Les effets électriques liés aux circulations d'eau dans les roches

Laurence Jouniaux

To cite this version:

Laurence Jouniaux. Les effets électriques liés aux circulations d'eau dans les roches. Géophysique [physics.geo-ph]. Université Louis Pasteur - Strasbourg I, 2007. tel-00137155

HAL Id: tel-00137155

https://theses.hal.science/tel-00137155

Submitted on 19 Mar 2007

Mémoire
Présenté par

Laurence JOUNIAUX

pour obtenir l'habilitation à diriger des recherches
de l'Université Louis Pasteur – Strasbourg I
Spécialité : Géophysique Interne

Les effets électriques liés aux circulations d'eau dans les roches

Soutenue le 15/01/2007 à
L'Institut de Physique du Globe de Strasbourg

devant la commission d'examen composée de :

Michel Dietrich	Examinateur
Jean Schmittbuhl	Examinateur
Guy Marquis	Rapporteur interne
Christian David	Rapporteur externe
Jean-Pierre Gratier	Rapporteur externe

TABLE DES MATIÈRES

A) RENSEIGNEMENTS SUR LA CANDIDATE

A-1. CURRICULUM VITAE

Nom : JOUNIAUX
Prénom : Laurence
née le 17/01/1967 à Gennevilliers (92)
Nationalité française

Adresse professionnelle :
École et Observatoire des Sciences de La Terre
IPGS, Physique des Roches
5 rue René Descartes, 67084 Strasbourg Cedex
Tel : 03 90 24 03 34 ; Fax : 03 90 24 01 25
Email : Laurence.Jouniaux@eost.u-strasbg.fr

EMPLOIS OCCUPÉS

sept. 2004 Mobilité vers l'EOST, Institut de Physique du Globe de Strasbourg, UMR7516, dans l'équipe « Physique des Roches »

oct. 1995 Chargée de Recherche au CNRS, section 11, Laboratoire de Géologie de l'École Normale Supérieure de Paris, URA1316 puis UMR8538, 24 rue Lhomond, Paris.

1994/95 *Lauréate d'une bourse Lavoisier du Ministère des Affaires Étrangères* pour effectuer un post-doc d'un an au Earth Resources Laboratory du Massachusetts Institute of Technology, Cambridge, États-Unis.

FORMATION

1994 Thèse de doctorat de l'Université Paris 6, préparée à l'École Normale Supérieure de Paris, Dpt TAO, laboratoire de Géologie, sous la direction de J.-P. Pozzi, soutenue le 31 mars 1994. *Spécialité* : Sciences de la Terre.

Sujet : **Effets électriques et magnétiques liés aux circulations de fluides dans les roches sous contraintes**. *Mention* : très honorable avec félicitations du jury.

Jury : Président : Xavier Le Pichon
Rapporteurs : Jean-Pierre Gratier
Yves Guéguen
Directeur de thèse : Jean-Pierre Pozzi
Examinateurs : Jean-louis Le Mouël
Patrick Lebon
Steve Pride
Ghislain de Marsily

RECHERCHE

Production scientifique en octobre 2006 : 25 articles publiés dans des revues internationales à comité de lecture, plus une sous presse et deux soumises, 26 communications dans des congrès internationaux, 15 communications dans des colloques nationaux, et 16 séminaires.

A-2. PUBLICATIONS

1. Revues à comité de lecture

Maineult, A., Jouniaux, L., and Y. Bernabé, Influence of the mineralogical composition on the self-potential response to advection of KCl concentration fronts through sand, soumis à ***Geophys. Res. Lett***.

Schmittbuhl, J., Steyer, A., Jouniaux, L., and R. Toussaint, Fracture morphology nad viscous transport, soumis à ***Geothermics***

26. Jouniaux, L., M. Zamora, and T. Reuschlé, Electrical conductivity evolution of non-saturated carbonate rocks during deformation up to failure, ***Geophys. J. Inter.***, sous presse, doi:10.1111/j.1365-246X.2006.03136.x, nov. 2006.

25. Guichet, X., L. Jouniaux, and N. Catel, Modification of streaming potential by precipitation of calcite in a sand-water system: laboratory measurements in the pH range from 4 to 12, ***Geophysical Journal International, 166, 445-,*** doi: 10.1111/j.1365-246X.2006.02922.x, 2006.

24. Bordes, C., Jouniaux, L., Dietrich, M., Pozzi, J.-P., and S. Garambois, Laboratory measurements of seismo-magnetic conversions in fluid-filled Fontainebleau sand, ***Geophys. Res. Lett***., Vol. 33, No. 1, L01302, 10.1029/2005GL024582, 2006

23. Bourlange, S., Jouniaux, L., and Henry, P., Permeability, compressibility, and friction coefficient measurements under confining pressure and strain, Leg 190, Nankai Trough. *In* Mikada, H., Moore, G.F., Taira, A., Becker, K., Moore, J.C., and Klaus, A. (Eds.), ***Proc. ODP, Sci. Results***, 190/196, 1–16, 2004. Online: http://www-odp.tamu.edu/ publications/190196SR/215/215.htm

22. Lei, X.-L., K. Masuda, O. Nishizawa, L. Jouniaux, L. Liu, W. Ma, T. Satoh, K. Kusunose, Detailed analysis of acoustic emission activity during catastrophic fracture of faults in rock, ***Jou. Struct. Geol***., 26, 247-258, doi:10.1016/S0191-8141(03)00095-6, 2004.

21. Guichet, X., L. Jouniaux, and J.-P. Pozzi, Streaming potential of a sand column in partial saturations conditions, ***J. Geophys. Res***., 108(B3), 2141, doi:10.1029/2001JB001517, 2003.

20. Henry, P., L. Jouniaux, E.J. Screaton, S. Hunze, and D.M. Saffer, Anisotropy of electrical conductivity record of initial strain at the toe of the Nankai accretionary wedge, ***J. Geophys. Res***.,108(B9), 2407, doi:10.1029/2002JB002287, 2003.

19. Doussan, C., Jouniaux, L., and J.-L. Thony, Temporal variations of SP and unsaturated water flow in loam and clay soils: a seasonal field study, ***J. of Hydrology***, 267, 3/4, 172-184, 2002.

18. Fontaine F., Rabinowicz, M., Boulègue J., and Jouniaux L., Constraints on hydrothermal processes on basaltic edifices: Inferences on the conditions leading to hydrovolcanic eruptions at Piton de la Fournaise, Réunion Island, Indian Ocean, ***Earth Planet. Sci. Lett***., 200, 1-14, 2002.

17. Pinettes, P., Bernard, P., Cornet, F., Hovhannissian, G., Jouniaux, L., Pozzi, J.-P., and V. Barthès, On the difficulty of detecting streaming potentials generated at depth, ***Pure and Applied Geophysics***, 159, 2629-2657, 2002.

16. Jouniaux, L., Masuda, K., Lei, X., Nishizawa, O., Kusunose, K., Liu,L., and W. Ma, Comparison of the microfracture localization in granite between fracturation and slip of a pre-existing macroscopic healed joint by acoustic emission measurements, ***J. Geophys. Res***., 106, 8687-8698, 2001.

15. Reppert, P.M., F.D. Morgan, D. Lesmes, and L. Jouniaux, Frequency dependent streaming potentials, ***Journal of Colloid and Interface Science,*** 234, 194-203, 2001.

14. Jouniaux, L., Bernard, M.-L., Zamora, M., and J.-P. Pozzi, Streaming potential in volcanic rocks from Mount Pelee, ***J. Geophys. Res***., 105, 8391-8401, 2000.

13. Jouniaux, L., Bernard, M.-L., Pozzi, J.-P., and M. Zamora, Electrokinetic in rocks: Laboratory measurements in sandstone and volcanic samples, ***Phys. Chem. Earth***, special issue on electrokinetics, 25, 329-332, 2000.

12. Jouniaux, L., J.-P. Pozzi, J. Berthier. and P. Massé, Detection of fluid flow variations at the Nankai Trough by electric and magnetic measurements in boreholes or at the seafloor, ***J. Geophys. Res***., 104, 29293-29309, 1999.

11. Liu, L., Ma, S., Ma, J., Lei, X., Kusunose, K., Nishizawa, O., and L. Jouniaux, Temporal and spatial distribution of microfractures in granites of different structures under triaxial compression and its significance in seismology, ***Chinese Science Bulletin***, 44, 1321-1324, 1999.

10. Liu, L., Ma, S., Ma, J., Lei, X., Kusunose, K., Nishizawa, O., and L. Jouniaux, effect of rock structure on statistic characteristics of acoustic emissions, ***Seismology and Geology***, 21, 377-386, 1999.

9. Masuda, K., Jouniaux, L., Nishizawa, O., Lei, X., Liu, L., Ma, W., Satoh, T. And K. Kusunose, Fracture planes observed with X-ray CT images and AE hypocenter distribution, ***Bull. Geol. Surv. Japan***, 48, 469-473, 1997.

8. Jouniaux, L. and Pozzi J.-P., Anomalous 0.1-0.5 Hz streaming potential measurements under geochemical changes: Consequences for electrotelluric precursors to earthquakes, ***J. Geophys. Res***., 102, 15335-15343, 1997**.**

7. Perrier, F., Petiau, G., Clerc, G., Bogorodsky, V., Choquier, A., Erkul, E., Jouniaux, L., Lesmes, D., Macnae, J., Marquis, P., Meunier, J.M., Nascimento, D., Oettinger, G., Schwarz, G., Toh, H., Valiant, M.J., Vozoff, K. and Yazici-Cakin, O., A one year systematic study of electrodes for long period measurements of the electric field in geophysical environments, ***Journal of Geomagnetism and Geoelectricity***, 49, 1677-1697, 1997.

6. Jouniaux, L., Dubet, L., Zamora, M. and Morat, P., Physical properties of limestone from the quarry of Meriel, ***C. R. Acad. Sci.*** Paris, t.322, série IIa, 361-367, 1996.

5. Jouniaux L. and Pozzi J.-P., Permeability dependence of streaming potential in rocks for various fluid conductivities, ***Geophys. Res. Letters***., 22, 485-488, 1995b.

4. Jouniaux L. and Pozzi J.-P., Streaming potential and permeability on saturated sandstones under triaxial stress: consequences for electrotelluric anomalies prior to earthquakes, ***J. Geophys. Res***., 100, 10197-10209, 1995a.

3. Jouniaux L., Lallemant S., and Pozzi J.-P., Changes in the permeability, streaming potential and resistivity of a claystone from the Nankai prism under stress, ***Geophys. Res. Letters*****,** 21, 149-152, 1994.

2. Pozzi J.-P., et Jouniaux L., Effets électriques des circulations de fluides dans les roches sédimentaires et prévision sismique, ***C. R. Acad. Sci. Paris***, t. 318, série II, 73-77, 1994.

1. Jouniaux L., Pozzi, J.-P., Brochot, M., et C. Philippe, Variation de résistivité sous contrainte triaxiale dans des grès de Fontainebleau saturés, ***C. R. Acad. Sci. Paris***, t. 315, Série II, 1493-1499, 1992.

2. Conférences invitées dans des congrès

Jouniaux, L. and M.L. Bernard, Streaming potential measurements on volcanic samples, ***solicited paper***, 23rd **E. G. S.**, Nice, ***Annales Geophysicae***, C271, 1998.

Jouniaux, L., Electrokinetic in porous media: effect of deformation, effect of permeability and effect of geochemical changes, ***communication invitée, 3rd Nordic Symposium on Petrophysics***, theme “ Electrical, Electrokinetic and fluid flow processes ”, Gothenborg, p. 4-8, 23-24 January, 1997.

3. Actes de colloque à comité de lecture

Jouniaux, L., Electrokinetic in porous media: the effects of deformation, permeability and geochemical changes, ***Nordic Petroleum technology Series II***, Ed. M.F. Middleton, Printed by Vasastadeus Bokbinderi AB, Göteborg, Sweden, 99-106, 1997.

4. Communications à des congrès internationaux

23. Bordes, C., Jouniaux, L., and M. Dietrich, Investigation of transient seismo-electromagnetic phenomena: an experiment within the Low Noise Underground Laboratory of Rustrel Pays d'Apt, **E. G. U**., Vienne, 2006.

22. Maineult, A., Bernabé Y., Jouniaux, L., and A. Deleforge, Effect of minor clay and mica phases on the SP response of KCl front transport, **E. G. U**., Vienne, 2006.

21. Bordes, C., Dietrich, M., Jouniaux, L., Garambois, S., Measurements of seismo-electromagnetic conversions in a cylindrical rock sample, **E. G. U**., Vienne, 2005.

20. Bourlange, S., Henry, P., Jouniaux, L., Relationships between fluids and deformations in the Nankai accretionary wedge, **E. G. U**., Vienne, 2005.

19. Bordes, C., L. Jouniaux, M. Dietrich, and J.-P. Pozzi, Seismo-electric and seismo-magnetic conversions in porous media, ***First International Conference, Small and medium scale underground science, Rustrel***, 22-24 Sept. 2004.

18. Guichet, X. and L. Jouniaux, Laboratory measurements of electrokinetic properties of sand composed of quartz and calcite, 27th **E. G. S.**, Nice, 2002.

17. Guichet, X., L. Jouniaux, and J.P. Pozzi, Streaming potential of a sand in partial saturation, **E. U. G. XI** , 2001.

16. Doussan, C., L. Jouniaux, and J.L. Thony, temporal variations of SP and unsaturated water flow in loam and clay soils: a seasonal field study, 26th **E. G. S.**, Nice, 2001.

15. Henry, P., Jouniaux, L., Screaton, E.J., Hunze, G., Saffer, D.M., and F. ODP Leg 190 Scientific party, Anisotropy of electrical conductivity in Nankai Trough sediments and ductile strain associated with decollement propagation, **A. G. U**., San Francisco, 2000.

14. Revil, A., Utama, Zamora, M., and L. Jouniaux, Electrical conductivity, streaming potential, and permeability of Fontainebleau sandstones, 25th **E. G. S.**, Nice, 2000.

13. Pozzi, J.-P., Jouniaux, L., Berthier, J., and P.Massé, Detection of fluid flow rate variations in accretionary prisms by electric and magnetic measurements, 24th **E. G. S.**, La Haye, ***Annales Geophysicae***, 1999.

12. Pinettes, P., Bernard, P., Cornet, F., Oganessian, G., Jouniaux, L., Pozzi, J.-P., Adler, P., and V. Barthès, Structural effects on streaming potentials artificially induced at 150 m depth, **A. G. U**., San Francisco, 1999.

11. Pozzi, J.-P. and L. Jouniaux, Streaming potential measurement as a precursor to failure, 23rd **E. G. S.**, Nice, ***Annales Geophysicae***, C272, 1998.

10. Philippe, C., L. Jouniaux, and J.-P. Pozzi, Electrokinetic monitoring of water flow in low consolidated medium, , 23rd **E. G. S.**, Nice, ***Annales Geophysicae***, C521, 1998.

9. Jouniaux, L. and Pozzi, J.-P., Streaming potential in rocks: implications for electrotelluric precursors to earthquakes, ***Electrokinetic phenomena '98***, Salzburg, L12, 1998.

8. Jouniaux, L. and Pozzi J.-P., Anomalous 0.1-0.5 Hz streaming potential measurements under geochemical changes, 22th **E. G. S.**, Vienne, ***Annales Geophysicae***, C46, 1997.

7. Zamora, M., Grandidier, I and Jouniaux L., Experimental study of elastic and electric earthquake precursors, , 22th **E. G. S.**, Vienne, ***Annales Geophysicae***, C54, 1997.

6. Jouniaux L. and Pozzi J.-P., Streaming potential measurements in laboratory: a precursory measurement of the rupture and Anomalous 0.1-0.5 Hz measurements under geochemical changes, ***International workshop on Seismo Electromagnetics***, NASDA, Tokyo, p.85-88, 3-5 March, 1997.

5. Berthier, J., Massé, P, Jouniaux, L and Pozzi J.-P., Detection of fluid flow rate variations in accretionary prisms by electric and magnetic measurements, 21th **E. G. S.**, La Haye, ***Annales Geophysicae***, C183, 1996.

4. Jouniaux L. et Pozzi J.-P., Streaming Potential and Permeability on Sediments. Consequences for Self-Potential Anomalies Measured in Seismic Area, **A. G. U**. Spring Meeting, Baltimore, ***E. O. S.***, april 19, 241-242, 1994.

3. Jouniaux L. et Pozzi J.-P., Laboratory measurements on streaming potential related to permeability on sandstones during deformation up to failure, 19th **E. G. S.**, Grenoble, ***Annales Geophysicae***, C95, 1994.

2. Jouniaux L. et Pozzi J.-P., Laboratory measurements on electrical effects related to fluid circulation in compressed rocks, 18th **E. G. S**., Wiesbaden, ***Annales Geophysicae***, C20, 1993.

1. Jouniaux L. et Pozzi J.-P., Laboratory measurements of electrical effects related to fluid circulation during deformation experiments up to failure, 7th **E. U. G**., Strasbourg, ***Terra abstracts***, 291-292, 1993.

5. Congrès ou colloques nationaux

16. Dietrich, M., S. Garambois, C. Bordes, L. Jouniaux, and J.-P. Pozzi, Field experiments, laboratory studies and numerical simulation of seismo-electromagnetic conversions in porous media, *Symposium International Déméter*, Toulouse, 14-16 juin 2006.

15. Bordes, C., Jouniaux, L., Dietrich, M., and J.P. Pozzi, Etude des conversions sismo-électriques dans un cylindre poreux par mesure en laboratoire à bas bruit, *Rencontres de Rustrel*, Rustrel, 28-30 septembre 2005.

14. Jouniaux, L., Electrofiltration dans une fracture, Atelier scientifique du Réseau Alsace de laboratoires en Ingéniérie et Sciences pour l'Environnement (*Réalise*), 2005.

13. Schmittbuhl, J., Jouniaux, L., Toussaint, R., and F. Brunet, Transport et érosion dans une fracture ouverte, Colloque ECCO-PNRH, Toulouse, décembre 2005.

12. Bordes, C., L. Jouniaux, M. Dietrich, and J.-P. Pozzi, Seismo-electromagnetic conversions in porous media: laboratory measurements at LSBB, Rustrel, France, *RST*, Strasbourg, 2004.

11. Doussan, C., L. Jouniaux, J.L. Thony, and A. Chanzy, Evolution temporelle du potentiel spontané et du flux d'eau non-saturé dans un sol sablo-limoneux et limono-argileux de cases lysimétriques, 3ième *colloque GEOFCAN*, 2001.

10. Jouniaux et al., Apport de la géophysique pour l’étude des circulations de fluides en subsurface, p.133, *Colloque PNRH*, mai 2000.

9. Albouy, et al., Compte Rendu des expérimentations menées sur le site INRA d’Avignon, p.139, *Colloque PNRH*, mai 2000.

8. Doussan, C., et L. Jouniaux, Suivi temporel de la polarisation spontanée et du potentiel hydrique pour un sol limoneux et argileux de cases lysimétriques, *Société Géologique de France* : *Les potentiels spontanés en science de la terre*, Paris, 366, 16 mars 2000.

7. Pinettes, P., Bernard, P., Cornet, F., Oganessian, G., Jouniaux, L., Pozzi, J.-P., and V. Barthès, On the difficulty of detecting streaming potentials generated at depth, *Société Géologique de France* : *Les potentiels spontanés en science de la terre*, Paris, 366, 16 mars 2000.

6. Pinettes, P., Bernard, P., Hovhanissian, G., Jouniaux, L., Pozzi, J.-P.,V. Barthès, Adler, P., and Cornet, F., Mesures in-situ d'électrofiltration à échelle hectométrique, *Société pour l'avancement de l'interprétation des diagraphies, Paris*, 1999.

5. Jouniaux, L. et Pozzi J.-P., Potentiel électrocinétique : marqueur de la microfissuration et précurseur de la rupture dans les grès de Fontainebleau, *5ième journée de la matière condensée, Société Française de Physique*, p.962, 28 août 1996.

4. Jouniaux L., Couplage électrocinétique, journée Fluides/Failles, E. N. S. Paris, 15 juin 1994.

3. Jouniaux L. et Pozzi J.P., Mesures de laboratoire sur les effets électriques liés aux circulations de fluides dans des roches déformées jusqu'à la rupture, Réunion scientifique DBT "fluides et failles", St Malo, 8-9 février, 1994.

2. Jouniaux L., Localisation et mesures électriques, *colloque GRECO géomatériaux*, Aussois, 23-24 novembre, 1992.

1. Pozzi J.-P. et Jouniaux L., Étude expérimentale des phénomènes électriques liés aux circulations de fluide dans les roches sous contrainte, relation avec la microfracturation, 14ème *R. S. T.*, Toulouse, *Soc. Géol. France Ed.*, 128, 1992.

6. Séminaires

16. Jouniaux, L., L'électrofiltration en milieu poreux comme marqueur des circulations de fluides, Laboratoire Domaines Océaniques, **Université de Bretagne occidentale, Brest**, 25 septembre 2002.

15. Jouniaux, L., L'électrofiltration en milieu poreux comme marqueur des circulations de fluides : application au volcanisme et aux zones de subduction, Laboratoire des matériaux des structures du génie civil, **LCPC Champs sur Marne**, 17 mars 1999.

14. Jouniaux, L., L'électrofiltration comme marqueur des circulations de fluides : application au volcanisme et aux zones de subduction, Unités de Sciences du sol, **INRA d'Avignon**, 23 février 1999.

13. Jouniaux, L., Bernard, M.-L., Zamora, M. et J.-P. Pozzi, Électrofiltration dans les roches volcaniques, Réunion du Comité National français de Géodésie et Géophysique, thème Précurseurs volcanologiques, **Institut de Physique du Globe de Paris**, 24 novembre 1998.

12. Jouniaux, L., Streaming potentials: Applications in Accretionary prisms and volcanoes, Solid Earth Physics Seminar, Division of Engineering and Applied Sciences, **Harvard University**, 2 novembre 1998.

11. Jouniaux, L., Streaming potential monitoring of subsurface fluid flow in the laboratory and on volcanoes, Dpt. of Geology and Geophysics, **Boston College**, 29 octobre 1998.

10. Jouniaux, L., Potentiel d'électrofiltration : Implications pour les précurseurs sismiques, séminaire de l'**Institut de Physique du Globe de Strasbourg**, 18 décembre 1997.

9. Jouniaux, L., Streaming potentials in rocks: Implications for seismic precursors, Solid Earth Physics Seminar, Division of Engineering and Applied Sciences, **Harvard University**, 1st august 1997.

8. Jouniaux, L., Streaming potential in rocks, **Geological Survey of Japan** (Tsukuba), janvier 1997.

7. Jouniaux, L., Effets électriques liés aux circulations de fluide dans les roches, séminaire interne du laboratoire de Géologie de l'**ENS** de Paris, 3 avril 1996.

6. Jouniaux L., Effets électriques liés aux circulations de fluide dans les roches, séminaire du Laboratoire LGIT-IRIGM, **Université de Grenoble**, 8 février 1996.

5. Jouniaux L., Streaming potential and permeability, **MIT**. borehole acoustics and logging and reservoir delineation **consortia annual meeting**, 19-21 avril 1995.

4. Jouniaux L., Laboratory measurements of streaming potential on sandstones and limestones: deformation, permeability, capillary model, séminaire du **Earth Resources Laboratory** du **MIT**, 14 octobre 1994.

3. Jouniaux L., conférence invitée, Électrocinétique dans les roches, Laboratoire de Phénomènes de Transport dans les Mélanges, **Meudon**, 10 juin 1994.

2. Jouniaux L., exposé "Effets électriques et magnétiques liés aux circulations de fluide dans les roches sous contraintes", laboratoire LETI, **CEA**, Grenoble, 13 avril 1994.

1. Jouniaux L., conférence invitée "Effets électriques liés aux circulations de fluide dans les roches", laboratoire LHMP, **ESPCI**, 18 mars 1994.

7. Chapitres dans des ouvrages

Jouniaux L. and Pozzi J.P., Streaming potential measurements in laboratory: a precursory measurement of the rupture and Anomalous 0.1-0.5 Hz measurements under geochemical changes, in *Atmospheric and Ionospheric Electromagnetic Phenomena Associated with Earthquakes*, Ed. M. Hayakawa,Terra Scientific Publishing, 873-880, 1999.

Jouniaux L. and Pozzi J.-P., Détection de la localisation dans les roches par mesures électriques, dans *Études en mécanique des matériaux et des structures*, Tome 2, Ed. Hermès, 153-156, 1995.

Jouniaux L. and Pozzi J.-P., Mesures électriques liées à la déformation et aux circulations de fluide, dans *Études en mécanique des matériaux et des structures*, Tome 3, Ed. Hermès, 205-210, 1995.

A-3. ENCADREMENT

1. Co-directions de thèse

Clarisse Bordes, Université Joseph Fourier, Grenoble.
Directeur de thèse : Michel Dietrich, LGIT Grenoble
Sujet : Étude expérimentale des phénomènes transitoires sismo-électromagnétiques, projet ACI sols et environnement.
Début de la thèse : septembre 2001; Encadrement 100 % en 2003 et 2004.
Thèse soutenue le 15 décembre 2005.
Actuellement Maître de Conférence à Pau

Sylvain Bourlange, Université Paris XI.
Directeur de thèse : Pierre Henry, ENS Paris
Sujet : Relations entre fluides et déformations dans le prisme d’accrétion de Nankai
Encadrement pour la partie expérimentale, Chapitre 3 de la thèse.
Thèse soutenue le 17 décembre 2003.
Actuellement Maître de Conférence à Nancy

Xavier Guichet, Université Paris 7.

Directrice de thèse : Maria Zamora, IPGParis

Sujet : Étude expérimentale des propriétés électriques des roches. Potentiels d'électrofiltration, suivi des mouvements de fluides en zones hydrothermales.

Encadrement 100 % sur 2 ans : janvier 2000 à janvier 2002

Thèse soutenue le 17 décembre 2002.

Actuellement en CDI à l'IFP

2. Encadrement de stages

Encadrement de stage de DEA :

Mourad Essalhi, « Phénomènes électrocinétiques et modélisation analogique d'écoulement », co-encadrante 15 %, EOST, ULP Strasbourg, rapport de stage 32 p., 2005

Xavier Laurencin, « Mesures pétrophysiques sur des roches ultrabasiques provenant d'une mine de nickel de Nouvelle Calédonie », co-encadrante, 20 %, EOST, ULP Strasbourg, rapport de stage, 55p., 2005

Encadrement de stage de maîtrise :

Maxime Mouyen, « Potentiel spontané dans une fracture », EOST, ULP Strasbourg, rapport de projet de recherche, 25p., 2006

Julia Holzhauer, « Mesures d'électrofiltration sur des échantillons de La Soutte », EOST, ULP Strasbourg, rapport de projet de recherche, 25 p., 2005

Encadrement tous les ans, pendant 7 ans, de deux élèves ingénieurs de l'École Nationale Supérieure d'Arts et Métiers, (ENSAM, Paris) : préparation du projet de fin d'étude du diplôme d'ingénieur, 20 % de leur temps sur l'année :

Yvan Cantou et Frédéric Hebert, « Phénomènes électrocinétiques dans les milieux poreux », PFE Str 42, 1999

Stevan LeGoff et Frédéric Pottier, « Étude du potentiel d'électrofiltration des roches », 37 p., 1998

Yann Boete et Stéphane Mazet, « Étude du potentiel d'électrofiltration des roches », 39 p., 1997

Damien Corneille et Samuel Jacquet, « Étude du potentiel d'électrofiltration et de la perméabilité de grès et de calcaires », PFE str17, 49 p., 1996

Laurent Belaich et Stéphane Declerck, « Étude du potentiel d'électrofiltration et de l'endommagement », PFE39, 1994

Marc Brochot et Emmanuel Vitrac, « Étude du potentiel d'électrofiltration et de la perméabilité », PFE48, 67 p., 1992

Claude Martz et Sébastien Roux, « Étude des propriétés magnétiques et électriques des roches en compression », PFE str 43, 27 p., 1991

3. Coopérations scientifiques extérieurs à l'EOST

Collaborations avec le MIT (1996-1998), le Geological Survey of Japan (1997-1999).

Séjour de 1 mois en 1996, au Massachusetts Institute of Technology, Earth Resources Laboratory, Cambridge, U.S.A.

Séjour de 2 mois en 1997 au Geological Survey of Japan, Tsukuba, Japon.

Collaborations avec le LGIT Grenoble, l'IPG Paris, l'Université de Clermont-Ferrand.

Séjours à la maison : *Congé maternité* du 26 avril au 16 août 1999 (3 mois ½).
Congé maternité du 29 octobre 2002 au 17 février 2003 (3 mois ½).

A-4. PARTICIPATION À DES JURYS

1. Jurys de thèse :

Invitée dans le jury de thèse de Anthony Finizola : *« Études de systèmes hydrothermaux de volcans actifs : Misti (Pérou) et Stromboli (Italie) ; approches géophysiques et géochimiques »*, dirigé par Jean-François Lénat et Mariano Valenza, Université Blaise Pascal Clermont-Ferrand II, juin 2002.

Rapporteur externe de la thèse de Oswald Conan Clint, *Electrical potential changes and acoustic emissions generated by fracture and fluid flow during experimental triaxial rock deformation*, PhD thesis from University College London, Londres, 18 février 2000.

Examinatrice de la thèse de S. Hautot *: Modélisation électrique et électromagnétique tri-dimensionnelle : caractérisation de la structure électrique de domaines géologiques et hydrogéologiques complexes*, Thèse de Doctorat de l'Université de Bretagne Occidentale, 25 janvier 1999.

Rapporteur (sous couvert de J.-P. Pozzi) de la thèse de B. Lorne : *Étude expérimentale du mécanisme de l'électrofiltration en laboratoire et sur un site naturel,* Thèse de doctorat de l'Institut de Physique de Globe de Paris, 19 décembre 1997.

2. Autres

Participation au jury d'admission d'un concours externe Assistants Ingénieurs (BAP C) en électronique, à l'Université Louis Pasteur de Strasbourg, 42 candidats, 12 auditions (2006).

Participation au jury d'admission d'un concours Ingénieur d'Études externe (BAP C) en « Instrumentation scientifique et techniques expérimentales », à l'université de Cergy-Pontoise (département des Sciences de la Terre et de l'Environnement) : une semaine d'auditions, 60 candidats (septembre 2005).

A-5. ENSEIGNEMENTS

- Participation aux cours du module « Physique des Matériaux et Écoulements », Master 2 Sciences de la Terre et 3$^{\text{ième}}$ année de l'École d'Ingénieurs de l'EOST.

- Participation aux cours de l'UV « Hydrogéophysique », Master 2 Sciences de la Terre et 3$^{\text{ième}}$ année de l'École d'Ingénieurs de l'EOST.

- Participation aux cours du module « Magnétisme » du Magistère de l'École Normale Supérieure de Paris.

A-6. CONTRATS DE RECHERCHE OBTENUS

Programmes français, européens ou internationaux :

Participation au programme **ACI - ECCO - PNRH** 2003, 2004 « Transport et érosion dans une fracture ouverte : étude des couplages chimio-électro-hydro-mécaniques par une approche expérimentale », coordonné par J. Schmittbuhl, IPG-Strasbourg. Participation au volet expérimental.

Participation au programme **ACI-FNS « ECCO »** Ecosphère continentale : processus expérimental, 2003, 2004, Waterscan : prospection et modélisation hydrogéophysique 4D, coordonné par P. Sailhac, IPG-Strasbourg

Dans le cadre du **Réseau Alsace de laboratoires en Ingéniérie et Sciences pour l'Environnement** (REALISE), projet scientifique 2004-2005, « Caractérisation des flux hydriques : détection des écoulements par méthode géophysique à différentes échelles et modélisation des écoulements multiphasiques » proposé dans l'axe « Le fonctionnement bio-physico-chimique de l'aquifère rhénan ». Ce projet est une collaboration entre les équipes « Physique des roches » et « Proche surface » de l'IPGS et de l'équipe « Hydrologie et transferts en milieu hétérogène » de l'Institut de Mécanique des Fluides et des Solides (IMFS) de Strasbourg.

Gestion de 4 keuros + 3keuros

Participation au projet **ANR « ECCO »** écosphère continentale risques environnementaux, ECOU - PREF « écoulements préférentiels dans les versants marneux fracturés. Quelle influence dans le déclenchement de glissements de terrain à contrôle hydrologique », coordonné par O. Maquaire et J. Schmittbuhl, 2005

Coordinatrice du thème sollicité : « Effets électriques et magnétiques sur les volcans : origine et modélisation » pour le programme **ACI - Catastrophes Naturelles** 2001 et 2002.

Gestion de 7 000 euros

Participation au programme **ACI - Eau et Environnement**, 2000, 2001 et 2002 « Compréhension des phénomènes sismo-électriques et sismo-magnétiques : expérimentations de terrain et de laboratoire, développements instrumentaux et méthodologiques, et simulations numériques » coordonné par M. Dietrich, LGIT Grenoble.

Gestion de 120 kF puis 4 keuros

Programme **INSU - PNRN** – Programme National de recherche sur la prévision et la prévention des Risques Naturels : Aléa Volcanique, « Étude des propriétés physiques des roches volcaniques nécessaires à l'interprétation des données de surveillance des volcans français d'outre mer (Montagne Pelée et Piton de la Fournaise) », 2000, 2001 : rédaction et gestion du projet et des rapports.

Gestion 50 kF

Programme **INSU – PRH puis PNRH** – Programme National de Recherches en Hydrologie, « Étude des potentialités de méthodes électriques (potentiel spontané, résistivité électrique) dans la caractérisation hydrodynamique et hydrologique du sol (détermination de caractéristiques hydrauliques, imagerie de l'infiltration, mesure de flux d'eau en non saturé) », coordonné par J.-P. Pozzi, puis C. Doussan, 1997 à 2001 : rédaction des projets et des rapports, gestion des projets.

Gestion de 173 kF puis 6 000 euros

Participation aux programmes :

INSU - PNRN risques sismiques (1995-1999) ;
CEE - Environmental and climate program-volcanic risk ;
Forpro - Géomécanique « *Couplage hydromécanique et électrofiltration » 1999* ;
INSU – Géomatériaux ;
GdR Géomécanique des roches profondes.

A-7. ANIMATION DE LA RECHERCHE, RESPONSABILITÉS COLLECTIVES

Organisatrice à l'***EGU*** (Vienne) de la session : *Self-Potential measurements: Applications and Interpretations,* 2006

Organisatrice d'un symposium à l'***EUG*** (Strasbourg) : *Self-potential measurements: applications and interpretations,* 2001

Co - organisatrice d'une réunion à la ***Société Géologique de France*** : *Les potentiels spontanés en Sciences de la Terre*, Paris, 16 mars 2000

Chairperson au cours du Workshop des membres fondateurs du Earth Resources Laboratory du Massachusetts Institute of Technology, Woodstock, Vermont, 11-15 juillet 1994

Suite à interview, publication d'un article de vulgarisation : «Pas un bruit, on scrute la terre» dans le magasine ulp.sciences, avril 2005, n°19, p.19, 2005

Reviewer pour : Geophysical Research Letters, Journal of Geophysical Research, National Science Fondation, Tectonophysics, Journal of Volcanology and Geothermal Resources, Phys. Chem. Earth.

2006 : membre élu du Conseil de laboratoire
membre élu de la Commission Recherche de l'EOST

A-8. AUTRES

Mesures au Laboratoire Souterrain à Bas Bruit (LSBB), à Rustrel, 2003-2004

Mesures sur le terrain au Mayet de Montagne : champs électrique et magnétique liés à une circulation d'eau forcée dans le sol, 1996

Participation à la campagne « International Campaign on electrodes for the long term monitoring of the Telluric field » (mai 1995-avril 1996) pour installer des électrodes sur le site de Garchy

Mesures sur le terrain : mesures de résistivité électrique, de potentiel spontané, du champ magnétique et mesures radar, à la surface d'une zone contaminée (huiles et solvants organiques) sur la base de l'American Air Force, Cape Cod, Massachusetts, oct. 1994

B) TRAVAUX SCIENTIFIQUES

Les effets électriques liés aux circulations d'eau dans les roches :

Compréhension et quantification du phénomène de l'électrofiltration dans les roches, signaux précurseurs de la rupture, applications aux zones volcaniques et aux zones de subduction - Conversions sismo-électromagnétiques.

INTRODUCTION

Mes débuts dans ce métier sont nés de la proposition de thèse (en 1991) de Jean-Pierre Pozzi, au laboratoire de Géologie de l'École Normale Supérieure de Paris (financement ANDRA), sur les effets électriques liés aux circulations d'eau dans les roches (électrofiltration). À l'époque, une certaine partie de la communauté des Sciences de la Terre espérait utiliser les signaux électriques mesurés en surface pour la détection des tremblements de terre. Un des arguments physiques était que les circulations d'eau dans la croûte terrestre peuvent être fortement perturbées lors d'un séisme (avant, pendant, mais aussi après) [*Muir-Wood and King*, 1993], ces variations de circulation d'eau pouvant elles-mêmes créer des variations de champ électrique que l'on peut essayer de détecter [*Bernard*, 1992]. J'étais assez sceptique sur la finalité de ce projet en terme prédictif, mais cette question de la génération de courants électriques par la circulation d'eau dans les roches avait aiguisé ma curiosité. C'est parce que des ions présents dans l'eau sont adsorbés sur les minéraux, et que la circulation d'eau entraîne une partie des ions, qu'il peut se créer un courant électrique. Je me suis donc lancée dans l'élaboration d'un dispositif expérimental permettant de mesurer ces effets électriques, liés aux circulations d'eau dans des échantillons de grès de Fontainebleau lors de leur déformation jusqu'à la rupture. Ma collaboration étroite avec des élèves ingénieurs de l'École Nationale Supérieure des Arts et Métiers (ENSAM) [*Jouniaux et al.*, 1992] a été salutaire pour résoudre les nombreux problèmes techniques. C'est ici que j'ai appris qu'il existe deux types de problèmes dans la vie : les problèmes de masse et les problèmes de fuite.

Pour mener à bien un tel sujet, j'ai dû développer mes connaissances à la fois sur les propriétés de transport dans les roches (perméabilité, conductivité électrique), sur les processus d'interactions entre les roches et l'eau, et sur la mécanique des roches. En parallèle, la proximité de l’équipe « Géodynamique », de Xavier Le Pichon, m’a amenée à m’intéresser aux circulations d’eau en zone de subduction, principalement dans les prismes d’accrétion.

J’ai soutenu ma thèse le 31 mars 1994. J’ai ensuite passé un an au MIT, grâce à une bourse Lavoisier du Ministère des Affaires Étrangères (co - financée à moitié par la CGG), où j’ai mis au point un dispositif expérimental de mesure d’électrofiltration en transitoire, c'est-à-dire la mesure du champ électrique transitoire induit par l’application d’un champ de pression d’eau transitoire (sinusoidal). Ce type de mesure permet de détecter des signaux électriques très faibles (puisque le signal attendu a une fréquence en principe connue), à l’instar des mesures de perméabilité dynamique (faites en appliquant une pression d’eau sinusoïdale). Je n’ai pas eu le temps d’utiliser pleinement cette expérience, mais j’ai formé le nouveau doctorant arrivant (Phil Reppert) à son utilisation [*Reppert et al.*, 2001].

J’ai ensuite été recrutée au CNRS au laboratoire de Géologie de l’École Normale Supérieure de Paris en 1995, et j’ai développé mes recherches par différentes approches sur les effets électriques et magnétiques liés aux circulations d’eau dans les roches, tant par des expériences de laboratoire que par des mesures in - situ ainsi que des modélisations, avec tout de même un développement plus avancé pour la mise en oeuvre de dispositifs expérimentaux originaux. J’ai continué ma collaboration avec l’équipe « Géodynamique », dont l’une des préoccupations était les circulations de fluides dans le prisme d’accrétion de Nankai (Japon). Et j’ai continué à m’intéresser aux « signaux précurseurs de la rupture » en laboratoire.

L’objectif de ce qui suit est de présenter mes travaux de recherche effectués depuis la thèse.

PRÉSENTATION SUCCINCTE DES RÉSULTATS

Mes thèmes de recherche concernent donc principalement les effets électriques liés aux circulations d’eau dans les roches. Les signaux électriques induits par les circulations d’eau sont appelés effets d’électrofiltration ou électrocinétiques et sont dus à la présence d’ions dans l’eau pouvant créer un courant électrique. Ce courant électrique engendre lui-même un champ magnétique. Ces effets reflètent principalement l’interaction électrique entre la roche et l’eau (appelée double- ou triple-couche électrique). En présence d’eau, des réactions chimiques et physiques se produisent à l’interface entre la roche et l’eau, dont il résulte un excédent d’ions négatifs liés à la roche, et par suite, un excédent d’ions positifs sur une couche de faible épaisseur au voisinage de l’interface, le reste du fluide restant neutre [voir Fig. B1 de *Guichet et* *al., GJI,* 2006, présenté dans la partie suivante]. Lorsque le fluide est en mouvement, ces ions positifs sont entraînés et engendrent ainsi un courant électrique, dit courant électrique de convection. Ce courant est contre-balancé par un courant de conduction (loi d'Ohm), et il en résulte une différence de potentiel électrique, on parle de potentiel d'électrofiltration ou potentiel électrocinétique.

La différence de potentiel électrique ainsi générée est proportionnelle au gradient de pression d'eau, ce qui en fait une méthode de choix pour la détection des circulations d'eau en subsurface. Les mesures en laboratoire sont effectuées de l'échelle centimétrique à l'échelle métrique et sont nécessaires pour contraindre les modèles de calcul des champs électriques et magnétiques induits par les circulations de fluides dans la croûte. Il est à noter que sur le terrain, les Potentiels Spontanés (PS), c'est-à-dire les potentiels électriques mesurés passivement entre deux électrodes, dont les mesures se sont largement développées ces dix dernières années, peuvent être induits par une circulation d'eau (soumise à une force liée à un gradient de pression), mais aussi par un flux de chaleur (soumis à une force liée à un gradient de température), ou encore par un gradient de concentration chimique. Ceci peut se voir dans les relations des flux couplés [*Onsager*, 1931 ; *Sill*, 1983] où chaque flux $\mathbf{J_i}$ (flux électrique, flux hydrique, flux de chaleur, flux de matière) est lié aux forces $\mathbf{X_j}$ (gradient de potentiel électrique, de pression hydrique, de température, de concentration) à travers les coefficients de couplage L_{ij} :

$$\mathbf{J_i} = \sum_j L_{ij} \mathbf{X_j} \tag{1}$$

Pour ma part, j'ai concentré mes recherches sur une meilleure quantification du champ électrique lié aux circulations d'eau dans les roches :

$$-\mathbf{I} = L_{11}\ \mathbf{grad}V + L_{12}\ \mathbf{grad}P \tag{2}$$

où **I** est la densité de courant électrique, *V* le potentiel électrique, *P* la pression hydrique, L_{11} correspond à la conductivité électrique du milieu (σ_r), et $L_{12} = C_s \times \sigma_r$. Le coefficient de couplage électrocinétique ou d'électrofiltration, C_s, peut-être mesuré en laboratoire. Le premier terme à droite de l'égalité dans l'équation (2) correspond au courant de conduction, le deuxième terme correspond au courant de convection. Il est à noter que le coefficient d'électrofiltration ne dépend pas en principe de propriétés telles que porosité ou perméabilité, ce qui amène le gradient de pression hydrique à jouer le premier rôle dans la génération des potentiels d'électrofiltration [pour plus de détails on peut consulter dans la partie qui suit, le paragraphe « Electrokinetic Phenomena » de *Jouniaux and Pozzi, JGR*, 1997, et l'appendice B de *Guichet et al., GJI*, 2006].

Cette thématique de recherche a donc un intérêt potentiel, et déjà en partie éprouvé, pour la détection à distance et la caractérisation des fluides dans le sous-sol. La communauté scientifique essaie de développer son potentiel en tant qu'outil d'imagerie, d'une part dans le domaine des ressources en eau : profondeur de nappe aquifère, suivi de transferts hydrauliques, caractérisation des flux contaminés, et d'autre part dans le domaine de la géophysique des réservoirs : détection d'hydrocarbones grâce aux conversions sismo-électromagnétiques.

Je décris dans les quatre parties suivantes mes recherches développées sur les thèmes : compréhension et quantification du phénomène d'électrofiltration dans les roches (i), signaux précurseurs de la rupture (ii), électrofiltration dans les zones volcaniques et zones de subduction (iii), et caractérisation des milieux superficiels par des excitations provoquées : conversions sismo-électro-magnétiques (iv). Chaque partie est illustrée d'une sélection d'articles. Toutes les références citées sont listées à la fin du mémoire.

Compréhension et quantification du phénomène de l'électrofiltration dans les roches

On verra dans cette partie les mesures d'électrofiltration faites sur des échantillons de roche afin de quantifier le coefficient de couplage électrocinétique C_s. On verra aussi les variations de potentiel d'électrofiltration lorsque la conductivité de l'eau varie. Les mesures faites lors de la précipitation de calcite dans un sable seront décrites, ainsi que les mesures effectuées lorsque la saturation en eau d'un sable est partielle. Enfin j'évoquerai les expérimentations de terrain auxquelles j'ai participé : sur le site INRA - Avignon, au Mayet de Montagne, et à Garchy. Cette partie sera illustrée par une sélection des articles suivants :

Pour les mesures en laboratoire :

- ***Photo*** du dispositif de mesure d'électrofiltration sur échantillons
- Guichet, X., L. Jouniaux, and N. Catel, Modification of streaming potential by precipitation of calcite in a sand-water system: laboratory measurements in the pH range from 4 to 12, ***Geophysical Journal International***, 2006.
- ***Photo*** du dispositif « Colonne » de mesure d'électrofiltration sur du sable
- Guichet, X., L. Jouniaux, and J.-P. Pozzi, Streaming potential of a sand column in partial saturations conditions, ***J. Geophys. Res.***, 2003.
- Reppert, P.M., F.D. Morgan, D. Lesmes, and L. Jouniaux, Frequency dependent streaming potentials, ***Journal of Colloid and Interface Science,*** 2001.
- Jouniaux, L. and Pozzi J.-P., Anomalous 0.1-0.5 Hz streaming potential measurements under geochemical changes: Consequences for electrotelluric precursors to earthquakes, ***J. Geophys. Res.***, 1997.
- Jouniaux, L., Dubet, L., Zamora, M. and Morat, P., Physical properties of limestone from the quarry of Meriel, ***C. R. Acad. Sci. Paris***, 1996.
- Jouniaux L. and Pozzi J.-P., Permeability dependence of streaming potential in rocks for various fluid conductivities, ***Geophys. Res. Letters***, 1995.

Pour les mesures de terrain :

- ***Coupure de presse*** « La Montagne » sur un forage effectué près de Volvic, 2001.
- Article de vulgarisation, sur la thèse de Mathieu Darnet, ***ulp.sciences***, 2005.
- Doussan, C., Jouniaux, L., and J.-L. Thony, Temporal variations of SP and unsaturated water flow in loam and clay soils: a seasonal field study, ***J. of Hydrology***, 2002.

- Pinettes, P., Bernard, P., Cornet, F., Hovhannissian, G., Jouniaux, L., Pozzi, J.-P., and V. Barthès, On the difficulty of detecting streaming potentials generated at depth, ***Pure and Applied Geophysics***, 2002.

Le principal encadrement que j'ai effectué, pour cette partie, a été celui de Xavier Guichet pour sa thèse de doctorat, soutenue en 2002.

● Quantification du coefficient de couplage électrocinétique

Pour mieux comprendre le mécanisme physique générateur des signaux d'électrofiltration, et le quantifier, j'ai mis au point une expérience afin de pouvoir étudier les effets d'électrofiltration sous différentes pressions d'eau, avec des fluides de salinités différentes, sur un grand nombre de roches consolidées (grès, calcaires, roches volcaniques) [*Jouniaux et al., CRAS, 1996 ; Jouniaux et al., 2000*], les mesures existant dans ce domaine à l'époque n'étant faites que sur des capillaires de verre ou des roches broyées. Cette expérience a été développée dans le cadre du programme DBT fluides et failles, INSU - PNRN risque volcanique, et CEE (Environmental and Climate Workprogram, Volcanic Risk). Il s'agit d'appliquer un gradient de pression hydrique entre les extrémités d'un échantillon et de mesurer la différence de potentiel électrique ainsi générée [voir photo du dispositif juste avant l'article *Guichet et al.*, *GJI*, 2006]. On mesure ainsi le coefficient de couplage $Cs = \Delta V/\Delta P$ (en V/Pa) car le courant électrique total I est nul dans l'équation (2).

De nombreuses mesures d'électrofiltration sur des roches variées, de caractéristiques physiques (porosité, perméabilité, conductivité électrique) et chimiques (interface grain/eau) différentes sont nécessaires, car le processus d'électrofiltration reflète l'interaction entre la roche et l'eau. J'ai montré que l'électrofiltration dans certaines conditions, sur des grès de Fontainebleau, des calcaires, et des roches volcaniques, dépend des propriétés de transport de la roche, telles la conductivité électrique ou la perméabilité [*Jouniaux and Pozzi*, *JGR*, 1995, *GRL*, 1995 ; *Jouniaux et al*, *CRAS*, 1996 ; *Jouniaux et al.*, *JGR*, 2000], principalement à travers la conductivité de surface (i.e., à l'interface), le facteur le plus influent sur l'électrofiltration dans les roches étant la conductivité du fluide On peut voir dans Jouniaux and Pozzi [*GRL*, 1995] que la forte dépendance du coefficient d'électrofiltration avec la perméabilité (Fig 1) est liée au fait que les mesures sont faites avec de l'eau très peu conductrice : dans ce cas on ne peut pas négliger la conductivité de surface par rapport à la conductivité volumique (de l'eau dans le réseau poreux). Les calculs montrent que dès que la conductivité de l'eau augmente à 0.1 ou 1 S/m, le coefficient de couplage ne dépend plus de la perméabilité [Fig.3]. Une meilleure connaissance de l’électrofiltration dans les roches était très attendue car on essayait d’imaginer une méthode indirecte de mesure de perméabilité grâce aux mesures du coefficient d’électrofiltration (aussi appelé coefficient de couplage électrocinétique) et d’électro-osmose [*Li et al.*, 1995], et des brevets avaient été déposés par la CGG (France) et Gaz Research Institute (Chicago, USA).

● Potentiels d’électrofiltration lors de variations géochimiques de l’eau

Des variations géochimiques de l’eau dans la croûte terrestre étant observées avant des séismes [*Tsunogai and Wakita*, 1995 ; *Toutain et al., 1997*], et des anomalies de champ électrique ou magnétique pouvant être mesurées avant des séismes [*Fraser-Smith et al.*, 1990 ; *Mizutani et al.*, 1979], il a semblé intéressant de suivre le potentiel d’électrofiltration lors de changements géochimiques de l’eau pendant des expériences de laboratoire (également sur des grès de Fontainebleau). J’ai montré que des signaux électriques de 0.1-0.5 Hz pouvaient apparaître lors de variations de conductivité électrique de l’eau [Fig. 3 dans *Jouniaux and Pozzi*, *JGR*, 1997], et par là-même il a été proposé que le phénomène d’électrofiltration puisse être générateur de signaux anormaux observés in - situ [*Jouniaux and Pozzi,* 1997]. Évidemment le passage de l’échelle du laboratoire à l’échelle du terrain n’est pas simple, mais il a été montré que ces signaux anormaux étaient observés uniquement dans des conditions « hors équilibre », c'est-à-dire lorsque la conductivité électrique de l’eau varie, ce qui peut être dû à des variations de circulations d’eau liées à des changements de contraintes tectoniques ou de perméabilité. Par la suite, d’autres expériences de laboratoire ont aussi montré que ce type de signal existait lorsque de l’eau très peu conductrice circulait dans un échantillon de granite Inada fraîchement fracturé [Fig. 17 dans *Yoshida*, 2001]

● Potentiels d’électrofiltration lors de précipitation de calcite

Il est en général supposé, pour les applications dans le domaine des Sciences de la Terre, que le couplage entre flux hydrique et flux électrique est négatif, c'est-à-dire que des cations sont majoritairement charriés dans le sens du flux hydrique. Cette hypothèse est en général vérifiée, mais dans les cas où des complexes calciques sont présents, la situation peut s’avérer bien plus compliquée [voir Fig. 2 de *Guichet et al., GJI*, 2006]. Connaître le signe de ce couplage est donc nécessaire pour interpréter le sens de l’écoulement de l’eau déduit de mesures de potentiel électrique. J’ai tenté de suivre l’électrofiltration lors de la précipitation de calcite dans un sable.

L'électrofiltration change effectivement de signe lors de la précipitation de calcite, et est accompagnée d'une diminution de la perméabilité [Fig. 5 dans *Guichet et al., GJI,* 2006]. Ces résultats ont été modélisés, et la sensibilité des modèles aux paramètres d'entrée a été étudiée. En particulier, les valeurs calculées des potentiels électriques en surface du minéral ont été représentés (potentiel zeta) pour une interface quartz-eau et calcite-eau en fonction du pH de l'eau. Ces potentiels ont été calculés en utilisant différentes valeurs de capacitances des couches présentes à l'interface minéral/eau (qui sont liées aux propriétés diélectriques de l'interface). Les valeurs de ces capacitances n'ont pas éte choisies comme paramètres ajustables : ce sont les valeurs calculées, à l'aide du modèle de triple couches, publiées dans la littérature géochimique. Il en résulte que la valeur calculée du potentiel de surface est sensible à ce paramètre et est représentée en grisé sur la figure 9 de *Guichet et al.* [*GJI*, 2006]. La valeur calculée du potentiel de surface dépend aussi de la conductivité de surface [Fig. 10 de *Guichet et al., GJI,* 2006]. Nous avons conclu que le potentiel électrique à l'interface minéral/eau de notre sable était négatif et controlé par une interface quartz-eau pour des pH inférieurs à 8.5 et était positif et controlé par une interface calcite-eau pour des pH supérieurs à 10.5. Afin d'interpréter les mesures de Potentiels Spontanés sur le terrain, il est donc indispensable de vérifier la nature du terrain pour savoir si le couplage d'électrofiltration attendu est positif ou négatif. En particulier sur les volcans, où les anomalies de température peuvent montrer un fort flux hydrothermal condensant près de la surface, et donc où l'altération et la présence de minéraux secondaires comme la calcite sont possibles. En particulier en cas de fortes anomalies de CO_2, la calcite peut précipiter dans une gamme de pH 4.5-5 [*Di Liberto et al.,* 2002].

● Potentiels d'électrofiltration dans un milieu poreux non saturé en eau

Les effets sur l'électrofiltration d'un milieu non saturé en eau, dont on pensait qu'ils augmentaient considérablement le signal électrique, et qui sont plus représentatifs des mesures effectuées in - situ en subsurface, ont été étudiés au laboratoire sur du sable [*Guichet et al., JGR,* 2003]. C'est une des questions majeures dans le domaine, à laquelle la communauté attendait une réponse, comme mis en avant lors de la réunion à la Société Géologique de France (2000). Une telle étude n'avait encore jamais été entreprise. Ce projet a été possible grâce à la construction d'une colonne de 1 m de haut et de 8 cm de diamètre pouvant contenir des sols non consolidés, et possédant 10 électrodes impolarisables et 10 capteurs de pression (*programme INSU - PNRH et ACI - Prévention des Catastrophes Naturelles*). J'ai co-dirigé pour ce faire la thèse de doctorat de Xavier Guichet [2002]. Nous avons montré que le coefficient de couplage électrocinétique n'augmente pas quand le milieu se désature, et qu'au contraire il diminue ou reste constant, bien que le milieu lui-même soit moins conducteur. Ces mesures posent encore des questions quant à leur interprétation exacte. En effet le coefficient de couplage peut s'exprimer de façon inversement proportionnelle au carré de la saturation partielle, en se basant sur la conductivité de la roche en fonction de la saturation partielle [*Archie*, 1942 ; *Waxman and Smits*, 1968 ; voir eq. (6) en supposant l'exposant d'Archie égal à 2, dans *Guichet et al*, *JGR*, 2003], ce qui implique un couplage d'électrofiltration très fort lorsqu'un milieu poreux se désature. Or les mesures montrent un coefficient de couplage qui diminue lorsque le sable se désature [Fig.11 de *Guichet et al.*, *JGR,* 2003], avec un coefficient de couplage proportionnel à la saturation partielle. C'est pourquoi cette thématique fait encore partie des projets (voir projets, partie C-2).

● Observations de Potentiels Spontanés sur le terrain

J'ai également participé aux mesures de Potentiel Spontané (PS) sur le terrain sur le site INRA - Avignon [*Doussan et al*., *JH,* 2002] pour savoir si le Potentiel Spontané peut être utilisé comme fluxmètre hydrique (*C. Doussan*, INRA*)*. Un suivi d'un an sur deux types de sols (sableux et argileux) dans des cases lysimétriques de 9 m^2 et de 2 m de profondeur (sols déconnectés du terrain par les côtés) a montré que les Potentiels Spontanés sont reliés à l'infiltration et à l'évaporation des eaux météoriques (que ce soit pour le sol sableux ou le sol argileux), mais nous n'avons pas pu trouver de relation linéaire stable avec le temps qui permette de calculer le flux hydrique d'après les mesures de PS, comme suggéré auparavant par Thony et al. [1997]. Par la suite, une modélisation de nos mesures, en milieu partiellement saturé, a été entreprise par Darnet and Marquis [2004], qui ont montré que le potentiel d'électrofiltration permet effectivement d'estimer la direction verticale du flux d'eau (infiltration ou évaporation) à l'échelle de quelques dizaines de centimètres (correspond à la séparation des électrodes).

J'ai également participé à une expérience sur un terrain granitique : une expérience pluridisciplinaire, sur le terrain au Mayet de Montagne a été organisée (*IPGP, CEA, ENS*) pour mesurer les champs électriques et magnétiques lors d'une circulation d'eau forcée controlée à 200 m de profondeur entre deux forages distants de 100 m, afin de savoir si des mesures électriques et magnétiques in - situ permettraient de détecter une variation de circulation d'eau en sous-sol. Ce type d'expérience, en étant « actif » et non « passif », effectuée à une échelle intermédiaire (centaine de mètres) est une étape clé de la compréhension de l'électrofiltration in situ et de son utilisation à plus grande échelle en « passif ». Des signaux électriques détectables ont été enregistrés uniquement à proximité de la source [*Pinettes et al*., *PAGEOPH, 2002*].

J'ai par ailleurs participé (en collaboration avec le Earth Resources Laboratory du MIT) à l'expérience internationale de campagne sur les électrodes pour les mesures du champ tellurique à long terme, organisée au centre de Garchy où plus de 100 électrodes ont été installées sur le terrain et suivies pendant un an pour déterminer leur stabilité et la possibilité de les utiliser pour des mesures in - situ à long terme [*Perrier et al*., 1997].

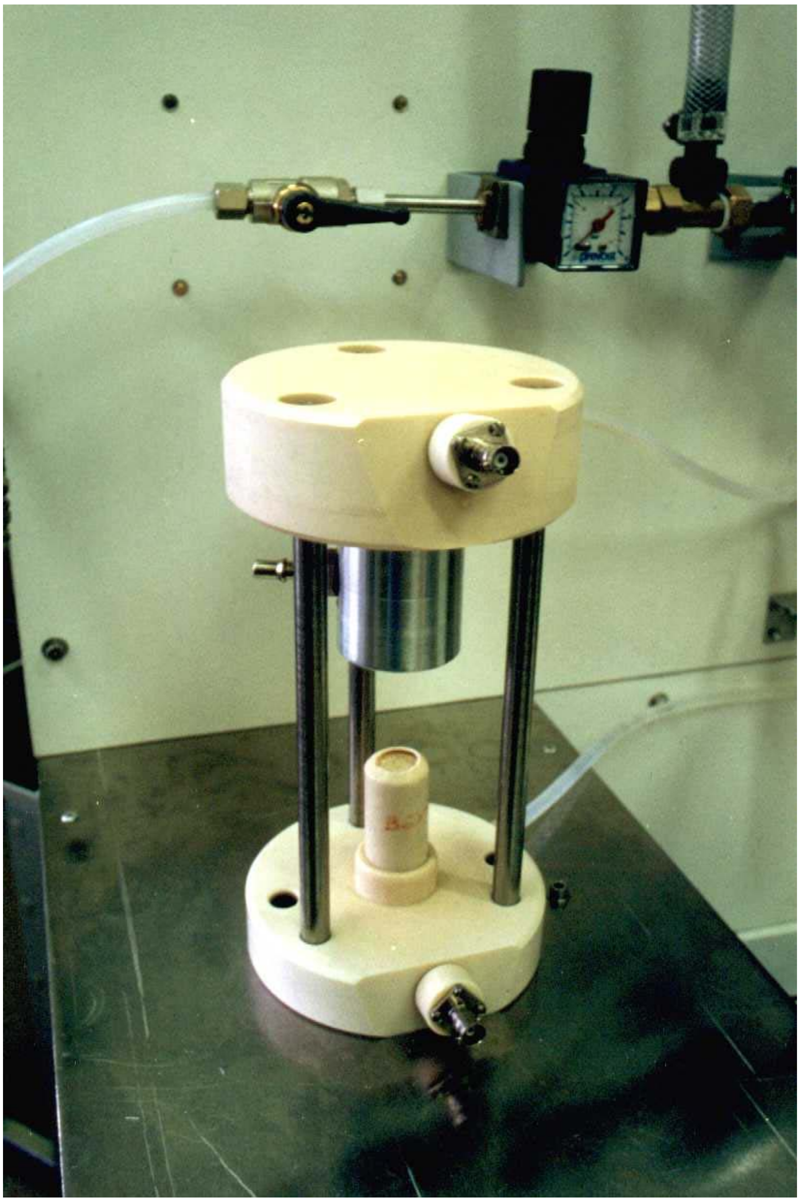

Geophys. J. Int. (2006) **166,** 445–460 doi: 10.1111/j.1365-246X.2006.02922.x

Modification of streaming potential by precipitation of calcite in a sand–water system: laboratory measurements in the pH range from 4 to 12

Xavier Guichet,[1] Laurence Jouniaux[2] and Nicole Catel[3]

[1] *Laboratoire des mécanismes de transfert en géologie,* UMR 5563, 38 *rue des* 36 *ponts,* 31400 *Toulouse, France.*
E-mail: Jouniaux@eost.u-strasbg.fr
[2] *Institut de Physique du Globe de Strasbourg, UMR* 7516, 5 *rue René Descartes,* 67000 *Strasbourg, France*
[3] *École Normale Supérieure, Laboratoire de Géologie, UMR* 8538, 24 *Rue Lhomond, Paris, France*

Accepted 2006 January 16. Received 2005 December 20; in original form 2005 July 1

SUMMARY

Spontaneous potentials associated with volcanic activity are often interpreted by means of the electrokinetic potential, which is usually positive in the flow direction (i.e. Zeta potential of the rock is negative). The water–rock interactions in hydrothermal zones alter the primary minerals leading to the formation of secondary minerals. This work addresses the study of calcite precipitation in a sand composed of 98 per cent quartz and 2 per cent calcite using streaming potential measurements. The precipitation of calcite as a secondary mineral phase, inferred by high calcite saturation indices and by a fall in permeability, has a significant effect on the electrokinetic behaviour, leading to a significant reduction in the Zeta potential (in absolute value) and even a change in sign.

The measured decrease in Zeta potential from -16 mV to -27 ± 4 mV takes place as the pH rises from 4 to 7, while it remains constant at -25 ± 1 mV as the pH increases from 8 to 10.5. For pH higher than 10.5, calcite precipitates and is expected to coat the quartz surface. The measured Zeta potential vary from -17 to $+8$ mV for pH ranging from 10.6 to 11.7 depending on the amount of precipitated calcite indicated by the decrease in permeability.

The observed change in sign of the electrical surface potential rules out the usual qualitative interpretation of SP anomalies in order to determine fluid circulations, even at pH lower than 9 if calcite is widely present as a secondary mineral phase, since the electrical surface potential of calcite depends also on CO_2 partial pressure and $[Ca^{2+}]$. Therefore, SP anomalies as measured in hydrothermal field, without mineralogical analyses of hydrothermal deposits, and without geochemical fluid survey, should be interpreted with caution.

Key words: electrical conductivity, electrical resistivity, fluids in rocks, laboratory measurement, permeability,volcanic activity.

1 INTRODUCTION

Spontaneous potential (SP) is an electrical geophysical method that measures naturally occurring voltage fields on the Earth's surface. Measurements of SP in the field are performed in various different geophysical contexts and are often interpreted by means of the electrokinetic or streaming potential, which represents the electrical potential induced by fluid flow through rock. In tectonically active zones, SP anomalies may be explained by a mechanism involving fluid movements between reservoirs triggered by strain perturbations (Bernard 1992), or by changes in pore pressure in fault zones (Fenoglio *et al.* 1995). The negative anomalies observed on the flanks of volcanoes are interpreted in terms of downward percolating rainfall, and can be linked to the depth of the water table (Zablocki 1978; Aubert *et al.* 1993). The positive anomalies observed in active volcanic areas originate from upward convective flows (Zablocki 1978; Aubert & Kieffer 1984), and are used to define hydrothermal zones (Corwin & Hoover 1979; Ishido *et al.* 1997; Michel & Zlotnicki 1998; Lénat *et al.* 2000; Finizola *et al.* 2002, 2003, 2004; Hase *et al.* 2005). Recent experiments have demonstrated that time variations of SP can be unambiguously identified and associated with time-varying fluid flow in geophysical systems from metric to kilometric scales (Perrier *et al.* 1998; Doussan *et al.* 2002; Pinettes *et al.* 2002; Trique *et al.* 2002), thanks to the improvement in long-term monitoring SP (Perrier *et al.* 1997; Perrier & Pant 2005). Electroseismic surveys are also based on electrokinetic phenomena and can be used to detect small changes in rock properties at interfaces, such as permeability and saturation state (Bordes *et al.* 2006; Garambois & Dietrich 2001, 2002; Beamish 1999). Moreover, the borehole electrokinetic response due to water injection (Marquis *et al.* 2002; Darnet *et al.* 2004) can yield an estimate of the fracture aperture (Hunt & Worthington 2000) or permeability (Murakami *et al.* 2001); and the inversion of SP anomalies (Gibert & Pessel 2001; Sailhac & Marquis 2001; Sailhac *et al.* 2004) can yield an estimate of aquifer hydraulic properties (Darnet *et al.* 2003). Measurements of SP have also been used in karst areas in the detection of groundwater flows (Erchul & Slifer 1987; Wanfang *et al.* 1999). Modelling of all these observations requires a good understanding of electrokinetic phenomena. We emphasize that it is fundamental to check for the presence of calcite in order to interpret field measurements of SP, such as in the case of streaming potentials in underground limestone quarries (Morat *et al.* 1995) or for the preservation of historical monuments (Pisarenko *et al.* 1996). Indeed the presence of calcite can induce a change in the streaming potential sign, which is generally positive in the flow direction (Ishido & Mizutani 1981; Jouniaux & Pozzi 1995a, 1997; Guichet *et al.* 2003; Maineult *et al.* 2004).

In hydrothermal areas, interaction between hot waters and the rocks through which they migrate alters the primary minerals and leads to the formation of secondary minerals. These processes result in changes in physical and chemical properties of the system. Karst areas are generally underlain by soluble calcareous rocks. Sinkholes, caves, result from dissolution of primary rocks. Sealing of fractured rocks can also occur, resulting in the precipitation of secondary minerals. Davis & Kent (1990) reported that the surface chemical properties of natural materials are modified by secondary minerals that are usually present as a minor fraction of the whole sample. We decided to focus our attention on calcite as a secondary mineral, because (i) Calcite is a common mineral constituent of limestones, and is a secondary mineral in numerous geological contexts, and (ii) the electrical properties of the calcite–water interface is still a controversial topic.

(i) In natural geophysical systems, calcite is a common mineral phase, modifying ground- and surface-water compositions. It acts as a buffer for pH in ground and surface waters, being able to modify the water chemistry because of its low solubility and rapid precipitation–dissolution kinetics (Langmuir 1971; Sigg *et al.* 2000). Waters in or close to equilibrium with calcite contain large amounts of Ca^{2+} and HCO_3^-; to a first approximation the concentration of HCO_3^- is twice the concentration of Ca^{2+} (Sigg *et al.* 2000). Many natural rivers show a calcite oversaturation with a CO_2 partial pressure ranging from atmospheric CO_2 partial pressure to 10^{-2} atm (Fig. 1). Thus, calcite acts as a buffer for many natural waters, and is expected to precipitate in many natural systems.

Calcite is present as a secondary mineral phase in volcanic terrains; Deutsch *et al.* (1982) showed that the water properties of the Columbia plateau basalt aquifer are determined by secondary calcite and Robert (2001) observed calcite in basalts from Northern Ireland, while Stoffers & Botz (1994) showed calcite formation associated with hydrothermal fluids emerging from the floor of Lake Tanganyika. In general the precipitation of secondary phases during the alteration of volcanic rocks is related to the thermal behaviour of the hydrothermal system. With decreasing temperature, the following crystallization sequence is observed: smectite → zeolite → calcite. These observations are based on field studies (Westercamp 1981; Robert *et al.* 1988) and also on experimental results (Robert & Goffé 1993). (Henley & Ellis 1983) gave a summary of the temperature range over which calcite alteration mineral has been observed in high-temperature hydrothermal systems associated with volcanism; calcite alteration mineral occurs from 100°C up to 300°C.

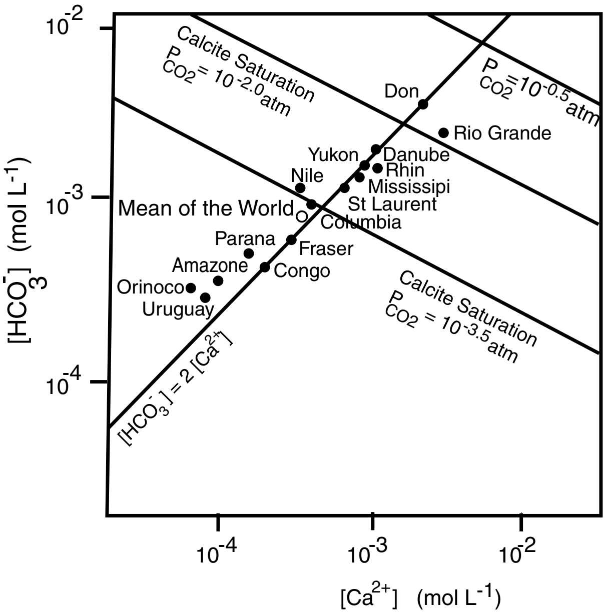

Figure 1. The concentration of HCO_3^- versus the concentration of Ca^{2+} for the main rivers of the world. The bold line shows the electroneutrality of waters buffered by calcite, for which HCO_3^- and Ca^{2+} are the main chemical species. The thin lines show calcite saturation for several CO_2 partial pressures (1 atm = 1.013 Pa). The waters of the main rivers fall into the bold line. (from Sigg *et al.* 2000).

(ii) Geochemists have investigated sorption processes onto calcite surfaces (Douglas & Walker 1950; Foxall *et al.* 1979; Zachara *et al.* 1991; Cicerone *et al.* 1992), as well as interactions at the molecular scale (Stipp & Hochella 1991). Nevertheless, the electrical properties of the calcite–water interface is still a controversial topic (Fig. 2), and the calcite surface reactions appear to be more complex than those involving silicates. Electrokinetic measurements are sometimes contradictory, yielding different results on natural calcite and on synthetic calcite, as well as depending on CO_2 partial pressure. For example in natural systems, the Ca^{2+} concentration ranges from 10^{-2} to 10^{-4} mol l^{-1} for systems where calcite acts as a buffer (Sigg *et al.* 2000). Measured calcite ζ potential ranges from 17 mV to -11 mV, while Ca^{2+} concentration ranges from 10^{-2} to $10^{-3.3}$ mol L^{-1} (Cicerone *et al.* 1992).

The two last decades, laboratory measurements have been performed to understand the variations of the streaming potential in fluid chemistry for various silicate minerals (Ishido & Mizutani 1981; Jouniaux & Pozzi 1995b; Lorne *et al.* 1999a,b; Pengra *et al.* 1999; Jouniaux *et al.* 2000; Guichet & Zuddas 2003; Guichet *et al.* 2003; Perrier & Froidefond 2003; Maineult *et al.* 2005; Lorne *et al.* 1999a) also reported the streaming potentials of four carbonate rocks at pH 8. However, it is surprising that the effect of secondary minerals in electrokinetic properties has not been studied. Modelling of SP observations in either hydrothermal or karst areas requires a good understanding of electrokinetic phenomena in dynamic systems where dissolution/precipitation can occur. In this study, we report streaming potential measurements on sand and show that precipitation of calcite as a secondary mineral phase has a significant effect on the electrokinetic behaviour: that is, the ζ-potential is reduced significantly (in absolute value) and can even change sign. Finally our measured surface potentials are compared to calculated surface potentials using a triple-layer model (TLM).

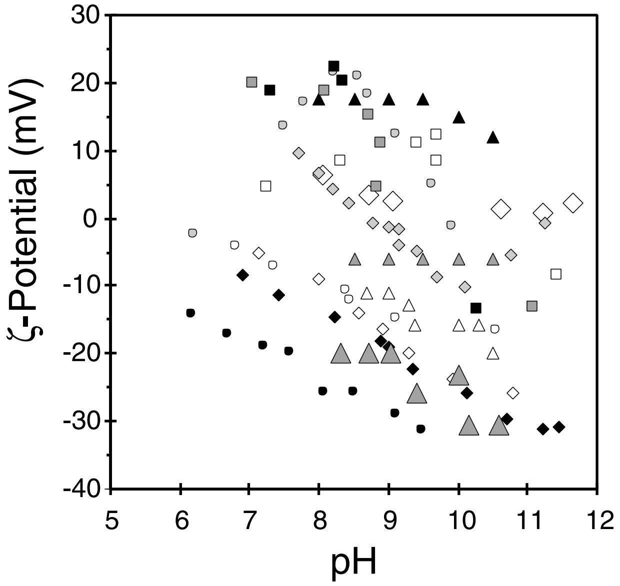

Figure 2. Variation of the ζ-potential of calcite as a function of pH. Squares show measurements of ζ-potential of Iceland Spar (empty squares after a few minutes, grey squares after one week, black squares after two months) performed by (Somasundaran & Agar 1967); Circles show measurements of ζ-potential performed by (Vdovic 2001) with natural samples (empty circles: limestone, black circles: lake sediment) and with synthetic sample (grey circles). Diamonds show measurements of ζ-potential of synthetic calcite performed by (Thompson & Pownall 1989) with various electrolytes (Black diamonds: NaCl (5×10^{-3} mol L^{-1}), Empty diamonds: NaCl (5×10^{-3} mol L^{-1})/$NaHCO_3$ (10^{-3} mol L^{-1}), Big Empty diamonds $CaCl_2$ (5×10^{-4} mol L^{-1}), pH values adjusted by additions of HCl/NaOH; Grey diamonds: NaCl (5×10^{-3} mol L^{-1})/ $NaHCO_3$ (10^{-3} mol L^{-1}), pH values adjusted by additions of $Ca(OH)_2$. Triangles show measurements of ζ-potential performed by (Cicerone *et al.* 1992) with a natural sample of Ficopomatus Enigmaticus (Big grey triangles) and with synthetic sample for various electrolytes (KCl (10^{-3} mol L^{-1}) solutions containing different amounts of added $CaCl_2$ (0 mol L^{-1}, empty triangles; 10^{-3} mol L^{-1} Grey triangles; 10^{-2} mol L^{-1} Black triangles).

2 SAMPLE AND METHODS

2.1 Electrical measurements

We performe laboratory streaming potential measurements of a sand composed of 98 per cent quartz and 2 per cent calcite using $CaCl_2$ solutions made up in distilled water for pH in the range 4-12. The sand is sieved, yielding a grain size ranging from 100×10^{-6} m to 500×10^{-6} m. Experiments are carried out at room temperature, which varies from 14.9°C to 19.5°C. A solution of $CaCl_2$, 5×10^{-4} mol l^{-1} is then prepared. The water used for making all solutions is freshly distilled with a MilliQ system. The solutions are made up and stored in glassware, thus atmospheric CO_2 does not equilibrate with the solution, which remains undersaturated with respect to atmospheric CO_2. Electrical surface potential of calcite can range from positive to negative values depending on CO_2 partial pressure, pH, and $[Ca^{2+}]$ (Pokrovsky *et al.* 1999). At the atmospheric CO_2partial pressure a pH corresponding to a zero surface charge can be observed. Since we do not observe any point of zero surface charge, the CO_2partial pressure of our experiments must be lower than the atmospheric CO_2partial pressure (Van Cappellen *et al.* 1993). The pH of the solution is adjusted with $Ca(OH)_2$ in the range 7–11.7, and with HCl in the range 4.4–7.

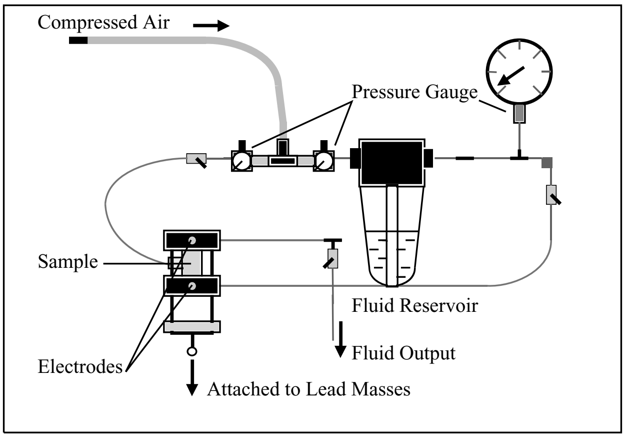

Figure 3. The water pressure is controlled by applying compressed air to a water reservoir at one end of the sample, while the other end is maintained at atmospheric pressure. The electric potential difference is measured between the ends of the sample by two silver-chloride non-polarizable electrodes: water saturated porous ceramics are used to prevent any gas or air bubble from being in contact with the electrode and remain saturated to keep the electrical contact. The electrodes are placed in the water circuit near the ends of the sample but not in the circulating water flow to avoid electrical noise due to water movement near the electrodes (Ahmad 1964). When calcite is precipitated during the experiments, the electrical potential difference measured by the electrodes without any fluid flow remains small (1–4 mV). The two electrodes are connected by coaxial wires to a high-input impedance voltmeter (>10 GΩ). The input impedance of the voltmeter is several orders of magnitude greater than the resistance of the sample (e.g. it is16 kΩ when water conductivity is 0.036 S m^{-1}), thus allowing accurate measurement of the electric potential.

The experiment setup is shown in Fig. 3. The reader can find a detailed description of the apparatus in (Jouniaux *et al.* 2000). In a typical experiment, a 1L-aliquot of aqueous solution from the reservoir is passed through the sample. The output solution is recirculated twice. Reliable measurements involve equilibrium between sand and aqueous solution: the electrical conductivity and the pH of the output solution are measured after the different steps of fluid circulation until the values become constant. Equilibrium is reached after waiting 24 hr (see Appendix A for details). Before measuring the electrokinetic coupling coefficient, the 1L aliquot of aqueous solution is again recirculated twice. A fraction of the output solution is sampled for chemical analysis.

The streaming potential ΔV is measured when the fluid is forced through the sample by applying a fluid pressure difference ΔP. To check the linearity between the applied pressure difference ΔP at the sample ends and the measured streaming potential difference ΔV, the solution is made to flow systematically with 5 pressure steps from 0.1 to 0.5×10^5 Pa. The coupling coefficient $\Delta V/\Delta P$ is determined from the slope of ΔV against ΔP (see examples in Fig. 4). The streaming measurements are described in Section 3 and the analysis of the effect of the precipitation of calcite as a secondary mineral phase is made in Section 4.

The permeability of the sample is also derived using Darcy's law. Since the sample permeability is high, more than 10^{-12} m^2 (see Table 1), the aqueous solution filling the pore space can be easily replaced through fluid circulation by fresh aqueous solution having a new pH. Experiments are performed on three samples of the same sand. The first sample runs are performed in the pH range from 7

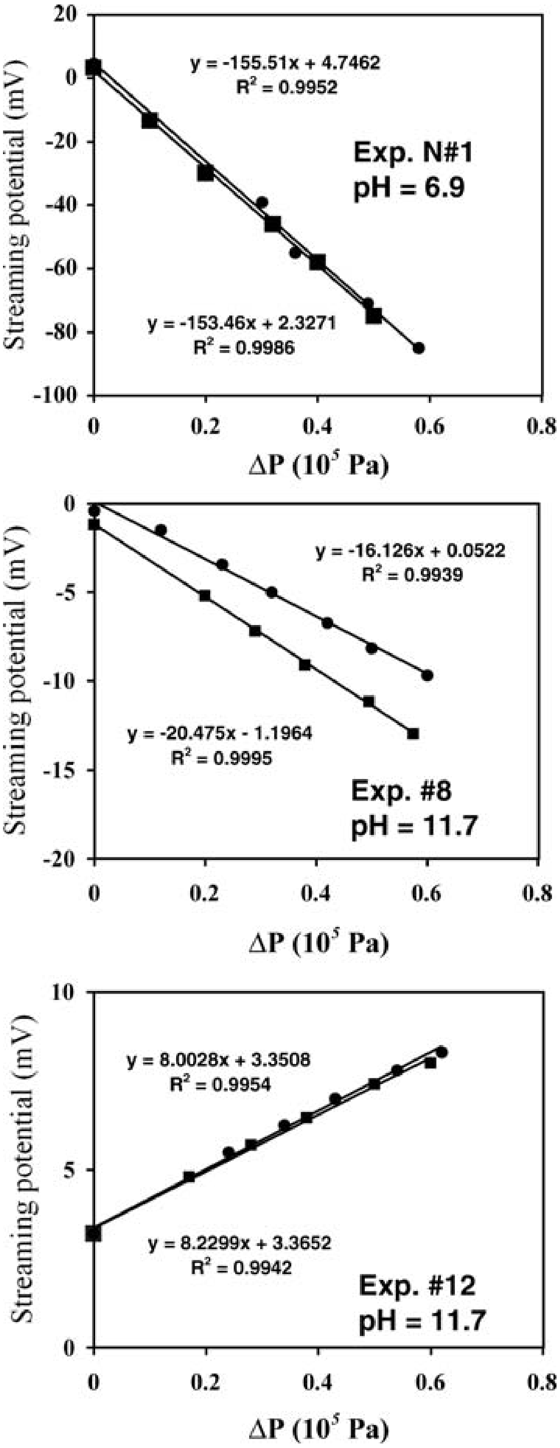

Figure 4. Streaming potential measured as a function of applied pressure during experiments 1, 8 and 12.

to 11.7 adding $Ca(OH)_2$; the second sample runs are performed in the pH range 9–11.7 to have a better analysis in this range. And the third sample runs are performed in the pH range 7–4 adding HCl (Table 1). We do not extend these measurements to pH below 4.4 and above 11.7, because then the ionic strength becomes significantly higher, and the interpretation of the experiments assuming a zeta potential non-dependent on the electrical conductivity is no more valid. Any decrease in permeability is thought to be related to calcite precipitation as discussed in Section 4.

Furthermore, the electrical conductivity of the sand σ_r is measured as a function of the electrical conductivity σ_f of the electrolyte in order to obtain the formation factor $F(F = \sigma_f/\sigma_r)$ and the surface electrical conductivity (see for instance: Waxman & Smits 1968).

2.2 Chemical analyses

It has been emphasized (Pokrovsky & Schott 1999) that there are three potential-controlling parameters of the interfacial properties of carbonates (pH, Alkalinity, $[Ca^{2+}]$), and that in previous carbonates electrokinetic studies, these parameters were unfortunately not measured. Therefore, pH, alkalinity and $[Ca^{2+}]$ were measured on the outflow solution collected after each experiment. We also measured Na^+ and Cl^-. A Perkin-Elmer 2380 spectrometer is used to determine the concentations of calcium and sodium. Calcium is determined by atomic absorption, and sodium by atomic emission. A Hitachi U 1100 spectrometer is used to determine the concentrations of chlorine and silicon. Chlorine is determined by stable complexation of mercury (II) thiocyanate. Silicon is determined by complexation of molybdic silicide, while alkalinity is determined by colorimetric titration with bromocresol green and methyl red.

2.3 ζ-potential calculations

Several models link the electrokinetic coupling coefficient $C_s = \Delta V/\Delta P$ to the physical properties of the fluid, the physical properties of the porous medium and the electric surface potential. We use the expression obtained with equation (11) from (Bussian 1983) and equation (46) from (Revil *et al.* 1999b):

$$C_s = \frac{\varepsilon\zeta/\eta\sigma_f}{1 + m(F-1)\xi}, \tag{1}$$

where

(i) ζ is defined as the electric potential on the shear plane (the closest plane to the rock surface over which fluid is moving)

(ii) $\varepsilon = \varepsilon_{\text{water}}\,\varepsilon_0$ is the electric permittivity of the fluid with $\varepsilon_{\text{water}}$ the relative dielectric constant of the fluid, which is calculated as a function of the temperature according to (Malmberg & Maryott 1956)'s law, and $\varepsilon_0 = 8.84 \times 10^{-12}$ F/m the electric permittivity of vacuum, and η is the dynamic shear viscosity of the circulating fluid, which is temperature-dependent, equal to 1.01×10^{-3} Pa s at 19.5°C and to 1.14×10^{-3} Pa s at 14.9°C.

(iii) σ_f is the electrical conductivity of the fluid, and $\xi = \sigma_s/\sigma_f$ with σ_s being the surface electrical conductivity of the sample.

(iv) F is the formation factor defined by Archie's first law:

$$F \equiv \Phi^{-m}$$

where Φ is the porosity, and m the first Archie's exponent (or the cementation exponent) of the rock.

Eq. (1) is used to derive the ζ-potential from our measurements of coupling coefficient C_s. Eq. (1) is valid in the high-salinity domain, that is, $\sigma_f \geq 5(m-1)\sigma_s$ (Bussian 1983), yielding a value equal to the high-salinity limit in the model of Revil *et al.* (1999b) and is also equivalent to the expression given by Jouniaux & Pozzi (1995a) in the case of m being equal to 2.

3 RESULTS

We describe here the results, but the interpretation of the electrokinetic behaviour as calcite is precipitated is discussed in Section 4

Table 1. Description of the experiments ; temperature, electrical conductivity, and pH of the electrolyte; measured electrokinetic coupling coefficient; ζ-potential inferred from eq. (1) using $F = 4.8$, $\sigma_s = 10^{-4}$ S m^{-1} and $m = 1.3$. Three samples have been used: sample 1 with pH solutions 7 to 11.7; sample 2 with pH solutions from 9 to 11.7; sample 3 with pH solutions from 7 to 4.4.

		Aqueous solution properties			Sample properties		
Experiment	Sample	Temperature °C	Electrical conductivity mS m^{-1}	pH	Permeability 10^{-12} m^2	Coupling Coefficient mV/MPa	ζ-Potential mV
1	1	19.5	12.7	6.9	–	−1545 ± 1	−29 ± 0.5
2	1	18.5	13.3	7.0	3.9 ± 0.5	−1173 ± 11	−23 ± 1.2
3	1	17.9	15.4	8.2	–	−1136 ± 1	−25 ± 1.4
4	1	17.1	15.4	8.4	–	−1157 ± 1	−26 ± 2
5	1	14.9	16.2	9.5	–	−1043 ± 1	−24 ± 3.3
6	1	15.7	17.2	10.1	4.0 ± 0.1	−1016 ± 15	−25 ± 3.3
7	1	18.8	19.0	10.7	1.5 ± 0.1	−412 ± 8	−11 ± 0.6
8	1	19.5	63.3	11.7	1.7 ± 0.4	−183 ± 22	−16 ± 2.1
9	2	18.3	12.1	9.0	4.4 ± 0.1	−1348 ± 8	−24 ± 1.3
10	2	18.3	17.4	10.5	4.4 ± 0.1	−1047 ± 4	−26 ± 1.3
11	2	18.4	26.7	11.0	3.2 ± 0.1	−435 ± 4	−17 ± 0.9
12	2	19.3	72.5	11.7	0.2 ± 0.1	81 ± 1	8 ± 0.3
13	3	17.0	13.2	7.5	5.6 ± 0.1	−1587 ± 12	−30 ± 2.7
14	3	16.7	14.2	7.4	5.5 ± 0.2	−1396 ± 43	−28 ± 3.3
15	3	16.4	15.4	7.1	5.6 ± 0.1	−1263 ± 5	−28 ± 2.8
16	3	16.4	16.9	6.6	5.5 ± 0.1	−1055 ± 3	−26 ± 2.6
17	3	18.2	23.8	6.5	5.7 ± 0.1	−650 ± 1	−22 ± 1.1
18	3	17.5	36.9	4.4	5.5 ± 0.1	−304 ± 16	−16 ± 1.9
19	3	18.2	36.2	5.8	5.5 ± 0.1	−314 ± 2	−16 ± 0.8
20	3	18.1	13.5	5.9	5.0 ± 0.1	−1078 ± 32	−21 ± 1.7
21	3	15.4	12.8	6.5	4.8 ± 0.1	−1702 ± 1	−31 ± 3.9

–Not measured.

since this interpretation is discussed using the permeability measurements (Section 3.1), the chemical analysis (Section 3.2) and the electrical measurements (Section 3.1).

3.1 Electrical properties and permeability of the sand

In order to determine the formation factor, the electrical conductivity of the sand is measured as a function of water electrical conductivity in the range 0.04–0.8 S m^{-1}. Electrical measurements yield a formation factor, F, of 4.8. The conductivity of the electrolyte after flowing through the sample is never lower than 1.2×10^{-2} S m^{-1}, which prevents us from determining the electrical surface conductivity of the sand. Revil & Glover (1998) reported a surface conductance of 8×10^{-9}S for quartz, independent on the electrolyte conductivity when this latter exceeds 10^{-2} S m^{-1}. Since the electrical conductivity of the water circulating in the sand is greater than 10^{-2} S m^{-1} (see Table 1), we assume that the specific surface conductance of the sand is 8×10^{-9} S. This is equivalent to a surface conductivity (i.e. 2× surface conductance divided by grain radius) of about 1.06×10^{-4} S m^{-1} for a mean grain diameter of 300 μm, in agreement with experimental values (Ruffet *et al.* 1991; Lorne *et al.* 1999a). The values of formation factor and surface conductivity given here are used in eq. (1) to obtain ζ-potentials from the electrokinetic measurements.

Fig. 5(a) shows the variation of sample permeability as a function of solution pH. Permeability of the samples is insensitive to pH over the range from 4 to 9, being $4.15 \pm 0.15 \times 10^{-12}$ m^2 for sample 1 and $4.37 \pm 0.04 \times 10^{-12}$ m^2 for sample 2. The permeability of sample 3 remains constant at $5.4 \pm 0.2 \times 10^{-12}$ m^2 for a pH range of 4.4–7.7. The permeability decreases when pH is higher than 9. We observe that the permeability of sample 1 decreases up to 1×10^{-12} m^2 at pH 11.7, and that the permeability of sample 2 falls to 0.2×10^{-12} m^2 at pH 11.7. This decrease of permeability can be shown to be related to calcite precipitation.

Fig. 5(b) shows the variation of the aqueous solution electrical conductivity as a function of the solution pH. The water electrical conductivity measurements are shown because the ζ-potential values are interpreted assuming a constant water conductivity. The solution electrical conductivity is constant at about $1.55 \pm 0.20 \times 10^{-2}$ S m^{-1} for pH in the range 5.9–10.7. Under either highly acidic or basic conditions, the solution electrical conductivity increases up to 7×10^{-2} S m^{-1} due to the addition of HCl at low pH and $Ca(OH)_2$ at high pH. The variation of the solution electrical conductivity is linked to the variation in the ionic strength (Fig. 5d) as calculated from the results of the chemical analyses (Table 2) and the WATEQ program (Plummer *et al.* 1976). The ionic strength is constant ($I = 2 \pm 0.2 \times 10^{-3}$ mol l^{-1}), while pH ranges from 5.5 to 11 except for experiment 17 (Fig. 5d). The ionic strength of experiments 8 and 12 (the most basic experimental conditions, pH 11.7) is not given because the electrical charge is unbalanced in this case.

Fig. 5(c) shows the variation of the ζ potential derived from eq. (1) for pH in the range 4–12. To calculate the ζ potential, we use $F = 4.8, \sigma_s = 1.06 \times 10^{-4}$ S m^{-1} and $m = 1.3$, the latter being a typical value for sand (Archie 1942). The formation factor is assumed to be constant, although it could be increased when permeability is decreased, specially for experiment n°12. Since the surface conductivity is small compared to the fluid conductivity, the value of $m(F-1)\xi$ in the eq. (1) is small compared to 1, so that the ζ-potential derived from eq. (1) assuming a formation factor value of 4.8, or a larger value possibly of 10, will only differ by 1 per cent. This error has been added in Table 1. The ζ-potential decreases from −16 to −27 ± 4 mV as the pH increases from 4 to 7. The ζ-potential is constant at −25 ± 1 mV from pH 8 to 10.5. For solution pH higher than 10.5, the ζ-potential is seen to increase in a less regular manner. The ζ-potential of sample 1 (experiment 7 at pH 10.7)

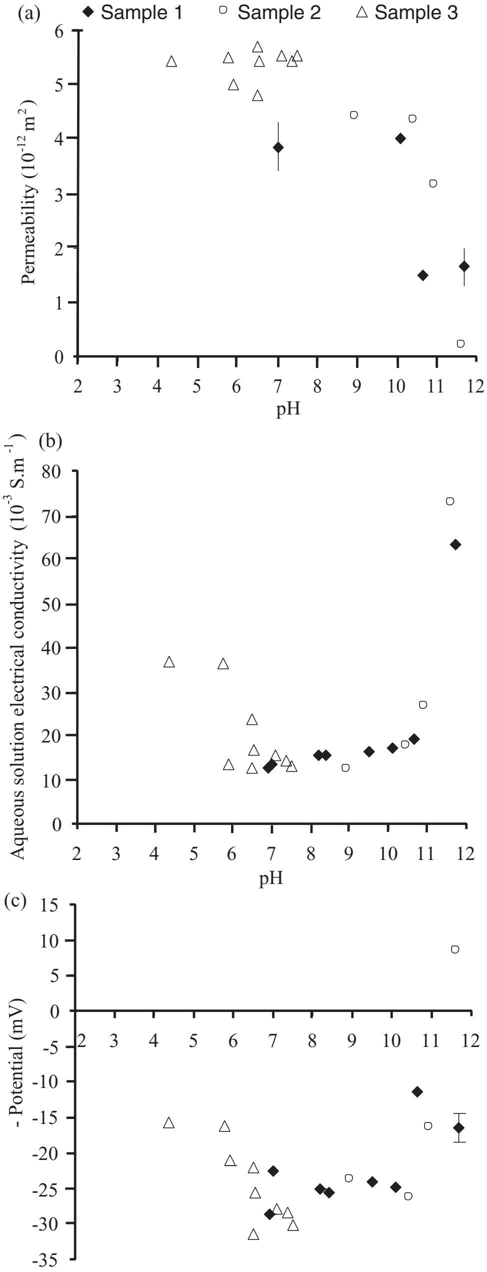

Figure 5. (a) Variation of the permeability of the samples as a function of pH (b) Variation of the electrical conductivity of the aqueous solutions, after flowing through the sand, as a function of pH (c) Variation of the ζ-potential derived from eq. (1) using $F = 4.8$, $\sigma_s = 10^{-4}$ S m^{-1} and $m = 1.3$, as a function of pH (d) Variation of the ionic strength of the aqueous solutions as a function of pH calculated using the chemical analyses and WATEQ program (Plummer *et al.* 1976). The ionic strength is not calculated for experiments run at pH higher than 11. Sample 1 was used with pH solutions from 7 to 11.7; sample 2 was used with ph solutions from 9 to 11.7; sample 3 was used with pH solutions from 7 to 4.4.

is equal to −11 mV. While the ζ-potential is negative for pH ranging from 4.4 to 11, a change of sign is observed with sample 2 at pH 11.7 (experiment 12) and the ζ-potential rises to +8 mV. At pH higher than 9, there is a decrease in the absolute value of ζ-potential, which even leads to a change of sign. This behaviour is thought to be related to the precipitation of calcite.

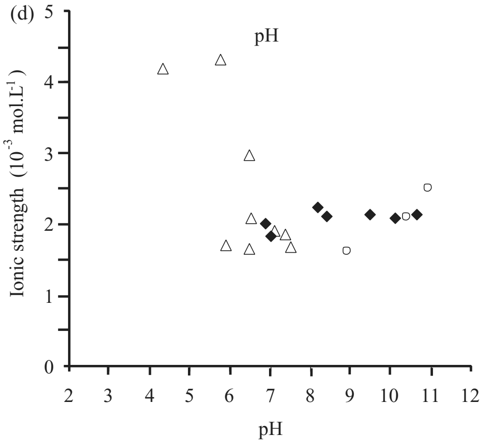

Figure 5. (*Continued.*

3.2 Chemical analysis

Table 2 groups together the chemical analyses of the aqueous solutions. Since the initial solution is obtained by dissolving $CaCl_2$ in distilled water, the major cation is Ca^{2+} and the major anion is Cl^-. The concentration of sodium is two orders of magnitude smaller than the concentration of calcium. We performed speciation calculations with the WATEQ program (Plummer *et al.* 1976), using the revised thermodynamic database of (Ball & Nordstrom 1991). The calculated aqueous speciation for calcium are shown in Fig. 6. For pH lower than 9, calcium does not form any complex in solution. In the pH range 9–12, the WATEQ calculations indicate the appearance of a $CaCO_3^0$ complex, which represents about 10 per cent of the calcium species. These speciation calculations are used to calculate ζ-potentials using the TLM model (Appendix B).

4 DISCUSSION

We now discuss the results, in particular the behaviour of zeta potential as a function of pH. We propose to interpret the measured ζ-potentials change of sign for pH larger than 11 by the calcite precipitation, using calculations of the surface electrical potential for both a quartz–water and a calcite–water interface.

4.1 Electrokinetic potentials

The ionic strength remains constant in the pH range 5.5–10.7 (Fig. 5d). Fig. 7 shows the evolution of ζ-potential at constant ionic strength ($I = 2 \pm 0.2 \times 10^{-3}$ mol l^{-1}) as a function of pH, that is, all experiments except n°s 8, 12, 17, 18 and 19 (Table 1). For comparison measurements from Lorne *et al.* (1999a) and Ishido & Mizutani (1981) are plotted. In the pH range from 4 to 10.5, the shape of the pH vs. ζ-potential dependence of our measurements is in good agreement with the results of Lorne *et al.* (1999a). The absolute values of the measurements reported by Ishido & Mizutani (1981) are larger, and the decrease with pH is much more abrupt. There are several possible reasons for this discrepancy:

(1) Sample preparation: Ishido & Mizutani (1981) carried out measurements with natural quartz that was crushed and cleaned with dilute nitric acid and then washed with distilled water. The samples were stored in distilled water for several months before being used. Lorne *et al.* (1999a) carried out measurements with crushed Fontainebleau sandstone that had not been cleaned with acid.

Table 2. Chemical analyses of the aqueous solutions sampled after the experiments. Uncertainties are 0.001×10^{-3} mol l^{-1}.

Experiment n°	Ca^{2+} 10^{-3} mol l^{-1}	Na^{+} 10^{-3} mol l^{-1}	Cl^{-} 10^{-3} mol l^{-1}	Alkalinity 10^{-3} mol l^{-1}	SiO_2 10^{-3} mol l^{-1}
1	0.624	0.023	1.128	0.384	0.007
2	0.589	0.009	1.016	0.272	0.004
3	0.694	0.147	1.185	0.352	0.006
4	0.679	0.005	0.979	0.528	0.006
5	0.709	0.004	1.001	0.544	0.007
6	0.734	0.009	0.860	0.576	0.009
7	0.709	0.006	1.016	0.592	0.010
8	0.931	0.006	0.987	0.432	0.023
9	0.514	$	0.818	0.368	0.005
10	0.644	$	0.894	0.960	0.010
11	0.828	$	0.931	0.944	0.017
12	1.238	$	0.937	1.280	0.021
13	0.524	$	0.922	0.320	0.004
14	0.584	$	1.058	0.304	0.004
15	0.609	$	1.086	0.272	0.005
16	0.674	$	1.255	0.240	0.006
17	0.938	0.005	1.932	0.256	0.010
18	1.317	0.007	2.863	0.136	0.007
19	1.352	0.007	3.032	0.160	0.008
20	0.514	0.004	1.001	0.224	0.005
21	0.519	0.007	1.142	0.192	0.003

$ Below determination threshold.

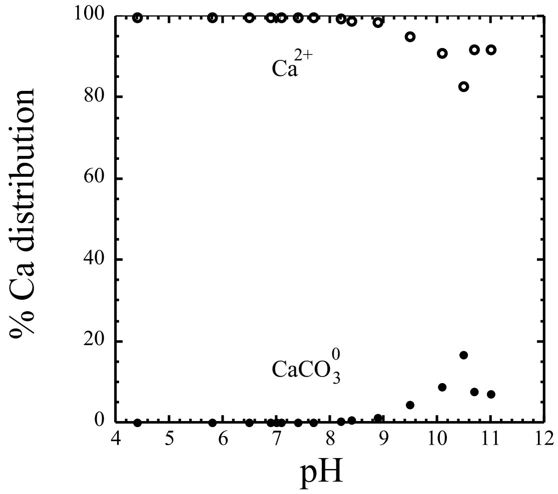

Figure 6. Aqueous speciation Ca calculated by WATEQ program (Plummer *et al.* 1976) using chemical analyses from present study (Table 1).

However, Lorne *et al.* (1999a) also ran an experiment with a crushed Fontainebleau sandstone that had been cleaned with hydrochloric acid, showing no significant change in the measured ζ-potential.

(2) Temperature: Lorne *et al.* (1999a) obtained a ζ-potential of about −25 mV at pH 6 using NaCl at 10^{-3} mol l^{-1}, performing their measurements at 22 ± 1°C. Ishido & Mizutani (1981) measured ζ-potentials of about −90 mV at pH 6 using KNO3 at 10^{-3} mol l^{-1}, and at a temperature of 45°C. These authors (1981) reported that ζ-potential decreases with increasing temperature, by about −0.65 mV/°C at pH 6.1. This would lead to a ζ-potential of about −75 mV at 22°C, a value which is still far from the value measured by Lorne *et al.* (1999a).

(3) Permeability: the permeability of our samples is about 5×10^{-12} m^2 for pH in the range 5.5–10.5. Lorne *et al.* (1999a,b) observed that the ζ-potential remains essentially constant for permeability ranging from 0.01×10^{-12} m^2 to 10×10^{-12} m^2, but decreases (in absolute value) at higher permeabilities. The permeability of the samples studied by Ishido & Mizutani (1981) is about 100×10^{-12} m^2. The discrepancy between our measurements and those of Ishido & Mizutani (1981) may be due to different permeabilities of the samples as noted by Ishido & Mizutani (1981), although the zeta potential is higher (in absolute value).

(4) Equilibrium time: Zeta-potential values deduced by Ishido & Mizutani (1981) were obtained after waiting 5–10 hr, whereas the values deduced by Lorne *et al.* (1999a) were obtained ‘when fluid conductivity was stable’, the sample could be ‘left in contact with the electrolyte for some days’, as noted by the authors, without giving any precise equilibrium time. It can not be concluded here that the high values of zeta potential (in absolute value) from Ishido & Mizutani (1981) are due to differences in equilibrium time.

The agreement of our data (using $CaCl_2$ at 0.015 S m^{-1}) with those (using NaCl at 0.01 S m^{-1}) of Lorne *et al.* (1999a) is quite surprising because ζ-potentials obtained with divalent cations should be twice lower than the values obtained with monovalent cations at similar ionic strength (Lorne *et al.* 1999a). Our measurement performed at pH 5.8 (−21 mV) is still higher than the zeta value of −11 mV from Lorne *et al.* (1999a) using $CaCl_2$ solution. Moreover, our measurements yield a ζ-potential of -27 ± 4 mV at pH 7, which is about twice lower in absolute terms than the data in the literature for quartz–water interface giving values of about −70 mV at an ionic strength of 10^{-3} mol l^{-1} (Pride & Morgan 1991), or −75 mV (Ishido & Mizutani 1981), which can be considered consistent with the fact that predominant cations are divalent cations in our study.

The measured ζ-potentials fall to −27 mV with increasing pH from 4 to 7, but remain constant at −25 mV from pH 8 to 10.5. This is surprising because the quartz surface is expected to become more negative with increasing pH, as the number of $>SiO^-$ sites increases. A further reason is that since the concentration of counter-ions Ca^{2+} is kept constant up to pH 9 (Fig. 6), the ζ-potential should decrease. The aqueous complex $CaCO_3$ appears at about pH 9. Its

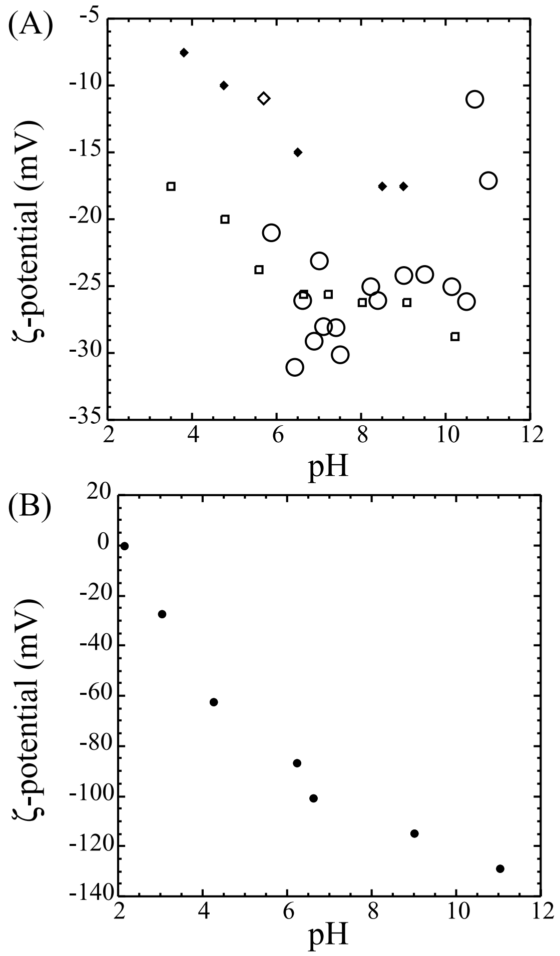

Figure 7. (a) Variation of the ζ-potential as a function of pH, at constant ionic strength of the aqueous solution $2 \pm 0.2 \times 10^{-3}$ mol l^{-1} (empty circles). Measurements from Lorne *et al.* (1999a) were performed with a crushed Fontainebleau sandstone, for NaCl aqueous solutions with pH adjusted by adding HCl or NaOH, and for KCl aqueous solutions with pH adjusted by adding HCl or KOH. These measurements were performed with a constant electrolyte resistivity of 100 Ω.m in the case of NaCl (empty squares) solutions (about 10^{-3} mol l^{-1}) and 25.5 Ω m (about 2×10^{-2} mol l^{-1}) in the case of KCl solutions (diamonds). Measurement using $CaCl_2$ solution is also reported (empty diamond): the inferred ζ-potential of −11 mV at $pH = 5.7$ for a fluid conductivity 13.5 mS m^{-1} (or 74 Ω m). (b) Measurements from Ishido & Mizutani (1981) were performed on Ishikawa quartz using aqueous solutions of KNO_3 (10^{-3} mol L^{-1}), with the temperature set at 45°C.

abundance increases up to pH 10.5 and then stays broadly constant at higher pH. The presence of $CaCO_3$ aqueous complexes decreases the amount of free Ca^{2+} in solution, so the measured ζ-potential should be more negative for pH higher than 8. The constant value of ζ-potential from pH 8 to 10.5 cannot be related to the appearance of aqueous complexes of Ca^{2+}.

4.2 Calcite precipitation

The measured ζ-potentials are scattered for pH higher than 10.5 (Fig. 7). We assume that this scattering is related to calcite precipitation, as inferred from saturation index calculations and from the decrease in permeability. The values of permeability of sample 1 (experiment 8) and sample 2 (experiment 12), at pH 11.7, are 1.7×10^{-12} m^2 and 0.2×10^{-12} m^2, respectively. These two values are smaller than the initial values obtained on sample 1 (sample 2) 4×10^{-12} m^2 (4.4×10^{-12} m^2) at neutral pH. This decrease in permeability is thought to be due to the precipitation of calcite. Using the WATEQ program (Plummer *et al.* 1976) and the chemical analyses of water samples in Table 2, we calculate the saturation indices of the calcite. This index is defined as the logarithm of the ionic activities product (IAP), that is, as the product of the Ca^{2+} activity and the CO_3^{2-} activity, divided by the calcite solubility product. Fig. 8 shows the variation of the calcite saturation index linked to permeability as a function of pH. Since the Ca^{2+} activity remains approximately constant, the increase of the saturation index with increasing pH is related to the increase of CO_3^{2-} activity with increasing pH (Fig. 6). The saturation index is less than 0 when pH ranges from 4.4 to 8.4, that is, the calcite of the sample undergoes dissolution. When pH is higher than 8.7, the saturation index is greater than zero, calcite precipitates from the solution and the permeability of the sample decreases. The calcite precipitate is expected to form a *coating* on the quartz grains. The higher the solution pH, the greater the amount of precipitated calcite, because (i) the saturation index increases, (ii) the duration of the experiment increases since the same sample remains in contact with a basic pH solution. The calcite *coating* gradually fills up the pore space and hydraulic pathways.

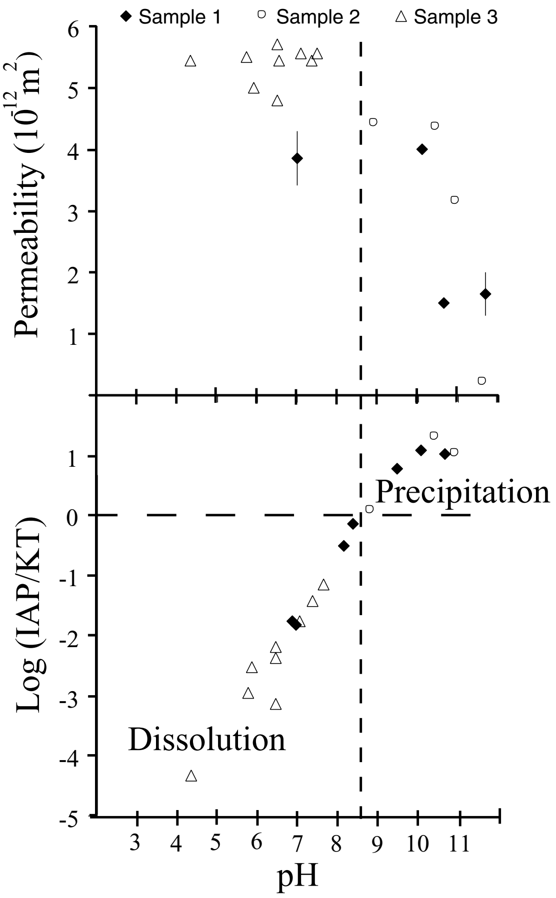

Figure 8. Saturation indices of calcite as a function of pH, associated with the variation in sample permeability. When the solution is oversaturated with respect to calcite, the permeability of the sample decreases.

4.3 Surface complexation model

We performed calculations of the surface electrical properties in order to achieve a semi-quantitative description of our measurements, and to investigate if calcite precipitation can lead to a reversal of sign of the ζ-potential. The zeta potential is first calculated for a quartz–water interface, and then for a calcite–water interface. The surface electrical properties of minerals are described by surface complexation models, which are based on a description of the formation of complexes on the surface of minerals, that is, between surface functional groups and dissolved species in the electrolyte. We choose TLM because consistent parameters of the model (i.e. capacitive constants, complexation constants) are available for numerous minerals. A mathematical description of TLM and a review of the quartz and calcite surfaces properties are given in Appendix B. The concentrations used for run calculations are the output species concentrations obtained from the WATEQ program (Plummer *et al.* 1976; Ball & Nordstrom 1991), using the results from the chemical analyses of water samples (Table 2). Equilibrium constants and capacitance constants are not adjustable parameters, but are values taken from the literature, and the sensitivity of the different possible values of these parameters on zeta-potential calculations has been achieved (see details in Appendix B and Fig. 9).

Quartz–Water Interface: Calculations were performed using the surface complexation reactions (Table 3), $C_1 = 1.4$ F m^{-2} or 0.81 F m^{-2}, $C_2 = 0.2$ F m^{-2} (see Appendix B for details), and total surface functional group densities of 10 and 25 sites nm^{-2} for pH in the range 4–8 and for pH higher than 8, respectively. Results of TLM calculations for a quartz–water interface are compared to our measurements in Fig. 9A. The calculated ζ-potentials decrease with increasing pH from 4.4 to 7.7, and remain constant in the pH range 8–10.5. The calculated ζ-potentials are in a good agreement with the measured ζ-potentials for pH ranging from 5.5 to 10. At pH 4.4, the calculated ζ-potential (around -6 mV) is higher than the measured ζ-potential (-16 mV). At pH higher than 10.5, the calculated ζ-potentials at a quartz–solution interface do not agree with the measured values.

Calcite–Water Interface: Calculations were performed using the surface complexation reactions (Table 4), $C_1 = 1.4$ F m^{-2}, $C_2 = 0.2$ F m^{-2}, and total surface functional group densities of 5 sites.nm^{-2} (see Appendix B for details). Results of TLM calculations for a calcite–water interface are compared to our measurements in Fig. 9B). Let us notice that the calculated ζ-potentials show a broad range of values depending on equilibrium constants published in recent geochemical literature (Van Cappellen *et al.* 1993; Pokrovsky *et al.* 1999; Fenter *et al.* 2000). Therefore, we are only able to provide a semi-quantitative interpretation of our measurements according to TLM results. TLM calculations do not agree with our measurements while pH increases from 4.4 to 10.5. The measured ζ-potentials show large variations and change of sign for pH higher than 10.5 (Fig. 7a). However, the magnitude of these variations can be compared with the magnitude of the range of TLM calculations values (Fig. 9B). TLM calculations also present a change of sign; electrical surface potentials calculated according to Van Cappellen *et al.* (1993)'s (or Pokrovsky *et al.* 1999's) equilibrium constants are always positive, whereas electrical surface potentials calculated according to Fenter *et al.* (2000)'s equilibrium constants became negative for pH larger than 8.

In summary, our ζ-potential measurements can be explained by a quartz–water interface when pH ranges from 5.5 to 8.5, and by a calcite–water interface when pH is greater than 10.5. When pH ranges from 8.5 to 10.5, the measured ζ-potentials are higher than the ζ-potentials calculated for a quartz–water interface and lower than the ζ-potentials calculated for a calcite–water interface. These measured ζ-potential values are probably representative of a surface composed by a mixture of quartz and calcite. Note that constant zeta potentials in the pH range 8.5 to 10.5 do not reflect the quartz–water interface usually described in the literature [Pride and Morgan,

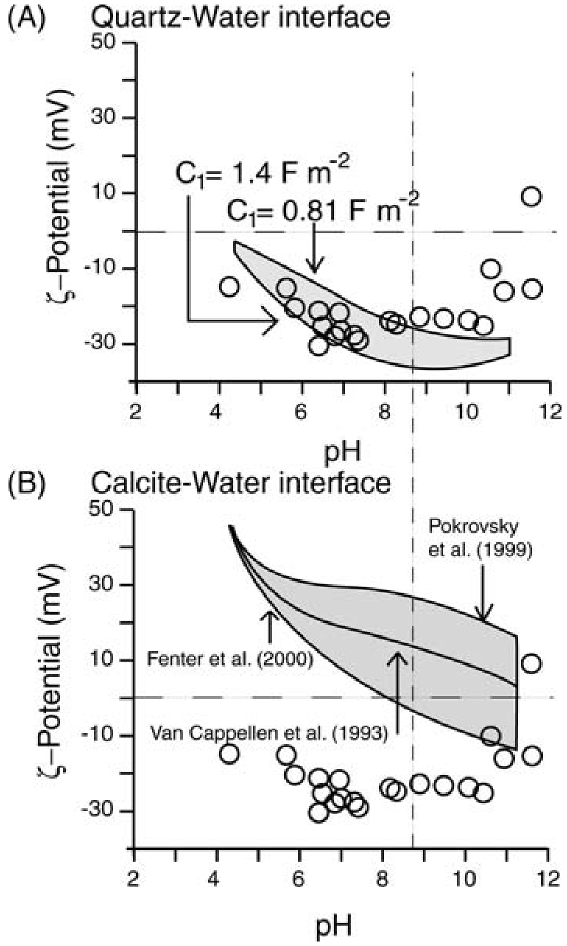

Figure 9. Results of the TLM calculation for (a) quartz–water interface, (b) calcite–water interface. The shadow parts show the sensitivity of the possible values of the electrical surface potentials as a fonction of input parameters (see Appendix B for details). The vertical dashed line is deduced from Fig. 8, and indicates the limit of oversaturation with respect to calcite (for pH greater than 8.7, the solutions are oversaturated with respect to calcite). The chemical surface reactions considered are grouped in Tables 3 and 4.

Table 3. Surface complexation reaction and equilibrium constants for the quartz–water interface used in the triple-layer model.

Surface reaction	Log *K*	Adsorption plane
$> \mathrm{SiOH\ H^+} \rightleftarrows > \mathrm{SiOH_2^+}$	$-1.3^{(a)}$	IHP
$> \mathrm{SiO^-} + \mathrm{H^+} \rightleftarrows > \mathrm{SiOH}$	$7.2^{(a)}$	IHP
$> \mathrm{SiO^-Ca^{2+}} \rightleftarrows > \mathrm{SiO^-Ca^{2+}}$	$-1.19^{(b)}$	β-plane
$> \mathrm{SiOH_2^+Cl^-} \rightleftarrows > \mathrm{SiOH_2^+} - \mathrm{Cl^-}$	$0.55^{(a)}$	β-plane

$^{(a)}$From Sverjensky & Sahai (1996) and Sahai & Sverjensky (1997b).
$^{(b)}$Calculated using equations (24), (35) and (36) from Sahai & Sverjensky (1997b).

Table 4. Surface complexation reaction and equilibrium constants for the calcite–water interface used in the triple-layer model.

Surface reaction	Log *K*	Reference
$> \mathrm{CO_3H^0} \rightleftarrows > \mathrm{CO_3^-} + \mathrm{H^+}$	−4.9	Van Cappellen *et al.* (1993)
	−2.8	Van Cappellen *et al.* (1993)
$> \mathrm{CO_3H^0} + \mathrm{Ca^{2+}} \rightleftarrows > \mathrm{CO_3Ca^+} + \mathrm{H^+}$	−4.4	Fenter *et al.* (2000)
	−1.7	Pokrovsky & Schott (1999)
$> \mathrm{CaOH_2^+} \rightleftarrows > \mathrm{CaOH^0} + \mathrm{H^+}$	−12.2	Van Cappellen *et al.* (1993)
$> \mathrm{CaOH^0} \rightleftarrows > \mathrm{CaO^-} + \mathrm{H^+}$	−17	Van Cappellen *et al.* (1993)
$> \mathrm{CaOH^0} + \mathrm{CO_2} \rightleftarrows > \mathrm{CaHCO_3^0}$	6	Van Cappellen *et al.* (1993)
$> \mathrm{CaOH^0} + \mathrm{CO_2} \rightleftarrows > \mathrm{CaCO_3^-} + \mathrm{H^+}$	−2.6	Van Cappellen *et al.* (1993)

1991], which shows a large decrease in zeta potential with increasing pH (see Fig. 7b). Our predicted values are flat in this pH range since our calculations are made using the [$\mathrm{Ca^{2+}}$] measured in our experiments. In this pH range, the predicted values for quartz–water interface are closer to the measurements than the predicted values for calcite–water interface, probably because of the unfinished coating of calcite on quartz grains since it is only the beginning of calcite precipitation (although it was not possible to quantify the calcite precipitation). The measured ζ-potentials change of sign for pH greater than 11, can be explained by the calcite precipitation inferred from the measured decrease of permeability and from chemical speciation calculations.

4.4 Electrical surface conductivity

We now discuss the sensibility of the inferred ζ-value to the surface conductivity value, as described by eq. (1). When calcite precipitates, it coats the quartz surface. Therefore, the electrical surface conductivity of the sand with a calcite coating is expected to be different than the electrical surface conductivity of the initial sand. To estimate the new electrical surface conductivity of the sand with calcite coating, we should measure the electrical conductivity of the sample versus the electrical conductivity of the fluid saturating the sample, for a set of fluid electrical conductivities ranging from demineralized water up to saline water (about 1S $\mathrm{m^{-1}}$). However, if the sample is saturated with demineralized water, the coating is expected to be dissolved. Therefore, to check the sensitivity of the ζ-potentials values deduced from eq. (1) with an electrical surface conductivity representative of carbonated rocks, we calculate ζ-potentials, for pH greater than 10, according to eq. (1) with a surface electrical surface conductivity equal to $1.4 \pm 0.5 \times 10^{-3}$ S $\mathrm{m^{-1}}$ (instead of 1.06×10^{-4} S $\mathrm{m^{-1}}$), which is the mean value of 14 electrical surface conductivities of carbonated rocks (M. Zamora, personal communication) (Fig. 10). The zeta potential is enhanced (in absolute value) by ~10 to 40 per cent, showing that it is important to know precisely this parameter. However, the general trend and obviously the change of sign observed in electrokinetic measurements (Fig. 10) are the same within our experimental errors.

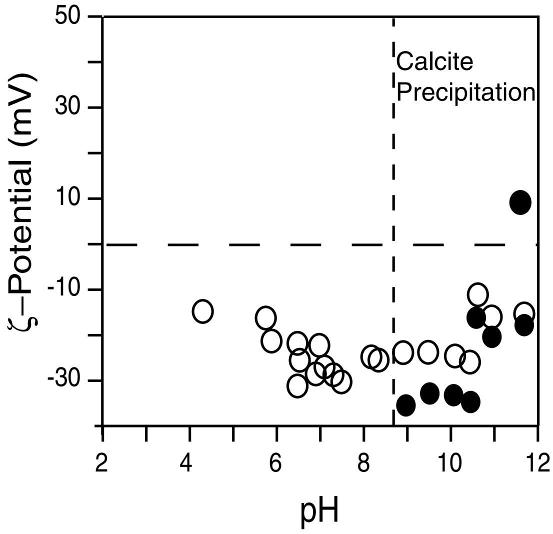

Figure 10. Check of the sensitiveness of ζ-potential values for various electrical surface conductivities when pH is greater than 8.7. ζ-potential deduced from eq. (1) using a surface electrical conductivity of 1.06×10^{-4} S $\mathrm{m^{-1}}$ (empty circles), and deduced from eq.(1) using a surface conductivity of 1.4×10^{-3} S $\mathrm{m^{-1}}$. The latter surface electrical conductivity is representative of carbonated rocks.

4.5 Consequences for field interpretations

It has been shown that large hydrothermal system without prominent surface area, and probably related to deeper intra-edifice system, can be recognized only through geophysical and geochemical measurements (Finizola *et al.* 2003). In order to interpret the SP surveys the streaming potential is always assumed positive in the flow direction. We would like to emphasize that this assumption is not correct when the zeta potential is positive instead of usually negative and we explore the field conditions needed to obtain a negative charge separation along the fluid flow.

The distribution of SP and $\mathrm{CO_2}$ anomalies observed on volcanoes is greatly influenced by the presence of structural limits such as crater, caldera or landslide faults. These discontinuities clearly constitute permeable drains on Stromboli (Finizola *et al.* 2003) allowing the escape of upward hot fluids and gas from the hydrothermal system: the electrical charge separation being usually positive in the flow direction, a positive SP anomaly is usually associated to a structural limit. In the summit area of Stromboli particularly a very dense survey was achieved for the first time in a similar context (Finizola *et al.* 2003), and the co-occurrence of SP, temperature and $\mathrm{CO_2}$ positive anomalies above the main faults lead to the conclusion that the transfer of hot hydrothermal fluids, heat and gases around the active area was controlled by the presence of more permeable paths along the fault. It was also observed a ‘cold zone’ interpreted as the filling of the craters by highly impermeable products, fluids, and heat only escaping along the border faults of the craters. In contrast, further from the active area, a previous study (Finizola *et al.* 2002) showed an inverse relationship between SP and $\mathrm{CO_2}$ anomalies at the scale of the island of Stromboli. High $\mathrm{CO_2}$ emanations were correlated with significant negative SP anomalies. This correlation was interpreted considering the permeable faults away from the active zone still allowing the upward migration of deep CO_2 degassing, but promoting the down-ward migration of ground water. This interpretation is in agreement with the assumption that charge separation is positive in the flow direction, but would be exactly the reverse assuming a reverse streaming potential. Moreover the occurrence of high-frequency SP signal closely associated with temperature anomalies, therefore, associated with high hydrothermal flux condensing close to the surface (Finizola *et al.* 2003) may have been interpreted considering the possibility of alteration and apparition of secondary minerals displaying a reverse zeta potential.

These results show the limits of the usual qualitative interpretation of the small-scale pattern of SP anomalies in order to determine local fluid circulations.

We now explore the field conditions needed to obtain negative charge separation along a fluid flow, meaning a positive zeta potential. We showed that this reverse sign in the streaming potential can be observed when secondary minerals such as calcite are present, for high pH values. These characteristics may not be evident to be observed on the hydrothermal systems of active volcanoes showing mixing between acid gas species such as H_2S, SO_2, HCl, HBr, HF, which lead to acid pH. However, calcite is often present in hydrothermal systems as an alteration product of volcanic rocks, precipitating on the walls of the rock cavities (Keller *et al.* 1979; Henley & Ellis 1983; Robert 2001). Evidences of high hydrothermal flux condensing close to the surface can be inferred by soil temperature elevation performed in the upper part of active volcanoes. These thermal anomalies are thought to coincide with permeable zones where uprising hot fluids escape (Finizola *et al.* 2003), leading to alteration and possibly to secondary minerals. Since electrical surface potential of calcite can range from positive to negative values depending on CO_2 partial pressure, pH, and $[Ca^{2+}]$ (Pokrovsky *et al.* 1999), either SP maxima or SP minima can be correlated to CO_2 maxima with the same fluid circulation direction even at pH lower than 9. Moreover calcite precipitation can also be effective on active volcano in acid environment: actually, in complex volcanic system, with a large output of magmatic CO_2 and low contribution of HCl, calcite can precipitate at low temperature such as 100°C–130°C or at higher temperature such as >300°C in a range of pH of 4.5–5 (Di Liberto *et al.* 2002).

5 SUMMARY AND CONCLUSION

The electrokinetic properties of the studied quartz–calcite sand are significantly affected when precipitation of calcite as a secondary mineral is observed. The ζ-potential is greatly reduced (in absolute value) and can even change sign. The electrical surface potentials calculated using TLM as a function of the pH, indicate that the electrical surface potential values are controlled by a quartz–water interface when pH ranges from 5.5 to 8.5, and by a calcite–water interface when pH is greater than 10.5.

SP method is frequently used on active volcanoes to evidence the hydrothermal systems and to outline their extension (Michel & Zlotnicki 1998; Lénat *et al.* 2000; Finizola *et al.* 2002, 2003, 2004). The small-scale patterns of SP and CO_2 anomalies are used to study tectonic fracture and structural limits. The electrokinetic coupling is always assumed to be positive in the flow direction—therefore, the negative anomalies are interpreted in terms of downward percolating rainfall, and the positive anomalies originate from upward convective flows (Zablocki 1976, 1978). This assumption is accurate if the surface electrical potential of the rocks is negative (see eq. 1). Surprisingly the SP studies do not check the nature of the rocks, whereas the surface electrical potential of the rock can be positive sometimes. In the field, only one experiment has been performed controlling CO_2 injection while measuring SP and showed an inversion in SP signals compared to the injection of neutral gas (Martinelli 2000). Calcite is often present in hydrothermal systems as an alteration product of volcanic rocks, precipitating on the walls of the rock cavities (Keller *et al.* 1979; Henley & Ellis 1983; Robert 2001). Since electrical surface potential of calcite can range from positive to negative values depending on CO_2 partial pressure, pH, and $[Ca^{2+}]$ (Pokrovsky *et al.* 1999), either SP maxima or SP minima can be correlated to CO_2 maxima with the same fluid circulation direction even at pH lower than 9. Moreover calcite precipitation can also occur in acid environment such as pH of 4.5–5 on active volcano with a large output of magmatic CO_2 and low contribution of HCl (Di Liberto *et al.* 2002).

Therefore, SP anomalies as measured in hydrothermal field, without mineralogical analyses of hydrothermal deposits, and without geochemical fluid survey, should be interpreted with caution, to infer fluid circulations.

ACKNOWLEDGMENTS

We thank G. Marolleau for the construction of the apparatus. We thank O. Pokrovsky, J. Schott, C. Robert for constructive remarks. We thank A. Finizola and T. Ishido for their constructive reviews. This research was supported by CNRS and by ACI- Prévention des Catastrophes Naturelles of the French Ministry of Research. Dr M. S. N. Carpenter carried out post-editing of a previous version of this final manuscript.

REFERENCES

Ahmad, M., 1964. A laboratory study of streaming potentials, *Geophys. Prospect.,* **12,** 49–64.

Ahrland, S., Grenthe, I. & Noren, B., 1960. The ion exchange properties of the silica gel I, *Acta Chemica Scandinavia,* **14,** 1059–1076.

Archie, G.E., 1942. The electrical resistivity Log as an aid in determining some reservoir characteristics, *Transactions AIME,* **146,** 54–62.

Aubert, M., Antraygues, P. & Soler, E., 1993. Interprétation des mesures de polarisation spontanées (PS) en hydrogéologie des terrains volcaniques. Hypothèse sur l'existence d'écoulements préférentiels sur le flanc sud du Piton de la Fournaise (île de la Réunion), *Bulletin de la Société Géologique de France,* **164**(1), 17–25.

Aubert, M. & Kieffer, G., 1984. Evolution d'une intrusion magmatique dans le flanc sud de l'Etna entre juin 1982 et juin 1983, Résultats de potentiel spontané (PS) et essai d'interprétation de l'éruption de 1983, *C. R. Académie des Sciences., Ser. II,* **298,** 379–382.

Ball, J.W. & Nordstrom, D.K., 1991. User's manual for WATEQ4F, with revised thermodynamic data base and test cases for calculating speciation of major, trace, and redox elements in natural waters, US Geological Survey.

Beamish, D., 1999. Characteristics of near- surface electrokinetic coupling, *Geophys. J. Int.,* **132,** 231–242.

Bernard, P., 1992. Plausibility of long distance electrotelluric precursors to earthquakes, *J. geophys. Res.,* **97**(B12), 17 531–17 546.

Bordes, C., Jouniaux, L., Dietrich, M., Pozzi, J.-P. & Garambois, S., 2006. First laboratory measurements of seismo-magnetic conversions in fluid-filled Fontainebleau sand, *Geophys. Res. Lett.,* **33,** L01302, doi:10.1029/2005GL024582.

Bussian, A.E., 1983. Electrical conductance in a porous medium, *Geophysics,* **48**(9), 1258–1268.

Cicerone, D.S., Regazzoni, A.E. & Blesa, M.A., 1992. Electrokinetic Properties of the Calcite/Water Interface in the presence of magnesium and organic matter, *Journal of Colloid and Interface Science,* **154**(2), 423–433.

Corwin, F.R. & Hoover, D.B., 1979. The self-potential method in geothermal exploration, *Geophysics,* **44**(2), 226–245.

Darnet, M., Maineult, A. & Marquis, G., 2004. On the origin of self-potential (SP) anomalies induced by water injections into geothermal reservoirs, *Geophys. Res. Lett.,* **31,** L19609, doi:10.1029/2004GL020922.

Darnet, M., Marquis, G. & Sailhac, P., 2003. Estimating aquifer hydraulic properties from the inversion of surface streaming potential (SP) anomalies, *Geophys. Res. Lett.,* **30,** 1679, doi:10.1029/2003GL017631.

Davis, J.A., James, R.O. & Leckie, J., 1978. Surface ionization and complexation at the Oxide/water interface, *Journal of Colloid and Interface Science,* **63,** 480–499.

Davis, J.A. & Kent, D.B., 1990. Surface complexation modeling in aqueous geochemistry, in *Mineral water interface geochemistry*, eds Hochella, M.F. & White, A.F., Mineralogical Society of America.

Deutsch, W.J., Jenne, E.A. & Krupka, K.M., 1982. Solubility equilibria in basalt aquifers: the Columbia Plateau, eastern Washington, USA, *Chemical Geology,* **36,** 15–34.

Di Liberto, V., Nuccio, P.M. & Paonita, A., 2002. Genesis of chlorine and sulphur in fumarolic emissions at Vulcano Island (Italy): assessment of pH and redox conditions in the hydrothermal system, *J. of Volcanol. Geotherm. Res.,* **116,** 137–150.

Douglas, H.W. & Walker, R.A., 1950. The electrokinetic behaviour of Iceland Spar against aqueous electrolyte solutions, *Transaction of the Faraday Society,* **46,** 559–568.

Doussan, C., Jouniaux, L. & Thony, J.-L., 2002. Temporal variations of SP and unsaturated water flow in loam and clay soils: a seasonal field study, *J. of Hydrology,* **267**(3/4), 172–184.

Dugger, D.L., Stanton, J.H., Irby, B.N., McConnell, B.L., Cummings, W.W. & Maatman, R.W., 1964. The exchange of twenty metal ions with the weakly acidic silanol group of silica gel, *The Journal of Physical Chemistry,* **68**(4), 757–760.

Erchul, R.A. & Slifer, D.W., 1987. the use of spontaneous potential in the detection of groundwater flow patterns and flow rate in karst areas, in *Karst Hydrology: Engineering and Environmental Applications*, pp. 217–227, in eds Beck, B.F. & Wilson, W.L., 2nd Multidisciplinary Conf on Sinkholes and the Environmental Impacts of Karst, Orlando, Florida.

Fenoglio, M.A., Johnston, M.J.S., Byerlee, Jim D., 1995. Magnetic and electric fields associated with changes in high pore pressure in fault zones; application to the Loma Prieta ULF emissions, *J. geophys. Res.,* **100,** 12 951–12 958.

Fenter, P., Geissbühler, P., DiMasi, E., Srajer, G., Sorensen, L.B. & Sturchio, N.C., 2000. Surface speciation of calcite observed in situ by high-resolution X-ray reflectivity, *Geochimica et Cosmochimica Acta,* **64**(7), 1221–1228.

Finizola, A., Lénat, J.-F., Macedo, O., Ramos, D., Thouret, J.-C., Sortino, F., 2004. Fluid circulation and structural discontinuities inside Misti volcano (Peru) inferred from self-potential measurements, *Journal of Volcanology and Geothermal Research,* **135,** 343–360, doi:10.1016/j.jvolgeores.2004.03.009.

Finizola, A., Sortino, F., Lénat, J.F., Aubert, M., Ripepe, M. & Valenza, M., 2003. The summit hydrothermal system of Stromboli. New insights from self-potential, temperature, CO2 and fumarolic fluid measurements, with structural and monitoring implications, *Bull. Volcanol.,* **65,** 486–504, DOI 10.1007/s00445–003-0276-z.

Finizola, A., Sortino, F., Lénat, J.F. & Valenza, M., 2002. Fluid circulation at Stromboli volcano from self-potential and CO2 surveys, *J. Volc. Geotherm. Res.,* **116,** 1–18.

Foxall, T., Peterson, G.C., Rendall, H.M. & Smith, A.L., 1979. Charge determination at calcium salt/aqueous solution interface, *Journal of the Chemical Society Faraday Transactions I,* **175,** 1034–1039.

Fuller, C.C. & Davis, J.A., 1987. Process and kinetic of Cd2+ sorption by a calcareous aquifer sand, *Geochimica et Cosmochimica Acta,* **51,** 1491–1502.

Garambois, S. & Dietrich, M., 2002. Full waveform numerical simulation of seismoelectromagnetic wave conversions in fluid-saturated stratified porous media, *J. geophys. Res.,* **107**(B7), doi:10.1029/2001JB000316.

Garambois, S. & Dietrich, M., 2001. Seismoelectric wave conversions in porous media : Field measurements and transfer function analysis, *Geophysics,* **66,** 1417–1430.

Gibert, D. & Pessel, M., 2001. Identification of sources of potential fields with the continuous wavelet transform: application to self-potential profiles, *Geophys. Res. Lett.,* **28,** 1863–1866.

Glover, P.W.J., Meredith, P.G., Sammonds, P.R. & Murrell, S.A.F., 1994. Ionic surface electrical conductivity in sandstone, *J. geophys. Res.,* **99,** 21 635–21 650.

Grahame, D.C., 1947. The electrical double layer and the theory of electrocapillarity, *Chemical review,* **41,** 441–501.

Guichet, X. & Zuddas, P., 2003. Effect of secondary minerals on electrokinetic phenomena during water-rock interaction, *Geophys. Res. Lett.,* **30,** 1714, doi:10.1029/2003GL017480.

Guichet, X., Jouniaux, L. & Pozzi, J.-P., 2003. Streaming potential of a sand column in partial saturations conditions, *J. geophys. Res.,* **108,** 2141, doi:10.1029/2001JB001517.

Hase, H., Hashimoto, T., Sakanaka, S., Kanda, W. & Tanaka, Y., 2005. Hydrothermal system beneath Aso volcano as inferred from self-potential mapping and resistivity structure, *J. Volc. Geotherm. Res.,* **143,** 259–277, doi:10.1016/j.jvolgeores.2004.12.005.

Henley, R.W. & Ellis, A.J., 1983. Geothermal systems ancient and modern: a geochemical review, *Earth Science Reviews,* **19,** 1–50.

Hunt, C.W. & Worthington, M.H., 2000. Borehole electrokinetic responses in fracture dominated hydraulically conductive zones, *Geophys. Res. Lett.,* **27**(9), 1315–1318.

Ishido, T. et al., 1997. Repeated self-potential of Izu-Oshima volcano, Japan, *J. Geomag. Geoelectr.,* **49,** 1267–1278.

Ishido, T. & Mizutani, H., 1981. Experimental and theoretical basis of electrokinetic phenomena in rock-water systems and its applications to geophysics, *J. geophys. Res.,* **86,** 1763–1775.

Jouniaux, L., Bernard, M.L., Zamora, M. & Pozzi, J.P., 2000. Streaming potential in volcanic rocks from Mount Pelée, *J. geophys. Res.,* **105**(B4), 8391–8401.

Jouniaux, L. & Pozzi, J.-P., 1997. Anomalous 0.1–0.5 Hz streaming potential measurements under geochemical changes: consequences for electrotelluric precursors to earthquakes, *J. geophys. Res.,* **102,** 15 335–15 343.

Jouniaux, L. & Pozzi, J.-P., 1995a. Streaming potential and permeability on saturated sandstones under triaxial stress: consequences for electrotelluric anomalies prior to earthquakes, *J. geophys. Res.,* **100,** 10 197–10 209.

Jouniaux, L. & Pozzi, J.-P., 1995b. Permeability dependence of streaming potential in rocks for various fluid conductivities, *Geophys. Res. Letts.,* **22,** 485–488.

Keller, G.V., Trowbridge Grose, L., Murray, J.C. & Skokan, C., 1979. Results of an experimental drill hole at the summit of Kilauea volcano, Hawaii, *J. Volc. Geotherm. Res.,* **5,** 345–385.

Kurosaki, S., 1954. The dielectric behavior of sorbed water on silica gel, *Journal of physical chemistry,* **58,** 320–324.

Langmuir, D., 1971. The geochemistry of some carbonate ground waters in central Pennsylvania, *Geochimica et Cosmochimica Acta,* **35,** 1023–1045.

Lénat, J.F., Fitterman, D. & Jackson, D.B., 2000. Geoelectrical structure of the central zone of the Piton de la Forunaise volcano (Réunion), *Bulletin of volcanology,* **62**(2), 75–89.

Lorne, B., Perrier, F. & Avouac, J.-P., 1999a. Streaming potential measurements: 1. Properties of the electrical double layer from crushed rock samples, *J. geophys. Res.,* **104,** 17 857–17 877.

Lorne, B., Perrier, F. & Avouac, J.-P., 1999b. Streaming potential measurements: 2. Relationship between electrical and hydraulic flow patterns from rock samples during deformation, *J. geophys. Res.,* **104,** 17 879–17 896.

Maineult, A., Bernabé, Y. & Ackerer, P., 2005. Detection of advected concentration and pH fronts from self-potential measurements, *J. geophys. Res.,* **110,** B11205, doi:10.1029/2005JB003824.

Maineult, A., Bernabé, Y. & Ackerer, P., 2004. Electrical response of flow, diffusion, and advection in a laboratory sand box, *Vadose Zone Journal,* **3,** 1180–1192.

Malmberg, C.G. & Maryott, A.A., 1956. Dielectric constant of water from 0° to 100°C, *Journal of Research of the National Bureau of Standard,* **56**(1), 2641.

Martinelli, G., 2000. The possible joint appearance of pre-seismic geochemical and geoelectrical anomalies in tectonically active areas, *Phys. Chem. Earth,* **25,** 337–341.

Marquis, G., Darnet, M., Sailhac, P., Singh, A.K. & Gérard, A., 2002. Surface electric variations induced by deep hydraulic stimulation : An example from the Soultz HDR site, *Geophys. Res. Lett.,* **29,** 10.1029/2002GL015046.

Michel, S. & Zlotnicki, J., 1998. Self-potential and magnetic surveying of La Fournaise volcano (Réunion Island): correlation with faulting, fluid circulation and eruption, *J. geophys. Res.,* **103**(B8), 17 845–17 857.

Mishra, S.K., 1978. The electrokinetics of apatite and calcite in inorganic electrolyte environment, *Int. J. Mineral Processing,* **5,** 69–83.

Morat, P., Le Mouël, J.-L., Pride, S. & Jaupart, C., 1995. Sur de remarquables oscillations de température, d'humiditè, de potential électrique observées dans une carrière souterraine, *C. R. Académie des Sciences., Ser. II,* **320,** 173–180.

Murakami, H., Hashimoto, T., Oshiman, N., Yamaguchi, S., Honkura, Y. & Sumitomo, N., 2001. Electrokinetic phenomena associated with a water injection experiment at the Nojima fault on Awaji Island, Japan, *The Island Arc,* **10,** 244–251.

Parks, G.A., 1965. The isoelectric points of solid oxides, solid hydroxides, and aqueous hydroxo-complex, *Chem. Rev.,* **65,** 177–198.

Parks, G.A., 1984. Surface and interfacial free energies of quartz, *J. geophys. Res.,* **89,** 3997–4008.

Pengra, D.B., Xi Li, S. & Wong, P., 1999. Determination of rock properties by low frequency AC electrokinetics, *J. geophys. Res.,* **104**(B12), 29 485–29 508.

Perrier, F. & Pant, S.R., 2005. Noise reduction in Long-term Self-potential monitoring with travelling electrode referencing, *Pure appl. Geophys.,* **162,** 165–179, doi:10.1007/s00024–004-2585–3.

Perrier, F. & Froidefond, T., 2003. Electrical conductivity ans streaming potential coefficient in a moderately alkaline lava series, *Earth planet. Sci. Lett.,* **210,** 351–363.

Perrier, F., Trique, M., Lorne, B., Avouac, J.-P., Hautot, S. & Tarits, P., 1998. Electric potential variations associated with lake level variations, *Geophys. Res. Lett.,* **25,** 1955–1958.

Perrier, F. et al., 1997. A one year systematic study of electrodes for long period measurements of the electric field in geophysical environments, *J. Geomag. Geoelect.,* **49,** 1677–1697.

Pinettes, P., Bernard, P., Cornet, F., Hovhannissian, G., Jouniaux, L., Pozzi, J.-P. & Barthès, V., 2002. On the difficulty of detecting streaming potentials generated at depth, *Pure appl. Geophys.,* **159,** 2629–2657.

Pisarenko, D., Morat, P. & Le Mouel, J.-L., 1996. Gn a possible mechanism of sandstone alteration: evidence from electric potential measurements, *C. R. Académie des Sciences, Ser. II,* **322,** 17–24.

Plummer, N.L., Jones, B.F. & Truesdell, A.H., 1976. WateQF—A Fortran IV version of WateQ, a computer program for calculating chemical equilibria of natural waters, pp. 61, US Geological Survey.

Pokrovsky, O. & Schott, J., 1999. Process at the magnesium-bearing carbonates-solution interface. II Kinetics and mechanism of magnesite dissolution, *Geochimica et Cosmochimica Acta,* **63,** 881–897.

Pokrovsky, O., Schott, J. & Thomas, F., 1999. Processes at the magnesium bearing carbontes-solution interface: I A surface speciation model for magnesite, *Geochimica et Cosmochimica Acta,* **63,** 863–880.

Pride, S. & Morgan, F.D., 1991. Electrokinetic dissipation induced by seismic waves, *Geophysics,* **56**(7), 914–925.

Revil, A. & Glover, P.W.J., 1998. Nature of surface electrical conductivity in natural sands, sandstones and clays, *Geophys. Res. Letts,* **25,** 691–694.

Revil, A., Schwaeger, H., Cathles, I.L.M. & Manhardt, P.D., 1999b. Streaming potential in porous media 2- Theory and application to geothermal systems, *J. geophys. Res.,* **104**(B9), 20033–20048.

Revil, A., Finizola, A., Sortino, F. & Ripepe, M., 2004. Geophysical investigations at Stromboli volcano, Ital: Implications for ground water flow and paroxysmal activity, *Geophys. J. Int.,* **157,** 426–440, doi:10.1111/j.1365–246X.2004.02181.x.

Robert, C., 2001. Hydrothermal alteration processes of the tertiary lavas of Nothern Ireland, *Mineralogical magazine,* **65**(4), 543–554.

Robert, C. & Goffé, B., 1993. Zeolitization of basalts in subaqueous freshwater settings: field observation and experimental study, *Geochimica et Cosmochimica Acta,* **57,** 3597–3612.

Robert, C., Goffé, B. & Saliot, P., 1988. Zeolitisation of a basaltic flow in a continental environmet: an example of mass transfer under thermal control, *Bulletin de minéralogie,* **111,** 207–223.

Ruffet, C., Gueguen, Y. & Darot, M., 1991. Complex conductivity measurements and fractal nature of porosity, *Geophysics,* **56,** 758–768.

Sahai, N. & Sverjensky, D.A., 1997a. Evaluation of internally consistent parameters for the triple-layer model by the systematic analysis of oxide surface titration data, *Geochimica et Cosmochimica Acta,* **61**(14), 2801–2826.

Sahai, N. & Sverjensky, D.A., 1997b. Solvation and electrostatic model for specific electrolyte adsorption, *Geochimica et Cosmochimica Acta,* **61**(14), 2827–2848.

Sailhac, P., Darnet, M. & Marquis, G., 2004. Electrical streaming potential measured at the ground surface: forward modeling and inversion issues for monitoring infiltration and characterizing the vadose zone, *Vadose Zone Journal,* **3,** 1200–1206.

Sailhac, P. & Marquis, G., 2001. Analytic potentials for the forward and inverse modeling of SP anomalies caused by subsurface fluid flow, *Geophys. Res. Lett.,* **28,** 1851–1854.

Schindler, P.W., Fürst, B., Dick, R. & Wolf, P.U., 1976. Ligand properties of surface silanol groups I, *Journal of Colloid and Interface Science,* **55,** 469–475.

Siffert, B. & Fimbel, P., 1984. Parameters affecting the sign and the magnitude of the electrokinetic potential of Calcite, *Colloids and Surfaces,* **11,** 377–389.

Sigg, L., Behra, P. & Stumm, W., 2000. *Chimie des milieux aquatiques*, Dunod.

Smallwood, P.V., 1977. Some aspects of the surface chemistry of calcite and argonite; Part I: an electrokinetic study, *Colloid and Polymer Sciences,* **256,** 881–886.

Somasundaran, P. & Agar, G.E., 1967. The zero point of charge of calcite, *Journal of Colloid and Interface Science,* **24,** 433–440.

Somasundaran, P. & Kulkarni, R.D., 1973. A new streaming potential apparatus and study of temperature effects using it., *Journal of Colloid and Interface Science,* **45**(3), 591–600.

Stipp, S.L. & Hochella, M.F., 1991. Structure and bonding environments at the calcite surface as observe with X-ray photoelectron spectroscopy (XPS) and low energy electron diffraction (LEED), *Geochimica et Cosmochimica Acta,* **55,** 1723–1736.

Stoffers, P. & Botz, R., 1994. Formation of hydrothermal carbonate in Lake Tanganyika, East-Central Africa, *Chemical Geology,* **115,** 117–122.

Stumm, W., Hohl, H. & Dalang, F., 1976. Interaction of metal ion with hydrous oxide surfaces, *Croatica Chemica Acta,* **48,** 491–504.

Sverjensky, D.A., 2001. Interpretation and prediction of triple-layer model capacitances and the structure of the oxide-electrolyte-water interface, *Geochimica et Cosmochimica Acta,* **65**(21), 3643–3655.

Sverjensky, D.A. & Sahai, N., 1996. Theoretical prediction of single-site surface-protonation equilibrium constants for oxides and silicates in water, *Geochimica et Cosmochimica Acta,* **60**(20), 3773–3797.

Tadros, T.F. & Lyklema, J., 1969. The electrical double-layer on silica in the presence of bivalent counter-ions, *Journal of Electroanalytical Chemistry and Interfacial Electrochemistry,* **22,** 1–17.

Thompson, A.B., 1971. P CO2 in low grade metamorphism; Zeolite, carbonate, clay mineral, Prehnite relation in system CaO-Al2O3-SiO2-CO2-H2O, *Contributions to mineralogy and petrology,* **33,** 145–161.

Thompson, D.W. & Pownall, P.G., 1989. Surface electrical properties of calcite, *Journal of Colloid and Interface Science,* **131,** 74–82.

Trique, M., Perrier, F., Froidefond, T., Avouac, J.-P. & Hautot, S., 2002. Fluid flow near reservoir lakes inferred from the spatial and temporal analysis of the electric potential, *J. geophys. Res.,* **107,** 2239, 10.1029/200JB000482.

Van Cappellen, P., Charlet, L., Stumm, W. & Wersin, P., 1993. A surface complexation model of the carbonate mineral-aqueous solution interface, *Geochimica et Cosmochimica Acta,* **57,** 3505–3518.

Vdovic, N., 2001. Electrokinetic behaviour of calcite - the relationship with other calcite properties, *Chemical Geology,* **177,** 241–248.

Wanfang, Z., Beck, B.F. & Stephenson, J.B., 1999. Investigation of grounwater flow in karst areas using component separation of natural potentila measurements, *Environmental Geology,* **37,** 19–25.

Waxman, M.H. & Smits, L.J.M., 1968. Electrical conductivities in oil-bearing shaly sands, *Transactions AIME,* **243,** 107–122.

Westercamp, D., 1981. Distribution and volcano-structural control of zeolites and others amygdales minerals in the island of Martinique, *J. Volc. Geotherm. Res.,* **11,** 353–365.

Zablocki, C.J., 1976. Mapping thermal anomalies on an active volcano by the self-potential mathod, Kilauea, Hawaii, in *Second U.N. Symposium on the development and use of geothermal resources*, pp. 1299–1309, San Francisco.

Zablocki, C.J., 1978. Streaming Potentials resulting from the descent of meteoric water—a possible mechanism for Kilauean self potential anomalies, *Geothermal Resources council Transactions,* **2,** 747–748.

Zachara, M.J., Cowan, C.E. & Resch, C.T., 1991. Sorption of divalent metals on calcite, *Geochimica et Cosmochimica Acta,* **55,** 1549–1562.

Zachara, M.J., Cowan, C.E. & Resch, C.T., 1993. Metal Cation/Anion adsorption on calcium carbonate: Implications to metal ion concentration in groundwater, in *Metals in Groundwater*, eds Allen, H.E., Perdue, E.M. & Brown, D.S., Lewis Publishers, Chelsea, MI.

APPENDIX A: EQUILIBRIUM TIME

We detail here how we checked that the equilibrium between the rock and the electrolyte was attained for sample 1. Measurements of electrokinetic coupling, pH, and fluid conductivity as a function of time are shown in Fig. A1. The initial water ($CaCl_2$ solution) has a conductivity 0.0127 S m^{-1} and pH 5.5. After 750 mL flowed through the sample, the conductivity and the pH of the output water are $\sigma_f =$ 0, 0116 S m^{-1} and $pH = 6.8$. Then we wait 21 hr before the output water is made to flow through the sample. The water is circulated twice 750 mL to check if the conductivity and pH are constant: at this time, if the conductivity and pH of the output water are constant, equilibrium is thought to be attained and streaming potential as a function of various applied pressures is measured. The linearity between the streaming potential and the applied pressure is checked and the electrokinetic coupling coefficient is deduced from 2 to 3 sets of measurements (see for examples Fig. 4). The measurements performed at time 22 hr are made with the initial solution (exp. 1), whereas measurements performed at time 44 hr (exp. 2) are performed using the initial solution added with $CaOH_2$, although the conductivity and pH are almost the same. These measurements lead to a ζ-potential of -29 and -23 mV, respectively. At time 70 hr the pH of the solution is increased up to 8.9 by adding $CaOH_2$. Electrokinetic measurements are performed after waiting 1 hr and the results show a large dispersion, probably because the equilibrium is not attained. These measurements were not taken into account. After waiting 20 hr (time 90 hr) the output water is made to flow trough the sample and the conductivity and pH of the ouput water are $\sigma_f =$ 0,0155 S m^{-1} and $pH = 8.3$. This water is recirculated twice in the sample and the conductivity and pH are constant: the electrokinetic coupling coefficient can be, therefore, quantified (exp. 3 and 4). Then the pH of water is increased up to 9.5 and after waiting 27 hr the output water is recirculated twice and the conductivity and pH are checked to be constant and the electrokinetic coupling coefficient is quantified (exp. 5). All the measurements have been performed using this experimental protocol.

The long run times needed to reach chemical equilibrium have already been emphasized by Davis & Kent (1990), who questioned the applicability of surface complexation models to carbonates. Furthermore, Zachara *et al.* (1993) observed that surface adsorption processes for divalent cations onto calcite and carbonates occur over two characteristic durations: one of a few hours, in relation to reversible reactions, and another of several days associated with irreversible reactions. The latter phenomena involve changes in the chemical bonding of the adsorbed divalent cations, inducing the formation of a recrystallized surface phase or a solid solution. The latter phenomena are not investigated in the present paper.

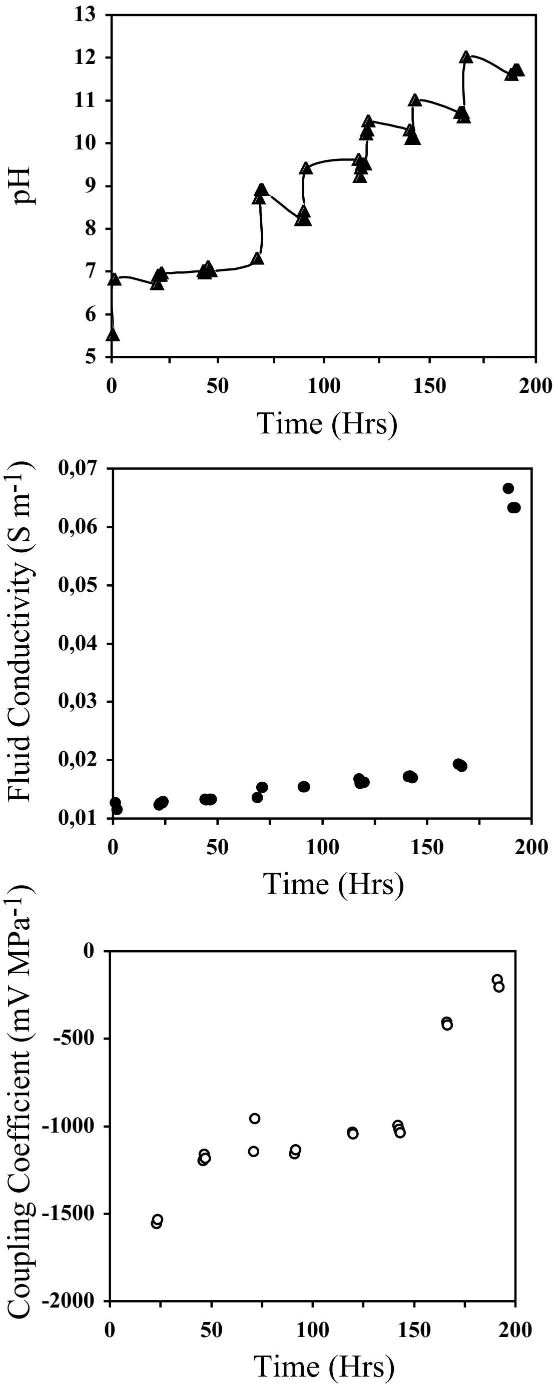

Figure A1. Measurements of the electrokinetic coupling, pH, and fluid conductivity, as a function of time.

Error sources

The error on each zeta potential deduced from eq. (1) was calculated by the sum of the errors on: the dielectric constant, the water conductivity, the viscosity, and the measured coupling coefficient. Temperature variation is taken into account for the dielectric constant. The error on fluid conductivity is ±0.4 per cent; the error on viscosity due to temperature variations is for most of the experiments between 1 and 5 per cent, but is between 9 and 13 per cent for the experiments performed a temperature below 16.5°; the error on the electrokinetic coupling coefficients is ±1 to ±5 per cent for most of the measurements, and ±12 per cent for exp. 8. Each error has been quantified on zeta potential (Table 1) and is included in the size of drawing in Figs 5, 7, 9 and 10. The surface conductivity is taken into account, however, since the exact value is not known precisely for pH higher than 9, this point has been developed in Section 4.4.

The measurements performed at time 22 hr are made with the initial solution (exp. 1) and lead to a zeta potential of −29 mV. The measurements performed with the initial solution on two other samples (exp. 13 and 21) lead to a zeta potential of −30 and −31 mV, respectively. Therefore, the variation from sample to sample leads to an error of ±3.5 per cent, which is, for most of the measurements, the same order of magnitude of the error due to the eq. (1).

APPENDIX B: ζ-POTENTIAL MODELLING ACCORDING TO TLM

We describe here the TLM, which is used to calculate zeta potentials of our sand/calcite–water interface to interpret the electrokinetic measurements as a function of pH (see Section 4).

The TLM distinguishes three planes to describe the electrical double layer. One plane, called the Inner Helmholtz Plane (IHP), for counter ions that are directly bound to the mineral structure and another plane, called the Outer Helmholtz Plane (OHP), for weakly bound counter ions (see Fig. B1) (Grahame 1947). The counter ions of the IHP are assumed to be chemically adsorbed, forming a chemical bond with the surface functional group. On the other hand, the counter ions of the OHP are assumed to be physically adsorbed and more labile. The TLM also takes account of a third plane, called the *d*-plane, associated with the smallest distance between the mineral surface and the counter ions in the diffuse layer. At every plane is related an electrical surface charge density σ and an electrical potential ϕ. The electrical surface charge densities and potentials are supposed to follow the Stern–Grahame relationships (Grahame 1947):

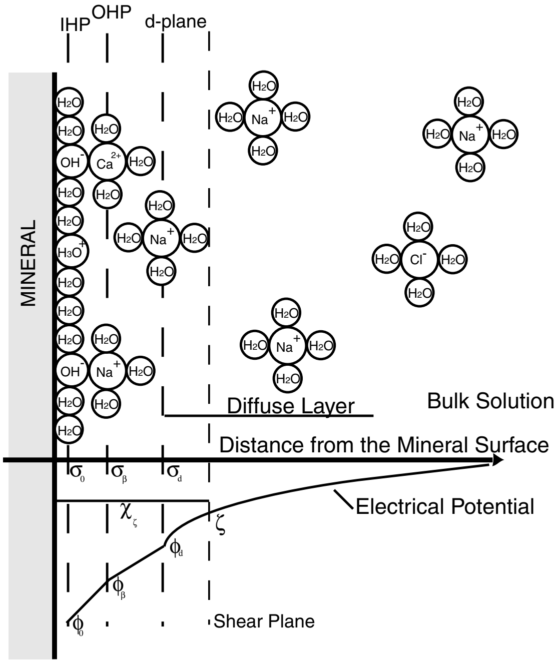

Figure B1. Schematic view of the mineral–water interface for oxide minerals, showing location of IHP and OHP, and the potential decay away from the surface (after Davis *et al.* 1978).

$$\begin{aligned}\phi_0 - \phi_\beta &= \sigma_0 / C_1 \\ \phi_\beta - \phi_d &= (\sigma_0 + \sigma_\beta)/C_2 \\ \sigma_0 + \sigma_\beta + \sigma_d &= 0\end{aligned} \tag{B1}$$

where the subscript 0, β and d refer to IHP, OHP, and d-plane, C_1 and C_2 the integral capacitances of the interfacial layers. The electrical potential on the d-plane is usually estimated by the Gouy–Chapman charge–potential relationship based on the bulk solution chemistry:

$$\sigma_d = 2\chi_d \sum_i eZ_i[i] \exp\left(\frac{-q_i\phi_d}{2kT}\right), \tag{B2}$$

where Z_i is the electrical charge of the ith ion in solution, e is the elementary electron charge, k is the Boltzmann's constant, T the absolute temperature, and χ_d is the Debye length equal to:

$$\chi_d = \sqrt{\varepsilon kT/e^2 \sum_i Z_i^2[i]}. \tag{B3}$$

The reader can find a comprehensible report of uses and results of the TLM in Davis & Kent (1990).

The Stern–Grahame model assumes that the surface of the mineral, the β-plane and the d-plane can be considered as plates of a planar condenser. The model of a planar condenser is appropriate if the thickness of the diffuse layer, around two Debye lengths, is small compared with the grain radius. In our study, the mean grain diameter is 3×10^{-4} m, and the Debye length is smaller than 10^{-9} m.

It has been proposed that the approximation be made that the slipping plane lies near the distance of closest approach of dissociated ions, that is, $\phi_d = \zeta$ (Davis & Kent 1990). The surface electrical potential of the d-plane can be determined by solving eqs (B2) and (B3) . In order to solve these equations, the electrical surface charge densities σ_0 and σ_β must be determined from the surface complexation reactions, which themselves depend on the surface functional groups and on the ionic species in the aqueous solution.

Quartz surface

We describe here the surface functional group used to model the quartz surface, and we detail the appropriate values of the total surface functional group density: for pH range 4–8 and for pH greater than 8 we use a total surface functional group density of 10 sites nm^{-2}, and 25 sites nm^{-2}, respectively.

The quartz surface has been extensively studied, and its properties can be modelled with silanol >SiOH group (Davis *et al.* 1978; Sahai & Sverjensky 1997a,b). Many experiments have been performed with silica gels (Ahrland *et al.* 1960; Dugger *et al.* 1964) and with natural silica (Somasundaran & Kulkarni 1973; Schindler *et al.* 1976; Ishido & Mizutani 1981; Lorne *et al.* 1999a). In summary, the OH^- and H^+ ions, termed potential-determining ions, are adsorbed onto the mineral surface and determine the charge density σ_0. Thus, the surface charge of quartz is a function of pH; the charge is positive for pH < pzc and negative for pH > pzc. The pzc of quartz is in the range 2 < pH < 4 (Parks 1965; Tadros & Lyklema 1969; Parks 1984; Glover *et al.* 1994; Lorne *et al.* 1999a). Since the pH of natural waters ranges from 4 to 10 (Sigg *et al.* 2000), the quartz surface is generally negatively charged. The major cations of natural waters (Ca^{2+}, Mg^{2+}, Na^+ and K^+) are found to be adsorbed onto the β-plane. Two reactions are possible with divalent cations (Ahrland *et al.* 1960; Dugger *et al.* 1964; Tadros & Lyklema 1969; Schindler *et al.* 1976; Stumm *et al.* 1976); the cation can form either a monodentate or a bidentate surface complex.

The surface parameters used for quartz in the present model are obtained from (Sahai & Sverjensky 1997a,b; Sverjensky & Sahai 1996) and are listed in Table 1. Since Ca^{2+} is the major ion during the experimental runs (Table 1), we ignore the other species such as Mg^{2+}, Na^+ and K^+. To simplify the calculation, we do not consider the formation of a bidentate surface complex of calcium. For pH in the range 4–8 and for pH higher than 8, we use total surface functional group densities of 10 and 25 sites.nm^{-2}, respectively.

Calcite surface

We describe here the surface functional group used to model the calcite surface, and we show the different possible values of the calcification reaction constants.

The surface electrical potential of calcite has been investigated by many geochemists over the last 50 yr (Douglas & Walker 1950; Somasundaran & Agar 1967; Smallwood 1977; Foxall *et al.* 1979; Siffert & Fimbel 1984; Thompson & Pownall 1989; Cicerone *et al.* 1992; Vdovic 2001) and measurements are sometimes contradictory (Fig. 2). For instance, the zero point of charge (pH_{pzc}) varies according to authors from 7 to 10.8 (Van Cappellen *et al.* 1993). Curves of ζ-potential versus pH show hysteresis loops (Thompson & Pownall 1989), while different electrokinetic behaviours are observed on natural or synthetic calcite, the ζ-potentials of natural calcite being systematically lower than the values obtained for synthetic calcite (Vdovic 2001).

In summary, Ca^{2+} and carbonate ions are the potential-determining ions (Somasundaran & Agar 1967; Foxall *et al.* 1979; Cicerone *et al.* 1992). H^+ and OH^- modify the surface electrical potential because they regulate the concentrations of Ca^{2+} and carbonate ions. Contradictory behaviours are observed at a given pH, because (i) the concentrations of the potential-determining ions are variable (Thompson & Pownall 1989; Cicerone *et al.* 1992); (ii) important dissolution and precipitation reactions imply that chemical equilibrium cannot be reached easily (Somasundaran & Agar 1967), and that—in the presence of other ions—the rapid exchange rates can transform the nature of the solid surface layer (Fuller & Davis 1987; Cicerone *et al.* 1992; Zachara *et al.* 1993). The most common approach to evaluate the validity of surface complexation theory is through measurements of surface charge (Fenter *et al.* 2000). However, calcite surface charge variation versus pH is difficult to measure by potentiometric titrations because of calcite's rapid dissolution (Charlet *et al.* 1990).

Therefore, different values of the calcification reaction constants are published in the literature. Van Cappellen *et al.* (1993) proposed a model with two surface functional groups, $>CaOH^0$ and $>CO_3H^0$, which can react with Ca^{2+}, carbonate ions, H^+ and OH^- (Table 4). The surface functional groups are based on X-ray photoelectron spectroscopic observations measured under ultra-high vacuum conditions (Stipp & Hochella 1991). The equilibrium constants are calculated to obtain a pH_{ZPC} near 8.2 with atmospheric CO_2 partial pressure. This model predicts that the calcite surface has distinct termination depending on solution composition (pH, pCa, and P_{CO2}) and shows a reaction constant $\log K = -2.8$ (Table 4). Fenter *et al.* (2000) present *in situ* X-ray reflectivity measurements of the calcite–water interface at pH ranging from 6.8 to 12.1 and low P_{CO2} which show that the calcite surface does not vary significantly over this range of experimental conditions, and can be explained without invoking changes other than protonation reactions in the surface speciation. Particularly Fenter *et al.*'s measurements do not require a calcification reaction as proposed by Van Cappellen *et al.* (1993): $> CO_3H^0 + Ca^{2+} \rightleftarrows\ > CO_3Ca^+ + H^+$, and a value of log $K < -4.4$ satisfies X-ray reflectivity measurements. On the other hand, Pokrovsky & Schott (1999) provide an higher estimate for the log K (-1.7) of the calcification reaction.

Finally, we use Van Cappellen's model, and the variability of calcification reaction constants on the calculated zeta potentials is taken into account (Fig. 9), using a total surface site density value of 5 sites per nm^2 as reported by Davis & Kent (1990).

Integral Capacitances of the interfacial layer

The values of the integral capacitances of the interfacial layers, C_1 and C_2, are related to the dielectric properties of the interface, particularly the water permittivity value. Despite the widespread application of such surface complexation models, the choice of the integral capacitance values is not straightforward because these values depend on the specific oxide and on the type of electrolyte, and cannot be directly measured (Sverjensky 2001). Usually C_1 and C_2 values are chosen as adjustable parameters, consistent with interfacial dielectric constant 80, and equal to 1–1.4 and 0.2 F m^{-2}, respectively (Davis & Kent 1990). Although measurements of the water permittivity at the interface are scarce and difficult, the water permittivity is supposed to be smaller near the mineral surface than within the bulk solution, <10 (e.g. Kurosaki 1954). Recently Sverjensky (2001) proposed a model consistent with interfacial dielectric constants ranging from 20 to 62, and obtained $C_1 = 0.81$ and 1.00 F m^{-2} for quartz with $CaCl_2$ electrolyte and NaCl electrolyte, respectively.

Calcite, and more generally carbonate minerals, develop relatively high surface charge, about 100 times higher than oxides, and show ζ-potential values of the same order of magnitude (Pokrovsky *et al.* 1999). Van Cappellen *et al.* (1993) propound that carbonate-water interface is thin and has highly structured (i.e. non-diffuse) electric double layer with high capacitance. It is likely, in the case of calcite, that Ca^{2+} and HCO_3^- (CO_3^{2-}) form inner-sphere specific interactions with the charged surface, leading to the formation of a very thin double layer (Pokrovsky *et al.* 1999). This could account for great difference in composition and structure of the EDL formed by oxides or by carbonates (Pokrovsky *et al.* 1999).

Finally we use $C_2 = 0.2$ F m^{-2} for quartz–water interface and for calcite–water interface, and $C_1 = 1.4$ F m^{-2} or 0.81 F m^{-2} for quartz–water interface, and $C_1 = 1.4$ F m^{-2} for calcite–water interface. The variability of the integral capacitance values on the calculated zeta potentials is shown in Fig. 9(a).

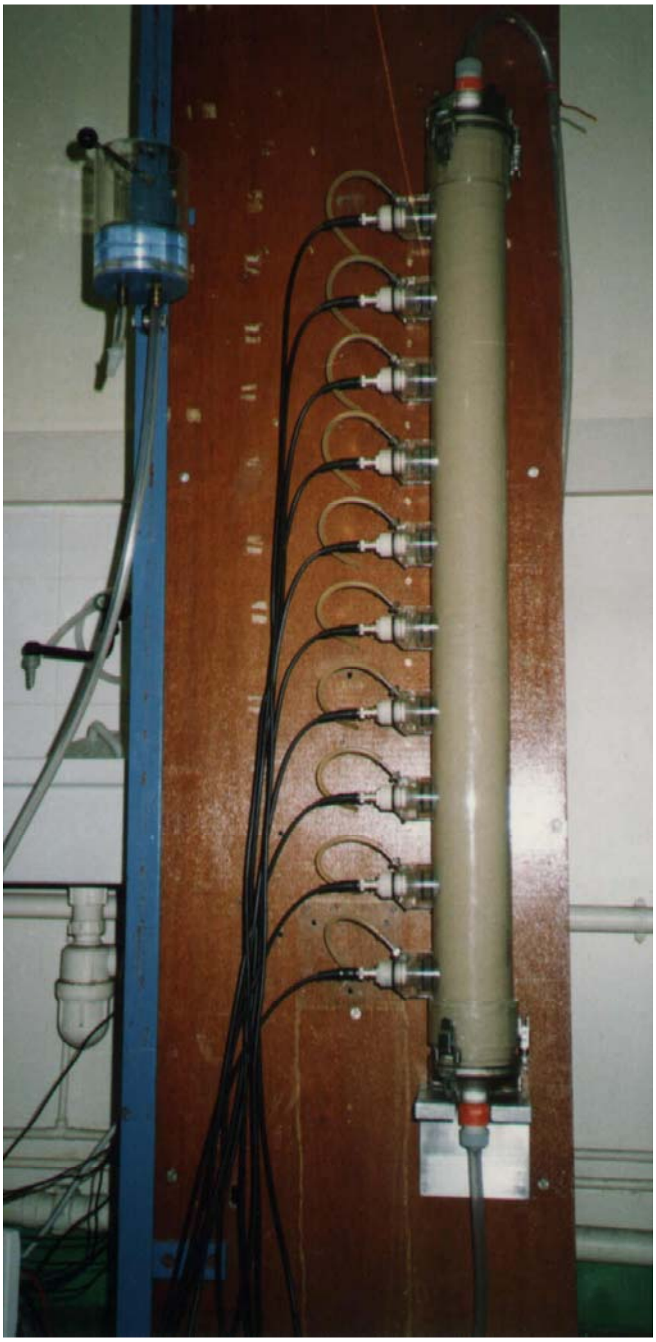

JOURNAL OF GEOPHYSICAL RESEARCH, VOL. 108, NO. B3, 2141, doi:10.1029/2001JB001517, 2003

Streaming potential of a sand column in partial saturation conditions

Xavier Guichet
École Normale Supérieure, Laboratoire de Géologie, Paris, France
Laboratoire des Géomatériaux, I.P.G.P., Université Paris (Denis Diderot), Paris, France

Laurence Jouniaux
École Normale Supérieure, Laboratoire de Géologie, Paris, France

Jean-Pierre Pozzi
École Normale Supérieure, Laboratoire de Géologie, Paris, France

Received 8 October 2001; revised 1 October 2002; accepted 31 October 2002; published 8 March 2003.

[1] The understanding of the streaming potential in partial water saturation conditions in porous media is of great interest for the interpretation of spontaneous polarization observations. We built a device which allows us to quantify the streaming potential at various saturation conditions using a sand column of 1-m height and 8-cm diameter. This is the first time that such a quantification has been performed. Different gases such as argon, nitrogen, and carbon dioxide are injected into the sand to decrease its water saturation, and to make the fluid flow within the sand. The measured electrokinetic coupling coefficient in partial saturation is either constant or decreases by a factor ~3 with decreasing water saturation from 100 to 40%, whereas the sand electrical resistivity is enhanced by a factor of ~5. *INDEX TERMS:* 5109 Physical Properties of Rocks: Magnetic and electrical properties; 5139 Physical Properties of Rocks: Transport properties; *KEYWORDS:* Streaming potential, partial saturation, electrokinetic, spontaneous potential, transport properties, porous media

Citation: Guichet, X., L. Jouniaux, and J.-P. Pozzi, Streaming potential of a sand column in partial saturation conditions, *J. Geophys. Res.*, *108*(B3), 2141, doi:10.1029/2001JB001517, 2003.

1. Introduction

[2] Spontaneous polarization (SP) anomalies are observed in several geophysical contexts. In tectonically active areas, the timescale of observed SP anomalies prior to earthquakes ranges from a few minutes to a few hours with an amplitude around 100 mV [for a review, see *Park et al.*, 1993]. On volcanoes, SP anomalies are used to define the lateral extent of the hydrothermal zone [*Finizola et al.*, 2002; *Ishido et al.*, 1997; *Jackson and Kauahikaua*, 1987; *Lénat et al.*, 2000; *Malengreau et al.*, 1994; *Zlotnicki et al.*, 1998, 1994] and show usually dipolar characteristics which can reach 4 V [*Finizola et al.*, 1998]. The thermoelectric effect, piezoelectric effect, or electrochemical effect have been proposed to explain SP anomalies, but the best candidate is the streaming potential, i.e., SP created by the motion of an electrolyte through a porous medium, related to a pressure gradient [*Zablocki*, 1978; *Zohdy et al.*, 1973]. Minerals forming the rock develop an electric double layer when in contact with an electrolyte, because the mineral surface is usually negatively charged. Qualitatively the fluid motion drags the electrical double layer with it, and a macroscopic separation of ions appears in the fluid, as the result of convection currents. The macroscopic electrical potential difference ΔV is called the streaming potential.

[3] In tectonically active zones, SP anomalies could be explained by a mechanism based on the fluid motions between reservoirs triggered by strain perturbations [*Bernard*, 1992], or by changes in high pore pressure in fault zones [*Fenoglio et al.*, 1995]. On volcanoes, the qualitative interpretation is that the negative anomalies observed on the flanks of volcanoes are associated with rainfall, which percolates downward. These negative anomalies can be related to the depth of the water table [*Aubert et al.*, 1993; *Zablocki*, 1978]. The positive anomalies observed on the active zone have their origin in upward convective flows [*Aubert and Kieffer*, 1984; *Zablocki*, 1978], and are used to define the hydrothermal zone. Electroseismic investigations are also based on the electrokinetic phenomena and are used to detect small rock interface property changes like permeability and saturation state [*Beamish*, 1999; *Garambois and Dietrich*, 2001].

[4] Modeling of all these observations needs a good understanding of electrokinetic phenomena. Therefore experimental studies have been performed for a better understanding of the electrokinetic effect at the level of the rock-electrolyte interface. Many streaming potential measurements have been made on crushed rocks at various temperatures or pH [*Ishido and Mizutani*, 1981; *Lorne et al.*, 1999a], on rock samples [*Jouniaux et al.*, 2000; *Jouniaux and Pozzi*, 1995, 1997; *Pengra et al.*, 1999], and during deformation [*Jouniaux et al.*, 1994; *Jouniaux and Pozzi*, 1995; *Lorne et al.*, 1999b; *Yoshida*, 2001]. However,

0148-0227/03/2001JB001517$09.00

only a few experiments have studied streaming potentials in two-phase flow conditions. *Antraygues and Aubert* [1993] measured the electrokinetic potential generated by wet steam flow in a vertical cylindrical column of porous material, using nonpolarising electrodes. They observed that the potential is mainly a function of the vapor flow rate, and an increase in the fraction of vapor can induce a large and long-lived increase in the potential differences along the vapor flow direction. Two-phase flow observations [*Antraygues and Aubert*, 1993; *Jiang et al.*, 1998; *Sprunt et al.*, 1994] are in agreement with the fact that partial saturation should increase the streaming potential, with or without a temperature effect, because the electrical resistance of the medium is increased.

[5] Measurements of streaming potentials of partially saturated rocks are therefore crucially needed since the partially saturated zone has to be taken into account to model and to interpret the SP observations. Indeed understanding and monitoring the distribution and transport of water using SP measurements has recently been reinvestigated [*Gibert and Pessel*, 2001; *Ishido and Pritchett*, 1999; *Sailhac and Marquis*, 2001]. Moreover, *Bernard* [1992] reported that strong local amplification was required for a streaming potential to be observed at long distances from its source. The effect of nonsaturating conditions on the streaming potential is expected to largely enhance the electrical signal, related to an enhancement of the electrical resistivity of the medium, and thus to be of great interest in the interpretation of SP observations. Nevertheless to take into account the electrokinetic coupling in partially saturated zones, geophysical methods must rely on accurate laboratory measurements for calibration.

[6] Measurements of streaming potential as a function of water saturation have not previously been reported in the literature. In this paper we measure the streaming potential in a column of sand in two-phase flow conditions, at various water saturations. Of specific interest to this study is the form and the magnitude of the coupling coefficient when the water content of the porous medium changes. Our measurements are the first quantification of the evolution of the electrokinetic coupling coefficient as a function of the water saturation. Attempts to model streaming potential in partial saturation state are also scarce, and hence we propound a phenomenological law describing the behavior of the coupling coefficient as a function of water saturation. Our measurements have also been compared to the model recently derived by *Revil et al.* [1999b].

2. Electrokinetic Phenomena

[7] In a saturated porous medium, and steady-state fluid circulation, a linear relation is observed between the macroscopic electrical potential difference ΔV and the applied pressure difference ΔP. The ratio $\Delta V/\Delta P$ is called the electrokinetic coupling coefficient (V/Pa):

$$C_{\mathrm{HS}} = \Delta V/\Delta P = (\varepsilon\zeta)/(\eta\sigma_f), \tag{1}$$

where ζ is the zeta potential defined as the electric potential on the shear plane, σ_f is the electric conductivity of the circulating fluid, $\varepsilon = \varepsilon_{\mathrm{water}}\,\varepsilon_0$ is the electric permittivity of the fluid with $\varepsilon_{\mathrm{water}}$ the relative dielectric constant of the fluid and $\varepsilon_0 = 8.84 \times 10^{-12}$ F/m the dielectric constant of vacuum, and $\eta = 10^{-3}$ Pa.s is the shear viscosity of the circulating fluid. The relative permittivity of water used is computed as a function of temperature according to results of *Malmberg and Maryott* [1956]. Equation (1) is obtained with the Helmholtz-Smoluchowski model, and it implies that the surface conductivity is small and negligible compared to the fluid conductivity σ_f, and that the convection and back currents are of equal magnitude and opposite along the same path [*Dukhin and Derjaguin*, 1974].

[8] Several models take into account the effects of surface electrical conductivity σ_s. For example, an empirical correction [*Ishido and Mizutani*, 1981; *Jouniaux et al.*, 2000; *Lorne et al.*, 1999a] replaces the electrolyte conductivity σ_f by the effective conductivity σ_{eff} in equation (1); the effective conductivity is defined by

$$\sigma_{eff} = F\sigma_r \tag{2}$$

where F is the formation factor and σ_r the electrical conductivity of the rock when the rock is saturated by a fluid, which has the same electrical conductivity than the fluid used for the electrokinetic measurement, and including possible surface conductivity.

[9] For a complete development of the equations governing the coupled electro-magnetics and flow of porous media, see *Pride* [1994], and *Revil et al.* [1999a, 1999b], and for further details on surface conductivity, see *Glover et al.* [1994] and *Revil and Glover* [1998].

[10] The effects of partial saturation S_w are not taken into account in equation (1). Recently *Revil et al.* [1999b] derived a new equation, which relates the electrokinetic coupling coefficient to the partial water saturation. The equation derived by *Revil et al.* [1999b] is rigorously valid for $m = n = 2$, with m being the Archie's first exponent ($m = -\ln F/\ln \Phi$ where Φ is the porosity) and n is Archie's second exponent ($\sigma_r(S_w < 1) = \sigma_r(S_w = 1)\, S_w^n$ where S_w is the water saturation) [*Archie*, 1942]. In the high-salinity domain (i.e., $\sigma_f \geq 5\,(m - 1)\sigma_s$), following the calculation process of *Revil et al.* [1999b] coupling results of Bussian's model [*Bussian*, 1983] with results of the model of *Pride* [1994], we have generalized their results to any values of m and n:

$$C(S_e \leq 1) = \frac{\varepsilon\zeta/\eta\sigma_f}{S_e^n\left(1 + m\left(\dfrac{F}{S_e^n} - 1\right)\dfrac{(\sigma_s/\sigma_f)}{S_e}\right)} \tag{3}$$

where S_e is the effective water saturation defined by

$$S_e = \begin{cases} \dfrac{S_w - S_{w0}}{1 - S_{w0}} & \text{as} \quad S_e > S_{w0} \\ 0 & \text{as} \quad S_e < S_{w0} \end{cases}. \tag{4}$$

where S_w is the water saturation and S_{w0} the water saturation below which there is no longer flow of the wetting phase. *Revil et al.* [1999b] foresaw an enhancement of the streaming potential with a decrease in the water saturation from unity to a critical value

$$S_e^c = \left(F\frac{\sigma_s}{\sigma_f}\right)^{1/(n+1)} \tag{5}$$

and that the coupling coefficient decreases below this critical value with decreasing water saturation until the S_{w0} water saturation value is reached.

[11] To take into account the influence of the partial saturation in equation (3), *Revil et al.* [1999b] used an equation for the electrical conductivity in partial saturation, which reduces in the high salinity domain to

$$\sigma_r = \frac{\sigma_f}{F} S_e^n + m\left(1 - \frac{S_e^n}{F}\right)\frac{\sigma_s}{S_e} \qquad (6)$$

This equation is obtained using empirical relationships developed by *Archie* [1942] and *Waxman and Smits* [1968]. However, equation (6) fails to explain the evolution of the electrical conductivity of a rock/fluid mixture below the critical water saturation S_e^c, since according to equation (6) the electrical conductivity of a rock/fluid mixture is expected to increase below the critical water saturation until the effective water saturation goes to zero. The increase of the electrical conductivity of a rock/fluid mixture with decreasing saturation has no physical meaning, since gas bubbles in the porous space behave like insulators. Therefore equation (3) can be only compared to measurements when the effective water saturation is greater than S_e^c.

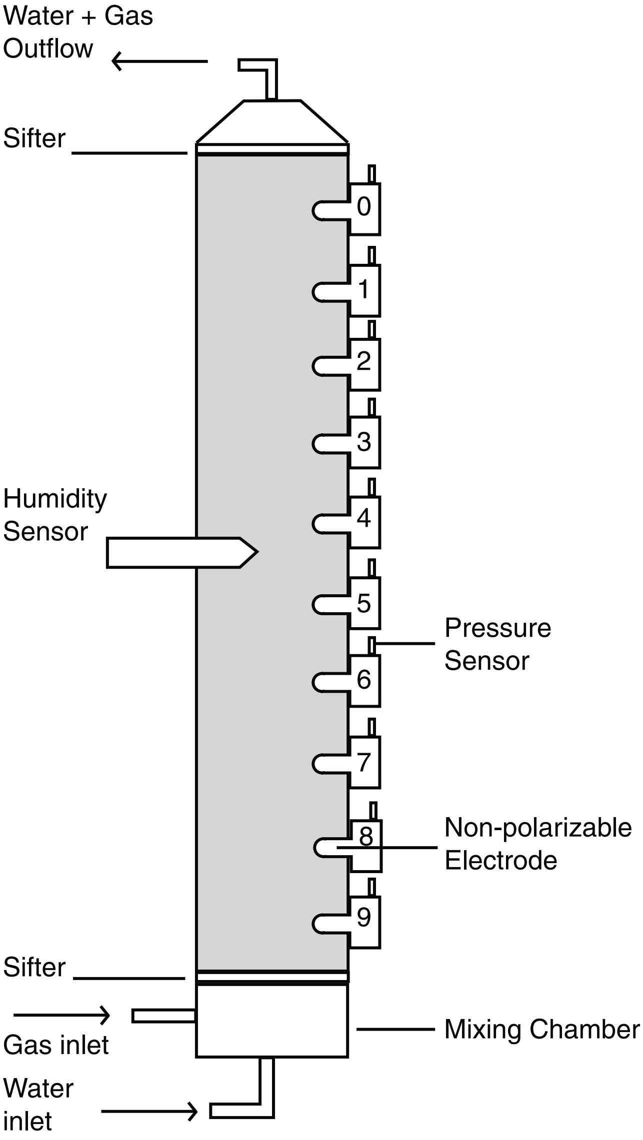

Figure 1. Sketch of the sand column of 1-m height and 8-cm diameter. Ten pressure sensors and electrodes are located along the column every 10 cm.

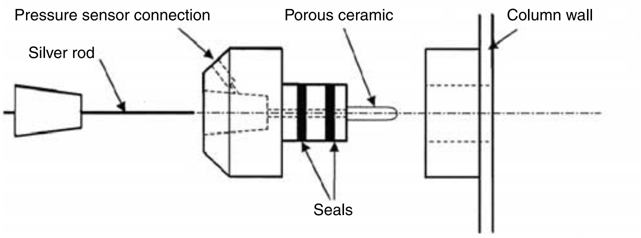

Figure 2. Sketch of an electrode.

[12] Equation (3) takes into account only the enhancement of the electrical potential caused by the insulating role of gas bubbles. In fact, the effects of gas bubbles in the pore are more complicated. There is a ζ-potential at the liquid-gas interface [*Graciaa et al.*, 1995]; the gas can react with the solution and change pH, and conductivity. These changes can be monitored but new ionic species due to gas dissolution can be adsorbed onto the mineral surface and can change the ζ-potential. The modification of the species adsorbed is not easy to take into account, and the reactions are not always known so that it is not possible to quantify a change in the ζ-potential.

3. Experimental Apparatus

[13] We use a 1-m high cylindrical column with an 8 cm inside diameter (Figure 1) that we fill with sand of known petrophysical properties. The water is made to flow through the sand column from bottom to top, using a reservoir located at incremental heights. Along the column, an electrode and a pressure sensor are placed every 10 cm. We monitor the humidity in the middle of the column by a capacitive sensor. At each end of the column sifters with 30 μm meshes allow measurement of the electrical resistivity of the whole column by an HP 4284A impedancemeter.

[14] We acquired the data in differential mode using high-resistance amplifiers and silver-silver chloride nonpolarising electrodes (Figure 2). They are grounded by coaxial wire, earthed at one of the 10 electrodes, which are numbered 0–9 from the top of the column (Figure 1). Each rod is put into a porous ceramic pot filled with deionised water, which is in contact with the porous medium, so that charge accumulation on the rods is avoided. The porous ceramics remain saturated unless a pressure of 0.1 MPa is applied, and therefore remain electrically conducting.

[15] Electrical surface conductivity is determined following the process drawn up by *Waxman and Smits* [1968]. A small device formed by a PVC cylinder 2.5 cm in diameter and 10 cm long, filled with the sand under study, enables us to measure the electrical conductivity of the sand for several electrolyte conductivities. Each measurement is made after waiting 1 day to ensure equilibrium between the electrolyte

Table 1. Measured Petrophysical Properties of the Sand[a]

Experiments	F	σ_s, S/m	n	Permeability, m^2
1–29	22	$<10^{-4}$	1.3	3×10^{-12}
30–43	15	$<10^{-4}$	1.3	3×10^{-12}

[a] F, formation factor; σ_s, electrical surface conductivity; n, Archie's second exponent.

and sand. We add sodium chloride in distilled water to control the conductivity of the electrolytes.

4. Method of Measurements

[16] The sand is sifted to have a mean grain diameter of 300 μm. In order to determine the initial mineralogy of the sand and possible mineralogical changes, we carry out X-ray diffraction analyses before any fluid circulation and after the circulation of each kind of gas.

[17] Once the column is filled with sand, we perform all the experiments for one kind of gas (argon or nitrogen), at various states of saturation. We only empty and refill the column with the same sand when we test a new gas.

[18] Deionised water is forced through the sand to saturate the pore space. The liquid-phase saturation S_w is measured with the capacitive sensor. First we check the linearity between fluid flow and pressure gradient for several heights of the water reservoir, and we calculate the permeability of the column using Darcy's law. Second a water reservoir height is chosen, and we check the linearity between the electrical potential gradient and the pressure gradient, leading to the saturated state coupling coefficient $C_m(S_w = 1)$.

[19] Then the reservoir is disconnected from the column. Gas is forced through the sand with a constant pressure of injection. The inlet pressure ranges from 29 to 32 kPa for argon injections, and from 23 to 30 kPa for nitrogen injections. The motion of the gas bubbles induces fluid flow, since gas circulation empties water from the column. Gas injection is maintained as long as necessary to reach a steady state, which is determined by the constant water flow rate. Flow rate values are around 10^{-3} l per min. Measurements of electrical potential and pressure of the steady state allow us to obtain an electrokinetic coefficient, for a partially saturated state $C_m(S_w)$. After each experiment, the electrical conductivity of the column is measured at 1 kHz, to determine Archie's second exponent.

[20] After circulation through the column, a sample of water is collected to measure pH and electrical conductivity. The chemical species, which are dissolved by circulation through the sand, are also tested.

5. Experimental Results

5.1. Petrophysical Properties of the Sand Column

[21] Table 1 lists the petrophysical properties of the sand column. X-ray diffraction revealed two kinds of sand minerals: quartz is the major component at around 98%, calcite the remaining 2%. After water circulation and gas injection, either argon or nitrogen, the major changes in composition are a decrease of the calcite peak associated with calcite dissolution. Calcite dissolution is revealed by chemical fluid analysis (Table 2), and the pH of the solutions (Tables 3 and 4) ranges from 6.8 to 8.7. The calcite-water-atmospheric CO_2 system balances at pH about 8.6 at room pressure and temperature [*Sigg et al.*, 2000].

[22] When the sand electrical conductivity is measured as a function of water conductivity, the conductivity of the fluid, which came out off the sand was never less than 4×10^{-3} S/m, even if the sand was saturated with distilled water. The increase of the fluid conductivity is related to exchange of ions between fresh distilled water and the rock matrix. Therefore the electrical surface conductivity of the sand cannot be measured exactly (Figure 3), but is estimated to be smaller than 2×10^{-4} S/m. *Revil and Glover* [1998] reported a surface conductance of 8×10^{-9} S for quartz, independent on the electrolyte conductivity when it exceeds 10^{-2} S/m. Electrical conductivities of the water circulating in the sand column are around 10^{-2} S/m (see Tables 3 and 4), so that we assume that the specific surface conductance of the sand is 8×10^{-9} S which is equivalent to a surface conductivity of about 1.0×10^{-4} S/m for a mean grain diameter of 300 μm. Note that the formation factor observed in Figure 3 is not the formation factor of the sand column; the sand is not packed down as it is in the column.

[23] Archie's second exponent n is deduced to be 1.3 according to equation (6) with negligible surface conductivity, by measuring the sand conductivity for several water saturations (Figure 4). *Waxman and Smits* [1968] reported that the n value is close to the value of Archie's first exponent m. *Archie* [1942] measured m of about 1.3 for relatively coarse granular media, giving confidence in the value of n that we deduced. The measured normalized

Table 2. Chemical Analyses of the Solutions After Flowing Through the Sand[a]

Experiment	Gas	Na^+, 10^{-3} mol/l	K^+, 10^{-3} mol/l	Ca^{2+}, 10^{-3} mol/l	Mg^{2+}, 10^{-3} mol/l	Cl^-, 10^{-3} mol/l	SO_4^{2-}, 10^{-3} mol/l	HCO_3^-, 10^{-3} mol/l	SiO_2, 10^{-3} mol/l	NH_4^+, 10^{-3} mol/l
1	none	0.191	0.095	0.719	0.010	0.257	0.036	1.515	0.218	···
18	argon	0.191	0.097	0.489	0.006	0.195	0.021	1.030	0.175	···
19–22	argon	0.213	0.097	0.559	0.005	0.186	0.065	1.394	0.184	···
23–25	argon	0.183	0.077	0.499	0.004	0.171	···	1.233	0.170	···
26–27	argon	0.178	0.072	0.584	0.003	0.210	0.021	1.313	0.166	···
33	nitrogen	0.161	0.036	0.514	0.019	0.149	···	1.010	0.180	0.025
34	nitrogen	0.174	0.059	0.599	0.016	0.171	···	0.909	0.161	0.026
35	nitrogen	0.148	0.056	0.367	0.009	0.460	···	···	0.082	0.010
39	nitrogen	0.148	0.026	0.302	0.007	0.282	0.052	0.534	0.170	0.017
41	nitrogen	0.157	0.023	0.402	0.009	0.138	···	1.010	0.184	0.027

[a] Amount of ion was not measured.

Table 3. Measurements of Coupling Coefficient $C_m(S_w \leq 1)$[a]

Experiment	Temperature, °C	Fluid Conductivity, μS/cm	pH	Saturation, S_w	C_m, mV/MPa	Error,%	Zeta Potential, mV	
							By equation (1)	By equation (8)
1	25.3	178	7.3	1	−1140	8	−29	. . .
2	20	99	8.0	1	−1750	5	−24	. . .
3	20.6	98	8.1	1	−1710	3	−24	. . .
4	19.8	93.5	8.0	1	−1780	1	−23	. . .
5	20.4	89.5	8.5	1	−1430	10	−18	. . .
6	21	91	8.4	1	−1660	4	−21	. . .
7	19.8	90.5	8.3	1	−1720	3	−22	. . .
8	20.4	90.5	8.3	1	−1730	4	−22	. . .
9	20.6	90	8.4	1	−1550	6	−20	. . .
10	20.8	102	8.7	1	−1660	5	−24	. . .
11	20.4	106.6	8.4	1	−1720	3	−26	. . .
12	20.4	105	8.5	1	−1760	2	−26	. . .
13	20.4	104	8.6	1	−1760	3	−26	. . .
14	20.6	99.2	8.5	1	−1740	4	−24	. . .
15	20.6	95.3	8.5	1	−1650	3	−22	. . .
16	21.3	264	8.1	1	−960	32	−36	. . .
17	24.6	145	7.9	0.81	−1290	4	−27	−22
18	25	146.8	8.0	0.73	−997	9	−21	−15
19	25	152	8.0	0.66	−866	13	−19	−13
20	24.6	164	8.1	0.65	−916	7	−22	−14
21	24.6	157	8.2	0.58	−1010	2	−23	−13
22	24.6	147	8.3	0.55	−1060	2	−22	−12
23	24.4	139	8.3	0.51	−1100	2	−22	−11
24	22.8	146	8.4	0.52	−721	12	−15	−8
25	23	133	8.5	0.48	−732	18	−14	−7
26	23.2	126	8.5	0.48	−860	14	−16	−7
27	23.2	126	8.6	0.46	−575	35	−10	−5
28	24.4	115.5	8.7	0.44	−669	30	−11	−5
29	24.4	105.5	8.7	0.43	−843	16	−13	−5

[a] Experiments 1–16 are conducted in saturated conditions and 17–29 are conducted when argon is forced through the sand column, at various water saturation S_w.

electrical resistivity is enhanced by a factor of about 5 while water saturation is decreased from 100 to 40%.

5.2. Coupling Coefficients Measurements

5.2.1. Saturated Sand Column

[24] The electric potential variations induced by pressure variations corresponding to water reservoir height of 0.6 m are shown in Figure 5. All potential measurements are referenced to electrode 0. The cause of the electrical noise with a period of about 60 s is not known. We note that the magnitude of the streaming potential is only about few mV, and measurements of streaming potential below 1 mV are difficult because of the noise. When a plateau is reached for both pressure and electrical potential, the changes in pressure and in potential are calculated from the initial state, for each electrode and pressure sensor couple. The potential varia-

Table 4. Measurements of Coupling Coefficient $C_m(S_c \leq 1)$[a]

Experiment	Temperature, °C	Fluid Conductivity, μS/cm	pH	Saturation, S_W	C_m, mV/MPa	Error, %
30	20	138	6.8	1	−1530	13
31	20	138	6.8	1	−1380	37
32	20	148	8.0	0.74	−2360	63
33	20	130	8.2	0.80	−1620	4
34	20	122	8.0	0.83	−1600	9
35	20	96	8.3	0.48	−1090	12
36	20	96	8.3	0.45	−1380	4
37	20	96	8.3	0.44	−1520	4
38	20	96	8.3	0.41	−1440	5
39	25	91	8.4	0.59	−1520	1
40	25	85	8.3	0.53	−1950	4
41	25.3	102	8.0	0.69	−1720	1
42	25.3	110.5	8.2	0.59	−2440	16
43	27.4	128	7.8	0.66	−1540	2

[a] Experiments 30–31 are conducted in saturated conditions and 32–43 are conducted when nitrogen is forced through the sand column, at various water saturation S_w.

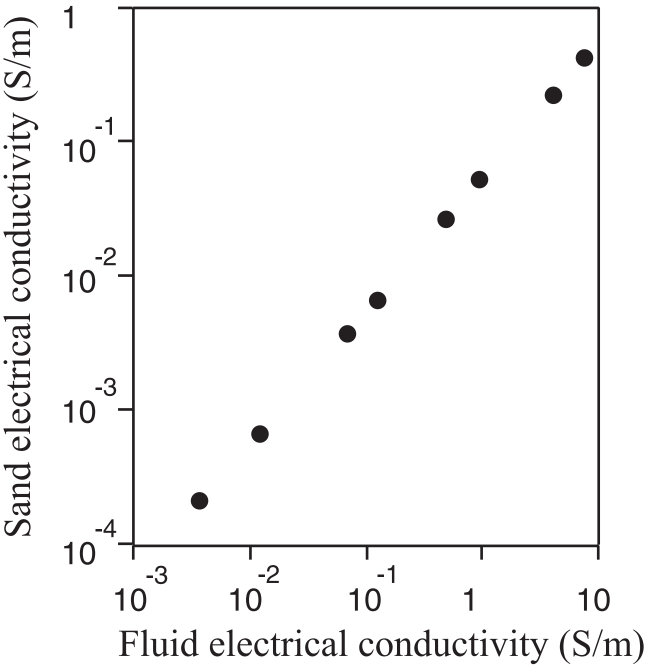

Figure 3. Electrical conductivity of the sand as a function of the electrical conductivity of NaCl solutions.

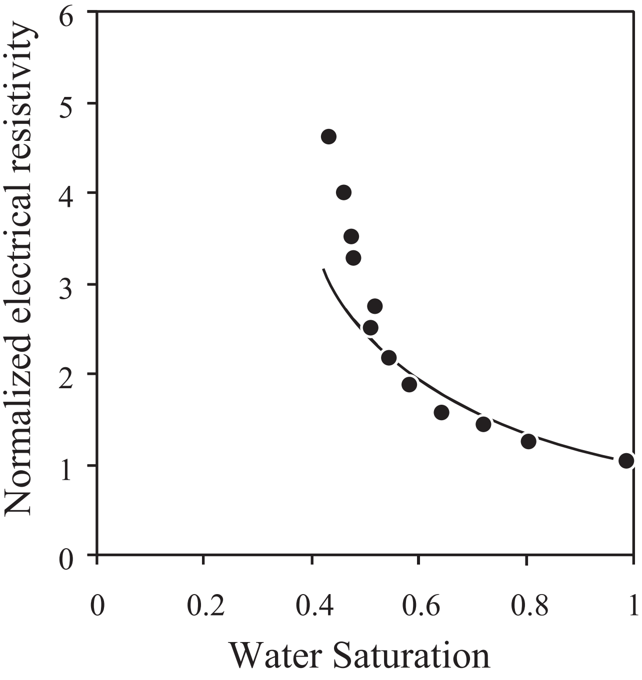

Figure 4. Normalized electrical resistivity of the sand as a function of water saturation. The curve fit to Archie's second law leads to n = 1.3.

tions of the eight electrodes as a function of the imposed pressure variation are shown in Figure 6. Linear regression (Figure 6) gives a value of the coupling coefficient: $C_m(S_w = 1) = -1140 \pm 92$ mV/MPa. In this experiment, (experiment 1 in Table 1) $\sigma_f = 1.78 \times 10^{-2}$ S/m, pH = 7.3.

5.2.2. Partially Saturated Sand Column

[25] A first result is that the streaming potential remains proportional to the driving pressure when the sand is not saturated (Figure 7). Measured coupling coefficients at various saturations are shown in Tables 3 and 4 when argon and nitrogen are made to flow respectively.

[26] The measured coupling coefficients range from −575 to −2440 mV/MPa, depending on water saturation, electrical conductivity, and pH of the electrolyte (Tables 3 and 4). The variation of the coupling coefficient versus water saturation is shown in Figure 8 for argon and nitrogen circulation. In the case of argon circulation, a decrease of the coupling coefficient (in absolute value) is observed with decreasing water saturation. While the water saturation varies from 1 to 0.4, the absolute value of the coupling coefficient is reduced by a factor of ~3. The coupling coefficients obtained with nitrogen circulation have large error bars, and it is difficult to distinguish a clear behavior versus water saturation. The coupling coefficient remains roughly constant.

[27] With decreasing water saturation, the electrical conductivity and the pH of the electrolyte also change as shown in Tables 3 and 4. Therefore the variations in coupling coefficients shown in Figure 8 may be also related to electrical conductivity and pH variations.

6. Discussion

[28] We begin by looking for a simple relation between water saturation and the measured coupling coefficients without taking into account changes in water pH and conductivity (Figure 8). In the case of argon circulation, it appears that the coupling coefficient decreases lineary with increasing water saturation:

$$C(S_w \leq 1) = AS_w + B \tag{7}$$

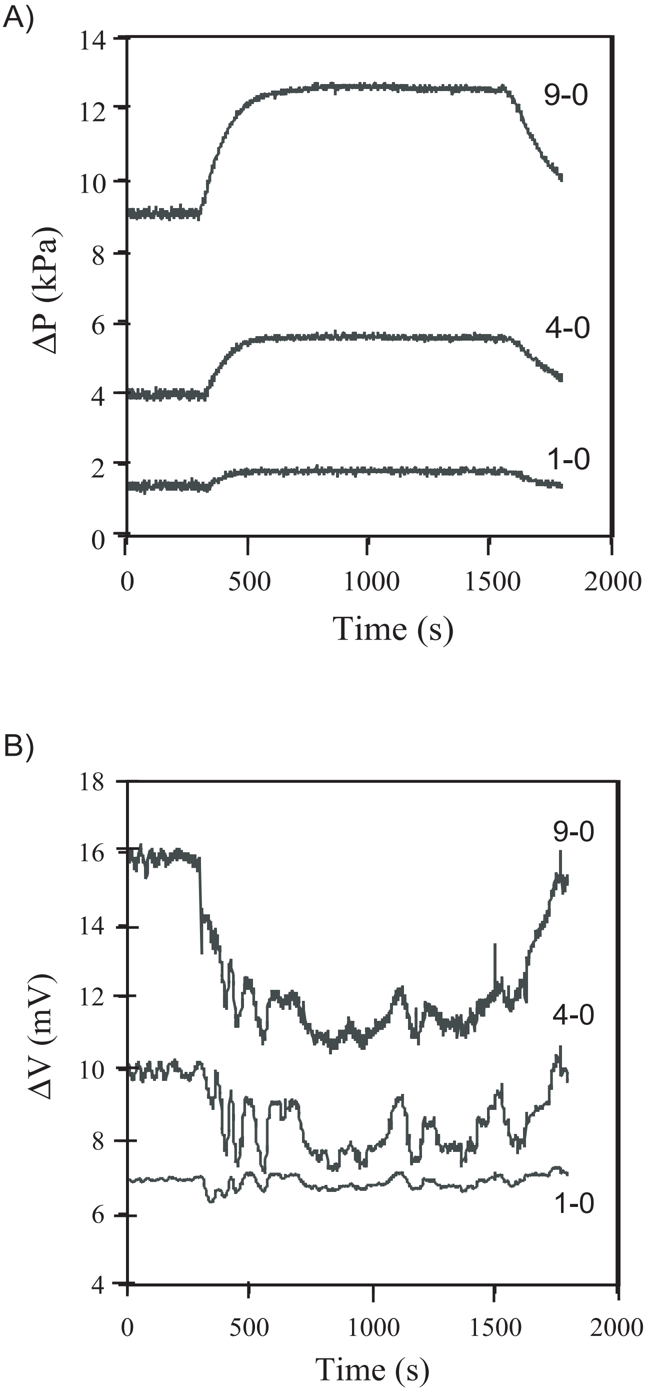

Figure 5. (a) Evolution of three pressure differences referenced to the sensor 0 with the reservoir located at around 60 cm above the top of the column. Water flows between 300 and 1600 s. (b) Evolution of three electrical potential differences referenced to the electrode 0, when water is forced through the sand column with the same conditions as in Figure 5a.

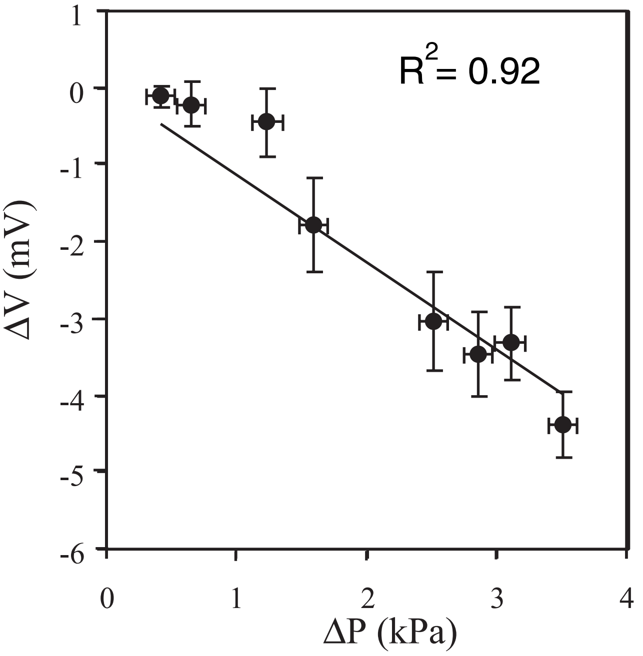

Figure 6. Streaming potential differences versus applied pressure differences in steady state and saturated state. The determination of the coupling coefficient is from the linear regression curve shown.

where *A* and *B* are constants. Since there is no fluid flow when the porous medium is totally dry, *B* should be equal to zero. When the water saturation equals unity, the simplest expression of the constant *A* is the Helmholtz-Smoluchowski relation (equation (1)). This relation is valid when the surface electrical conductivity of the sample is negligible. Since the surface electrical conductivity for our sample is too low to be measured, we assume that equation (1) is valid. Therefore equation (7) becomes

$$C(S_w \leq 1) = \frac{\varepsilon\zeta}{\eta\sigma_f} S_w \tag{8}$$

We have to take into account the variation of the ζ-potential with fluid conductivity in order to compare our measurements to the coupling coefficient calculated according to

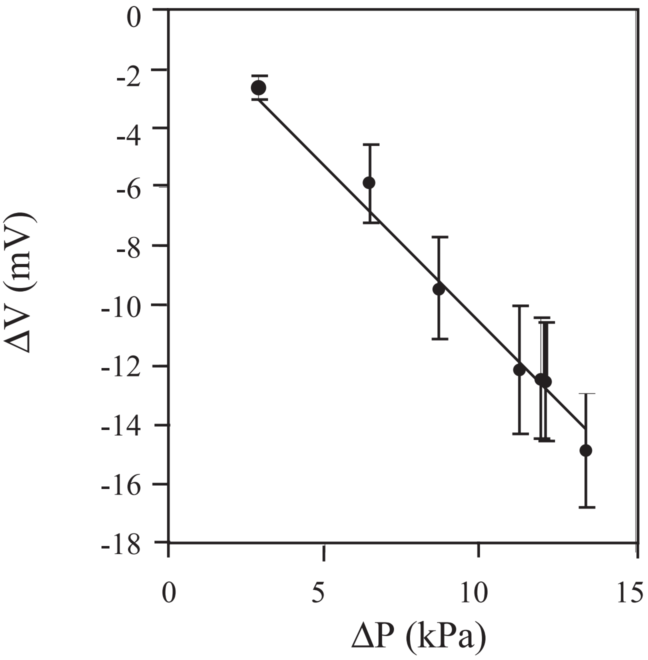

Figure 7. Streaming potential differences versus applied pressure differences in steady state and partially saturated state. The determination of the coupling coefficient is from the linear regression curve shown.

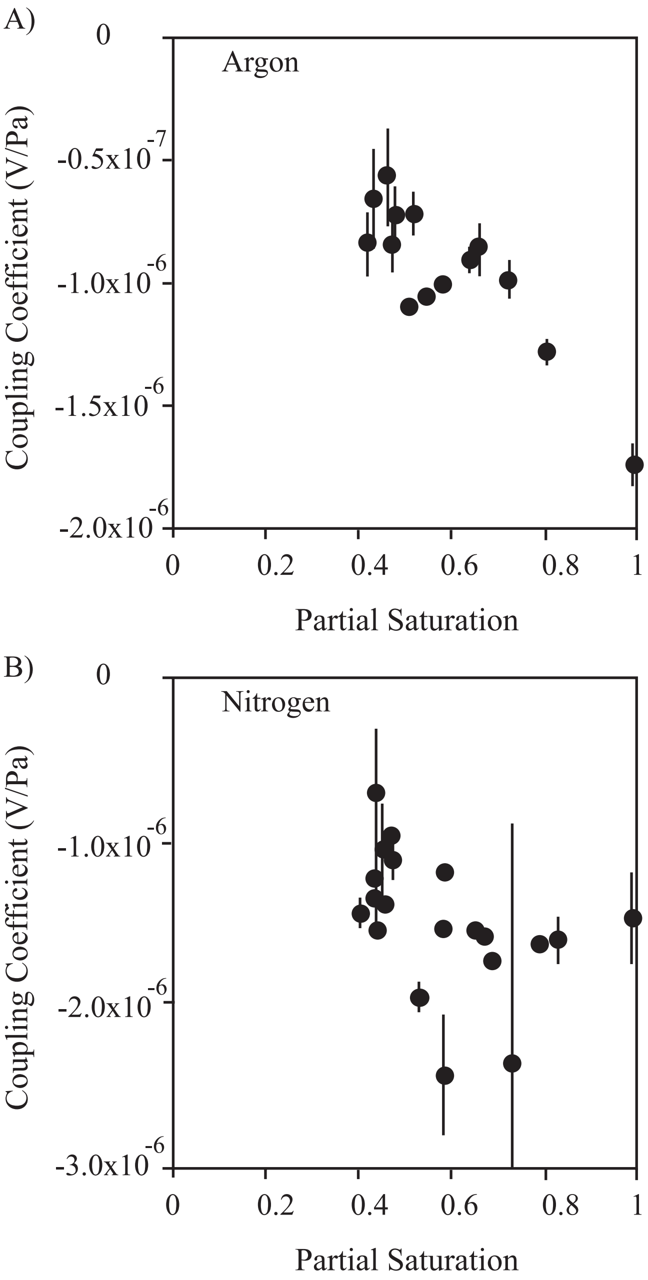

Figure 8. Variation of the measured coupling coefficient versus water saturation. Water pH and conductivity changes are reported in Tables 3 and 4. (a) Argon circulation. (b) Nitrogen circulation.

equation (8). To compute equation (8), all the parameters are measured except the ζ-potential. Since the ζ-potential originates at the water-rock interface and is related to the water composition [*Davis and Kent*, 1990; *Ishido and Mizutani*, 1981], we make the assumption that the ζ-potential is not influenced by the saturation state for our experiments. This assumption can be justified by (1) nitrogen and argon are inert gases which do not change the chemical composition of the circulating water, (2) the liquid phase remains the wetting phase because the water saturation is always greater than 0.4 (Tables 3 and 4). Point (2) is deduced from our electrical resistivity measurements (Figure 4); indeed in water wet systems, the electrical resistivity of rocks shows two domains as a function of water saturation. In the first, the resistivity increase is associated with the removal of bulk water, the normalised resistivity, and the water saturation are linear in a log resitivity-linear saturation plot, and the resistivity increase is about 1 order of magnitude; in the second, the resistivity increase is partly caused by water inside the network which is physically isolated by gas bubbles. The film of water wetting the grain surface provides a path for electrical flow, and the normalised resistivity shows an increase of several orders in magnitude in a log linear plot versus water saturation. The reader can find, for example, measurements of electrical resistivity versus water saturation in the work of *Roberts and Lin* [1997] and simulation in the work of *Suman and Knight* [1997]. In our study, the normalised electrical resistivity is increased only by about ~5 (Figure 4), so that the current path is provided by bulk water, meaning that the electrical double layer is not disturbed by gas bubbles.

[29] Next we seek an empirical expression from which to estimate ζ-potential versus water conductivity to insert into equation (8). Using our measurements performed in saturated state at pH = 8.3 ± 0.25, the ζ-potential according to equation (1) is related to the electrolyte electrical conductivity in the range $10^{-2} - 2.5 \times 10^{-2}$ S/m by a logarithmic relation (Figure 9)

$$\zeta(V) = -0.0146\ln(\sigma_f) - 0.0854 \tag{9}$$

meaning that the ζ-potential decreases with increasing fluid conductivity, which is the reverse of the usual variation. Actually the ζ-potentials measured on crushed Fontainebleau sandstones by *Lorne et al.* [1999a] show an increase, with increasing fluid electrical conductivity, of about 20 mV per decade in the range 10^{-4} to 10^{-1} S/m, in agreement with the compilation of *Pride and Morgan* [1991]

$$\zeta(\mathrm{mV}) \propto 20\log_{10}(\sigma_f) \tag{10}$$

We do not discuss here this unusual variation of ζ-potential with fluid electrical conductivity. Knowing the fluid electrical conductivity for each experiment, the ζ-potential is calculated using equation (9), and the electrokinetic coupling coefficient is computed with equation (8) for various saturation states, and compared to the measured electrokinetic coupling coefficient in Figure 10. In the case of argon circulation, the calculated coupling coefficients are in reasonable agreement with the measured coupling coefficients (Figure 10a). On the other hand, equation (8) fails to explain the measurements in the case of nitrogen circulation (Figure 10b). When using equation (10) to describe the variation of zeta potential with water conductivity, the results are roughly the same.

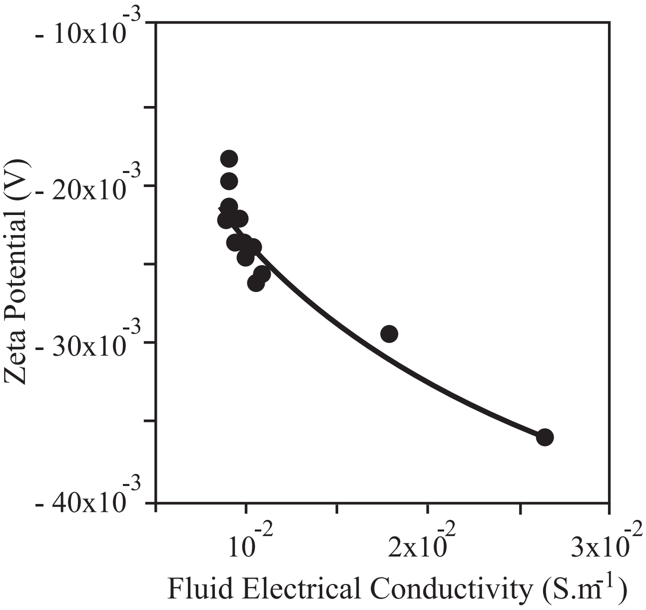

Figure 9. Variation of the ζ-potentials deduced using equation (1) from the measured coupling coefficients in saturated state (experiments 1–16) as a function of the fluid electrical conductivity. The pH values are in the range 7.3–8.7.

[30] Since a relatively good estimate of the coupling coefficient in partial saturation is obtained in Figure 10a for argon circulation, we compare the ratio $C_m(S_w < 1)/C_m(S_w = 1)$ of the measured coupling coefficient in partial water saturation to the measured coupling coefficient of the saturated sand, with the ratio

$$\frac{C(S_w \leq 1)}{C(S_w = 1)} = S_w \tag{11}$$

in order to interpret the evolution of the measured coupling coefficient versus water saturation. To compare the ratio $C_m(S_w < 1)/C_m(S_w = 1)$ to the ratio as in equation (11), experiments in saturated and in partially saturated states must be conducted with the same pH and electrical conductivity of the electrolyte. Otherwise we will not be able to discern the variations of the coupling coefficient related to electrolyte properties from the variations of the coupling coefficient related to the partial saturation condition. The ζ-potential depends on the electrical conductivity and on the pH of the electrolyte, but the partial saturation is not assumed to have an influence on the ζ-potential [*Revil et al.*, 1999b]. Thus the ζ-potential is deduced from our measurements according to equation (8), and empirical relations are used to correct pH and fluid electrical conductivity variations. To perform pH corrections, we use the experimental law determined by *Lorne et al.* [1999a] for crushed Fontainebleau sandstones, which relates the ζ -

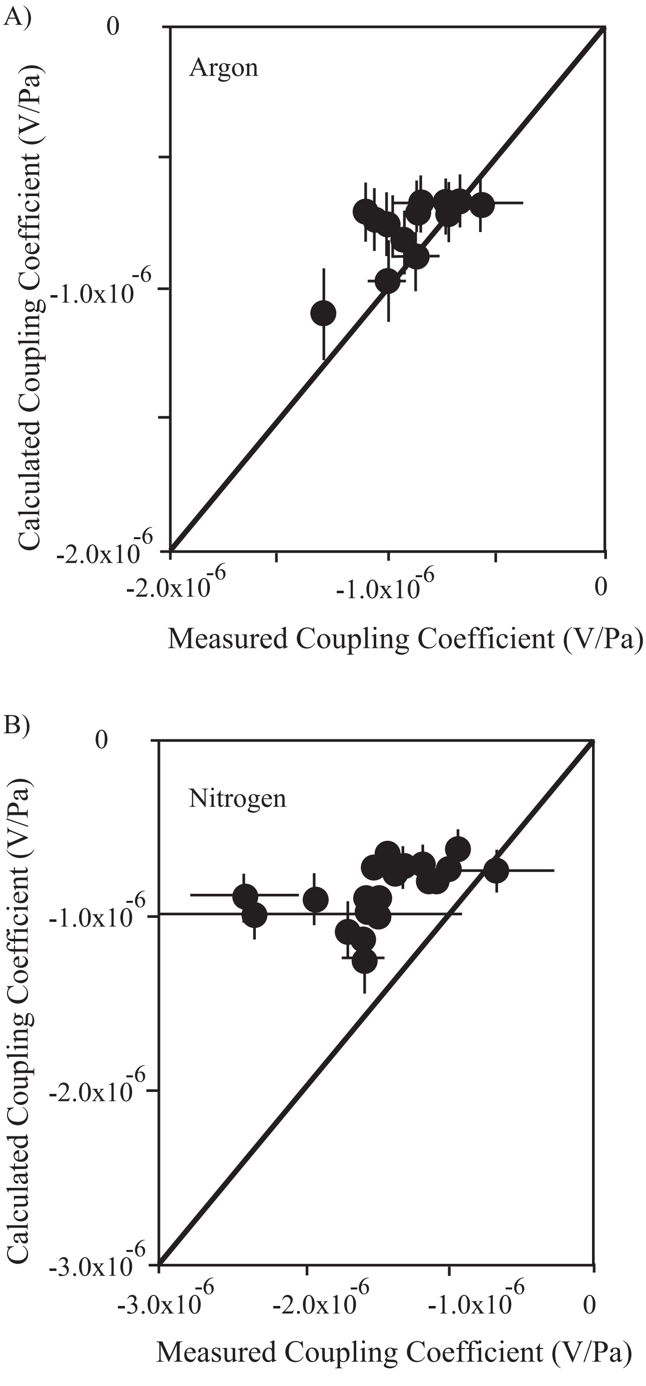

Figure 10. Coupling coefficient in partial saturation state. Comparison between the prediction of the coupling coefficient from equation (8) using equation (9) to calculate the ζ-potential and our measurements. The line has a slope of unity to compare measured and calculated values.

potential (in V) measured at pH = pH$_0$ to the ζ-potential at pH = pH$_1$ through a linear relation

$$\zeta(\mathrm{pH}_1) = (\mathrm{pH}_0) - (\mathrm{pH}_1 - \mathrm{pH}_0) \times 1.45 \times 10^{-3} \qquad (12)$$

[31] Electrolyte conductivity corrections are made using either equation (9) or equation (10). The ratio C_m (S_w < 1)/ C_m(S_w = 1) that would have been measured at a fixed pH (pH = 8) and a fixed fluid electrical conductivity (1.4 × 10^{-2}) is calculated using the corrected ζ-potential values in accordance with equation (13)

$$\frac{C_m(S_w \leq 1)}{C_m(S_w = 1)} = \frac{\zeta(S_w \leq 1)}{\zeta(S_w = 1)} \times S_w \qquad (13)$$

[32] When argon is made to flow, the saturation ranges from approximately 40 to 80% (Figure 11). The normalized

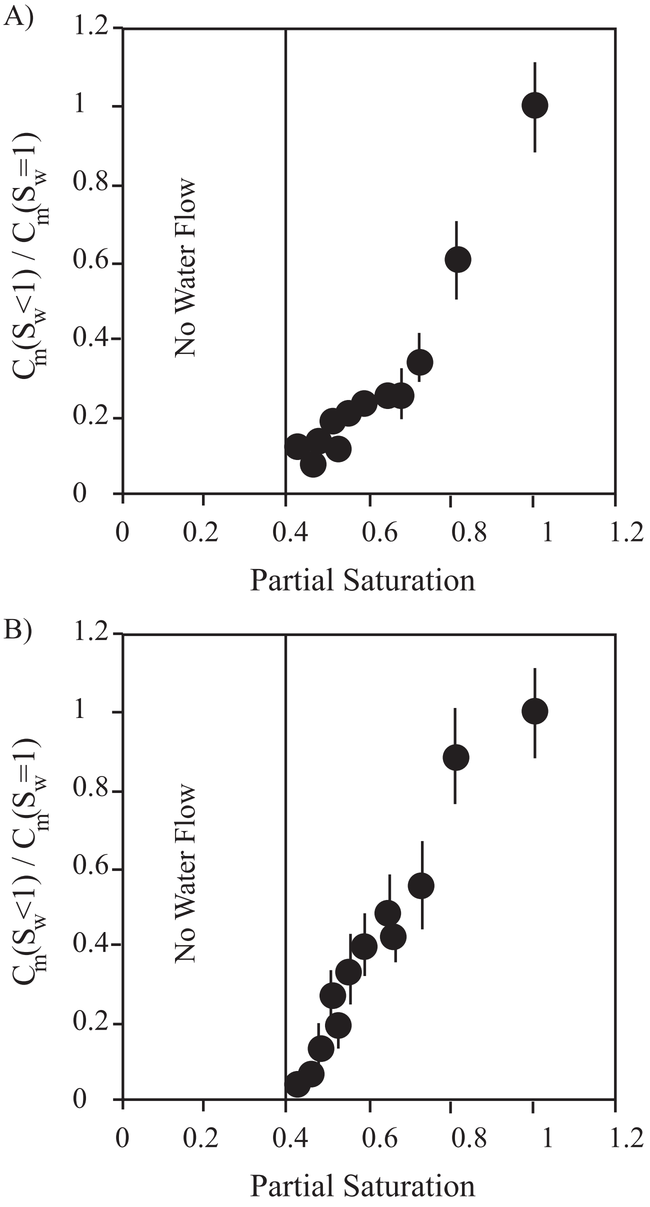

Figure 11. Normalized coupling coefficient $C_m(S_w < 1)/C_m(S_w = 1)$ versus water saturation. The ζ-potential is assumed to be insensitive to water saturation, and is calculated using equation (8). The gas injected is argon. (a) The experimental results are corrected for pH (equation (12)) and fluid electrical conductivity (equation (9)) variations in ζ-potential are corrected to a pH value of 8 and a fluid electrical conductivity value of of 140 μS/cm. (b) The experimental results are corrected for pH (equation (12)) and fluid electrical conductivity (equation (10)) variations in ζ-potential are corrected to a pH value of 8 and a fluid electrical conductivity of 140 μS/cm.

coupling coefficient decreases while the water saturation decreases, and equals zero as the water saturation reaches 40%. The behavior of the normalized coupling coefficient is not greatly affected by the ζ-potential changes versus water conductivity according to either equation (9) (Figure 11a) or equation (10) (Figure 11b). The normalized coupling coefficient is not in agreement with equation (11), but decreases according to a rough linear relation with water saturation. The phenomenological equation (8) does not take into account the water saturation S_{w0} under which the water in the porous media does not flow. According to Figure 11, the water saturation S_{w0} can be estimated to be about 40%. Note that when the water saturation is 40% (experiment 29 in Table 3), the water starts to flow out of the column 75 min after the beginning of the gas circulation. Our measurements in the case of argon can be explained by equation (8) if the water saturation is replaced by the effective water saturation. We do not observe any enhancement of the coupling coefficient with two-phase flow as reported by *Antraygues and Aubert* [1993] and *Sprunt et al.* [1994]. Nevertheless, the electrical resistivity of the porous medium increases by a factor of $\sim$5 when the water saturation ranges from 100 to 40% (Figure 4). During experiments, *Antraygues and Aubert* [1993] injected wet steam in a vertical column. Initially their medium was not saturated, and was at room temperature. The steam warmed and condensed into the column. The authors did not control humidity, and could not distinguish the effect of partial saturation from the effect of temperature. An increase of temperature enhances the ζ-potential, and therefore the coupling coefficient [*Ishido and Mizutani*, 1981]. *Sprunt et al.* [1994] performed experiments on limestone samples, in which they injected gas bubbles. They observed an increase of 2 orders of magnitude in the coupling coefficient in partial saturation. However, they did not use nonpolarising electrodes; futhermore the authors mentioned that gas bubbles were trapped in the electrode enclosures, and that the voltage was unstable during the passage of the bubbles. Therefore the increase of the coupling coefficient observed by *Sprunt et al.* [1994], was probably due to bubbles being trapped in the electrodes, which cannot occur in our experimental setup because porous ceramics were used.

[33] Finally if we assume that the water saturation S_{w0} is close to 40%, we can calculate the coupling coefficient in partial saturation conditions according to equation (3), for an effective saturation greater than the critical saturation S_e^c, which is in our case about 50%. In Figure 12, the calculated coupling coefficient, assuming a ζ-potential independent of water saturation (using equation (9)), is plotted versus the measured coupling coefficient. The calculated coupling coefficients are not in agreement with the measured ones.

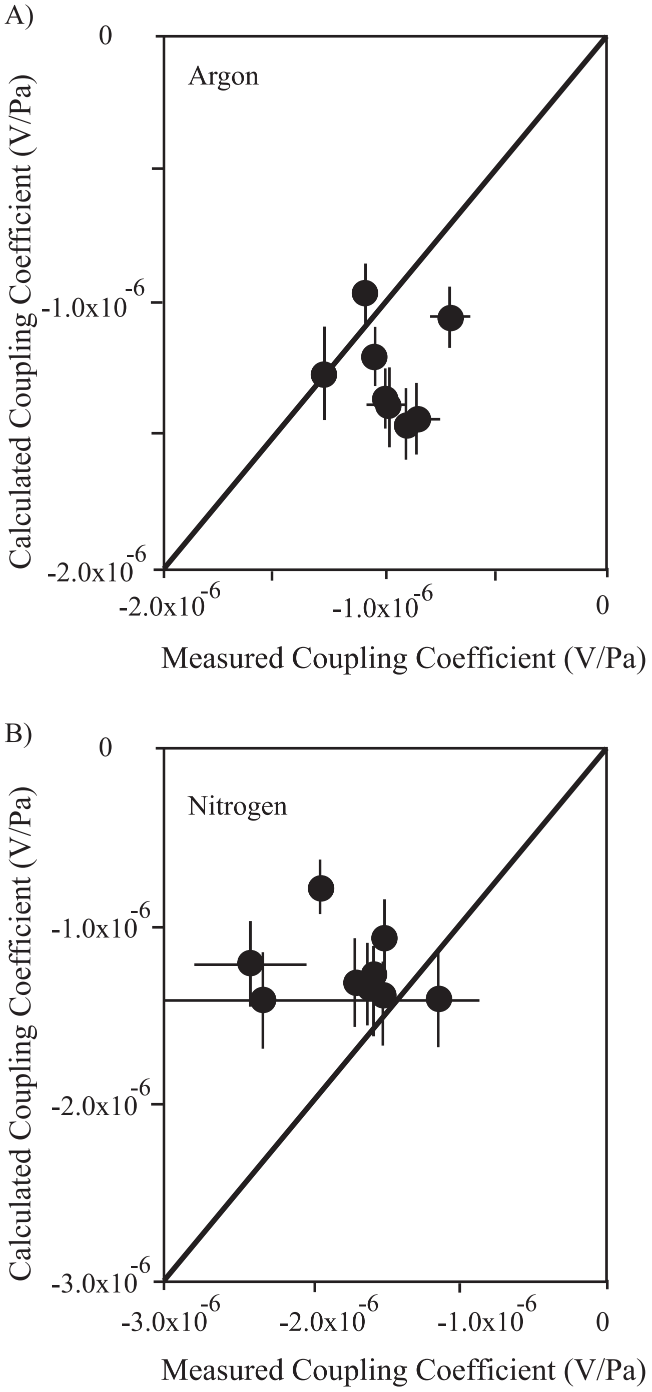

Figure 12. Coupling coefficient in partial saturation state. Comparison of the prediction of the coupling coefficient in equation (3) derived by *Revil et al.* [1999b] and our measurements, with the effective water saturation greater than the critical saturation S_e^c (about 50% for our sand). The ζ-potential is calculated according to equation (9). The line has a slope of unity to compare measured and calculated values. (a) Argon circulation. (b) Nitrogen circulation.

[34] We carried out experiments with carbon dioxide to take into account chemical changes in two-phase flow conditions. When carbon dioxide is forced through the sand column, the pH of the solution ranges from 5.8 to 7.9, and the electrical conductivity of the solution ranges from 1.6×10^{-2} to 0.18 S/m. Carbon dioxide circulation leads to lower pH and higher electrical conductivity of the solution than argon and nitrogen circulation does, because carbon dioxide is a reagent gas at room pressure and temperature. When the electrical conductivity of the solution increases, the coupling coefficient decreases (equation 1). Thus for a given pressure difference, the induced voltages are smaller and their measurement is more difficult. The increase of 1 order of magnitude in the electrical conductivity of the solution

makes the determination of the coupling coefficient in saturated and in partially saturated state unreliable for the pressure differences that we can reach. Therefore we cannot deduce either an increase or a decrease of the electrokinetic coupling coefficient with decreasing saturation when carbon dioxide is used. However, if the electrokinetic coupling coefficient had been enhanced by a factor 10, we would have been able to measure it.

7. Conclusion

[35] The measured electrokinetic coupling coefficient in partial saturation is either constant or decreases by a factor of ~3 with decreasing water saturation from 100 to 40%, whereas the electrical resistivity is enhanced by a factor of ~5. Our measurements show that the critical saturation below which there is no longer fluid flow, and therefore no electrokinetic coupling, is about 40% for our sand. Our measurements are the first to provide the evolution of the coupling coefficient versus water saturation. Nevertheless we observe two different behaviors, so that it is not possible to provide a general evolution of the streaming potential in the partially saturated state. We hope that these measurements will motivate further theoretical and experimental investigations of electrokinetic phenomena in the partially saturated state.

[36] The main conclusion of our study for geophysical interpretation is that the electrokinetic coupling coefficient does not increase with decreasing water saturation. During laboratory measurements, the convection current due to fluid flow is exactly balanced by the conduction current. To interpret self potential measurements performed in the field, the convection current has to be calculated in partially saturated crust taking into account the increase of the electrical resistivity, but the electrokinetic coupling coefficient itself is not enhanced.

[37] **Acknowledgments.** We thank J.L. Thony and J.P. Laurent for providing us basic equipment of the sand column. We thank G. Marolleau for his help in the construction of the apparatus, N. Catel for water analysis, and L. Mamou for the X-ray diffraction analyses. This paper has been greatly improved by constructive remarks from the associated editor Kathy Whaler, the reviewer T. Ishido, and an anonymous reviewer. This research was supported by CNRS and by ACI Prévention des Catastrophes Naturelles. This is a CNRS-INSU-PNRH contribution 324 (thème circulation des fluides dans la croûte), and a CNRS-INSU-PNRN contribution 324 (Thème risques volcaniques).

References

Antraygues, P., and M. Aubert, Self potential generated by two phase flow in a porous medium: Experimental study and volcanological application, *J. Geophys. Res.*, *98*, 22,273–22,281, 1993.

Archie, G. E., The electrical resistivity Log as an aid in determining some reservoir characteristics, *Trans. Am. Inst. Min. Metall. Pet. Eng.*, *146*, 54–62, 1942.

Aubert, M., and G. Kieffer, Evolution d'une intrusion magmatique dans le flanc sud de l'Etna entre juin 1982 et juin 1983, Résultats de potentiel spontané (PS) et essai d'interprétation de l'éruption de 1983, *C. R. Acad. Sci., Ser. II*, *298*, 379–382, 1984.

Aubert, M., P. Antraygues, and E. Soler, Interprétation des mesures de polarisation spontanées (PS) en hydrogéologie des terrains volcaniques. Hypothèse sur l'existence d'écoulements préférentiels sur le flanc sud du Piton de la Fournaise (île de la Réunion), *Bull. Soc. Géol. France*, *164*, 17–25, 1993.

Beamish, D., Characteristics of near-surface electrokinetic coupling, *Geophys. J. Int.*, *132*, 231–242, 1999.

Bernard, P., Plausibility of long distance electrotelluric precursors to earthquakes, *J. Geophys. Res.*, *97*, 17,531–17,546, 1992.

Bussian, A. E., Electrical conductance in a porous medium, *Geophysics*, *48*(9), 1258–1268, 1983.

Davis, J. A., and D. B. Kent, Surface complexation modeling in aqueous geochemistry, in *Mineral Water Interface Geochemistry*, edited by M. F. Hochella and A. F. White, Mineral. Soc. of Am., Washington, D.C., 1990.

Dukhin, S. S., and B. V. Derjaguin, Electrokinetic phenomena, in *Surface and Colloid Science*, edited by E. Matijevic, chap. 1, pp. 1–48, John Wiley, New York, 1974.

Fenoglio, M. A., M. J. S. Johnston, and J. D. Byerlee, Magnetic and electric fields associated with changes in high pore pressure in fault zones: Application to the Loma Prieta ULF emissions, *J. Geophys. Res.*, *100*, 12,951–12,958, 1995.

Finizola, A., D. Ramos, and O. Macedo, Self potential studies of hydrothermal systems structure on Misti and Ubinas volcanoes south Peru, *XXIII Gen. Assem. EGS, Nice*, C194, 1998.

Finizola, A., F. Sortino, J. F. Lénat, and M. Valenza, Fluid circulation at Stromboli volcano from self-potential and CO_2 surveys, *J. Volcanol. Geotherm. Res.*, *116*, 1–18, 2002.

Garambois, S., and M. Dietrich, Seismoelectric wave conversions in porous media: Field measurements and transfer function analysis, *Geophysics*, *66*(5), 1417–1430, 2001.

Gibert, D., and M. Pessel, Identification of sources of potential fields with the continuous wavelet form: Application to self-potential profiles, *Geophys. Res. Lett.*, *28*, 1863–1866, 2001.

Glover, P. W. J., P. G. Meredith, P. R. Sammonds, and S. A. F. Murrell, Ionic surface electrical conductivity in sandstone, *J. Geophys. Res.*, *99*, 21,635–21,650, 1994.

Graciaa, A., G. Morel, P. Saulnier, J. Lachaise, and R. S. Schechter, The zeta-potential of gas bubbles, *J. Colloid Interface Sci.*, *172*, 131–136, 1995.

Ishido, T., and H. Mizutani, Experimental and theoretical basis of electrokinetic phenomena in rock-water systems and its applications to geophysics, *J. Geophys. Res.*, *86*, 1763–1775, 1981.

Ishido, T., and J. W. Pritchett, Numerical simulation of electrokinetic potentials associated with subsurface fluid flow, *J. Geophys. Res.*, *104*, 15,247–15,259, 1999.

Ishido, T., T. Kikuchi, N. Matsushima, Y. Yano, S. Nakao, M. Sugihara, T. Tosha, S. Takakura, and Y. Ogawa, Repeated self-potential of Izu-Oshima volcano, Japan, *J. Geomagn. Geoelectr.*, *49*, 1267–1278, 1997.

Jackson, D. B., and J. Kauahikaua, Regional self-potential anomalies at Kilauea volcano, *U.S. Geol. Surv. Prof. Pap.*, *1350*, 947–959, 1987.

Jiang, Y. G., F. K. Shan, H. M. Jin, L. W. Zhou, and P. Sheng, A method for measuring electrokinetic coefficients of porous media and its potential application in hydrocarbon exploration, *Geophys. Res. Lett.*, *25*, 1581–1584, 1998.

Jouniaux, L., and J.-P. Pozzi, Streaming potential and permeability on saturated sandstones under triaxial stress: Consequences for electrotelluric anomalies prior to earthquakes, *J. Geophys. Res.*, *100*, 10,197–10,209, 1995.

Jouniaux, L., and J.-P. Pozzi, Anomalous 0.1–0.5 Hz streaming potential measurements under geochemical changes: Consequences for electrotelluric precursors to earthquakes, *J. Geophys. Res.*, *102*, 15,335–15,343, 1997.

Jouniaux, L., S. Lallemant, and J.-P. Pozzi, Changes in the permeability, streaming potential and resistivity of a claystone from the Nankai prism under stress, *Geophys. Res. Lett.*, *21*, 149–152, 1994.

Jouniaux, L., M. L. Bernard, M. Zamora, and J. P. Pozzi, Streaming potential in volcanic rocks from Mount Pelée, *J. Geophys. Res.*, *105*, 8391–8401, 2000.

Lénat, J. F., D. Fitterman, and D. B. Jackson, Geoelectrical structure of the central zone of the Piton de la Forunaise volcano (Réunion), *Bull. Volcanol.*, *62*(2), 75–89, 2000.

Lorne, B., F. Perrier, and J.-P. Avouac, Streaming potential measurements, 1, Properties of the electrical double layer from crushed rock samples, *J. Geophys. Res.*, *104*, 17,857–17,877, 1999a.

Lorne, B., F. Perrier, and J.-P. Avouac, Streaming potential measurements, 2, Relationship between electrical and hydraulic flow patterns from rock samples during deformation, *J. Geophys. Res.*, *104*, 17,879–17,896, 1999b.

Malengreau, B., J. F. Lénat, and A. Bonneville, Cartographie and temporal observation of self-potential (SP) anomalies at Piton de la Fournaise, *Bull. Soc. Géol. France*, *165*, 221–232, 1994.

Malmberg, C. G., and A. A. Maryott, Dielectric constant of water from 0° to 100°C, *J. Res. Natl. Bur. Stand. U.S.*, *56*(1), 2641, 1956.

Park, S. K., M. J. S. Johnston, T. R. Madden, F. D. Morgan, and H. F. Morrison, Electromagnetic precursors to earthquakes in the ULF band: A review of observations and mechanisms, *Rev. Geophys.*, *31*, 117–132, 1993.

Pengra, D. B., S. Xi Li, and P. Wong, Determination of rock properties by low frequency AC electrokinetics, *J. Geophys. Res.*, *104*, 29,485–29,508, 1999.

Pride, S., Governing equations for the coupled electrmagnetics and acoustics of porous media, *Phys. Rev. B*, *50*, 15,678–15,696, 1994.

Pride, S., and F. D. Morgan, Electrokinetic dissipation induced by seismic waves, *Geophysics*, *56*(7), 914–925, 1991.

Revil, A., and P. W. J. Glover, Nature of surface electrical conductivity in natural sands, sandstones and clays, *Geophys. Res. Lett.*, *25*, 691–694, 1998.

Revil, A., P. A. Pezard, and P. W. J. Glover, Streaming potential in porous media, 1, Theory of the zeta potential, *J. Geophys. Res.*, *104*, 20,021–20,031, 1999a.

Revil, A., H. Schwaeger, I. L. M. Cathles, and P. D. Manhardt, Streaming potential in porous media, 2, Theory and application to geothermal systems, *J. Geophys. Res.*, *104*, 20,033–20,048, 1999b.

Roberts, J. J., and W. Lin, Electrical properties of partially saturated Topopah spring tuff: Water distribution as a function of saturation, *Water Resour. Res.*, *33*(4), 577–588, 1997.

Sailhac, P., and G. Marquis, Analytic potential for the forward and inverse modeling of SP anomalies caused by subsurface fluid flow, *Geophys. Res. Lett.*, *28*, 1851–1854, 2001.

Sigg, L., P. Behra, and W. Stumm, *Chimie des Milieux Aquatiques*, Dunod, Paris, 2000.

Sprunt, E. S., T. B. Mercer, and N. F. Djabbarah, Streaming potential from multiphase flow, *Geophysics*, *59*, 707–711, 1994.

Suman, R. J., and R. Knight, Effects of pore structure and wettability on the electrical resistivity of partially saturated rocks—A network study, *Geophysics*, *62*(4), 1151–1162, 1997.

Waxman, M. H., and L. J. M. Smits, Electrical conductivities in oil-bearing shaly sands, *Trans. AMIE*, *243*, 107–122, 1968.

Yoshida, S., Convection current generated prior to rupture in saturated rocks, *J. Geophys. Res.*, *106*, 2103–2120, 2001.

Zablocki, C. J., Streaming potentials resulting from the descent of meteoric water—A possible mechanism for Kilauean self potential anomalies, *Trans. Geotherm. Resour. Counc.*, *2*, 747–748, 1978.

Zlotnicki, J., M. Feuillard, and G. Hammouya, Water circulation on La Soufrière volcano inferred by self-potential surveys (Guadeloupe, Lesser Antilles). Renew of volcanic activity?, *J. Geomagn. Geoelectr.*, *46*, 797–813, 1994.

Zlotnicki, J., G. Boudon, J. P. Viodé, J. F. Delarue, A. Mille, and F. Bruère, Hydrothermal circulation beneath Mount Pelée inferred by self potential surveying. Structural and tectonic implications, *J. Volcanol. Geotherm. Res.*, *84*, 73–81, 1998.

Zohdy, A. A. R., L. A. Anderson, and L. J. P. Muffler, Resistivity, self-potential, and induced-polarization surveys of a vapor-dominated geothermal system, *Geophysics*, *38*(6), 1130–1144, 1973.

X. Guichet, L. Jouniaux, and J.-P. Pozzi, Laboratoire de Géologie and CNRS UMR 8538, École Normale Supérieure, 24 rue Lhomond, 75231 Paris Cedex 05, France. (xavier.guichet@ens.fr; jouniaux@geologie.ens.fr; pozzi@geologie.ens.fr)

Journal of Colloid and Interface Science **234,** 194–203 (2001)
doi:10.1006/jcis.2000.7294, available online at http://www.idealibrary.com on IDEAL®

Frequency-Dependent Streaming Potentials

Philip M. Reppert,*[1] Frank Dale Morgan, David P. Lesmes,† and Laurence Jouniaux‡

Earth Resources Laboratory, Department of Earth Atmospheric and Planetary Sciences, Massachusetts Institute of Technology, E34-356a, 42 Carleton Street, Cambridge, Massachusetts 02142; †Department of Geology and Geophysics, Boston College, Chestnut Hill, Massachusetts 02167; and ‡Laboratoire de Géologie, URA1316, Ecole Normale Supérieure, 24 Rue Lhamond, 75231 Paris Cedex 05, France

Received June 23, 2000; accepted October 16, 2000

An experimental apparatus and data acquisition system was constructed to measure the streaming potential coupling coefficients as a function of frequency. The purpose of the experiments was to measure, for the first time, the real and imaginary portion of streaming potentials. In addition, the measured frequency range was extended beyond any previous measurements. Frequency-dependent streaming potential experiments were conducted on one glass capillary and two porous glass filters. The sample pore diameters ranged from 1 mm to 34 μm. Two frequency-dependent models (Packard and Pride) were compared to the data. Both Pride's and Packard's models have a good fit to the experimental data in the low- and intermediate-frequency regime. In the high-frequency regime, the data fit the theory after being corrected for capacitance effects of the experimental setup. Pride's generalized model appears to have the ability to more accurately estimate pore sizes in the porous medium samples. Packard's model has one unknown model parameter while Pride's model has four unknown model parameters, two of which can be independently determined experimentally. Pride's additional parameters may allow for a determination of permeability. © 2001 Academic Press

Key Words: **electrokinetic; streaming potential; dynamic; frequency; ac.**

INTRODUCTION

The phenomenon of streaming potentials has been studied for many years. This has led to applications in such diverse fields as chemistry, biology, and geophysics (1–5). The overwhelming majority of this work has been in the area of dc streaming potentials, while very little work has been done in the area of frequency-dependent streaming potentials. Past theoretical and experimental work dealing with the frequency response of streaming potentials has dealt with single-frequency, low-frequency, and frequency response measurements. Single-frequency streaming potential measurements are made at one frequency while varying the pressure in order to get plots of streaming potentials versus pressure without using a flow-through apparatus (6). Low-frequency measurements are used to extrapolate the frequency-dependent streaming potential value to the dc limit. This is done for the purposes of determining the zeta or surface potentials (7, 8). Low-frequency measurements are also used to determine the effective pore size and hydraulic permeability (9). Frequency-response measurements examine the frequency-dependent behavior of streaming potentials (10, 11). Packard (10) proposed a frequency-dependent streaming potential theory for capillaries where the streaming potential coupling coefficient remains constant at its dc value until the critical frequency is approached by the sinusoidal driving force. At frequencies higher than the critical frequency, the streaming potential coupling coefficient decays with increasing frequency. Packard's experiments were performed on a limited number of capillary samples of large radii (2.083–0.589 mm) and with no changes in solution chemistry. Packard was able to achieve a maximum measuring frequency of 200 Hz. Cooke (11) attempted to duplicate Packard's work, but with limited success; he could not match his capillary data to the theoretical curves of Packard. Cooke's data for porous glass filters appears to have the expected trend predicted by Packard's theory. On closer examination, however, Packard's theory cannot be satisfactorily fitted to Cooke's data. No one to date has satisfactorily fitted frequency-dependent streaming potential data to theoretical curves for porous media of any pore diameter or for capillaries with diameters less than 155 μm.

In 1994, Pride (12) proposed a generalized theory for frequency-dependent streaming potentials in porous media. This theory relates the transport properties and pore-geometry parameters to the samples' streaming potential frequency-response behavior. No experimental work has been performed to validate Pride's theory.

The understanding of frequency-dependent streaming potentials is vital to Earth scientists who study the electromagnetic signals generated by seismic/acoustic waves propagating in the earth. Earth scientists believe that these electromagnetic signals are generated by oscillatory fluid flow in rocks relative to the mineral matrix (13). This relative flow induces a streaming current, which oscillates as an electric dipole at the same frequency as the seismic/acoustic wave exciting the medium. This frequency-dependent streaming current has a countercurrent that flows through the conductive part of the rock (bulk fluid) to develop a frequency-dependent streaming potential.

---

[1] To whom correspondence should be addressed. Present address: Department of Geological Sciences, 338 Brackett Hall, Clemson University, Clemson, SC, 29634. Fax: (864) 656-1041. E-mail: reppert@clemson.edu.

0021-9797/01 $35.00

Frequency-dependent streaming potentials induced by a seismic wave are often referred to as the seismoelectric effect (14, 15). Some Earth scientists believe that the streaming potential frequency response may be useful in determining *in situ* permeability (16, 17).

In this paper, the real and imaginary streaming potential frequency response for a capillary is developed based on Packard's model, which is then compared to Pride's model. Then a discussion of the experimental system and methodology is provided. This is followed by a presentation of the first data where the complex frequency response for one glass capillary and two porous glass filters is presented. These experiments cover a frequency range of 1–500 Hz.

DC STREAMING POTENTIALS

Streaming potentials are a subset of electrokinetic phenomena, which includes electroosmosis, electrophoresis, and sedimentation potentials. Electrokinetic phenomena are a consequence of a mobile space charge region that exists at the interfacial boundary of two different phases. This region is commonly referred to as the electrical double layer (EDL). The most simplified approximations of the EDL can be represented by a parallel-plate capacitor (Helmholtz model) or a charge distribution that decays exponentially away from the surface, Gouy–Chapman model (18). A more accurate model takes into account the finite size of ions by combining the Helmholtz and Gouy–Chapman models where a fixed layer exists at the surface (Stern layer) and a diffuse layer extends from the fixed layer into the bulk solution (Gouy–Chapman diffuse layer). This model is often referred to as the Stern model of the electrical double layer. More specifically the interfacial region, shown schematically in Fig. 1, consists of the inner Helmholtz plane (IH) where ions are adsorbed to the surface and the outer Helmholtz plane (OH) where ions are rigidly held by electrostatic forces and cannot move. The closest plane to the surface at which fluid motion can take place is called the slipping plane. The slipping plane has a potential defined as the zeta potential (ζ), which is a characteristic of the solid and liquid that constitute the interface. The diffuse layer extends from the OH into the bulk of the liquid phase. The distance at which the diffuse layer potential (ψ_0) has been reduced to ψ_0/e is referred to as the Debye length. This is often used as a measure of how far the diffuse layer extends into the bulk fluid.

Streaming potentials occur when relative motion between the two phases displaces ions tangentially along the slipping plane by viscous effects in the liquid. This displacement of ions generates a convection current (I_{conv}) and has properties similar to an ideal current source. For a capillary, I_{conv} is defined by

$$I_{\text{conv}}(r) = \int v(r)\rho_c(r)\,\mathrm{d}r, \qquad [1]$$

in which $v(r)$ is the fluid particle velocity, dr is an infinitesimal part of the cross section, and $\rho_c(r)$ is the charge distribution in the capillary. The solution to this integral can be found in a variety of texts and is given by

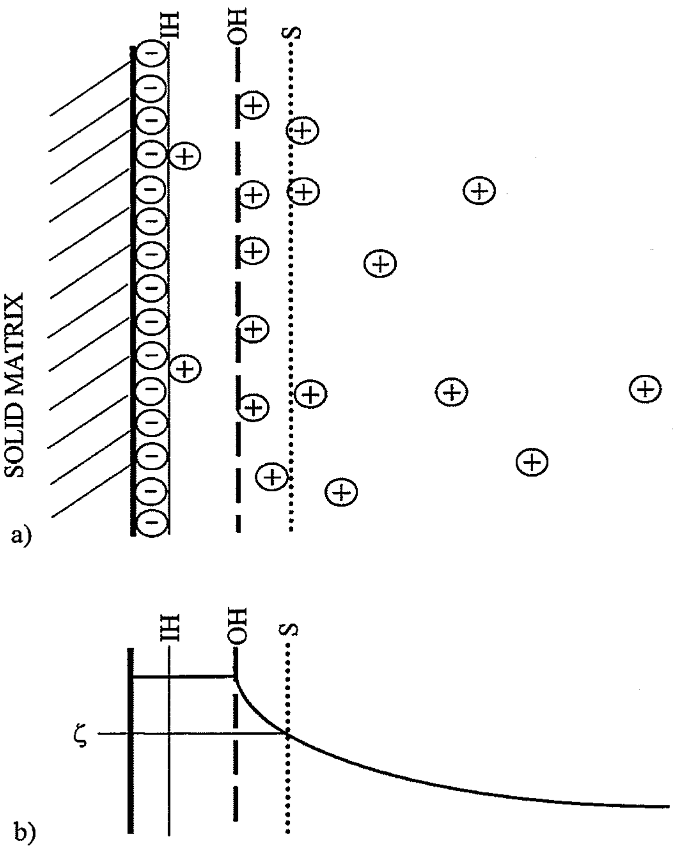

FIG. 1. (a) The Stern model of the electrical double layer. (b) One of the possible potential distributions of the Stern model. This model assumes that in the Stern layer the potential varies linearly.

$$I_{\text{conv}}(r) = \frac{\pi \varepsilon a^2 \zeta \Delta P}{\eta l}, \qquad [2]$$

where ε is the permittivity of the fluid, a is the radius of the capillary, l is the length of the capillary, ΔP is the pressure across the sample, η is the viscosity of the fluid, and ζ is the zeta potential.

In steady-state equilibrium the convection current must be balanced by a conduction current (I_{cond}) (18). Hence by ohms law,

$$I_{\text{cond}}(r) = \frac{\pi \sigma a^2}{l}\Delta V, \qquad [3]$$

where σ is the fluid conductivity and ΔV is the voltage measured across the sample. Equating the convection and conduction currents, which must be equal at equilibrium, leads to the Helmholtz–Smoluchowski equation (18)

$$\Delta V = \frac{\varepsilon \zeta}{\eta \sigma}\Delta P. \qquad [4]$$

It should be noted when viewing Eq. [4] that it does not include geometry terms for the specimen. The ratio $\Delta V/\Delta P$ is referred to as the cross-coupling coefficient or simply the coupling coefficient in the rest of the paper. When the capillary or pore-space thickness approach the dimensions of the diffuse layer (0.1 μm for 0.001 M solution), surface effects must be considered (2, 4). The radii of the samples used in our experiments are much larger than the Debye length; hence, these effects are not be addressed.

AC STREAMING POTENTIALS

The basic principles of ac streaming potentials are presented following the methodology of Packard (10). To better understand the physics of ac streaming potentials, appropriate comparisons are made to the frequency-dependent hydraulic problem previously solved by others (19).

The basic electrokinetic principles of dc and ac streaming potentials are the same. The difference is in the hydrodynamic part of the solution where the constant pressure of the dc case is replaced by a sinusoidal pressure in the ac case. Therefore, the starting point for the derivation must go back to the hydrodynamic problem where the Navier–Stokes equation,

$$\rho\frac{\partial\bar{v}(r,\omega)}{\partial t}\exp(-i\omega t) = -\nabla P(\omega)\exp(-i\omega t)+\eta\nabla^2\bar{v}(r,\omega)\exp(-i\omega t), \quad [5]$$

is shown with a sinusoidal driving pressure applied across the sample. Equation [5] can be rearranged into the form

$$\left[\frac{\partial^2}{\partial r^2}+\frac{1}{r}\frac{\partial}{\partial r}+k^2\right]v(r,\omega)=\frac{\Delta P(\omega)}{\eta l}, \quad [6]$$

where the gradient of the pressure has been replaced by $\Delta P(\omega)/l$ and

$$k^2=\frac{-i\omega\rho}{\eta}. \quad [7]$$

It is apparent that the solution can be expressed using Bessel functions, with the general solution to Eq. [6] expressed as

$$\bar{v}(r,\omega)=-\frac{\Delta P(\omega)}{k^2 l\eta}+C_1J_0(\text{kr})+C_2Y_0(\text{kr}). \quad [8]$$

The applied boundary conditions are $v(r,\omega)=0$, when $r=a$; $v(r,\omega)=$ finite, when $r=0$, and also noting $Y_0(0)=\infty$, which then requires that $C_2=0$. This leads to

$$C_1=-\frac{\Delta P(\omega)}{\eta l k^2}\frac{1}{J_0(\text{ka})}. \quad [9]$$

Substituting Eq. [9] into Eq. [8] gives

$$\bar{v}(r,\omega)=\frac{\Delta P(\omega)}{\eta l k^2}\left[\frac{J_0(\text{kr})}{J_0(\text{ka})}-1\right] \quad [10]$$

as the frequency-dependent velocity inside a capillary. Integrating Eq. [10] over the cross-sectional area of the capillary gives

$$v(\omega)=\frac{\Delta P(\omega)}{\eta l k^2}\left[\frac{2}{\text{ka}}\frac{J_1(\text{ka})}{J_0(\text{ka})}-1\right] \quad [11]$$

as the average fluid velocity inside a capillary, which is the frequency-dependent hydraulic solution for a capillary.

Now that the frequency-dependent fluid flow inside a capillary has been presented, Eq. [10] can be substituted into Eq. [1] to give

$$I_{\text{conv}}(\omega)=\int 2\pi r\rho_c(r)\bar{v}(r,\omega)\,\text{dr}, \quad [12]$$

which is the frequency-dependent convection current inside a capillary, where the charge density in the capillary in cylindrical coordinates is given by

$$\rho_c(r)=-\varepsilon\nabla^2\psi_0(r)=-\frac{\varepsilon}{r}\frac{\partial}{\partial r}\left(r\frac{\partial\psi_0(r)}{\partial r}\right). \quad [13]$$

Integrating Eq. [12] from the center of the capillary to the slipping plane under the assumption that the capillary radius is large compared to the Debye length of the EDL (10, 12) gives

$$I_{\text{conv}}(\omega)=-\frac{2\pi\varepsilon a\zeta\,\Delta P(\omega)}{\eta l k}\frac{J_1(\text{ka})}{J_0(\text{ka})} \quad [14]$$

as the frequency-dependent convection current for a capillary.

As in the DC case, at equilibrium, the convection current must be balanced by a conduction current. The conduction current is determined using Ohm's law, where the conduction current is given by

$$I_{\text{cond}}(\omega)=\Delta V(\omega)\pi a^2\frac{\sigma}{l}. \quad [15]$$

Setting the convection current equal to the conduction current gives

$$C(\omega)=\frac{\Delta V(\omega)}{\Delta P(\omega)}=\left[\frac{\varepsilon\zeta}{\sigma\eta}\right]\frac{-2}{\text{ka}}\frac{J_1(\text{ka})}{J_0(\text{ka})}. \quad [16]$$

This is the ac Helmholtz–Smoluchowski equation in a form similar to that presented by Packard (10), where $C(\omega)$ is the frequency-dependent cross-coupling coefficient. The ac Helmhotz–Smoluchowski equation reduces to the dc form in the limit as ω goes to zero, which can be demonstrated using Bessel function recursive relations or by taking the low-frequency approximation of Eq. [16]. Figure 2 shows the real and imaginary

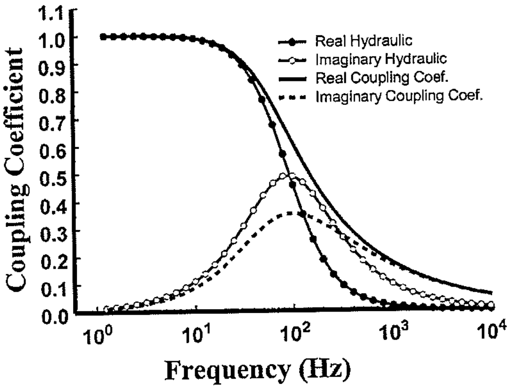

FIG. 2. Theoretical comparison of the frequency-dependent hydraulic solution, Eq. [11] and the frequency-dependent streaming potential solution. The real and imaginary portions of both solutions are shown. The coupling coefficients are normalized.

portions of the ac coupling coefficient, Eq. [16], and a plot of the frequency-dependent hydraulic equation, Eq. [11]. Figure 3 shows the phase part of Eqs. [11] and [16]. It can be seen in these two figures that the general behavior of the two equations is similar. In particular, the low-frequency behavior is identical but the high-frequency behavior diverges as one goes to higher frequencies.

At first examination of frequency-dependent streaming potentials and frequency-dependent hydraulics, it might be expected that the two phenomena would have identical behavior, since the frequency-dependent streaming potential behavior is governed by the frequency-dependent fluid flow. The different responses of the ac Helmholtz–Smoluchowski equation, Eq. [16], and the frequency-dependent hydraulic equation, Eq. [11], are easier to understand by looking at the series and asymptotic approximations for the low- and high-frequency cases, respectively. Following the methodology of Crandall (20) (which was developed for the acoustic case), the low-frequency and high-frequency approximations are made. The two separate equations are then combined to form a single equation.

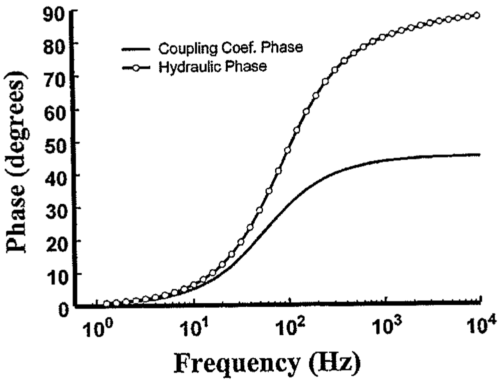

FIG. 3. Phase comparison of the frequency-dependent coupling coefficients and frequency-dependent hydraulics, where the phase is 0° for both curves at 0 Hz.

Starting with the ac Helmholtz–Smoluchowski expression, Eq. [16], and substituting the low-frequency approximations of the Bessel functions (20) J_0 and J_1, with

$$J_0(x) = \sum_{n=0}^{\infty} \frac{(-1/4x^2)^k}{k!\Gamma(n+1)} \qquad [17]$$

and

$$J_1(x) = \frac{x}{2} \sum_{n=0}^{\infty} \frac{(-1/4x^2)^k}{k!\Gamma(n+2)}, \qquad [18]$$

where x represents ka and ka < 1. Substituting these two approximations into Eq. [16] and taking the Lim $n \to \infty$ gives

$$\begin{aligned}\frac{\Delta V(\omega)}{\Delta P(\omega)} &= \lim_{n\to\infty}\left[\frac{\varepsilon\zeta}{\sigma\eta}\right]\left[\frac{2}{\text{ka}}\left\{\frac{\frac{x}{2}\sum_{n=0}^{\infty}\frac{(-1/4x^2)^k}{k!\Gamma(n+2)}}{\sum_{n=0}^{\infty}\frac{(-1/4x^2)^k}{k!\Gamma(n+1)}}\right\}\right]\\ &= \left[\frac{\varepsilon\zeta}{\sigma\eta}\right]\left[\frac{2}{\text{ka}}\frac{x}{2}\right]. \qquad [19]\end{aligned}$$

Since $x = \text{ka}$, the low-frequency approximation reduces to

$$\underset{\text{ka}<1}{C}(\omega) = \frac{\Delta V(\omega)}{\Delta P[\omega]} = \left[\frac{\varepsilon\zeta}{\sigma\eta}\right] = \frac{\Delta V}{\Delta P}. \qquad [20]$$

The high-frequency approximation used for the Bessel functions J_0 and J_1 are given by

$$\frac{J_1(x\sqrt{-i})}{J_0(x\sqrt{-i})} = -i, \qquad [21]$$

which can be found in Crandall (20) or which can be easily proven using the asymptotic approximations of Abramowitz and Stegun (21). In Eq. [16],

$$\text{ka} = a\sqrt{-\frac{i\rho\omega}{\eta}}, \qquad [22]$$

from which the following substitution is made in Eq. [22]:

$$x\sqrt{-i} = a\sqrt{-\frac{i\rho\omega}{\eta}} = a\sqrt{\frac{\rho\omega}{\eta}}\sqrt{-i}. \qquad [23]$$

Then substituting Eq. [21] and Eq. [23] into Eq. [16] gives

$$\underset{\text{ka}>10}{C(\omega)} = \left[\frac{\varepsilon\zeta}{\sigma\eta}\right]\left[\frac{-2i}{\text{ka}}\right] = \left[\frac{\varepsilon\zeta}{\sigma\eta}\right]\left[\frac{-2i}{a\sqrt{\frac{-i\rho\omega}{\eta}}}\right]. \qquad [24]$$

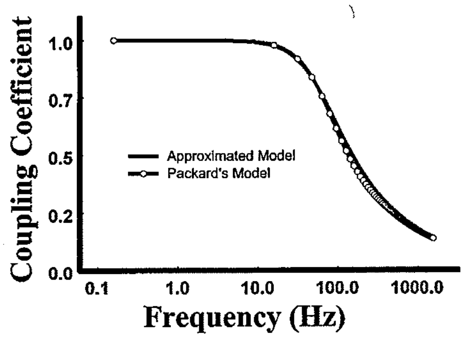

FIG. 4. Normalized comparison of the Bessel function solution, Eq. [16], to the approximated Bessel function solution, Eq. [26].

Equation [24] can then be modified to

$$\underset{\mathrm{ka}>10}{C(\omega)} = \left[\frac{\varepsilon\zeta}{\sigma\eta}\right]\left[\frac{-2}{a}\sqrt{\frac{\eta}{\omega\rho}}\left(\frac{1}{\sqrt{2}} - \frac{1}{\sqrt{2}}i\right)\right]. \qquad [25]$$

Combining the low-frequency and high-frequency approximations gives

$$\mathrm{CA}(\omega) = \left[\frac{\varepsilon\zeta}{\sigma\eta}\right]\left[1 - \frac{2}{a}\sqrt{\frac{\eta}{\omega\rho}}\left(\frac{1}{\sqrt{2}} - \frac{1}{\sqrt{2}}i\right)\right], \qquad [26]$$

where $\mathrm{CA}(\omega)$ represents the approximated cross-coupling coefficient. In Fig. 4, the solution using Bessel function approximations, Eq. [26], is plotted against the Bessel function solution of Eq. [16]. It can be seen in Fig. 4 that the two solutions are nearly identical. There is a slight divergence in the intermediate-frequency range, $1 > \mathrm{ka} > 10$, which was not accounted for in the approximation. However, the error is smaller than measurements can detect.

It can be seen in Eq. [26] and Figs. 2, 3, and 4 that as the frequency is increased inertial effects start to retard the motion of the fluid within the pore space. This occurs as the fluid makes a transition from viscous dominated flow to inertial dominated flow. At the higher frequencies the flow becomes inefficient, requiring more energy to move the same amount of liquid the same distance. Therefore at frequencies higher than the transition from viscous to inertial flow, more pressure is required to shear the same quantity of ions from the diffuse zone than when strictly in the viscous flow regime. It can also be seen in Eq. [26] and Fig. 2 that at higher frequencies the real and imaginary parts of the coupling coefficient solution are decreasing at the same rate. This explains the 45° phase angle found at high frequencies in Fig. 3.

One might ask why the frequency-dependent hydraulics and frequency-dependent streaming potentials do not have the same behavior. By comparing the form of the frequency-dependent streaming potential (FSP) approximate solution to the frequency-dependent hydraulic (FDH) solution, valuable insight into the physics that causes the difference in behavior between FDH and FSP solutions can be obtained. This comparison is made using Eqs. [20], [25], and [26] of the FSP approximation and Eq. [11] of the (FDH) solution. The low-frequency approximation to Eq. [11] is (20)

$$\underset{\mathrm{ka}<1}{H(\omega)} = \left(\frac{8}{a^2} + \frac{4}{3}i\rho\omega\right)^{-1}, \qquad [27]$$

where $H(\omega)$ represents the frequency-dependent hydraulic solution. When $\mathrm{ka} < 1$, the real term in Eq. [27] dominates over the imaginary term. This implies that at low frequencies the flow is real (no vorticity present) and as the frequency is increased an inertial component starts to develop in the flow (vorticity present). However, when $\mathrm{ka} < 1$ the inertial term remains insignificant and the flow is essentially viscous. Therefore, both low-frequency FDH and FSP solution approximations approach the dc limit at low frequencies.

The high-frequency approximation of the FDH equation is given by (20)

$$\underset{\mathrm{ka}>10}{H(\omega)} = \left(i\rho\omega + \frac{1}{r}2\eta\sqrt{\frac{\rho\omega}{2\eta}}(1+i)\right)^{-1}, \qquad [28]$$

where $(2\eta/\rho\omega)^{1/2}$ is the viscous skin depth. When examining Eq. [28], it can be seen that the bulk of the fluid is governed by the imaginary terms and thus inertial flow exists. However, when the viscous skin depth is sufficiently small, a second-order effect starts to dominate and the imaginary term starts to decrease at the same rate as the real term, giving rise to a diminished propagation velocity. It becomes apparent from the approximation analysis that the high-frequency solution causes the difference between the frequency-dependent hydraulics and the frequency-dependent streaming potential behavior. When the integral of Eq. [12] is evaluated, most of the contribution to the integral occurs along the wall of the capillary where most of the charge distribution is located. This region near the wall is also where the second-order effect of the hydraulic solution starts to dominate. Consequently, the frequency-dependent streaming potential exhibits high-frequency behavior that follows the form of the second-order effect of the hydraulic solution.

AC STREAMING POTENTIALS IN POROUS MEDIA

A model for ac streaming potentials in a porous medium derived from first principles was developed by Pride (12). Pride's version of the ac Helmholtz–Smoluchowski equation is given by

$$\mathrm{CP}(\omega) = \frac{\Delta V(\omega)}{\Delta P(\omega)}$$

$$= \left[\frac{\varepsilon\zeta}{\eta\sigma}\right]\left[1 - i\frac{\omega}{\omega_{\mathrm{t}}}\frac{m}{4}\left(1 - 2\frac{d}{\Lambda}\right)^2\left(1 - i^{\frac{3}{2}}d\sqrt{\frac{\omega\rho}{\eta}}\right)^2\right]^{-\frac{1}{2}}, \qquad [29]$$

where CP(ω) represents the AC coupling coefficient for porous media using Pride's model, d is the Debye length, and Λ is a typical pore radius representing a weighted volume-to-surface ratio (19). The transition frequency

$$\omega_t \equiv \frac{\phi}{\alpha_\infty k_0}\frac{\eta}{\rho}, \quad [30]$$

as defined by Pride (12), separates the low-frequency viscous flow regime from the high-frequency inertial flow regime. In Fig. 2 the transition frequency occurs where the hydraulic imaginary curve intercepts the hydraulic real curve. Porosity is given by ϕ tortuosity by α_∞, and the dc permeability by k_0. The dimensionless number m is defined as

$$m \equiv \frac{\phi}{\alpha_\infty k_0}\Lambda^2, \quad [31]$$

which is also a function of the pore microgeometry, which reduces to 8 for a capillary. Closer examination of the ac porous media coupling coefficient, Eq. [29], reveals that to a first-order approximation the response is determined by the transition frequency ω_t and the dc coupling coefficient.

Figure 5 shows the normalized real and imaginary parts of the theoretical ac coupling for three capillaries of different radius using Eq. [16]. The obvious characteristic of the curves is that the transition frequency shifts with changing radius of the capillary. This relationship is easily evident when looking at the equation for the transition frequency, Eq. [30], and realizing that the dc permeability for a capillary is

$$k_0 = \frac{a^2}{8}. \quad [32]$$

The transition frequency for capillary then becomes

$$\omega_t(\text{cap}) = \frac{8}{a^2}\frac{\eta}{\rho}. \quad [33]$$

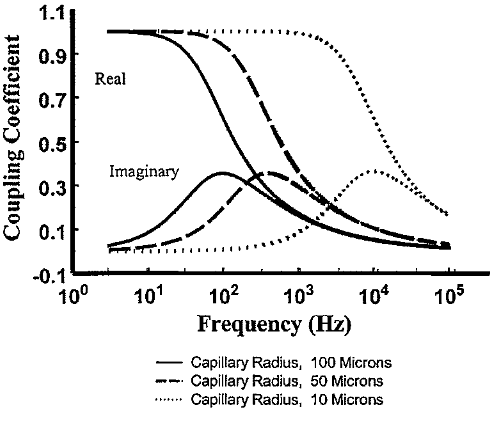

FIG. 5. Normalized coupling coefficient of the real and imaginary components for three capillaries of different radii.

COMPARISON OF PACKARD'S AND PRIDE'S MODELS

Pride (12) generated his model by creating low-frequency and high-frequency models separately and then combining them into a single combined model. Equations [34] and [35] show Pride's low-frequency and high-frequency models, respectively, when capillary geometry terms are used and second-order effects are neglected. Capillary geometry terms imply that $m = 8$, $\phi = 1$, $\alpha_\infty = 1$, $\Lambda = a$, and $k_0 = (a^2)/8$, where a is the capillary radius. Second-order effects occur when the Debye length is large compared to the capillary radius:

$$\mathrm{CP_{LAC}} = \frac{\varepsilon\zeta}{\eta\sigma} \quad [34]$$

$$\mathrm{CP_{HAC}} = -2\left[\frac{\varepsilon\zeta}{\eta\sigma}\right]\frac{i^{\frac{1}{2}}\delta}{\Lambda}. \quad [35]$$

Equation [35] can be rewritten as

$$\mathrm{CP_{HAC}} = \left[\frac{\varepsilon\zeta}{\eta\sigma}\right]\left[\frac{-2}{a}\sqrt{\frac{\eta}{\rho\omega}}\sqrt{i}\right], \quad [36]$$

where δ is the viscous skin depth and is given by $(2\eta/\rho\omega)^{1/2}$. Equation [36] can also be rewritten as

$$\mathrm{CP_{HAC}} = \left[\frac{\varepsilon\zeta}{\eta\sigma}\right]\left[\frac{-2}{a}\sqrt{\frac{\eta}{\rho\omega}}\left(\frac{1}{\sqrt{2}} - \frac{1}{\sqrt{2}}i\right)\right], \quad [37]$$

which clearly shows that the real and imaginary parts of the high-frequency solution are identical to Eq. [25] in the Bessel function approximation. One possibility of combining the low-frequency and high-frequency solutions into a single model is

$$\mathrm{CP}(\omega) = \left[\frac{\varepsilon\zeta}{\eta\sigma}\right]\left[1 - \frac{2}{a}\sqrt{\frac{\eta}{\omega\rho}}\left(\frac{1}{\sqrt{2}} - \frac{1}{\sqrt{2}}i\right)\right], \quad [38]$$

where capillary geometry is used and second order-effects are neglected.

The simplified version of Pride's model, Eq. [38], as opposed to the full equation, is compared to Packard's equation for two reasons. First, the second-order effects do not affect the model within the range of frequency or concentrations for which Pride's model is defined. Second, the simplified model of Pride, Eq. [38], is identical to the approximated form the Packard's model, Eq. [26]. This implies, when using capillary geometry terms and neglecting second-order effects, that Pride's model is identical to Packard's model when the series and asymptotic approximations are used.

A visual comparison of Packard's and Pride's models can be made by looking at Fig. 4, where Eqs. [16] and [38] are compared. A slight discrepancy between the two curves becomes apparent, which is addressed earlier in this paper. To completely approximate the Bessel function, the range where ka is greater than one but less than 10 must be addressed. Packard addresses this range because the Bessel function form inherently covers the whole range. It appears from the comparison of Packard's Bessel function form to Pride's model that Pride's model does not completely address this region. When Fig. 4 is compared to actual measurements, however, it is difficult to resolve the difference between the two curves when experimental error is accounted for in the data. Consequently, Pride's model is adequate in this region.

EXPERIMENTAL APPROACH

The approach used to collect the streaming potential data was to hold the capillary or porous filter stationary and oscillate the fluid back and forth through the sample using a sinusoidal driving pressure at one end while having the other end open to the atmosphere. Silver silver–chloride electrodes were placed on either side of the sample in fluid ports to keep them out of the fluid flow path (22). The frequency response of the electrodes was measured using a four-electrode method and found to be flat in the region used in this experiment. The electrode measurements were also verified through the use of a capacitive coupled antenna placed around the outside of the sample. The pressure was monitored on the high-pressure and atmospheric-pressure sides of the sample by miniature hydrophones that have a flat frequency response from 1 to 20 kHz. The acrylic apparatus, which holds the sample, electrodes, and hydrophones, is shown schematically in Fig. 6. The enclosure around the sample and preamplifiers is constructed of Mu-metal. Mu-metal is used because of its superior electromagnetic shielding properties. The acrylic housing that holds the sample is additionally enclosed in an aluminum housing, and the electromechanical shaker that produces the driving pressure is enclosed in a separate steel box. This large quantity of shielding is required for two reasons. The first is that the laboratory is an electrically noisy environment. The second is that the pressure source is being generated by an electromechanical transducer, which is driven at the same frequency as the measured streaming potential. The driving transducer and associated leads emit enough electromagnetic signal (EMF) at the same frequency being measured to sometimes affect the measured results. Depending on the pore or capillary diameters, the resistance of the sample could be several hundred megaohms, which causes the sample to act as an antenna for the EMF fields produced by the electromechanical transducer. The acrylic housing has 50 kg of lead placed on it to reduce any sample vibration.

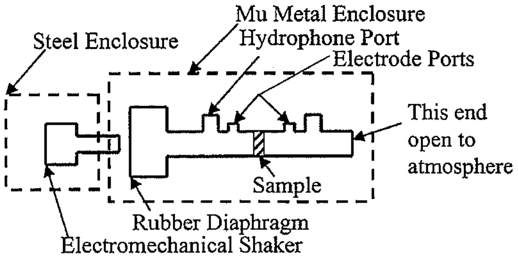

FIG. 6. A simplified schematic representation of the test cell and pressure source. The apparatus is constructed of Plexiglas and bolted to a heavy metal plate.

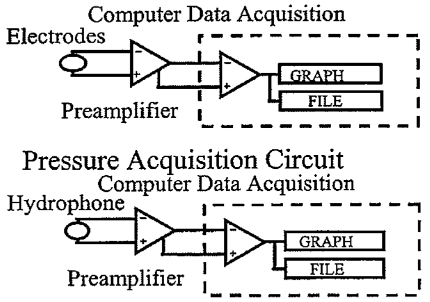

FIG. 7. A simplified representation of the streaming potential data acquisition circuit is shown. A Labview 12-bit AD board was used to acquire the data in the computer.

The waveforms were sampled using two instrument preamplifiers and a 12-bit analog-to-digital board with 24.8-μV resolution. Electrometers or FET preamplifiers were required as input buffers due to the high impedance of the samples (.5 MΩ to 1 GΩ). A schematic representation of the data acquisition system is shown in Fig. 7. The data were analyzed using spectral analysis with a Hanning window applied to the data prior to spectral analysis. In addition to spectral analysis, the time-domain voltage and pressure were monitored at each driving frequency. The raw data were saved for possible future processing. Cross-correlation analysis of the signals was also performed as a verification of the amplitude spectrum measurements.

DATA/RESULTS

To test Packard's and Pride's models experimentally, the pore diameters of the samples must be known. The pore diameter is used as an adjustable parameter in the models to fit the theory to the data. Actual pore diameters are then compared to the experimentally determined pore diameters. The pore diameters of the glass samples were provided by the manufacturer.

The glass samples consist of a capillary and two porous filters. Capillary 1 has an inner diameter that ranges from 0.8 to 1.1 mm, and a length of 60 cm. Porous Filter A has manufacturer-determined pore diameters ranging from 145 to 175 μm, an overall diameter of 1 cm, and a thickness of 2 mm. Porous Filter B has manufacturer-determined pore diameters ranging from 70 to 100 μm, an overall diameter of 1.9 cm, and a thickness of 1 cm.

The experiments were carried out using 10^{-3} and $10^{-3.7}$ M KCl with a pH of 5.5. Assuming a concentration of 10^{-4} M KCl, the Debye length was found to be much less than the radius of the pore space. Therefore, second-order effects can be neglected in Pride's model.

Figure 8 shows the measurements of the coupling coefficient versus frequency for Capillary 1 along with a theoretical curve

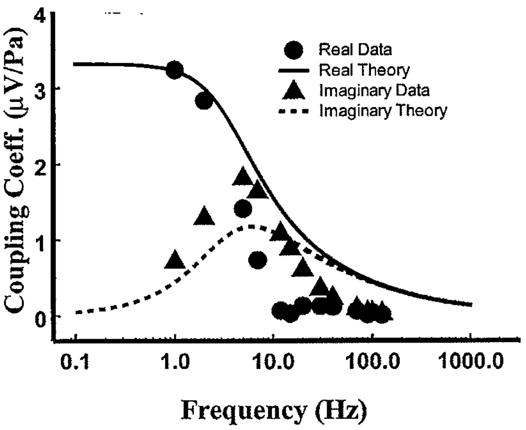

FIG. 8. Cross-coupling real and imaginary uncorrected data for Capillary 1 plotted along with the theory for a 0.8-mm capillary.

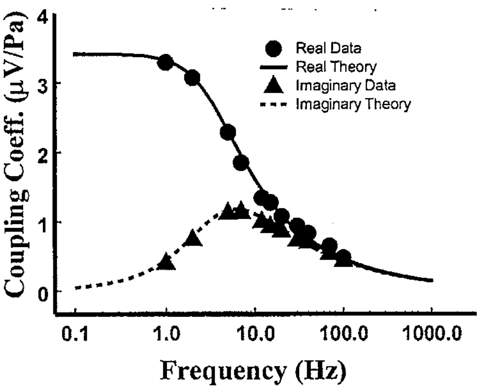

FIG. 10. Corrected cross-coupling real and imaginary data for 60-mm-long, 0.8-mm-diameter capillary plotted along with the theory for a 0.8-mm capillary. Error bars are not shown because they fall within the size of the data points.

for Eq. [26]. It can be seen that the data do not have a satisfactory fit to the theory. In addition to the streaming potential data of Fig. 8, the frequency-dependent impedance of the sample and measuring circuit was also determined and is shown in Fig. 9. The impedance of the sample and measuring circuit was determined using a four-electrode method. The RC of the circuit was found to have a resistance of 1 GΩ and a capacitance of 25 pF. The resistance was determined to be on the order of the resistance of a 0.8-mm capillary filled with $10^{-3.7}$ M KCl. The capacitance was found to be on the order of the input capacitance of the amplifier and the capacitance of the wire leads. The data in Fig. 8 were then corrected for this impedance by normalizing the real and imaginary portions of the impedance at the particular frequencies of the streaming potential measurement. This normalized impedance was then divided into the data. The corrected data are shown in Fig. 10, where a good correlation between the theory and the data is evident. At the higher frequencies, signal-to-noise problems caused the fit to have a little more scatter. The transition frequency determined from the fit of the theoretical curve is 7.1 Hz, which gives a capillary diameter of 0.8 mm. This is in agreement with the manufacturer-provided diameter of 0.8–1.1 mm for this type of capillary. Looking at Fig. 10, it can be seen that for the higher frequencies, inertial flow essentially dominates in Capillary 1.

The corrected data for Porous Filter A, shown in Fig. 11, are plotted against Eq. [26]. As can be seen, the theory fits the data well. Fitting the theoretical curve to the data for Porous Filter A gives a pore radius of 65 μm and a transition frequency of 269 Hz. The manufacture-provided pore radii for the Porous Filter A are 72.5–87 mm.

Figure 12 shows the corrected data for Porous Filter B along with the best-fit theoretical curve. Porous filter B has its best fit to Pride's theory, Eq. [26], using a 40-μm pore radius and a transition frequency of 710 Hz. Recall that the pore radii provided by the manufacturer for Porous Filter B are 35 to 50 μm. The data for Porous Filter B fits the theory very well in the low-frequency and the intermediate-frequency regions. At the higher frequencies, there is a little more scatter than at the low frequencies due to poor signal-to-noise ratio.

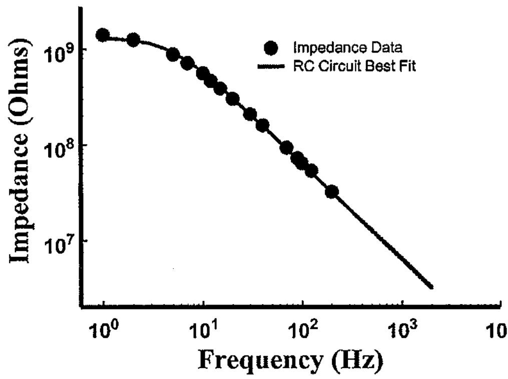

FIG. 9. Capillary 1 impedance data plotted with the best RC circuit response. The resistance and capacitance of the RC circuit are 1 GΩ and 25 pF, respectively.

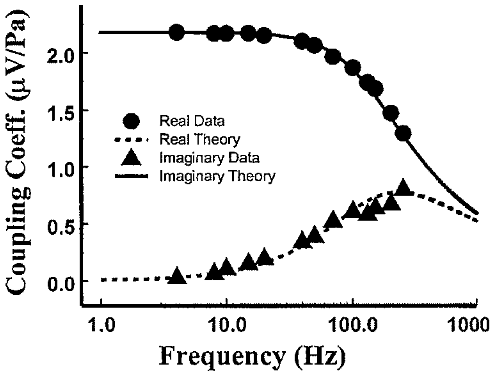

FIG. 11. Porous Filter A corrected cross-coupling real and imaginary data plotted with the theoretical response. The transition frequency was determined to be 269 Hz, which gives a pore radius of 65 μm. The manufacturer provided pore radius for porous filter B ranges from 72.5 to 87 μm. Error bars are not shown because they fall within the size of the data points.

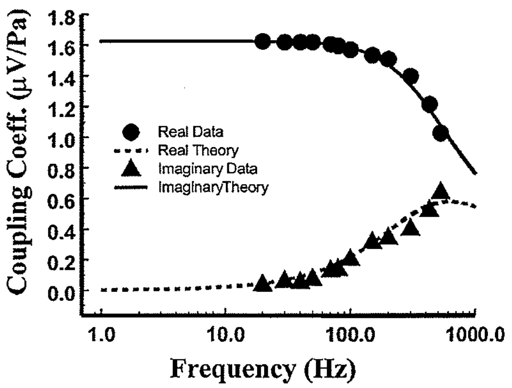

FIG. 12. Porous Filter B corrected cross-coupling frequency response data plotted along with the theoretical response. The transition frequency was determined to be 710 Hz, which gives a pore radius of 40 μm. The manufacturer provided pore radius for porous filter B ranges from 35 to 50 μm. Error bars are not shown because they fall within the size of the data points.

It appears from the data that the experimentally determined pore radii tend toward the low range of radii provided by the manufacturers. This may imply that the frequency-dependent streaming potential response is controlled by the smallest pore geometry in a fluid path. Further research is required to say for certain why the frequency response tends toward the smaller pore sizes. At the present time it appears to be related only to the hydrodynamic portion of the problem.

DISCUSSION AND APPLICATIONS

The emphasis of this study has been to examine, for the first time, complex streaming potentials and to extend the frequency range covered by this type of experiment. As a consequence of this study Packard's and Pride's theories have been verified over a range of pore sizes. Both Packard's and Pride's theories fit the data nearly identically. The transition frequency is the important parameter to be determined uniquely, for both capillaries and porous filters, from frequency-dependent streaming potential curves. From the transition frequency, the pore size can be determined. The transition frequency can be determined graphically from the data or by curve fitting the theory to the data and then determining the transition frequency from the theory. Packard's theory for a capillary is related to the capillary radius and the viscosity and density of the fluid. In Pride's model one additional parameter (m) is included if the second-order parameters are neglected and Λ is taken as the pore radius. The second-order effect parameters are important only where the pore sizes are very small and/or the electrolyte concentration is very low.

The data collected on glass filters with pore diameters much larger than the diffuse zone indicate that the curves generated using Pride's and Packard's theories cannot be distinguished from each other. This result confirms the analysis done earlier in the paper. What is different between the theories is that Pride's model includes second-order effects, which are eliminated in the approximation made during the solution of Eq. [16], Packard's model. In this respect, Pride's model appears to be more complete and general, but the accuracy in these regions has not been confirmed. From the data thus far collected on porous filters, it can be concluded that the curves generated by Packard's and Pride's models can accurately fit the data. Therefore, both Packard's and Pride's models give identical results when used with realistic frequency ranges and solution chemistries as shown from the theoretical analysis and the experimental data.

SUMMARY/CONCLUSION

Real and imaginary parts of frequency-dependent streaming potentials were measured for the first time. A comparison of streaming potential data to proposed models has been presented for various pore sizes. Although there is a slight discrepancy between the capillary model and the generalized model, overall both Packard's and Pride's models fit the frequency-dependent streaming potential capillary data. For porous media, both Packard's capillary model and Pride's porous media model fit the data, which allows the pore size to be estimated. The difference between the two models comes from the model parameters used to fit the curve. When using Pride's model, if either m or Λ are know a priori, it allows determination of the other parameter. From the results thus far presented, the frequency streaming potential response may be governed by the smallest pore geometry in the fluid path.

Currently plans are underway to extend the frequency range of the experiment to 20–30 kHz. This will allow study of a wider range of samples, including rocks. Studying a broader sampling of rocks will help us to understand the relationship between frequency-dependent streaming potentials and permeability as alluded to by others (16, 17). A set of samples with well-defined geometries will better help to confirm how well the models can predict pore size and whether the response is governed by the pore-throat size. Last, performing frequency-dependent studies at higher temperatures and pressures will help us to ascertain what is happening to the solution chemistry and electrical double layer at *in situ* temperatures and pressures for rocks. This understanding has importance to the oil industry as well as to Earth scientists for the study of earthquake nucleation (23).

ACKNOWLEDGMENTS

We thank the United States Air Force for their grant in support of this work. We also thank Dereck Hirst and the MIT Laboratory of Nuclear Science Machine Shop personnel for their invaluable help in constructing the test cell and other required equipment. This work was partially supported by DOE Grant DE-FG02-00ER15041, a Lavoisier grant from the French Foreign office, and the Compagine Général de Géophysique (France).

REFERENCES

1. Kurtz, R. J., Findl, E., Kurtz, A. B., and Stormo, L. C., *J. Colloid Interface Sci.* **57**, 28–39 (1976).

2. Levine, S., Marriott, J. R., Neale, C., and Epstein, N., *J. Colloid Interface Sci.* **52,** 136–149 (1975).
3. Rice, C. L., and Whitehead, R., *J. Phys. Chem.* **69**(11) (1965).
4. Morgan, F. D., Williams, E. R., and Madden, T. R., *J. Geophys. Res.* **94,** 12,449–12,461 (1989).
5. Ishido, T., and Mizutani, H., *J. Geophy. Res.* **86,** 1763–1775 (1981).
6. Sears, A. R., and Groves, J. N., *J. Colloid Interface Sci.* **65,** 479 (1977).
7. Pengra, D. P., Shi, L., Li, S. X., and Wong, P., "MRS Symposium Proceedings, Boston, December 1995."
8. Wong, P., U.S. Patent 5,417,104 (1995).
9. Li, S. X., Pengra, D. B., and Wong, P., *Phy. Rev. E* **51,** 5748–5751 (1995).
10. Packard, R. G., *J. Chem. Phys.* **21,** 303–307 (1953).
11. Cooke, C. E., *J. Chem. Phys.* **23,** 2299–2303 (1955).
12. Pride, S. R., *Phys. Rev. B.* **50,** 15,678–15,696 (1994).
13. Thompson, A. H., and Gist, G. A., *The Leading Edge*, **December,** 1169 (1993).
14. Haartsen, M. W., and Pride, S. R., *in* "64th Ann. Internat. Mtg. Soc. Expl. Geophys., Expanded Abstracts," pp. 1155–1158, 1994.
15. Zhu, Z., Cheng, C., and Toksöz, M. N., *in* "64th Ann. Internat. Mtg. Soc. Expl. Geophys., Expanded Abstracts," pp. 26–29, 1994.
16. Mikhailov, O. V., Haartsen M. W., and Toksöz, M. N., *Geophysics* **62,** 1–9 (1997).
17. Reppert, P. M., and Morgan, F. D., *in* "Transactions of the 99th Annual Meeting of the American Geophysists Union," T32H-04, 1998.
18. Overbeek, J. Th., *in* "Irreversible Systems" (H. R. Kruyt, Eds.), Vol. 1. Elsevier, New York, 1952.
19. Johnson, D. L., Koplik, J., and Schwartz, L. M., *Phys. Rev. Lett.* **57,** 2564–2567 (1986).
20. Crandall, I. B., "Theory of Vibrating Systems and Sound." Van Norstrand, New York, 1926.
21. Abramowitz, M., and Stegun, I. A., "Handbook of Mathematical Functions With Formula, Graphs, and Mathematical Tables." U.S. National Bureau of Standards, 1964.
22. Morgan, F. D., *in* "Lecture Notes in Earth Sciences" (S. Bhattacharji, G. M. Friedman, H. J. Neugebauer, and A Seilacher, Eds.), Vol. 27, Springer-Verlag, Berlin/New York (1989).
23. Morgan, F. D., *Eos Trans.* AGU, F173 (1995).

JOURNAL OF GEOPHYSICAL RESEARCH, VOL. 102, NO. B7, PAGES 15,335-15,343, JULY 10, 1997

Laboratory measurements anomalous 0.1-0.5 Hz streaming potential under geochemical changes: Implications for electrotelluric precursors to earthquakes

Laurence Jouniaux and Jean-Pierre Pozzi

Laboratoire de Géologie de l'École Normale Supérieure, Centre National de la Recherche Scientifique, Paris, France

Abstract. Streaming potentials resulting from flow of various salt solutions in rock were measured on saturated sediments (Fontainebleau sandstones). The streaming potential ΔV was found to be proportional to the driving pore pressure ΔP. Pulses of amplitude 15-40 mV in the frequency range of 0.1 to 0.5 Hz were observed when the conductivity of the injected water was decreased and the fluid flow rate was relatively low, corresponding to a Darcian velocity of 17 to 30 cm/h. The amplitudes of these pulses are 47% to 133% of the corresponding steady components of the ΔV values. Such geochemically induced effects may possibly be responsible for the frequency signals from 0.1 to 0.5 Hz that were sometimes observed before an earthquake.

Introduction

Monitoring of electric and magnetic anomalies has been proposed as a possible means for predicting earthquakes because many authors reported observations of signals prior to earthquakes [*Myachkin et al.*, 1972; *Sobolev*, 1975; *Mizutani and Ishido*, 1976; *Corwin and Morrison*, 1977; *Varotsos and Alexopoulos*, 1984a,b; *Murakami et al.*, 1984; *Miyakoshi*, 1986; *Fujinawa and Takahashi*, 1990; *Gruszow et al.*, 1995]. *Fujinawa et al.* [1992] observed impulsive signals of duration ranging from about 1 s to several tens of seconds in the vertical geoelectric field before, during, and after a minor volcanic eruption on Izu-Oshima Island in Japan. Large increases in ULF magnetic signals were observed by *Fraser-Smith et al.* [1990] starting 3 hours before the October 18, 1989, Loma Prieta M7.1 earthquake, at 7 km from the epicenter. However, no significant ULF magnetic field signals were observed far from the epicenter (at 81 km) when the M6.7 Northridge earthquake occurred on January 17, 1994 [*Fraser-Smith et al.*, 1994]. ELF (10 Hz to 15 kHz) electromagnetic signals at frequencies below 450 Hz were recorded by low-altitude satellites passing over the Spitak Armenian region and anomalies were observed less than 3 hours before the strong aftershocks of the December 7, 1988, Spitak M6.7 earthquake [*Serebryakova et al.*, 1992]. Comparative analysis between observations near Loma Prieta and near Spitak were performed by *Molchanov et al.* [1992].

The steady (or dc) component of electric or magnetic anomalous signals may possibly be attributed to electrokinetic effects of fluid. *Corwin and Morrison* [1977] thought that the anomalous signal they observed was produced by a fluid flowing into a dilatant region prior to an earthquake. *Mizutani and Ishido* [1976] invoked electrokinetic effects to explain their observed signals of 5 to 10 nT. The electrokinetic effects may be produced by fluid percolation in the crust, driven by a pore pressure gradient related to precursory deformation. This model was first proposed by *Mizutani et al.* [1976], who assumed that dilatancy prior to earthquakes [*Nur*, 1972; *Scholz et al.*, 1973] enhances the permeability of the medium and allows the fluid to flow in the vicinity of the fault. *Dobrovolsky et al.* [1989] proposed that a long-distance elastic effect induced a fluid flow and an electrokinetic effect near the electrodes of measurement. *Bernard* [1992] proposed that the electric anomalies measured far from an epicenter could be an electrokinetic signal induced by the triggering of fluid instabilities at the measurement site responding nonlinearly to precursory strain.

Miyakoshi [1986] concluded that their observation of anomalous electric signals in Japan was due to the change of the self-potential of the fractured fault rock in which one electrode was fixed, the other electrode being at a constant potential serving as a reference. He noted that fluid was flowing through the Yamasaki fault, but did not attribute this anomaly to changes in the water migration through the fault, based on consideration of the time constant of the anomaly. Another interpretation for electric and magnetic signals was given by *Jouniaux and Pozzi* [1995a] on the basis of laboratory measurements: The electrokinetic coupling coefficient of the rock near the electrode could be changed before earthquakes because the zeta potential is enhanced by fracturing, when stresses rise to over 75% of the yield stress that ruptures the seismic zone. This increse in zeta potential could lead to an electrokinetic potential anomaly [*Jouniaux and Pozzi*, 1995a]. *Draganov et al.* [1991] suggested that the magnetic anomalies observed at the Earth's surface before the Loma Prieta earthquake [*Fraser-Smith et al.*, 1990] were the results of magnetic fields induced by fluid flow of conductivity 4 S/m and velocity 4 cm/s at a seismogenic depth of 5 km. However, such conditions are not likely to be met as noted by *Fenoglio et al.* [1995].

The oscillatory nature of the signals observed by *Fraser-Smith et al.* [1990] has been attributed by *Fenoglio et al.* [1995] to an electrokinetic effect associated with unsteady fluid flow during failure of faults. *Fenoglio et al.* [1995] suggested that the stop-and-go fracture propagation associated with rapid fluid flow in a shear fracture 17 km deep could generate magnetic signals measurable at the surface as a result of electrokinetic effects.

The preceding discussion shows that many authors have invoked electrokinetic phenomena to explain electric and

Paper number 97JB00955.
0148-0227/97/97JB-00955$09.00

magnetic anomalies observed prior to earthquakes near or far from the epicenter region. Streaming potentials refer to the electrical signals produced when a fluid flows in a porous medium and this effect can be quantified through experimental results. Few laboratory data of geophysical interest on streaming potential are available [*Ahmad*, 1964, *Somasundaran and Kulkarni*, 1973; *Ishido and Mizutani*, 1981; *Massenet and Van Ngoc*, 1985; *Morgan et al.*, 1989; *Morat et al.*, 1992; *Antraygues and Aubert*, 1993; *Jouniaux et al.*, 1994; *Pozzi and Jouniaux*, 1994; *Jouniaux and Pozzi*, 1995a,b].

We present in this paper some laboratory measurements of streaming potentials on a saturated Fontainebleau sandstone (quartz content more than 99%), using various conductivities of salt solutions. In particular, we report the observation of the occurrence of unusual signal pulses having a duration of a few seconds under the condition of changing fluid conductivity. These findings may be relevant to recent reports of changes in the geochemistry of groundwater as a precursor to earthquakes [*Tsunogai and Wakita*, 1995; *Toutain et al.*, 1997].

Electrokinetic Phenomena

Electrokinetic phenomena arise from the existence of some electrical double layers that are formed at the solid-liquid interface. The currently accepted model for the rock-fluid interface is derived largely from the work of *Stern* [1924]. The double layer is made up of a stationary layer of ions (the Helmholtz layer) adsorbed to the surfaces of the minerals comprising the rock, and a diffuse mobile layer (the Gouy-Chapman zone) on the aqueous side of this interface that extends into the liquid phase (for detailed description, see *Adamson* [1976], *Dukhin and Derjaguin* [1974], and Hunter [1981]).

When a fluid is made to flow through a porous medium, there will be an occurrence of a potential, the so-called streaming potential, across the sample in the flow direction because of the relative motion between the solid and the liquid. On the closest plane to the surface on which fluid motion takes place, the potential is defined as the ζ potential, which is the potential that is manifested in streaming-potential measurements. Streaming potentials generated by fluids moving through porous media or capillaries are governed by the Helmholtz-Smoluchowski equation as discussed below [*Overbeek*, 1952; *Nourbehecht*, 1963]. In a porous medium the electric current density I (A/m^2) and the fluid flow J (m/s) are coupled according to the following equations:

$$-\mathbf{I} = \frac{\sigma_f}{F}\mathbf{grad}V - \frac{\varepsilon\zeta}{\eta F^o}\mathbf{grad}P \qquad (1)$$

$$-\mathbf{J} = -\frac{\varepsilon\zeta}{\eta F^o}\mathbf{grad}V + \frac{k}{\eta}\mathbf{grad}P \qquad (2)$$

where V is the electric potential, P is the fluid pressure, σ_f and ε are the electrical conductivity and the dielectric constant of the fluid, ζ is the zeta potential, η the dynamic viscosity of the fluid, k is the permeability of the porous medium. F^o is the formation factor ($\sigma_{fluid}/\sigma_{rock}$, ratio between fluid and rock conductivities) with a very high fluid conductivity (typically, 0.1 S/m for a lot of rocks [see *Ruffet*, 1993]) when surface conduction is absent, and F is the formation factor for the fluid conductivity being studied (i.e., possibly with surface conductivity). The first term on the right-hand side in (1) represents Ohm's law, and the second term in (2) represents Darcy's law. In a steady state equilibrium the convection current (due to grad P) is balanced by the conduction current (due to grad V). Equating these currents leads to the ratio $\Delta V/\Delta P$ called the streaming-potential cross-coupling coefficient C_s, or simply, the coupling coefficient:

$$C_s = \frac{\Delta V}{\Delta P} = \frac{\varepsilon\zeta}{\eta\sigma_f}\frac{F}{F^o} \qquad (3)$$

which is the Helmholtz-Smoluchowski equation [*Dukhin and Derjaguin*, 1974]. The above equations are given here because they are found in different forms in the *literature [Ishido and Mizutani*, 1981; *Morgan et al.*, 1989; *Pride*, 1994]. ΔV is the generated potential, and ΔP is the applied pore-pressure difference. For a complete development of the equations governing the coupled electromagnetics and acoustics of the porous media, see *Pride* [1994]; for further details on surface conductivity, see *Revil et al.* [1996]. Equation (3) implies that the currents are of equal magnitude and opposite flow along the same path. When surface conductivity is negligible, F=F^o, and we have

$$C_s = \varepsilon\zeta/\eta\sigma_f \qquad (4)$$

Double Layer For Quartz-Water Systems

The streaming potential is due to the motion of the diffuse layer induced by the applied fluid pressure gradient along the interface. The double layer for quartz-water systems is described here from a chemical point of view.

Population Distribution of Sites at Quartz-Water Interface

Dove and Elston [1992] quantified the distribution of surface species on pure quartz in a solution of several values of sodium concentration and *p*H (at 25°C). For a quartz surface in pure water the authors calculated how sites at the mineral surface are distributed at *p*H 5. Note that at *p*H 5 the activity of H_3O^- ions is 10^{-5} which is 10^4 times greater than the activity of OH^- ions (10^{-9}). *Dove and Elston* [1992] noted that an increase in sodium concentration of the bulk solution redistributes the population balance of surface complexes in favor of more SiO^- and $SiONa^+$. However, their predictions for a solution of 10^{-4} M NaCl and *p*H 5 showed a predominant site fraction SiOH of 99.85% and a site fraction SiO^- of 0.15%. A more concentrated solution of 0.2 M NaCl still shows that surface sites are dominated by SiOH (99.52%) with a site fraction of SiO^- and SiONa of only 0.43% and 0.05%, respectively. These estimates indicate that all of the experiments conducted in the present study had surfaces which were dominated by more than 99% of the neutral complex and which had negative deprotonated complex SiO^-. As a consequence, the cations of electrolyte solutions are electrostatically attracted to this negative surface and anions are repulsed.

Species That Can Form at Quartz-Water Interface

The hydrated counterions Na^+ present in the diffuse layer are thought to be maintained at some distance from the rock surface by the hydratation water around each cation and the water adsorbed on the surface. The outer Helmholtz plane defines the closest distance approached by the hydrated counterions Na^+ at which distance the potential is Φ_h. Note that there is an excess of cations in the diffuse layer. Strongly adsorbed ions such as hydrogen interact closely with unsaturated oxygens in the innermost layer.

Position and State of the Species at Quartz-Water Interface

The exact position of the shear plane at a quartz-water interface is not clear. A common assumption is that zeta potential is identical to Φ_h, meaning that the hydraulic flow shears the diffuse layer up to the surface, the first layer of counterions that constitute the Helmholtz layer being mobile. This assumption would be justified at low ionic strengths (10^{-4} and 10^{-3} M) and at *p*H values below 9 [*Li and De Bruyn*, 1966]. The motion of the diffuse layer induced by the applied pore pressure is carrying an excess of hydrated Na^+ ions and H_3O^+ ions. Therefore an excess of positive charge exists at one end of the sample where the fluid pressure is the smallest whereas a deficit in positive charges exists at the other end of the sample where the fluid pressure is the highest. As a result the electrokinetic coupling coefficient $\Delta V/\Delta P$ is negative, leading to a negative zeta potential.

The effect of *p*H on zeta potential is well known: the negative zeta potential can increase and become zero and may even be positive. The isoelectric point is the *p*H for which the zeta potential is zero. *Li and De Bryun* [1966] showed from electrokinetic measurements of NaCl solutions on pure quartz an isoelectric point at *p*H value lower than 2. *Sharma et al.* [1987] showed from measurements on baked and unbaked sandstone oxide and Ottawa sand with NaCl solution of 10^{-2} and 10^{-3} M at 25°C that the isoelectric point was between 2 and 3.5. *Ishido and Mizutani* [1981] measured an isoelectric point at *p*H 2 for quartz in solution of 10^{-3} N KNO_3. Therefore the zeta potential is expected to be negative for *p*H values above 2-3.5.

Experimental Procedure

Our experiments were conducted using Fontainebleau sandstone composed of more than 99% pure quartz with grain size of about 250 µm. In a previous study [*Jouniaux and Pozzi*, 1995a] we showed that the formation factor $F°$ was 91, the porosity 11%, and the permeability $6.5\text{x}10^{-14}$ m^2 (65 mD). Measurements were made on sample F313 using a pressure cell described by *Jouniaux and Pozzi* [1995a]. The sample was cut into a cylinder 50 mm long and 25 mm in diameter. The sample was subsequently dried at 70°C in vacuum for 8 hours. Then it was saturated with distilled water of resistivity $2\text{x}10^3$ Ωm.

The first set of measurements (Figures 1 and 2) were performed when the sample was subjected to a quasi-hydrostatic pressure such that the axial stress was 12±0.5 MPa and confining pressure was 11±0.1 MPa. The press is servocontrolled in displacement; thus the strain was constant. The streaming potential was measured using different NaCl concentrations, starting with distilled water of *p*H 5, which had a resistivity of 1030 Ωm, up to a concentration of $9\text{x}10^{-4}$ mol/L, which had a resistivity of 103 Ωm. The intermediate solutions had resistivities of 720 Ωm and 490 Ωm.

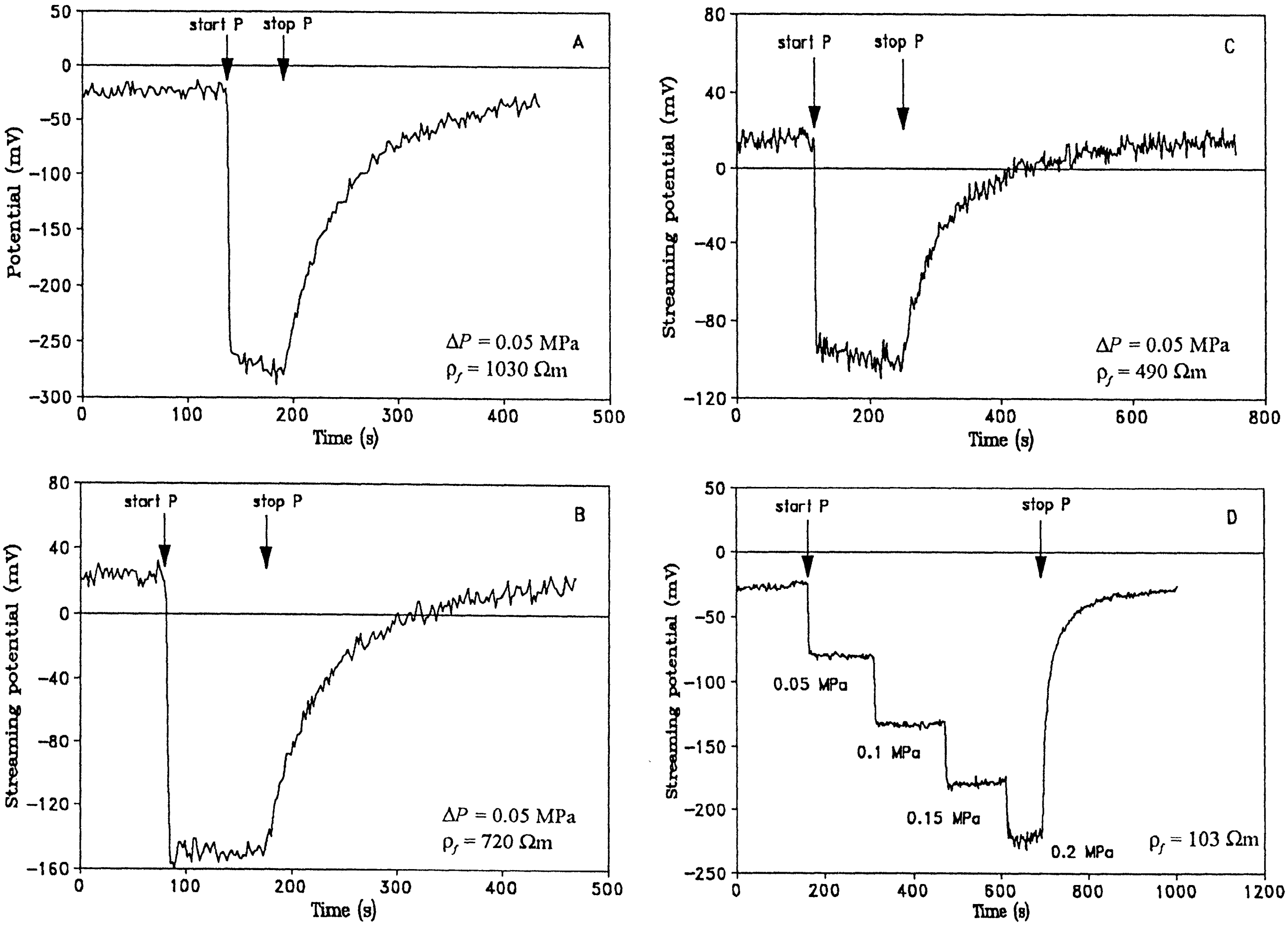

Figure 1. Examples of measured streaming potential (ΔV) when a pore pressure difference ΔP is applied from "start P" to "stop P" for four fluids of different resistivity ρ_f.

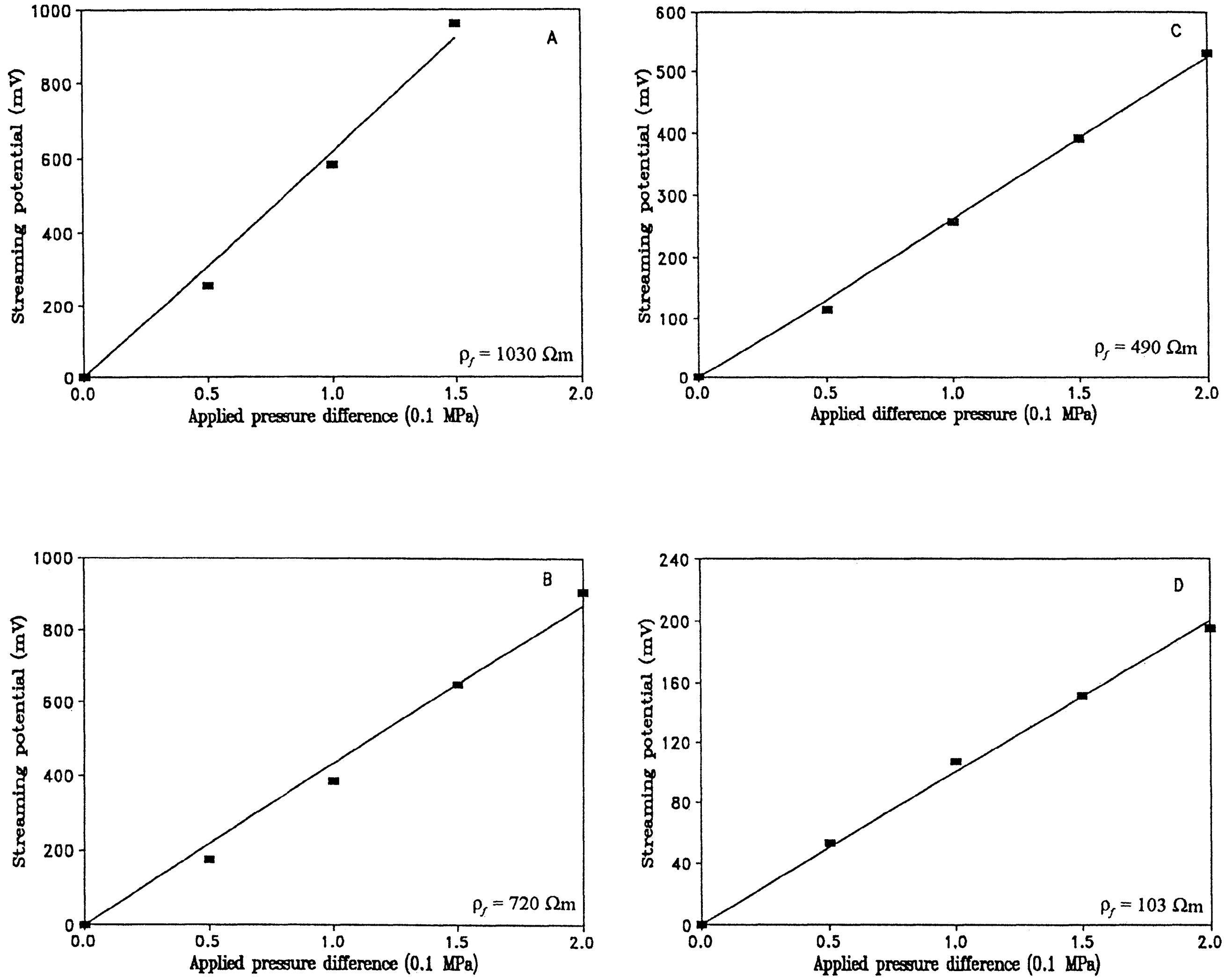

Figure 2. Measured streaming-potential values (in absolute value) versus applied pore pressure difference ΔP for the four fluids corresponding to those of Figure 1.

After these measurements with salt solutions, measurements with distilled water were performed, leading to transient streaming potentials (Figure 3). These measurements were performed during the beginning of a deformation cycle, when the axial stress and confining pressure were 10±1 MPa and 10.0±0.1 MPa, 24.5±0.5 MPa and 10.7±0.1 MPa, 67±2 MPa and 11.3±0.1 MPa, 118±2 MPa and 11.3±0.1 MPa, respectively, for the four measurements shown in Figure 3. The sample strength was 262 MPa.

The electrodes used in our experiment are made of beryllium-bronze with a 3 mm hole at the center and two linked circular grooves allowing the fluid to flow uniformly in the axial direction through the sample. The upper and lower electrodes are isolated from the conductive press and the cell by an insulating alumina piston and an insulating pastille, respectively. The dielectric constant of the fluid ε_{H2O} is 7.04-7.18 x 10^{-10} F/m at temperatures between 17°C and 24°C.

Resistivity Measurement

The resistance of the sample was measured with an HP 4284A impedance meter at a frequency of 4 kHz [*Ruffet et al.*, 1991] as for all previous measurements. The fluid in the cylindrical hole of the insulating piston and the insulating pastille is in contact with the sample [*Jouniaux and Pozzi*, 1995a] and can provide a conduction path outside of the sample. The resistance R_w of this exterior conduction path which was measured is in parallel with the conduction path through the sample. The effective resistance between the electrodes R_m is

$$1 / R_m = (1 / R_s) + (1 / R_w) \qquad (5)$$

where R_s is the resistance of the sample. The resistivity ρ_w of the fluid which was used for the calculation of R_w, was measured after the fluid flowed out of the cell and as soon as the flow was stopped by using a conductivity cell. This procedure allows us to use the resistivity of the sample (ρ_s) and the resistivity of the fluid (ρ_w) to approximately represent the values that were present during the streaming-potential measurement.

Streaming Potential Measurement

The streaming potential was measured during fluid flow by an HP 34401A voltmeter with an input resistance of more than 10^{10} Ω. The resistance of the water in the insulating piston (R_w) is taken into account. In this case the total electrical current is

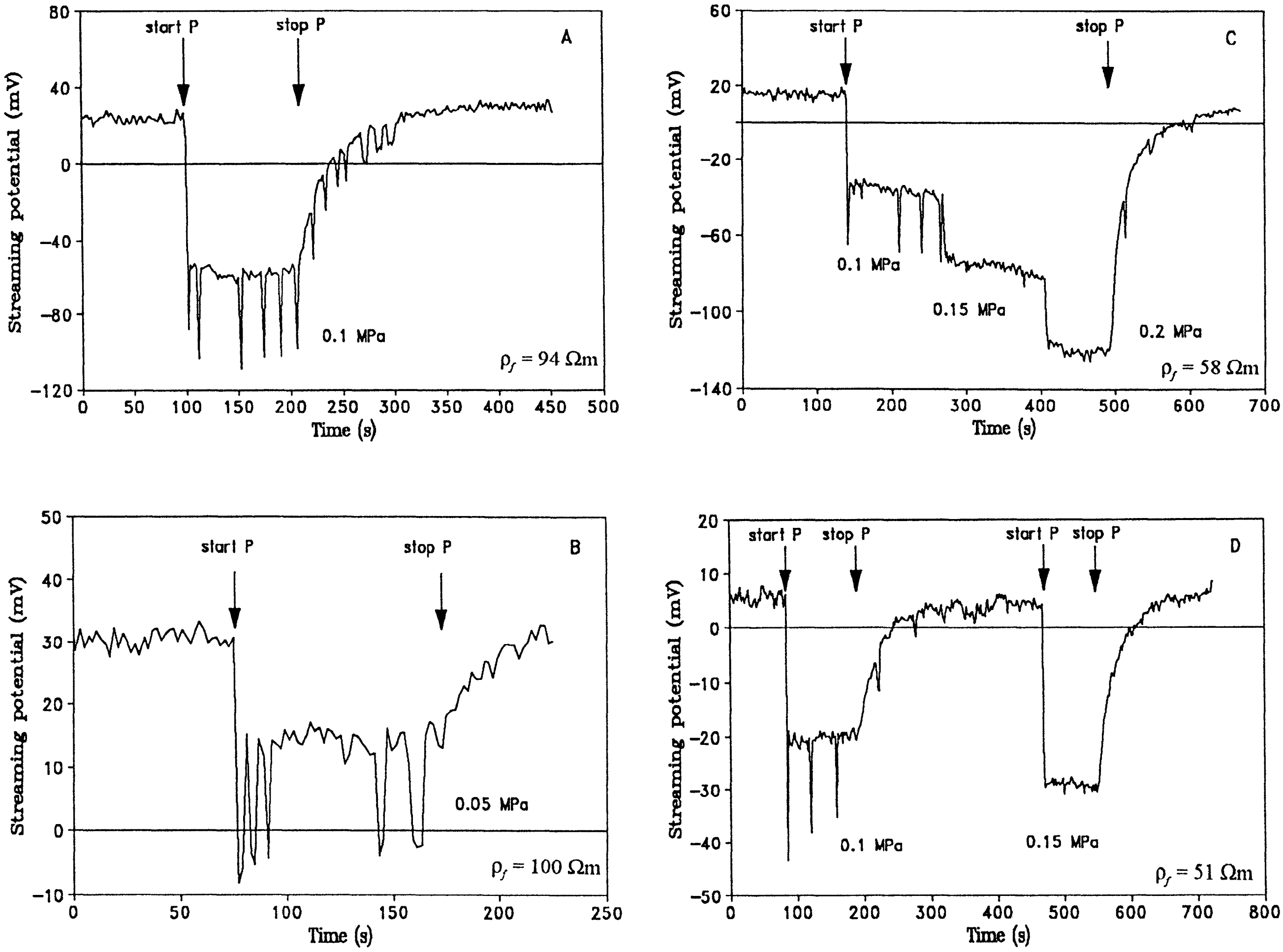

Figures 3. Streaming-potential measurements for different fluid resistivities (a) 94 Ωm, (b) 100 Ωm, (c) 58 Ωm and (d) 51 Ωm. The 0.1-0.5 Hz pulses were observed only for low fluid flow rate when ΔP = 0.05 or 0.1 MPa and when the injected water was less conductive than the previous solution. The electrokinetic coupling coefficients are (a) -85 mV/0.1 MPa, (b) -30 mV/0.1 MPa, (c) -61 mV/0.1 MPa, and (d) -24 mV/0.1 MPa.

no longer zero in the sample. Under this condition, (3) may be modified as follows:

$$\frac{\Delta V}{\Delta P} = C_s / (1+\frac{R_s}{R_w}) \qquad (1')$$

C_s being the electrokinetic coupling coefficient that would have been measured without this leakage current outside the sample (when $R_w >> R_s$). Data were recorded, once per second, with a PC computer and an IEEE interface. The different fluids were made to flow through the sample from the most resistive to the least until the measured resistivity of the fluids flowing out of the sample was constant. We then began the streaming-potential measurements. The confining pressure was applied manually by a pump. The pore pressure difference ΔP was applied by using a pump and measured by using a manometer. The pump is manually controlled; typical error in a measured pressure difference of 0.1 MPa is ±0.01 MPa for the F313 sample. The applied pore pressure difference was kept constant usually for 50 to 200 s. Fluid flow rate and fluid resistivity were measured during streaming-potential measurement, and the values given are average for the 50-200 s durations.

Results

We first describe the steady state streaming-potential measurements and then focus on pulses of 2-9 s duration that were observed when the input solution was replaced by a less conductive one and when the water flow was relatively low.

Steady State Streaming Potential Measurements

A typical streaming-potential variation when a pressure difference of 0.05 MPa was applied is shown in Figure 1a for a solution which is distilled water having a resistivity of 1030 Ωm. The potential was -25 mV when the fluid was not flowing through the sample and dropped to about -275 mV when the pressure was applied. The streaming potential is therefore -250 mV. Similar measurements were performed with pressure differences of 0.1 MPa and 0.15 MPa. The streaming potential is shown to be proportional to the applied pore pressure (Figure 2a). From the slope of the best fit line in Figure 2a, we obtain an apparent electrokinetic coupling coefficient $\Delta V/\Delta P$ of -614 mV/0.1 MPa, and a corrected coefficient C_s of -1331 mV/0.1 MPa after taking into account the resistance of the fluid in the cylindrical hole of the piston (R_w) (1'). The linearity between the streaming potential and the applied pore pressure is an important result and is not accepted by all investigators [*Middleton*, 1996].

When a more conductive salt solution of resistivity 720 Ωm (corresponding to a concentration of NaCl of 1.5x10^{-4} mol/L) was used under a pore pressure difference of 0.05 MPa, the streaming potential was -175 mV (Figure 1b). The streaming potentials for four different pore pressure differences are shown in Figure 2b, which gives a $\Delta V/\Delta P$ coefficient of -435 mV/0.1 MPa, and a C_s coefficient of -734 mV/0.1 MPa. Similar results for a salt solution of resistivity 490 Ωm corresponding to a NaCl concentration of 2x10^{-4} mol/L are shown in Figures 1c and 2c. The coefficient C_s is -404 mV/0.1 MPa. The results for the salt solution of resistivity 103 Ωm corresponding to a NaCl concentration of 9x10^{-4} mol/L are shown in Figures 1d and 2d. When the fluid is not flowing through the sample, the electric potential was -25 mV, it dropped to -78 mV when ΔP was 0.05 MPa, -132 mV when ΔP was 0.1 MPa, -176 mV when ΔP was 0.15 MPa and -220 mV when ΔP was 0.2 MPa. These measurements lead to a C_s coefficient of -157 mV/0.1 MPa.

When using more conductive fluid of resistivity 11 Ωm (9.5x10^{-3} mol/L of NaCl), 1.1 Ωm (0.1 mol/L), or 0.11 Ωm (1.45 mol/L of NaCl), the streaming potential was no longer constant for a constant applied pore pressure. The potential for the most conductive solution was too small to measure. Table 1 summarizes the electrokinetic coupling coefficient (C_s in mV/0.1 MPa) for the four solutions.

Transient streaming potential measurements

Distilled water of *p*H 5 and resistivity 3x10^3 Ωm was made to flow through the sample seven days (time needed to process the previous data) after the above-mentioned measurements. The solution flowing out of the cell became 30 times more conductive than the injected water with a resistivity of about 100 Ωm, still 10^3 less conductive than the most conductive solution used earlier (0.1 Ωm). Streaming potential was measured when the fluid resistivity became constant. Fluid flow rate through the sample was about 2.4 x 10^{-8} m^3/s when ΔP = 0.05 MPa and 4.2 x 10^{-8} m^3/s when ΔP = 0.1 MPa. Since the pore volume of the sample is 2.7 x 10^{-6} m^3, the residence time of fluid in the sample is about 2 min when ΔP = 0.05 MPa, and 1 min when ΔP = 0.1 MPa. As the exchange rate for sodium ions is of the order of 10^{-9} s, we assumed that the fluid conductivity inside the sample is the same as that measured after the fluid flowed through the sample. The measured permeability was 4.9x10^{-14} m^2, showing a 25% decrease compared to value measured just before the above-mentioned measurements with salt solutions (6.5x10^{-14} m^2; see *Jouniaux and Pozzi* [1995a] for the method). In all the experiments described below the injected fluid was distilled water. The electrokinetic coupling coefficient C_s is equal to the measured electrokinetic coupling coefficient $\Delta V/\Delta P$ as the resistance R_w of the exterior conduction path is important compared to the resistance of the sample R_s. Indeed the insulating piston is full of distilled water whereas it was full of salt water for the previous measurements (the resistance R_w is 49.4 MΩ, while the resistance of the sample is in the range 303-618 kΩ).

Table 1. Electrokinetic Coupling Coefficients C_s for Various Solutions of Resistivity ρ_f

NaCl, mol/L	Pure Water	1.5x10^{-4}	2x10^{-4}	9x10^{-4}
ρ_f, Ωm	1030	720	490	103
C_s, mV/0.1 MPa	-1331	-734	-404	-157

Table 2. Electrokinetic Coupling Coefficient C_s and 0.1-0.5 Hz Pulse Amplitude

ρ_f, Ωm	94	100	60	51
C_s, mV/0.1 MPa	-85	-30	-30	-24
Pulse amplitude, mV	40	20	30	15-25

As shown in Figure 3a when a pressure difference of 0.1 MPa was applied, the potential decreases from 25 mV to about -60 mV. After flowing through the sample, the solution has a resistivity of 94±1 Ωm. The electrokinetic coupling still defined from the dc component, is -85±20 mV/0.1 MPa. Superimposed on the dc signal are some 40 mV pulses with a duration of 2-6 s. In another experiment the resistivity of the fluid was 100±5 Ωm after flowing through the sample. The potential decreased from 30 mV to 15 mV when the applied pressure difference was 0.05 MPa. The electrokinetic coupling coefficient deduced from this measurement is -30±9 mV/0.1 MPa. Again pulses of amplitude 20 mV and duration of 4.5-9 s were observed (Figure 3b). Other measurements with various applied pressure differences are shown in Figures 3c and 3d. Such pulses were seen when the applied pressure difference was 0.1 MPa but not seen for larger applied pressure differences (0.15 MPa and 0.2 MPa). The fluid resistivity after flowing through the sample is 58±8 Ωm in Figure 3c and 51±5 Ωm in Figure 3d. The electrokinetic coupling coefficients deduced from these measurements are -61±5 mV/0.1 MPa and -24±5 mV/0.1 MPa in Figures 3c and 3d, respectively. The amplitudes of the pulses are about 15 to 25 mV and the duration 2-8 s. Table 2 summarizes the electrokinetic coupling coefficient (C_s in mV/0.1 MPa) and pulses corresponding to the different solution resistivities (ρ_f in Ωm).

Discussion

From the above-mentioned steady state measurements reported previously [*Jouniaux and Pozzi*, 1995a], the streaming potential is roughly proportional to the fluid resistivity with a slope of 1.2 mV/0.1 MPa/Ωm (Figure 4). This result leads to a roughly estimated zeta potential of -17 mV, using (4) with the assumptions that F=F^o and ε and η are constant. Note that zeta potential depends on salt concentration [*Pride and Morgan*, 1991] and that ε is of the order of 2-3 x 10^{-10} F/m for salt solutions. For all concentrations used, the surface species on sandstones are expected to be 99% SiOH as discussed in the description of the quartz-water systems. Since solutions of *p*H 5

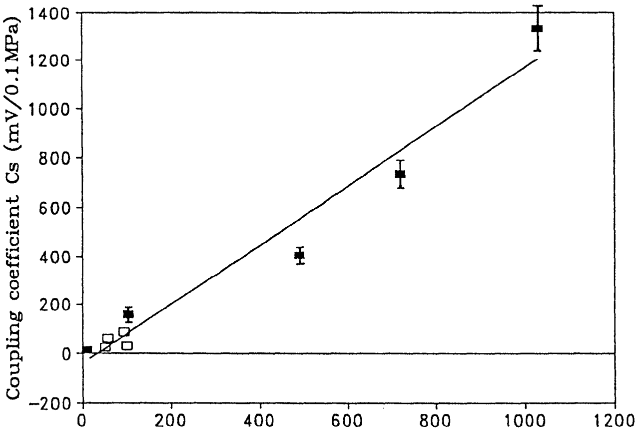

Figure 4. Electrokinetic coupling coefficient (mV/0.1 MPa) versus fluid resistivity obtained from steady state (solid squares) and transient (open squares) measurements.

are used in our study, a negative zeta potential is consistent with the studies on the isoelectric point.

The electrokinetic coupling coefficient based on the transient streaming potential measurements (open squares in Figure 4) is qualititatively consistent with the steady state measurements made previously (solid squares in Figure 4).

Note that the transient streaming-potential pulses were observed only (1) when the injected fluid is less conductive than the previous solution by a factor 10^3, and (2) when the applied pressure difference is as small as 0.05 MPa or 0.1 MPa, corresponding to a Darcian velocity of 17 cm/h (4 m/d) to 30 cm/h (7.4 m/d). The amplitudes of these pulses are about 15 to 40 mV, which represent 47%, 133%, 60%, and 60 to 100% of the measured signals in the examples shown in Figures 3a, 3b, 3c, and 3d, respectively. Note that for each measurement the fluid resistivity is approximately constant (with some fluctuations as shown by the error bars) and did not change sufficiently to induce the observed pulses. A variation of 50% in water resistivity, for example, would induce a variation of 50% in streaming potential as C_s is proportional to the fluid resistivity (3). Moreover in all the streaming-potential measurements performed in our laboratory, usually on sandstone and limestone samples, pulses in the measurements were only observed when less conductive water was made to flow through a previously salted sample. The opposite arrangement, when a more conductive water was made to flow through the sample, never produced such pulses.

The appearance of the pulses suggests that more H_3O^- cations and hydrated counterions Na^+ of the diffuse layer are suddenly carried along by the fluid. These charges may have resulted from the salt deposited in the rock, part of which is put into the solution when the distilled water is used. Indeed the decrease in the permeability by 1/4 between the first measurement and the measurements performed 7 days later shows that some salt deposit very likely exists on the surface of the rock. If certain heterogeneity of salt deposit on the surface of the rock could explain some sudden increase of carried cations (hydrated ions Na^+) it cannot explain the frequency of these pulses (0.1 to 0.5 Hz) because the exchange rate for sodium ion is of the order of 10^{-9} s. Since all our measurements were performed on the sample subjected to stresses below the rupture (strength less than 45%), we do not think that microcracks could give rise to these pulses. Moreover no such pulses were observed when the sample was stressed from 50% of the strength up to rupture. In view of electrokinetic coupling coefficient given by (3) not being dependent on sample size, we think that these pulses are not related to sample size and similar pulses can be observed in geophysical field experiments.

In our opinion, these pulses may arise from random or transient breaks of fluid through pore throats the size of which have been reduced by salt deposits. This suggestion is consistent with the observation that the pulses disappeared at higher pressure difference (salt deposit has been swept away from the pore throats).

Possible Implications for Electrotelluric Earthquake Precursors

The streaming-potential pulses observed in our laboratory experiments can be used to explain certain oscillary electromagnetic signals observed in the field before some earthquakes.

Variations in groundwater flow before and after earthquakes have often been reported in the literature. For example, a sudden hot-spring erupted in the epicentral region several months before the 1923 Kanto M=7.9 earthquake [*Wakita*, 1982]. Water level changes of about 5 to 10 cm were reported prior to the 1976 Tangshan earthquake in China [*Jin*, 1985]. Along the San Andreas fault in California, changes in water levels up to 16 cm are observed to accompany some creep events [*Roeloffs et al.*, 1989]. Abnormal increases in water flow lasting 6 to 12 months have been measured in springs and wells at distances of the order of 50 km from the epicenter, beginning a few days after some earthquakes, especially those generated along some major normal faults. Expelled water volumes were 0.2 to 0.5 km^3 for two earthquakes of magnitude 7 and 7.3 studied by *Muir-Wood and King* [1993].

More recently, geochemical evidence of ground-water changes were reported before earthquake [*Toutain et al.*, 1997; *Tsunogai and Wakita*, 1995]. *Tsunogai and Wakita* [1995] reported geochemical evidence of precursory groundwater changes observed at a distance of 20 km from the epicenter of the M=7.2 Kobe earthquake on January 17, 1995. Chlorine ion (Cl^-) and sulfate ion (SO_4^{2-}) concentration of water from a 100 m deep well began to increase 6 months before the earthquake. Four days before the earthquake, the Cl^- concentration was about 10% higher than the average background level. Tsunogai and Wakita stated that chemical changes observed before the earthquake could be attributed to the introduction of groundwater enriched in Cl^- and SO_4^{2-} to the artesian layer of the wells and coming from the fracture zone. They suggested that changes of groundwater flow may occur by a change either in regional tectonic stress or in permeability. Increased groundwater discharge was observed in many parts of the aftershock region [*King et al.*, 1995].

The above-mentioned examples illustrate that the chemical composition of water can be changed in places affected by earthquake-related variations of groundwater flow, though the mechanism needed to explain these changes is still uncertain [*Dobrovolsky at al.*, 1989; *Draganov et al.*, 1991; *Bernard*, 1992; *Fenoglio et al.*, 1995]. However it is likely that water flowing in some rock layer can introduce changes in conductivity. In such cases, electrokinetic signals including pulses of duration 2-9 s may be produced by fluid flow, as suggested by our laboratory measurements. Our interpretation involves electrokinetic effects not at the source but near the site of measurements, for an electromagnetic field is easily attenuated in the conductive Earth [*Honkura*, 1992]. Our suggestion of fluid breaking through salt deposit pore throats is similar to the physical mechanism proposed by *Fenoglio et al.* [1995], which involves nonuniform fluid flow in the Earth resulting from pressure decrease due to dilatancy, partial blockage by silica deposition, and clearing of deposition as the pressure increases. The paths of fluid flow, of electric currents, and the changes in chemical composition in the Earth are, of course, more complex and could induce more complicated signals.

The dc component of streaming potential could be observed by measuring the vertical electric field, or the horizontal electric field if a lateral heterogeneity in the electrokinetic coupling coefficient values exists as suggested by *Fitterman* [1979]. Indeed, the vertical component should be dominant because it is proportional to the vertical driving pore pressure and to the the electrokinetic coupling coefficient (no heterogeneity in C_s is needed).

Could we explain the observation that no electric coseismic anomalies are observed for most earthquakes? Our laboratory measurements show that the pulses were observed only when the fluid flow was relatively low and when less conductive fluid was flowing through the rock. If these conditions are met, the observation of pulses of 0.1 to 0.5 Hz can be attributed to electrokinetic effects caused by groundwater flow changes before the earthquake.

Conclusion

Transient streaming-potential variations with pulses of amplitude 15-40 mV and frequency 0.1 to 0.5 Hz were observed under geochemical changes. Such geochemically induced effects may possibly be responsible for the signals of frequency 0.1 to 0.5 Hz that were sometimes observed before an earthquake.

Acknowledgments. This paper has been greatly improved by the reviewers P. M. Dove, Y. Fujinawa and A. C. Fraser-Smith. This research was supported by CNRS/INSU. It is a collaboration with C. Philippe, ENSAM Paris. This is a CNRS-INSU-DBT contribution 78 thème fluides et failles, a CNRS-INSU-PNRN contribution thème risques sismiques, and a CNRS-INSU-PRH contribution thème circulation des fluides dans la croûte.

References

Adamson, A. W., *Physical Chemistry of Surfaces*, Wiley-Interscience, New York, 1976.

Ahmad, M., A laboratory study of streaming potentials, *Geophys. Prospect.*, *12*, 49-64, 1964.

Antraygues, P., and M. Aubert, Self potential generated by two-phase flow in a porous medium: Experimental study and volcanological applications, *J. Geophys. Res.*, *98*, 22,273-22,281, 1993.

Bernard, P., Plausibility of long distance electrotelluric precursors to earthquakes, *J. Geophys. Res.*, *97*, 17,531-17,546, 1992.

Corwin, R. F., and H. F. Morrison, Self-potential variations preceding earthquakes in Central California, *Geophys. Res. Lett.*, *4*, 171-174, 1977.

Dobrovolsky, I. P., N. I. Gershenzon, and M. B. Gokhberg, Theory of electrokinetic effects occuring at the final stage in the preparation of a tectonic earthquake, *Phys. Earth Planet. Inter.*, *57*, 144-156, 1989.

Dove, P. M., and S.F. Elston, Dissolution kinetics of quartz in sodium chloride solutions: Analysis of existing data and a rate model for 25C, *Geochim. Cosmochim. Acta*, *56*, 4147-4156, 1992.

Draganov, A. B., U. S. Inan, and Yu.N. Taranenko, ULF magnetic signatures at the Earth surface due to groundwater flow: A possible precursor to earthquakes, *Geophys. Res. Lett.*, *18*, 1127-1130, 1991.

Dukhin, S. S., and B.V. Derjaguin, *Surface and Colloid Science*, vol. 7, edited by E. Matijevic, John Wiley, New York, 1974.

Fenoglio, M. A., M. J. S. Johnston, and J. D. Byerlee, Magnetic and electric fields associated with changes in high pore pressure in fault zones: Application to the Loma Prieta ULF emissions, *J. Geophys. Res.*, *100*, 12,951-12,958, 1995.

Fitterman, D. V., Theory of electrokinetic-magnetic anomalies in a faulted half-space, *J. Geophys. Res.*, *84*, 6031-6040, 1979. (Correction, *J. Geophys. Res.*, *86*, 9585-9588, 1981.)

Fraser-Smith, A.C., A. Bernardi, P.R. McGill, M.E. Ladd, R.A. Helliwelll and O.G. Villard Jr., Low-frequency magnetic field measurements near the epicenter of the Ms 7.1 Loma Prieta earthquake, *Geophys. Res. Lett.*, *17*, 1465-1468, 1990.

Fraser-Smith, A. C., P. R. McGill, R. A. Helliwell, and O.G. Villard Jr., Ultra-low frequency magnetic field measurements in southern California during the Northridge earthquake of 17 January 1994, *Geophys. Res. Lett.*, *21*, 2195-2198, 1994.

Fujinawa, Y., and K. Takahashi, Emission of electromagnetic radiation preceding the Ito seismic swarm of 1989, *Nature*, *347*, 376-378, 1990.

Fujinawa, Y., T. Kumagai, and K. Takahashi, A study of anomalous underground electric field variations associated with a volcanic eruption, *Geophys. Res. Lett.*, *19*, 9-12, 1992.

Gruszow, S., J. C. Rossignol, C. Pambrun, A. Tzanis, and J.L. Le Mouël, Characterisation of electric signals observed in the Ioannina region (Greece), *C.R. Acad. Sci. Paris*, *320*, part IIa, 547-554, 1995.

Honkura, Y., Electric fields in the conducting crust for oscillating electric dipole sources, in *Proceedings of the International Workshop on Low-Frequency Electrical Precursors*, *Rep. 92-15*, edited by S. K. Park, , Inst. of Geophys. and Planet. Phys., Univ. of Calif., Riverside, 1992.

Hunter, R. J., *Zeta Potential in Colloid Science*, Academic, San Diego, Calif., 1981.

Ishido, T., and H. Mizutani, Experimental and theoretical basis of electrokinetic phenomena in rock-water systems and its applications to geophysics, *J. Geophys. Res.*,*86*, 1763-1775, 1981.

Jin, A., Some results of observations and studies on Earth resistivity in China (abstract), *Eos Trans. AGU*, *66*(46), 1066-1067, 1985.

Jouniaux, L., and J.-P. Pozzi, Streaming potential and permeability of saturated sandstones under triaxial stress: Consequences for electrotelluric anomalies prior to earthquakes, *J. Geophys. Res.*, *100*, 10,197-10,209, 1995a.

Jouniaux, L., and J.-P. Pozzi, Permeability dependence of streaming potential in rocks for various fluid conductivities, *Geophys. Res. Lett.*, *22*, 485-488, 1995b.

Jouniaux, L., S. Lallemant, and J.-P. Pozzi, Changes in the permeability, streaming potential and resistivity of a claystone from the Nankai prism under stress, *Geophys. Res. Lett.*, *21*, 149-152, 1994.

King, C.-Y., N. Koizumi, and Y. Kitagawa, Hydrogeochemical anomalies and the 1995 Kobe earthquake, *Science*, *269*, 38-39, 1995.

Li, H. C., and P. L. De Bruyn, Electrokinetic and adsorption studies on quartz, *Surf.Sci.*, *5*, 203-220, 1966.

Massenet, F., and P. Van Ngoc, Experimental and theoretical basis of self-potential phenomena in volcanic areas with reference to results obtained on Mount Etna, *Earth Planet. Sci. Lett.*, *73*, 415-429, 1985.

Middleton, M. F., The relationship of streaming potential and applied pressure to pore geometry (abstract) *Ann. Geophys. Eur. Geophys. Soc.*, 178, 1996.

Miyakoshi, J., Anomalous time variation of the self-potential in the fractured zone of an active fault preceding the earthquake occurrence, *J. Geomagn. Geoelectr.*, *38*, 1015-1030, 1986.

Mizutani, H., and T. Ishido, A new interpretation of magnetic field variation associated with Matsushiro earthquake, *J. Geomagn. Geoelectr.*, *28*, 179-188, 1976.

Mizutani, H., T. Ishido, T. Yokokura, and S. Ohnishi, Electrokinetic phenomena associated with earthquakes, *Geophys. Res. Lett.*, *3*, 365-368, 1976.

Molchanov, O. A., Y. A., Kopytenko, P. M., Voronov, E. A. Kopytenko, T.G. Matiashvili, A. C. Fraser-Smith, and A. Bernadi, Results of ULF magnetic field measurements near the epicenters of the Spitak (Ms = 6.9) and Loma Prieta (Ms = 7.1) earthquakes: Comparative analysis, *Geophys. Res. Lett.*, *19*, 1495-1498, 1992.

Morat, P., J.-L. Le Mouël, G. Nover, and G. Will, Annual variation of the water saturation of a highly porous rock driven by a seasonal temperature variation and measured by an array of electrodes, *C. R. Acad. Sci. Paris, 315, Ser. II*, 1083-1090, 1992.

Morgan, F. D., E. R. Williams, and T. R. Madden, Streaming potential properties of Westerly granite with applications, *J. Geophys. Res.*, *94*, 12,449-12,461, 1989.

Muir-Wood, R., and G. C. P. King, Hydrological signatures of earthquake strain, *J. Geophys. Res.*, *98*, 22,035-22,068, 1993.

Murakami, H., H. Mizutani, and S. Nabetani, Self-potential anomalies associated with an active fault, *J. Geomagn. Geoelectr.*, *36*, 351-376, 1984.

Myachkin, V.I., G.A. Sobolev, N.A. Dolbilkina, V.N. Morozow, and V.B. Preobrazensky, The study of variations in geophysical fields near focal zones of Kamchatka, *Tectonophysics*, *14*, 287-293, 1972.

Nourbehecht, B., Irreversible thermodynamic effects in inhomogeneous media and their applications in certain geoelectric problems, Ph.D., thesis, Mass. Inst. of Technol., Cambridge, 1963.

Nur, A., Dilatancy, pore fluids, and premonitory variations of ts/tp travel times, *Bull. Seismol. Soc. Am.*, *62*, 1217-1222, 1972.

Overbeek, J. T. G., Electrochemistry of the double layer, in *Colloid Science*, vol. 1, *Irreversible Systems*, edited by H. R. Kruyt, pp.115-193, Elsevier, New York, 1952.

Pozzi, J.-P., and L. Jouniaux, Electrical effects of fluid circulation in sediments and seismic prediction, *C. R. Acad. Sci. Paris, 318, Ser. II*, 73-77, 1994.

Pride, S.R., Governing equations for the coupled electromagnetics and acoustics of porous media, *Phys. Rev. B*, *50*, 15,678-15,696, 1994.

Pride, S.R., and F.D. Morgan, Electrokinetic dissipation induced by seismic waves, *Geophysics*, *56*, 914-925, 1991.

Revil, A., M. Darot, and P.A. Pezard, From surface electrical properties to spontaneous potentials in porous media, *Surv. Geophys.*, *17*, 331-346, 1996.

Roeloffs, E. A., S. S. Burford, F.S. Riley, and A.W. Records, Hydrologic effects on water level changes associated with episodic fault creep near Parkfield, California, *J. Geophys. Res.*, *94*, 12,387-12,402, 1989.

Ruffet, C., La conductivité électrique complexe dans quelques roches crustales, PhD. Thesis, Université Strasbourg I, 1993.

Ruffet, C., Y. Gueguen, and M. Darot, Complex conductivity measurements and fractal nature of porosity, *Geophysics*, *56*, (6), 758-768, 1991.

Scholz, C. H., L. R. Sykes, and Y. P. Aggrawal, Earthquake prediction : A physical basis, *Science, 181*, 803-810, 1973.

Serebryakova, O. N., S. V. Bilichenko, V. M. Chmyrev, M. Parrot, J. L. Rauch, F. Lefeuvre, and O. A. Pokhotelov, Electromagnetic ELF radiation from earthquake regions as observed by low-altitude satellites, *Geophys. Res. Lett.*, *19*, 91-94, 1992.

Sharma, M. M., J.F. Kuo, and T. F. Yen, Further investigation of the surface charge properties of oxide surfaces in oil-bearing sands and sandstones, *J. Colloid Interface Sci.*, *115*, 9-16, 1987.

Sobolev, G. A., Application of electric method to the tentative short-term forecast of Kamchatka earthquakes, *Pure Appl. Geophys.*, *113*, 229-235, 1975.

Somasundaran, P. and R..D. Kulkarni, A new streaming potential apparatus and study of temperature effects using it, *J. Colloid Interface Sci.*, *45*, 591-600, 1973.

Stern, O., Zür theorie der electrolytischen doppelschicht, *Z. Elecktrochem.*, *30*, 508-516, 1924.

Toutain, J.-P., M. Munoz, F. Poitrasson, and A.C. Lienard, Springwater chloride ion anomaly prior to a Ml=5.2 pyrenean earthquake, , *Earth Planet. Sci. Lett.*, in press, 1997.

Tsunogai, U. and H. Wakita, Precursory chemical changes in ground water: Kobe earthquake, Japan, *Science*, *269*, 61-63, 1995.

Varotsos, P., and K. Alexopoulos, Physical properties of the variations of the electric field of the Earth preceding earthquakes, I, *Tectonophysics, 110*, 73-98, 1984a.

Varotsos, P., and K. Alexopoulos, Physical properties of the variations of the electric field of the Earth preceding earthquakes, II, Determination of epicenter and magnitude, *Tectonophysics, 110*, 99-125, 1984b.

Wakita, H., Changes in groundwater level and chemical composition, in *Earthquake Prediction Techniques*, edited by T. Asada, pp. 175-216, Univ. of Tokyo Press, Tokyo, 1982.

L. Jouniaux and J.-P. Pozzi, Laboratoire de Géologie de l'École Normale Supérieure , URA 1316 du CNRS, 24, rue Lhomond, 75231 Paris Cédex 05, France. (e-mail: jouniaux@magnetit.ens.fr; pozzi@magnetit.ens.fr)

(Received June 13, 1996; revised March 15, 1997;
accepted March 27, 1997.)

Étude des propriétés physiques du calcaire de la carrière de Mériel

C.R. Acad. Sci. Paris,
t. 322, série II a,
p. 361 à 367,
1996

Laurence Jouniaux, Luc Dubet, Maria Zamora et Pierre Morat

L. J. : Laboratoire de Géologie de
l'École Normale Supérieure,
24, rue Lhomond,
75231 Paris Cedex 05, France ;

L. D. et M. Z. : Laboratoire
de Géomatériaux, Institut
de Physique du Globe de Paris,
4, place Jussieu, 75252 Paris Cedex 05,
France ;

P. M. : Laboratoire de
Géomagnétisme, Institut
de Physique du Globe de Paris,
4, place Jussieu, 75252 Paris Cedex 05,
France.

Résumé Dans le but d'obtenir les données nécessaires à la modélisation des phénomènes électriques observés dans la carrière laboratoire de Mériel, quelques propriétés physiques de la roche qui forme cette carrière ont été étudiées. La perméabilité moyenne de cette roche est de 230 mD. De fortes hétérogénéités de la perméabilité ont été observées à l'échelle du décimètre. Le facteur de formation est d'environ 3,5, montrant que le réseau poreux est bien connecté. Le coefficient de couplage électrocinétique est de l'ordre de –0,50 V/MPa, pour une eau dont la résistivité est de 200 Ωm, et les effets de conductivité de surface sont négligeables. Les vitesses des ondes élastiques (P et S) sont reliées à la porosité par une relation linéaire.

Mots-clés : Propriétés électriques, Propriétés élastiques, Propriétés de transport, Calcaire de Mériel.

Abstract **Physical properties of limestone from the quarry of Mériel**

In order to model the electrical phenomena observed in the laboratory quarry (at Mériel, France) we performed systematic measurements of the physical properties of the quarry rocks. We showed that the permeability is heterogeneous at decimetre scale and its average value is 230 mD. The formation factor is 3.5, showing that the porous network is well connected. The electrokinetic coupling coefficient is –0.50 V/MPa for a fluid resistivity of 200 Ωm and the effects of surface conductivity are negligible. Elastic wave velocities are connected to porosity by a linear relationship.

Keywords: Electrical properties, Elastic properties, Transport properties, Mériel limestone.

Abridged English Version

INTRODUCTION

Electrokinetic phenomena are thought to be responsible for some electric or magnetic anomalies measured before seismic activity (Mizutani *et al.*, 1976; Bernard, 1992) or on volcanoes (Zlotnicki and Le Mouël, 1988; Aubert and Dana, 1994). In the Mériel quarry (limestone) changes of self-potential have been related to atmospheric pressure changes (Morat *et al.*, 1992; Morat and Le Mouël, 1992). To understand and to model these changes we measured the physical properties of the quarry rocks.

TRANSPORT PROPERTIES

Previous measurements have shown porosity values in the range 28-46% with a peak around 37-41% (Denis *et al.*, 1987) in quarry rock. Porosity of rock samples varies from 33 to 39% and permeability from 74 to 312 mD (**table I**). The access radii distribution shows peaks at 16 and 0.15 µm for CM1A sample and 10, 0.2 and 0.03 µm for CM1B sample (**fig. 2**). The smallest radii are thought to decrease the permeability.

ELECTRIC PROPERTIES

Electric measurements have been performed in a triaxial press (Jouniaux and Pozzi, 1995 *a*; Pozzi and Jouniaux, 1994). The formation factor F value is 3.3. The Archie's law cementation index m ($F = \Phi^{-m}$) is that for a weakly consolidated sample ($m = 1.14$). Permeability k can be computed using Paterson's relation $k = cm^2 F^{-1}$ (with m the hydraulic radius and c a geometric constant), taking

Note

présentée par Jean-Paul Poirier.

remise le 15 mars 1995, ***acceptée après révision le*** 11 décembre 1995.

1250-8050/96/03220361 • $ 2.00 © Académie des Sciences

m_1 = 5 µm (k_1=3.57 D), m_2 = 0.1 µm (k_2 = 1.43 mD) and considering that there are 2 families of pores in series. The *ad hoc* relation $(1/k) = (1/k_1) + (1/180\ k_2)$ allows a value of permeability of 240 mD to be calculated. The electrokinetic coupling coefficient $\Delta V/\Delta P = (\varepsilon\zeta/\eta\sigma)\ (FF/FF^{\circ})$ (Dukhin and Derjaguin, 1974) has been measured (**table II, fig. 3**) with a fluid resistivity of 200 Ω.m, where ε, η and σ are electric permittivity, fluid viscosity and fluid conductivity respectively. *FF* is the measured formation factor, *FF°* the formation factor with high salinity fluid and ζ the electric potential at the rock/fluid interface. The ζ potential has been deduced from these measurements and is equal to –3.5 mV. The non-permeability dependence of streaming potential shows that the surface conductivity is negligible (Jouniaux and Pozzi, 1995 *b*).

ELASTIC PROPERTIES

Elastic wave velocities have been measured on saturated and dry samples (**table III**) in 3 directions using the experimental device reported in Zamora and Poirier (1990). *P*-wave velocity is increased with saturation whereas S wave velocity is decreased. The effect of saturation on *P*-wave velocities can be explained by the Gassmann equation. Values of *S*-wave velocities predicted by this theory are too high. This effect has already been observed (Blangy *et al.*, 1993). Figure 4 shows *P*- and *S*-wave velocities as a function of porosity in dry and saturated cases. We observe a linear dependence of velocities on porosity. The linear porosity dependence of *P*- and *S*-wave velocities could be used to infer *in situ* porosity values by measuring velocity of elastic waves on the rock surface.

CONCLUSION

Permeability has been shown to vary from 100 to 300 mD. The electrokinetic coupling coefficient is –0.50 V/MPa with a fluid resistivity of 200 Ωm, compared with –0.02 to –2 V/MPa for Fontainebleau sandstones. Moreover, the surface conductivity is negligible compared with fluid conductivity. The formation factor is 3.5 showing a very well connected network. The dependence on porosity of velocity of *P* and *S* waves is linear. These properties could be used to understand and to model self-potential changes measured in Mériel quarry and are thought to be due to electrokinetic phenomena.

INTRODUCTION

La recherche de phénomènes physiques qui annonceraient les séismes et les éruptions volcaniques est un sujet d'actualité. Des variations de la conductivité électrique et du potentiel spontané ont été clairement reliées à l'activité volcanique (Zlotnicki et Le Mouël, 1988). Les potentiels électrocinétiques produits par les mouvements de fluide dans les roches pourraient expliquer les signaux observés avant les séismes (Mizutani *et al.* 1976 ; Bernard, 1992) et sur les volcans (Aubert et Dana, 1994). C'est dans ce cadre de prédiction, que des mesures *in situ* dans la carrière de Mériel ont été entreprises. Des mesures de résistivité électrique (Morat *et al.*, 1992) et de potentiel électrique (Morat et Le Mouël, 1992) sont effectuées depuis plusieures années et les variations du potentiel électrique ont été clairement reliées aux variations de la pression atmosphérique dans la galerie. Pour modéliser ces variations du potentiel, nous avons entrepris de caractériser les propriétés physiques du calcaire de Mériel, en particulier sa porosité, la géométrie de son réseau poreux, sa perméabilité, la conductivité électrique, le coefficient de couplage électrocinétique et la vitesse des ondes élastiques.

PROPRIÉTÉS DE TRANSPORT

Le calcaire de Mériel est un calcaire biodétritique grossier d'âge Lutétien (Éocène), formé par accumulation en mer peu profonde de débris coquilliers plus ou moins cimentés. L'observation au microscope montre des débris organogènes (0,1-0,5 mm de diamètre) difficilement identifiables et

Tableau I Porosité et perméabilité à l'eau et à l'air. Les directions 1 et 2 correspondent aux deux directions de mesure.

Porosity and permeability. Directions 1 and 2 correspond to the two directions of measurement.

Éprouvette	Porosité (%)	Perméabilité à l'air (mD)			Perméabilité à l'eau (mD)
		Direction 1	Direction 2	Moyenne	
CM1	35,5	112	372	242	
CM2	36,2	309		309	
CM3	34,3	161	264	212	
CM4	33,3	108		108	
CM5	38,7	268	319	293	
CM6	35,0				156
CM7	35,0				74

une porosité importante laissée libre par le ciment calcique peu abondant. Denis *et al.* (1987) ont montré que ce calcaire est hétérogène à l'échelle du décimètre. Sa porosité varie entre 28 et 46 % avec un maximum entre 37 et 41 %.

Pour effectuer notre étude, 6 blocs de calcaire on été prélevés dans la carrière. Dans cinq de ces blocs, un cube de 50 mm de côté fut découpé, pour mesurer les propriétés élastiques et la porosité, et une ou deux carottes (découpées dans deux directions perpendiculaires) de 22 mm de diamètre pour mesurer la perméabilité à l'air. Les mesures électriques et de perméabilité à l'eau furent effectuées dans deux carottes de 25 mm de diamètre et 48 mm de long prélevées dans le dernier bloc.

La porosité des différentes éprouvettes fut mesurée par la méthode de la triple pesée. Les résultats montrent que la porosité des blocs étudiés varie entre 33 et 39 % (**tableau I**). La perméabilité à l'air k_A fut mesurée avec un perméamètre à air à charge variable. La perméabilité de cette roche est relativement faible vu sa porosité importante (**tableau I**) et montre une forte hétérogénéité provoquée par un zonage de la roche (**fig. 1**). On remarque sur cette photo deux zones distinctes, l'une où les pores sont abondants et fins et l'autre où ils sont gros et dispersés. C'est dans cette dernière que la

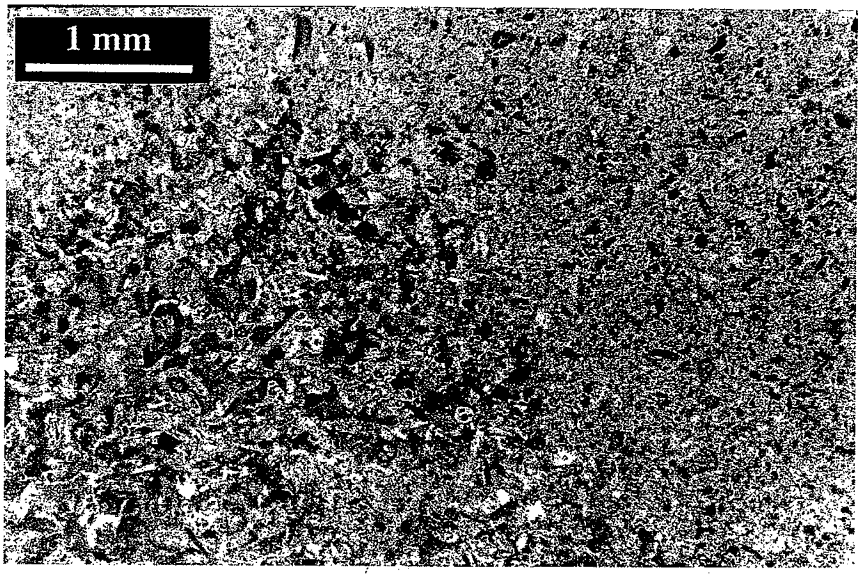

Fig. 1 Lame mince de la roche imprégnée d'une résine.
La couleur noire est la couleur de la résine occupant l'espace poreux.

Thin section of the rock impregnated with epoxy. Resin in the pore spaces shows were as black patches.

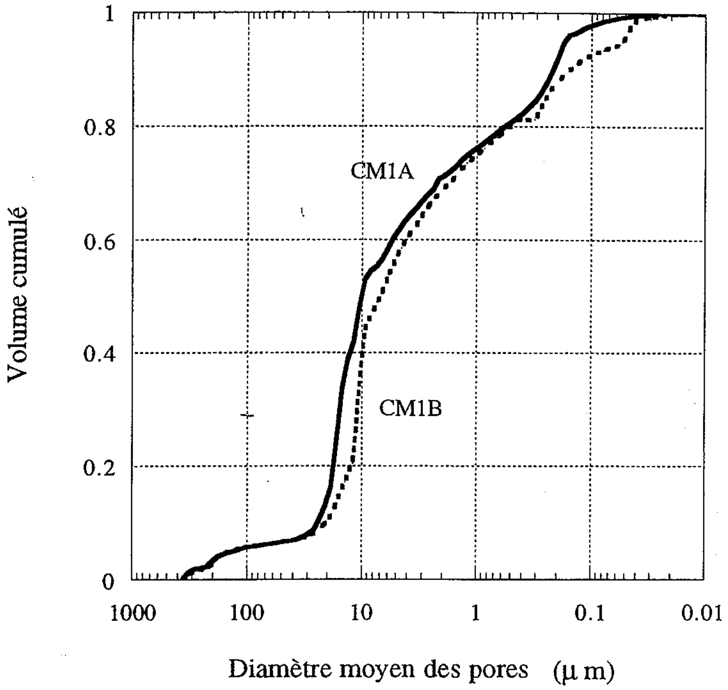

Fig. 2 Courbes porosimétrie au mercure pour les échantillons CM1A et CM1B.

Mercury porosimetry saturation curves for CM1A and CM1B samples.

perméabilité sera plus forte. Le bloc CM1 est celui qui présente une plus forte hétérogénéité, l'écart entre la perméabilité obtenue dans les deux directions de mesure est de 54 %. Dans les deux éprouvettes ayant servi à mesurer la perméabilité, des mesures de porosimétrie au mercure furent effectuées. L'éprouvette CM1A, qui est la plus perméable, présente une distribution des rayons d'accès bimodale, avec un maximum centré vers 16 μm et un autre moins important vers 0,15 μm. L'éprouvette CM1B, la moins perméable, présente trois pics, un vers 10 μm, c'est le plus important, et deux autres vers 0,2 et 0,03 μm respectivement (**fig. 2**). Ce sont sans doute ces très faibles rayons d'accès qui font diminuer la perméabilité. La perméabilité à l'eau k_E a été mesurée sur les échantillons CM6 et CM7 par la méthode du débit et déduite de la loi de Darcy. On observe que les perméabilités à l'eau et à l'air sont à peu près du même ordre (**tableau I**).

PROPRIÉTÉS ÉLECTRIQUES

La conductivité électrique et le potentiel électrocinétique ont été mesurés dans les échantillons CM6 (saturé) et CM7 (sec). L'eau utilisée est de l'eau distillée de pH = 5. Quand l'eau parcourt l'échantillon, elle se charge d'ions au contact de la matrice, et sa résistivité après passage dans l'échantillon est de 210 à 220 Ωm. Pendant les expériences, les échantillons sont jaquettés dans une cellule triaxiale (Jouniaux et Pozzi, 1995 *a*, Pozzi et Jouniaux, 1994). La conductivité électrique est mesurée à une fréquence de 4 kHz. Le potentiel électrocinétique ΔV est mesuré toutes les secondes, par un multimètre à haute impédance d'entrée ($>10^{10}$ Ω), quand l'eau circule dans l'échantillon sous une différence de pression ΔP de 0,05 à 0,2 MPa.

Le facteur de formation F (résistivité de l'échantillon/résistivité de l'eau) est de 3,3 pour l'échantillon CM6. Dans le cas de l'échantillon CM7, le rapport résistivité de l'échantillon/résistivité de l'eau, égal à F/S_w^2, avec S_w^2 le volume d'eau/volume des pores, est de 3,6. Ces mesures montrent que la saturation de cet échantillon pendant les expériences est de 96 % et que son réseau poreux est assez bien connecté. On peut déduire de ces mesures une loi d'Archie simple $F = \Phi^{-1,14}$ dont l'exposant est petit, ce qui montre que ce calcaire est mal consolidé, en bon accord avec les observations effectuées sur les lames minces. La perméabilité peut

Tableau II Propriétés électriques. L'échantillon CM6 est saturé et l'échantillon CM7 est sec.

Electrical properties. CM6 sample is saturated and CM7 is dry.

éprouvette	Contrainte axiale (MPa)	Pression de confinement (MPa)	Facteur de Formation	Coefficient de couplage électrocinétique (V/MPa)
CM6	7,5	5	3,3	–0,51
CM7	0,6	0,5	3,6	–0,47

être calculée en utilisant la relation de Paterson (1983), $k = cm^2 F^{-1}$, avec m le rayon hydraulique. Pour $m_1 = 5$ µm, $k_1 = 3{,}57$ D et pour $m_2 = 0{,}1$ µm, $k_2 = 1{,}43$ mD. En considérant les pores de différentes tailles en série, une moyenne harmonique *ad hoc* du type $1/k = (1/k_1) + (1/180\ k_2)$ permet de calculer une perméabilité de 240 mD.

Le coefficient de couplage électrocinétique est le potentiel électrocinétique ΔV par unité de pression d'eau ΔP et $\Delta V/\Delta P = (\varepsilon\zeta/\eta\sigma)(FF/FF^{\circ})$ (Dukhin and Derjaguin, 1974), où ε, η et σ sont respectivement la permittivité électrique, la viscosité et la conductivité du fluide. FF est le facteur de formation mesuré, FF° le facteur de formation avec de l'eau très conductrice, et ζ le potentiel électrique à l'interface roche/fluide. Les conditions d'expérience, le facteur de formation, et le coefficient de couplage électrocinétique (quand la résistivité de l'eau est de 200 Ωm) sont données dans le tableau II. La figure 3 montre une mesure typique du potentiel électrocinétique sur un échantillon quand l'eau circule sous des différences de pression variées. La différence de perméabilité d'un facteur 2 entre les deux échantillons n'a pas entraîné une différence de coefficient de couplage électrocinétique, montrant ainsi que les effets de conductivité de surface sont négligeables (Jouniaux et Pozzi, 1995 *b*). Ces mesures permettent de calculer un potentiel ζ d'environ -3,5 mV ($\varepsilon = 7{,}08.10^{-10}$ F/m, $\eta = 10^{-3}$ Pa.s et $\sigma = 4{,}65$ mS/m) en considérant les effets de conductivité de surface négligeables, c'est-à-dire $FF = FF^{\circ}$.

PROPRIÉTÉS ÉLASTIQUES

Pour chaque éprouvette, la vitesse des ondes élastiques P et S a été mesurée dans trois directions perpendiculaires, avec une technique classique de propagation d'ondes ultrasonores (1 MHz) à pression atmosphérique. La démarche expérimentale et le dispositif utilisés sont décrits par Zamora et Poirier (1990). Ces mesures furent effectuées d'abord dans l'éprouvette préalablement séchée à l'étuve à 70°C pendant 48 h, puis dans l'éprouvette saturée sous vide avec de l'eau distillée. Les résultats de ces mesures sont donnés dans le tableau III. L'anisotropie des ondes P est inférieure à 8 % dans le cas sec et sensiblement plus faible dans le cas saturé. La saturation de la roche avec de l'eau augmente la vitesse des ondes P (entre 0 et 10 %) et diminue celle des ondes S (entre 6 et 24 %). Dans le cas des ondes P, l'effet de la saturation est relativement bien interprétée par la théorie de Gassmann (1951), l'écart entre les valeurs mesurées et celles prédites par la théorie est inférieur à 4 %. Dans le cas des ondes S, les valeurs prédites par cette théorie sont plus élevées que celles mesurées, la différence pouvant aller jusqu'à 12 %. Cet effet a déjà été observé par d'autres auteurs et a été expliqué par une perte de rigidité de la matrice lors de la saturation (Blangy *et al.*, 1993). L'effet de la porosité peut être observé sur la figure 4. On remarque que la vitesse des ondes P et S diminue linéairement avec la porosité. Les lois obtenues par régression linéaire sont données dans cette figure. Dans tous les cas, le coefficient de corrélation est supérieur à 0,93. La dépendance linéaire de la vitesse avec la porosité est en bon accord avec la théorie de Kuster et Toksöz (1974) qui prévoit, dans la gamme de porosité couverte par

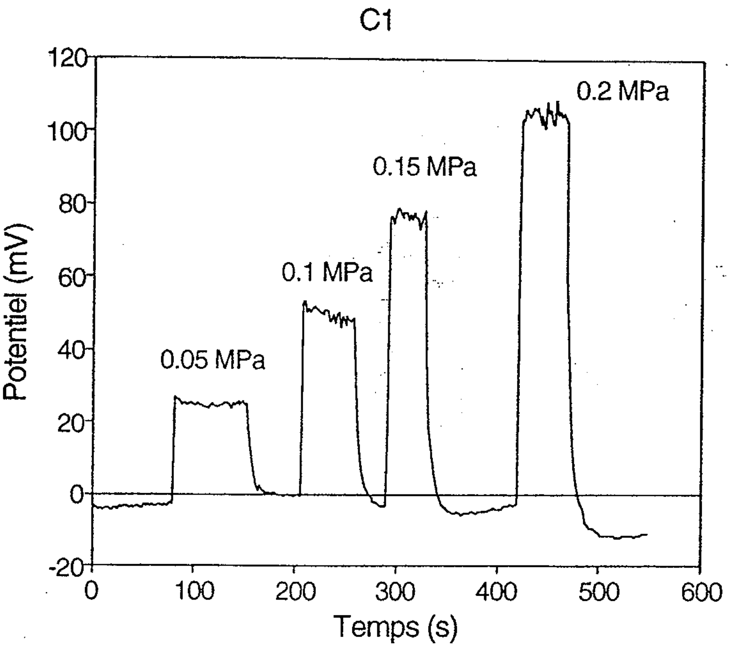

Fig. 3 Mesure typique du potentiel électrocinétique quand l'eau circule dans l'échantillon sous plusieurs différences de pression d'eau.

Streaming potentiel measurements with various driving pore pressures in the sample.

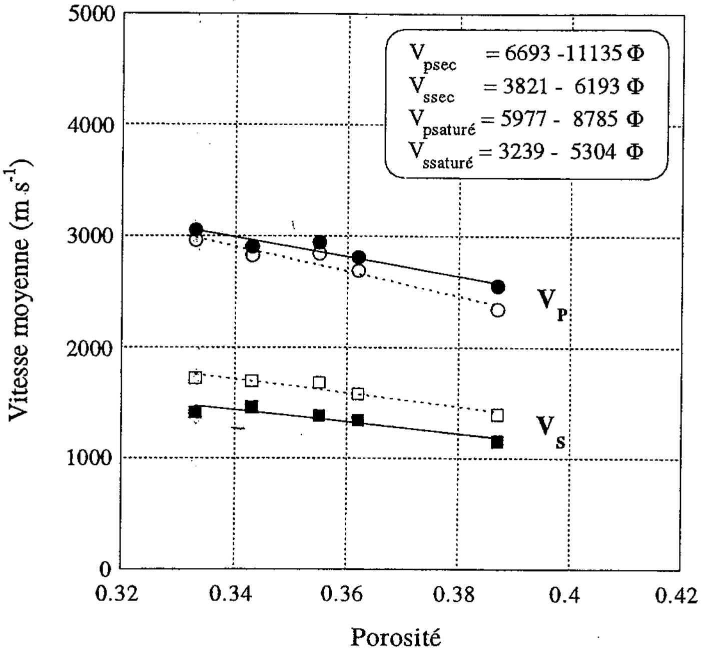

Fig. 4 Vitesse des ondes *P* et *S* en fonction de la porosité. Les symboles vides et pleins correspondent respectivement aux mesures effectuées sur la roche sèche et saturée avec de l'eau.

P and *S* wave velocities as a function of porosity. Open and solid symbols correspond respectivelly to dry and saturated measurements.

Tableau III Vitesse moyenne et anisotropie (définie par $A = ((V_{max} - V_{min}) / V_{moyenne}) \times 100$) des ondes élastiques dans les cas sec et saturé avec de l'eau.

Average wave velocities and anisotropy (defined as $A = ((V_{max} - V_{min}) / V_{average}) \times 100$) of elastic waves in dry and saturated conditions.

Éprouvette	V_{PM} (m s^{-1})	V_{SM} (m s^{-1})	A_P (%)
CM1 sec	2839	1682	4
CM1 saturé .	2940	1383	1
CM2 sec	2685	1581	8
CM2 saturé .	2807	1345	4
CM3 sec	2821	1696	3
CM3 saturé .	2900	1460	1
CM4 sec	2872	1723	6
CM4 saturé .	3050	1413	6
CM5 sec	2340	1399	1
CM5 saturé .	2550	1155	1

nos échantillons, une variation quasi-linéaire de la vitesse avec la porosité quand le facteur de forme des pores est relativement élevé, ce qui est le cas dans le calcaire étudié (Cattin, communication personelle). La variation linéaire de la vitesse des ondes *P* et *S* avec la porosité pourait fournir un moyen pour obtenir la porosité *in situ* de la roche dans les piliers grâce à la mesure de la vitesse des ondes élastiques effectuées à la surface de ces piliers.

CONCLUSION

Différentes propriétés physiques de la roche formant la carrière ont été étudiées : la perméabilité varie de 100 et 300 mD. Des fortes hétérogénéités de la perméabilité ont été observées à l'échelle du décimètre. Le coefficient de couplage électrocinétique est de l'ordre de –0,50 V/MPa quand la résistivité de l'eau est 200 Ωm, comparé à –0,02 à –2 V/MPa dans le grès de Fontainebleau pour la même résistivité de l'eau. De plus, les effets de conductivité de surface sont négligeables. Ces données devraient permettre de mieux modéliser les potentiels électriques observés dans la carrière, dont on pense que l'origine peut être électrocinétique. Le facteur de formation est d'environ 3,5, montrant que le réseau poreux est bien connecté. La vitesse des ondes élastiques varie linéairement avec la porosité, fournissant peut-être ainsi un moyen non destructif d'obtenir la porosité de la roche dans les piliers, à partir de mesures de ces grandeurs effectuées en surface des piliers.

Remerciements : Nous remercions Y. Géraud de l'ENS Lyon qui à gracieusement effectué les mesures de porosimétrie au mercure, B. Zinszner et M. Masson pour leur aide lors des mesures de perméabilité, D. Jeannette pour les imprégnations et Y. Guéguen pour ses remarques constructives.
C'est une contribution 31 du CNRS (URA 1316, URA 729 et URA 734)-INSU-DBT, thème fluides et failles.

RÉFÉRENCES BIBLIOGRAPHIQUES

AUBERT, M. et DANA, I., 1994. Interprétation des profils radiaux de polarisation spontanée (PS) en volcanologie. Possibilités d'application de la méthode PS à la surveillance des volcans actifs, *Bull. Soc. géol. France*, 165, p. 113-122.

BERNARD, P., 1992. Plausibility of long distance Electrotelluric precursors to Earthquakes, *J. Geophys. Res.*, 97, p. 17,531-17,546.

BLANGY, J. P., STRANDENES, S., MOOS, D. et NUR, A., 1993. Ultrasonic velocities in sands- revisited, *Geophysics*, 58, p. 344-356.

DENIS, A., DURVILLE, J.L., MASSIEU, E. et THORIN, R., 1987. Problèmes posés par un calcaire très poreux dans l'étude de la stabilité d'une carrière souterraine, *Bull. liaison, Labo. P. et Ch.*, 152, p. 69-74.

DUKHIN, S.S. et DERJAGUIN, B.V., 1974. *Surface and Colloid Science*, 7, MATIJEVIC, John Wiley and Sons, New York.

GASSMANN, F., 1951. Über die Elastizität poroser Medien : Vierteljahrschr. der Naturforsch. *Gesellschaft Zurich*, 96, p. 1-21.

JOUNIAUX, L. et POZZI, J.P., 1995 *a*. Streaming potential and permeability on saturated sandstones under triaxial stress: consequences for electrotelluric anomalies prior to earthquakes, *J. Geophys. Res.*, 100, p. 10197-10209.

JOUNIAUX, L. et POZZI, J.P., 1995 *b*, Permeability dependence of streaming potential in rocks for various fluid conductivities, *Geophys. Res. Lett.*, 22, p. 485-488.

KUSTER, G. T. et N. TOKSÖZ, 1974. Velocity and attenuation of seismic waves in two-phase media: Part I. Theoretical formulations, *Geophysics*, 39, p. 587-606.

MIZUTANI, H., ISHIDO T., YOKOKURA, T. et OHNISHI, S., 1976. Electrokinetic phenomena associated with earthquakes, *Geophys. Res. Lett.*, 3, p. 365-368.

MORAT, P. et Le MOUËL, J.L., 1992. Signaux électriques engendrés par des variations de contrainte dans des roches poreuses non saturées, *C. R. Acad. Sci. Paris*, 315, série II, p. 955-963.

MORAT, P., LE MOUËL, J.L., NOVER, G. et WILL, G., 1992. Variation annuelle de la saturation d'une roche de grande porosité induite par la variation saisonnière de la température extérieure et mesurée par voie électrique, *C. R. Acad. Sci. Paris*, 315, série II, p. 1083-1092.

PATERSON, M. S., 1983. The equivalent channel model for permeability and resistivity in fluid-saturated rock. A reappraisal, *Mechanics of Materials*, 2, p. 345-352.

POZZI, J.P., et JOUNIAUX, L., 1994. Effets électriques des circulations de fluides dans les roches sédimentaires et prévision sismique, *C. R. Acad. Sci. Paris*, 318, série II, p. 73-77.

ZAMORA, M. et POIRIER, J.P., 1990. Experimental study of acoustic anisotropy and birefringence in dry and saturated Fontainebleau sandstone, *Geophysics*, 55, p. 1455-1465.

ZLOTNICKI, J. et LE MOUËL, J. L., 1988. Volcanomagnetic effects observed on Piton de la Fournaise volcano (Reunion Island), *J. Geophys. Res.*, 30, p. 9157-9171.

GEOPHYSICAL RESEARCH LETTERS, VOL. 22, NO. 4, PAGES 485-488, FEBRUARY 15, 1995

Permeability dependence of streaming potential in rocks for various fluid conductivities

Laurence Jouniaux and Jean-Pierre Pozzi

Laboratoire de Géologie & CNRS URA 1316, École Normale Supérieure, Paris, France.

Abstract. Streaming potentials have been measured on sandstone and limestone samples in a large range of permeabilities. The electrokinetic coupling coefficient increases with permeability and we explain this effect by the related variation of surface conductivity. A model is proposed to study this effect for various fluid conductivities and it is shown that the dependence of the electrokinetic coupling coefficient on permeability is stronger for high fluid resistivity and is weaker for lower fluid resistivity. When fluid resistivity is below 1 Ω.m permeability and streaming potential are no more related.

Introduction

Observations of self-potential (SP) anomalies by surface measurements have been reported from numerous tectonically active areas in the world. The streaming potential effect in the crust may be promising to explain low frequency electric and magnetic precursors to earthquakes [Mizutani et al., 1976; Bernard, 1992]. Electrokinetic effects are often proposed to explain SP anomalies on volcanoes [Zlotnicki and Le Mouël, 1990; Aubert and Dana, 1994] and in geothermal areas [Corwin and Hoover, 1979], or used to monitor subsurface flow in geotechnical constructions [Merkler et al., 1989]. Streaming potentials can be quantified through experimental results. Few streaming potential data of geophysical interest are available [Somasundaran and Kulkarni, 1973; Ishido and Mizutani, 1981; Morgan et al., 1989; Antraygues and Aubert, 1993]. Effects of high pressure, high temperature, or changes of permeability on streaming potential have not been systematically analysed. Note that permeability varies by 11 orders of magnitude in the Earth's crust and can vary by 5 orders of magnitude in a given geological layer. We present streaming potential measurements on sandstone and limestone samples covering a large range of permeabilities and we propose a model to quantify the effect of permeability on streaming potential with various fluid conductivities.

Electrokinetic phenomena

When a fluid is made to flow through a porous medium there is an occurence of a potential called streaming potential across the sample caused by the relative motion between the solid and the liquid. Electrokinetic phenomena are due to the existence of an electric double layer formed at the solid-liquid interface [Stern, 1924]. The double layer is made up of a layer of ions adsorbed on the surface of the matrix and of a diffuse mobile layer extending into the liquid phase. The zeta potential is the electric potential on the plane closest to the surface of the matrix on which fluid is in motion. Phenomenologically the general relation between the electric current density i and the thermodynamical forces grad V and grad P [Overbeek, 1952; Nourbehecht, 1963] is from irreversible thermodynamics

$$i = -L_{11}\,\mathrm{grad}\,V - L_{12}\,\mathrm{grad}\,P \quad (A/m^2) \tag{1}$$

where P is the pore pressure, V the electric potential, L_{11} the conductivity and L_{12} the cross-coupling coefficient. The first term is the conduction current (Ohm's law) and the second term is called convection current. Ishido and Mizutani [1981] used a capillary model to formulate the electrokinetic phenomena in porous media. The specific conductivity of the sample σ_r has been expressed in terms of tortuosity t (actual flow path/bulk length measure), porosity Φ, specific internal area A_s (total internal pore surface area/volume of the sample), and specific surface conductance k_s (assumed to be due to the excess ions in the electrical double layer) assuming identical tortuosity for bulk and surface conduction and for fluid flow:

$$L_{11} = \sigma_r = \Phi t^{-2} \sigma_f + t^{-2} k_s A_s \tag{2}$$

$$L_{12} = -\Phi t^{-2} \frac{\varepsilon \zeta}{\eta} \tag{3}$$

where σ_f, ε and η are the electric conductivity, the electric permittivity and the shear viscosity of fluid, and ζ the zeta potential [Pfannkuch, 1972; de Groot and Mazur, 1962]. In a steady state equilibrium the convection current is balanced by the conduction current and the generated potential ΔV is related to the applied pore pressure difference ΔP by

$$\frac{\Delta V}{\Delta P} = \frac{\varepsilon \zeta}{\eta\,(\sigma_f + \frac{k_s A_s}{\Phi})} \tag{4}$$

The ratio ΔV/ΔP is the electrokinetic coupling coefficient which is independant on the size of the specimen under consideration. When surface conductivity is absent $k_s A_s/\Phi$ is negligible compared to σ_f then $\Delta V/\Delta P = \varepsilon\zeta/\eta\sigma_f$ which is the Helmholtz-Smoluchowski equation [Dukhin and Derjaguin, 1974]. Note that ΔV/ΔP can be positive or negative depending on the sign of ζ potential.

Experimental procedure

The relation between permeability k and streaming potential was investigated on saturated limestone and Fontainebleau sandstone samples. Fontainebleau sandstones do not contain clay and show uniform sized quartz grains ranging from 100 to 300 μm. Measurements on sandstones have been made on intact samples covering a large range of permeabilities from 1.5×10^{-16} m^2 to 1.2×10^{-12} m^2. One sample of limestone has been studied during permeability changes under deformation. An increasing deviatoric stress was applied to this sample and C12, C11, C10 refer to three states of deformation of the limestone sample. This

Paper number 94GL03307
0094-8534/95/94GL-03307$03.00

sample was collected in an underground quarry where SP measurements have been clearly correlated with changes of the atmospheric pressure [Morat and Le Mouël, 1992]. The streaming potential was measured during fluid flow by a voltmeter with an input resistance above 10^{10} Ω.m. Permeability was measured either by the steady state flow method or the transient flow method. The resistance of the sample was measured by an impedancemeter at 4 kHz frequency. The high pressure cell and the experimental procedure have been detailed in [Jouniaux and Pozzi, in press]. The streaming potential was measured on sandstones with distilled water of pH = 5 and resistivity r_f = 1000 Ω.m, and on limestone with water resistivity of 200 Ω.m.

Experimental results

The formation factor was computed from the measurements of the rock resistivity and of the fluid resistivity ($FF = r_{rock}/r_{fluid}$). The c factor is a numerical constant determined by the actual pore shape [Wyllie and Spangler, 1952] (0.5 for circular pores, 0.6 for equilateral triangular cross-section, 0.33 for a slot) was deduced from the observed thin sections (Table 1).

We observed negative electrokinetic coupling coefficients in all these experiments; the reported values are the absolute values of the electrokinetic coupling coefficient. The electrokinetic coupling coefficients measured on Fontainebleau sandstones are shown in figure 1 (empty squares).

The electrokinetic coupling coefficients measured on a limestone sample are shown in figure 2 (empty squares). These measurements show an electrokinetic coupling coefficient proportional to $k^{0.23}$.

Model

We explain this behavior by the effect of surface conductivity. Surface conductivity can be important when fluid resistivity is high or when pore size r is not large compared to the Debye length κ^{-1} (double layer length)

$$\kappa^{-1} = \sqrt{\frac{\varepsilon kT}{e^2 \sum\limits_i C_i z_i^2}}$$

where z_i is the valence of the ionic species with concentration C_i, k is the Boltzman's constant, T the temperature and e the electronic charge. Note that the Debye length is proportional to the square root of the fluid resistivity.

Table 1. Characterisation of the samples. F are sandstones and C are limestone. Permeability k is in 10^{-15} m^2 and ΔV/ΔP measured and computed are in mV/0.1MPa.

S	Φ	k	FF	c	ΔV/ΔP meas.	ΔV/ΔP comp.
F82	4.3%	0.15	16.7	0.33	11	65
C10		1.1	1.8	0.5	17.1	18.9
C11		2.6	2.6	0.5	23.4	26.3
F17		5			65	
F01		86			310	
C12	37%	156	3.3	0.5	55.6	44.6
F9IY	9.9%	180	36	0.5	1166	1199
FK5	10%	250	158	0.5	4002	2337
F34	11.9%	250	30.6	0.5	1287	1221
F44	13%	287	45	0.5	661	1642
F2	20%	1220	77	0.5	6642	3011

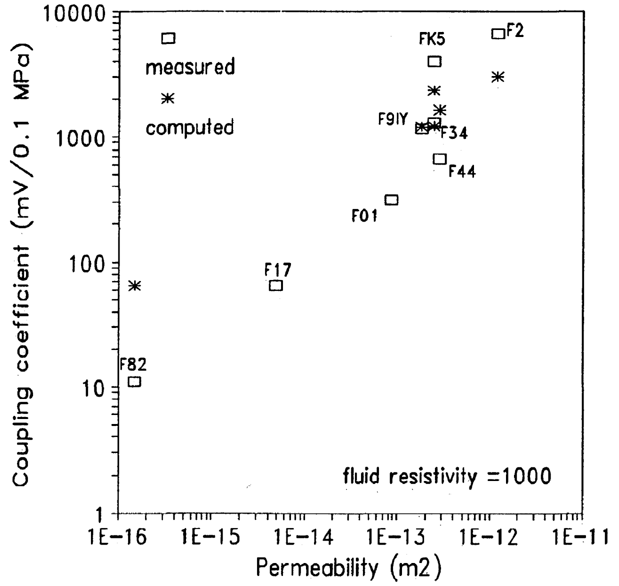

Figure 1. Electrokinetic coupling coefficient as a function of permeability when fluid resistivity is 1000 Ω.m. Empty squares are measured values and stars are computed values from eq.(5).

Bröz and Epstein [1976] have measured that surface conductivity in borosilicate glass capillaries with ζ potential of about 55 mV is not negligible for κr up to 40. The authors compared their measurements to the model from Rice and Whitehead [1965] and Levine et al. [1975] who computed that surface conductivity was not negligible for κr up to 100 in some cases: the ζ potential deduced from the Helmholtz-Smoluchowski equation can be underestimated of a few % when κr = 100, of 20% when κr is about 15-25 and of 40% when κr is about 5-10.

In our case the distilled water with pH = 5 induces a Debye length of 0.13 μm. The sample F2 which is the most permeable one has an average pore size of 50 μm. Therefore κr = 385 and we assumed that surface conductivity was not important for this sample. ζ potential was then computed from the Helmholtz-Smoluchowski equation for the sample F2 and was found to be -97 mV. This value is consistent with other values of ζ potential on quartz deduced from measurements or from theory [Li and De Bruyn, 1966; Pride and Morgan, 1991]. Furthermore ζ potential is expected to be of the same order of magnitude for all these Fontainebleau sandstones because the mineralogy is nearly identical. As the other samples have smaller pore size we assumed that surface conductivity was present. The smaller the permeability is, the smaller the pore sizes in sandstones are expected to be, and the apparent dependence of the electrokinetic coupling coefficient on permeability can be mainly due to the surface conduction effect.

We propose to interpret the permeability dependence of electrokinetic coupling coefficient using the capillary model and the Carman-Kozeny law. Indeed $k = c\,\Phi\, m^2/t^2$ where $m = \Phi/A_s$ is the hydraulic radius. Tortuosity can be taken into account through the formation factor F using $t^2 = \Phi F$ which implies $k = c\, m^2 F^{-1}$ [Wyllie and Spangler, 1952; Paterson, 1983]. The electrokinetic coupling coefficient can be thus expressed as a function of permeability

$$\frac{\Delta V}{\Delta P} = \frac{\varepsilon \zeta}{\eta \left(\sigma_f + \frac{k_s \sqrt{c}}{\sqrt{k}\sqrt{F}} \right)} \qquad (5)$$

As the conduction current equilibrates the convection current which is constant, when sample conductivity is enhanced by surface conductivity the electrokinetic gradient is decreased. The dielectric constant of water is $\varepsilon/\varepsilon_0 = 80$ at 25°C, the shear viscosity is 10^{-3} Pa·s at 20°C and the effect of temperature on η was taken into account.

Fontainebleau sandstones

Measurements of rock conductivity with different fluid conductivities allowed us to overestimate the surface conductance [Jouniaux and Pozzi, in press]. Ruffet [1993] measured surface conductance on Fontainebleau sandstones of 2×10^{-10} to 8×10^{-10} Ω^{-1}. Here k_s was estimated to 5×10^{-9} Ω^{-1}. The ζ potential was deduced as explained above and is $\zeta = -97$ mV. Values of electrokinetic coupling coefficient computed from eq.(5) are shown in figure 1 (stars). This computation shows roughly the behavior of the electrokinetic coupling coefficient with permeability.

This model was used to predict the effect of permeability on electrokinetic coupling coefficient of the used samples when fluid conductivity is higher. These predictions are shown in figures 2 and 3. The ζ potential was considered to be the same as before, that is an approximation. Indeed for pure quartz ζ potential can change from -100 mV for a fluid resistivity of 10^3 Ω.m to -50 mV for a fluid resistivity of 10 Ω.m [Pride and Morgan, 1991]. A different value for ζ potential would not change the amplitude of variation of the electrokinetic coupling coefficient with permeability, but only its intrinsic value as shown by eq. (5). Note that for a given fluid conductivity the ζ potential is constant.

The electrokinetic coupling coefficient is proportional to $k^{0.33}$ when fluid resistivity is 200 Ω.m (Fig. 2), is proportional to $k^{0.27}$ when fluid resistivity is 100 Ω.m (Fig. 3) and is proportional to $k^{0.09}$ when fluid resistivity is 10 Ω.m. The electrokinetic coupling coefficient is constant when fluid conductivity is 1 Ω.m (Fig. 3).

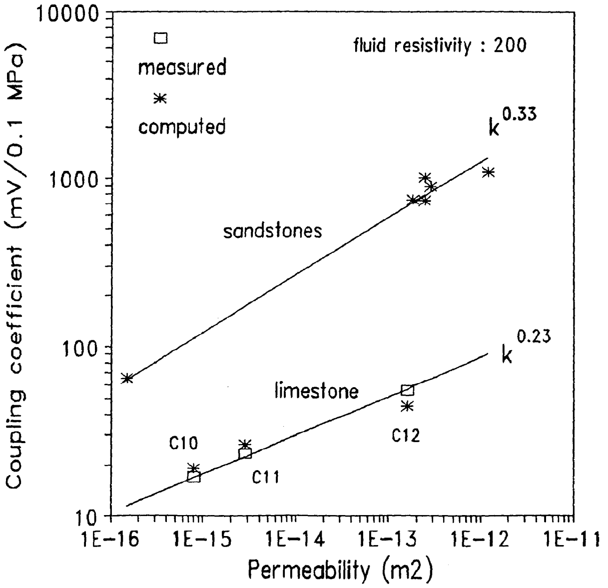

Figure 2. Electrokinetic coupling coefficient as a function of permeability when fluid resistivity is 200 Ω.m. Empty squares are measured values for the limestone, stars are computed values from eq.(5) and slopes of straightlines are proportional to $k^{0.33}$ and to $k^{0.23}$.

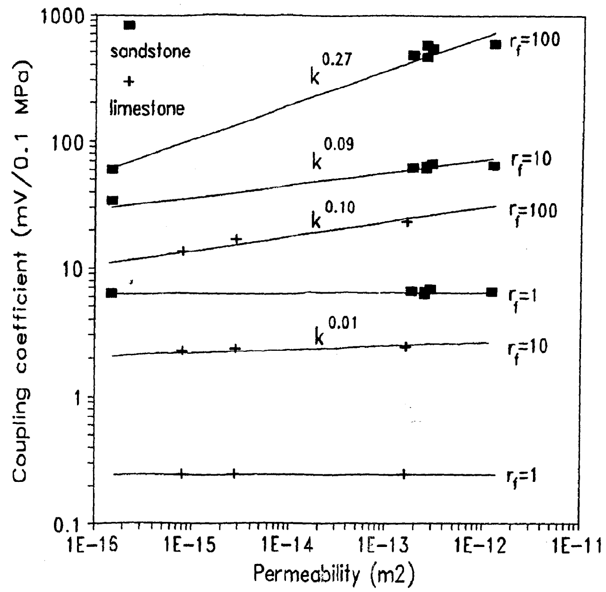

Figure 3. Predicted values of electrokinetic coupling coefficient versus permeability computed using eq.(5) for sandstones(filled square) and limestone(plus) with various fluid resistivities(r_f). Straightlines are deduced from the model and slopes are proportional to $k^{0.27}$, to $k^{0.09}$, to $k^{0.10}$ and to $k^{0.01}$.

Limestone sample

Permeability of the limestone sample was decreased by deformation. The electrokinetic coupling coefficient was computed using eq.(5) in three states of deformation (C12, C11 and C10). The ζ potential was deduced from measurements on the non-deformed state (C12) when permeability was high using the Helmholtz-Smoluchowski equation and assuming that surface conductivity was not important. ζ potential was found to be - 4 mV. Surface conductance k_s was estimated to 5×10^{-10} Ω^{-1}. Values of electrokinetic coupling coefficient computed from eq.(5) are shown in figure 2 (stars). This computation shows that the electrokinetic coupling coefficient is proportional to $k^{0.23}$ when fluid resistivity is 200 Ω.m. The predicted effect of fluid conductivity is shown in figure 3. The electrokinetic coupling coefficient is proportional to $k^{0.10}$ when fluid resistivity is 100 Ω.m and is proportional to $k^{0.01}$ when fluid resistivity is 10 Ω.m. The electrokinetic coupling coefficient is constant when fluid resistivity is 1 Ω.m.

Discussion and Conclusion

Measurements of electrokinetic coupling coefficient on sandstones and limestone of various permeabilities show that the electrokinetic coupling coefficient is related to permeability. This correlation is strong when fluid resistivity is high. This behavior is explained by the contribution of surface conductivity. A capillary model allowed us to quantify this effect. This model can roughly account for the permeability dependence of electrokinetic coupling coefficient considering the surface conductivity effect. We used this model to compute the effect of permeability on electrokinetic coupling coefficient with various fluid conductivities. When fluid resistivity is high the electrokinetic coupling coefficient strongly depends on permeability and this dependence is more important for sandstones than for limestone.

By chemical analysis calcium was found in fluid after flowing through the sandstone samples. This calcium is supposed to be responsible of a large part of surface conductivity in Fontainebleau sandstones. When fluid is more conductive the effect of permeability is less important and for a fluid conductivity of 1 Ω.m this model shows that the electrokinetic coupling coefficient is no longer dependent on permeability. Models usually use an average water resistivity of 10^2 Ω.m in the Earth's crust, that means that the electrokinetic coupling coefficient will be affected by changes of permeability. In some area where sea water is predominant, with a resistivity less than 1 Ω.m, it is likely that the electrokinetic coupling coefficient will not be affected by changes of permeability.

Acknowledgments. This study is a collaboration with ENSAM (Laboratoire de mécanique des structures). We thank the referees for their very useful comments and suggestions. This research was supported by ANDRA and the GRECOgéomatériaux. This is a CNRS-INSU-DBT contribution n°5, thème fluides et failles.

References

Antraygues, P. and Aubert, M., Self Potential Generated by Two-Phase Flow in a Porous Medium: Experimental Study and Volcanological Applications, *J. Geophys. Res.*, 98, 22273-22281, 1993.

Aubert, M. et Dana, I., Interpretation des profils radiaux de polarisation spontane (PS) en volcanologie. Possibilites d'application de la methode PS a la surveillance des volcans actifs, *Bull. Soc. geol. France*, t. 165, 2, 113-122, 1994.

Bernard, P., Plausibility of Long Distance Electrotelluric Precursors to Earthquakes, *J. Geophys. Res.*, 97, 17531-17546, 1992.

Broz, Z. and Epstein, N., Electrokinetic flow through porous media composed of fine cylindrical capillaries, *J. Colloid and Interface Science*, 56, 605-612, 1976.

Corwin, R.F. and Hoover D.B., The self potential method in geothermal exploration, *Geophysics*, 44, 226-245, 1979.

De Groot, S.R. and Mazur, P., *Non equilibrium thermodynamics*, North Holland (Ed.), Amsterdam, 1962.

Dukhin, S.S. and Derjaguin, B.V., *Surface and Colloid Science*, 7, edited by E. Matijevic, John Wiley and sons, NY, 1974.

Ishido, T. and Mizutani, H., Experimental and theoretical basis of electrokinetic phenomena in rock-water systems and its applications to geophysics, *J. Geophys. Res.*, 86, 1763-1775, 1981.

Jouniaux, L. and Pozzi, J.P., Streaming potential and permeability on satured sandstones under triaxial stress : consequences for electrotelluric anomalies prior to earthquakes, *J. Geophys. Res.*, in press.

Levine, S., Marriott, J.R., Neale, G. and Epstein, N., Theory of Electrokinetic Flow in Fine Cylindrical Capillaries at High Zeta-Potentials, *J. Colloid Interface Sci.*, 52, 136-149, 1975.

Li, H.C., and De Bruyn P.L., Electrokinetic and adsorption studies on quartz, *Surface Science*, 5, 203-220, 1966.

Merkler, G.P., Militzer, H., Hötzl, H., Armbruster, H. and Brauns, J. (Eds), *Detection of subsurface flow phenomena*, Lecture notes in Earth Sciences, vol. 27, Springer-Verlag (Ed), 1989.

Mizutani, H., Ishido, T., Yokokura, T. and Ohnishi S., Electrokinetic phenomena associated with earthquakes, *Geophys. Res. Lett.*, 3, 365-368, 1976.

Morat, P. et Le Mouël, J.L., Signaux électriques engendrés par des variations de contrainte dans des roches poreuses non saturées, *C. R. Acad. Sci. Paris*, t. 315, Série II, 955-963, 1992.

Morgan, F.D., Williams, E.D. and Madden, T.R., Streaming potentials properties of Westerly granite with applications, *J. Geophys. Res.*, 94, 12449-12461, 1989.

Nourbehecht, B., Irreversible thermodynamic effects in inhomogeneous media and their applications in certain geoelectric problems, Ph. D. Thesis, M.I.T., Cambridge, USA, 1963.

Overbeek, J.Th. G., Electrochemistry of the double layer, *Colloid Science*, vol. 1, Irreversible Systems, Ed. H.R. Kruyt, Elsevier, New York, 115-193, 1952.

Paterson, M.S., The equivalent channel model for permeability and resistivity in fluid-saturated rock– A re-appraisal, *Mechanics of Materials*, 2, 345-352, 1983.

Pfannkuch, H.O., On the correlation of electrical conductivity properties of porous systems with viscous flow transport coefficients, in *Fundamentals of Transport Phenomena in Porous Media*, 42-54, Elsevier, NY, 1972.

Pride, S. R. and Morgan, F. D., Electrokinetic dissipation induced by seismic waves, *Geophysics*, 56, 914-925, 1991

Rice, C.L. and Whitehead, R., Electrokinetic Flow in a Narrow Cylindrical Capillary, *J. Phys. Chem.*, 69, 4017-4123, 1965.

Ruffet, C., La conductivité électrique complexe dans quelques roches crustales, Thèse, Université Louis Pasteur, Strasbourg, 1993.

Somasundaran, P. and Kulkarni, R.D., A new streaming potential apparatus and study of temperature effects using it, *J. Colloid and Interface Science*, 45, 591-600, 1973.

Stern, O., Zür theorie der elektrolischen doppelschicht, *Z. Elektrochem.*, 30, 508, 1924.

Wyllie, M.R.J. and Spangler, M.B., Application of electrical resistivity measurements to problem of fluid flow in porous media, *Bull. AAPG*, 36, N°2, 359-403, 1952.

Zlotnicki, J. and Le Mouël, J.L., Possible electrokinetic origin of large magnetic variations at La Fournaise volcano, *Nature*, 343, 633-635, 1990.

L. Jouniaux and J.-P. Pozzi, Laboratoire de Géologie & CNRS URA 1316, École Normale Supérieure, 24 rue Lhomond, 75231 Paris Cédex 05, France, (e-mail : pozzi@magnetit.ens.fr or laurence@erl.mit.edu).

(Received September 9, 1994; revised November 25, 1994; accepted November 25, 1994.)

Volvic "La Montagne" du 13.03.2001 éd. Riom

Une plaque en hommage à la science

Une plaque a été inaugurée, mercredi, à l'endroit où fut mis en chantier le forage de Moulet-Marcenat qui permet, depuis le 14 juin 1991, d'alimenter mille foyers en eau potable.

Ce forage est le résultat d'un travail d'équipe qui a rassemblé les scientifiques et les ingénieurs du génie civil. La plaque vient rappeler que le forage a bénéficié d'une nouvelle méthode de prospection géophysique, la « polarisation spontanée », mise au point par un universitaire clermontois, Maurice Aubert.

Le physicien — désormais à la retraite — considère que « c'est la découverte à laquelle il tient le plus ». Il explique que sa méthode consiste en une mesure, en surface, des potentiels (c'est-à-dire les « charges ») électriques que produit l'eau lorsqu'elle percole dans un milieu poreux et vient lécher les scories. Il suffit alors de se positionner précisément sur le talweg (la plus grande pente d'une vallée) pour mesurer le débit de l'eau.

Camille Bertrand, président du Syndicat mixte des utilisateurs d'eau de la région de Riom (SMUERR), a salué ce forage « comme l'opération qui l'aura le plus marqué durant son mandat ». Il a tenu à rappeler que le forage de reconnaissance avait reçu le soutien financier de l'Agence de l'eau et du département, et le forage lui-même, celui de la commune de Volvic.

Maurice Aubert devant la plaque célébrant son invention.

texte de la plaque apposée sur le bâtiment abritant le forage de Moulet-Marcenat (63) et inaugurée le 7 mars 2001.

Le forage de Moulet-Marcenat est le premier ouvrage d'exploitation d'eau souterraine implanté grâce à une nouvelle méthode de prospection géophysique (polarisation spontanée). Cette méthode a été mise au point par Maurice Aubert, physicien à l'Université Blaise Pascal, Clermont-Fd .

L'eau est puisée à 80 mètres de profondeur dans une ancienne vallée comblée par des coulées volcaniques dont le fond atteint 115 mètres. Ce forage a été mis en service en 1991.

Prix de thèses

244 thèses ont été soutenues en 2004 à l'ULP. La Société des amis des universités de l'Académie de Strasbourg, le Conseil général du Bas-Rhin et le Conseil scientifique de l'ULP donnent un coup de chapeau à une dizaine de docteurs. Une belle occasion pour découvrir les travaux de trois jeunes scientifiques primés.

Une baguette de sourcier pour les géophysiciens

"Ce site est le volcan de Tecapa au Salvador sur lequel nous avons installé un réseau de suivi de potentiels spontanés. C'est sur ce volcan que se trouve aussi la deuxième centrale géothermique de Gesal (compagnie de géothermie salvadorienne). Au total, 25 % de l'électricité du Salvador est fourni par Gesal."

Comment trouver l'emplacement d'une réserve d'eau souterraine sans creuser le sol ? En mesurant à la surface les champs électriques générés par les mouvements des fluides dans le sous-sol.

À l'Institut de physique du globe de Strasbourg (IPGS), Mathieu Darnet a mis au point une technique de détection basée sur le phénomène d'électrocinétisme : le mouvement des fluides (eau, hydrocarbures, gaz, etc.) dans le sol et les interactions physico-chimiques entre ces fluides et les minéraux génèrent des courants électriques variables selon la nature de la roche, la vitesse de l'écoulement du fluide... Le signal électrique induit est un bon indicateur de la présence de fluides en circulation. L'idée est de mesurer ce signal pour localiser la réserve d'eau. Un simple voltmètre et des électrodes adaptées au sol suffisent à réaliser ces mesures. Les chiffres relevés permettent de cartographier les écoulements souterrains et de les suivre en temps réel. Mathieu a effectué ses mesures sur le site géothermique de Soultz-sous-Forêts en Alsace. Il a aussi testé sa méthode au Salvador dans le cadre d'un post-doctorat financé par la société Shell.

Mathieu est un jeune docteur heureux, il a réussi à obtenir "*la reconnaissance de l'université pour un travail de thésard souvent méconnu et laborieux*". Aujourd'hui, il a intégré la vie professionnelle au sein de la société Shell pour la prospection de sites pétroliers. A l'IPGS, la recherche poursuit son cours ; le travail de Mathieu va servir à développer de nouvelles méthodes de détection des pollutions causées en particulier par les hydrocarbures.

D.C. & S.K.

Mathieu Darnet **a soutenu sa thèse intitulée *Caractérisation et suivi de circulations de fluides par la mesure de Potentiels Spontanés (PS)* en novembre 2003, sous la direction de Guy Marquis, unité mixte de recherche ULP/CNRS 7516, IPGS.**

Lauréats 2004

Prix Société des amis des universités de l'Académie de Strasbourg
> M. Mathieu Darnet (Dir. de thèse : G. Marquis)
> M^{lle} Sandy Dubaele (Dir. de thèse : J.M. Egly)
> M. Luc Dupuis (Dir. de thèse : J.P. Loeffler)
> M. Romuald Ginhoux (Dir. de thèse : M. de Mathelin)
> M^{lle} Bahaâ Salem (Dir. de thèse : J. Suffert)
> M^{lle} Annette Schenck (Dir. de thèse : J.L. Mandel)
> M. Alexandre Specht (Dir. de thèse : M. Goeldner)

Prix du Conseil général du Bas-Rhin
> M^{me} Anne Puissant (Dir. de thèse : C. Weber)

Prix Raymond Poincaré
> M. François Dahmani (Dir. de thèse : T. Delzant)

Prix du Conseil scientifique de l'ULP
> M^{lle} Claire Wyart (Dir. de thèse : D. Chatenay et L. Bourdieu)

Journal of Hydrology 267 (2002) 173–185

Journal of Hydrology

www.elsevier.com/locate/jhydrol

Variations of self-potential and unsaturated water flow with time in sandy loam and clay loam soils

Claude Doussan[a,*], Laurence Jouniaux[b], Jean-Louis Thony[c]

[a]*INRA, Unité Climat, Sol & Environnement, Domaine Saint Paul, Site Agroparc, 84914 Avignon Cedex 9, France*
[b]*Ecole Normale Supérieure, Laboratoire de Géologie, UMR 8538, 24, rue Lhomond, 75231 Paris Cedex 05, France*
[c]*Laboratoire d'étude des Transferts en Hydrologie et Environnement, BP53-F-38041 Grenoble Cedex 09, France*

Abstract

Accurate assessment of soil–water fluxes is essential in soil physics due to its direct implications in environmental, agronomical or hydrological applications. Field estimations of soil–water fluxes by 'classical' hydraulic methods are often difficult to obtain. Moreover, water fluxes are highly variable in space and time. The obtainment of a reasonable estimate for this variable would require numerous measurement sites. However, such a requirement is rarely met. Thony et al. [CR Acad. Sci. Paris, Earth Planetary Sci. 325 (1997) 317] presented the experimental evidence of a linear relationship between the self-potential (SP) and the unsaturated soil–water flux. Therefore, this relationship would allow the indirect assessment of the water flux using electrical measurements. Such an approach would appear much more flexible and easier to perform than the current hydraulic measurements. The aim of this study is to experimentally investigate the existence and robustness of the flux–SP relationship for different soil types and pedoclimatic conditions.

The soil–water fluxes and the SP were monitored in a long-term experiment involving two types of soils, contrasting in hydraulic and electric properties. The soils were placed in lysimeters which were instrumented with tensiometers and TDR probes for monitoring hydraulic heads and moisture content, respectively. Unpolarizable SP electrodes, temperature sensors and suction cups (for collecting pore water) were also installed in the lysimeters. The SP and the fluxes were measured or calculated in the 30–40 cm depth section.

Results show that the variations of the SP with time were clearly linked to both rainfall events and evaporation. However, in the long-term, the linear relationship between the unsaturated water flux and the SP evolves from strongly correlated to almost not correlated. The slope (sensitivity) of the flux–SP relationship varies with the soil type, decreasing with more electrically conductive soil. Taking into account a varying soil–electrode contact greatly improves the flux–SP relationship at the scale of the rainfall event, particularly when considering infiltration and drainage phases separately. Nevertheless, at the scale of a year, with alternated rainfalls and evaporation phases, the robustness of the relationship decreases (i.e. the coefficients of the relationship vary between events). This variability could be related to time variations in electrical conductivity, not so much to that of the soil–water, but rather to that of the water from the salted soil mud added to the SP electrodes at the time of installation.

This study points out methodological problems associated with the measurement of SP in shallow unsaturated soils over the long-term and the need for designing specific electrodes for this purpose. However, in deep soils beneath the root zone, environmental conditions generally vary slowly and lightly in comparison to surface horizons. In this case and with our present set of SP measurement devices, the flux–SP relationship could be more stable than in the surface soil horizons and useful for examining aquifer recharge, capillary rises or contaminant transfer. © 2002 Elsevier Science B.V. All rights reserved.

Keywords: Unsaturated flow; Self-potential; Soil; Fluxmeter

---

* Corresponding author. Fax: +33-4-3272-2238.
E-mail address: doussan@avignon.inra.fr (C. Doussan).

PII: S0022-1694(02)00148-8

1. Introduction

The fact that the water flow in a porous medium induces electric fields has been known for a long time (Ahmad, 1964). Such evidence has been observed in different geologic settings such as volcanoes, tectonically active areas, in the vicinity of dams or lakes, or in quarries (Mitzutani et al., 1976; Ishido, 1989; Morat and Le Mouël, 1992; Aubert and Dana, 1994; Hashimoto and Tanaka, 1995; Perrier et al., 1998). However, a quantitative relationship between the flow and the electric field is most often assumed rather than observed because simultaneous detailed measurements of the electric and hydraulic parameters are seldom available.

The self-potential (SP) is generated by the existence of a natural gradient of electric potential. In field situations, SP may arise: (i) from a thermoelectric potential, consequence of a temperature gradient, (ii) from a chemical potential, consequence of chemical gradients, and (iii) from a streaming potential, electrokinetic phenomena, consequence of fluid pressure gradients. SP anomalies are often assumed to result primarily from electrokinetic phenomena because the thermoelectric and chemical coefficients are smaller than the electrokinetic coefficient (Perrier et al., 1999; Jouniaux et al., 2000).

In a saturated porous medium, the differential motion between the fluid and the solid induces electrokinetic phenomena. Minerals forming the porous medium, which are usually negatively charged, create an electric double layer in the pore fluid. A strong electric field is created perpendicular to the surface of the mineral, which attracts cations and repulses anions in the vicinity of the solid–liquid interface. The electric double layer is made up of: (i) the Stern layer, which includes the hydration of the virgin surface as well as ions weakly bound to the surface, and (ii) the Gouy diffuse layer, where Coulomb forces are counterbalanced by thermal agitation (for detailed description see Adamson (1976), Dukhin and Derjaguin (1974) and Hunter (1981)). The streaming potential is due to the motion of the diffuse layer along with fluid flow, induced by a pressure gradient. The shear plane in the fluid, i.e. the zero velocity surface, is located within the diffuse layer. The electric potential along this surface is called the zeta potential.

Fluids moving through porous media or capillaries generate streaming potentials that are governed by the Helmholtz–Smoluchowski equation as discussed below (Overbeek, 1952; Nourbehecht, 1963).

In a saturated porous medium the electric current density I (A/m^2) and the fluid flow J (m/s) are coupled according to the following equations:

$$-I = \frac{\sigma_f}{F}\,\mathrm{grad}\ V - \frac{\varepsilon\zeta}{\eta F^0}\,\mathrm{grad}\ P \tag{1}$$

$$-J = -\frac{\varepsilon\zeta}{\eta F^0}\,\mathrm{grad}\ V + \frac{k}{\eta}\,\mathrm{grad}\ P \tag{2}$$

where V is the electric potential, P the fluid pressure, σ_f and ε the electrical conductivity and the dielectric constant of the fluid, respectively, ζ the zeta potential, η the dynamic viscosity of the fluid and k is the permeability of the porous medium. F^0 is the formation factor, i.e. the ratio between fluid and rock electrical conductivity ($\sigma_{\mathrm{fluid}}/\sigma_{\mathrm{rock}}$) for a high fluid conductivity when electrical surface conductivity is negligible, and F is the formation factor for the fluid conductivity being studied (i.e. possibly with electrical surface conductivity). The first term on the right-hand side in Eq. (1) is Ohm's law, and the second term in Eq. (2) is Darcy's law. At steady state, the convection current (related to grad P—Eq. (1)) is balanced by the conduction current (related to grad V—Eq. (1)). Equating these currents leads to the ratio $\Delta V/\Delta P$, called the streaming-potential cross-coupling coefficient C_s, or simply, the coupling coefficient according to Eq. (3):

$$C_s = \frac{\Delta V}{\Delta P} = \frac{\varepsilon\zeta}{\eta\sigma_f}\frac{F}{F^0} \tag{3}$$

which is the Helmholtz–Smoluchowski equation (Dukhin and Derjaguin, 1974). ΔV is the generated electric potential difference and ΔP is the pore-pressure difference, between two points in the porous medium. The above equations are recalled here because they are found in different forms in the literature (Ishido and Mizutani, 1981; Pride, 1994). For a complete development of the equations governing the coupled electromagnetics and flow through porous media, see Pride (1994) and Revil (1999a,b). Eq. (3) implies that the currents are of equal magnitude and opposite along the same path. When the surface conductivity is negligible, $F = F^0$, and

Eq. (3) can be written as:

$$C_s = \frac{\Delta V}{\Delta P} = \frac{\varepsilon\zeta}{\eta\sigma_f} \tag{4}$$

Eq. (3) or (4) can be rewritten in terms of fluid flow, taking into account Darcy's law for a saturated porous medium:

$$F = \frac{K}{C_s}\Delta V \tag{5}$$

where F is the (Darcy) flux of water and K is the saturated hydraulic conductivity. When interpreting the SP data as the result of an electrokinetic process, Eq. (5) shows that a linear relationship is also expected between the water flux and the SP for a saturated porous medium.

The linear relationships represented in Eq. (4) or (5) between the pressure gradient or the water flux and the electric potential have been observed and validated for different unconsolidated or consolidated sediments and rocks (Ahmad, 1964; Jouniaux and Pozzi, 1995; Lorne et al., 1999; Jouniaux et al., 2000). However, very few measurements of the SP for conditions of *unsaturated* fluid flow are available, particularly for soils. The field experiments of Thony et al. (1997), where the soil–water fluxes and the electric potentials were measured independently during a rainfall event, brought evidences of the existence of a linear relationship between the unsaturated water flux in soil and the SP.

Estimation of soil–water fluxes is essential in soil physics due to its direct implications in environmental, agronomical or hydrological purposes (i.e. estimation of drainage, evaporation, transfer of pollutants, aquifer recharge, infiltration/runoff partition, etc.). Field estimation of soil–water fluxes is usually done either by mass balance, such as the 'zero flux method' (Vachaud et al., 1978), or by direct application of the Darcy's law extended for unsaturated flow. The latter requires an initial determination of the soil hydrodynamic characteristics (water retention, unsaturated hydraulic conductivity) as a function of water potential (or soil moisture) on soil core samples in the laboratory (Tamari et al., 1993). However, these widely used hydraulic methods present some difficulties. They are rather difficult to set-up and manage, time consuming, they require specific equipment (for measuring the soil moisture and water potential) and problems can be encountered during the data interpretation process. Moreover, water fluxes (as well as hydraulic conductivity or soil moisture) are highly variable in time and space and an accurate determination of these properties at different scales would require a high number of measuring sites. These requirements are rarely met due to the time needed and the complexity of the measurements. Therefore, new ways and devices for estimating soil–water fluxes would be very helpful, such as an 'unsaturated fluxmeter'. Gee et al. (1999) presented a design using a heat pulse, but the estimation of the flux is not straightforward. Based on the fact that SP measurements could be easier to perform than the hydraulic methods and based on the possible linearity of the SP–flux relationship, this study aims at estimating soil–water fluxes from SP measurements in soils. Therefore, questions have to be answered regarding: (i) the stability of such a relationship, in different soil types and pedoclimatic conditions, (ii) its robustness with time and the sensitivity of the signal, and (iii) the influence of environmental factors on the relationship.

This article attempts to experimentally address these questions, and more specifically the stability and reproducibility of the relationship between the SP and the unsaturated soil–water fluxes, at a space scale intermediate between the laboratory column and the field, i.e. the scale of a few square meters in lysimeters.

2. Materials and methods

2.1. Experimental sites

The experimental sites consist of two non-weighting lysimeters each of about 9 m^2 surface area and 2 m depth, located in the south of France (Avignon, lat.: 43°55′00″N, long.: 4°52′47″E) in the INRA experimental fields (Fig. 1). One lysimeter is packed with a sandy loam soil and the other with a clay loam soil. The soils were kept bare during the experiment. The climate of the region is Mediterranean and shows a large inter annual variability.

2.2. Instrumentation

Hydraulic heads were measured with automatic

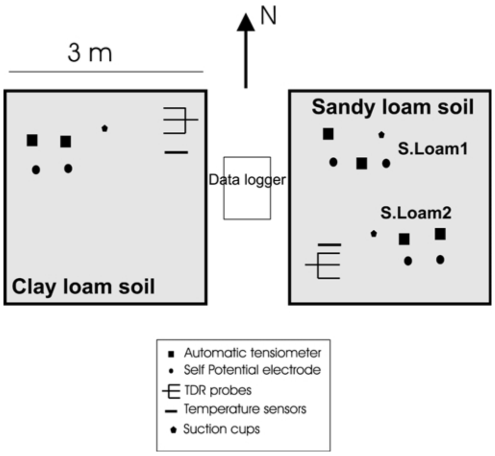

Fig. 1. Schematic map of the experimental sites (two lysimeters filled with clay loam or sandy loam) including probes locations. S. Loam 1 and S. Loam 2 are the two measuring points in the sandy loam.

tensiometers (SDEC, France) at two depths: 30 and 40 cm. SP measurements were performed with unpolarizable electrodes ($Pb/PbCl_2$ type, Petiau, 2000; SDEC-France) at identical depths installed at about 20 cm from the tensiometers. These electrodes were selected for their long-term stability and low noise characteristics (Perrier et al., 1997; Petiau, 2000). The electrodes were vertically installed in the soil. Soil from the site, which was mixed with NaCl saturated water to form mud, was added at the bottom of the holes in which the SP electrodes were inserted. Adding this mud allowed us to get identical geochemical conditions near all the electrodes and a good soil–electrode contact. Moisture content was measured with a set of TDR probes (Time Domain Reflectometry, Trase system) implanted at 5, 15, 30 and 40 cm depths. Soil temperature was also monitored at these depths with Pt-thermistances. Temperature, SP and hydraulic heads measurements were recorded with a data logger (CR10X, Campbell) of high input impedance. Two data acquisition locations (i.e. a pair of electrodes and tensiometers) were chosen in the sandy loam lysimeter (herein called S. Loam 1 and S. Loam 2) and one in the clay loam lysimeter. Electrodes in the sandy loam were referenced to the same electrode buried at 40 cm. The SP was measured as $V_{40\text{cm}} - V_{30\text{cm}}$, where V is the electric potential at the indicated depth. Suction cups were also installed at 35 cm depth in order to sample the soil pore water and to determine the electrical conductivity of the solution. Two suctions cups were installed in the same way as the electrodes, i.e. with salted soil mud, to estimate time variations of the electrical conductivity of the mud pore water.

2.3. Water flux determination and SP correction

Mean water flux at 35 cm depth was calculated by Darcy's law using hydraulic heads measured at 30 and 40 cm depth. The hydraulic conductivity was calculated for the mean matric potential of the 30–40 cm depth section. Unsaturated hydraulic conductivity (which depends on the moisture content or matric potential in unsaturated flow—Hillel, 1974) and water retention (i.e. relationship between moisture content and matric potential) were determined in the laboratory using the Wind evaporation method (Tamari et al., 1993) on soil cores sampled at the end of the experiment. Fig. 2 presents these hydrodynamic characteristics of the sandy loam.

The SP was corrected for temperature variations at 35 cm depth using the sensitivity coefficient of these electrodes, that is 0.21 mV/°C (Petiau, 2000).

3. Results

Water potential variations. Time variations of total water potential over a 6 month period are shown in Fig. 3. After a rainy autumn in 1999 that refilled the soil with water after the summer, the winter 2000 was a very dry season with almost no rain. Potential evapotranspiration (~ 2 mm d^{-1}, data not shown) was rather low, but sufficient to induce evaporation during this period. This explains why the water potential dropped from about -1.5 m to between -5 and -6 m in the sandy loam. In the clay loam, the fall of the water potential was much steeper, from -4 m to less than -8 m in February, unfortunately below the working range of tensiometers. In the early spring 2000, a series of rainfalls occurred more or less regularly. This induced a quick rise of the water potential in the sandy loam, which reacted rapidly to the rain at 30–40 cm depth. The water potential in the clay loam recovered much more slowly during this rainy period. In the late spring/beginning of summer, the water potential of both soil types sharply declined

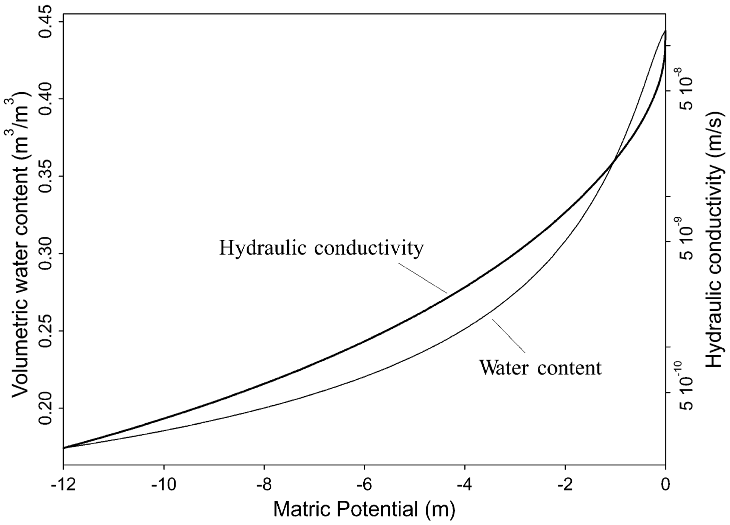

Fig. 2. Hydrodynamic characteristics (water retention and hydraulic conductivity) of the sandy loam soil used in the experiments as a function of matric potential.

because of the increase in potential evapotranspiration ($\sim 5.5-6$ mm d^{-1}). As a consequence, the tensiometers were brought out of the working range. It should be noted that, in the case of the sandy loam soil, although the overall tendency is similar for the two measurement points (S. Loam 1 and S. Loam 2), the amplitude of variation differs, showing some heterogeneity in the hydraulic behaviour of the soil.

3.1. Self-potential variations

Self-potential variations, i.e. $V_{40\mathrm{cm}} - V_{30\mathrm{cm}}$: the

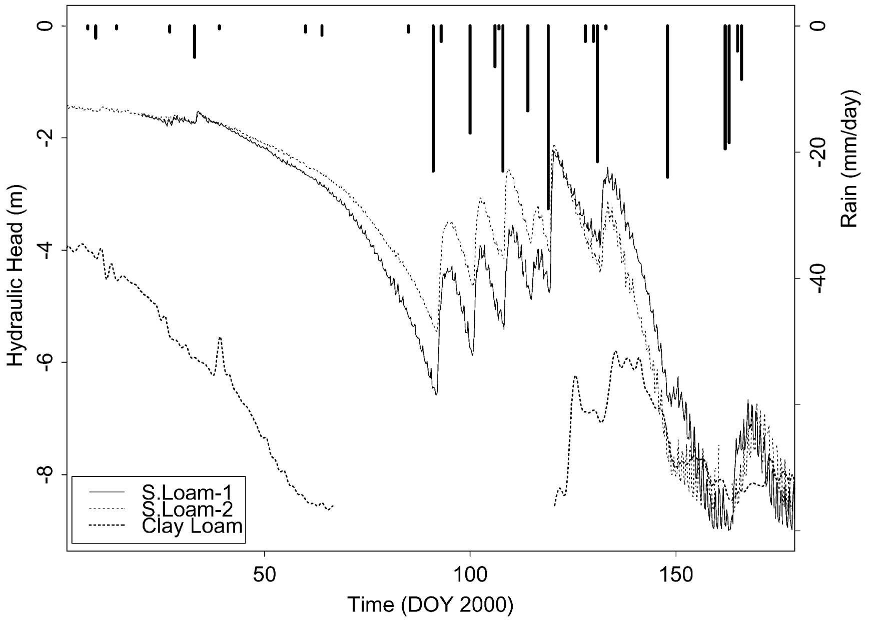

Fig. 3. Time variation of the mean hydraulic head (or total water potential) at 35 cm depth for the two measuring points (S. Loam 1 and S. Loam 2) in the sandy loam lysimeter, and in the clay loam lysimeter. Daily rainfall is also presented (vertical lines).

electric potential difference between 40 and 30 cm depth, are presented in Fig. 4 for the two types of soil. The amplitude of variation for the sandy loam was about 60 mV over the year and 40 mV between January and June. In the clay loam, variations are less pronounced with a yearly amplitude of about 20 mV. The electric field at 35 cm depth (approximated by $(V_{40\mathrm{cm}} - V_{30\mathrm{cm}})/\Delta z$ with $\Delta z = 10$ cm) ranges between -150 mV/m and $+400$ mV/m in the sandy loam and between -150 mV/m and $+40$ mV/m in the clay loam. These variations are much higher than those found by Thony et al. (1997), which ranged between -1 and $+35$ mV/m during a single rainfall event. Diurnal variations of about 1 mV are also noticeable in the sandy loam, whereas in the clay loam the electric signal appears much less noisy. When comparing the electric data at the two measuring points in the sandy loam, the pattern of variation looks similar but the different amplitudes of the signals denotes some heterogeneity in the lysimeter, as it was the case for water. The high rates of variation of the SP observed in the sandy loam are most often linked to rainfall events that started at the beginning of spring (day 91, Fig. 4). The events resulted in a delayed peak in the SP data. The SP measurements are here interpreted as electrokinetic processes, so that the measured electric field is induced by infiltration of water in soil and the high pressure gradient associated (see Eq. (4)). The zeta potential and the water electrical conductivity are expected to be constant or slightly varying for a given soil type (see Section 3.3). However, some variations of the SP seem unrelated to rainfalls, e.g. in winter (around day 20). In the clay loam, time variations are generally much smoother but also show some jumps (e.g. around day 60 and 130) with no clear relation to rainfall events. In particular, the strong variation around day 60 happened in the dry winter period (see rains in Fig. 4).

3.2. Unsaturated water flux

Time variations of mean water fluxes at 35 cm depth, calculated from the observed water potential gradients and from the calculated hydraulic conductivity, are presented in Fig. 5. For the sandy loam, the calculated water flux at the beginning of the period appears to be noisy because the hydraulic gradients are very small. This indicates that water in the soil is near hydrostatic equilibrium and a small error in pressure measurements induces a large variation of low fluxes. A clear upward water flux (evaporation) started around day 50 (February) and levelled off on day 91 (end of March), when rain started. From that moment on, fluxes were directed downward (infiltration), with more or less pronounced peaks appearing slightly after the rainfall events. The base line of infiltration went back to zero (null flux) at the end of spring. The differences between the two measurement points of the sandy loam are clearly seen in Fig. 5, where the infiltration rates are greater than 0.6 cm d^{-1} in S. Loam 1, whereas they do not exceed 0.2 cm d^{-1} in S. Loam 2.

In the clay loam, less flux data are available because tensiometers were at the limit of, or out of the working range part of the time. However, fluxes are much smaller than in the sandy loam and the water dynamics look completely different showing, in particular, higher fluxes at the beginning of the year 2000.

3.3. Unsaturated flux–self-potential relationship

The SP and the unsaturated water fluxes appear to be related to each other (Figs. 4 and 5). They show the same global trends and peaks. However, it is shown in Fig. 6 and in Table 1 that a simple linear correlation between the fluxes and the SP (i.e. $\mathrm{Flux} = a\mathrm{SP} + b$) is relatively weak for the whole period including evaporation and infiltration, between days 30 and 140. The slope of the flux–SP relationship seems to be much higher in the sandy loam than in the clay loam, probably because the clay loam electrical conductivity is greater than that of the sandy loam. In the rest of the discussion the focus will be set more specifically on the sandy loam because more data are available, but the results and conclusions are qualitatively the same for both soil types.

When looking at the scale of a single rainfall event, contrasted results are obtained concerning the flux–SP relationship. For example, Fig. 7 and Table 1 present data for the first rainfall in the spring for the sandy loam soil. A strong linear correlation is observed between the fluxes and the SP for the S. Loam 1 point. This correlation is greatly increased when the fluxes and the SP are daily averaged, as in

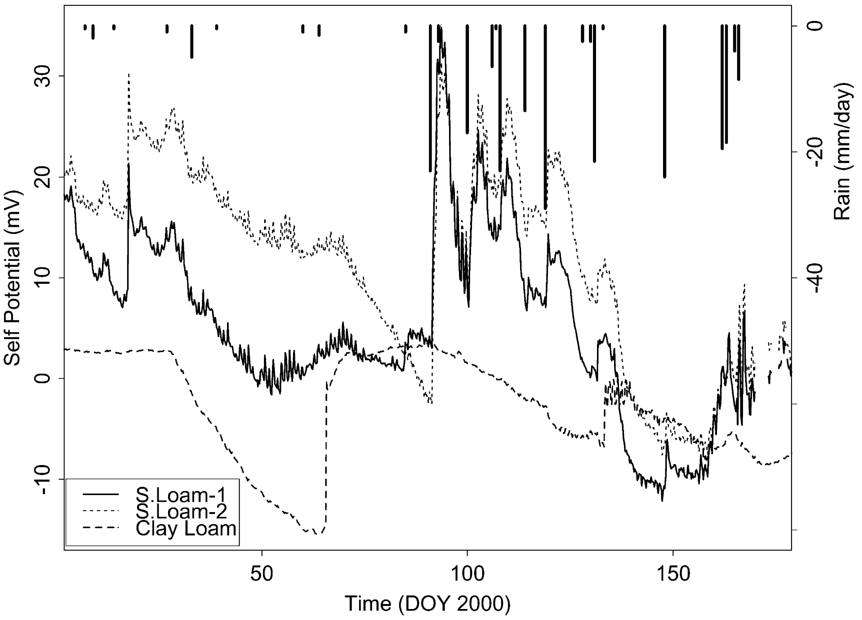

Fig. 4. Time variation of the self-potential between 30 and 40 cm depths (i.e. $V_{40\mathrm{cm}} - V_{30\mathrm{cm}}$, where V is the electric potential at indicated depth) for the two measuring points (S. Loam 1 and S. Loam 2) in the sandy loam lysimeter, and in the clay loam lysimeter. Daily rainfall is also presented (vertical lines).

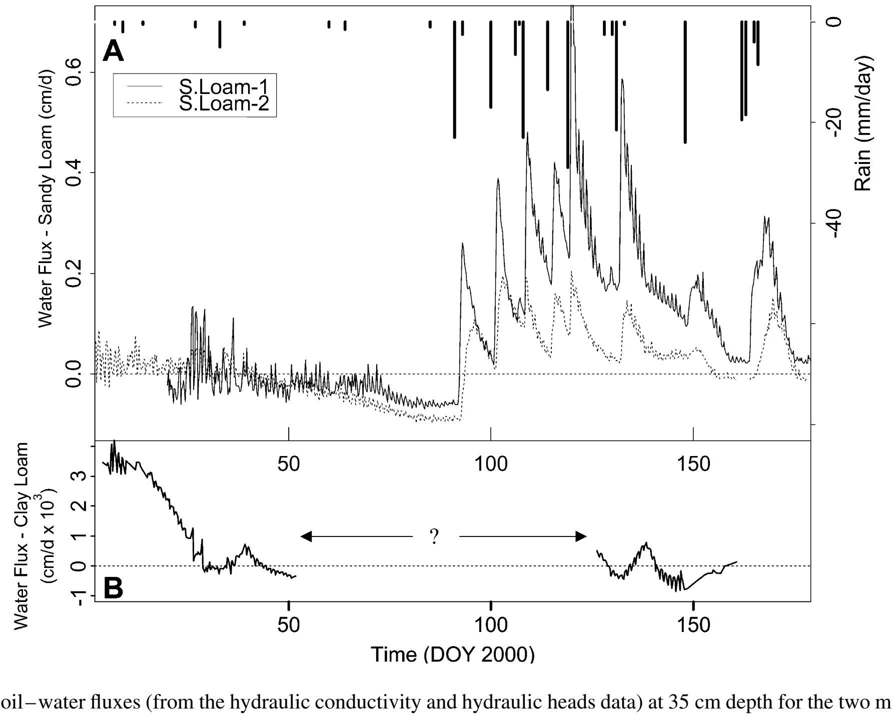

Fig. 5. Calculated soil–water fluxes (from the hydraulic conductivity and hydraulic heads data) at 35 cm depth for the two measuring points (S. Loam 1 and S. Loam 2) in the sandy loam lysimeter (A) and in the clay loam lysimeter (B). The ‘?’ mark signifies that hydraulic heads could not be measured at that time and therefore water flux is not available. Daily rainfall is also presented (vertical lines).

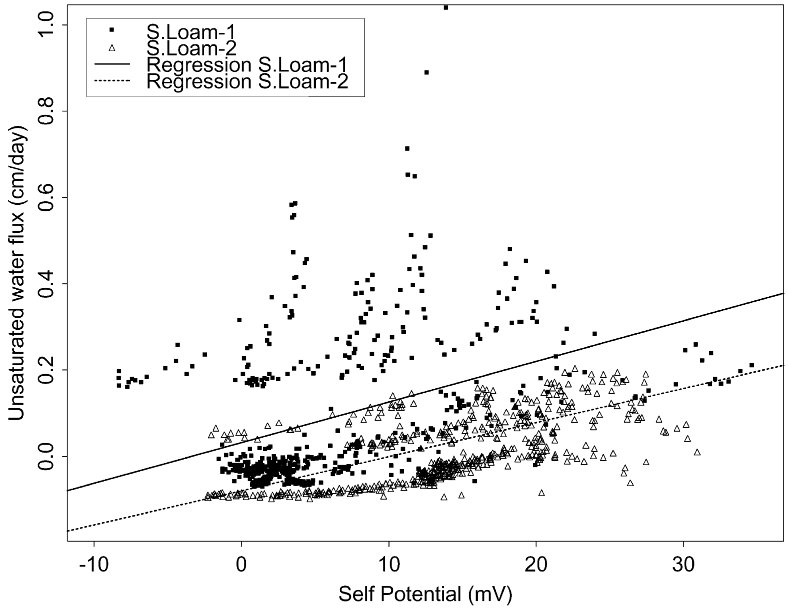

Fig. 6. Relationship between SP at 30 and 40 cm depth (i.e. $V_{40cm} - V_{30cm}$, where V is the electric potential at indicated depth) and the soil–water flux at 35 cm depth for the two measuring points (S. Loam 1 and S. Loam 2) in the sandy loam lysimeter for the period 30–140 day of year 2000, encompassing evaporation and infiltration phases. Regression lines Flux $= a\mathrm{SP} + b$ are also shown (see Table 1 also).

Thony et al. (1997) experiment, reaching nearly the same correlation level ($r^2 = 0.912$) in the two experiments. Nevertheless, this correlation vanishes for the S. Loam 2 point (Fig. 7).

Some processes altering the SP signal and consequently the flux–SP relationship may explain such variations. When examining the SP records (Fig. 4), abrupt variations of SP are observed that are not related to infiltration (e.g. around day 20 in the sandy loam and day 65 in the clay loam). This suggests that some miscontact between the soil and the electrode may have occurred in this long-term experiment. Miscontact may be directly due to variations in the soil–water saturation near the electrodes, or variations in the electrode porous material that separates the (gel) electrolyte from the soil. It may also be indirectly related to swelling and shrinkage of the soil that leads to cracks at the soil–electrode interface. If we use the water saturation to take into account the effects of varying soil–electrode contact (as in some plant root water uptake models for simulating the soil–root contact, Jensen et al., 1993), the relationship between the fluxes and the SP can be

Table 1
Coefficients of the linear regression between SP (i.e. $V_{40cm} - V_{30cm}$, where V is the electric potential at indicated depth) and soil–water flux at 35 cm depth (Flux $= a\mathrm{SP} + b$) for a 3 month period (for the two measuring points of the sandy loam lysimeter and for the clay loam lysimeter) and for the first rainfall event (23 mm) in spring 2000 (for the two measuring points of the sandy loam lysimeter)

Time period/site	a (cm d^{-1} mV^{-1})	b (cm d^{-1})	r^2
Days 30–140/S. Loam 1	0.0094	0.032	0.171[a]
Days 30–140/S. Loam 2	0.0064	−0.074	0.342[a]
Days 1–140/Clay Loam	1.93×10^{-4}	1.16×10^{-3}	0.470[a]
Rainfall 1 (days 91–101)/S. Loam 1	0.0077	−0.054	0.751[a]
Rainfall1 (days 92–101)/S. Loam 2	6×10^{-4}	0.031	0.0060

[a] 1% confidence level.

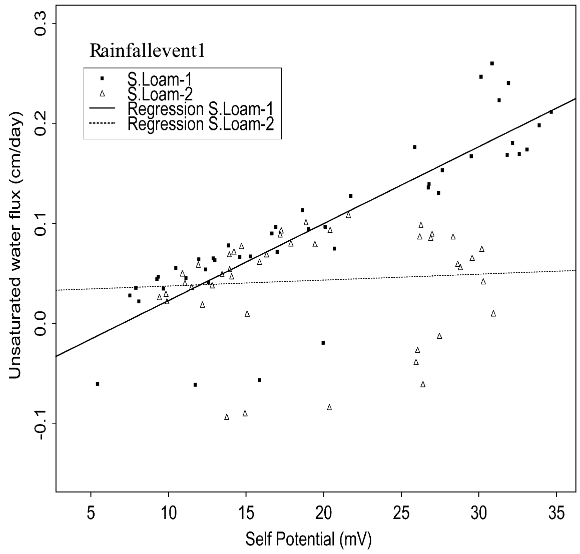

Fig. 7. Relationship between SP at 30 and 40 cm depth (i.e. $V_{40\text{cm}} - V_{30\text{cm}}$, where V is the electric potential at indicated depth) and the soil–water flux at 35 cm depth for the two measuring points (S. Loam 1 and S. Loam 2) in the sandy loam lysimeter for the first rainfall event of spring 2000 (23 mm). Regression lines Flux = $a\text{SP} + b$ are also shown (see Table 1 also).

rewritten as:

$$\text{Flux} = \left(a\frac{\theta}{\theta_s} + b\right)\text{SP} + \left(c\frac{\theta}{\theta_s} + d\right) \tag{6}$$

where θ is the volumetric water content and θ_s is the volumetric water content at saturation. θ/θ_s is the water saturation.

At the scale of a rainfall event, Eq. (6) significantly improves the regression fits (see Table 2), as can be seen in Fig. 8A showing the soil–water fluxes estimated by linear regression (Eq. (6)) and measured for the first rainfall event. However, the fitted coefficients (a, b, c, d—Eq. (6)) vary between the different rainfall events, meaning that Eq. (6) is not stable with time. To increase its stability, Eq. (6) was fitted by splitting the infiltration and drainage phases of the different rainfall events. An example of the results of this fitting procedure is given in Fig. 8B and in Table 2 for the first rainfall event. A good fit of the fluxes corresponding to the different rainfall events can be obtained by applying this procedure. However, even in this case, Eq. (6) is not stable with time and the coefficients are both site and event-dependent.

The SP–unsaturated flux relationship can effectively be improved by taking into account the soil–electrode contact with the saturation variations. However, the instability of this relationship tends to show that other processes can induce a shift in the SP signal. One of these processes could be time variations of the pore water electrical conductivity (see Eq. (4)). On the studied site, where soils are calcareous, the soil–water electrical conductivity was rather buffered at 35 cm depth with a mean value of 500 ± 49 μS cm^{-1}. On the other hand, the pore water of the salted soil mud that was in contact with the electrodes showed a drastic variation of electrical conductivity (Fig. 9). This may have induced a variable ‘electric’ environment between the electrodes, as well as differences in the electric field sampled by the electrodes, and caused an additional SP drift with time.

4. Conclusion

The existence of a linear relationship between the

Table 2
Coefficients of the linear regression between SP (i.e. $V_{40\text{cm}} - V_{30\text{cm}}$, where V is the electric potential at indicated depth) and soil–water flux at 35 cm depth, taking into account a variable soil–SP electrode contact through water saturation, Eq. (6)). Data for the first rainfall event (23 mm) in spring 2000 and the two measuring points of the sandy loam lysimeter. Regression is calculated either by considering the total period of infiltration and drainage or by fitting independently the infiltration and drainage phases

Time period/site/process	a (cm d^{-1} mV^{-1})	b (cm d^{-1} mV^{-1})	c (cm d^{-1})	d (cm d^{-1})	r^2
Rainfall 1 (days 91–101)/S. Loam 1	−0.061	0.0394	2.194	−1.208	0.827
Rainfall1 (days 92–101)/S. Loam 2	0.0645	−0.0435	1.643	−0.812	0.898
Rainfall1 (days 91–93)/S. Loam 1/infiltration	0.0184	−0.0071	4.899	−2.51	0.997
Rainfall1 (days 93–101)/S. Loam 1/drainage	−0.0963	0.061	0.943	−0.562	0.934
Rainfall1 (days 92–96)/S. Loam 2/infiltration	0.0388	−0.0304	2.593	−1.335	0.958
Rainfall1 (days 96–101)/S. Loam 2/drainage	0.006	−0.0018	1.149	−0.638	0.917

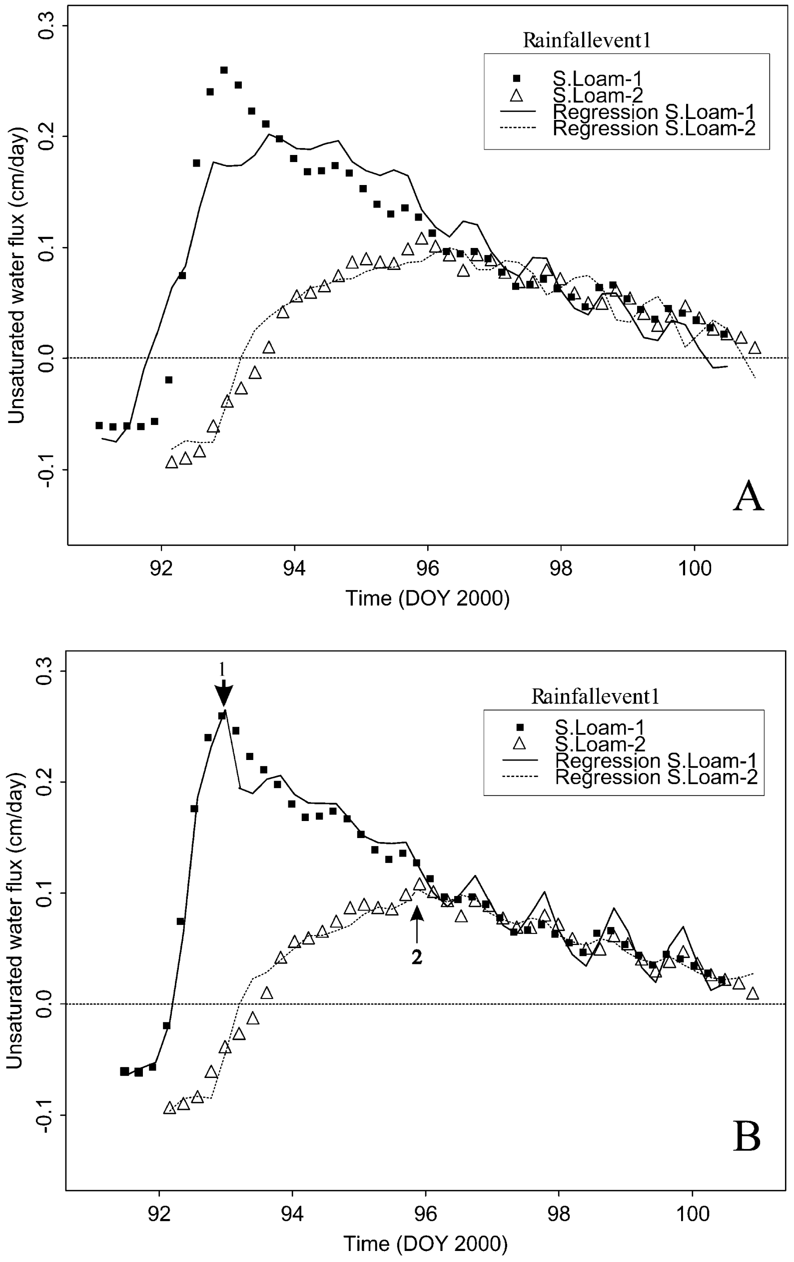

Fig. 8. (A) Comparison between the calculated soil–water fluxes and the field estimated water fluxes for the two measuring points (S. Loam 1 and S. Loam 2) in the sandy loam lysimeter. The flux–SP relationship Eq. (6) taking into account a variable soil–electrode contact through water saturation, is used to calculate flux. Data for the first rainfall event of spring 2000 (23 mm), see Table 2 also. (B) Same as A, but the flux–SP relationship (6) is fitted independently to the infiltration and drainage phases of the rainfall event (see Table 2 also). Arrows show the end of the infiltration phase and the beginning of drainage for the two measuring points.

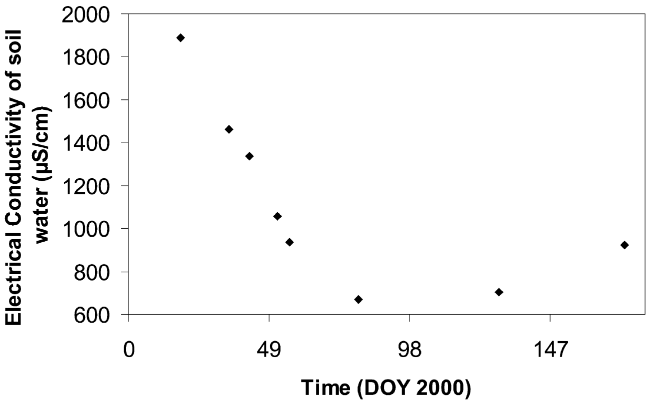

Fig. 9. Variation with time of the pore water electrical conductivity of the NaCl salted soil mud collected with suction cups installed similarly to the SP electrodes (sandy loam soil).

unsaturated water fluxes in soils and the SP could be very useful in research fields linked to soil physics. Thony et al. (1997) gave an experimental evidence of such a relationship. Estimation of water fluxes in soil is essential, but is difficult to obtain and highly variable in space and time. Indirect estimation of water fluxes by electrical measurements could lead to the design of an unsaturated fluxmeter that would be much more flexible and much easier to set-up than current measurements. The aim of this study was to investigate the existence and robustness of such a flux–SP relationship for different soil types and pedoclimatic conditions than in Thony et al. (1997) experiment.

Soil–water fluxes and SP were monitored in a long-term experiment involving two soil types, contrasting in hydraulic and electric properties, placed in lysimeters under the same meteorological conditions.

Measured time variations of SP are clearly linked to both rainfall events and evaporation. However, in the long-term, the quality of the linear relationship between the unsaturated water flux and SP ranged from a strong to a weak correlation. The slope of the flux–SP relationship seems to vary with the soil type and decreases with a more electrically conductive soil. Taking into account a varying soil–electrode contact, through water saturation (Eq. (6)), greatly improves the flux–SP relationship at the scale of a rainfall event, particularly when considering infiltration and drainage phases. Nevertheless, at the scale of a year, with alternated rainfalls and evaporation phases, the relationship (6) is not so robust (i.e. the coefficients of Eq. (6) vary between events). This variability could be attributed to variations in the electrical conductivity, not so much of the soil–water which is rather constant on the studied sites, but more of the salted mud that was added to the SP electrodes during their set-up. A variability of the flux–SP relationship is also observed between neighbouring data acquisition points in the same lysimeter, but this could be due to heterogeneity in the soil hydrodynamic characteristics. Estimation of this variability is currently undertaken.

This study points out methodological problems in measuring the SP in the shallow unsaturated zone, for long-term monitoring, in relation to water fluxes. The SP electrodes generally give accurate results in regular geophysical uses because of short-term measurements (e.g. mineral exploration) and/or burying at sufficient depths to avoid variations of saturation and temperature. A great amount of salted clay, in rather big holes, is also added. In these regular uses, SP variations linked to soil–water fluxes are most of the time considered as noise in the signal. In the case where the upper few meters of the soil and its hydrodynamics are of interest, very large variations of saturation, water potential, and temperature will occur throughout the season. Consequently, a design of electrodes maintaining electrical contact with varying conditions is essential. Important design parameters shape the electrode to avoid crack formation and the nature of the porous medium separating the electrolyte from soil, which should not desaturate in dry conditions. Set-up conditions are also important, which should be as little disturbing as possible, and the effect of added salted mud should be much more specifically studied for this kind of SP application. The salted mud can lixiviate and its concentration can vary during periods of high drainage. This last point also stresses out the problem of agricultural fields where fertilizers are periodically added that may modify soil–water electrical conductivity.

However, with the present measurement devices, in the cases of slowly fluctuating conditions within a limited range, as it is often the case in deep soils beneath the root zone (where variations of temperature, saturation and chemistry of the soil solution are low), more stable flux–SP relationships with time could possibly be obtained. In this case, the use of SP data would be of great interest for examining/monitoring aquifer recharge, capillary rises or contaminant transfer.

Laboratory studies, with controlled temperature, water fluxes, and soil properties are needed to design electrical measurement devices better and also to get better insights into the unsaturated fluxes–SP relationship.

Acknowledgments

This study benefited from a grant INSU-CNRS ‘Programme National de Recherche en Hydrologie (PNRH)’ no PNRH-62-200—Research program ‘Apport des méthodes géophysiques en hydrologie’. The authors thank Yves Dudal for kindly reviewing the language of the manuscript.

References

Adamson, A.W., 1976. Physical Chemistry of Surfaces, Wiley-Interscience, New York.

Ahmad, U., 1964. A laboratory study of streaming potentials. Geophys. Prospect. XII, 49–62.

Aubert, M., Dana, I., 1994. Interpretation of the self-potential radial profiles in vulcanology. Possibilities of the SP method for monitoring the actives vulcanoes. Bull. Soc. Geol. Fr. 165, 113–122.

Dukhin, S.S., Derjaguin, B.V., 1974. In: Matijevic, E., (Ed.), Surface and Colloid Science, vol. 7. Wiley, New York.

Gee, G.W., Ward, A.L., Kirkham, R.R., Ritter, J.C., 1999. A water-flux meter for unsaturated soils. Proceedings of the Annual Meeting ASA, CSSA, SSSA, 31 October–4 November, Salt Lake City, USA, 173.

Hashimoto, T., Tanaka, Y., 1995. A large self-potential anomaly on Unzen vulcano, Shimabara peninsula, Kyushu island, Japan. Geophys. Res. Lett. 22, 191–194.

Hillel, D., 1974. L’eau et le sol—Principes et processus physiques, Vander Editions, Louvain, Belgium.

Hunter, R.J., 1981. Zeta Potential in Colloid Science, Academic Press, London.

Ishido, T., 1989. Self-potential generation by subsurface water flow through electrokinetic coupling, Detection of subsurface flow phenomena, lecture notes in earth science, 27. Springer, New York, p. 121–131.

Ishido, T., Mizutani, H., 1981. Experimental and theoretical basis of electrokinetic phenomena in rock–water systems and its applications to geophysics. J. Geophys. Res. 86, 1763–1775.

Jensen, C.R., Svendsen, H., Andersen, M.N., Lösch, R., 1993. Use of the root contact concept, an empirical leaf conductance model and pressure volume curves in simulating crop water relations. Plant Soil 149, 1–26.

Jouniaux, L., Pozzi, J.P., 1995. Streaming potentials and permeability of saturated sandstones under triaxial stress. Consequences for electrotelluric anomalies prior to earthquakes. J. Geophys. Res. 100, 10197–10209.

Jouniaux, L., Bernard, M.L., Zamora, M., Pozzi, J.P., 2000. Streaming potential in volcanic rocks from Mount Pelée. J. Geophys. Res. 105 (B4), 8391–8401.

Lorne, B., Perrier, F., Avouac, J.P., 1999. Streaming potential measurements—2. Relationships between electrical and hydraulic flow patterns from rock samples during deformation. J. Geophys. Res. 104, 17879–17896.

Mitzutani, H., Ishido, T., Yokokura, T., Ohnishi, S., 1976. Electrokinetic phenomena associated with earthquakes. Geophys. Res. Lett. 3, 365–368.

Morat, P., Le Mouël, J.L., 1992. Signaux électriques engendrés par des variations de contrainte dans des roches poreuses non saturées. C. R. Acad. Sci. Paris, Serie II 315, 955–963.

Nourbehecht, B., 1963. Irreversible thermodynamic effects in inhomogneous media and their applications in certain geoelectric problems. PhD Thesis, Massachusetts Institute of Technology, Cambridge.

Overbeek, J.Th.G., 1952. Electrochemistry of the double layer. In: Kruyt, H.R., (Ed.), Colloid Science, Irreversible Systems, vol. 1. Elsevier, New York, pp. 115–193.

Perrier, F., Petiau, G., Clerc, G., Bogorodsky, V., Erkul, E., Jouniaux, L., Lesmes, D., Macnae, J., Meunier, J.M., Morgan, D., Nascimento, D., Oettinger, G., Schwarz, G., Toh, H., Valliant, M.J., Vozoff, K., Yaziciçakin, A., 1997. A one year systematic study of electrodes for long period measurements of the electric field in geophysical environments. J. Geomagn. Geoelectr. 49, 1677–1696.

Perrier, F., Trique, M., Lorne, B., Avouac, J.P., Hautot, S., Tarits, P., 1998. Electrical variations associated with yearly lake level variations. Geophys. Res. Lett. 25, 1955–1958.

Perrier, F., Trique, M., Aupiais, J., Gautam, U., Shrestha, P., 1999. Electric potential variations associated with periodic spring discharge in western Nepal. CR Acad. Sci. Paris, Serie II 328, 73–79.

Petiau, G., 2000. Second generation of Lead–Lead Chloride electrodes for geophysical applications. Pure Appl. Geophys. 157, 357–382.

Pride, S.R., 1994. Governing equations for the coupled electromagnetics and acoustics of porous media. Phys. Rev. B: Condens. Matter 50, 15678–15696.

Revil, A., Pezard, P.A., Glover, P.W., 1999A. Streaming potential in porous media—1. Theory of the zeta potential. J. Geophys. Res. 104 (B9), 20021–20031.

Revil, A., Schwaeger, H., Cathles, L.M., Manhardt, P.D., 1999b. Streaming potential in porous media—2. Theory and application to geothermal systems. J. Geophys. Res. 104 (B9), 20033–20048.

Tamari, S., Bruckler, L., Halbertsma, J., Chadoeuf, J., 1993. A simple method for determining soil hydraulic properties in the laboratory. Soil Sci. Soc. Am. J. 57, 642–651.

Thony, J.L., Morat, P., Vachaud, G., Le Mouël, J.L., 1997. Field characterization of the relationship between electrical potential gradients and soil water flux. CR Acad. Sci. Paris, Earth Planetary Sci. 325, 317–321.

Vachaud, G., Dancette, C., Sonko, M., Thony, J.L., 1978. Méthodes de caractérisation hydrodynamique in situ d'un sol non saturé. Application à deux types de sols du Sénégal en vue de la détermination des termes du bilan hydrique. Ann. Agro. 29, 1–36.

Pure appl. geophys. 159 (2002) 2629–2657
0033–4553/02/122629–29 $ 1.50 + 0.20/0

Pure and Applied Geophysics

On the Difficulty of Detecting Streaming Potentials Generated at Depth

PATRICK PINETTES,[1,2,3] PASCAL BERNARD,[1] FRANÇOIS CORNET,[1]
GAGUIK HOVHANNISSIAN,[4] LAURENCE JOUNIAUX,[5]
JEAN-PIERRE POZZI,[5] and VÉRONIQUE BARTHÉS[6]

Abstract — In order to investigate how a streaming potential coefficient measured in the laboratory, at a typical scale of 10 cm, can be incorporated into a field model, with a typical scale of 1 to 10 km, we measured the electric field induced by water flows forced at 150 m depth through a 10-m wide granite fractured zone. The water flows were obtained by pumping cyclically 10 m of water from a borehole that cut the fractured zone at depth, and contemporaneously reinjecting it into another borehole located 50 m away. After one day a steady-state fluid flow regime was reached, with pumping cycles lasting 45 minutes, indicating a hydraulic conductivity of 10^{-5} m s^{-1} and a specific storage coefficient of 3.25×10^{-6} m^{-1}. The expected self-potential at the surface was an anomaly with two maxima of opposite sign and 2 μV amplitude each, both located 160 m away from the middle of the borehole heads, the signal being divided by two 500 m away from the middle of the borehole heads (in agreement with WURMSTICH and MORGAN, 1994). Instead, we observed an electrical signal of 8 mV midway between the borehole heads, and smaller than 5 mV, 33 m away from the borehole heads. The discrepancy observed between the data and the model can be explained by fluid flow leakages that occurred close to the water-table head, represented about 20% of the total water flow, and activated smaller but closer electric sources. This experiment thus illustrates the practical difficulty of detecting streaming potentials generated at depth. It shows in particular that in fractured zones, and hence in the vicinity of a major active fault small water flows located distantly from an energetic targeted source, but close to some of the electrodes of the network, can sometimes drastically distort the shape of the expected anomaly. Models of possible electrical earthquake precursors therefore turn out to be more speculative than expected.

Key words: Electro-kinetic phenomena, streaming potentials, self-potential, earthquake and volcanic precursors, geothermal exploration, electric methods.

---

[1] Département de Sismologie, UMR CNRS 7580, Institut de Physique du Globe de Paris, 4 Place Jussieu, 75252 Paris cedex 05, France. E-mails: bernard@ipgp.jussieu.fr, cornet@ipgp.jussieu.fr

[2] Observatoire Royal de Belgique, Avenue circulaire 3, B-1180 Bruxelles, Belgium.

[3] Now at Institut des Sciences de la Terre, de l'Eau et de l'Espace de Montpellier, Université des Sciences et Techniques du Languedoc - Montpellier 2, Case courrier 56, Place Eugène Bataillon, 34095 Montpellier cedex 05, France. E-mail: pinettes@dstu.univ-montp2.fr

[4] Centre de Recherche en Géophysique, CNRS, 58150 Pouilly sur Loire, France.

[5] Laboratoire de Géologie, UMR CNRS 8538, École Normale Supérieure, 24 rue Lhomond, 75 231 Paris cedex 05, France. E-mails: Laurence.Jouniaux@ens.fr, Jean-Pierre.Pozzi@ens.fr

[6] Laboratoire d'Électronique, de Technologies et d'Instrumentation, Commissariat à l'Énergie Atomique, 17 rue des Martyrs, 38054 Grenoble cedex 9, France.

1. Introduction

It has long ago been suspected that low-frequency electro-telluric and magnetic anomalies might sometimes precede tectonic events. Recently, such anomalies were observed in association with volcanic activities at La Fournaise volcano, France (ZLOTNICKI and LE MOUËL, 1990; MICHEL and ZLOTNICKI, 1998), at Mount Unzen volcano, Japan (HASHIMOTO and TANAKA, 1995), as well as in other places (see JOHNSTON, 1997 for review). Various magnetic or electric anomalies were also reported before major earthquakes (see PARK *et al.*, 1993 for review), in particular before the M_S 7.1 Loma Prieta earthquake (FRASER-SMITH *et al.*, 1990; BERNARDI *et al.*, 1991; FENOGLIO *et al.*, 1993) and, possibly, in Greece with the debated "VAN method" (LIGHTHILL, 1996).

Three questions arise from these observations: (1) Do they correspond to technical artifacts or to geophysical phenomena? (2) If they are of geophysical origin, are they indeed correlated with the suspected tectonic events? (3) If they actually are associated with tectonic events, which geophysical phenomena created them?

Measurements of long-term electro-telluric potentials are usually performed with so-called "non-polarizing" electrodes. A recent experiment conducted at Garchy, France enabled a comparison of various electrode designs to be made *in situ* during one year (PERRIER *et al.*, 1997). It revealed that some designs and installation methods are better than others, depending on the external conditions and the local resistivity. Furthermore, it quantified the short- (< some hours), mid- (hours to days) and long- (>days) term drifts of each design.

The validity of the correlations between the observations and the tectonic events can sometimes be established without any doubt, for instance, when the excitations and anomalies are repeated (see, e.g., ZLOTNICKI and LE MOUËL, 1990 at La Fournaise volcano). But for scarce events like earthquakes, the correlations are generally more difficult to establish (see, e.g., the purposed VAN correlations between the Greek $M > 4.5$ earthquakes and the electro-telluric observations conducted there by the VAN group, GELLER, 1996).

Many physical phenomena are known to induce electric or magnetic fields in response to tectonic stresses (see JOHNSTON, 1997 and PARK *et al.*, 1993 for review). Among them, streaming potentials (ADAMSON, 1990) appear to be the best candidate for explaining electric or magnetic anomalies induced by volcanic or earthquake activity (see ZLOTNICKI and LE MOUËL, 1990 and ADLER *et al.*, 1999 for the La Fournaise volcano; HASHIMOTO and TANAKA, 1995 for the Mount Unzen volcano; BERNARD, 1992, GRUSZOW *et al.*, 1996, PINETTES *et al.*, 1998, and PHAM *et al.*, 1998, 1999 for the VAN observations; and FENOGLIO *et al.*, 1995 for the Loma Prieta observations).

PERRIER *et al.* (1998) and TRIQUE *et al.* (1999) recently observed repeated electrical signals associated with recurrent pore pressure variations induced by reappearing artificial lake level variations. They indicated that this observation can be explained with streaming potentials induced in a perched aquifer located below one of the electrodes. A comparison between the streaming potential coefficient required by their model and that measured in the laboratory with rock samples coming from the site confirmed the interpretation. Streaming potentials can thus generate observable potentials at the scale of hundreds of meters, with shallow sources.

The results of PERRIER *et al.* (1998) and TRIQUE *et al.* (1999) do not enlighten us regarding the possible ability of streaming potentials to generate observable anomalies with deep buried sources (>100 m). The physical conditions at depth are generally far different from those in the laboratory (different *p*H, temperature, pressure and characteristic lengths, etc.). Therefore the only way to model data originating from such situations consists of extrapolating results from standard laboratory experiments (e.g., ISHIDO and MIZUTANI, 1981; MORGAN *et al.*, 1989; JOUNIAUX and POZZI, 1995, 1997; LORNE *et al.*, 1999a,b).

REVIL *et al.* (1999a,b) recently derived a general formal theory of streaming potentials in porous media. Their model depends on many assumptions. It is in particular restricted to temperatures lower than about 100 °C. BERNABÉ (1992) conducted theoretical experiments to test the upscaling of electro-kinetic phenomena for heterogeneous media. He showed that several discrepancies are expected between the micro- and macroscopic equations. Moreover, he found that the electrical current and potential gradients should be considerably more localized in highly heterogeneous networks than in homogeneous ones. He did not investigate the effects of temperature and pressure. Using a finite-difference approach for modeling steady-state streaming potentials generated by standard oil well pumping in typical North American reservoirs (500 $\mathrm{m}^3\ \mathrm{day}^{-1}$ pumpings of 100-m wide reservoirs buried at 500-m depth with a streaming potential coefficient of 100 mV MPa^{-1}, a permeability of 150 mD and a resistivity of 50 Ω m), WURMSTICH and MORGAN (1994) showed that bell-shape potential anomalies are expected at the surface, with a maximum of the order of 500 μV close to the production well, and a rapid decay of the signal away from the well (amplitude divided by 5 about 3 km from the well). ISHIDO and PRITCHETT (1999) recently tested the effect of a dilatant strain inducing 20 MPa of depressure 6 km around a vertical fault zone of 5-km width, 4-km height, 10-m thickness and 7-km depth. They showed that signals up to 60 mV km^{-1} are expected at the surface, provided that a 0.1 S m^{-1} conductive channel of 1-km width and 100-m thickness is present from 100 m below the surface down to the fault zone depth.

None of these upscalings are presently controlled by direct *in situ* measurements. In fact, the available data are restricted to poorly constrained experiments, such as that of ISHIDO *et al.* (1983), who measured the self-potential generated at the surface of hot water eruptions induced by sudden openings of head valves of 700-m deep cased wells in the Takinoue geothermal area of Japan. They observed signals of the order of 5 mV with electric lines located 20 and 150 m from the production wells. This observed value is bigger than the calculations of WURMSTICH and MORGAN

(1994), however the reservoir was deeper and thicker than that tested by WURMSTICH and MORGAN (1994) (600 and 200 m, respectively). The permeability and resistivity were furthermore ten times smaller than that tested by WURMSTICH and MORGAN (1994). ISHIDO *et al.* (1983) explain their result with crude assumptions, for example that the electrical currents are supposed purely horizontal and radial. They conclude that the streaming potential coefficient at the source is 5 times smaller than that tested by WURMSTICH and MORGAN (1994), but they do not confirm it with direct measurement, and they do not investigate the effect of diphasic flows that are likely to occur at depth and that are known to enhance the streaming potentials (e.g., MORGAN *et al.*, 1989).

While theories extrapolated from laboratory experiments are in agreement with field experiments when the sources are superficial, discrepancies thus still exist in the case of buried electric sources, in particular when the media are heterogeneous or fractured. Experimental studies enabling the signal generated at the surface by streaming potentials induced at depth through fractured media to be constrained, are therefore required.

The aim of the present study is to investigate this very last point. By presenting the results of an experiment conducted in 1996, in a granite area, and consisting of the measurement of the electric potential generated at the surface and at depth by forced water flows induced at 150-m depth, through a 10-m wide subhorizontal fractured zone. After a brief description of the experiment, we show that streaming potentials were observed in association with the hydraulic excitations. A detailed quantification of the model generally proposed for explaining them illustrates that the surface measurements cannot be explained by the targeted deep electric source. They were due rather to smaller but shallower streaming potential sources, incidently activated and whose effects dominated at the surface. These results have fundamental implications in earthquake precursors research.

2. *The Mayet de Montagne Experiment of September 1996*

The test site at the Mayet de Montagne is located in central France, 25 km to the southeast of Vichy. It was originally chosen in 1984 for conducting large-scale *in situ* experiments on forced water circulations in a granite area (CORNET, 1988). Eight 200 m or more deep boreholes were drilled in granite and cut a major subhorizontal altered zone located at about 150-m depth (Fig. 1a). The average thickness of this zone is 8 m, as attested by its thermal signature (Fig. 1b). At the surface, the distance between the boreholes is of the order of 50 m (Fig. 2).

At the beginning of the experiment, the subsurface water level was −8.4 m in borehole III-2 and −13.7 m in boreholes III-3 and III-8. The fluid circulation through the altered zone was forced by pumping water regularly from borehole III-2 and reinjecting it immediately in borehole III-8 *via* a standard plastic pipe installed

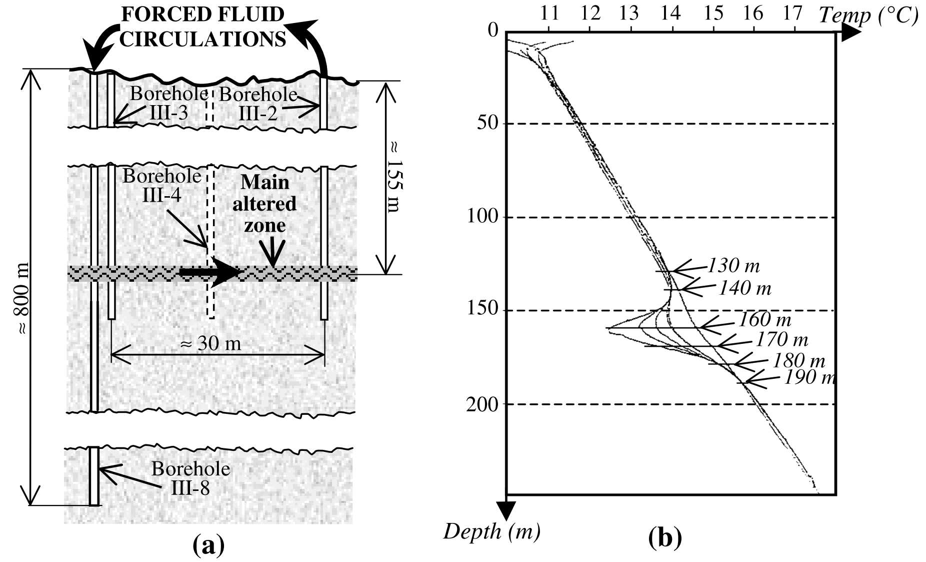

(a) (b)

Figure 1
(**a**) Schematic cross section of the aquifer and the instrumented boreholes. Less active subhorizontal aquifers are present, though not represented. (**b**) Available thermal soundings at borehole III-4 (1982/06/03, 1982/09/14, 1983/04/27 and 1983/05/18). From CORNET (1984, Fig. 21).

between the borehole heads. The flow was driven by a down-hole electric pump placed 29.9 m down borehole III-2. The pump was programmed to start pumping automatically when the water level in this well reached -18.2 m, and to stop when the water level fell to -28.2 m. The pump rate during the pumping periods was constant and equal to about 2.15 l s^{-1}. One day and a half after the beginning of the experiment, a steady-state fluid flow regime was reached, with pumping periods lasting $101 \text{ s} \pm 1$ s, and pumping cycles testing $45'5'' \pm 30$ s.

In order not to induce excessive electric noise close to borehole III-2, the pump was automatically isolated from the local 220 V power supply network whenever it was off (i.e., $43'24''$ during each $45'5''$ pumping cycle, i.e., 96.3% of the time). The pipe between boreholes III-2 and III-8 was electrically insulated, and no permanent water was present at the surface (either anthropogenic or as rainfall). Thus, there was no electrical connection at the surface between boreholes III-2 and III-8, except possibly during seconds when the pump was active and when water was forced to fall from borehole III-8 head into the water table head there. Boreholes III-2, III-3, III-4 and III-6 were not cased, and borehole III-8 was cased only from 165 m on (hence, deeper than the altered zone).

The surface electrode network was sized according to the *a priori* characteristic length of the experiment, that is the aquifer depth, 150 m (Fig. 2). In addition, two electrodes were installed in borehole III-3, at 137-m and 152-m depths, in order to sample the vertical electric field. An active resistive barometer was installed 30 m

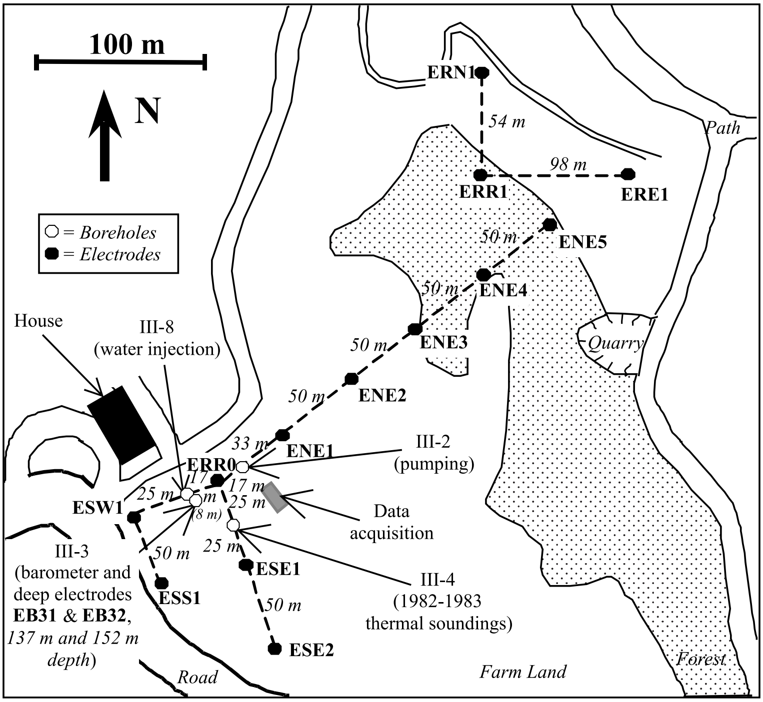

Figure 2
Schematic view of the experiment. The electrodes are located in 5 m radius circles centered on the points. The site was originally chosen for conducting large scale *in situ* experiments on forced water circulations in a granite area (CORNET, 1988).

down in borehole III-3 in order to measure the water level 8 m to the southeast of borehole III-8 (see Fig. 2). The activity of the pump was also recorded.

The electrodes were made of Pb/$PbCl_2$ with a kaolinite absorber (CLF-Na design of PERRIER *et al.*, 1997, Table 1). They were installed in opened plastic buckets filled with local soil with NaCl in excess saturation, and buried at an average depth of 50 cm (PERRIER *et al.*, 1997, Fig. 1b). The maximum possible drift is expected to be of the order 5 μV/day (PERRIER *et al.*, 1997, Fig. 4).

The voltage differences between each electrode and the reference electrode ERR0 were measured by an IOTech DaqBook 216. Fourteen of its single-ended inputs were connected to its internal 16 bits over ± 5 V Analog-to-Digital Converter. The instrument was programmed to work at 10 Hz, without anti-aliasing analog filters between the electrodes and the analog input. The connection between the electrodes and the acquisition system was ensured *via* wires soldered to the electrode wires and protected by self-amalgamating strips. The input impedance presented to the electrodes was that of the logger, i.e., 100 MΩ in parallel with 100 pF (see full specifications of the DaqBook 216 at IOTech web site: http://www.iotech.com/catalog/daq/daqbook.pdf).

The signals emanating from the barometer and the pump were digitized by another data logger, a Data Electronics Datataker DT500. This logger had two differential analog inputs connected to its internal 16 bits over ±2.5 V Analog-to-Digital Converter, and was programmed to work at 1 Hz (see full specifications of the DT500 at the Data Electronics web site: http://www.datataker.com/downloads/products/DT500600new.pdf).

The data were saved in two passes: (i) At first, in real time, in the internal buffer memory of the loggers; (ii) then with a delay of some seconds for the DaqBook and of some hours for the Datataker, in the hard disk of portable PCs that were connected to the loggers *via* parallel ports. All the loggers and the PCs, as well as the barometer, were powered by three 12 V 38 Ah batteries, whereas those of the PCs were permanently on charge *via* standard 12 V car battery chargers connected to the local 220 V power supply network.

3. Observations

The Mayet de Montagne site is located on farm land, with many electrical fences active in the vicinity. In order to test the possible effect of these electrical fences on the local electric noise, we stopped the closest one (located about 50 m to the southeast of our experiment) for half an hour, and compared the signals measured before and during the test. The corresponding data are presented in Figure 3 in terms of power spectra. It can be seen that quite significant noise is present between 2 and 15 s, which is partially contributed by the electrical fences. This noise is however not expected to produce aliasing of the data provided that the sampling frequency is greater than 1 Hz, which is the case in all the data presented in this paper.

The power spectra from measurements between the electrodes in borehole III-3 (EB31 and EB32) were also measured when the closest electric fence was connected, and then disconnected. The results are similar to that of Figure 3. The noise observed at the surface was therefore not significantly attenuated with depth, at least down to 150 m. This indicates either that an important part of the noise is generated close to the aquifer (for instance close to a borehole filled with water up to the surface and well connected with the aquifer at 150-m depth), or that it is induced in the logging wires close to the surface.

The electric potential of all the electrodes referenced to electrode ENE5 is presented in Figure 4 for the total duration of the experiment. Similar curves are obtained when the reference is changed to any electrode, except ERE1 or ESS1. It results that all the electrodes except ERE1 and ESS1 are stable and behave compatibly with the observations of Perrier *et al.* (1997). The visible drift on electrode ESS1 during the first three hours probably corresponds to a stabilization problem. It is not important since it has a total amplitude of about 25 mV and eventually vanishes. The long-term drift visible on electrode ERE1 is, on the (**a**) ENE1-ERR0, fence connected (16/09/1996-11:20:00 → 16/09/1996-11:50:00)

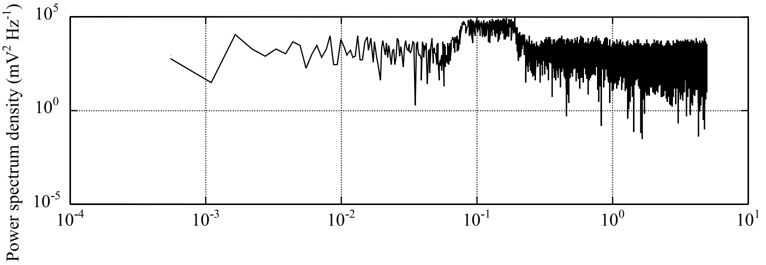

(**b**) ENE1-ERR0, fence disconnected (16/09/1996-12:20:00 → 16/09/1996-12:50:00)

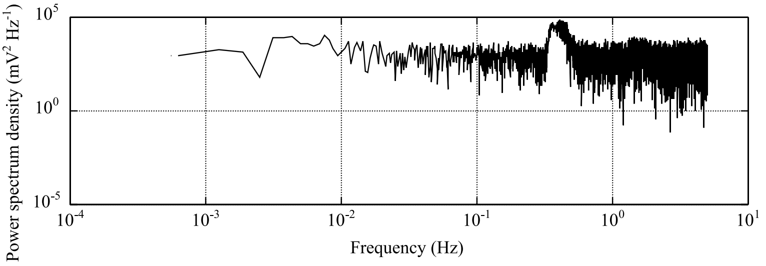

Figure 3
Power spectrum of the voltage differences between electrodes ENE1 and ERR0 during 20 minute periods. (**a**) Period during which the closest electrical fence was connected. (**b**) Period during which it was not connected.

contrary, serious, since it has a total amplitude of about 200 mV and never vanishes. The data issuing from that electrode are thus excluded.

The electric potentials expected at the surface in response to our excitations are of the order of fractions of μV, as detailed later. Such signals clearly cannot be detected directly in the raw data, where the noise level is thousands of times greater in amplitude (Fig. 4). Indeed, an eye comparison in the time domain between the pressure and electrical signals reveals no visible correlation between any electrical signal and the pressure or pump signals. Yet, as our excitation is characterized in the frequency domain by a single peak at 45 minutes plus its harmonics, a better signal-to-noise ratio is expected in the spectral domain. We thus compared the power spectrum of the pressure with the power spectra of some of the voltage differences, and it revealed common peaks at 45 minutes for the pressure and all the voltage differences that include electrode ERR0 (Fig. 5). A less defined peak could also be seen on ESW1-EB32 and ESW1-EB31 data, once again at 45 minutes.

The signals detected at 45 minutes can be due either to streaming potentials induced by the forced fluid circulations, or to artificial noises induced by possible electrical leakage of the electric pump. In both cases the periodicity of the expected noise is of the order of 45 minutes, however while in the former case its duration should be governed by the duration of the fluid flows (i.e., 45 minutes), in the latter

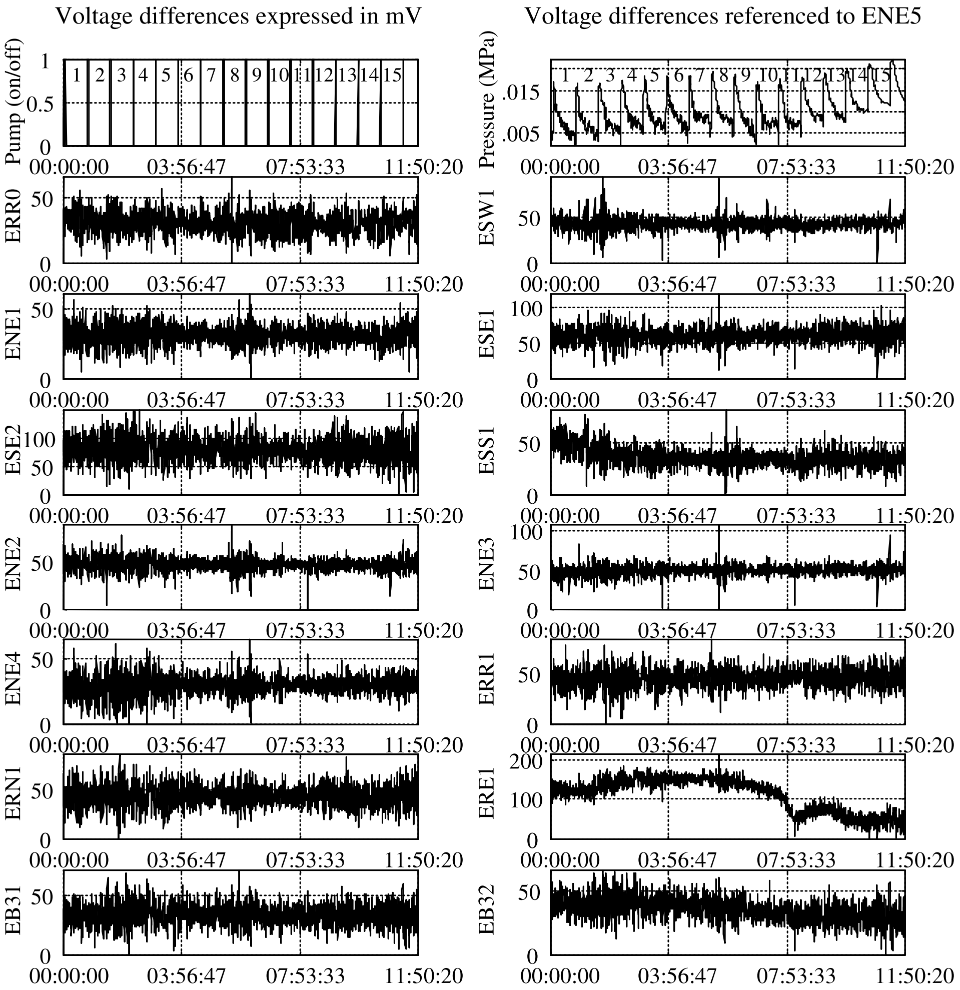

Figure 4
Electric potential of all the electrodes referenced to electrode ENE5. The monitorings began on 1996/09/25–18:45:50, after the steady-state fluid flow regime was reached. The data, originally sampled at 10 points per second for the electric potentials and at 1 point per second for the pump and pressure signals, were filtered at 50 s with a sixth-order nondephasing low-pass Butterworth filter and roughly desampled to 1 point every 10 seconds. The long-term drift visible on the pressure signal is not significant, since it is due to the slow discharge of the standard 12 V battery that was powering the instrument during the experiment. The long-term drift visible on electrode ERR1 on the contrary reveals a severe problem, which lead us to reject the data. The slow stabilization visible on electrode ESS1 during the first three hours of measurements, as well as the high frequency noises visible during cycles number 2, 3, 8, 9, 10 and 15, are not important, and did not imply rejection of the data.

case it should be governed by the duration of the possible electrical leakage (at most 100 s, see Section 2). We examined the data in the time domain, after having stacked them on each pumping cycle except the perturbed ones (cycles 2 3 8 9 10 15

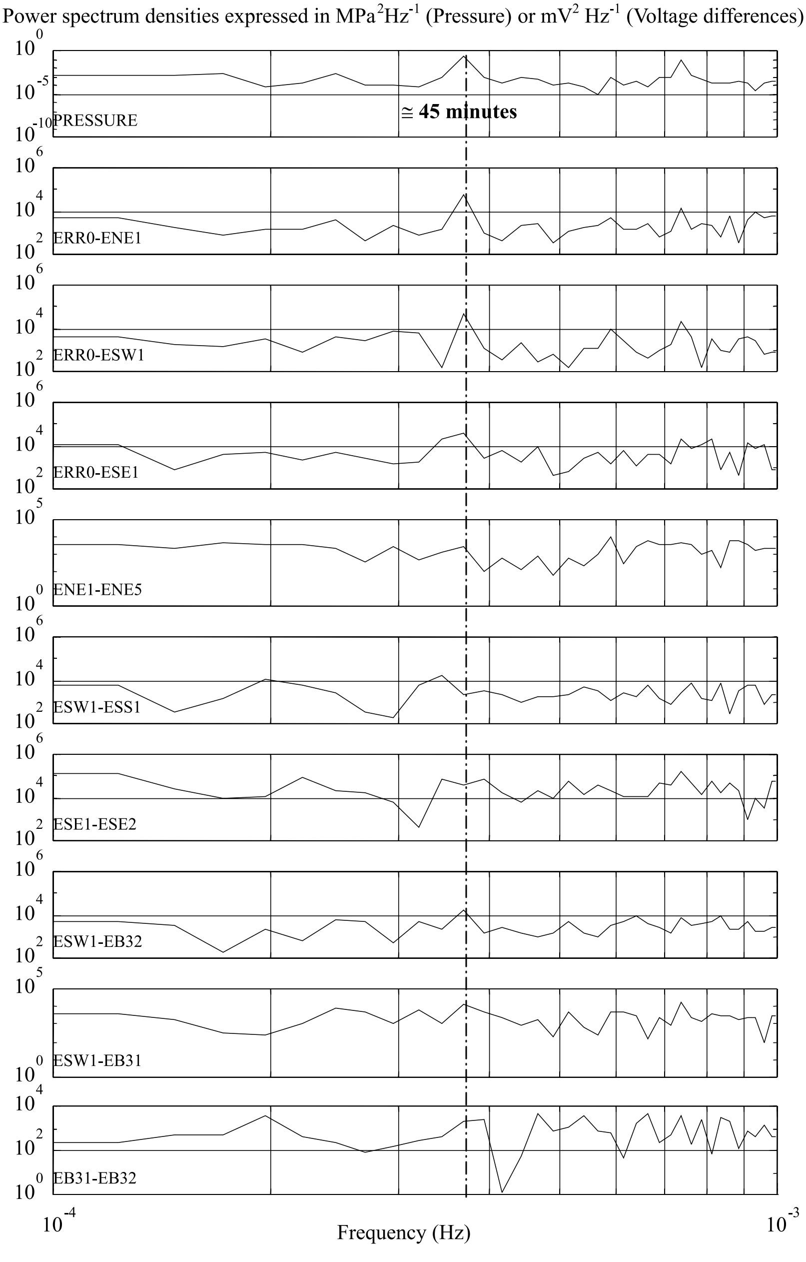

Figure 5

Power spectra of the pressure and some of the measured voltage differences between 1996/09/25-18:48:13 and 1996/09/26-06:05:09 (hence during the total duration of the experiment). The data, originally sampled at 10 points per second for the electric fields and at 1 point per second for the pressure, were filtered at 50 s with a sixth-order nondephasing low-pass Butterworth filter and roughly desampled to 1 point every 10 seconds, before the estimation of the spectra. Frequency picks at 45 minutes are clearly visible in the pressure, ERR0-ENE1, ERR0-ESW1 and ERR0-ESE1 signals. Smaller picks appear at the same frequency for ESW1-EB32 and ESW1-EB31.

of Fig. 4). The corresponding results are presented in Figure 6. The signal that generates the peak visible at 45 minutes in the spectra is clearly visible on ERR0-ENE1 and ERR0-ESW1 (Figs. 6a, b). It continues about 45 minutes, therefore it cannot be due to the pump. It moreover cannot be due to a filter effect, as the data were filtered at 250 s before the stack, i.e., at a period which is negligible compared to the duration of the excitation (45 minutes). Consequently, it is very likely that this signal corresponds to streaming potentials induced by the forced fluid circulations.

No signal corresponding to the peak visible at 45 minutes in the spectra of ERR0-ESE1 can be seen on ERR0-ESE1 (Fig. 6c). We therefore cannot conclude whether this peak is due to streaming potentials induced by the forced fluid circulations, or to any other electric source.

The time signals corresponding to the 45-minute peaks appearing in the power spectra of ESW1-EB32 and ESW1-EB31 are hardly detectable in Figures 6f and g. Yet a close look at the data reveals a small signal that emerges slightly from the noise during the first 7 minutes of the monitoring (Figs. 6f and g). As it persists longer than 250 s, it very likely corresponds to streaming potentials induced by the forced fluid circulations.

The reason why the EB31-EB32 combination does not monitor any signal is due to the fact that EB31 and EB32 are installed in the same borehole, close to each other (15 m), so that they are permanently short circuited. Contrastingly, ESW1 and EB32 and EB31 are separated by the granite bedrock which is resistive enough so as not to cancel the electric potential present between the electrodes.

The amplitudes of the signals detected in association with the forced fluid circulations were of the order of 5 mV for ERR0-ENE1, 8 mV for ERR0-ESW1 and 2.5 mV for ESW1-EB32 and ESW1-EB31 (Figs. 6a,b,f and g).

4. *Modeling*

When a fluid is forced to percolate through a permeable rock, an electrical current appears. It is called the *convection* current. It is proportional to the pressure gradient

$$\overrightarrow{j_{\mathrm{conv}}} = \frac{\varepsilon \times \zeta}{\eta} \times \vec{\nabla}(P) = C \times \sigma \times \vec{\nabla}(P) \ , \tag{1}$$

where ε is the dielectric constant of the fluid, ζ is the zeta potential of the fluid/rock interface, η is the dynamic viscosity of the fluid and P is the pressure (C being the streaming potential coefficient and σ the electrical conductivity of the fluid). Such an electrical current creates an electric potential V, which in turn creates a second electrical current, the *conduction* current, that is proportional to the potential gradient

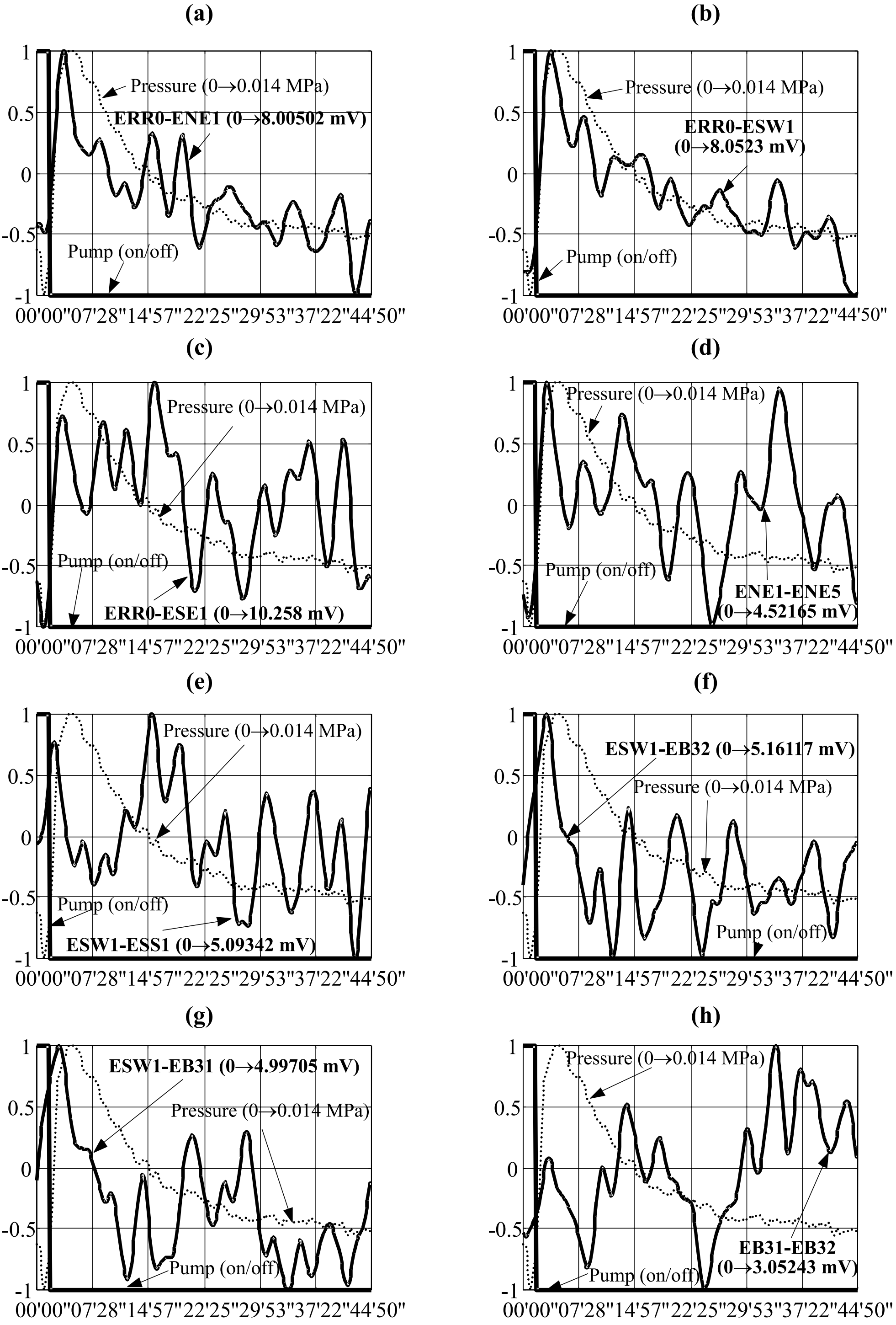
(a)
Pressure (0→0.014 MPa)
ERR0-ENE1 (0→8.00502 mV)
Pump (on/off)
1
0.5
0
-0.5
-1
00'00"07'28"14'57"22'25"29'53"37'22"44'50"
(b)
Pressure (0→0.014 MPa)
ERR0-ESW1 (0→8.0523 mV)
Pump (on/off)
1
0.5
0
-0.5
-1
00'00"07'28"14'57"22'25"29'53"37'22"44'50"
(c)
Pressure (0→0.014 MPa)
Pump (on/off)
ERR0-ESE1 (0→10.258 mV)
1
0.5
0
-0.5
-1
00'00"07'28"14'57"22'25"29'53"37'22"44'50"
(d)
Pressure (0→0.014 MPa)
Pump (on/off)
ENE1-ENE5 (0→4.52165 mV)
1
0.5
0
-0.5
-1
00'00"07'28"14'57"22'25"29'53"37'22"44'50"
(e)
Pressure (0→0.014 MPa)
Pump (on/off)
ESW1-ESS1 (0→5.09342 mV)
1
0.5
0
-0.5
-1
00'00"07'28"14'57"22'25"29'53"37'22"44'50"
(f)
ESW1-EB32 (0→5.16117 mV)
Pressure (0→0.014 MPa)
Pump (on/off)
1
0.5
0
-0.5
-1
00'00"07'28"14'57"22'25"29'53"37'22"44'50"
(g)
ESW1-EB31 (0→4.99705 mV)
Pressure (0→0.014 MPa)
Pump (on/off)
1
0.5
0
-0.5
-1
00'00"07'28"14'57"22'25"29'53"37'22"44'50"
(h)
Pressure (0→0.014 MPa)
Pump (on/off)
EB31-EB32 (0→3.05243 mV)
1
0.5
0
-0.5
-1
00'00"07'28"14'57"22'25"29'53"37'22"44'50"

$$\overrightarrow{j_{\text{cond}}} = -\sigma \times \overrightarrow{\nabla}(V) \tag{2}$$

and that tends to cancel the convection current. The total electric charge is conservative, thus when the permanent electric regime is reached, and in absence of any other electrical current source, the divergence of the total electrical current is equal to zero

$$\overrightarrow{\nabla}\left[\sigma \times \overrightarrow{\nabla}(V)\right] = \overrightarrow{\nabla}\left[C \times \sigma \times \overrightarrow{\nabla}(P)\right] \ . \tag{3}$$

Though the altered zone is intrinsically fractured, it can be approximated with an equivalent continuous porous medium (DE MARSILY, 1986, pp. 65–72). The volume fluid flow thus contains two terms. One is proportional to the gradient pressure

$$\overrightarrow{J_{\text{Darcy}}} = -\frac{\kappa}{\eta} \times \overrightarrow{\nabla}(P) \ , \tag{4}$$

where κ is the rock permeability. The other is proportional to the second force of the system, the potential gradient

$$\overrightarrow{J_{\text{osmo-electric}}} \propto \overrightarrow{\nabla}(V) \ . \tag{5}$$

According to the Onsager reciprocal relations, the coefficients in Equations (1) and (5) must be the same (DE GROOT and MAZUR, 1962), so

$$\overrightarrow{J_{\text{osmo-electric}}} = C \times \sigma \times \overrightarrow{\nabla}(V) \ . \tag{6}$$

In the altered zone of the Mayet de Montagne, κ can be estimated to be of the order of 10^{-12} m^2 (Fig. 7), η about 10^{-3} Pa s (the water was approximately at 20°C), $\sigma = 3.2 \times 10^{-2}$ S m^{-1} (measured directly in the field), C about 100 mV MPa^{-1} (ISHIDO and MIZUTANI, 1981; MORGAN *et al.*, 1989; JOUNIAUX and POZZI, 1995, 1997; LORNE *et al.*, 1999a, b), $\|\overrightarrow{\nabla}(P)\|$ between 10^{-2} MPa m^{-1} and 10 Pa m^{-1} (Fig. 8b and Eq. (1)), and $\|\overrightarrow{\nabla}(V)\|$ at most 0.6 mV km^{-1} (Fig. 12 at 137 m depth). $\left\|\overrightarrow{J_{\text{Darcy}}}\right\|$ is thus expected to be between 10 μm s^{-1} and 10 nm s^{-1}, while $\left\|\overrightarrow{J_{\text{osmo-electric}}}\right\|$ is expected to be at most of the order of 1.8×10^{-15} m s^{-1}, i.e. always negligible with respect to $\left\|\overrightarrow{J_{\text{Darcy}}}\right\|$. Hence, the hydraulic and electric problems, can be solved independently.

◀

Figure 6

Pressure and voltage differences stacked on each pumping cycle but the perturbed ones (cycles 1 2 3 8 9 10 15 removed). The data, originally sampled at 1 point per second for the pressure and the pump (respectively 10 points per second for the voltage differences), were filtered at 50 s (respectively 250 s) with a sixth-order (respectively fourth-order) nondephasing low-pass Butterworth filter, and roughly desampled to 1 point every 10 seconds. A signal continuing about 45 minutes is clearly visible on ERR0-ENE1 and ERR0-ESW1, and another one lasting about 7 minutes slightly emerges from the noise on ESW1-EB32 and ESW1-EB31.

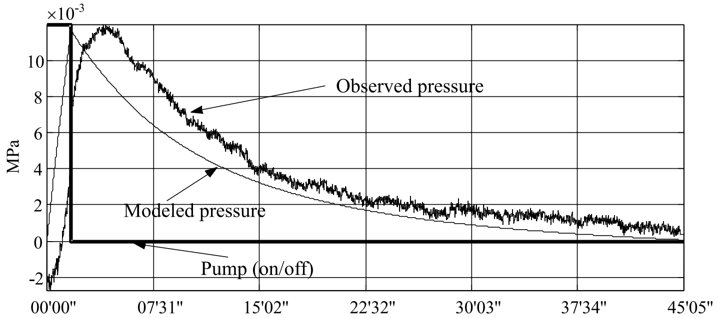

Figure 7
Modeled pressure after 14 fluid injections and for $S_{seq} = 3.25 \times 10^{-6}$ m^{-1} and $K_{eq} = 10^{-5}$ m s^{-1} (that is for $\alpha_{eq} \approx 3.3 \times 10^{-10}$ Pa^{-1} – so that $\phi_{eq} \times \beta_f \ll \alpha_{eq}$ whatever ϕ_{eq} – and $\kappa_{eq} \approx 1$ D) and observed pressure after stacking on 15 pumping cycles in borehole III-3. The data are sampled at 1 point per second.

The altered zone behaves like a confined aquifer. With the hydraulic head h defined as $h = \frac{P}{\rho \times g} + z$, where P is the pressure, ρ the mass of water per unit volume, g the acceleration due to gravity, and z the elevation measured positively upwards, it therefore follows (DE MARSILY, 1986, Chapter 5.3) that

$$\overrightarrow{\nabla}^2(h) = \frac{S}{T} \times \frac{\partial h}{\partial t} + \frac{Q_s}{T} \quad , \tag{7}$$

where Q_s is the water flow rate per unit surface area withdrawn from the aquifer and $S = S_s \times e = \rho \times g \times \phi \times \left(\beta_f - \beta_s + \frac{\alpha}{\phi}\right) \times e$ the storage coefficient of the aquifer. Here S_s is the specific storage coefficient, ϕ is the porosity, β_f, β_s and α are the fluid, mineral and soil compressibility coefficients, and e is the aquifer thickness. The parameter $T = K \times e = \frac{\kappa \times \rho \times g}{\eta} \times e$ is the aquifer transmissivity, where K is the hydraulic conductivity.

No analytical solution of Equation (7) is known for the present geometry, with two boreholes. But as noted by DE MARSILY (1986, pp. 190–191), CARLSAW and JAEGER (1986, pp. 341–344) derived a particular solution for the analog heat conduction problem with one borehole only. PAPADOPOULOS and COOPER (1967) adapted this solution to hydrogeology for $r = a$, when a constant fluid flow rate Q is withdrawn from a confined aquifer of thickness e, storage coefficient S and transmissivity T, through a borehole of radius a. The hydraulic head then follows $h_{(r,t)}$

$$\frac{2}{\pi^2} \times \frac{S \times Q}{T} \times \int_0^{\infty} du \times \left[1 - \exp\left(-\frac{T}{S} \times \frac{t}{a^2} \times u^2\right)\right]$$
$$\times \frac{J_0\left(\frac{r}{a} \times u\right) \times [u \times Y_0(u) - 2S \times Y_1(u)] - Y_0\left(\frac{r}{a} \times u\right) \times [u \times J_0(u) - 2S \times J_1(u)]}{u^2 \times \left\{[u \times J_0(u) - 2S \times J_1(u)]^2 + [u \times Y_0(u) - 2S \times Y_1(u)]^2\right\}} \tag{8}$$

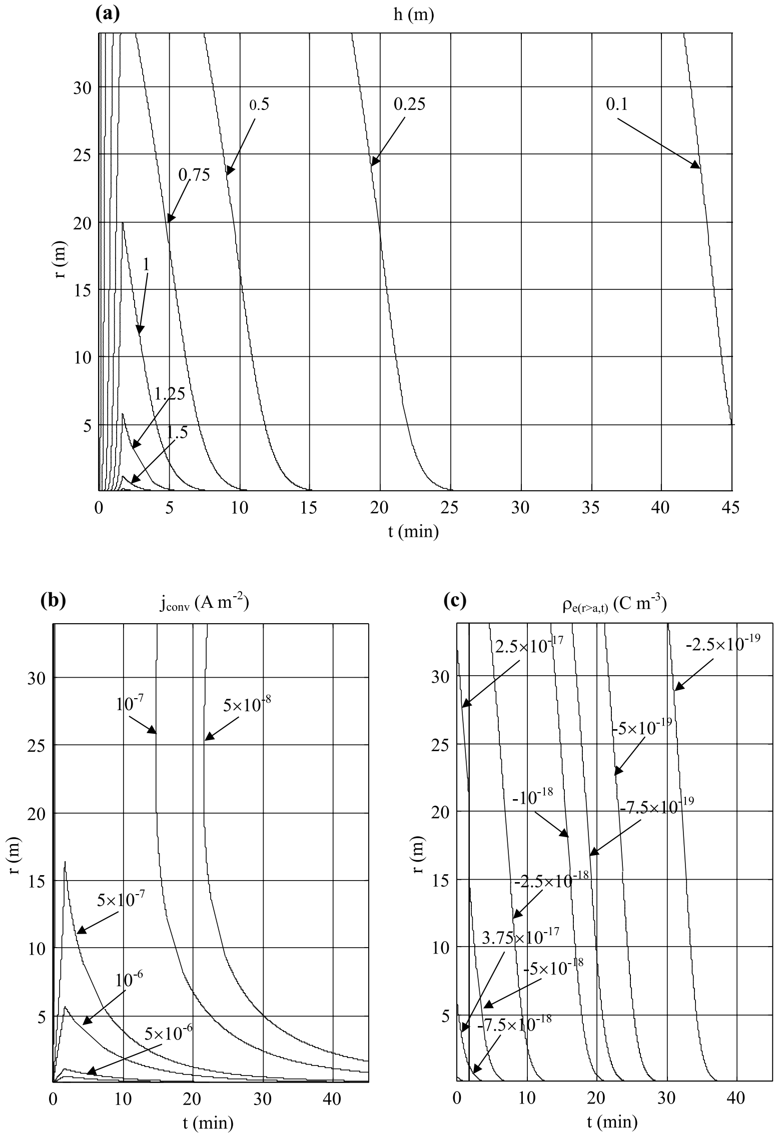

Figure 8
(**a**) Hydraulic head derived from Equation (8) and $S_{seq} = 3.25 \times 10^{-6}$ m^{-1} and $K_{eq} = 10^{-5}$ m s^{-1}. (**b**) Convection electrical current derived from Equation (1), the definition of the hydraulic head and $h_{(r,t)}$ curves of Figure 8a. (**c**) Equivalent electric charge density derived from Equation (11) and $h_{(r,t)}$ curves of Figure 8a.

where J_v and Y_v are the Bessel functions of the first and second kinds, of the order v. This solution is adapted to our problem since we want to estimate the first order of the hydraulic head, and the induced hydraulic head step is equal to 10 m, while the distance between the boreholes is equal to more than three times 10 m, i.e., it is always large compared to the influence distance between one borehole and the other.

In the Mayet de Montagne, $a = 8.25$ cm, $Q = 2.151\ \mathrm{s}^{-1}$, and $e = 8$ m. The only unknowns of the hydrogeological problem were thus the equivalent specific storage coefficient S_{seq} and the equivalent hydraulic conductivity K_{eq} of the altered zone. We determined them by comparing the pressure measured in borehole III-3 with the results of numerical estimates of Equation (8) with S_{seq} varying from 10^{-7} to $10^{-2}\ \mathrm{m}^{-1}$, and K_{eq} varying from 10^{-9} to $10^{-2}\ \mathrm{m\ s}^{-1}$. The best fit was found for $S_{seq} = 3.25 \times 10^{-6}\ \mathrm{m}^{-1}$ and $K_{eq} = 10^{-5}\ \mathrm{m\ s}^{-1}$ (Fig. 7). Taking $\eta = 1.002 \times 10^{-3}$ Pa s, $g = 9.81\ \mathrm{m\ s}^{-1}$, $\rho = 10^3\ \mathrm{kg\ m}^{-3}$, $\beta_f = 5 \times 10^{-10}$, $\beta_s = 2 \times 10^{-11}\ \mathrm{Pa}^{-1}$ (DE MARSILY, 1986, p. 108), these values correspond to an equivalent soil compressibility $\alpha_{eq} = 3.3 \times 10^{-10}\ \mathrm{Pa}^{-1}$ and an equivalent permeability $\kappa_{eq} = 1$ D (so that $\phi_{eq} \times \beta_f \ll \alpha_{eq}$ whatever the equivalent porosity ϕ_{eq}). This value of S_{seq} implies that it is dominated by the soil compressiblity, thus the ability of the Mayet de Montagne aquifer to store water is controlled by the rock matrix compressiblity and not by the fluid or mineral compressibility. Such values of S_{seq} and K_{eq} are realistic for a granite fractured zone (DE MARSILY, 1986, Chapter 5).

Two important points should be emphasized at this step of the modeling. It can be seen in Figure 7 that the pressure measured into borehole III-3 does not immediately grow after water is injected in borehole III-8. It first drops, by about 0.0025 MPa in about 15 s, before it finally grows, with a delay of about 1 minute with respect to the modeled pressure. At the end of the pumping cycle the pressure in borehole III-3 is equal to its level immediately before water was injected into borehole III-8. It is possible that the first minute drop may be due to fractures located in the vicinity of borehole III-3, put in tension when water is injected into borehole III-8 and sucking water from borehole III-3 when the drained regime between boreholes III-8 and III-3 is not yet established (Fig. 9).

The second point that should be emphasized is the fact that the maximum pressure measured in borehole III-3 is equal to 0.016 MPa, while we expected *a priori* a greater signal, of the order of less than 0.1 MPa, that is the height of water injected in borehole III-8. The maximum pressure at $r = a$ deduced from the numerical simulations of Figure 8a (0.02 MPa) confirms this impression, as it is considerably smaller than the maximum pressure *a priori* induced in borehole III-8 (about 0.1 MPa). It shows that borehole III-8 obviously does not behave like borehole III-2, probably because, unlike borehole III-2, it is drilled down to 780 m, so that it is connected to deeper aquifers which clearly absorb a significant part of the water withdrawn from borehole III-2. The induced fluid flow is therefore less symmetric than expected.

In the altered zone, C and σ can be assumed constant. Equation (3) thus becomes

$$\vec{\nabla}^2(V) - C \times \vec{\nabla}^2(P) = 0\ . \tag{9}$$

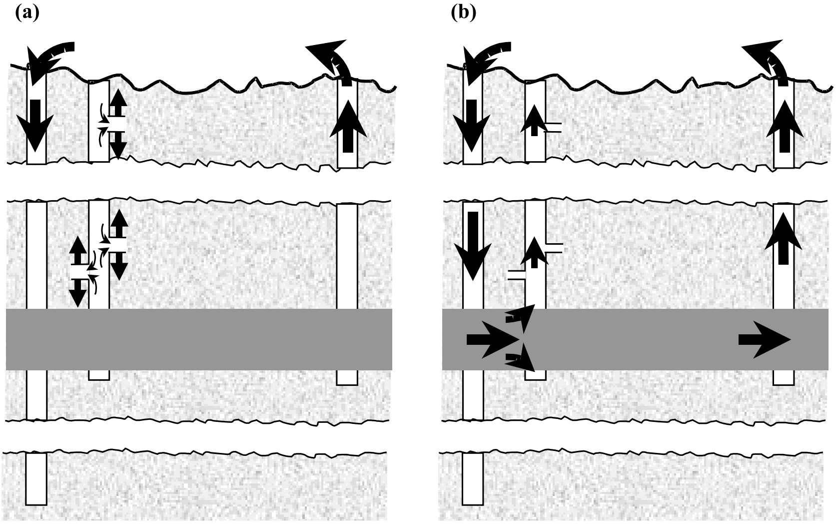

Figure 9
(**a**) At first, during the first minute of the water injection in borehole III-8, the drained regime in the aquifer is not yet established, and the fractures that are located in the vicinity of borehole III-3 are put in tension and suck water from borehole III-3. The pressure in borehole III-3 drops down. (**b**) One minute after the water injection in borehole III-8, the drained regime in the aquifer (or in fractures interconnecting boreholes III-8 and III-3) is established, so that water is drained from borehole III-8 to borehole III-3, and induces the pressure in borehole III-3 to increase.

By analogy with the standard Poisson equation (which is valid here because the electric conductivity is of the order of 10^{-2} S m^{-1} and the characteristic times are greater than 1 min, so that $\frac{\sigma}{\omega \times \varepsilon} \gg 1$, where ω is the pulsation), an equivalent volumetric electric charge $\rho_{e_{(r,t)}}$ thus develops where the pressure Laplacian is not negligible

$$\rho_{e_{(r,t)}} = -\varepsilon \times C \times \vec{\nabla}^2(P) \ , \tag{10}$$

that is, according to Equation (7) and to the definition of the hydraulic head

$$\rho_{e_{(r>a,t)}} = -\rho \times g \times \varepsilon \times C \times \frac{S}{T} \times \frac{\partial h}{\partial t} \ . \tag{11}$$

In the case where there is only one borehole, $\rho_{e_{(r,t)}}$ can be derived from $h_{(r,t)}$ curves calculated with Equation (8) and $S_{seq} = 3.25 \times 10^{-6}$ m^{-1} and $K_{eq} = 10^{-5}$ m s^{-1}. With C negative, $\rho_{e_{(r,t)}}$ is positive close to borehole III-8 when the water is pumped, and negative the remainder of time (Fig. 8c). An opposite surface electric charge develops at the interface of the altered zone and the borehole so that the total electric charge is always equal to zero. The electric charge Q_0 corresponding to this surface electric charge is equal to the mean time of the volume integral of $\rho_{e_{(r,t)}}$ in the altered zone during the pumping cycles minus the pumping periods

$$Q_0 = \frac{1}{2705-102} \times \int_{t\in[102;2705]} \left\{ \iiint_{r\in[0.0825;+\infty],\theta\in[0;2\pi],z\in[0;8]} \rho_{e_{(r,t)}} \times dr \times rd\theta \times dz \right\} \times dt \ . \tag{12}$$

In the case where there are two boreholes, the circumstances are more complex. While the surface electric charge that develops at the interface of the altered zone and the boreholes is unchanged, the volume electric charge $\rho_{e\ 2\ \text{boreholes}_{(r,\theta,t)}}$ that appears in the altered zone is the algebraic sum of the volume electric charge $\rho_{e\ \text{borehole}\ 1_{(r_1,t)}}$ that is generated there by the first borehole, and the volume electric charge $\rho_{e\ \text{borehole}\ 2_{(r_2,t)}}$ (of opposite sign) that is generated at the same place by the other borehole (Fig. 10). *A priori*, $\rho_{e\ \text{borehole}\ 1_{(r_1,t)}}$ and $\rho_{e\ \text{borehole}\ 2_{(r_2,t)}}$ cannot be derived from $\rho_{e_{(r,t)}}$ calculated with Equation (11) and $h_{(r,t)}$ curves calculated with Equation (8), since the presence of the two boreholes prevents the assumption of axial symmetry made in Equation (8) from being valid. Yet, as noted before, the characteristic length of the excitation (i.e., the induced hydraulic head step, 10 m) is large compared to the influence distance between one borehole and the other (34 m), so $\rho_{e_{(r,t)}}$ can be used for calculating $\rho_{e\ \text{borehole}\ 1_{(r_1,t)}}$ and $\rho_{e\ \text{borehole}\ 2_{(r_2,t)}}$, provided that the integration is limited to the area between the boreholes ($X \in [\pm 17]$ m, see Fig. 10), where the fluid flow is mainly restricted in the steady-state regime. The resultant electric charge thus follows

$$Q_1 = \frac{1}{2705-102} \times \int_{t\in[102;2705]} 2 \times \left\{ \iiint_{X\in[0;17],z\in[0;8]} \left[\rho_{e_{\text{borehole}\ 1_{(r_1,t)}}} - \rho_{e_{\text{borehole}\ 2_{(r_2,t)}}}\right] \times dr \times rd\theta \times dz \right\} \times dt \tag{13}$$

where r_1, r_2 and X are given in Figure 10.

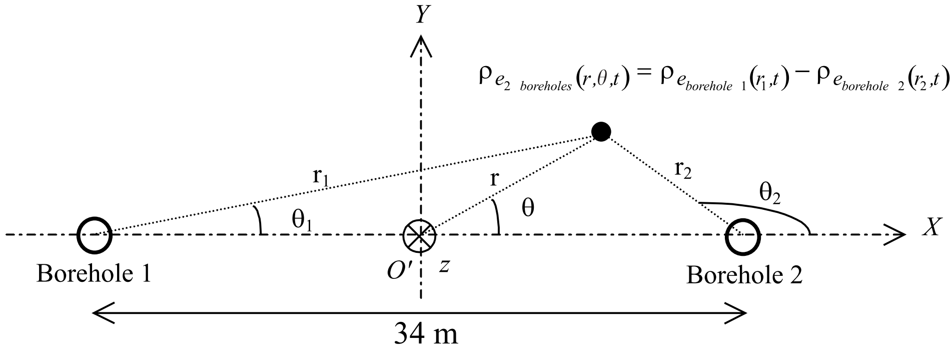

Figure 10
Geometrical conventions for the calculation of the electric charge that develops in the altered zone in case of two boreholes (viewed from above).

In practice, we truncated the integration in r (respectively θ) to [0;17] m (respectively [0;$\pi/2$] Rad), so the given value of Q_1 is an underestimate of its real value by at most the ratio between the total surface that should have been taken into consideration in the integration and the surface that has actually been taken into consideration, that is 3.

Q_0 and Q_1 can be concentrated at the barycenter positions of $\rho_{e_{(r,t)}}$ and $\rho_{e_{2\ \mathrm{boreholes}(r,\theta,t)}}$ for the estimation of their effect at the surface, distant from the sources. With $\rho_{e_{(r,t)}}$ of Figure 8c and Equations (12) and (13), we found that Q_0 is equal to 8.2×10^{-15} C and concentrated at the center of the boreholes, while Q_1 is equal to 7.3×10^{-16} C and concentrated 4.4 m from the center of the boreholes. The corresponding electric quadrupole is given in Figure 11.

The last step in the modeling consists of estimating how the electric potential generated at depth can reach the surface. In the nucleation zone of an impending earthquake, few data are generally available to constrain the electric structure. The medium is generally assumed to be either homogeneous or horizontally stratified. We thus decided to neglect, in the *a priori* model of Le Mayet de Montagne, the vertical electric conductivity contrast between the conductive boreholes and the resistive embedding rocks. The medium was rather assumed to be horizontally stratified, with an electric conductivity of 10^{-4} S m^{-1} down to 150 m (typical conductivity for a granite, see e.g., GUÉGUEN and PALCIAUSKAS, 1994), 3.2×10^{-2} S m^{-1} between 150 and 158 m (conductivity of the water measured in the field), and 10^{-4} S m^{-1} below. With these assumptions we found (see Appendix for details of the calculation) that the voltage difference generated by the model is equal to 1 μV for ERR0-ENE1 and ERR0-ESW1, and 10 μV for ESW1-EB32 and ESW1-EB31 (Fig. 12). These values are appreciably smaller than what was actually measured in the field, by a factor of about −5,000 for ERR0-ENE1, 8,000 for ERR0-ESW1 and 250 for ESW1-EB32 and ESW1-EB31.

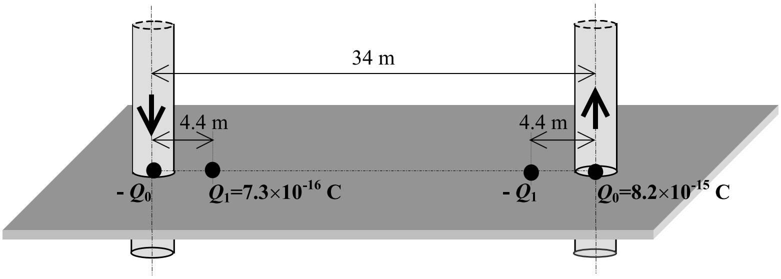

Figure 11
Schematic representation of the electric quadrupole that contributes to the electric potential measured with the surface electrodes.

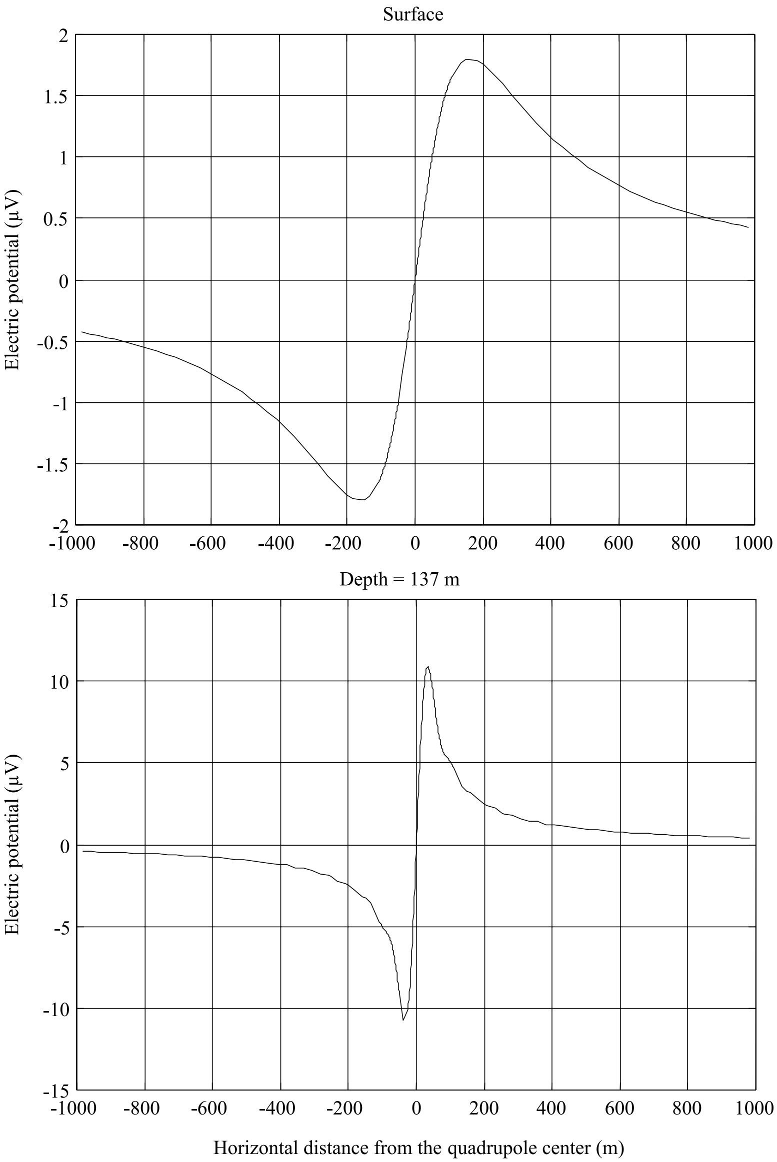

Figure 12
Electric potential expected at the surface and at depth by the electric quadrupole of Figure 11 embedded in a horizontally stratified medium with an electric conductivity of 10^{-4} S m^{-1} down to 150 m, 3.2×10^{-2} S m^{-1} between 150 and 158 m (measured directly in the field), and 10^{-4} S m^{-1} below.

5. Discussion

The assumption consisting of concentrating the electric charges at the density barycenters is not realistic for the estimation of the effect of the targeted streaming potential source 17 m above it, at 137 m depth. The discrepancy observed between the data recorded with ESW1-EB32 and ESW1-EB31 and the model predictions there are thus due to the fact that our simplifications are too crude at depth. The signals recorded with ESW1-EB32 and ESW1-EB31 therefore attest that a streaming potential source located at 155-m depth has actually been activated. The question is thus whether the source that created the surface observations is the deep targeted one, or another one, incidently activated.

Two phenomena were neglected in the *a priori* model and perhaps led us to underestimate the electric field generated at the surface. First, we did not allow for vertical resistivity contrasts that exist between the boreholes (which were full of water, and hence rather conductive) and the surrounding rocks (dry and resistive) in the model. Such contrasts are known to trap the electric field between the source and the surface, and to enhance the induced effects at the surface (see, e.g., ISHIDO and PRITCHETT, 1999). WURMSTICH and MORGAN (1994) quantified this effect when they studied the impact of casings on steady-state streaming potentials generated by standard oil well pumping (about 500 m^3 day^{-1}) in typical North American reservoirs (100-m wide, 150 mD permeable, and 50 Ω resistive at 500-m depth). They showed that the distortions induced by the casings on the surface electric potential contour lines are restricted to the vicinity of the borehole heads, within regions delimited by at most 10 times the boreholes radii (WURMSTICH and MORGAN, 1994, Fig. 3). In the Mayet de Montagne, the radii of the boreholes were equal to about 10 cm, and the electrodes were located at least 17 m from the borehole heads. The effect of the vertical resistivity contrasts, if it existed, was thus limited to at most 1 m around the borehole heads, consequently it is very unlikely to have generated the 5 or 8 mV monitored with ERR0-ENE1 and ERR0-ESW1.

The second effect that may have led us to underestimate the surface electric field is the fact that fluid flow leakages gathering up to 20% of the total fluid flow between boreholes III-2 and III-3 are known to occur close to the water table heads (CORNET, personal communication, 1996). These leakages may have created smaller but shallower streaming potential sources. Few constraints are available regarding the location and geometry of the fractures that interconnect boreholes III-2, III-3 and III-8. We know from visual coring analysis in borehole III-4 that altered granite is present from 6 to 8 m down in this borehole. In Figure 13 we test a plausible electrokinetic leakage source that we associate with this fracture zone. We assume that a 2-D horizontal fracture of 500-μm width is present 6 m below the surface, and that it generates an electric dipole of 1.75×10^{-15}C, representing 20% of the charge *a priori* induced at depth. In order not to have a zero signal at ERR0, we locate the negative charge below borehole III-8 and the positive charge about 5 m to the northeast of

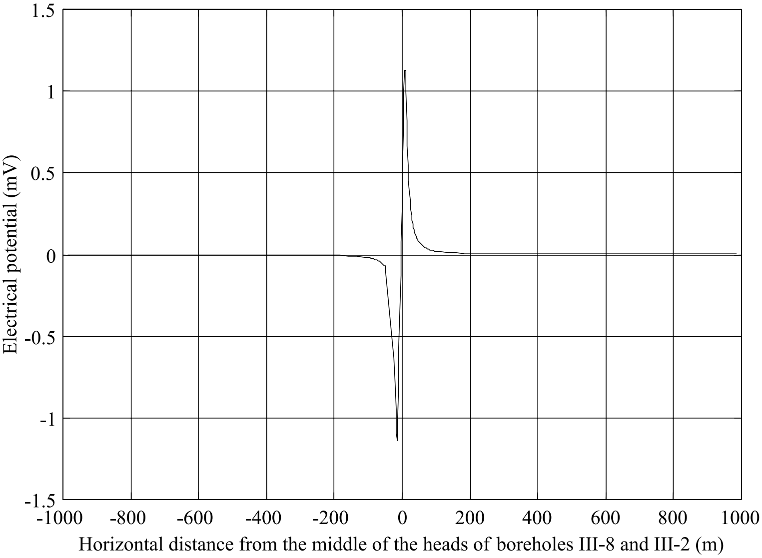

Figure 13
Electric potential expected at the surface by a horizontal electric dipole of charge $Q = 1.75 \times 10^{-15}$ C and length 22.5 m embedded at 6-m depth in a horizontally stratified medium with an electric conductivity of 10^{-4} S m^{-1} down to 6 m–250 μm, 3.2×10^{-2} S m^{-1} between 6 m–250 μm and 6 m + 250 μm, and 10^{-4} S m^{-1} below.

electrode ERR0. The electric potential generated at the surface has then a larger maximum amplitude than the previous one, however it is more concentrated in space (Fig. 13). The potential expected at ERR0 is equal to 4 mV and the voltage differences ERR0-ENE1 and ERR0-ESW1 are equal to 0.3 and 0.5 mV. These signs are in agreement with the measurements, while the amplitudes are 15 times lower than the measurements. With a small displacement of one of the charges towards electrode ERR0, or with the assumption that the fracture is 3-D and not 2-D, it is possible to generate the measured surface electric potential. It is conceivable, therefore, that the observations made at the surface were dominated by shallow fluid flow leakages.

The effects of the shallow electric source at depth are very slight. In particular, they are smaller in the vicinity of electrodes EB31 and EB32, than that of the previous source. The electric potentials measured in borehole III-3 were thus dominated by the deeply activated streaming potential source.

6. *Conclusion*

The main aim of the study was to determine whether streaming potentials generated at depth can, in practice, be detected with a surface electrode network.

We induced overpressures of 0.1 MPa at 150 m depth in a subhorizontal granite fractured zone, and measured the electric potential at the surface and at depth. The permanent fluid flow regime was reached after one day, indicating a hydraulic conductivity of 10^{-5} m s^{-1} and a specific storage coefficient of 3.25×10^{-6} m^{-1}. An electric potential of about 5 mV was detected in association with the induced fluid flow. We modeled the streaming potentials associated with the hydraulic excitation, and found that a surface signal about 5,000 times smaller than the measurements was expected. The uncertainties associated with the model are too insignificant to explain the discrepancy. The electric potentials detected at the surface were thus generated by another electric source, incidentally activated. We tested the effect of a very shallow source (6 m depth), associated with fluid flow leakages that are known to occur in the site, close to the water table heads. We found that it generates a surface electric potential compatible with the measurements. Therefore, it was considered likely that the observed surface electric potential was dominated by shallow fluid flow leakage.

Two electrodes were installed at depth, in the vicinity of the targeted deep streaming potential source. They recorded a signal associated with the forced fluid flow, and obviously due to the targeted deep streaming potential source.

It is consequently an established fact that, although we did activate a deep streaming potential source, our surface measurements were dominated by a smaller but shallower source, incidentally activated. This result thus illustrates the intrinsic difficulty of detecting streaming potentials generated at depth using surface electrode networks, in particular in fractured areas where side sources like our leakage source are expected to be numerous. It also points out that detecting streaming potentials in a farm land is very difficult because of the high electric noise generated by the electric fences present, nearby.

BERNARD (1992) estimated the surface electric potential induced by plausible streaming potentials associated with hypothesized preseismic strains. He showed that the electric potential decays very rapidly with distance (as the inverse of the square of the distance), and cannot propagate far horizontally unless adequate horizontal channels are present between the source and the electrodes. We now add that electric potential is likely to be distorted by smaller but shallower streaming potentials triggered by fluid flows on adjacent faults or fractures. Such side sources are expected to be numerous close to major active fault zones, since the distribution of fault sizes in such regions is known to be fractal. Models of possible electrical earthquake precursors thus prove to be more speculative than expected. In particular, even though it remains possible that assumed preseismic strains could sometimes generate detectable streaming potentials at the surface, using surface electrode networks to locate such sources appears to be very difficult.

Appendix: Electric Potential in a Horizontally Stratified Medium

Following BERNARD (1992) and PINETTES *et al.* (1998), we found that the electric potential generated by a unipolar electrical current I buried at the depth z_0 in a stratified conductive medium consisting of two horizontal layers of conductivities σ_1 from $H = 0$ down to H_1, and σ_2 from H_1 down to H_2, lying over a half-space of conductivity σ_3 follows

$$V_{(r,z=0,z_0\in[0,H_1])} = \frac{I}{2\pi\sigma_1}\times\int_0^{+\infty} dk\times J_0(kr) \times\frac{(1+R')\times sh[k(H_1-z_0)]+\frac{\sigma_1}{\sigma_2}\times(1-R')\times ch[k(H_1-z_0)]}{(1+R')\times ch(kH_1)+\frac{\sigma_1}{\sigma_2}\times(1-R')\times sh(kH_1)} \tag{14-a}$$

$$V_{(r,z=0,z_0\in[0,H_1])} = \frac{I}{2\pi\sigma_1}\times\int_0^{+\infty} dk\times J_0(kr)\times ch(kz) \times\frac{(1+R')\times sh[k(H_1-z_0)]+\frac{\sigma_1}{\sigma_2}\times(1-R')\times ch[k(H_1-z_0)]}{(1+R')\times ch(kH_1)+\frac{\sigma_1}{\sigma_2}\times(1-R')\times sh(kH_1)} \tag{14-b}$$

$$\begin{aligned} V_{(r,z\in[z_0,H_1],z_0\in[0,H_1])} = {} & \frac{I}{4\pi\sigma_1}\times\frac{1}{\sqrt{r^2+(z-z_0)^2}} \\ & +\frac{I}{2\pi\sigma_1}\times\int_0^{+\infty} dk\times J_0(kr) \\ & \times\left\{\frac{(1+R')\times sh[k(H_1-z_0)]+\frac{\sigma_1}{\sigma_2}\times(1-R')\times ch[k(H_1-z_0)]}{(1+R')\times ch(kH_1)+\frac{\sigma_1}{\sigma_2}\times(1-R')\times sh(kH_1)}\times ch(kz)\right. \\ & \left.-\frac{e^{-kz_0}}{2}\times e^{kz}\right\} \end{aligned} \tag{14-c}$$

$$\begin{aligned} & V_{(r,z\in[H_1,H_2],z_0\in[0,H_1])} \\ & =\frac{I}{2\pi\sigma_2}\times\int_0^{+\infty} dk\times J_0(kr) \\ & \times\left\{e^{kH_1}\times e^{-kz}\times\frac{\left[ch[k(H_1-z_0)]\times ch(kH_1)-\frac{1-R'}{1+R'}\times sh[k(H_1-z_0)]\times sh(kH_1)\right]}{(1+R')\times ch(kH_1)+\frac{\sigma_1}{\sigma_2}\times(1-R')\times sh(kH_1)}\right. \\ & -R'\times e^{-kH_1}\times e^{kz} \\ & \left.\times\frac{\left[ch[k(H_1-z_0)]\times ch(kH_1)-\frac{1-R'}{1+R'}\times sh[k(H_1-z_0)]\times sh(kH_1)\right]}{(1+R')\times ch(kH_1)+\frac{\sigma_1}{\sigma_2}\times(1-R')\times sh(kH_1)}\right\} \end{aligned} \tag{14-d}$$

$$V_{(r,z\in[H_2,+\infty],z_0\in[0,H_1])} = \frac{I}{2\pi\sigma_3} \times \int_0^{+\infty} dk \times J_0(kr) \times e^{kH_1} \times e^{-kz}$$
$$\times \left\{ \frac{(1+R) \times ch[k(H_1 - z_0)] \times ch(kH_1)}{(1+R') \times ch(kH_1) + \frac{\sigma_1}{\sigma_2} \times (1-R') \times sh(kH_1)} \right.$$
$$\left. - \frac{\frac{(1-R')\times(1+R)}{1+R'} \times sh[k(H_1 - z_0)] \times sh(kH_1)}{(1+R') \times ch(kH_1) + \frac{\sigma_1}{\sigma_2} \times (1-R') \times sh(kH_1)} \right\} , \tag{14-e}$$

when $0 \le z_0 \le H_1$,

$$V_{(r,z=0,z_0\in[H_1,H_2])} = \frac{I}{2\pi\sigma_2} \times \int_0^{+\infty} dk \times J_0(kr)$$
$$\times \frac{\left[e^{-k(z_0-H_1)} - R'e^{k(z_0-H_1)}\right]}{(1+R') \times ch(kH_1) + \frac{\sigma_1}{\sigma_2} \times (1-R') \times sh(kH_1)} \tag{15-a}$$

$$V_{(r,z\in[0,H_1],z_0\in[H_1,H_2])} = \frac{I}{2\pi\sigma_2} \times \int_0^{+\infty} dk \times J_0(kr) \times ch(kz)$$
$$\times \frac{\left[e^{-k(z_0-H_1)} - R'e^{k(z_0-H_1)}\right]}{(1+R') \times ch(kH_1) + \frac{\sigma_1}{\sigma_2} \times (1-R') \times sh(kH_1)} \tag{15-b}$$

$$V_{(r,z\in[H_1,H_2],z_0\in[H_1,H_2])}$$
$$= \frac{I}{4\pi\sigma_2} \times \frac{1}{\sqrt{r^2 + (z-z_0)^2}} + \frac{I}{4\pi\sigma_2} \times \int_0^{+\infty} dk \times J_0(kr)$$
$$\times \left\{ \frac{\left[e^{-k(z_0-2H_1)} - R'e^{kz_0}\right] \times \left[ch(kH_1) - \frac{\sigma_1}{\sigma_2} \times sh(kH_1)\right]}{(1+R') \times ch(kH_1) + \frac{\sigma_1}{\sigma_2} \times (1-R') \times sh(kH_1)} \times e^{-kz} - 2R'e^{-2kH_1} \right.$$
$$\left. \times \frac{ch[k(z_0 - H_1)] \times ch(kH_1) + \frac{\sigma_1}{\sigma_2} \times sh[k(z_0 - d_1)] \times sh(kH_1)}{(1+R') \times ch(kH_1) + \frac{\sigma_1}{\sigma_2} \times (1-R') \times sh(kH_1)} \times e^{kz} \right\} \tag{15-c}$$

$$V_{(r,z\in[H_2,+\infty],z_0\in[H_1,H_2])}$$
$$= \frac{I}{2\pi\sigma_2} \times \int_0^{+\infty} dk \times J_0(kr) \times e^{-kH_2} \times \left(e^{kH_1} - R\right)$$
$$\times \frac{ch[k(z_0 - H_1)] \times ch(kH_1) + \frac{\sigma_1}{\sigma_2} \times sh[k(z_0 - H_1) \times sh(kH_1)}{(1+R') \times ch(kH_1) + \frac{\sigma_1}{\sigma_2} \times (1-R') \times sh(kH_1)} \times e^{-kz} , \tag{15-d}$$

when $H_1 \le z_0 \le H_2$,

$$V_{(r,z=0,z_0\in[H_2,+\infty])} = \frac{I}{\pi(\sigma_2+\sigma_3)} \times \int_0^{+\infty} dk \times J_0(kr) \times \frac{e^{-k(z_0-H_1)}}{(1+R') \times ch(kH_1) + \frac{\sigma_1}{\sigma_2} \times (1-R') \times sh(kH_1)} \tag{16-a}$$

$$V_{(r,z\in[0,H_1],z_0\in[H_2,+\infty])} = \frac{I}{\pi(\sigma_2+\sigma_3)} \times \int_0^{+\infty} dk \times J_0(kr) \times \frac{e^{-k(z_0-H_1)}}{(1+R') \times ch(kH_1) + \frac{\sigma_1}{\sigma_2} \times (1-R') \times sh(kH_1)} \times ch(kz) \tag{16-b}$$

$$\begin{aligned} &V_{(r,z\in[H_1,H_2],z_0\in[H_2,+\infty])} \\ &= \frac{I}{2\pi(\sigma_2+\sigma_3)} \times \int_0^{+\infty} dk \times J_0(kr) \\ &\times \left\{ e^{-k(z_0-2H_1)} \times \frac{\left[ch(kH_1) + \frac{\sigma_1}{\sigma_2} \times \frac{3-R'}{1+R'} \times sh(kH_1)\right]}{(1+R') \times ch(kH_1) + \frac{\sigma_1}{\sigma_2} \times (1-R') \times sh(kH_1)} \times e^{-kz} \right. \\ &\left. + e^{-kz_0} \times \frac{\left[ch(kH_1) + \frac{\sigma_1}{\sigma_2} \times \frac{1-3R'}{1+R'} \times sh(kH_1)\right]}{(1+R') \times ch(kH_1) + \frac{\sigma_1}{\sigma_2} \times (1-R') \times sh(kH_1)} \times e^{kz} \right\} \end{aligned} \tag{16-c}$$

$$\begin{aligned} &V_{(r,z\in[H_2,+\infty],z_0\in[H_2,+\infty])} \\ &= \frac{I}{4\pi\sigma_3} \times \frac{1}{\sqrt{r^2+(z-z_0)^2}} + \frac{I}{2\pi(\sigma_2+\sigma_3)} \int_0^{+\infty} dk \times J_0(kr) \\ &\times \left\{ \left[e^{2kH_1} + e^{-2kH_2} - \frac{\sigma_2+\sigma_3}{2\sigma_3} \times (1+R') \times e^{2kH_2} \right] ch(kH_1) \right. \\ &+ \frac{\sigma_1}{\sigma_2} \left[(3-R') \times e^{2kH_1} + \frac{1-3R'}{1+R'} \times e^{-2kH_2} - \frac{\sigma_2+\sigma_3}{2\sigma_3} \times (1-R') \times e^{2kH_2} \right] \\ &\left. \times sh(kH_1) \right\} / \left\{ (1+R') \times ch(kH_1) + \frac{\sigma_1}{\sigma_2} \times (1-R') \times sh(kH_1) \right\} \\ &\times e^{-kz_0} \times e^{-kz} \ , \end{aligned} \tag{16-d}$$

when $H_2 \leq z_0$, with

$$R = \frac{\sigma_3 - \sigma_2}{\sigma_2 + \sigma_3} \ , \tag{17-a}$$

$$R' = R \times e^{-2k(H_2-H_1)} \ , \tag{17-b}$$

where J_v and $Y_v$are the Bessel function of the first and second kind, respectively, of the order v.

The source codes for programs corresponding to these solutions of the Laplace equation as well as for Equation (8) can be downloaded at the Royal Observatory of Belgium website: http://homepage.oma.be/patrickp/Softwares/Sources.html.

Acknowledgments

We would like to thank Pierre Adler and Jean-Louis Le Mouél for their very fruitful advice when we tried to calculate the Bessel solutions of the Laplace function in the case where the studied property contrasts are vertical. We are also grateful to Dr. G. Olhoeft and a anonymous referee for their constructive and helpful reviews. This work was supported by the DBT Thème "Fluides et Failles" and PNRN programs, INSU/CNRS, as well as by the E.C. Environment and Climate Program, Topic Seismic Risk, Contracts #ENV4V-CT96-0276 and ENV4-CT97-5086. This is IPGP contribution 1755.

REFERENCES

ADAMSON, A. W. (5th ed.), *Physical Chemistry of Surfaces* (Wiley-Interscience, New York, 1990).

ADLER, P., LE MOUËL, J.-L., and ZLOTNICKI, J. (1999), *Electro-kinetic and Magnetic Fields Generated by Flow through a Fractured Zone: A Sensitivity Study for La Fournaise Volcano*, Geophys. Res. Lett. *26*, 795–798.

BERNABÉ, Y. (1992), *Streaming Potential in Heterogeneous Networks*, J. Geophys. Res. *103*, 20,827–20,841.

BERNARD, P. (1992), *Plausibility of Models of Electro- telluric Anomalies Observed at Large Distances from Areas of Earthquake Preparation*, J. Geophys. Res. *97*, 17,531–17,546.

BERNARDI, A., FRASER-SMITH, A. C., MCGILL, P. R., and VILLARD, O. G. Jr. (1991), *ULF Magnetic Field Measurements near the Epicenter of the M_s 7.1 Loma Prieta Earthquake*, Phys. Earth Planet. Inter. *68*, 45–63.

CARLSAW, H. S. and JAEGER, J. C. (2nd ed.), *Conduction of Heat in Solid* (Charendon Press, Oxford, 1986) pp. 342–344.

CORNET, F. H., *Expérimentation à faible profondeur sur une méthode d'exploitation de la chaleur des roches profondes peu perméables, Vol. 1* (Rapport final pour le contrat CEE EGD-1-002 F, CEE, Bruxelles, 1984).

CORNET, F. H., *Projet Mayet de Montagne: Étude in situ de la percolation forcée d'eau en milieu granitique* (Rapport final Géothermie Profonde Généralisée, CNRS, Paris, 1988).

DE GROOT, S. R. and MAZUR, P., *Nonequilibrium Thermodynamics* (Elsevier, Amsterdam, 1962) pp. 405–452.

DE MARSILY, G., *Quatitative Hydrogeology – Groundwater Hydrology for Engineers* (Academic Press, San Diego, 1986).

FENOGLIO, M. A., FRASER-SMITH, A. C., BEROZA, G. C., and JOHNSTON, M. J. S. (1993), *Comparison of Ultra-low Frequency Electro-magnetic Signals with Aftershock Activity during the 1989 Loma Prieta Earthquake Sequence*, Bull. Seismol. Soc. Am. *83*, 347–357.

FENOGLIO, M. A., JOHNSTON, M. J. S., and BYERLEE, J. D. (1995), *Magnetic and Electric Fields Associated with Changes in High Pore Pressure in Fault Zones – Application to the Loma Prieta ULF Emissions*, J. Geophys. Res. *100*, 12,951–12,958.

FRASER-SMITH, A. C., BERNARDI, A., MCGILL, P. R., LADD, M. E., HELLIWELL, R. A., and VILLARD, O. G. Jr. (1990), *Low-frequency Magnetic Field Measurements near the Epicenter of the M_s 7.1 Loma Prieta Earthquake*, Geophys. Res. Lett. *17*, 1465–1468.

GELLER, R. J., ed. (1996), *Debate on "VAN"*, Geophys. Res. Lett. *23*, 1291–1452.

GRUSZOW, S., ROSSIGNOL, J.-C., TZANIS, A., and LE MOUËL, (1996), *Identification and Analysis of Electromagnetic Signals in Greece: The case of the Kozani Earthquake VAN Prediction*, Geophys. Res. Lett. *23*, 2025–2028.

GUÉGUEN, Y. and PALCIAUSKAS, V., *Introduction to the Physics of Rocks* (Princeton Univ. Press, Princeton, 1994).

HASHIMOTO, T. and TANAKA, Y. (1995), *A Large Self- Potential Anomaly on Unzen Volcano, Shimabara Peninsula, Kyushu Island, Japan*, Geophys. Res. Lett. *22*, 191–194.

ISHIDO, T. and MIZUTANI, H. (1981), *Experimental and Theoretical Basis of Electrokinetic Phenomena in Rock-water Systems and its Application to Geophysics*, J. Geophys. Res. *86*, 1763–1775.

ISHIDO, T., MIZUTANI, H., and BABA, K. (1983), *Streaming Potential Observations, Using Geothermal Wells and in situ Electro-kinetic Coupling Coefficient under High Temperature*, Tectonophysics *91*, 89–104.

ISHIDO, T. and PRITCHETT, J. W. (1999), *Numerical Simulation of Electro-kinetic Potentials Associated with Subsurface Fluid Flow*, J. Geophys. Res. *104*, 12,247–12,259.

JOHNSTON, M. J. S. (1997), *Review of Electric and Magnetic Fields Accompanying Seismic and Volcanic Activity*, Surveys Geophys. *18*, 441–475.

JOUNIAUX, L. and POZZI, J.-P. (1995), *Streaming Potential and Permeability of Saturated Sandstones under Triaxial Stress: Consequences for Electro-telluric Anomalies Prior to Earthquakes*, J. Geophys. Res. *100*, 10,197–10,209.

JOUNIAUX, L. and POZZI, J.-P. (1997), *Laboratory Measurements Anomalous 0.1-0.5 Hz Streaming Potential under Geochemical Changes: Implications for Electro-telluric Precursors to Earthquakes*, J. Geophys. Res. *102*, 15,335–15,343.

LIGHTHILL, SIR J., ed., *A Critical Review of VAN – Earthquake Prediction from Seismic Electric Signals* (World Sci., River Edge, N. I., 1996).

LORNE, B., PERRIER, F., and AVOUAC, J.-P. (1999a), *Streaming Potential Measurements: 1. Propertties of the Electrical Double Layer from Crushed Rock Samples*, J. Geophys. Res. *104*, 17,857–17,877.

LORNE, B., PERRIER, F., and AVOUAC, J.-P. (1999b), *Streaming Potential Measurements: 2. Relationship between Electric and Hydraulic Flow Patterns from Rock Samples during Deformation*, J. Geophys. Res. *104*, 17,879–17,886.

MICHEL, S. and ZLOTNICKI, J. (1998), *Self-potential and Magnetic Surveying of La Fournaise Volcano (Réunion Island): Correlations with Faulting, Fluid Circulation, and Eruption*, J. Geophys. Res. *103*, 17,845–17,857.

MORGAN, F. D., WILLIAMS, E. R., and MADDEN, T. R. (1989), *Streaming Potential Properties of Westerly Granite with Applications*, J. Geophys. Res. *94*, 12,449–12,461.

PAPADOPOULOS, I. S. and COOPER, H. H. Jr. (1967), *Drawdown in a Well of Large Diameter*, Water Resour. Res. *3*, 241–244.

PARK, S. K., JOHNSTON, M. J. S., MADDEN, T. R., MORGAN, F. D., and MORRISON, H. F. (1993), *Electromagnetic Percursors to Earthquakes in the U.L.F Band: A Review of Observations and Mechanisms*, Rev. Geophys. *31*, 117–132.

PERRIER, F. E., PETIAU, G., CLERC, G., BOGORODSKY, V., ERKUL, E., JOUNIAUX, L., LESMES, D., MACNAE, J., MEUNIER, J. M., MORGAN, D., NASCIMENTO, D., OETTINGER, G., SCHWARZ, G., TOH, H., VALIANT, M. J., VOZOFF, K., and YAZICI-ÇAKIN, O. (1997), *A One Year Study of Electrodes for Long-period Measurements of the Electric Field in Geophysical Environments*, J. Geomag. Geoelectr. *49*, 1677–1696.

PERRIER, F., TRIQUE, M., LORNE, B., AVOUAC, J.-P., HAUTOT, S., and TARITS, P. (1998), *Electric Potential Variations Associated with Yearly Lake Level Variations*, Geophys. Res. Lett. *25*, 1955–1958.

PHAM, V.-N., BOYER, D., CHOULIARAS, G., LE MOUËL, J.-L., ROSSIGNOL, J.-C., and STAVRAKAKIS, G. N. (1998), *Characteristics of Electro-magnetic Noise in the Ioanninae Region (Greece); A Possible Origin for so-called "Seismic Electric Signal" (SES)*, Geophys. Res. Lett. *25*, 2229–2232.

PHAM, V.-N., BOYER, D., LE MOUËL, J.-L., CHOULIARAS, G., and STAVRAKAKIS, G. N. (1999), *Electromagnetic Signals Generated in the Solid Earth by Digital Transmission of Radio-waves as a Plausible Source for Some so-called "Seismic Electric Signal"*, Phys. Earth Planet. Inter. *114*, 141–163.

PINETTES, P., BERNARD, P., ARTRU, J., BLUM, P.-A., VERHILLE, R., MILAS, P., and VEIS, G. (1998), *Strain Constraint on the Source of the Alleged VAN Precursor of the 1995 Aigion Earthquake*, J. Geophys. Res. *103*, 15,145–15,155.

REVIL, A., PEZARD, P. A., and GLOVER, P. W. J. (1999a), *Streaming Potential in Porous Media 1. Theory of the Zeta Potential*, J. Geophys. Res. *104*, 20,021–20,031.

REVIL, A., SCHWAEGER, H., CATHLES III, L. M., MANHARDT, P. D. (1999b), *Streaming Potential in Porous Media 2. Theory and Application to Geothermal Systems*, J. Geophys. Res. *104*, 20,033–20,048.

TRIQUE, M., RICHON, P., PERRIER, F., AVOUAC, J.-P., and SABROUX, J.-C. (1999), *Radon Emanation and Electric Potential Variations Associated with Transient Deformation in the Vicinity of Reservoir Lakes*, Nature *399*, 137–141.

WURMSTICH, B. and MORGAN, F. D. (1994), Modelling of Streaming Potential Response by Oil Well Pumping, Geophys. *59*, 46–56.

ZLOTNICKI, J. and LE MOUËL, J.-L. (1990), *Possible Electro-kinetic Origin of a Large Magnetic Variations at La Fournaise Volcano*, Nature *343*, 633–636.

(Received March 28, 2000, accepted April 14, 2001)

Signaux précurseurs de la rupture

On verra dans cette partie des mesures d'électrofiltration, de conductivité électrique, d'émissions acoustiques, lors de déformation et de rupture d'échantillons (grès, calcaire, granite). Cette partie sera illustrée par une sélection des articles suivants :

- Jouniaux, L., M. Zamora, and T. Reuschlé, Electrical conductivity evolution of non-saturated carbonate rocks during deformation up to failure, ***Geophys. J. International,*** 2006.
- Lei, X.-L., K. Masuda, O. Nishizawa, L. Jouniaux, L. Liu, W. Ma, T. Satoh, K. Kusunose, Detailed analysis of acoustic emission activity during catastrophic fracture of faults in rock, ***Journal of Strucural Geology***, 2004.
- ***Photo*** de la presse et de la cellule de déformation du Geological Survey of Japan, et d'un échantillon du granite du Mayet de Montagne.
- Jouniaux, L., Masuda, K., Lei, X., Nishizawa, O., Kusunose, K., Liu,L., and W. Ma, Comparison of the microfracture localization in granite between fracturation and slip of a pre-existing macroscopic healed joint by acoustic emission measurements, ***J. Geophys. Res***., 2001.
- Article de vulgarisation de F. Jestin : Prévision des séismes : vers une méthode fiable ? ***La Recherche***, 1995.
- ***Photo*** de la presse triaxiale pour les mesures d'électrofiltration sous déformation.
- Jouniaux L. and Pozzi J.-P., Streaming potential and permeability on saturated sandstones under triaxial stress: consequences for electrotelluric anomalies prior to earthquakes, ***J. Geophys. Res***., 1995.
- Jouniaux L., Pozzi, J.-P., Brochot, M., et C. Philippe, Variation de résistivité sous contrainte triaxiale dans des grès de Fontainebleau saturés, ***C. R. Acad. Sci. Paris***, 1992.

● Potentiels d'électrofiltration et déformation jusqu'à la rupture

J'avais étudié les effets électriques en tant que précurseurs de la rupture en laboratoire sur des grès de Fontainebleau, lors de déformations fragiles. J'ai montré que le potentiel d'électrofiltration est un marqueur de la déformation et un précurseur de la rupture : il augmente à partir d'environ 75 % de la contrainte de rupture, à cause de l'augmentation du potentiel électrique à l'interface roche/eau quand de nouvelles surfaces sont créées dans la bande de cisaillement (fracturation intra- et inter-granulaire) [*Jouniaux and Pozzi, JGR, 1995* ; *Pozzi and Jouniaux, GRL, 1994* ; *Jouniaux et al., 2000*]. D'autres expérimentations ont également montré une augmentation du potentiel d'électrofiltration de 30 % à 50 % associé au début de la dilatance dans des grès de Fontainebleau [*Lorne et al.*, 1999].

● Conductivité électrique et déformation jusqu'à la rupture

Par la suite, en collaboration avec le laboratoire de Géomatériaux de l'IPGP dans le cadre du programme INSU - PNRN risques sismiques, des mesures de vitesse des ondes P et S, ainsi que de leur anisotropie, ont été couplées aux mesures électriques (et à leur anisotropie) pendant des expériences de déformation uniaxiale. Ces expériences complètent les premières mesures de variation de conductivité électrique pendant la déformation triaxiale [*Jouniaux et al., CRAS, 1992*] qui avaient montré, lorsque la saturation en eau est totale (et en condition drainée), que la conductivité électrique diminue dans un premier temps, puis augmente à partir de la dilatance. Il avait été suggéré qu'il serait possible d'identifier des régions de nucléation de séismes à travers des mesures électriques standard [*Lockner and Byerlee*, 1986], en discutant les résultats expérimentaux en conjonction avec les modèles de dilatance-diffusion [*Scholz et al.*, 1973 ; *Brace*, 1975]. Pourtant, la croûte terrestre supérieure est anormalement résistive électriquement [*Hyndman and Shearer*, 1989 ; *Marquis and Hyndman*, 1992], ce qui pourrait être lié à la non-saturation totale en eau et à la présence de CO_2 [*Olhoeft*, 1981 ; *Nesbitt*, 1993]. Je me suis donc intéressée aux variations de conductivité électrique lorsque la saturation en eau n'est pas complète, en condition non drainée. Il s'avère que l'on observe une augmentation continue de la conductivité électrique lors de la déformation jusqu'à la rupture, dès que la saturation initiale est de 80-85 % au lieu de 100 % [Fig. 4 dans *Jouniaux et al.*, *GJI*, 2006], sans comportement spécial lors de la dilatance. Lors de la compression, le volume poreux diminue, mais la saturation relative augmente dès lors que la saturation initiale n'est pas totale et que l'échantillon n'est pas drainé (volume d'eau constant). Lors de la dilatance, le volume poreux augmente et la saturation relative décroît, mais le chemin connecté d'eau se retrouve au final augmenté, et la conductivité électrique augmente. La modélisation de cette évolution, en déformation triaxiale, en condition non saturé et non drainé n'est pas aisée. Nous avons proposé une loi en puissance pour la variation de la conductivité dans ces conditions, dans le domaine compactant (avant la dilatance) [Fig. 8 dans *Jouniaux et al.*, *GJI*, 2006]. Il faut noter que les variations de conductivité électrique mesurées sont faibles : de l'ordre de 1 à 4 %. Cette étude à saturation partielle pose donc la question de la validité des conclusions déduites des expériences en saturation totale pour l'application à plus grande échelle aux séismes.

● Émissions acoustiques et déformation jusqu'à la rupture : comportement d'un joint naturel recristallisé

En complément de ces travaux « précurseurs de la rupture », j'ai initié une collaboration avec le Geological Survey of Japan (GSJ), reconnu internationalement dans le domaine de mesure des émissions acoustiques en laboratoire. Cette collaboration a d'ailleurs été pérennisée à l'ENS, dont plusieurs étudiants sont allés au GSJ. Les émissions acoustiques ont été mesurées lors d'expériences de compression triaxiale d'échantillons de granite du Mayet de Montagne (*programme INSU - PNRN risques sismiques, collaboration F. Cornet, IPGP*) et ont montré une localisation de la déformation bien avant la rupture, à la fois lors de la fracturation, et lors d'un glissement sur un joint naturel recristallisé [*Masuda et al.,* 1997 *; Liu et al.,* 1999a ; 1999b ; *Jouniaux et al., JGR,* 2001 ; *Lei et al., JSG,* 2004]. Le but de l'expérience était de comparer les émissions acoustiques émises « par le joint recristallisé » (appelé JS pour Joint Sample) par rapport à celles émises par un échantillon intact (appelé HS pour Homogeneous Sample) fracturé de manière classique, comparaison à la fois du nombre d'émissions acoustiques et de leur localisation. Le joint recristallisé (calcite, prehnite, et fluorine), avait été orienté de façon à être le plan de glissement ou de fracturation final. Le glissement s'est effectivement produit sur ce joint : l'échantillon a subi une diminution de volume [Fig. 2b, JS sample dans *Jouniaux et al.*, *JGR*, 2001] et le glissement s'est produit à la fin de cette compaction, au moment où la dilatance aurait commencé (s'il n'y avait pas eu de joint recristallisé dans l'échantillon). Il est remarquable que lors de la déformation du joint recristallisé, autant d'émissions acoustiques, si ce n'est plus, par rapport à l'échantillon intact, ont été enregistrées. De plus, les émissions acoustiques se localisent sur le futur plan de rupture, bien avant la rupture, que ce soit pour le joint recristallisé, mais aussi pour l'échantillon intact [Fig.3 dans *Jouniaux et al.*, *JGR*, 2001]. Cette expérience permettra peut-être de mieux interpréter des mesures de tomographie acoustique prévues in situ par le laboratoire de Géomatériaux de l'IPGP, sur un bloc de granite dans la carrière du Mayet de Montagne.

Geophys. J. Int. (2006)

doi: 10.1111/j.1365-246X.2006.03136.x

Electrical conductivity evolution of non-saturated carbonate rocks during deformation up to failure

Laurence Jouniaux,[1] Maria Zamora[2] and Thierry Reuschlé[3]
[1]*Institut de Physique du Globe de Strasbourg, CNRS* UMR7516, 5, *rue René Descartes,* 67084 *Strasbourg Cedex, France.*
E-mail: Laurence.Jouniaux@eost.u-strasbg.fr
[2]*Institut de Physique du Globe de Paris, France*
[3]*Institut de Physique du Globe de Strasbourg, CNRS* UMR7516, *France*

Accepted 2006 July 10. Received 2006 July 10; in original form 2005 April 11

SUMMARY

We present electrical conductivity measurements (at a fixed frequency of 1 kHz) performed on three directions on limestone samples from the quarry of Meriel, during uniaxial tests of deformation up to failure. Samples were saturated from 100 to 80 per cent by drainage. The samples showed brittle fracture with Young's modulus in the range 10–13 MPa. Formation factor (sample resistivity divided by water resistivity) values range between 2 and 4. In saturated conditions the electrical measurements reflect the initial rock compaction, followed by dilatancy due to new axial cracks formation and finally crack coalescence, fracture localization and failure. The conductivity increase is related to the crack porosity Φ_c, which starts to increase at relatively low stress (31 per cent of strength). The magnitude of the electrical conductivity variation is 1–4 per cent of the initial value. We show that when saturation is decreased the conductivity increase occurs earlier during the deformation process, from 68 to 17 per cent of strength for 100 to 80 per cent of water saturation, respectively, so that the decrease in conductivity at low stress is less and less present. The induced relative rock conductivity variation in non-saturated and undrained conditions is the result of two competing effects: the relative porosity variation and the relative saturation variation during the deformation process. During compaction the electrical conductivity can show either a small decrease or a small increase; since the size of the partially saturated pores and cracks is reduced, the water occupies a larger percentage of the pore space, and then conductivity can be increased at this stage. We show a *continuous* increase of the conductivity both during the compaction and the dilatancy phases when the initial saturation is about 80–85 per cent. Finally a power law is shown between conductivity and stress, so that the relative electrical conductivity increase is larger as one goes along the compression process.

Just before failure, at 90–95 per cent of strength, the rate increase in horizontal conductivity drops, so that the anisotropy between axial and radial conductivity is about 0.5–2 per cent. At failure a drastic increase of this anisotropy can be seen, up to 5–6 per cent (CME21, CME24 and CME13 samples).

Key words: deformation, electrical anisotropy, electrical conductivity, fluids in rocks, laboratory measurements, rock fracture.

INTRODUCTION

Electrical resistivity can be used in geophysics to investigate the structure or the deformation of the crust (Henry *et al.* 2003; Le Pennec *et al.* 2001; Jouniaux *et al.* 1999; Pezard 1990). Since the electrical resistivity is related to mechanical properties (Glover *et al.* 2000; David *et al.* 1999; Bernabé 1986, 1995; Jouniaux *et al.* 1994), it can be used to detect fracture (Nover *et al.* 2000), or used for *in situ* stress determination (Cornet *et al.* 2003). The electrical conductivity is a combination of electrolytic conduction for the fluid-filled fractures and surface conduction for conductive alteration minerals, and depends on the degree of water saturation of the rock (Guichet *et al.* 2003). Therefore, it is also used to investigate the migration of fluids through crustal rocks, and to image active fault zones up to 10 km depth (Eberhart-Philipps *et al.* 1995).

Electrical properties of rocks have been studied in an attempt to find a physical basis for earthquake prediction. Changes in complex resistivity during laboratory creep experiments have suggested that it may be possible to identify earthquake nucleation regions through the use of standard electrical remote sensing techniques

(Lockner & Byerlee 1986). Changes in rock conductivity (DC or low-frequency measurements) under deformation up to failure in triaxial experiments have been measured in laboratory and showed first a decrease in conductivity at low stresses, and then an increase in conductivity when stresses are further increased (Brace & Orange 1968; Brace 1975; Jouniaux *et al.* 1992; Glover *et al.* 1997). The rate of conductivity increase was shown to be larger when water was flowing through the sample (Jouniaux *et al.* 1992). Some of these experimental results were discussed in conjunction with the dilatancy–diffusion model to interpret the field observations of pre-seismic changes in crustal resistivity (Scholz *et al.* 1973; Brace 1975). However, as noted sometime ago, many negative field observations have challenged the dilatancy–diffusion model (Takano *et al.* 1993).

Most of the previous experimental studies have focused on the resistivity changes under saturated conditions, which may not be representative of the shallow crust. Indeed, as a result of the magnetotelluric studies, it is well established that the upper crust is often anomalously resistive in comparison to the lower crust. This transformation occurs at depth of 13 to 20 km and is characterized by a decrease in resistivity of 1–3 orders of magnitude. The transition from high to low resistivity correlates with crustal temperature of about 400°C (Hyndman & Hyndman 1968; Hyndman & Shearer 1989; Marquis & Hyndman 1992; Thouret & Marquis 1994). An explanation for this anomalously resistive upper crust arises from the behaviour of fluids in the H_2O-CO_2 system. When a H_2O-CO_2 solution cools to temperature of 300°–400°C, a CO_2-rich phase will begin to separate from the aqueous solution (Nesbitt 1993). The resistivity of this CO_2-rich phase should be several orders of magnitude larger than the remaining aqueous solution (Olhoeft 1981). This may be especially effective in the upper brittle crust where permeability is largely a product of a few, relatively large fractures (Brace 1980). Consequently, even though fractures in the upper crust are probably largely saturated with a moderately conductive aqueous solution, the upper crust may be anomalously resistive due to the insulating properties of discrete CO_2-rich bubbles passing through the system (Nesbitt 1993). This leads to the conclusion that we need to know the behaviour of the electrical conductivity of rocks during deformation in non-saturated and non-drained conditions.

When the rock is not fully saturated the conductivity increases throughout the compaction (in uniaxial experiments: Parkhomenko & Bondarenko 1960; Yamazaki 1965, 1966), and the amplitude of conductivity increase drops when the saturation is increased (Yamazaki 1966). To have a better understanding of the rock structure evolution during deformation up to failure, and to track some precursory changes before rupture, we have focused on measurements of electrical properties of rock during deformation, and particularly the electrical anisotropy which has not been measured in previous studies. Since the electrical conductivity is related to the water content and to the porous structure, specially crack connectivity, it can reflect the evolution of the rock structure during deformation.

It is usually accepted that faulting in compressive brittle fracture is induced by coalescence of microcracks formed prior to faulting, these microcracks being randomly distributed and subparallel to the maximum compressive stress (Brace *et al.* 1966), and the coalescence occurring near the peak stress. During the linear part of volumetric strain–stress evolution the minerals distort elastically and grains or part of grains shift slightly under the applied stress and slide relative to each another (Brace *et al.* 1966). New cracks appear at pre-existing intergranular boundaries at the onset of dilatancy, and then at 50–75 per cent of peak stress new transgranular cracks appear (Tapponier & Brace 1976; Fonseka *et al.* 1985). Small cracks grow steadily up to their coalescence leading to a macroscopic instability (Ashby & Sammis 1990). At later stages of deformation extensive crushing of particles into fine-grained gouge becomes important (Wong 1982).

Electrical data obtained during uniaxial compression tests reflect the initial rock compaction, followed by dilatancy due to new axial crack formation and finally crack coalescence, fracture localization and failure. We present the results of uniaxial compression tests run on limestone samples partially and fully saturated with water. This is the first time, in our knowledge, that the electrical anisotropy is quantified during deformation, since electrical measurements have been performed in three directions. Moreover, in non-saturated conditions, unlike previous studies focused on very low saturations, we performed measurements at relatively high water saturation such as 80–100 per cent, which is more representative of the shallow crust.

EXPERIMENTAL PROCEDURE

The studied samples come from the quarry of Meriel, France (Jouniaux *et al.* 1996; Morat & Le Mouël 1992; Morat *et al.* 1992). Meriel limestone is a bioclastic Lutetian limestone. The thin section of this limestone is shown in Fig. 1. The sample was impregnated with blue epoxy resin to reveal the pore spaces and cracks. The rock is not homogeneous since some isolated large pores can be present. The grains and pores are aligned in the bedding plane (the *X* direction). The porosity of studied samples, measured by triple weight, varies from 35.4 to 37.6 per cent (Table 1). Measurements carried out on

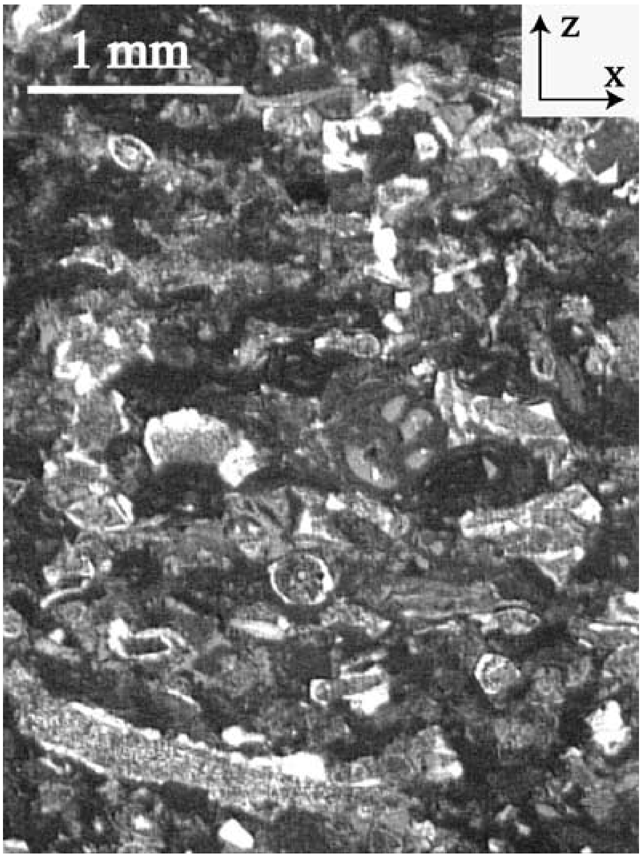

Figure 1. Thin section of Meriel limestone. The porous network is represented by blue epoxy.

Table 1. Porosity, water saturation, Young's modulus (E), peak stress, strain at peak stress, initial rock conductivity values, and water conductivity, for the studied samples.

	CME21	CME22	CME24	CME23	CME13	CME32
Porosity (per cent)	36.1	37.1	36.3	37.2	35.4	37.6
Water saturation (per cent)	100	95	91	87.6	85	80
E (MPa)	10.5	11.8	12.0	11.3	13.5	12.2
Peak stress (MPa)	4.0	4.5	4.1	4.5	4.9	4.7
Strain at peak stress (per cent)	0.68	0.63	0.86	0.70	0.69	0.63
σ_{0x} (S m^{-1})	0.28	0.26	0.25	0.24	0.22	0.25
σ_{0y} (S m^{-1})	0.28	0.27	0.26	0.28	0.22	0.25
σ_{0z} (S m^{-1})	0.52	0.53	0.44	0.48	0.40	0.41
σ_{f} (S m^{-1})	1.027	1.008	1.008	1.008	0.967	0.994

some samples taken beside our samples show that air permeability (measured by the constant flow technique) ranges from 74 to 374 × 10^{-15} m^2 (Jouniaux *et al.* 1996), and the access radii distribution shows peaks at 16 and 0.15 μm. These carbonate rocks have been chosen for their high porosities, so that the expected electrical conductivity variation induced by the deformation should be a low one compared to the amplitude variation expected for low-porosity rocks. For this study six parallelepedic (50 × 50 × 100 mm) samples were cut in the same block of rock. The rectangular geometry was chosen because it is more convenient for electrical anisotropy measurements and for further studies using acoustic sensors.

Samples were saturated under vacuum with salted (0.1 M NaCl) water (water conductivity was measured by a WTW LF330 conductivimeter and is ~1 S m^{-1}, see Table 1), at six saturation levels ranging from 100 to 80 per cent. The electrical conductivity of the water is thought to be homogeneous inside the sample once it is saturated. Partial water saturation S_{w} was achieved by drainage of the sample, that is by drying the sample using a vacuum pump and placing it in a dessicator during 24 hr. The weight of the sample was measured to deduce the water saturation, the weight being measured before and after runs.

Samples were deformed up to failure under uniaxial compression at strain rate 3.5 to 6 × 10^{-7} s^{-1}. Typical experiment lasted 4–5 hr. Loading stress was increased in small steps and stress was held at 19 to 23 levels for periods of time 10–20 min to collect electrical data. The loading force and the axial displacement were measured, leading us to deduce the axial stress and the axial strain. The horizontal strains were not measured, so that the volumic deformation of the rock was not monitored.

Conductivity of the sample (a scheme of the sample is shown in Fig. 2) was measured in three directions (horizontal: x, y; axial or vertical: z) by a two-electrodes technique at a frequency of 1 kHz, using an HP impedance bridge. Electrodes consisted in silver paint on each surface. Impedance response of the sample at frequencies between 100 Hz and 20 kHz showed a quasi-pure resistance with no capacitive effect (angle of the impedance is 0.08° to 1°) and a fixed frequency of 1kHz was chosen for our measurements during deformation because it is often the frequency at which the out-of-phase conductivity is minimized. Measurements at a fixed frequency 1 kHz were, therefore, performed for each step in axial stress. It allows us to compare our measurements to other available data (Jouniaux *et al.* 1992; Glover *et al.* 1997). The application of an electrical field gives rise to different physical and physico-chemical processes both in the bulk and on the interfaces of components (Knight & Endres 1990). Since the water used showed a conductivity of about 1 S m^{-1}, and since the used frequency is 1 kHz, it is thought that we are in the regime where the conductivity is dominated by volumic conductivity through water in pores and cracks and that surface conductivity is negligible. That is why the internal surface to volume ratio of the pores, which controls the relative importance of surface conduction processes in porous rocks (David *et al.* 1993) was not measured.

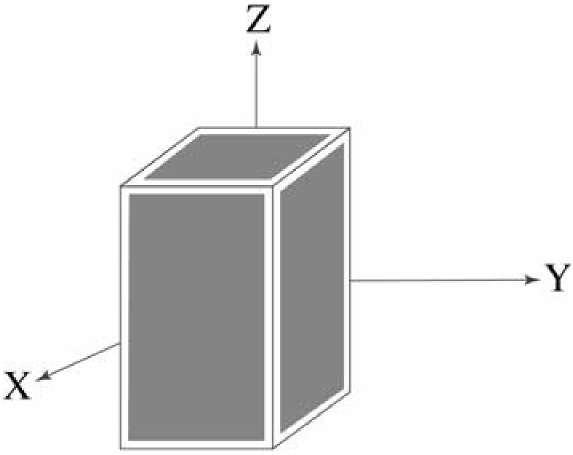

Figure 2. Scheme of the sample.

By measuring the electrical potential in one direction (x, y, or z) when a parallel current flows through a cross section of a sample, the impedancemeter measures the complex impedance Z of the sample, and the angle θ. The resistance R of the sample is deduced as $Z\cos(\theta)$. The conductivity of the sample is then calculated as $\sigma = (L/RS)$ where L is the length of the sample, and S is the section area. Therefore, the error on the rock conductivity is the sum of the errors on the measured resistance, the measured length, and the calculated section, and is ±0.9 per cent. Anisotropy of conductivity between x, y, and z direction has been calculated as followed: $\sigma_{\mathrm{xz}} = (\sigma_{\mathrm{z}} - \sigma_{\mathrm{x}})/\sigma_{\mathrm{x}}$, and its relative variation has been plotted. Note that experiments are performed in undrained regime.

Typical resistance measurements were of the order of 65 to 81 ohm in horizontal directions, and of 140 to 181 ohm in the axial direction, which lead to resistivity values of 3.6–4.5 to 1.9–2.5 ohm m. The initial values of rock conductivities from 0.2 to 0.5 S m^{-1} are given in Table 1.

RESULTS

Since the sample is shortened during the axial compression test, its strain is the axial displacement measured by the press divided by the initial length of the sample. The axial stress is the loading force divided by the cross section of the sample, and the strength of the sample is the axial stress at failure.

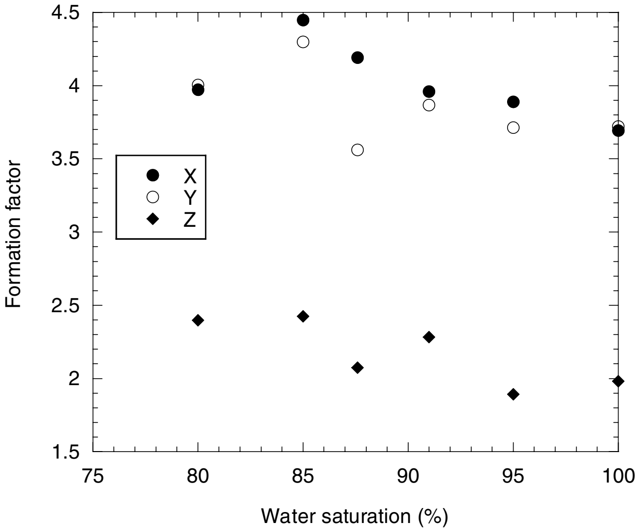

Figure 3. Initial formation factor in the three directions *X*, *Y* and *Z* versus water saturation of the samples.

Mechanical behaviour

Samples have been deformed up to 0.6–0.9 per cent in axial strain. They showed brittle axial fracture, the maximum stress ranged from 4.1 to 4.9 MPa, and Young's modulus, obtained in the linear part of the curve, was 10–13 MPa (Table 1).

Electrical behaviour

Initial formation factors (water conductivity divided by rock conductivity) are 3.5–4.5 in horizontal directions and 1.9–2.4 in the axial direction (consistent with Jouniaux *et al.* 1996), showing that the samples are about twice more conductive in the axial direction than in the horizontal plane. Since the water conductivity σ_f is about 1 S m^{-1}, the initial value of rock conductivities are between 0.2 and 0.5 S m^{-1}. Initial formation factors F_z, F_x, F_y have been plotted versus saturation (Fig. 3) and show a light decrease with increasing saturation.

Variations of the rock conductivity in *X*, *Y* and *Z* directions and variations of the anisotropy σ_{xy}, σ_{zx}, and σ_{zy} during the experimental tests have been plotted in Fig. 4. The magnitude of variation is about 2–4 per cent of the initial rock conductivity value.

We now describe the behaviour of the electrical conductivity of the six studied samples during the compression tests up to failure.

Sample CME21 was fully saturated and its porosity was 36.1 per cent. The electrical conductivities first decrease. At 73 per cent

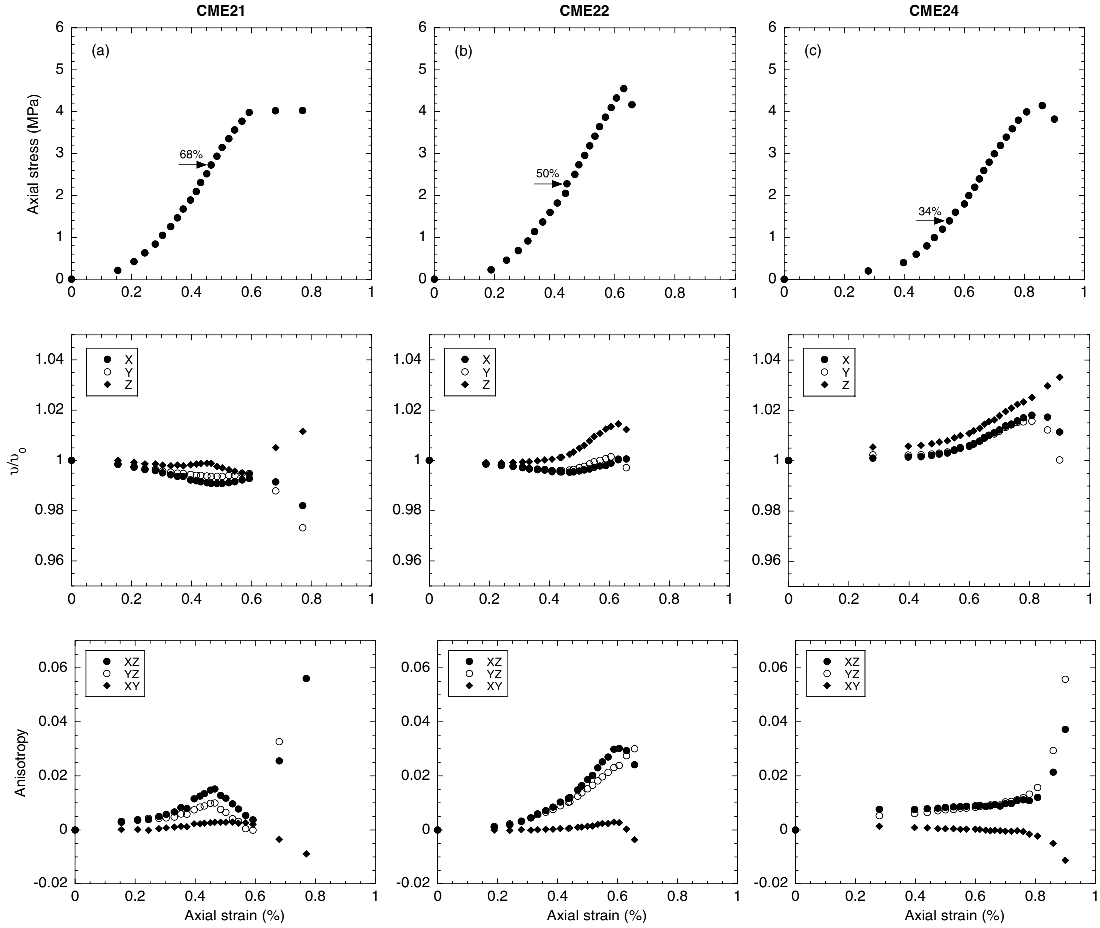

Figure 4. Axial stress, rock conductivity, and electrical anisotropy versus axial strain. 4a: CME21 sample; 4b: CME22 sample; 4c: CME24 sample; 4d: CME23 sample; 4e: CME13 sample and 4f: CME32 sample.

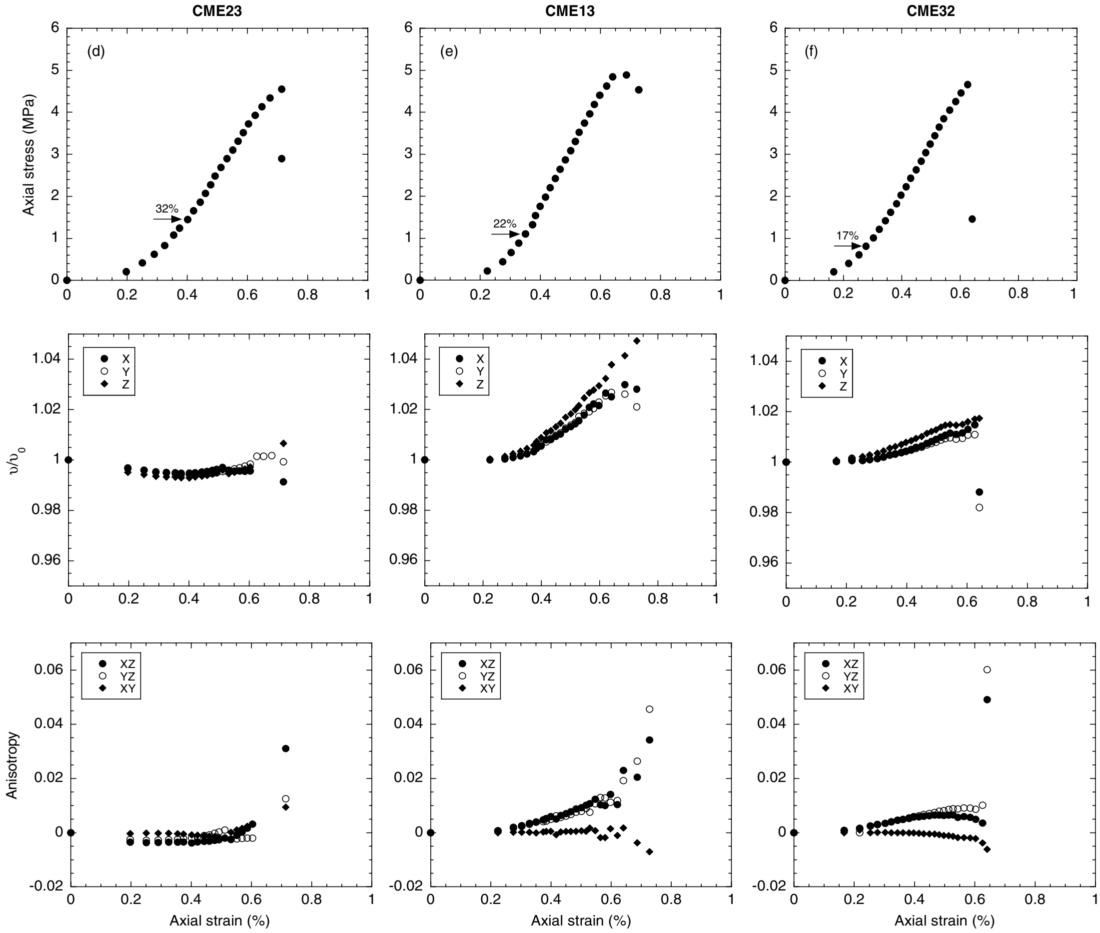

Figure 4. (*Continued.*)

of the strength the horizontal conductivities increase up to failure, the total variation being about 1 per cent. The axial conductivity tends to increase at low stress (37 per cent of strength), but then decreases well before failure (68 per cent of strength). At failure the axial conductivity increases by 2 per cent, whereas the horizontal conductivities decrease by 1–2 per cent, σ_{x} decreasing less than σ_{y} (Fig. 4a).

Sample CME22 was saturated at 95 per cent. The horizontal conductivities decrease by 0.5 up to 55 per cent of strength, and then increase by 0.5 per cent up to failure. The axial conductivity increases slowly at low stresses, and then increases more rapidly by 1.5 from 45 per cent of the strength to final rupture. Just before failure, at 95 per cent of strength, the rate increase is dropping, except for σ_{x} (Fig. 4b).

Sample CME24 was saturated at 91 per cent. The electrical conductivities slowly increase up to 34 per cent of strength, and then increase more rapidly, by 1.5–2 per cent for σ_{x}, σ_{y} and 3 per cent for σ_{z} up to failure. Before failure, at 91 per cent of strength the rate increase of the horizontal conductivities is dropping (Fig. 4c).

Sample CME23 was saturated at 87.6 per cent. The electrical conductivities first decrease by 0.5–0.7 up to 32 per cent of strength. Then the electrical conductivity increase up to failure, by 0.8 and 1.4 per cent for σ_{y} and σ_{z}, respectively, except for σ_{x} that decreases from 60 per cent of strength up to failure. Before failure, at 82 per cent of strength the rate increase in σ_{y} is dropping. Note that some σ_{x} data are missing, due to technical problems (Fig. 4d).

Sample CME13 was saturated at 85 per cent. The electrical conductivities first slowly increase up to 22 per cent of strength, then increase up to failure, by 3 per cent for σ_{x} and σ_{y}, and 4 per cent for σ_{z}. Before failure, at 95 per cent of strength, the rate increase of the horizontal conductivities is dropping (Fig. 4e).

Sample CME32 was saturated at 80 per cent. The electrical conductivities slowly increase up to 17 per cent of strength, and then increase more rapidly up to failure by 1–1.5 per cent, with a dropping in rate increase at 85 per cent of strength (Fig. 4f).

DISCUSSION

Electrical conductivity at various saturations (intact samples)

The resistivity of the samples roughly increases when water saturation is decreased, as shown in Fig. 3. This behaviour is consistent with the fact that the mineral grains act as an insulating matrix and conduction occurs solely through the pore fluid. The expression used to describe the variation of formation factor F with saturation S_{w} and porosity Φ is usually $F = \Phi^{-m} S_{\mathrm{w}}^{-n}$ (Archie 1942). Since we compare different samples in Fig. 3, it may explain the roughly feature of the increase of formation factor with decreasing saturation. When the sample is fully saturated (sample CME21), the m-value deduced from this expression is 1 ± 0.2 (consistent with

Jouniaux *et al.* 1996), which is a low value for cementation exponent in carbonates (Focke & Munn 1985; Sen *et al.* 1997). The *n*-value deduced from the axial formation factor results (Fig. 3) is about 1, consistent with the observation that the *n*-value is close to the *m*-value (Waxman & Smits 1968). For the horizontal results, their dispersion does not allow us to derive a *n*-value. Especially the lower horizontal formation factor value at 80 per cent water saturation and the dispersion observed at 87.6 per cent saturation may be due to some heterogeneities in the horizontal lithology of the concerned samples.

Since our samples were saturated from 100 to 80 per cent, we may assume that we are not in the low-saturation regime where the conductivity involves surface conduction. In low-saturation regime, a dramatic decrease in resistivity occurs when saturation is increased, up to the presence of a few monolayers of water on the internal rock surfaces (Knight & Dvorkin 1992). These few monolayers of water correspond to water saturation of 4 to 10 per cent for the studied sandstones by Knight & Dvorkin (1992) and have been interpreted as the thickness of water layers for which the behaviour of water changes from that of a surface phase to that of a bulk phase (Knight & Dvorkin 1992). It can, therefore, be assumed that by using saturation between 80 and 100 per cent, the main mechanism involved in the conductivity will be the conductivity of bulk water.

Effect of uniaxial compression on the electrical conductivity of fully saturated sample (CME21)

When the rock is saturated, and in drained conditions, the axial electrical conductivity is thought first to decrease, and then to increase with compression. At the beginning of the deformation process, the closure of pores and subhorizontal cracks full of water induces a decrease in conducting paths and the conductivity of the rock decreases. Then, when new axial cracks form in the rock and when water is available, these cracks become new conducting paths, and the conductivity of the rock increases. This behaviour has been observed in triaxial experiments on crystalline rocks (Brace & Orange 1968), on Fontainebleau sandstone (Jouniaux *et al.* 1992), and on Darley Dale sandstone (Glover *et al.* 1997). It has been shown by Brace & Orange (1968) that the increase of conductivity begins about when the rock becomes dilatant and that a rapid increase in conductivity accompanies the rapid increase in volume. Most of the time the magnitude of conductivity increase is much more larger than the magnitude of conductivity decrease. This is not the case in our experiments, maybe because in uniaxial compression tests, the crack closure at low stress, which leads to a decrease in conductivity when in drained conditions, is more important than in triaxial compression tests, where the hydrostatic stress applied to the sample prior to triaxial testing has already partly closed the initial cracks.

In our study, measurements on CME21 sample which was fully saturated, show first a decrease and then an increase in horizontal conductivities, as expected for the axial conductivity. Note that the horizontal conductivity of a granite sample under triaxial deformation increased too (Brace & Orange 1968). However, the behaviour of the axial conductivity is more complex with an unusual transient increase at about 70 per cent of strength, roughly corresponding to the local minimum in the horizontal conductivity curves. Indeed in our uniaxial undrained experiments the sample is not connected to a water reservoir as it is usually the case in triaxial experiments, so that the available water volume is only the initial water volume present in the rock. The transient vertical conductivity increase may thus be explained by the differential closure of subhorizontal cracks with their water content being expelled into the opening vertical cracks. The following light decrease may then be due to a transient lack of water in the new axial cracks forming in the sample. Further closing of subhorizontal cracks leads to the increase of water saturation in axial cracks resulting, when combined to their coalescence, in the increase in axial conductivity and the decrease in horizontal conductivities at failure.

The increase rate of axial conductivity from 40 to 70 per cent of strength is 0.13 per cent/MPa, of the same order as the one observed by Brace & Orange (1968) on Pottsville sandstone (0.14 per cent/MPa), and lies between the values obtained by Glover *et al.* (1997) on Darley Dale sandstone (0.06 per cent/MPa) and those measured by Jouniaux *et al.* (1992) on Fontainebleau sandstone (0.2 to 0.6 per cent/MPa). At failure, the 2 per cent increase in the axial conductivity and the decrease in horizontal conductivities confirm the subverticality of the final macroscopic fracture.

The conductivity increase is usually related to the crack porosity Φ_c, corresponding to new formed cracks, which is the difference between the actual volume change and the elastic volume change. The conductivity through cracks σ_c, which is obtained by subtracting crack-free conductivity (that would be the linear decrease of the conductivity from the beginning of the compression test, Fig. 5(a): straight line) from total conductivity (the measured conductivity, Fig. 5(a): empty squares), was calculated and compared to the crack porosity by Brace & Orange (1968). These authors showed that the crack conductivity was proportional to the crack porosity, so that $\sigma_c/\sigma_f = \Phi_c^m$ with $m = 1$ for their studied crystalline rocks, whereas for the Pottsville sandstone $m = 2$. The *m*-value, deduced from two independent measurements (volume change and conductivity

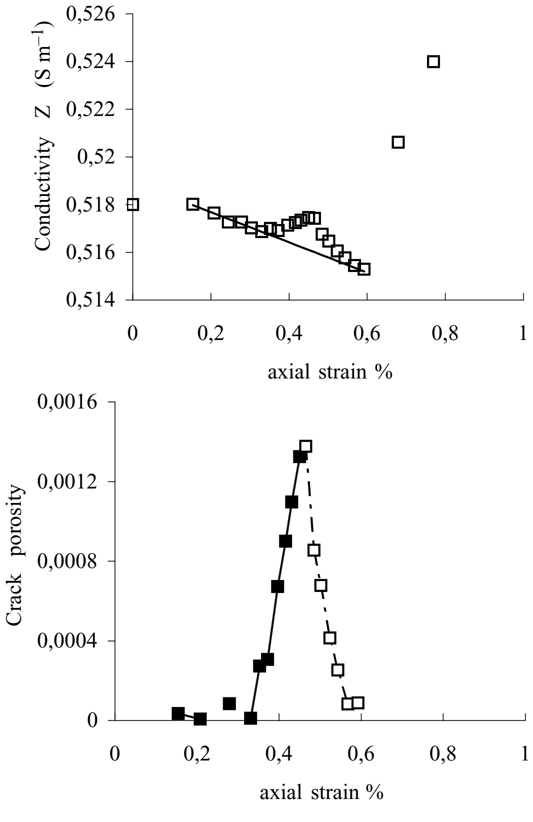

Figure 5. (a) Measured axial conductivity and the linear decrease of conductivity during the compression phase, for CME21 sample. (b) Crack porosity Φ_c during compression, deduced from $\sigma_c/\sigma_f = \Phi_c^m$ with $m = 1$.

change), was shown to be constant during compression up to the failure (Brace & Orange 1968). The same approach has been used by Glover *et al.* (1996), who assumed a *m*-value equal to 2 to compute a damage parameter which is the crack porosity. The crack porosity Φ_c has been computed for CME21 sample (Fig. 5b), with the *m*-value deduced from the measurements of porosity and formation factor before the deformation test ($m = 1$), and assuming that this *m*-value is constant during compression, as shown by Brace & Orange (1968). It can be seen that the crack porosity starts to increase at 0.33 per cent of axial strain, meaning 31 per cent of strength, and increases up to 0.46 per cent of strain (68 per cent of strength). When the rock is saturated, the conductivity change can, therefore, be related to the crack porosity and according to this analysis, the compression of the sample leads first to a decrease in volume, and then to a volume increase up to 68 per cent of strength. As noted previously a partial desaturation of new forming cracks may happen leading to a transient decrease of axial conductivity and, therefore, a transient decrease of the deduced crack porosity (Fig. 5b, dotted-line), before their drastic increase as failure approaches.

Since the cracks induced by the deformation are created in the axial direction, this analysis is not suitable for horizontal electrical measurements. Moreover, note that the crack porosity is related to the electrical conductivity change only if the cracks are filled with water, which is not the case for the following not-fully saturated conditions.

Effect of water saturation on the electrical conductivity behaviour during uniaxial compression tests

The largest variation in electrical conductivity during compression is usually in the axial direction (except for CME23 sample), in accordance to the fact that cracks are created in the axial direction during these uniaxial experiments. There is no obvious relation between the amplitude of conductivity increase and the water saturation, at least for the studied saturation range. When the water saturation is decreased, the electrical conductivity increase occurs earlier during compression (Fig. 6), so that the decrease in conductivity at low stress is less and less present (except for CME23 sample). The increase in conductivity occurs at 68, 50, 34, 32, 22 and 17 per cent of strength (see Fig. 4) for the decreasing saturations of 100, 95, 91, 87.6, 85 and 80 per cent, respectively. In order to compare the mechanical behaviour of the different samples, the axial stress has been plotted versus the axial strain on a single graph for the six studied samples (Fig. 7). The samples show a similar mechanical behaviour, except sample CME24 which shows a rather compliant initial behaviour maybe due to the presence of subhorizontal flaws. Therefore, the differences in the electrical conductivity variation during the compression will not be attributed to a possible mechanical difference, except possibly for the sample CME24.

Previous experiments on sedimentary rocks of high porosity (40–55 per cent) under uniaxial compression at various water saturation from 2 to 25 per cent showed an increase in electrical conductivity with stress (Yamazaki 1965; 1966). The conductivity increase was 0.5 per cent on lapilli tuff at 25 per cent water saturation, 2.5 per cent on tuffaceous sandstone at 9.5 per cent of water saturation; and 1 per cent on pumice tuff at 5.6 per cent of water saturation. When the initial water saturation was increased from 2 to 25 per cent in lapilli tuff samples, the magnitude of conductivity increase during the uniaxial compression tests dropped from 11 to 0.5 per cent (Yamazaki 1966). As already mentioned by Brace & Orange (1968), when the rock is partially saturated, water films form only a partial network in the rock, and at low stress when cracks and pores are closed and porosity reduced, the connectivity of these films is increased. So that the initial conductivity is small and then increases with stress. Note that only a small water amount is needed to form a connected path throughout the sample, as low as one-fifth of a monolayer of water on the internal rock surfaces, corresponding to water saturation below 1 per cent for the sandstones studied by Knight & Dvorkin (1992).

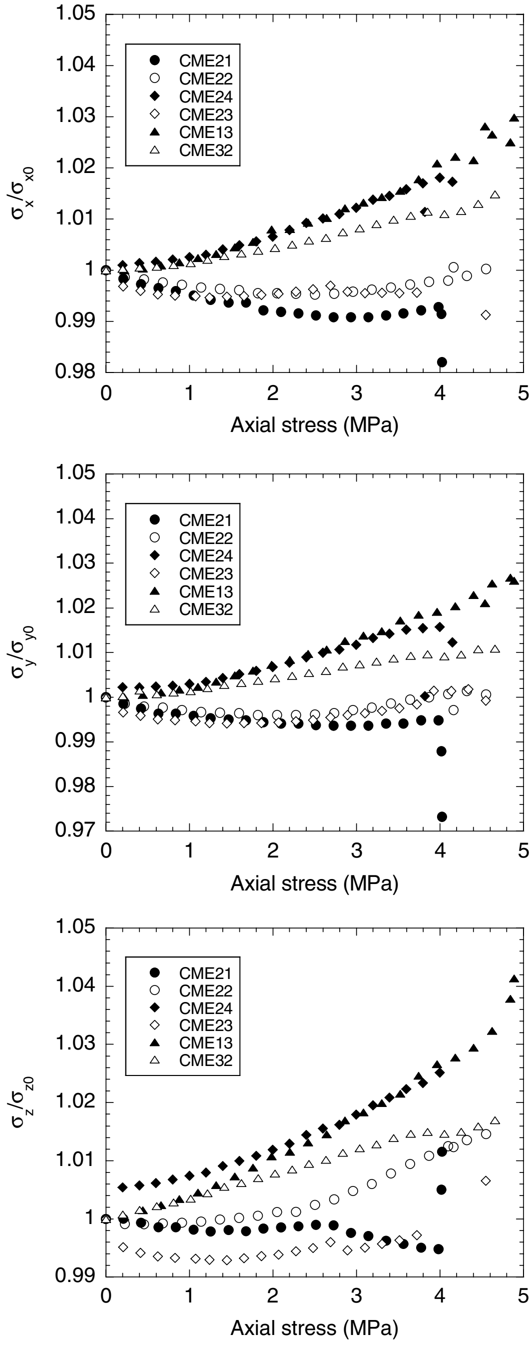

Figure 6. Rock conductivity versus axial stress for the six studied samples.

However, the exact quantification of the involved processes both during the compression and in non-saturated and undrained conditions is hardly feasible. Some modelling exists that explains

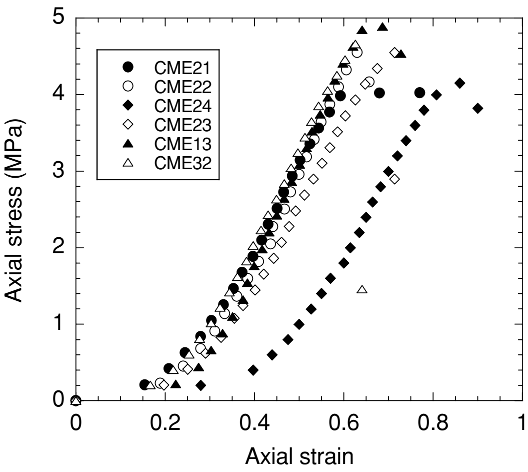

Figure 7. Axial stress versus axial strain for the six studied samples.

the decrease of electrical conductivity during the drainage of samples, leading to a decrease in water saturation, but without any deformation (see e.g. Brovelli *et al.* 2005). Other modelling exists that explains the effect of stress (P), in hydrostatic conditions and in saturated and drained conditions, on the electrical conductivity (Kaselow & Shapiro 2004). From Archie's law in saturated conditions $F = \Phi^{-m}$, these authors deduced a variation of the rock electrical conductivity σ_r as $\log(\sigma_f/\sigma_r) = A + KP - B\exp(-DP)$, the coefficients A, K, B, and D being fitting parameters for a given set of measurements. The first and second terms are related to the variation of the stiff porosity, and the last term is related to the compliant porosity. Note that in our case the pressure is the axial stress and not the hydrostatic pressure. From Fig. 6 it seems that the behaviour of the samples can be split into two groups: for the first group corresponding to samples with higher water saturation values (100, 95 and 87.6 per cent, meaning samples CME21, CME22, and CME23) the electrical conductivity decreases during the compaction phase before increasing at higher stress values, for the second group corresponding to lower water saturation values (85 and 80 per cent, meaning CME13 and CME32) the electrical conductivity increases from the beginning of the compression, the sample CME24 may be not comparable because of its different initial mechanical behaviour (Fig. 7).

In our case we should consider Archie's law in unsaturated conditions (see above). The induced relative variation of the rock conductivity is given by:

$$\frac{\delta\sigma_r}{\sigma_r} = \frac{\delta\sigma_f}{\sigma_f} + m\frac{\delta\Phi}{\Phi} + n\frac{\delta S_w}{S_w}$$

Water conductivity σ_f being constant, the first term is equal to zero. We can, therefore, see that two competing effects are present in non-saturated and undrained conditions: the relative variations of porosity Φ and saturation S_w during compression.

At low stress, when the rock volume is decreasing and pores or subhorizontal cracks are closing, the saturation is increasing since the water volume is constant. The water is expelled from closing cracks and distributed in the still open porous network. At this stage, the porosity decreases (the second term is negative) and the saturation increases (the last term is positive). The result of these competing effects depends on the initial saturation: a small decrease or almost constant axial and horizontal conductivity is observed for the first group of samples (higher water saturation), a small increase is observed for the second group (lower water saturation) (Figs 4 and 6).

When stress is further increased the electrical conductivity of partially saturated rocks increases, both in axial and horizontal directions. This increase occurs earlier during the compression process when the initial water saturation is lower (Figs 4 and 6). During dilatancy the porosity increases and the saturation decreases, so that the two terms in the equation of the conductivity variation are still in competition. The result of these competing effects shows that the connected path of water is eventually enhanced, both in the axial and horizontal directions (Fig. 6).

We finally plot the logarithm of the rock conductivity versus the axial stress (Fig. 8) in order to quantify the effect of stress on the

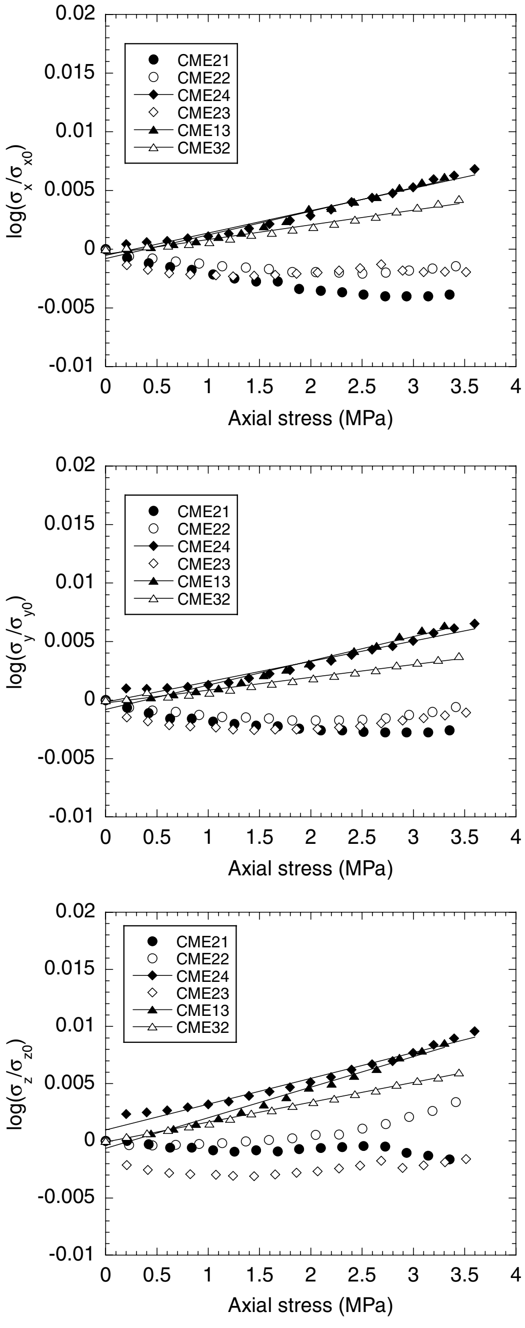

Figure 8. Logarithm of the rock conductivity versus axial stress for the six studied samples.

evolution of rock conductivity in a similar way as that followed by Kaselow & Shapiro (2004). This analysis is done before the dilatancy onset at about 3.5 MPa (Fig. 7) to only take into account the initial crack population.

For highly saturated samples CME21 (100 per cent) and CME22 (95 per cent) the variation of the logarithm of the conductivity is not a straight line, neither for CME23 sample. On the contrary, for lower saturation, that is for samples CME32 (80 per cent), CME13 (85 per cent) and CME24 (91 per cent), a linear relationship exists in the axial (z) direction between the logarithm of the rock conductivity and stress with a slope of 0.0017, 0.0027 and 0.0023 MPa^{-1}, respectively, confirming that there is no clear relation between the amplitude of electric conductivity variation during compression and the initial water saturation value, at least in the studied range. In the horizontal directions, the slopes are 0.0011, 0.002, 0.0017 (in y direction), and 0.0013, 0.002 and 0.0019 (in x direction) for samples CME32, CME13 and CME24, respectively. The slope is, therefore, about 35 per cent larger in axial direction than in the horizontal directions, which is consistent with the fact that cracks are created in the axial direction. Moreover, note that in undrained and non-saturated conditions, the linear relationship observed between log σ_{r} and stress means that the relative increase in the electrical conductivity is larger as one goes along the compression.

Evolution of the anisotropy of electrical conductivity during compression

The plots of the electrical conductivity anisotropy (Fig. 4) show that there is no anisotropy in the radial plane. The anisotropy between axial and radial directions is larger, about 1 to 4 per cent, because during compression new cracks are created in the axial direction. We note that there is usually a continuous small increase in the anisotropy between axial and radial directions during the compression test, except the transient decrease in sample CME21. It results that the anisotropy between axial and radial directions is about 0.5–2 per cent just before failure. At failure a drastic increase of this anisotropy can be seen, up to 5–6 per cent (CME21, CME24 and CME13 samples).

CONCLUSION

When the rock is fully saturated the electrical conductivity first decreases, and then increases during the uniaxial compression test. Although our experiments are performed on highly porous sedimentary rocks, the magnitude of the rock conductivity variation is of the same order, meaning 1–4 per cent, as the one measured usually on granite or sandstone, and most of the time under triaxial deformation. We show that when saturation is decreased the conductivity increase occurs earlier in the compression process, from 68 to 17 per cent of strength for 100 to 80 per cent of water saturation, respectively. Therefore, the decrease in conductivity at low stress is less and less present. Continuous increase of electrical conductivity due to compression is measured as soon as the saturation is decreased to 85 per cent. For low saturation levels such as 80–85 per cent, the compression phase leads to an increase in axial conductivity, roughly following a power-law $\sigma_r \sim 10^{0.002P}$, where P is the axial stress in MPa. It is usually suggested to interpret the field observations of pre-seismic change in crustal resistivity in the light of laboratory measurements performed in saturated conditions. Although an upscaling of laboratory measurements to *in situ* measurements is not simple, we suggest that *a continuous increase* of electrical conductivity due to compression should be probably expected as soon as the rocks are not fully saturated. These non-saturated conditions are more representative of the shallow crust. However at the scale of the sample the electrical conductivity increase is only about 1–4 per cent. Moreover a drastic increase in the anisotropy of electrical conductivity at fracture could be expected, and at the scale of the sample the anisotropy between axial and radial directions can be observed up to 5–6 per cent at rupture.

ACKNOWLEDGMENTS

This work was supported by CNRS-INSU-PNRN Risques Sismiques and GdR Géomécanique des roches profondes. We thank G. Nover and an anonymous referee for their constructive comments.

REFERENCES

Archie, G.E., 1942. The electrical resistivity log as an aid in determiningsome reservoir characteristics, *Trans. Am. Inst. Min. Meta. & Petrol.. Eng.,* **146,** 54–67.

Ashby, M.F. & Sammis, C.G., 1990. The damage mechanics of brittle solidsin compression, *Pure appl. Geophys.,* **133,** 489–521.

Bernabé, Y., 1986. Pore volume and transport properties changes duringpressure cycling of several crystalline rocks, *Mech. Mater.,* **5,** 235–249.

Bernabé, Y., 1995. The transport properties of networks of cracks and pores, *J. geophys. Res.,* **100,** 4231–4241.

Brace, W.F., 1975. Dilatancy-related electrical resistivity changes in rocks, *Pure appl. Geophys.,* **113,** 207–217.

Brace, W.F., 1980. Permeability of crystalline and argillaceaous rocks, *Inter. J. Rock Mech. Min. Sci. Geomech. Abst.,* **17,** 241–251.

Brace, W.F. & Orange, A.S., 1968. Electrical resistivity changes in saturated rocks during frature and frictional sliding, *J. geophys. Res.,* **73,** 1433–1445.

Brace, W.F., Paulding, B.W. & Scholz, C., 1966. Dilatancy in the fracture of crystalline rocks, *J. geophys. Res.,* **71,** 3939–3953.

Brovelli, A., Cassiani, G., Dalla, E., Bergamini, F., Pitea, D. & Binley, A.M., 2005. Electrical properties of partially saturated sandstones: novel computational approach with hydrogeophysical applications, *Water Resour. Res.,* **41,** W08411, doi:10.1029/2004WR003628.

Cornet, F.H., Doan, M.L. & Fontbonne, F., 2003. Electrical imaging and hydraulic testing for a complete stress determination, *Int. J. Rock Mech. Min. Sci.,* **40,** 1225–1241,.

David, C., Darot, M. & Jeanette, D., 1993. Pore structures and transportproperties of sandstone, *Transp. Porous Media,* **11,** 161–177.

David, C., Menendez, B. & Darot, M., 1999. Influence of stress-inducedand thermal cracking on physical properties and microstructure of La Peyratte granite, *Int. J. Rock Mech. Min. Sci.,* **36,** 433–448.

Eberhart-Philipps, D., Stanley, W.D., Rodriguez, B.D. & Lutter, W.L., 1995. Surface seismic and electrical methods to detect fluids related to faulting, *J. geophys. Res.,* **100,** 12 919–12 936.

Focke, J.W. & Munn, D., 1985. Cementation exponents in Middle Easterncarbonate reservoirs, presented at Middle Eastern Oil Show, Bahrain, Soc; Pet. Eng., *Pap. SPE 13735,* 431–442.

Fonseka, G.M., Murell, S.A.F. & Barnes, P., 1985. Scanning electron microscope and acoustic emission studies of crack development in rocks, *Int. J. Rock Mech. Min. Sci. & Geomech. Abstr.,* **22,** 273–289.

Glover, P.W.J., Gomez, J.B., Meredith, P.G., Boon, S.A., Sammonds, P.R. & Murrel, S.A.F., 1996. Modelling the stress-strain behavior of saturatedrocks undergoing triaxial deformation using complex electrical conductivitymeasurements, *Surv. Geophys.,* **17,** 307–330.

Glover, P.W.J., Gomez, J.B., Meredith, P.G., Hayashi, K., Sammonds, P.R. & Murrel, S.A.F., 1997. Damage of saturated rocks undergoing triaxial deformation using complex electrical conductivity measurements:experimental results, *Phys. Chem. Earth,* **22,** 57–61.

Glover, P.W.J., Gomez, J.B. & Meredith, P.G., 2000. Fracturing in saturated rocks undergoing triaxial deformation using complex electrical conductivity measurements: Experimental study, *Earth planet. Sci. Lett.,* **183,** 201–213.

Guichet, X., Jouniaux, L. & Pozzi, J.P., 2003. Streaming potential of as and column in partial saturations conditions, *J. geophys. Res.,* **108,** 2141, doi:10.1029/2001JB001517.

Henry, P., Jouniaux, L., Screaton, E.J., Hunze, S. & Saffer, D.M., 2003. Anisotropy of electrical conductivity record of initial strain at the toe ofthe Nankai accretionary wedge, *J. geophys. Res.,* **108,** 2407, doi:10.1029/2002JB002287.

Hyndman, R.D. & Hyndman, D.W., 1968. Water saturation and high electricalconductivity in the lower continental crust, *Earth planet. Sci. Lett.,* **4,** 427–432.

Hyndman, R.D. & Shearer, P.M., 1989. Water in the lower continental crust: modelling magnetotelluric and seismic reflection results, *Geophys. J. Int.,* **98,** 343–365.

Jouniaux, L., Pozzi, J.P., Brochot, M. & Philippe, C., 1992. Resistivity changes induced by triaxial compression in saturated sandstones from Fontainebleau (France), *C. R. Acad. Sci. Paris,* **315,** Série II, p. 1493–1499.

Jouniaux, L., Lallemant, S. & Pozzi, J.P., 1994. Changes in the permeability, streaming potential and resistivity of a claystone from theNankai prism under stress, *Geophys. Res. Lett.,* **21,** 149–152.

Jouniaux, L., Dubet, L., Zamora, M. & Morat P., 1996. Physical properties of limestone from the quarry of Mériel, *C. R. Acad. Sci. Paris,* **322,** série IIa, 361–367.

Jouniaux, L., Pozzi, J.P., Berthier, J. & Massé, P., 1999. Detectionof fluid flow variations at the Nankai Trough by electric and magnetic measurements in boreholes or at the seafloor, *J. geophys. Res.,* **104,** 29 293–29 309.

Kaselow, A. & Shapiro, S.A., 2004. Stress sensitivity of elastic moduli and electrical resistivity in porous rocks, *J. Geophys. Eng.,* **1,** 1–11.

Knight, R. & Dvorkin, J., 1992. Seismic and electrical properties of sandstones at low saturations, *J. geophys. Res.,* **97,** 17 425–17 432.

Knight, R. & Endres, A., 1990. A new concept in modeling the dielectricresponse of sandstones: defining a wetted rock and bulk water system, *Geophysics,* **55,** 586–594.

Le Pennec, J.-L. *et al.*, 2001. Electrical conductivity and pore-space topology of Merapi lavas: implications for the degassing of porphyritic andesite magmas, *Geophys. Res. Lett.,* **28,** 4283–4286.

Lockner, D.A. & Byerlee, J.D., 1986. Changes in complex resistivity during creep in granite, *Pure appl. Geophys.,* **124,** 659–676.

Marquis, G. & Hyndman, R.D., 1992. Geophysical support for aqueous fluids in the deep crust: seismic and electrical relationships, *Geophys. J. Int.,* **110,** 91–105.

Morat, P. & Le Mouël, J.L., 1992. Signaux électrique sengendrés par des variations de contrainte dans des roches poreuses nonsaturées, *C. R. Acad. Sci. Paris,* **315,** Série II, 955–963.

Morat, P., Le Mouël, J.L., Nover, G. & Will, G., 1992. Variation annuelle de la saturation d'une roche de grande porosité induite par la variation saisonnière de la température extérieure et mesurée par voie électrique, *C. R. Acad. Sci. Paris,* **315,** Série II, 1083–1092.

Nesbitt, B.E., 1993. Electrical resistivities of crustal fluids, *J. geophys. Res.,* **98,** 4301–4310.

Nover, G., Heikamp, S. & Freund, D., 2000. Electrical Impedance Spectroscopy used as a tool for the detection of fractures in rock samples exposed to either hydrostatic or triaxial pressure conditions, *Nat. Hazards,* **21,** 317–330.

Olhoeft, G.R., 1981. Electrical properties of granite with implications forthe lower crust, *J. geophys. Res.,* **86,** 931–936.

Parkhomenko, E.I. & Bondarenko, A.T., 1960. Effect of unilateral pressure on electrical resistance of rocks, Bull. Acad. Sci. USSR, *Geophysics Ser.,* **2,** 214–219 (English version).

Pezard, P., 1990. Electrical properties of Mid-Ocean ridge basalt and implications for the structure of the upper oceanic crust in Hole 504B, *J. geophys. Res.,* **95,** 9237–9264.

Scholz, C.H., Sykes, L.R. & Aggarwal, Y.P., 1973. Earthquake prediction: a physical basis, *Science,* **181,** 803–810.

Sen, P.N., Kenyon, W.E., Takezaki, H. & Petricola, M.J., 1997. Formation factor of carbonate rocks with microporosity: model calculations, *J. Petroleum Science and Engineering,* **17,** 345–352.

Takano, M., Yamada, I. & Fukao, Y., 1993. Anomalous electrical, resistivity of almost dry marble and granite under axial compression, *J. Phys. Earth,* **41,** 337–346.

Tapponier, P. & Brace, W.F., 1976. Development of stress-Inducedmicrocracks in Westerly granite, *Int. J. Rock Mech. Min. Sci. Geomech. Abstr.,* **13,** 103–112.

Thouret, L.R. & Marquis, G., 1994. Deep fluids and electrical conductivity of the lower continental crust, *C.R. Acad. Sci. Paris,* **318,** Ser. II, 1469–1482.

Waxman, M.H. & Smits, L.J.M., 1968. Electrical conductivities in oil-bearing shaly sands, *Trans. AMIE,* **243,** 107–122.

Wong, T.-f., 1982. Micromechanics of faulting in Westerly granite, *Int. J. Rock Mech. Min. Sci. Geomech. Abstr.,* **19,** 49–64.

Yamazaki, Y., 1965. Electrical conductivity of strained rocks, laboratory experiments on sedimentary rocks, *Bull. Earthquake Research Institute,* **43,** 783–802.

Yamazaki, Y., 1966. Electrical conductivity of strained rocks, further experiments on sedimentary rocks, *Bull. Earthquake Research Institute,* **44,** 1553–1570.

PERGAMON

Journal of Structural Geology 26 (2004) 247–258

JOURNAL OF STRUCTURAL GEOLOGY

www.elsevier.com/locate/jsg

Detailed analysis of acoustic emission activity during catastrophic fracture of faults in rock

Xinglin Lei[a,b,*], Koji Masuda[a], Osamu Nishizawa[c], Laurence Jouniaux[d], Liqiang Liu[b], Wentao Ma[b], Takashi Satoh[a], Kinichiro Kusunose[c]

[a]*Institute of Geoscience, GSJ/National Institute of Advanced Industrial Science and Technology (AIST), Higashi 1-1-1, Tsukuba, Ibaraki 305-8567, Japan*
[b]*Institute of Geology & Laboratory of Tectonophysics, China Seismological Bureau, Beijing, China*
[c]*Institute of Geo-Resource and Environment, GSJ/National Institute of Advanced Industrial Science and Technology (AIST), Higashi 1-1-1, Tsukuba, Ibaraki 305-8567, Japan*
[d]*Laboratoire de Geologie, Ecole Normale Superieure, France*

Abstract

The detailed time-space distribution of acoustic emission (AE) events during the catastrophic fracture of rock samples containing a pre-existing joint or potential fracture plane is obtained under triaxial compression using a high-speed 32-channel waveform recording system, and the results are discussed with respect to the prediction and characterization of catastrophic fault failure. AE activity is modeled quantitatively in terms of the seismic *b*-value of the magnitude–frequency relation, the self-excitation strength of the AE time series, and the fractal dimension of AE hypocenters. Consistent with previous studies on rock samples containing a fracture plane with several asperities, the present analyses reveal three long-term phases of AE activity associated with damage creation on heterogeneous faults, each clearly identifiable based on the above parameters. A long-term decreasing trend and short-term fluctuation of the *b*-value in the phase immediately preceding dynamic fracture are identified as characteristic features of the failure of heterogeneous faults. Based on the experimental results it is suggested that precursory anomalies related to earthquakes and other events associated with rock failure are strongly dependent on the heterogeneity of the fault or rock mass. A homogeneous fault or rock mass appears to fracture unpredictably without a consistent trend in precursory statistics, while inhomogeneous faults fracture with clear precursors related to the nature of the heterogeneity.

Keywords: Rock sample; Acoustic emission; Microcracking; Fault nucleation

1. Introduction

The study of damage formation in jointed or bulk rock under stress is a subject of widespread interest, with relevance to both artificial applications such as optimization of geothermal recovery, oil recovery, safe design of nuclear waste repositories, and rock bursts, and natural processes such as volcanism and seismology. For many reasons, it is important to be able to predict the time, location and intensity of potential rock fracture. Fracture development in stressed rock has been observed extensively in the laboratory by a number of methods. One approach is the direct observation of samples by scanning electron microscopy (SEM) (e.g. Zhao, 1998) or optical microscopy (e.g. Cox and Scholz, 1988). Another method involves monitoring the hypocenter distribution of acoustic emission (AE) events caused by microcracking activity (e.g. Lockner et al., 1991; Lei et al., 1992, 2000c). Direct observation is a useful technique for both brittle and ductile deformation, but is limited in that only the surface of the test specimen can be observed. In contrast, AE techniques provide an analysis of the microcracking activity inside the rock volume, but are insensitive to ductile deformation, which does produce appreciable AE activity. However, AE techniques have an important advantage over other techniques in that tests can be performed under confining pressure, which is very important in the simulation of underground conditions.

The recent development of high-speed multi-channel waveform recording technology has made it possible to monitor the hypocenters of AEs associated with spontaneously/unstably fracturing processes in stressed rock samples with high precision. Such a system is capable of recording AE waveforms in 32 channels at sampling rates of

---

[*] Corresponding author. Correspondence address: Institute of Geoscience, GSJ/National Institute of Advanced Industrial Science and Technology (AIST), Higashi 1-1-1, Tsukuba, Ibaraki 305-8567, Japan. Tel. +81-298-61-2468; fax: +81-298-61-3697.

E-mail address: xinglin-lei@aist.go.jp (X. Lei).

0191-8141/03/$ - see front matter © 2003 Elsevier Ltd. All rights reserved.
doi:10.1016/S0191-8141(03)00095-6

up to 5000 events per second, and have been successfully used to study the quasi-static nucleation of intact brittle rocks based on detailed AE data. The present authors applied this technique to the analysis of hornblende schist (Lei et al., 2000c) and granitic rocks (Lei et al., 2000a), and later to study of the fracture of mudstone containing quartz veins, which play a role as strong asperities (Lei et al., 2000b). More recently, the present authors observed that the microcracking activity associated with the fracture of an inhomogeneous fault proceeds in three stages with a spatial hierarchical structure (Lei et al., 2003).

The present report presents the experimental results for four samples with a naturally healed macroscopic joint and widely differing healing strength and asperity distributions. High-speed waveform recording technology was employed to monitor the detailed time–space distribution of AE activity during the catastrophic fracture of the four rock samples under triaxial compression. This report focuses on the experimental facts related to the temporal change of some quantitative statistics of AE activity, including the event rate, seismic *b*-value, self-excitation strength and fractal dimension of the hypocenter distribution.

2. Experiments and data analyses

2.1. Samples and experiments

Four samples having a macroscopic joint or potential fracture plane were prepared to simulate four kinds of faults of widely differing healing strength or asperity distribution. As all samples fractured along this pre-existing joint or potential fracture plane, the general term ‘fault’ is used to refer to that feature in this paper. For convenience, these samples are labeled SF (strong fault with homogeneous healing strength distribution), HF (fault with heterogeneous healing strength distribution), AF (fault with weak segments and strong asperities), and WF (weak fault with homogeneous strength distribution). The terms ‘strong’ and ‘weak’ are based on the fracture strength of the sample. As there is no way to know the detailed distribution of healing strength on the fault plane, the terms ‘homogeneous’ and ‘heterogeneous’ are mainly given in terms of optical microscope and naked eye observations, and as such are qualitative descriptions.

The host rock for the SF sample is a granitic porphyry, and is almost entirely free of microcracking (see Lei et al. (2000a) for reference). The main rock-forming minerals are quartz, plagioclase, and K-feldspar, with a grain size distribution of ~1 mm to ~1 cm (peak ~5 mm). As illustrated in Fig. 1a, no visible cracks can be seen by microscope observation along the fault in the SF sample. Therefore, the SF sample represents a strongly healed fault in a coarse-grained granitic porphyry.

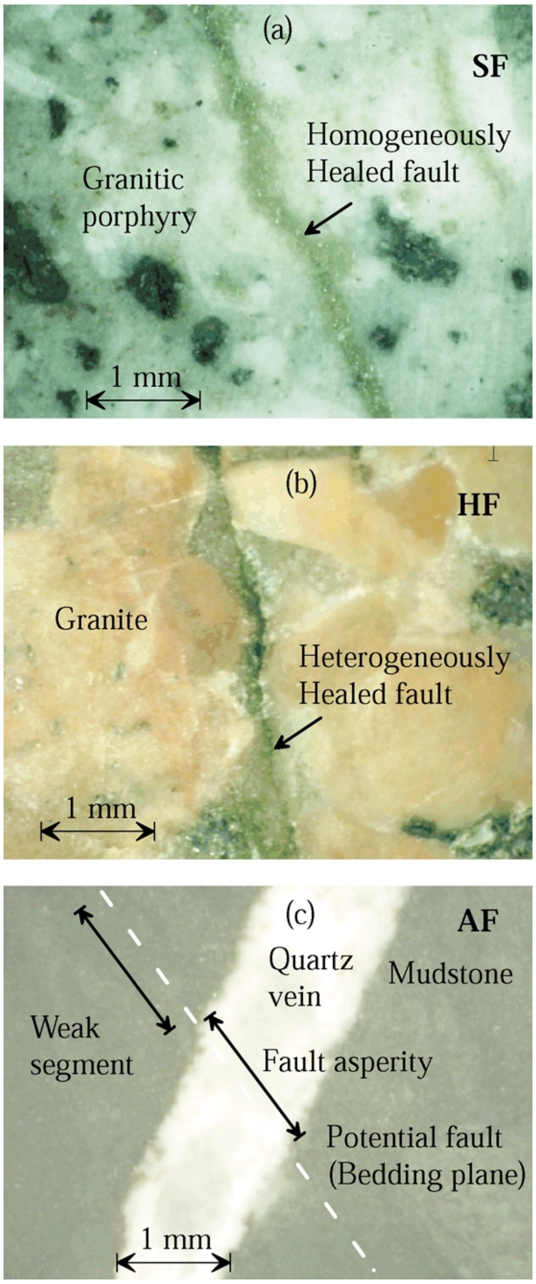

Fig. 1. Photomicrographs showing pre-existing or potential faults in the (a) SF, (b) HF and (c) AF samples.

The HF sample is a coarse-grained granite containing quartz, K-feldspar, biotite and muscovite hornblende (Jouniaux et al., 2001). This sample has a significantly higher density of pre-existing microcracks than the SF sample. In addition, there are also some heterogeneously distributed cracks along the fault plane, as shown in Fig. 1b. Thus, the HF sample models a heterogeneously healed fault in coarse-grained granite.

The WF sample is a mudstone with well-oriented planar structure. The final fracture plane was created along the bedding plane of the mudstone, at an angle of ~25° to the maximum stress axis of the sample. Since the bedding plane makes this sample significantly weaker than the SF and HF samples, the WF sample models a homogeneous weak fault that may undergo ductile deformation under confining pressure.

The AF sample is similar to the WF sample but contains quartz veins at an angle of ~70° to the fracture plane (Fig. 1c). The quartz veins are either 1 or 3 mm thick, but are much stronger than the surrounding mudstone. Accordingly, the AF sample is a model of a weak fault with a few strong asperities or barriers.

All samples used in this study contain a potential fault oriented at an angle of 25 ~ 30° to the maximum stress direction. These potential faults were ruptured during triaxial compressive test, giving four typical models of shear faults with widely differing strength distributions.

All samples were obtained as cylinders of 100 mm in length and 50 mm in diameter. The aspect ratio of these samples (2:1) is smaller than the usual 2.5:1 used in many experiments. All samples were dried under normal room conditions for more than one month and then compressed under a constant stress-rate (0.04 ~ 0.1 MPa/s) loading and constant confining pressure of 60 MPa (40 MPa for the HF sample) at room temperature (~25 °C).

Friction between the sample ends and the end-pieces plays a role in constraining horizontal deformation around the ends of the samples. The end effects under these conditions for fine-grained samples are generally more important than for coarse-grained samples because the latter exhibit appreciable dilatancy prior to failure (Lei et al., 1992). In this study, the test samples contain a potential fault, which is weaker than the host rocks. Therefore, as the dilatancy in these host rocks will be several times smaller than in the case of homogeneous intact rock, end effects are not considered to be a serious problem in this study.

A total of 32 piezoelectric transducers (PZT) (5 mm in diameter, resonant frequency of 2 MHz) were mounted on the surface of each test sample and the two end caps to detect AE signal from microcracking events. A series of eight cross-type strain gauges (16 channels) were mounted on the surface of the test samples to measure local axial and circumferential strains. The local volumetric strain (ε_v) was calculated from the axial (ε_a) and circumferential (ε_c) strains according to the equation $\varepsilon_v = \varepsilon_a + 2\varepsilon_c$. The strain gauges were located on both the pre-existing fault and the host rock, and the 16 channels were sampled with a dynamic range of 16 bits and a maximum sampling frequency of 1 kHz.

As introduced by Lei et al. (2000c), the high-speed waveform recording system used in this study records the maximum amplitudes (dynamic range of 100 dB) in two channels and waveforms (sampling rate of 20 MHz, 12-bit resolution) in 32 channels. The waveform recorder has a discrete A/D converter and 16 MB memory buffers for each channel. The sampling length is set to 1024 words (50 μs) for each event, corresponding to a total waveform recording capacity of 8192 events. The mask time (minimum trigger interval) for waveform recording was ~200 μs, which is sufficient for recording the full tail of typical detectable AE signals (generally about 50–200 μs in length), ensuring no major event loss. The system records 32 (channels) × 2048 (sampling length in bytes) × 5000 (1/mask-time) bytes (total 33 MB) of waveform data per second in FIFO (first-in first-out) mode.

The waveform data was transferred and stored on a personal computer so as to free up memory for subsequent recordings without influencing the waveform recording process, providing virtually unlimited recording capacity. As the transfer of data from the waveform recorder to the computer including hypocenter determination and disk access, took about 0.3 s for each event, real-time hypocenter monitoring was possible only when the AE rate was lower than 3 events/s. At higher rates, the hypocenters were determined with a time delay dependent on the amount of data accumulated in the memory of the waveform recorder.

The velocities along multiple paths were measured using an 18-channel fast-switching system to switch the selected sensor from receiver to detonator and connect the sensor to a pulse generator. Switching all 18 selected sensors one by one took about 1 s. After the experiment, the data obtained using this system allowed the precise velocity structure in the test sample to be reconstructed at each measuring time by travel–time tomography.

Since there is no major loss of AE events even for an event rate of the order of several thousand events per second, it is possible to map out the spontaneous acceleration from quasi-static to dynamic rupture of a fault under constant stress (creep) or constant stress-rate loading conditions by monitoring the detailed spatio-temporal distribution of AE events. This is a more advanced way to study the non-linear faulting process than the method employed in previous studies, which involved stabilization of the failure process through control of the axial stress in order to maintain a low constant rate of AE occurrence (e.g. Lockner et al., 1991). Although constant strain-rate loading has been used in many experimental studies, constant stress loading is also a meaningful loading method for simulating the tectonic forces and conditions in many artificial applications such as tunnels and mines.

2.2. Preliminary data analysis

The main data used in this study includes (1) event rates calculated from the maximum amplitude data, (2) seismic *b*-values for the magnitude–frequency relationship as calculated from the maximum amplitude data, (3) hypocenters determined using the first arrival times at the 32 receivers, (4) the fractal dimension of the hypocenter distribution, and (5) the self-excitation strength for AE occurrence. As a trigger threshold higher than the maximum amplitude recording was employed for waveform recording, the hypocenter data is a subset of the maximum amplitude data. The maximum amplitudes are used to calculate a relative magnitude that is comparable with seismic magnitude for small earthquakes. The noise level after pre-amplification with a gain of 20 dB was less than 45 dB, providing an effective dynamic range of more than 55 dB, which corresponds to a relative magnitude range of about 2.75. The b-values are calculated from the relative magnitude data using the maximum likelihood method (Aki, 1965; Utsu, 1965) for a running window of 500 events and a step of 125 events. The standard error is estimated to be between 0.03 and 0.08 for a b-value between 0.5 and 1.5. The path attenuation, which is not considered in the calculation of b-values, appears to have no statistically significant effect on the b-values, and the maximum amplitude data recorded by two sensors mounted at opposite positions on the cylinder surface of the sample give similar results. Hypocenters were re-determined after each test using the measured P velocity during the test. The location error is estimated to be less than 2 ~ 3 mm for most events (Lei et al., 1992), as estimated directly from AE hypocenters in the AF sample.

2.3. Fractal analysis

A two-point correlation integral was applied to examine the spatial clustering of the hypocenters of AE events. The two-point correlation is defined as follows (e.g. Hirata, 1987; Lei et al., 1992).

$$C(r) = \frac{2N_r(R < r)}{N(N-1)} \tag{1}$$

where $N_r(R < r)$ is the number of hypocenter pairs separated by less than r, and N is the total number of AE events analyzed. If the hypocenter distribution is self-similar, $C(r)$ is proportional to r^D, where D is the fractal dimension determined by a least-squares fit of a log–log plot. If a set of hypocenters in a three-dimensional volume is fractal, the fractal dimension will be between 0 and 3.0. Here, $D = 0$ indicates that all hypocenters fall within a discrete volume, while $D = 3.0$ represents the distribution of hypocenters throughout the volume without areas of concentration. Smaller values therefore reflect higher degrees of clustering, and a value itself can represent many patterns of distribution. For example, $D = 2.0$ may represent both a planar distribution and a volumetric distribution with clustering. Similarly, $D = 1.0$ may represent a linear distribution or a volumetric distribution with strong clustering. Hence, the D value must be considered with respect to the general nature of the hypocenter distribution.

2.4. Self-excitation model of AE occurrence

It has been found that AE events do not occur randomly, but rather have a time-dependent probability distribution (Nishizawa and Noro, 1990; Lei et al., 2000c). Lei et al. (2000c) observed that in most cases, the following conditional function models the instantaneous probability of AE occurrence in a short interval:

$$\lambda(t) = \mu_0 + p_1 t + \sum_{t_i < t} g(t - t_i) \tag{2}$$

$$g(t) = a_0 e^{-\beta t} \tag{3}$$

where μ_0 is a constant expressing the stationary Poisson process, $p_1 t$ is the trend component, t_i is the timing of the ith event, and $g(t)$ is the impulse response function used to express the effect of excitation of the preceding event on succeeding events. Integrating the impulse function $g(t)$ gives

$$s = \int_0^\infty g(t)\mathrm{d}t = \int_0^\infty a_0 e^{-\beta t}\mathrm{d}t = \frac{a_0}{\beta} \tag{4}$$

which is a value expressing the strength of the effect of excitation associated with the preceding event on succeeding events, or equivalently, the degree of positive feedback in the dynamics. Following Lei et al. (2000c), this integral is called the self-excitation strength. The parameters in the model are determined based on maximum likelihood theory (see Lei et al. (2000c) for details).

3. Results

Fig. 2 shows the differential stress and cumulative number of AE events against the axial strain (shortness) observed near the fractured fault for all tests. The fracture strengths (maximum differential stress) for the SF, HF, AF, and WF samples were 720, 300, 280, and 150 MPa, respectively. The fault in the SF sample was strong, while that in the WF was weak, as expected. Accordingly, the SF sample fractured suddenly with only a small number of AE events prior to dynamic fracture followed by numerous

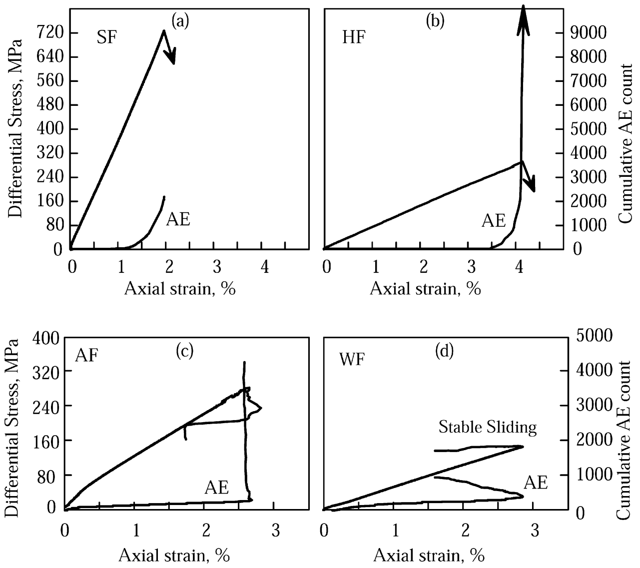

Fig. 2. Differential stress and cumulative AE counts plotted against local axial strain near the fault in the test samples. All samples were loaded at a constant stress rate. Notes that the axial strain is a local measurement.

aftershocks, representing typical brittle fracture behavior (Fig. 2a). The WF sample exhibited ductile rupture behavior with no remarkable AE activity (Fig. 2d). Samples HF and AF have an intermediate fracture strength between that of the SF and WF samples, and exhibited violent AE activity prior to dynamic rupture (Fig. 2b and c). As summarized in Table 1, the AE activity during the fracture process can be grouped into three typical long-term stages according to the time–space statistics of AE events: primary, secondary and nucleation. The term 'pre-nucleation' is also used to refer collectively to the primary and secondary phases. This progression of the fracture process is consistent with the results for an inhomogeneous fault having several mechanical/geometrical asperities presented in the authors' previous paper (Lei et al., 2003). However, new data in this study shows that the statistical characteristics of each stage vary according to the fault type. Event rates, *b*-values and other statistics differ significantly between these phases.

3.1. SF sample

Fig. 3 shows the temporal change in axial strain, differential stress, event rate, *b*-value and self-excitation strength of AEs in the SF sample. The AE activity prior to dynamic rupture is very low, initiating at a stress of ~60% of the peak stress (Fig. 3a). After initiation, the event rate increases slowly with time and stress (Fig. 3b). The *b*-value increases from ~0.75 to 1.0 with increasing stress (Fig. 3c). The secondary phase is characterized by a gradual increase in the event rate and slight decrease in the *b*-value with increasing stress (Fig. 3b and c). The nucleation phase is very short (a few seconds), with only a small number of foreshocks. After the dynamic fracturing, about 2500 aftershocks were observed, accompanied by a high *b*-value of ~1.2. In the primary phase, the self-excitation strength is weak (<0.2), but from the secondary phase to the nucleation phase, this value increases gradually to ~1.0 up to dynamic fracture (Fig. 3d).

Fig. 4 shows an X-ray computed tomography (CT) scan of the sample after the experiment, along with projected hypocenters on planes perpendicular and parallel to the fault plane. In the primary and secondary phases, the AE hypocenters are distributed throughout the sample volume without remarkable concentration, although some small clusters are apparent. As shown in Fig. 5a, the primary phase has two distinct fractal distributions, with a transition at around 8 mm, which is roughly equivalent to the dominant grain size. The clustering of microcracking therefore appears to be controlled by the spatial distribution of grain size. The long-range fractal dimension D_{l} (>8 mm) is 2.25, and therefore represents the distribution of clusters in the sample, and the short-range fractal dimension D_{s}

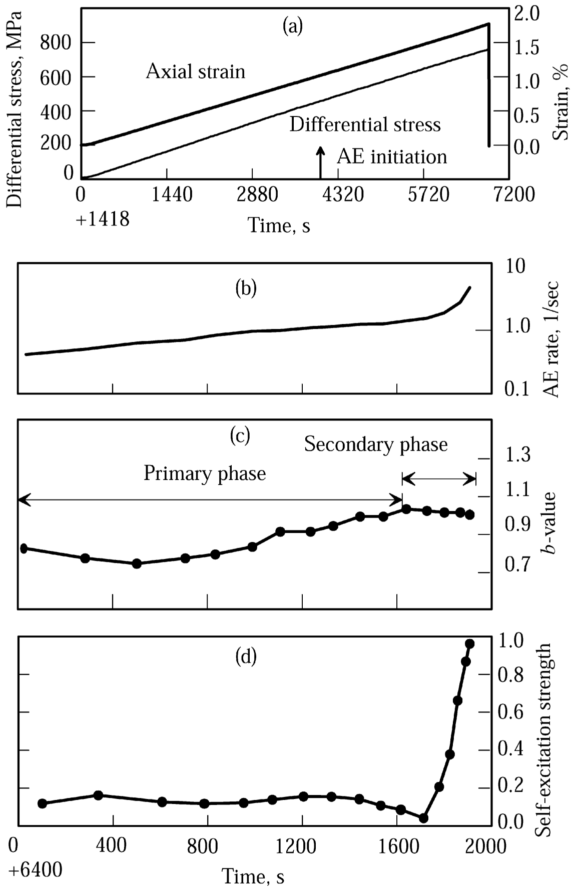

Fig. 3. Basic results for the SF sample: (a) differential stress and axial strain; (b) AE rate; (c) *b*-value; and (d) self-excitation strength after AE initiation. The error bars for the *b*-value are smaller than the symbols in this plot.

Table 1
Summary of the main experimental results

Sample	Fracture strength (MPa)	Statistics	Primary phase	Secondary phase	Nucleation phase
SF	720	AE count	~1,500	~540	~200
		b-value	0.8 → 1.05	1.05 → 1.0	
		D	2.25/1.06	1.87	
HF	300	AE count	~500	~1200	~58,000
		b-value	1.1 → 1.3	1.3 → 1.0	1.0 → 0.5
		D	2.00	1.60	1.25/2.25
AF	280	AE count			~4200
		b-value			1.2 → 0.6
		D			1.0
WF	150				

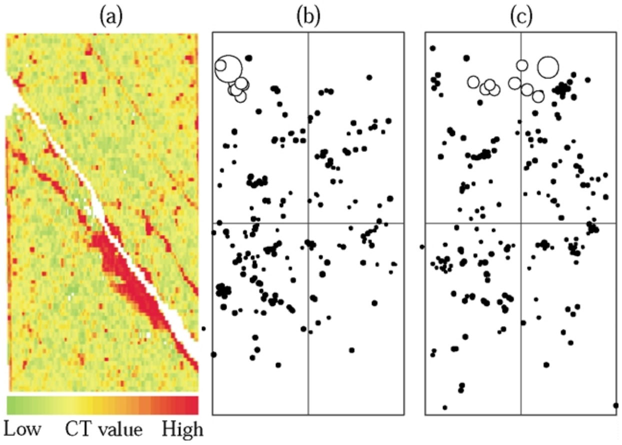

Fig. 4. (a) X-ray CT scan image for the SF sample (the CT value reflects the density of the material matrix). (b) and (c) The AE hypocenters in the SF sample projected to a plane (b) perpendicular and (c) parallel to the rupture plane. Solid circles indicate the events in the pre-nucleation phases; open circles (shown twice as large for clarity) indicate the foreshocks in the nucleation phase.

(<8 mm) is 1.06, reflecting the distribution of hypocenters inside the clusters. This result indicates that the typical size of clusters in the primary phase is about 8 mm. In the secondary phase, D_l decreases to 1.87 while D_s increases to 1.87 (Fig. 5b). Since the nucleation phase included only a few events, it is impossible to calculate the fractal dimension for that phase. However, it can be seen that the foreshocks in the nucleation phase are concentrated at the initiation site on the fault plane (empty circles in Fig. 4b and c). The last (and largest) event produced a very strong waveform, and most likely represents the beginning of dynamic fracture along the pre-existing fault.

3.2. HF sample

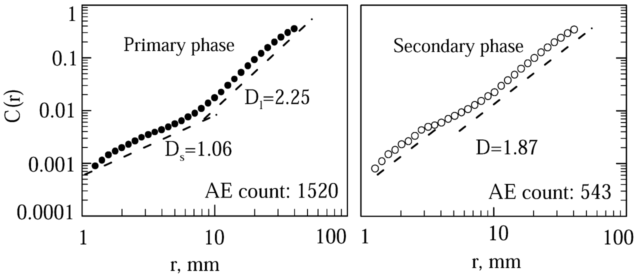

Fig. 5. Correlation integral function for hypocenters in the SF sample against distance using logarithmic coordinates. The fractal dimensions estimated from the slope are also shown.

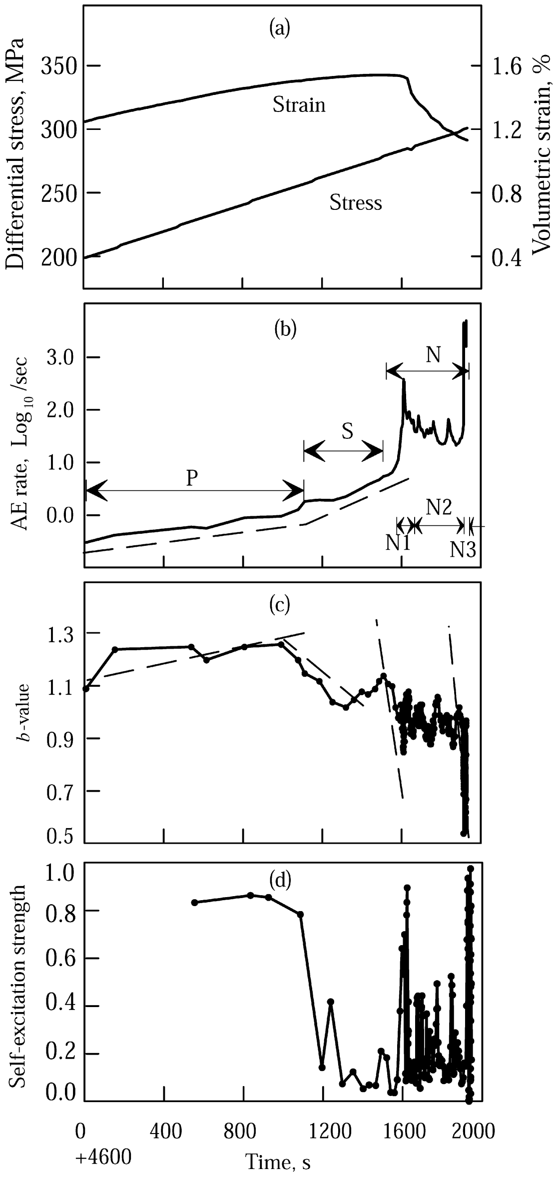

Fig. 6. Basic results for the HF sample: (a) axial stress and volumetric strain against time. Volumetric strain is calculated from the axial and circumferential strains recorded using a cross-type strain gauge near the fracture plane and as such is a local value; (b) logarithmic AE rate against time; (c) *b*-value against time; and (d) self-excitation strength against time. P, S, and N indicate the primary, secondary, and nucleation phases, and the nucleation phase is further divided into sub-phases N1, N2, and N3.

Fig. 6 shows the results for the HF sample. This sample clearly demonstrates the three stages of the fracturing process. Fig. 7 is a magnified view of the final 20 s (N3 in Fig. 6b). Large numbers of AE events occurred in all three phases, providing a clear picture of the process. In the primary phase, AE activity initiates at a stress of ~65% of the peak stress, and the event rate increases gradually with time and stress (Fig. 6b). The *b*-value increases slightly from 1.1 to 1.3, with an average of 1.2 (Fig. 6c). In the secondary phase, the event rate increases with time and stress at a significantly larger slope than the primary phase. The *b*-value decreases with increasing stress from an initial value of ~1.3 to ~1.0 (Fig. 6c). In the nucleation phase, the event rate increases rapidly to 400 AEs/s (N1 in Fig. 6b), followed by a decrease to ~40 AEs/s and fluctuation for about 250 s (N2 in Fig. 6b). Finally, the AE rate increases suddenly to ~5000 AEs/s (N3 in Figs. 6b and 7a), while the *b*-value decreases from ~1.0 to the global minimum of ~0.5 with large fluctuations (Fig. 7b). This nucleation behavior appears to be associated with the particular

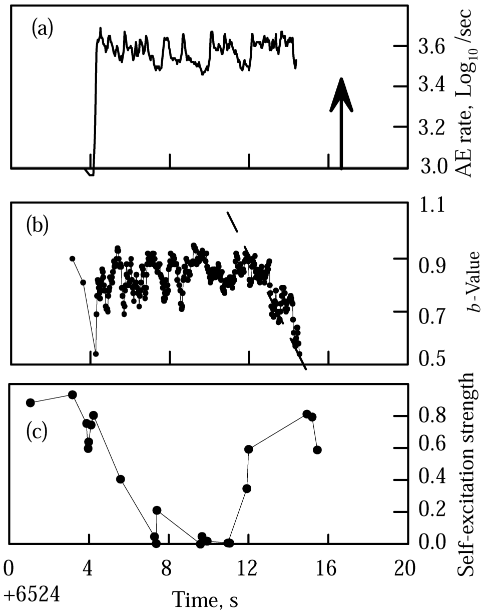

Fig. 7. Detailed view of: (a) the event rate, (b) *b*-value, and (c) self-excitation in the N3 phase shown in Fig. 6. Arrow in (a) indicates the onset of dynamic fracture.

structure of the fault. The fault has an extensional jog at its upper end (Fig. 8a). The first local maximum of the event rate in N1 in fact corresponds to the dense cluster of microcracking around the jog. After the fracture of the extensional jog, the accelerated faulting nucleation process is relaxed due to the sub-critical stress on other unfractured areas of the fault plane.

The average self-excitation strength in the primary phase is 0.8, while that in the secondary phase is less than 0.2, indicating that preceding events tend to trigger successive events in the primary phase, but not in the secondary phase. The nucleation phase is characterized by a highly variable self-excitation strength of 0.5 ~ 1.0. In the N1 (faulting initiation) and N3 (accelerated fault growth) regions in particular, the self-excitation strength reaches the maximum value of ~ 1.0 (Figs. 6d and 7c).

The most notable feature of the nucleation phase is the short-term contemporaneous fluctuations of the AE rate, *b*-value and self-excitation strength. A local minimum in the *b*-value corresponds to local maxima of both the AE rate and self-excitation strength. After viewing the results of all tests, it is clear that this kind of short-term fluctuation is related to the heterogeneous structure of the fault plane. This will be discussion later in more detail.

The hypocenter distribution in the three phases is shown in Fig. 8, along with a CT image of the sample after the experiment. The hypocenters in the primary phase are distributed throughout the sample volume, with some concentration on a small fault to the lower-left of the main fault (Fig. 8b). The fractal dimension is 2.0 (Fig. 9a), and the correlation integral function has a bend at ~ 10 mm, indicating a typical cluster size of ~ 10 mm, which again is equivalent to the predominant grain size of the sample. In the secondary phase, most AEs occur on the pre-existing fault plane (Fig. 8c), and the fractal dimension decreases to 1.6 (Fig. 9b). In the nucleation phase, the hypocenter distribution reveals several dense clusters on the fault plane (Fig. 8e). The long-range and short-range fractal dimension are $D_l = 1.0 \sim 1.38$ and $D_s = 2.25$ (Fig. 9c). These values, and the fact that D_s is much larger than D_l, indicate that clusters are limited to a few sites, but that microcracking events within each cluster fall on the fault plane. The typical cluster size changes between N1, N2 and N3, reflecting the progressive fracture of asperities of different size.

As the main fault ruptured down towards the lower end cap and not to the free surface, the end cap may have affected the nucleation process (N2 to N3). If this is the case, the end cap may have acted as a barrier for shear rupture. Therefore, the longer nucleation process observed for this

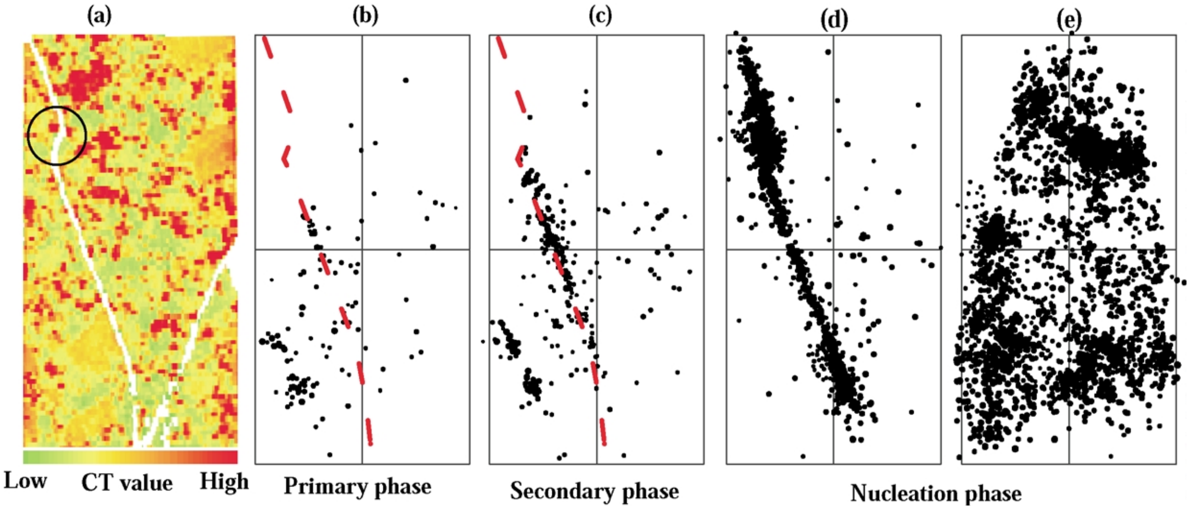

Fig. 8. (a) X-ray CT scan image of the HF sample after the experiment, taken perpendicular to the fault plane. (b)–(d) Plots of AE hypocenters projected onto a plane perpendicular to the fault plane for the (a) primary, (b) secondary and (c) nucleation phases. (e) AE hypocenters in the nucleation phases projected onto a plane parallel to the fault plane.

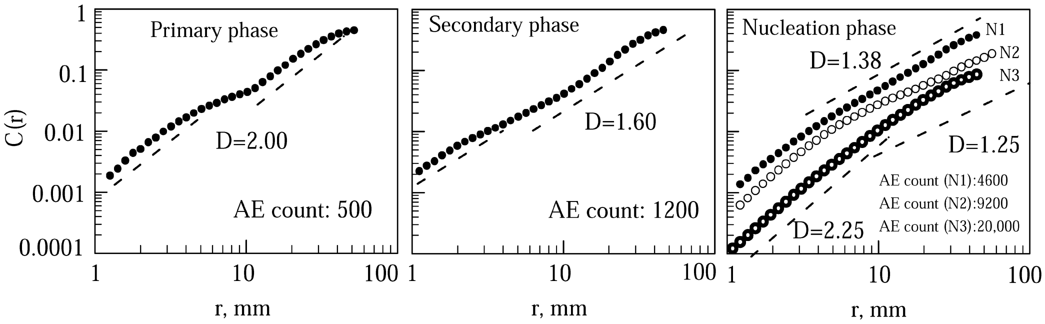

Fig. 9. Correlation integral function for the hypocenters in the HF sample against distance using logarithmic coordinates. The fractal dimensions estimated from the slope are also shown.

sample may be due in part to end effects. However, the progression of the nucleation phase, and fluctuation of the event rate and *b*-value would not be affected appreciably.

3.3. AF and WF samples

Four experiments have been conducted using samples similar to the AF sample, as detailed in previous work (Lei et al., 2000b). Here, the important common results are summarized, and some new analytical results are presented. Figs. 10–13 show the results for one of the AF samples. AEs initiate suddenly and increase rapidly near the peak stress. The *b*-value exhibits fluctuations on a decreasing trend from an initial value of 1.2 ~ 1.4 to a global minimum of 0.5 ~ 0.7 (Fig. 11). As indicated in Fig. 11a, the sample was manually unloaded at the onset of dynamic fracture in order to save the sample from excessive damage. The self-excitation strength before unloading is large (0.5 ~ 1.0). These features of AE activity are similar to the nucleation phase of the SF and HF samples, demonstrating that only the nucleation phase produces high AE activity in AF samples. The primary and secondary phases include only a few weak events, precluding meaningful statistical analysis.

The AE hypocenters are distributed at asperities (intersections of the quartz veins and the fracture plane) where large dilatancy was observed following the rapid increase of AE activity (v2 in Fig. 11a). The hypocenter distribution has a fractal dimension of ~1.0 (Fig. 14), which is consistent with the arrangement of asperities along a line of 1 or 3 mm in width on the fault plane. Hypocenters map out the asperities on the fault plane precisely, allowing a direct estimation of the location error to be made, in this case (<2 ~ 3 mm). Off-asperity segments of the fault exhibit ductile behavior with large compressive deformation but no remarkable AE activity (Lei et al., 2000b). Therefore, fault nucleation appears to be controlled by the asperities of the quartz veins. During loading, stress is concentrated mainly at narrow veins of high strength. The precursory microcracking activity is caused by fracturing of the asperities. Dense microcracking moves from one asperity to another, giving rise to the short-term fluctuations in the *b*-value and event rate. Similar to the HF sample, local maxima of event rate and self-excitation strength, and local minima of *b*-values correspond to dense spatial clusters.

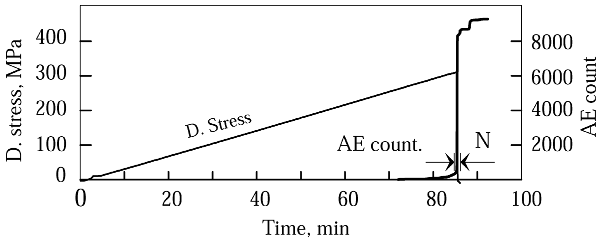

Fig. 10. Experimental results for the AF sample. Differential stress and AE count are plotted against time.

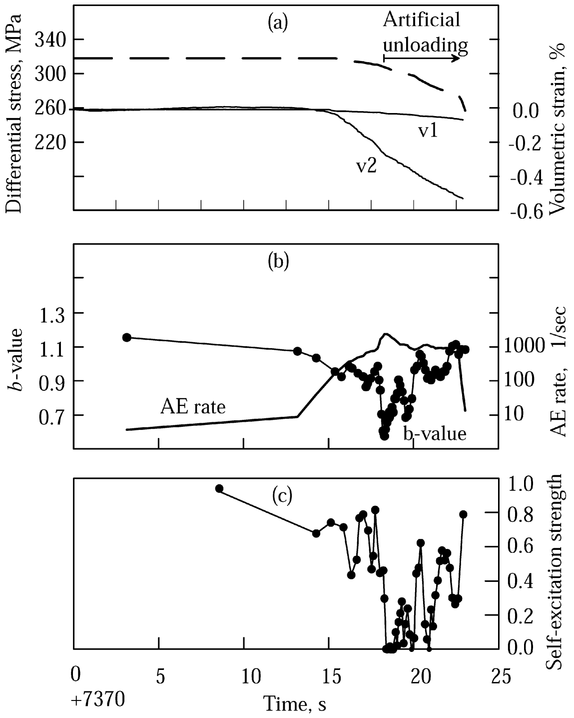

Fig. 11. Detail of the nucleation phase N in Fig. 10. (a) The differential stress and strains at asperities (v2) and off-asperities (v1), (b) logarithmic AE rate and *b*-value, and (c) self-excitation strength are plotted against time. The axial stress was released manually when the dynamic rupture was initiated in order to save the sample from excessive damage.

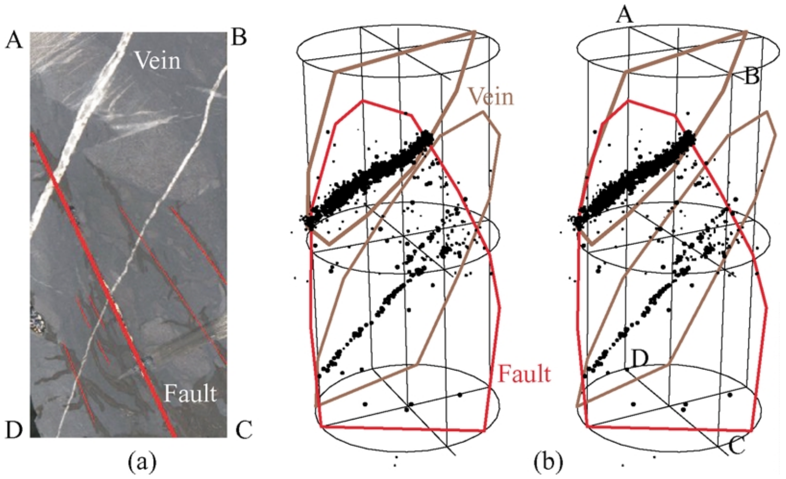

Fig. 12. (a) Photograph of a section of the AF sample after the experiment. (b) Stereo images of all AE hypocenters, showing veins and faults.

The WF sample exhibits a completely different deformation pattern, with a stable or ductile rupture process and very low AE activity (Fig. 2d). Examination of the results for both the AF samples and the WF sample reveals that strong asperities appear to control the nucleation process of rupture. The fracture strength of the WF sample is 150 MPa, while the average for the AF samples is 280 MPa. Although the total area of asperities on the AF fault constitutes only a small fraction of the total fault area, these asperities increase the strength of the fault by 130 MPa, demonstrating that such asperities are very strong and influence the seismic behavior of a fault considerably.

4. Discussion

4.1. Physics behind the three phases of microcracking

AE activities in stressed rock can be theoretically modeled by stress-aided corrosion theory for sub-critical crack growth of a macroscopic crack (e.g. Atkinson, 1984) and a population of microcracks (Meredith et al., 1990; Main et al., 1992, 1993). These models predict a negative relationship between the *b*-value and remote stress, as well as high-order nonlinear crack growth prior to dynamic fracture with a corresponding rapid decrease in the *b*-value. However, in the primary phase, particularly for the SF sample, the *b*-value of AE events exhibits a slightly positive relationship with stress, indicating that earlier microcracking may be governed by some mechanism other than subcritical crack growth. In fact, in the primary stage, major microcracking could be the result of an initial opening or rupturing of pre-existing microcracks or defects.

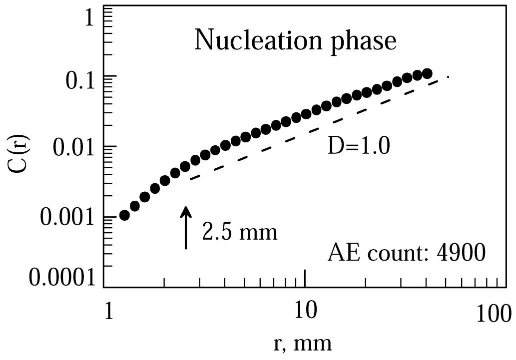

Fig. 13. Correlation integral function for the hypocenters in the AF sample against distance using logarithmic coordinates. The fractal dimensions estimated from the slope are also plotted.

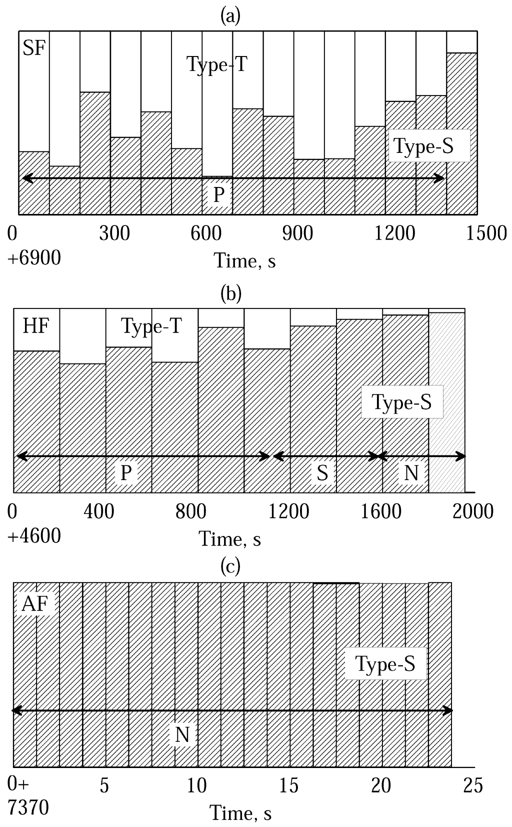

Fig. 14. Cracking mode distribution in the test samples based on the first motion of P-waves. Type-T and Type-S indicate tensile and shear cracking.

Pre-existing microcracks generally heal with a wide range of healing strength, thus separation of the crack walls is more likely to occur than growth of the crack front into unfractured rock. Since extension strength is much lower than shear strength, the opening of pre-existing microcracks can be considered to be an important cracking mode in the primary phase, particularly at relatively low stress.

The cracking mode itself can be determined statistically using the method proposed by Lei et al. (1992). Here, the ratio of up (dilatation) to down (compression) first motions is used to distinguish between tensile cracking (Type T) and shear or shear-dominated cracking (Type S), defined as up/(up + down). To maintain reliability of the data, only data having more than eight reliable first motions were used in this analysis. From a preliminary manual consideration of the ratio, cracking with an up–down ratio larger than 0.75 is considered to be tensile, and all other cracking to be shear or shear-dominated. This analysis revealed that extension cracking is dominant in the primary phase for the SF sample (Fig. 14a). As larger pre-existing microcracks have a higher probability for rupture at lower stress than smaller cracks, this results in a slight increase in b-value in primary phase with increasing stress.

The low self-excitation strength in the primary phase for the SF sample is also consistent with this model. In the HF sample, however, the primary phase is characterized by high self-excitation strength. This is probably associated with the earlier fracture of a small sub-fault on the lower side of the main fault, as indicated by the concentration of hypocenters in that region.

In the secondary phase, the event rate increases with stress according to a power law, but with a significantly higher exponent than that of the primary phases. The seismic b-value decreases with stress, which is consistent with the sub-critical crack growth model mentioned above. Increasing AE rate, decreasing b-values, weak self-excitation strength, and an increase in the predominance of the shear-cracking mode are the important features of the secondary phase. These results indicate that following the increase in crack density and mean crack length, sub-critical crack growth and coalescence of neighboring cracks becomes gradually more important. Therefore, interaction between cracks appears to be a key factor in the secondary phase.

The nucleation stage is the most interesting and important phase in the catastrophic fracture of rock samples with heterogeneous faults. The term ‘nucleation’ is used rather than ‘tertiary’ here for the rapidly increasing microcracking prior to dynamic rupture because this phase corresponds to the nucleation process of the final unstable rupture of the fault in the test sample. In homogeneous brittle rock, the initiated shear fault grows quasi-statically with a process zone at the fault front and is governed by progressive triggering of tensile microcracking, as determined by both microscopic examination (Cox and Scholz, 1988) and AE monitoring (Lei et al., 2000c). The process zone of a shear fault may also include a minor shear microcracking component depending on the material under investigation (Zang et al., 2000).

In rock samples, the pre-existing macroscopic faults are first-order heterogeneities, and the non-uniform healing strength distribution of the fault is a second-order heterogeneity. In the case of a fault with heterogeneous healing strength, AE hypocenters in the nucleation phase do not show a clear fault front, rather, faulting is initiated at several sites in succession in a competing manner, resulting in the observed large amplitude fluctuations in the event rates and b-values. Weaker areas and smaller asperities can rupture earlier than stronger areas and larger asperities, and the rupture can be obstructed at the boundary of a strong asperity or barrier, resulting in a short hiatus. Dense microcracking may then occur in the strong asperity when the local stress exceeds the strength of the asperity. A stronger asperity will therefore result in a longer hiatus and consequently higher event rate and lower b-value after the hiatus. When an asperity is fractured, aftershocks occur in the asperity area in a relatively lower shear stress environment, resulting in a higher b-value. This model reasonably explains the large simultaneous short-term fluctuations in event rate, b-value and self-excitation strength observed in the nucleation phase for these samples.

Once the final fault is initiated at one or several key positions, which may be the edges of asperities or fractured areas, the faulting process will be governed by non-linear crack growth, or in other words, the progressive fracture of asperities. Hence, the nucleation phase represents a transition from linear behavior to non-linear behavior. This is considered to be the reason why the change from the secondary phase to the nucleation phase in the experimental results is so abrupt.

The duration of the nucleation phases for the SF, AF, and HF samples are <2, 50, and 300 s (N1: 50 s, N2: 235 s, N3: 15 s), respectively. Although the N2 and N3 periods in the nucleation phase for the HF sample may be affected by the lower cap, the timing of fault nucleation appears to be positively related to the degree of heterogeneity. Highly homogeneous faults such as in the SF sample may exhibit an unpredictable failure style, whereas heterogeneous faults such as that in the HF sample fail in a predictable manner with remarkable precursory anomalies in the statistics of AE activity, indicative of microcracking.

The results of this and previous studies demonstrate that the fracture of fine-grained samples and samples containing faults or joints (Lockner et al., 1991; Satoh et al., 1996; Lei et al., 2003) is characterized by clear localization of hypocenters in the nucleation phase, while this is not commonly observed for intact coarse-grained rock samples with high densities of pre-existing microcracks (Zang et al., 1998; Lei et al., 2000b). In the former case, a thin shear fracture plane initiates and grows, observed as low background activity. In the later case, a wide shear zone forms and grows, with higher background activity. As pre-existing cracks and mineral grains appear to be the most important factor controlling the local strength of rock, the different nucleation behavior reflects the stress redistribution in a rock sample after the initiation of shear fracture.

4.2. Implication of experimental results

The present experimental results demonstrate that damage creation and catastrophic fracture of faults in rocks is characterized by three typical stages of microcracking. Explicit precursory behaviors were observed in the nucleation phase preceding the dynamic rupture of heterogeneous faults. The microcracking activity can be quantitatively described in terms of the event rate, seismic *b*-value, self-excitation strength, and fractal dimension of the hypocenter distribution. These parameters are closely related to the heterogeneous structure of the fault, such as the distribution of healing strength and asperities. According to the self-similarity of the geological structure, these laboratory-scale experimental results are considered to be basically applicable to larger scales of industrial application and natural earthquakes. Therefore, the statistics of detailed AE or microseismic data can be expected to provide useful parameters for monitoring the status of active faults and identifying potential asperities on a fault plane.

AE data prior to dynamic rupture can be treated as foreshocks (Lei et al., 2003). The present experimental results revealed a precursory *b*-value anomaly: a slight increase and then drop from $1.0 \sim 1.2$ to about 0.5. This result is in agreement with the theoretical model of subcritical crack growth (Meredith et al., 1990; Main et al., 1992, 1993), indicating that a decreasing *b*-value reflects stress enhancement due to fracture growth in asperities, and in particular the boundaries of asperities. This long-term tendency is also consistent with that observed before some large earthquakes such as the 1984 Nagano and 1985 Tonga earthquakes (Meredith et al., 1990), the Mw 7.8 Cape Kronotsky, Kamchatka, earthquake on 5 December 1997 (Zuniga and Wyss, 2001), and the Mw 7.9 off-Etorofu (Iturup), Kurile Islands, earthquake on 3 December 1995 (Hurukawa, 1998), as well as volcanic eruptions (Vinciguerra, 1999).

Statistical studies have also shown that variation in the *b*-value of foreshocks is a common feature of natural earthquakes. For example, by comparing *b*-values for long-term seismicity and foreshocks occurring within hours and days prior to a mainshock, Molchan et al. (1999) found that the *b*-value drops by half during the foreshock period. However, this result represents a statistical average, and not the behavior of individual foreshock sequences. Unfortunately, most large natural earthquakes are not preceded by a large number of identifiable foreshocks. To interpret this, two factors must be considered. One is the incompleteness of small earthquake data due to the magnitude threshold for detection. The other is that a well-developed natural fault might be quite homogeneous on small scales, particularly at seismogenic depths, resulting in a low cutoff of magnitude. Clearly, further work is required to evaluate the importance of these factors.

Some studies have found that asperities in the crust can be predicted from the detailed *b*-value distribution calculated from seismic data including earthquakes of magnitude smaller than one (e.g. Wyss et al., 2000). However, it remains difficult to observe all small earthquakes in the upper crust, and it is even more difficult to detect the stress–strain status of a fault at depth. Therefore, experimental approaches such as that adopted in the present study provide an alternative means of clarifying the relationships between fault rupture and fault structure. The validity of rules obtained through experimental studies when applied to seismic activity in the earth also remains an important scientific challenge. To this end, detailed studies on induced microseismicity in mineral fields and dams on an intermediate scale can be expected to provide further data allowing the reliable extension of laboratory results to the analysis of tectonic earthquakes.

5. Conclusion

Through the use of a high-speed multi-channel waveform recording system, the detailed time-space distribution of AE activity was examined during the fracture of four rock samples containing faults of widely differing strength distribution under triaxial compression. The experimental results are generally in agreement with previous data on the fracture of inhomogeneous faults. The AE events were characterized in terms of event rates, seismic *b*-values, the self-excitation strength, and the fractal dimension of the hypocenter distribution. Three long-term microcracking phases: primary, secondary and nucleation, can be identified based on the changes in these parameters. In the primary phase, the AE rate increases gradually with stress, corresponding to early microcracking (mainly tensile mode) during the loading period. In the secondary phase, the event rate increases markedly, indicative of increased interaction between cracks. The nucleation phase appears as a sudden sharp increase in the event rate, and represents the initiation and acceleration of the final rupture. The *b*-values in the three phases also exhibit different trends. In the primary phase, the *b*-value takes an average of ~ 1.2 and increases slightly with increasing stress. In the secondary phase, the *b*-value starts to decrease slowly, and in the nucleation phase, the *b*-value decreases rapidly. The fractal dimension for scales larger than the typical cluster size, which generally corresponds to the dominant grain size, decreases from ~ 2.2 in the primary phase to $1.0 \sim 1.4$ in the nucleation phase.

In the secondary and nucleation phases, the event rate and *b*-value also exhibit large simultaneous short-term fluctuations. The simultaneous local maximum in the event rate and local minimum in the *b*-value are considered to represent spatial clustering around an asperity on the rupture fault. These short-term fluctuations in the event rate and *b*-value are characteristic of the heterogeneous healing strength and asperity distribution on the fault plane.

The present experimental results demonstrate that the predictability of catastrophic fault fracture is strongly dependent on the fault heterogeneity. A homogeneously healed fault is notably unpredictable, whereas a fault of non-homogeneous healing strength or asperity distribution undergoes a predictable fracturing process with a remarkably clear nucleation phase that can be observed as a precursory anomaly of the *b*-value or other statistical parameters of AE activity. The appearance of a nucleation phase with decreasing *b*-value, a non-linearly increasing event rate and spatio-temporal clustering can therefore be considered to be a signal of the initiation of catastrophic fracture. This paper focused on the experimental facts; a new constitutive model will be examined as part of future work after more data has been collected.

Acknowledgements

This work was supported by the National Institute of Advanced Industrial Science and Technology of Japan (AIST) and a grant (No. G1998040704) from the Ministry of Science and Technology of China. The authors would like to thank M.V.M.S. Rao and two anonymous referees for helpful comments and suggestions on improvements to the manuscript.

References

Aki, K., 1965. Maximum likelihood estimate of *b* in the formula $\log N = a - bm$ and its confidence. Bulletin Earthquake Research Institute of Tokyo University 43, 237–239.

Atkinson, B.K., 1984. Subcritical crack growth in geological materials. Journal of Geophysical Research 89, 4077–4114.

Cox, S.J.D., Scholz, C.H., 1988. Rupture initiation in shear fracture of rocks: an experimental study. Journal of Geophysical Research 93, 3307–3320.

Hirata, T., 1987. Omori's power law aftershock sequences of microfracturing in rock fracture experiment. Journal of Geophysical Research 92, 6215–6221.

Hurukawa, N., 1998. The 1995 off-Etorofu earthquake: joint relocation of foreshocks, the mainshock, and aftershock and implications for the earthquake nucleation process. Bulletin of Seismological Society of America 88, 1112–1126.

Jouniaux, L., Masuda, K., Lei, X.-L., Nishizawa, O., Kusunose, K., Liu, L., Ma, W., 2001. Comparison of the microfracture localization in granite between fracturation and slip of a pre-existing macroscopic healed joint by acoustic emission measurements. Journal of Geophysical Research 106, 8687–8698.

Lei, X.-L., Nishizawa, O., Kusunose, K., Satoh, T., 1992. Fractal structure of the hypocenter distribution and focal mechanism solutions of AE in two granites of different grain size. Journal of Physics of the Earth 40, 617–634.

Lei, X.-L., Kusunose, K., Nishizawa, O., Cho, A., Satoh, T., 2000a. On the spatio-temporal distribution of acoustic emissions in two granitic rocks under triaxial compression: the role of pre-existing cracks. Geophysical Research Letter 27, 1997–2000.

Lei, X.-L., Nishizawa, O., Kusunose, K., Cho, A., Satoh, T., 2000b. Compressive failure of mudstone samples containing quartz veins using rapid AE monitoring: the role of asperities. Tectonophysics 328, 329–340.

Lei, X.-L., Kusunose, K., Rao, M.V.M.S., Nishizawa, O., Satoh, T., 2000c. Quasi-static fault growth and cracking in homogeneous brittle rock under triaxial compression using acoustic emission monitoring. Journal of Geophysical Research 105, 6127–6139.

Lei, X.-L., Kusunose, K., Satoh, T., Nishizawa, O., 2003. The hierarchical rupture process of a fault: an experimental study. Physics of the Earth and Planetary Interiors 137, 213–228.

Lockner, D.A., Byerlee, J.D., Kuksenko, V., Ponomarev, A., Sidorin, A., 1991. Quasi-static fault growth and shear fracture energy in granite. Nature 350, 39–42.

Main, I.G., Meredith, P.G., Sammonds, P.R., 1992. Temporal variations in seismic event rate and *b*-values from stress corrosion constitutive laws. Tectonophysics 211, 233–246.

Main, I.G., Sammonds, P.R., Meredith, P.G., 1993. Application of a modified Griffith criterion to the evolution of fractal damage during compressional rock failure. Geophysics Journal International 115, 367–380.

Meredith, P.G., Main, I.G., Jones, C., 1990. Temporal variations in seismicity during quasi-static and dynamic rock failure. Tectonophysics 175, 249–268.

Molchan, G.M., Kronrod, T.L., Nekrasova, A.K., 1999. Immediate foreshocks: time variation of the *b*-value. Physics of the Earth and Planetary Interiors 111, 229–240.

Nishizawa, O., Noro, H., 1990. A self-exciting process of acoustic emission occurrence in steady creep of granite under uniaxial stress. Geophysical Research Letter 17, 1521–1524.

Satoh, T., Shivakumar, K., Nishizawa, O., Kusumase, K., 1996. Precursory localization and development of microfracture along the ultimate fracture plane in amphibolite under triaxial creep. Geophysical Research Letters 23, 865–868.

Utsu, T., 1965. A method for determining the value of *b* in a formula $\log N = a - bm$ showing the magnitude–frequency relation for earthquakes (in Japanese). Geophysical Bulletin 13, pp. 99–103, Hokkaido University, Hokkaido, Japan.

Vinciguerra, S., 1999. Seismic scaling exponents as a tool in detecting stress corrosion crack growth leading to the September–October 1989 flank eruption at Mt. Etna volcano. Geophysical Research Letter 26, 3689–3692.

Wyss, M., Schorlemmer, D., Wiemer, S., 2000. Mapping asperities by minima of local recurrence time: San Jacinto–Elsinore fault zones. Journal of Geophysical Research 105, 7829–7844.

Zang, A., Wagner, F.C., Stanchits, S., Dresen, G., Andresen, R., Haidekker, M., 1998. Source analysis of acoustic emissions in Ave granite cores under symmetric and asymmetric compressive loads. Geophysical Journal International 135, 1113–1130.

Zang, A., Wagner, F.C., Stanchits, S., Janssen, C., Dresen, G., 2000. The fracture process zone in granite. Journal of Geophysical Research 105, 23651–23661.

Zhao, Y., 1998. Crack pattern evolution and a fractal damage constitutive model for rock. International Journal of Rock Mechanics and Mining Science 35, 349–366.

Zuniga, F.R., Wyss, M., 2001. Most- and least-likely locations of large to great earthquakes along the Pacific coast of Mexico estimated from local recurrence time based on *b*-values. Bulletin of Seismological Society of America 91, 1717–1728.

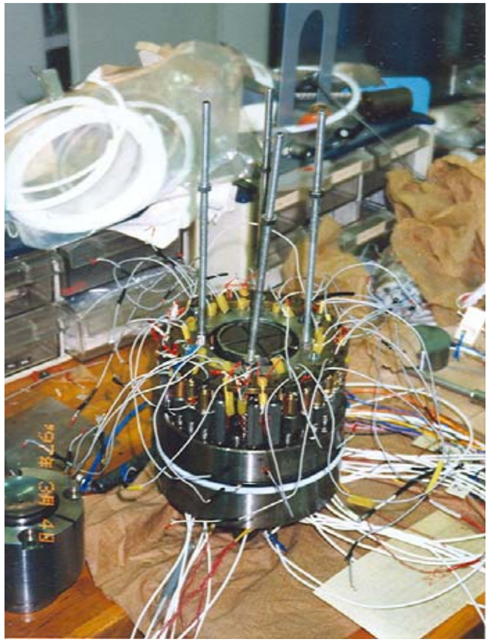

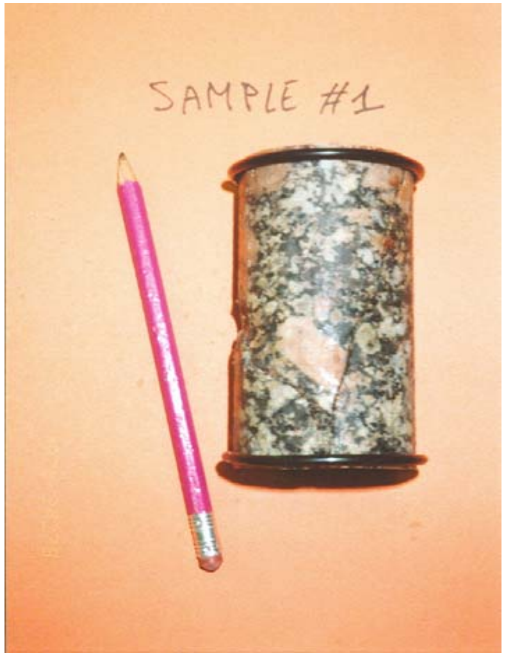

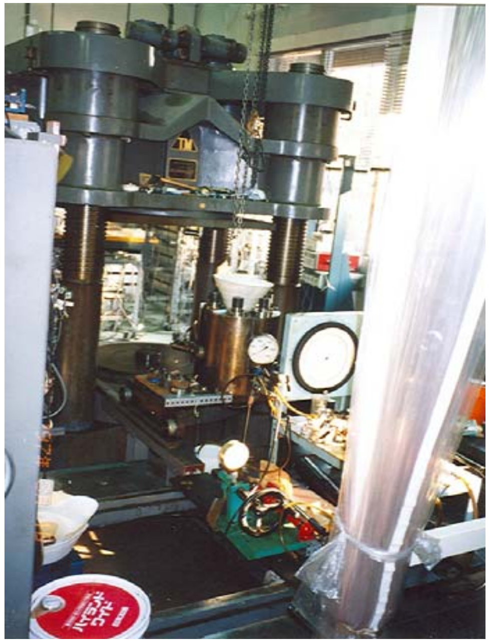

Dispositif expérimental du Geological Survey of Japan

Échantillon du granite du Mayet de Montagne

JOURNAL OF GEOPHYSICAL RESEARCH, VOL. 106, NO. B5, PAGES 8687–8698, MAY 10, 2001

Comparison of the microfracture localization in granite between fracturation and slip of a preexisting macroscopic healed joint by acoustic emission measurements

Laurence Jouniaux
École Normale Supérieure de Paris, Unité Mixte de Recherche 8538, CNRS, Paris, France

Koji Masuda, Xinglin Lei, Osamu Nishizawa, and Kinichiro Kusunose
Geological Survey of Japan, Tsukuba, Japan

Liqiang Liu and Wentao Ma
China Seismological Bureau, Beijing, China

Abstract. Experiments of fracturation and slip of a preexisting macroscopic healed joint have been performed under triaxial deformation on granite from Mayet de Montagne (France). This granite shows high grain-scale inhomogeneity. Acoustic emissions have been recorded and hypocenters have been determined during the entire experiments. For both rupture experiment and slip experiment, precursory localization of microfractures in the final rupture plane has been observed in the early stage of deformation, well before the dilatancy. It is likely that not only initial closure of favorably oriented cracks but also breaking of partially cemented grains or slipping between grains may occur in the pseudoelastic phase and are already localized on the final rupture plane where the shear stress seems to be concentrate. This behavior is observed in both cases where stress heterogeneity and rupture nucleation are controlled by (1) medium-scale heterogeneity at the grain scale (HS sample) or (2) macroscopic heterogeneity in the form of a preexisting healed joint (JS sample). The sample with the healed joint exhibited ~ 1.6 times more acoustic emission events than the intact sample. The presence of the healed joint significantly weakened the sample.

1. Introduction

It is usually accepted that faulting of brittle rocks is induced by coalescence of microcracks formed prior to faulting. These microcracks are initially randomly distributed and subparallel to the maximum compressive stress [*Brace et al.*, 1966], and the coalescence occurs near the peak stress. During the linear part of the rock deformation, minerals distort elastically and grains or part of grains shift slightly under the applied stress and slide relative to one another [*Brace et al.*, 1966]. Microcracks deform or close depending on their orientations. However, new cracks appear at preexisting intergranular at the onset of volume increase and then at 50-75% of peak stress new transgranular cracks appear [*Tapponier and Brace*, 1976; *Fonseka et al.*, 1985]. The growth of microcracks is associated to mismatch of grain boundaries, differences in elastic moduli between minerals, intracrystalline flaws, and shear along grain boundaries [*Taponnier and Brace*, 1976]. Model for the deformation and failure of brittle rock has been developed from the mechanics of tensile microcracks [*Costin*, 1983; *Main*, 1991]. Another model of failure of brittle solids has been developed considering crack initiation, crack propagation, and crack linkage [*Nemat-Nasser and Horii*, 1982; *Ashby and Hallam*, 1986]. Both axial and shear cracks play significant roles in the faulting process; small cracks grow stabily until their length is comparable with their spacing. When they interact, an instability develops to give final failure [*Ashby and Sammis*, 1990], and at later stages of deformation, extensive crushing of particles into fine-grained fault gouge is important [*Wong*, 1982].

In this paper we describe two experiments of rock deformation under triaxial stress up to fracture strength on two granite samples: an intact sample (HS), and a sample having a preexisting macroscopic healed joint (JS) from the bottom to the top of the sample with an angle of ~20° to the axial direction and ~ 1 mm in aperture. Therefore the JS sample is constrained to have a fracture running from the top to the bottom of the sample. Note that these samples have different grain sizes and are not as homogeneous as material usually used in other experiments. The preexisting healed joint was thought to control the rupture initiation. This healed joint was expected to slip during the deformation or the final stage of deformation. However, it was not known if this healed joint acts as strong or weak component, depending on the nature and degree of cementation. Acoustic emission (AE) were observed by counting the cumulative number and by determinating the source location.

One goal of our experiments was to know if the eventual rupture plane would appear earlier in the loading history by showing an increased and localized AE activity, when a preexisting joint exists. Samples were loaded up to failure, and

Paper number 2000JB900411.
0148-0227/01/2000JB900411$09.00

since brittle fracture involves the growth of microcracks, acoustic signals were spontaneously generated from this microcracking. Indeed, AE are high-frequency elastic waves generated by the localized relaxation of stress or displacement as a local dislocation or by crack propagation. Note that the observed AE are probably the result of unstable crack propagation, meaning rapid microcrack growth [*Lockner*, 1993]. The microcrack damage is anisotropic and AE source location can detect the three-dimensional distribution of microfractures. We address the question of when the macroscopic fracture plane can be first identified from AE locations when an intact sample is fractured and when a slip occurs on a preexisting healed joint.

2. Experimental Setup

Two samples of granite from Mayet de Montagne (France) were cut into cylinders of 100 mm length by 50 mm diameter. This granite contains quartz (1 to 5 mm diameter), K-feldspar (grains up to 3 cm diameter), biotite, and muscovite (1 to 3 mm diameter) hornblende. The grain size to sample ratio for the largest quartz grains is therefore ~ 0.1, which is large compared to other experiments described in the literature. Images of the intact samples were made under X-ray tomography, one cross section each millimeter being scanned. The same procedure was used after the experiments in order to see the fracture using a nondestructive method. The first sample was an intact sample (HS), and the second sample contained a preexisting throughgoing macroscopic joint (JS). This macroscopic joint contains calcite, prehnite and fluorine [*Clavaud et al.* , 2000]. Flat areas ~ 1 cm in width were ground on the cylindrical surface at 60° intervals around the circumference in order to glue the piezoelectric transducers (PZT). PZT transducers function not only as receivers of acoustic signals but also as acoustic sources. Eighteen PZT transducers (2 MHz resonant frequency, 5 mm in diameter) were used for acoustic emission (AE) detection, six for *P* wave velocity measurements and four to eight for *S* wave velocity measurements. The elastic wave velocities in the axial and radial directions were measured during the experiment by exciting the appropriate piezoelectric sensors (PZT 19 and 20 measured vertical *P* wave, PZT a and 1, b and 2, measured horizontal *P* wave, see Figures 1a and 1b) with a pulse generator, and AE events that occurred during the velocity measurements could not be detected. Velocity measurements were performed for each 25 MPa increment of axial stress during the first part of the experiment, then for each 50 MPa because of the real-time results of velocity measurements. This provided the velocity values used for the AE hypocenter determination.

Six cross-strain gauge pairs, each 6 mm length, were cemented to the sample surface with epoxy resin to measure the local strains at the central portion of the sample (A, B, C, D, E and F in Figure 1). After the gauges and the transducers were glued on the sample, the stainless steel end pieces were attached to each end of the sample. Then the sample and the end pieces were coated with several layers of silicon rubber in order to isolate the sample from the oil used as the fluid-confining pressure medium. The sample assembly was then fixed to the base of a pressure vessel, and all electric leads were connected (with shield wires for each AE sensor) and tested. The pressure vessel was placed in a servocontrolled loading frame and the confining pressure tubing connecting to the pump. After all gauges and PZT were connected to the data acquisition system, uniformity of the axial loading was checked from strain gauge outputs. The confining pressure was set at 40 MPa and was held constant thoughout the experiment. The loading rate was 0.052 MPa/s.

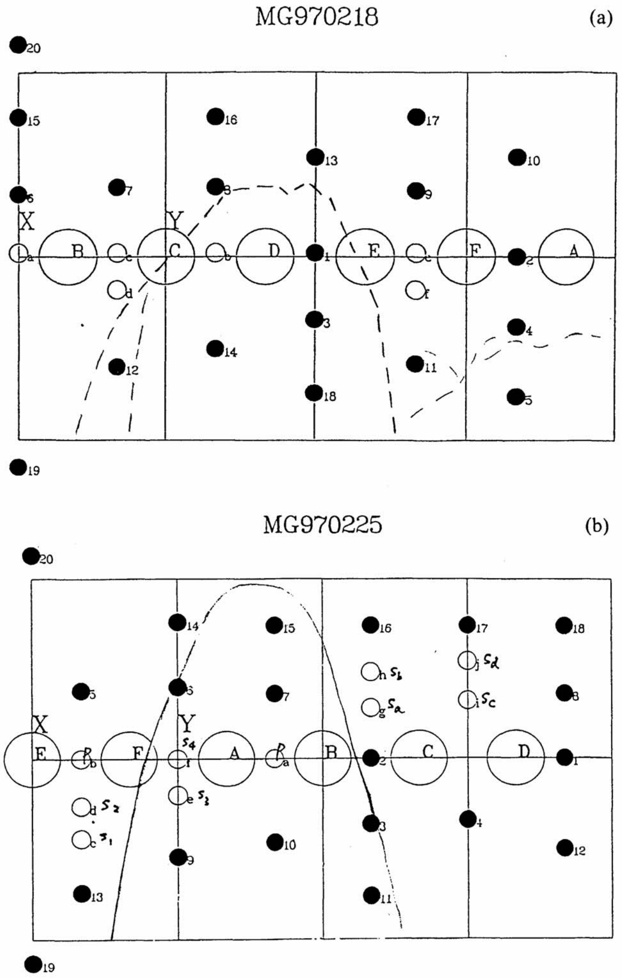

Figure 1. Sample scheme with strain gauges (large circles A to F) and transducers (small circles) locations. Length of sample is 100 mm, and circumference of sample is 314 mm. Transducers 19 and 20 are located on the ends of the sample. Scheme for (a) HS sample and (b) JS sample. The line on Figure 1b represents the location of the healed joint, and dashed line on Figure 1a represents the finale rupture.

3. Data Acquisition System

One data acquisition system collected the values of axial load, confining pressure, strain gauges outputs, and AE counts. No measurements were performed with a smaller time period than 40 s. Another data acquisition system was used to detect, digitize, and store the AE waveforms and elastic waveforms from the transducers. This system is based on the one detailed by *Satoh et al.* [1987] and has been improved [*Nishizawa*, 1997; *Satoh and Nishizawa*, 1997; *Lei et al.*, 1997]. The system digitizes the waveform at a rate of 20 MHz for each channel, for as many as 32 channels. AE hypocenters were determined automatically by picking the first arrival of the *P* wave [*Yokota et al.*, 1981; *Satoh et al.*, 1987; *Masuda et al.*, 1990]. The method calculating AE hypocenters is basically the same as that one used for seismic

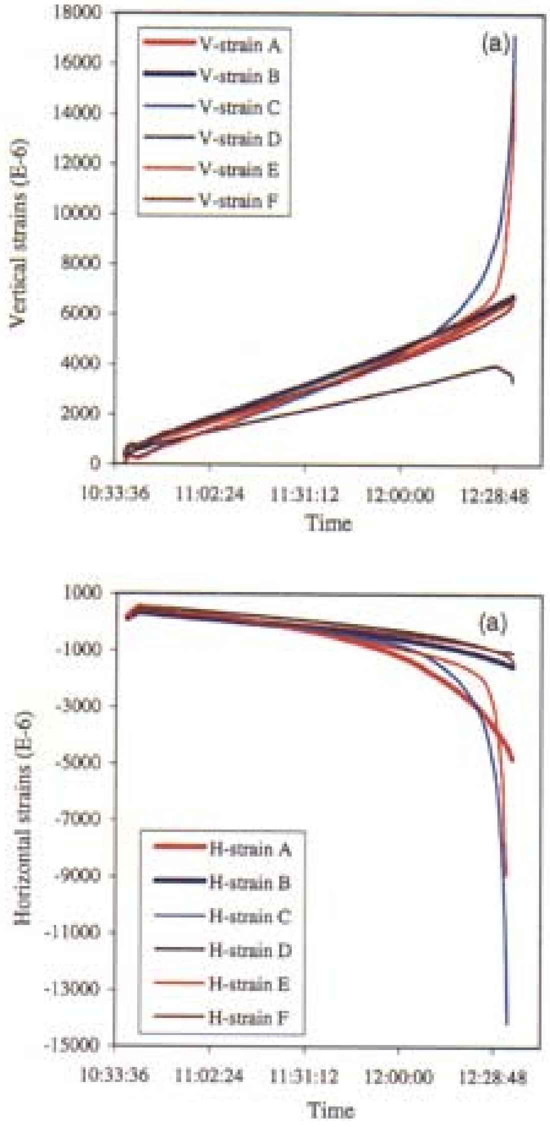

Plate 1a. Vertical and horizontal strains measured from the six different strain gauges for HS sample.

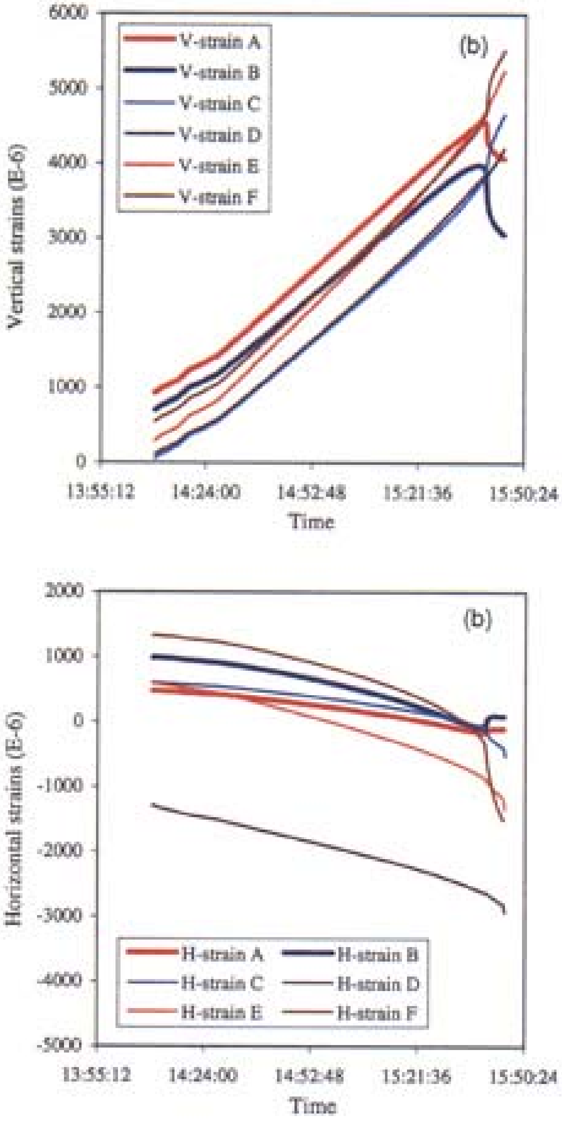

Plate 1b. Same as Plate 1a except for JS sample. Different behavior from strain gauges A and B can be observed.

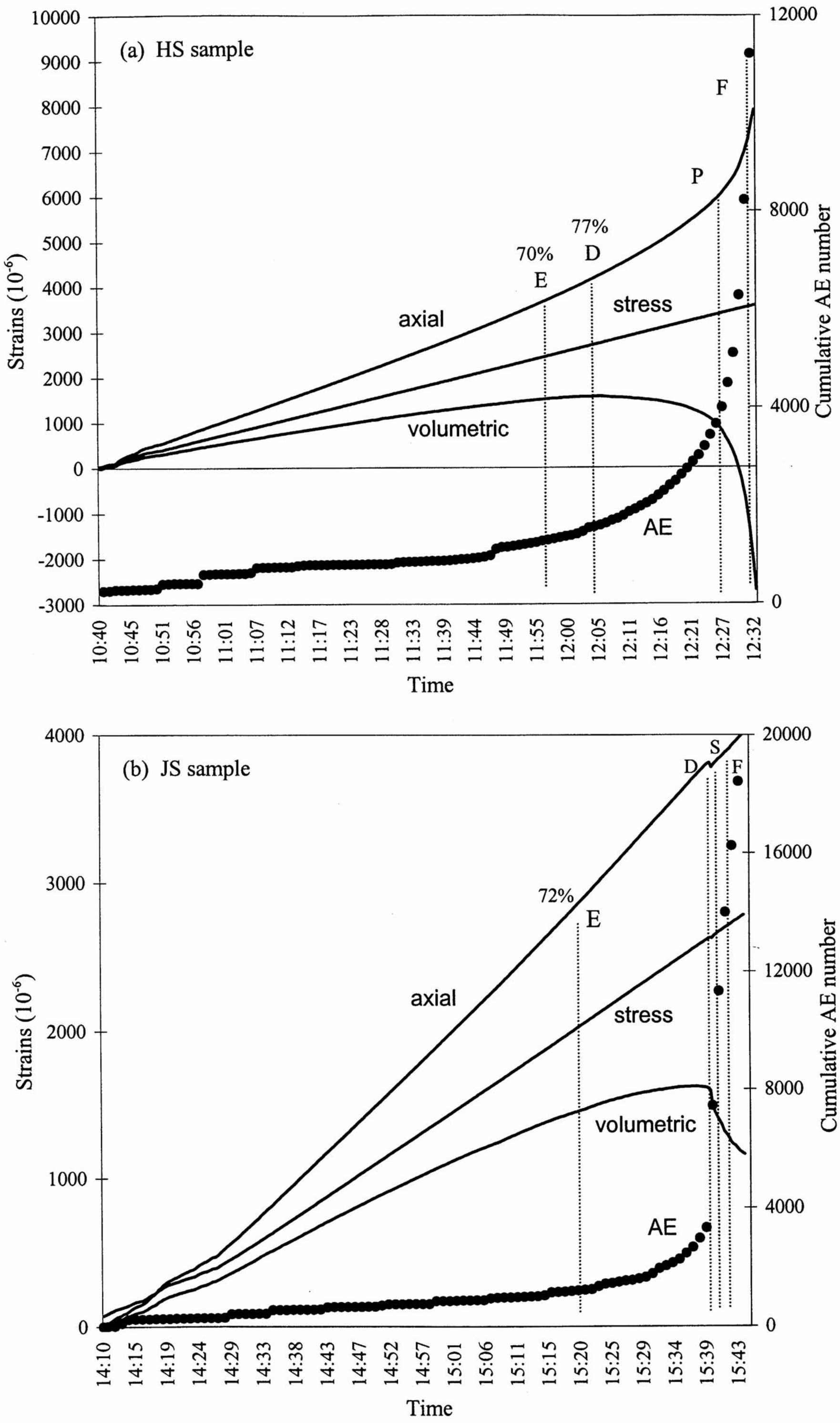

Figure 2. Differential stress, axial strain, volumetric strain evolution and AE cumulative number during the triaxial compression for (a) HS sample and (b) JS sample. Stress is in 10^5 Pa on the axis of strains. E is the end of the linear part in differential stress-vertical strain curve, D is the beginning of increasing volumetric strain, and S is the slip.

events. Those AE hypocenters determined within an error smaller than 2 mm were selected for plotting. Several hypocenters are located outside the sample because of poor conditions for convergence when events occur close to the surface. Thus the results are more accurate within the sample but not too close to the sample boundaries.

4. Results

4.1. Mechanical Behavior

The strain gauges responses during the experiment are plotted in Plates 1a and 1b. The vertical and volumetric strains, the differential stress (axial stress minus confining pressure), and the

Table 1. Mechanical Characteristics for the Homogeneous Sample (HS) and the Sample With a Joint (JS)[a]

Sample	Strength, MPa	*E*, GPa	ν	$\mu = \tau / \sigma_n$
HS	358	67.2	0.32	1.12
JS	278	69.2	0.28	1.22

[a] *E* is the Young'modulus, ν is the Poisson ratio, and μ is the friction (τ / σ_n).

AE cumulative number are shown in Figures 2a and 2b. The strength of HS sample was larger than the one of JS sample (Table 1), showing that the sample of the same material, but with the preexisting joint, was weaker than the intact sample. The deformation (differential stress-vertical strain curve) is linear up to 70% and 72% of strength (E point) for HS and JS sample, respectively. The Young's modulus *E* and the Poisson ratio ν have been deduced from the linear part of the differential stress-vertical strain curve (Table 1).

For the linear deformation part the imposed loading rate induced vertical strain rates of $8.1\text{x}10^{-7}$ s^{-1} and $7.6\text{x}10^{-7}$ s^{-1} for HS and JS samples, respectively, and horizontal strain rates of $2.6\text{x}10^{-7}$ s^{-1} and $2.1\text{x}10^{-7}$ s^{-1} for HS and JS samples, respectively. The maximum vertical shortening was 0.8% and 0.4% for HS and JS samples, respectively.

The HS sample exhibits a typical volumetric change during the deformation; volume decreases by 0.16% during the first 86 min of the experiment (up to point D), and then volume increases by 0.43% at the onset of dilatancy (from the differential stress 270 MPa, point D) during the next 26 min. This indicates the growth of new microcracks. The strains of gauges C and E are more important than the other gauges because the final rupture plane was located throughout gauges C and E (Plate 1a and Figure 1a). Dynamic failure occurred at peak stress after a period of strain hardening.

The volume of JS sample was first decreased by 0.16%, similar to the intact sample, during the first 91 min of the experiment, and then began to slip when the differential stress was 260 MPa (S point). We did not observe some dilatancy during slip (at least absolute dilatancy of the total volume of the sample) as sometimes described [*Rudnicki and Chen*, 1988]. Note that there is no purely elastic (linear) volume changes, even at low stress, for the JS sample. A stress drop of 0.3 MPa was measured at the time of failure (in a time accuracy of 40 s). The slip, which cut the sample into two parts, was very clear since the behavior of the two strain gauges (A and B) glued on one part of the sample showed opposite behavior to the four other strain gauges glued on the other part of the sample (Figure 1b and plate 1b) (location of these strain gauges in regard to the slip being made after the experiment).

The final main rupture plane for JS sample was the same as the plane of the healed joint and was at an angle of ~20° compared to the axial stress direction, and for HS sample was at an angle ~32° (Figures 3 and 4). The shear and normal stresses resolved on a rupture plane inclined at an angle of α from the vertical are as follows [*Jaeger*, 1959; *Nicolas*, 1984]:

$$\tau = \frac{\sigma_1 - \sigma_3}{2} \sin(2\alpha)$$

$$\sigma_n = \frac{\sigma_1 + \sigma_3}{2} - \frac{\sigma_1 - \sigma_3}{2} \cos(2\alpha),$$

where σ_1 is the axial stress and σ_3 is the confining pressure.

At peak stress for HS sample the shear and the normal stresses on the fault inclined at the angle 32-34° from vertical are $\tau = 163.6 \pm 2.8$ MPa and $\sigma_n = 146.3 \pm 11.9$ MPa. For JS sample the shear and normal stresses on the healed joint when slip occurred (at an angle 18-23° from vertical) are $\tau = 90.9 \pm 9.3$ MPa and $\sigma_n = 74.5 \pm 5.9$ MPa. The friction $\mu = \tau / \sigma_n$ [*Byerlee*, 1978] on the rupture plane at peak stress is 1.12 ± 0.11 (HS sample) and on the healed joint when the slip occurred is 1.22 ± 0.22 (JS sample). These values are difficult to compare each other because the normal stresses are different. Shear stress versus normal stress for a large number of experiments (fracturation and sliding) on various materials has been reported and shows $\tau = 0.85\ \sigma_n$ for $\sigma_n < 200$ MPa [*Byerlee*, 1978; *Scholz*, 1990]. The friction deduced in our experiments (1.12 and 1.22) is higher than $\tau / \sigma_n = 0.85$ deduced by *Byerlee* [1978], higher than $\tau / \sigma_n = 0.86$ deduced from experiment of friction on blocks of granite at normal stress 70 MPa [*Dieterich*, 1972], and higher than $\tau / \sigma_n \sim 0.6$ deduced from experiment of gouge layer (quartz sand) sheared within Westerly granite surfaces in wet conditions at normal stress 100 MPa [*Marone et al.*, 1990]. We would expect a higher friction for the fracture experiment than for the sliding of the healed joint experiment at a given normal stress. This was observed when friction has been measured on Westerly granite in fracturing and sliding experiments [*Byerlee*, 1967]. For sliding experiments a law $\tau = 0.5 + 0.6\sigma_n$ was observed, leading to $\tau / \sigma_n = 0.5/\sigma_n + 0.6$ (τ and σ_n in kbar) equal to 1.27 when normal stress is 74.5 MPa (case of JS sample), which is closed to what we observed when slip occurred on the healed joint (friction equal 1.22 for JS sample). For fracturing experiments of Westerly granite the shear stress needed to fracture the sample was higher than for sliding (at a given normal stress) [*Byerlee*, 1967], so that for a normal stress of 146 MPa (HS sample) the friction would be 0.94 for sliding experiment and 1.55 for fracturing experiment. We deduced a friction of 1.12 for the experiment of fracturation (HS sample), which is lower than what was observed for Westerly granite fracturation but still higher than what was observed for Westerly granite sliding.

In summary, the HS sample fractured after an important volumetric change including dilatancy, with a high strength and an inferred friction coefficient 1.1, whereas the JS sample showed a slip (the joint itself fractures before it slides as it will be shown by acoustic emissions) after a compaction without showing significant dilatancy, with a lower strength, and an inferred friction coefficient 1.2. The presence of the healed joint weakened the strength of the sample.

4.2. *P* Wave Velocities

The values of *P* wave velocities were ~5.7-6.0 km/s for both samples. The evolution of vertical and horizontal *P* wave velocity during the deformation is detailed in Table 2. During the deformation of JS sample the velocities do not vary until the differential stress is 235 MPa, which is almost the end of the volume decrease of the sample. During the deformation of HS sample the vertical *P* wave velocity first increased from 5 to 5.96 km/s and then decreased when differential stress is ~130 MPa, which is well before the end of compaction, and then increased again. The horizontal *P* wave velocity first decreased or increased, depending on the orientation in the horizontal plane, and then decreased when the differential stress is ~130 MPa until the end of the experiment.

4.3. Acoustic Emissions

The cumulative number of AE events occurring during the experiments is shown in Figure 2. The total number of AE was

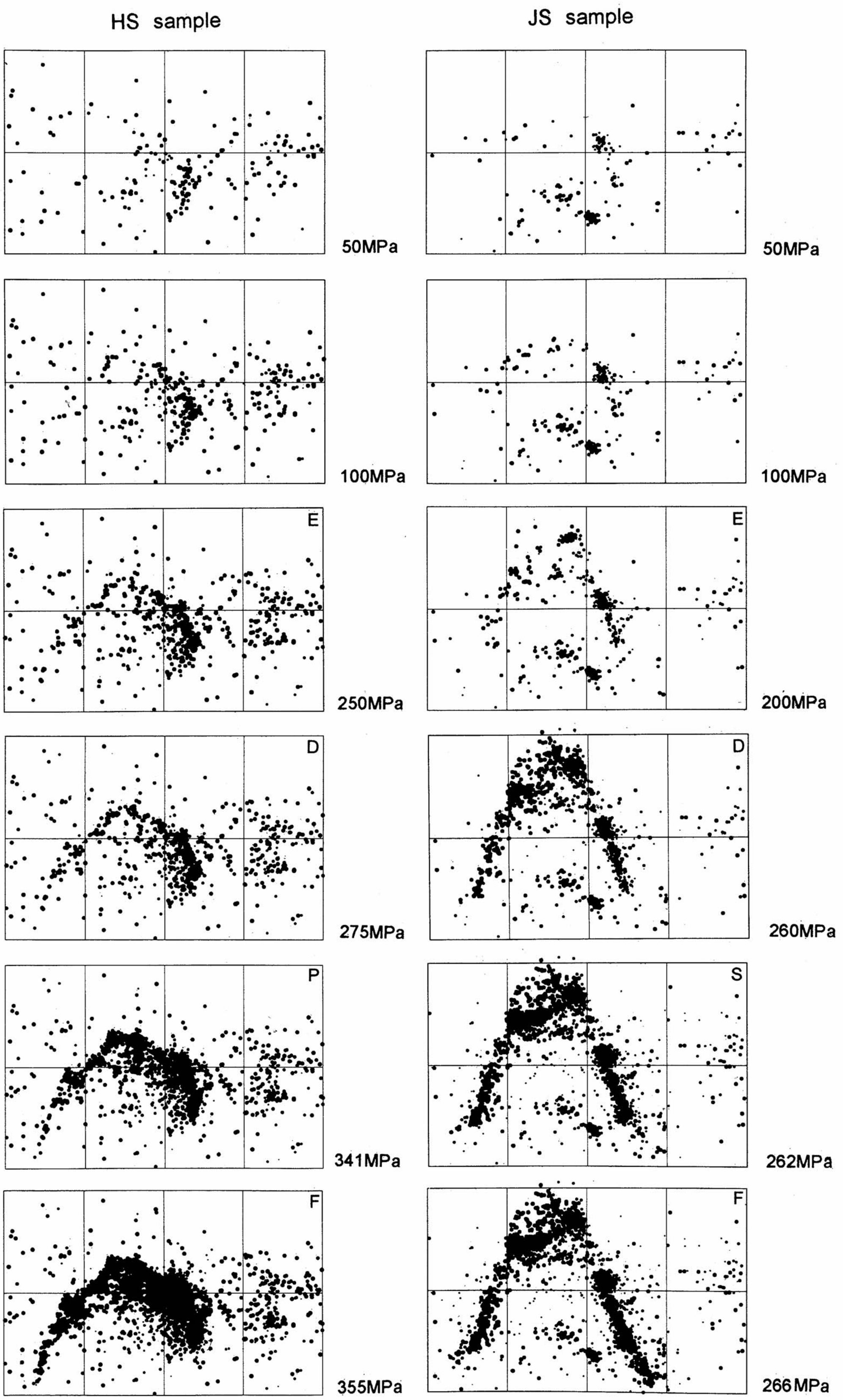

Figure 3. Evolution of the AE hypocenters location (lateral projection) during the triaxial compression at various differential stress values for HS sample and JS sample (letters refer to Figure 2). Length and circumference of the sample are 100 mm and 314 mm, respectively. The AE events of JS sample are distributed on the preexisting macroscopic joint.

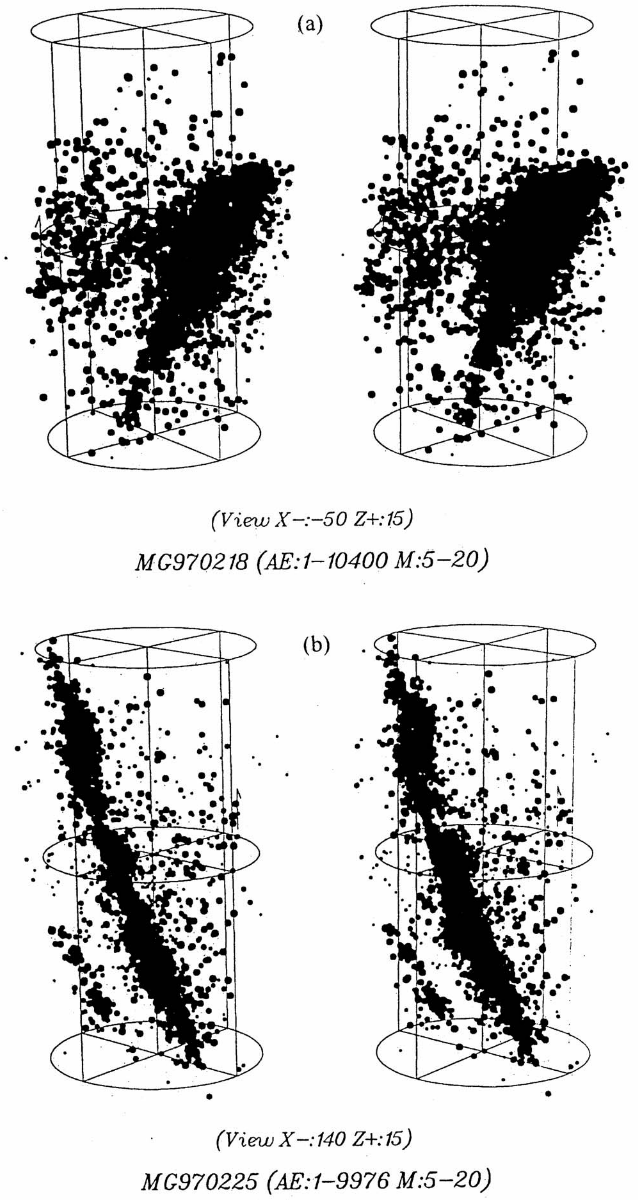

Figure 4. Stereographic projection of the AE hypocenters for (a) HS and (b) JS samples. Length and diameter of the sample are 100 mm and 50 mm, respectively.

11,207 and 18,411 for HS and JS samples, respectively. AE activity was observed during the linear elastic phase (up to E point). The AE rate was roughly constant up to 56% (200 MPa) and 72% (200 MPa) of the strength for HS and JS samples, with an AE rate larger at the very beginning of the compression for HS sample compared to JS sample. The end of the constant AE rate for HS sample coincides with the end of the linearity between differential stress and volumetric strain (56%). At the end of the compression phase (point D) both samples showed a decrease in volume of 0.16%. For HS sample, AE events were 14% (~1600 AE) of the total amount of events, and the differential stress was 275 MPa meaning 77% of the strength. For JS sample, just before the slip occurred, AE events were 13-14% (~2500) of the total amount of AE events, and the differential stress was 253-257 MPa meaning 91-92% of the strength. At this point the behavior of both samples is quite similar, except that the JS sample exhibits ~1.6 times more AE events in absolute value. It would mean that the deformation at this stage induces more microcracks or slipping in the sample containing the joint than in the intact sample, and particularly within the healed joint.

The AE hypocenter locations (deduced from a number of sensors between 5 and 20) are shown in Figure 3 when the differential stress was 50 MPa and then 100 MPa and the final rupture plane is not yet localized. Another plot of the hypocenters when the differential stress was 250 MPa for HS sample and 200 MPa for JS sample, meaning the end of elastic phase (point E), shows the progression of the localization of the hypocenters on the final rupture plane. The final plane of rupture can already be seen in both experiments. Note that the AE distribution is distributed throughout the volume for HS sample but is planar on the preexisting joint for JS sample. The localization of the hypocenters at the end of the compression phase at 275 MPa and 260 MPa for HS and JS samples is shown as point D. At this point it is clearly shown that the future plane of rupture is already well localized before any dilatancy. Finally, the hypocenter locations are shown near the rupture (95% and 99% of strength, points P and F) (Figures 2 and 3) for HS sample and just at the slip and after the slip for JS sample (points S and F).

5. Discussion

Some observations showing that the start of AE activity corresponds to the onset of dilatancy, defined as the beginning of the nonlinear part of the axial stress-volumetric strain curve (volume increases relative to elastic changes), have been reported (*Scholz* [1968a] and *Meredith et al.* [1990] for a granite sample and *Takahashi and Abé* [1987]). On the other hand, AE activity prior to the onset of dilatancy has also been observed [*Scholz*, 1968b; *Kurita and Fujii*, 1979; *Gowd*, 1980; *Ohnaka and Mogi*, 1982; *Fonseka et al.*, 1985; *Meredith at al.*, 1990; *Kusunose et*

Table 2. *P* Wave Velocity Values During the Deformation for HS and JS Samples[a]

Differential Stress, MPa	P_V, km/s	P_{H1}, km/s	P_{H2}, km/s
	HS Sample		
0	5.00	5.26	5.49
9.9	5.66	6.25	5.95
34.9	5.84	6.10	5.99
59.9	5.88	5.99	6.02
84.9	5.95	6.02	6.10
109.9	5.96	6.17	6.02
159.8	5.95	5.99	6.02
209.8	5.88	6.02	5.95
259.7	5.95	5.88	5.95
314.7	6.04	5.65	5.75
	JS Sample		
0	5.86	5.70	5.70
39.9	5.90	5.70	5.70
59.9	5.97	5.70	5.70
209.8	5.97	5.70	5.70
234.7	6.00	5.50	5.50

[a] P_V is the vertical *P* wave velocity (maximum error of ±0.5% and ±0.35% for HS and JS samples, respectively), P_{H1} and P_{H2} are the horizontal *P* wave velocity (maximum error of ±0.2% and ±0.1% for HS and JS samples, respectively).

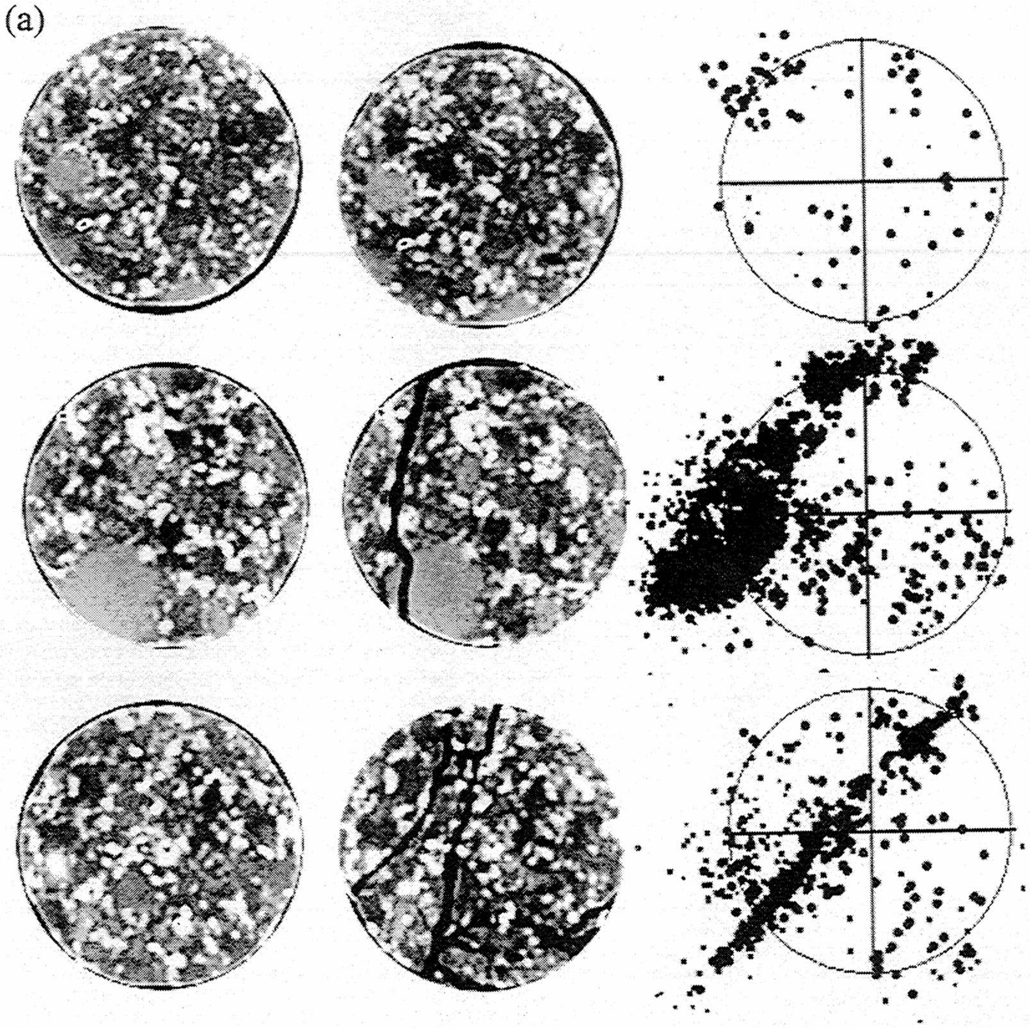

Figure 5. Scanner X images of three cross sections of (a) HS and (b) JS samples, (left) before the experiment, (middle) after the rupture, and (right) projections of the AE hypocenters. Diameter of the sample is 50 mm. Cross sections at the top and bottom are at 30 mm from the ends of the sample, and cross section in the middle corresponds to the middle of the sample. Diameter of cross sections is ~50 mm. Large grains are feldspar. Large black channel is the rupture.

al., 1991]. Such activity is associated with initial closure under compression of favorably oriented cracks already present, together with sliding of crack faces. Compaction-induced AE has been interpreted as due to friction between interlocking grains, the breaking of partially healed portions and asperities on preexisting crack surfaces during compaction, and closure of preexisting cracks under stress, at large angles to the compression axis [*Gowd*, 1980; *Meredith et al.*, 1990; *Ohnaka and Mogi*, 1982]. The permanent AE activity during our experiments, meaning the existence of AE activity well before the dilatancy, suggests that even a low-porosity rock such as a granite cannot be purely elastic in the linear part of the stress-strain curve because the generation of AE involves locally inelastic processes [*Ohnaka and Mogi*, 1982].

Then AE activity is usually found to increase exponentially when the deviatoric stress is increased [*Scholz*, 1968b; *Kurita and Fujii*, 1979; *Gowd*, 1980; *Ohnaka and Mogi*, 1982; *Meredith et al.*, 1990]. This increase in acoustic activity is usually attributed to atomic bond breaking and the creation of new stress-induced cracks that are successively produced [*Sondergeld and Estey*, 1981]. Then the rapid acceleration of AE activity before and during failure is usually explained by the growth process of large cracks and by their coalescence.

In some case, an apparent seismic quiescence is observed. *Liakopoulou-Morris et al.* [1994] measured the AE during the fault nucleation and sliding and strengthening of a sandstone sample under constant strain rate. They showed that during the fault nucleation the AE event rate increased very slowly in the linear quasi-elastic phase and accelerated markedly in the strain-hardening phase, consistent with dilatant microcrack growth. During the period of postpeak strain softening, a decrease in AE events was observed, implying an apparent seismic quiescence. During the sliding phase, characterized by a relatively constant differential stress, the variations in AE rate were much smaller than in the nucleation phase. In the case of HS sample, no stress decrease was measured, as can be observed in postpeak strain softening, implying coalescence of existing microcracks to form a throughgoing fault. In the case of JS sample the slip was different from stable sliding under quasi-constant differential stress usually observed after postpeak strain softening and

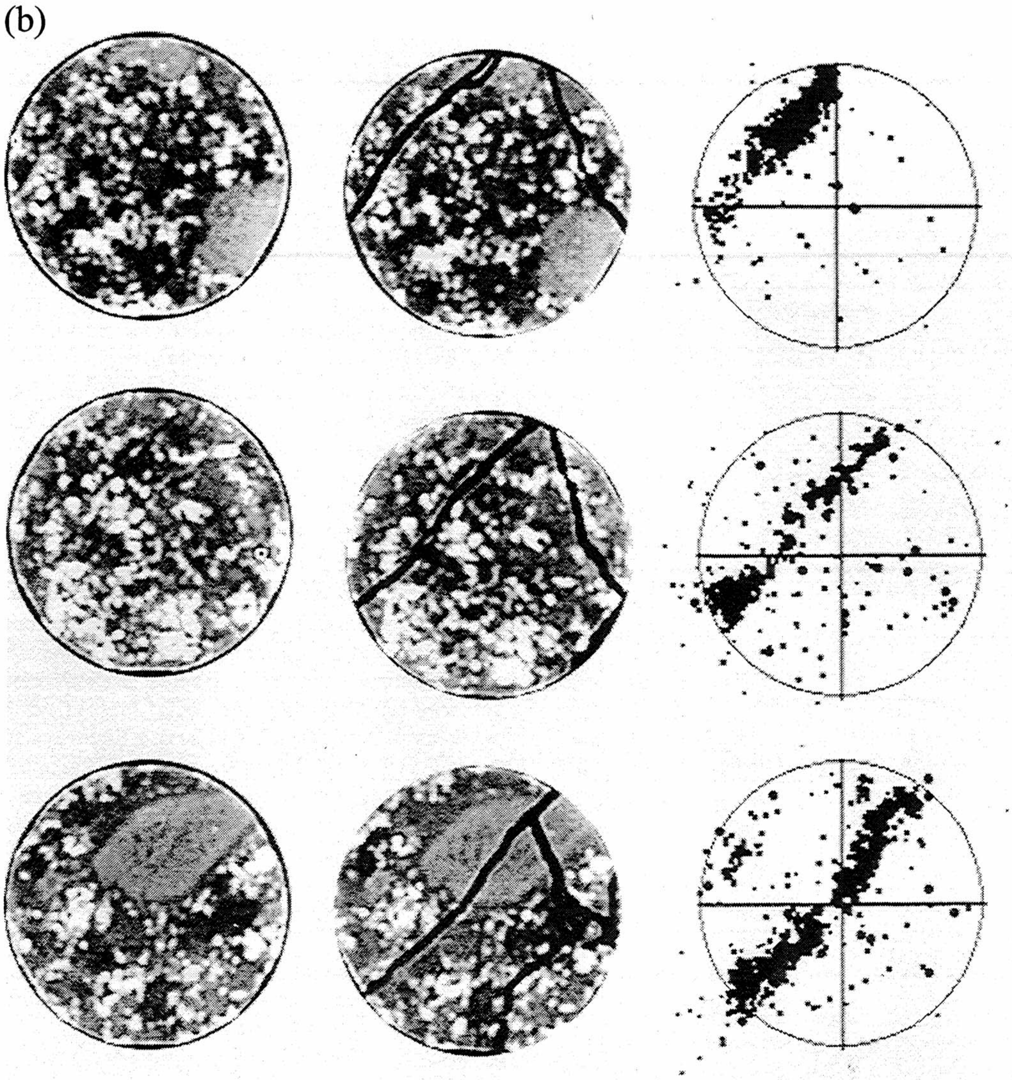

Figure 5. (continued)

unstable dynamic failure [*Gowd*, 1980; *Meredith et al.*, 1990; *Liakoupoulou-Morris et al.*, 1994; *Baddari et al.*, 1996]. The slip of the healed joint of JS sample occurred under a drop of differential stress of ~0.3 MPa. *Meredith et al.* [1990] noted that only when a period of strain softening preceded dynamic rupture, was AE rate flattenned and decreased to a period of apparent seismic quiescence. Since a post peak strain softening was not observed in our experiments, the absence of a kind of quiescence is not in contradiction with these earlier observations.

The early localization of the main final rupture plane, well before dilatancy (see points E and D in Figures 2 and 3), deduced from the hypocenters of the AE measurements in our experiments of fracturation in one hand, and of slipping in the other hand, differs from the usual inference from previous studies [e.g., *Scholz*, 1968c]. Indeed, during a cyclic loading experiment on Oshima granite [*Satoh et al.*, 1990] the AE hypocenters did not concentrate preferentially on the ultimate fracture planes, but they concentrated around a part of the main fault plane prior to the ultimate fracture. The sample fractured in a brittle manner, and there was no postpeak stage. The AE hypocenters formed a number of clusters in which hypocenters aligned in the directions parrallel or conjugate to the main fault. *Satoh et al.* [1990] concluded that the most plausible mechanisms of fault development was shear linking of an axial crack array [*Wong*, 1982]. In triaxial compression experiments on granite and sandstone samples by controlling axial stress to maintain constant AE rate, the fault growth and shear fracture have been followed quasi-statically [*Lockner et al.*, 1991, 1992]. In that case the postpeak weakening curve corresponds to propagation of the macroscopic fault plane across the sample, and microcracking, as determined by AE locations, remained uniformly distributed in the central portion of the granite samples until after peak stress. The low and uniformly distributed events reflected homogeneous microcracking during the loading phase. There was no obvious precursor in AE event locations (meaning clustering of AE) to indicate the position of the nucleation zone, so that it was concluded that microcracks were sparse and damage remained diffuse until near peak stress. Note that in sandstone samples, significant AE was occurring by ~40% of peak stress and was interpreted as indicating the presence of a weak zone. In another experiment of symmetric loading of granite sample the clustering of events was also found only after the failure [*Zang et al.*, 1998]

When some precursor localization (meaning precursor

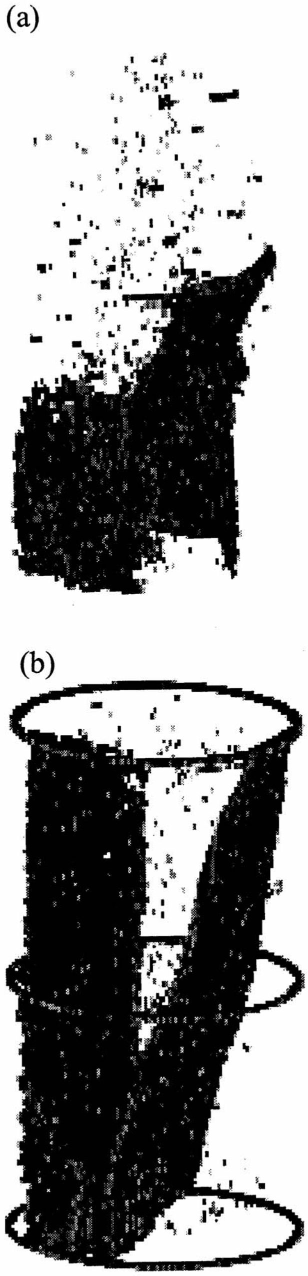

Figure 6. Three-dimensional scanner X image of the fracture planes of samples (a) HS and (b) JS. Length and diameter of the sample are 100 mm and 50 mm, respectively.

behavior of AE) is observed, it is usually deduced that it is induced by a weak zone. For example, during the uniaxial cycling of a Westerly granite sample, strong spatial clustering of hypocenters has been observed and was thought to be induced by nonhomogeneous dilatancy development [*Sondergeld and Estey*, 1981]. During another triaxial creep experiment on amphibolite [*Satoh et al.*, 1996], precursory localization of AE hypocenters was observed. This precursory nucleation and development of a macroscopic fracture plane was induced by a preexisting macroscopic defect. Moreover, no significant precursory localization of AE hypocenters on the final fracture plane before failure has been reported in rock sample free of preexisting macroscopic defects. In another experiment, when deforming a granite sample under uniaxial compression with a constant stress rate, *Shah and Labuz* [1995] observed that the microseismic activity was more or less uniformly distributed on the sample until ~85% of the maximum loading, when concentration of AE hypocenters was observed.

In both cases of HS sample and JS sample the precursory localization of the final rupture plane is clearly observed as soon as the end of the pseudo-elastic phase (E point in Figure 2) and well before the dilatancy (D point), meaning that the damage does not remain diffuse and uniformly distributed. In the case of JS sample the healed joint controls the stress heterogeneity and therefore the final rupture, and the AE distribution is planar. In the case of HS sample the heterogeneity in grain size controls the stress heterogeneity and therefore the rupture nucleation, and the AE distribution is volumic distributed.

Scanner X images of the cross sections of our granite samples have been performed, before and after the experiment (Figure 5), and have been rebuilded in three dimensions (Figure 6). Minerals and grain sizes of this granite are very different, from 1 mm to 3 cm. Large grains in Figure 5 are feldspar. This inhomogeneity may be a main difference of our experiment compared to other samples used in previous experiments. It is likely that the grain-scale inhomogeneity and differences in elastic moduli between minerals can influence the local stress field significantly. Geometry of the fracture can be seen in Figure 6 and corresponds to the AE distribution plotted in Figure 4. For JS sample the plane indicated by AE location was formed during the deformation of the rock. The other plane (Figure 6b) was formed just before the final rock fracture in the very short time or at the same time of the final fracture. That is why this plane is not accompanied by AE and its location is very close (and parallel) to the surface.

An interpretation of fault growth, based on optical and scanning electron microscope observation of Berea sandstone samples retrieved at different stages of deformation, has been proposed by *Menendez et al.* [1996]. They observed that in the brittle regime, shear localization does not develop until the postfailure stage and that very little intragranular cracking occurred before the peak stress was attained. As stress concentrations at grain contacts are not sufficient to initiate stress-induced extensile cracking, they proposed that the local *shear* stress concentrations are sufficiently high to cause the grains to move relative to one another by rotation and slip. This intergranular cracking, probably related to the shear rupture of cemented grain contacts, could also induce dilatancy and AE activity in the prefailure stage. Then, in the close vicinity of the peak stress, intragranular fractures develop in isolated clusters, and the coalescence of a high density of clusters results in shear localization [*Menendez et al.*, 1996]. Note that this study was performed on Berea sandstone of relative high porosity compared to the low-porosity rock granite used here.

Whatever is the exact mechanism involved in the fracturing (HS sample) and in the slipping (JS sample) of our granite samples, the acoustic emission hypocenters are localized on the final rupture plane in the early stage of deformation process, involving locally inelastic processes. It is likely that not only initial closure of favorably oriented cracks but also breaking of partially cemented grains contacts or sliping between grains may occur in the pseudoelastic phase, distributed on the final rupture plane, where the shear stress seems to be concentred. This behavior is observed in both cases where stress heterogeneity and rupture nucleation are controlled by (1) medium-scale heterogeneity at the grain scale (HS sample) or (2) macroscopic heterogeneity in the form of a preexisting healed joint (JS sample).

6. Conclusion

Localization of the rupture in one experiment and localization of the slip of a preexisting macroscopic healed joint in the other experiment, on the granite from Mayet de Montagne, have been observed in the early stage of deformation, whatever controls the stress heterogeneity and rupture nucleation: (1) medium-scale heterogeneity at the grain scale (HS sample) or (2) macroscopic heterogeneity in the form of a preexisting healed joint (JS sample). Since the early localization of the rupture was not reported in previous experiments in the literature, using other samples with a smaller grain size to sample ratio, a comparison should be made on different granite samples with various grain sizes and various degrees of heterogeneity, using the same technology, in order to understand the different behaviors of the different granite samples.

Acknowledgments. F. Cornet (IPGParis) is thanked for providing the granite samples from Mayet de Montagne (France). The initial project of these experiments has benefitied from discussions with M. Zamora and J.-P. Pozzi (ENS Paris). We thank Pierre Bésuelle for fruitful discussions. This paper was greatly improved by the associate editor Ian Main. We thank S. Yoshida for his review. This research is a CNRS-INSU-PNRN contribution 258 (Thème risques sismiques) and was partly supported by CNRS and ANDRA through the GdR FORPRO (Research Action 99-VIII) and corresponds to the GdR FORPRO contribution 2000/17 A.

References

Ashby, M.F., and S.D. Hallam, The failure of brittle solids containing small cracks under compressive stress states, *Acta Metall.*, *34*, 497-510, 1986.

Ashby, M.F., and C.G. Sammis, The damage mechanics of brittle solids in compression, *Pure Appl. Geophys.*, *133*, 489-521, 1990.

Baddari, K., G. A. Sobolev, and A.D. Frolov, Similarity in seismic precursors at different scales, *C. R. Acad. Sci. Paris, Ser. IIa*, *323*, 755-762, 1996.

Brace, W.F., B.W. Paulding, and C. Scholz, Dilatancy in the fracture of crystalline rocks, *J. Geophys. Res.*, *71*, 3939-3953, 1966.

Byerlee, J., Frictional characteristics of granite under high confining pressure, *J. Geophys. Res.*, *72*, 3639-3647, 1967.

Byerlee, J., Friction of rocks, *Pure Appl. Geophys.*, *116*, 615-626, 1978.

Clavaud, J.B., M. Zamora, F. Cornet, G. Michard, P. Zuddas, J.M. Boffa, and J.P. Hulin, Permeability change by dissolution or precipitation effects in granite with a single fracture, paper presented at XXV General Assembly, Eur. Geophys. Soc., Nice, France, 2000.

Costin, L.S., A microcrack model for the deformation and failure of brittle rock, *J. Geophys. Res.*, *88*, 9485-9492, 1983.

Dieterich, J.H., Time-dependent friction in rocks, *J. Geophys. Res.*, *77*, 3690-3697, 1972.

Fonseka, G.M., S.A.F. Murell, and P. Barnes, Scanning electron microscope and acoustic emission studies of crack development in rocks, *Int. J. Rock Mech. Min. Sci. Geomech. Abstr.*, *22*, 273-289, 1985.

Gowd, T.N., Factors affecting the acoustic emission response of triaxially compressed rock, *Int. J. Rock Mech. Min. Sci. Geomech. Abstr.*, *17*, 219-223, 1980.

Jaeger, J.C., The frictional properties of joints in rock, *Geofis. Pura Appl.*, *43*, 148-158, 1959.

Kurita, K., and N. Fujii, Stress memory of crystalline rocks in acoustic emission, *Geophys. Res. Lett.*, *6*, 9-12, 1979.

Kusunose, K, X. Lei, O. Nishizawa, and T. Satoh, Effect of grain size on fractal structure of acoustic emission hypocenter distribution in granitic rock, *Phys. Earth Planet. Inter.*, *67*, 194-199, 1991.

Lei, X., O. Nishizawa, T. Satoh, and K. Kusunose, An AE data processing program for windows (in Japanese with English abstract), *Bull. Geol. Surv. Jpn.*, *48*, 447-457, 1997.

Lei, X., K. Kusunose, M.V.M.S. Rao, O. Nishizawa, and T. Satoh, Quasi-static fault growth and cracking in homogeneous triaxial compression using acoustic emission monitoring, *J. Geophys. Res.*, *105*, 6127-6139, 2000.

Liakopoulou-Morris, F., I.G. Main, B.R. Crawford, and B.G.D. Smart, Microseimic properties of a homogeneous sandstone during fault nucleation and frictional sliding, *Geophys. J. Int.*, *119*, 219-230, 1994.

Lockner, D., The role of Acoustic emission in the study of rock fracture, *Int. J. Rock Mech. Min. Sci. Geomech. Abstr.*, *30*, 883-899, 1993.

Lockner, D.A., and J.D. Byerlee, How geometrical constraints contribute to the weakness of mature faults, *Nature*, *363*, 250-252, 1993.

Lockner, D.A., J.D. Byerlee, V. Kuksenko, A. Ponomarev, and A Sidorin, Quasi-static fault growth and shear fracture energy in granite, *Nature*, *350*, 39-42, 1991.

Lockner, D.A., J.D. Byerlee, V. Kuksenko, A. Ponomarev, and A. Sidorin, Observations of quasistatic fault growth from acoustic emissions, in *Fault Mechanics and Transport Properties of Rocks*, edited by B. Evans and T.-F. Wong, pp. 3-29, Academic, San Diego, Calif., 1992.

Main, I.G., A modified Griffith criterion for the evolution of damage with a fractal distribution of crack lengths: Application to seismic event rates and *b*-values, *Geophys. J. Int.*, *107*, 353-362, 1991.

Marone, C., C. B. Raleigh, and C.H. Scholz, Frictional behavior and constitutive modeling of simulated fault gouge, *J. Geophys. Res.*, *95*, 7007-7025, 1990.

Masuda, K., O. Nishizawa, K. Kusunose, T. Satoh, M. Takahashi, and R.L. Kranz, Positive feedback fracture process induced by nonuniform high-pressure water flow in dilatant granite, *J. Geophys. Res.*, *95*, 21,583-21,592, 1990.

Menendez, B., W. Zhu, and T.-F. Wong, Micromechanics of brittle faulting and cataclastic flow in Berea sandstone, *J. Struct. Geol.*, *18*, 1-16, 1996.

Meredith, P.G., I.G. Main, and C. Jones, Temporal variations in seismicity during quasi-static and dynamic rock failure, *Tectonophysics*, *175*, 249-268, 1990.

Moore, D.E., and D.A. Lockner, The role of microcracking in shear-fracture propagation in granite, *J. Struct. Geol.*, *17*, 95-114, 1995.

Nemat-Nasser, S., and H. Horii, Compression-induced nonplanar crack extension with application to splitting, exfoliation, and rockburst, *J. Geophys. Res.*, *87*, 6805-6821, 1982.

Nicolas, A., *Principes de Tectonique*, Masson, Paris, 1984.

Nishizawa, O., New multi-wire type and co-axial type feedthroughs for an oil pressure-medium vessel (in Japanese with English abstract), *Bull. Geol. Surv. Jpn.*, *48*, 431-438, 1997.

Ohnaka, M., and K. Mogi, Frequency characteristics of acoustic emissions in rocks under triaxial compression and its relation to the fracturing process to failure, *J. Geophys. Res.*, *87*, 3873-3884, 1982.

Reches, Z., and D.A. Lockner, Nucleation and growth of faults in brittle rocks, *J. Geophys. Res.*, *99*, 18,159-18,173, 1994.

Rudnicki, J.W., and C.H. Chen, Stabilization of rapid frictional slip on a weakening fault by dilatant hardening, *J. Geophys. Res.*, *93*, 4745-4757, 1988.

Satoh, T., and O. Nishizawa, A high speed, multi-channel waveform recording system for AE measurement (in Japanese with English abstract), *Bull. Geol. Surv. Jpn.*, *48*, 439-446, 1997,

Satoh, T., K. Kusunose, and O. Nishizawa, A minicomputer system for measuring and processing AE waveforms-High speed digital recording and automatic hypocenter determination (in Japanese with English abstract), *Bull. Geol. Surv. Jpn.*, *38*, 295-303, 1987.

Satoh, T., O. Nishizawa, and K. Kusunose, Fault development in Oshima granite under triaxial compression inferred from hypocenter distribution and focal mechanism of acoustic emission, *Tôhoku Geophys. J., Sci. Rep. Tôhoku Univ., Ser. 5*, *33*, 241-250, 1990.

Satoh, T., K. Shivakumar, O. Nishizawa, and K. Kusunose, Precursory localization and development of microfractures along the ultimate fracture plane in amphibolite under triaxial creep, *Geophys. Res. Lett.*, *23*, 865-868, 1996.

Scholz, C.H., The frequency-magnitude relation of microfracturing in rock and its relation to earthquakes, *Bull. Seismol. Soc. Am.*, *58*, 399-415, 1968a.

Scholz, C.H., Microfracturing and the inelastic defomation of rock in compression, *J. Geophys. Res.*, *73*, 1417-1432, 1968b.

Scholz, C.H., Experimental study of the fracturing process in brittle rock, *J. Geophys. Res.*, *73*, 1447-1454, 1968c.

Scholz, C. H., *The Mechanisms of Earthquakes and Faulting*, pp. 53-66, Cambridge Univ. Press, New York, 1990.

Shah, K.R., and J.F. Labuz, Damage mechanisms in stressed rock from acoustic emission, *J. Geophys. Res.*, *100*, 15,527-15,539, 1995.

Sondergeld, C.H., and L.H. Estey, Acoustic emission study of microfracturing during the cyclic loading of Westerly granite, *J. Geophys. Res.*, *86*, 2915-2924, 1981.

Takahashi, H., and H. Abé, Fracture mechanics applied to hot, dry rock geothermal energy, in *Fracture Mechanics of Rock*, edited by B.K. Atkinson, pp. 254-257, Academic, San Diego, Calif., 1987.

Tapponier, P., and W.F. Brace, Development of stress-Induced microcracks in Westerly granite, *Int. J. Rock Mech. Min. Sci. Geomech. Abstr.*, *13*, 103-112, 1976.

Wong, T.-F., Micromechanics of faulting in Westerly granite, *Int. J. Rock Mech. Min. Sci. Geomech. Abstr.*, *19*, 49-64, 1982.

Yokota, T., S. Zhou, M. Mizoue, and I. Nakamura, An automatic measurement of arrival time of seismic waves and its application to an on-line processing system (in Japanese with English abstract), *Bull. Earthquake Res. Inst. Univ. Tokyo*, *55*, 449-484, 1981.

Zang, A., F.C. Wagner, S. Stanchits, G. Dresen, R. Andresen, and M.A., Haidekker, Source analysis of acoustic emissions in Aue granite cores under symmetric and asymmetric compressive loads, *Geophys. J. Int.*, 135, 1113-1130, 1998.

L. Jouniaux, Laboratoire de Géologie de l'Ecole Normale Supérieure de Paris, UMR 8538, 75231 Paris Cedex 05, France. (jouniaux@geologie.ens.fr)

K. Kusunose, X. Lei, K. Masuda, and O. Nishizawa, Geological Survey of Japan, Higashi 1-1-3, Tsukuba, Ibaraki 305, Japan. (kin@gsj.go.jp; lei@gsj.go.jp; masuda@gsj.go.jp; osamu@gsjkouji.gsj.go.jp)

L. Liu and W. Ma, Institute of Geology and Laboratory of Tectonophysics, China Seismological Bureau, Beijing, China.

(Received February 28, 2000; revised October 25, 2000;
accepted November 6, 2000.)

PRÉVISION DES SÉISMES : VERS UNE MÉTHODE FIABLE ?

LES VARIATIONS ANORMALES DU CHAMP ÉLECTRIQUE TERRESTRE QUI PRÉCÈDENT SOUVENT LES SÉISMES CONSTITUENT-ELLES UN MOYEN FIABLE DE PRÉVISION ?

Parmi les nombreux signaux précurseurs des séismes, il est fréquent de détecter des anomalies du champ électrique de la Terre. On a donc cherché à les exploiter pour mettre au point une méthode fiable de prévision des séismes. La plus célèbre et la plus controversée est la méthode VAN élaborée par trois physiciens grecs dans les années 1980 (voir « Prévision des séismes : la longue marche des physiciens grecs » dans *La Recherche* de juin 1986). P. Varotsos, K. Alexopoulos et K. Nomicos défendent l'idée que tout séisme est précédé d'un signal électrique anormal, mesurable par des électrodes implantées dans le sol, et que la date et le lieu de tout tremblement de terre peuvent être déterminés avec une bonne précision(1). Cependant, certains séismes n'ont pas été prévus par la méthode VAN tel que celui de Kalamata, en Grèce, le 13 septembre 1986, pourtant particulièrement destructeur (voir « La méthode VAN pour la prédiction des séismes : pourquoi les géophysiciens sont-ils sceptiques ? » dans *La Recherche* de mars 1990). Comment adhérer totalement à la méthode si elle ne prévoit pas tous les tremblements de terre ? De grands progrès restent donc à accomplir avant que ce genre de démarche ne soit entièrement fiable.

En particulier, les mécanismes physiques responsables de ces signaux électriques restent un sujet de controverse. Afin de mieux les comprendre, Laurence Jouniaux et Jean-Pierre Pozzi, du laboratoire de géologie de l'Ecole normale supérieure à Paris, ont effectué récemment des mesures de potentiel électrique et de perméabilité sur des échantillons de grès de Fontainebleau(2). Ces travaux étaient destinés à étudier les phénomènes électriques liés aux circulations de fluides (eau et sels dissous) dans les roches. Au moment des tremblements de terre, on observe souvent des perturbations qui sont dues à la déformation des roches. Ainsi, après un séisme, le débit des sources peut augmenter de façon importante. Or ces circulations de fluides peuvent créer des variations de potentiel électrique, comme l'a montré une équipe japonaise dès 1976(3). C'est le phénomène de l'électrofiltration : quand un liquide circule à travers un milieu perméable, on y mesure une différence de potentiel due à des interactions entre le solide et le liquide. Le phénomène d'électrofiltration est l'un des mécanismes physiques envisagés actuellement pour expliquer les signaux électriques précurseurs des séismes. Peut-on montrer qu'il s'agit bien de ce phénomène ? Quels sont les facteurs qui influencent les variations du potentiel d'électrofiltration ? Peut-on en déduire quelles sont, sur le terrain, les configurations les plus favorables pour mesurer ces signaux électriques anormaux ? Les récents travaux en laboratoire de L. Jouniaux et J.P. Pozzi, en tentant de répondre à toutes ces questions, permettent de mieux comprendre les relations entre signaux électriques et circulations de fluides dans les roches et de les quantifier dans un cas proche des mesures sur le terrain, d'où le choix de sédiments ordinaires comme les grès de Fontainebleau. Jusqu'à présent, ce type d'expériences n'avait pas été réalisé sur des roches intactes mais sur des roches ou minéraux broyés(4), situation peu conforme à la réalité.

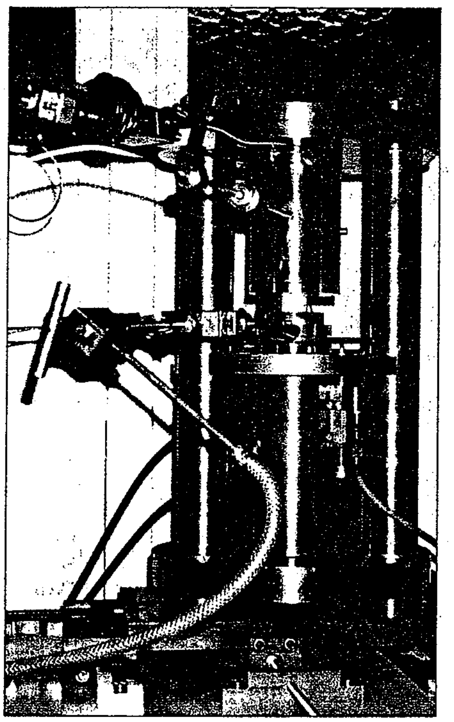

Figure 1. On mesure fréquemment avant les séismes des signaux électriques anormaux. L'un des mécanismes physiques envisagés actuellement est en rapport avec la circulation des fluides de la croûte terrestre, souvent perturbée au moment des tremblements de terre. Ces circulations de fluides peuvent créer des variations de potentiel électrique. Dans le but d'étudier ce phénomène, appelé électrofiltration, de récentes expériences ont été réalisées au laboratoire de géologie de l'Ecole normale supérieure à Paris sur de petits échantillons de grès de Fontainebleau. Le rôle des fluides de la croûte terrestre est joué par de l'eau distillée. Un piston applique une pression verticale sur l'échantillon. Celui-ci se déforme alors progressivement jusqu'à sa rupture qui représente un véritable minitremblement de terre. Ces expériences permettent de mieux comprendre les relations qui existent entre la déformation des roches avant un séisme, la circulation des fluides et les signaux électriques. (Cliché L. Jouniaux/ENS Paris)

Les variétés de grès ont été sélectionnées pour couvrir une gamme de perméabilités la plus vaste possible. Chaque échantillon cylindrique, de cinq centimètres de hauteur, est saturé en eau distillée, laquelle joue le rôle des fluides de la croûte terrestre. Sa circulation est induite par une différence de pression aux deux extrémités du petit cylindre (fig. 1). Un premier type d'expériences, sans déformer l'échantillon, montre que plus celui-ci est perméable, plus son potentiel d'électrofiltration est fort(2). Dans un deuxième temps, une presse applique une pression verticale sur l'échantillon. Celui-ci se déforme progressivement jusqu'à sa rupture. A son échelle, cette rupture représente un véritable petit tremblement de terre. Dans ce deuxième type d'expériences, on sait que la déformation se traduit d'abord par une compaction, puis par l'apparition de microfissures, ce qui entraîne des changements de la perméabilité. En effet, la compaction diminue la perméabilité alors que l'apparition de microfissures l'augmente, et plus particulièrement juste avant la rupture (fig. 2). Le potentiel d'électrofiltration reste alors stable jusqu'à l'apparition des fissures et augmente ensuite fortement jusqu'à la rupture.

Qu'apportent ces résultats, un peu arides à première vue, à la compréhension des variations du champ électrique enregistrées avant un séisme ? Tout d'abord, ces expériences montrent que la perméabilité est un paramètre qui influence fortement le comportement du potentiel d'électrofiltration. On peut donc s'attendre, sur le terrain, à mesurer un potentiel d'électrofiltration d'autant plus élevé que la roche est perméable, toutes choses égales par ailleurs. En outre, à proximité de la faille, de même que dans l'échantillon, la perméabilité évolue au cours de la déformation précédant le séisme et peut alors entraîner

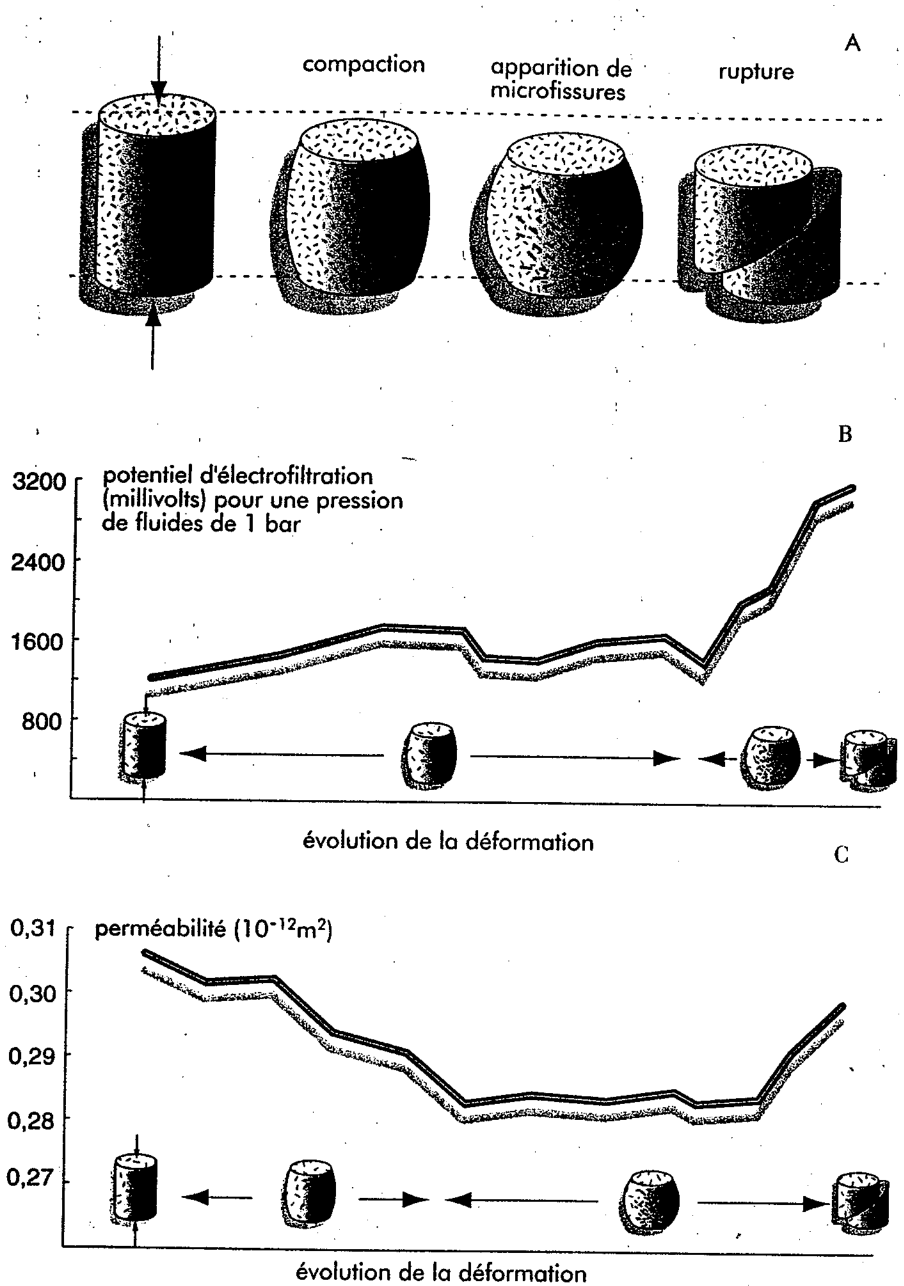

© LA RECHERCHE

Figure 2. Dans les expériences où l'on déforme l'échantillon, la déformation se traduit d'abord par une compaction, puis par l'apparition de microfissures (A), ce qui entraîne des changements de la perméabilité. En effet, la compaction diminue la perméabilité alors que l'apparition de microfissures l'augmente, et plus particulièrement juste avant la rupture (B). Le potentiel d'électrofiltration reste alors stable jusqu'à l'apparition des fissures et augmente ensuite fortement jusqu'à la rupture (C). Ces expériences montrent que la perméabilité est un paramètre qui influence les variations du potentiel d'électrofiltration et confirment que celui-ci est un bon signal précurseur de séisme, grâce à sa brusque augmentation juste avant la rupture.

des variations du potentiel d'électrofiltration. Les résultats obtenus confirment ainsi que grâce à sa forte augmentation juste avant la rupture, le potentiel d'électrofiltration est un bon signal précurseur des séismes.

L. Jouniaux et J.-P. Pozzi proposent également un mécanisme pour expliquer les variations anormales enregistrées à grande distance de l'épicentre. En effet, une des objections faites au phénomène de l'électrofiltration concerne la déformation due au futur séisme à de grandes distances de la faille. On estime que cette déformation y est généralement trop faible pour entraîner des mouvements de fluides suffisants(5). Pourtant, des variations du potentiel électrique sont enregistrées loin de l'épicentre. Une équipe de chercheurs de l'Institut de physique de la Terre à Moscou a montré en 1989 que des circulations d'eau horizontales dans une nappe phréatique ne peuvent pas provoquer d'importants potentiels électriques en surface loin des régions épicentrales(6). Des mouvements d'eau verticaux sont nécessaires. C'est ce que suggèrent L. Jouniaux et J.-P. Pozzi par l'intermédiaire d'échanges entre les nappes aquifères profondes et superficielles. Dans leurs expériences, l'intensité du potentiel d'électrofiltration peut atteindre cinquante millivolts pour une différence de pression de fluide aussi faible que dix millibars, pression typiquement mesurée à la base d'une colonne de dix centimètres d'eau. Loin de l'épicentre, des mouvements de fluides même extrêmement faibles, comme la baisse de niveau d'une nappe phréatique de dix centimètres, peuvent donc engendrer des signaux tout à fait mesurables.

Enfin, ces expériences apportent des résultats importants pour mesurer les variations du potentiel d'électrofiltration dans les meilleures conditions. Nous avons vu que, à circulation de fluides et déformation de la roche égales, plus une roche est perméable plus son potentiel d'électrofiltration est fort. Sur le terrain, on mesure une différence de potentiel entre deux électrodes. Si les perméabilités des roches autour des deux électrodes sont identiques, la différence des deux potentiels sera négligeable. En revanche, si les perméabilités sont très différentes, la différence de potentiel sera très élevée. Or il est classique dans une même formation géologique que la perméabilité varie d'un facteur mille d'un point à un autre. Cette condition de variation de perméabilité est donc très facile à satisfaire sur le terrain. Jusqu'à présent, on recherchait la présence d'une hétérogénéité latérale, faille ou terrains différents, afin d'obtenir une différence de potentiel significative, condition plus difficile à obtenir.

En simulant des mini tremblements de terre sur quelques centimètres cubes de grès saturés en eau distillée, ces expériences se révèlent donc fondamentales pour comprendre les causes physiques des signaux électriques précurseurs des séismes. Cependant, le pas entre le laboratoire et le terrain reste à franchir, la nature étant plus complexe que prévu… Ces résultats prometteurs sur des roches et des fluides simples ne peuvent qu'inciter à continuer dans cette voie sur des échantillons plus hétérogènes et de plus grande taille. Ainsi, c'est dans ce sens que vont P. Morat et J.-P. Le Mouël de l'Institut de physique du globe de Paris qui s'intéressent actuellement aux mêmes phénomènes mais à une échelle plus grande, celle d'une carrière de calcaires(7). Il reste à espérer que les chercheurs seront bientôt en mesure de nous indiquer où planter nos électrodes pour détecter des signaux électriques précurseurs des séismes, interprétables à coup sûr.

FLORENCE JESTIN

(1) P. Varotsos et K. Alexopoulos, *Tectonophysics, 110*, 73, 1984.
(2) L. Jouniaux et J.P. Pozzi, *J. Geophys. Res.*, 1994-1995.
(3) H. Mizutani *et al., Geophys. Res. Letters*, 3, 365, 1976.
(4) F.D. Morgan *et al., J. Geophys. Res., 94*, 12449, 1989.
(5) P. Bernard, *J. Geophys. Res., 97*, 17531, 1992.
(6) I.P. Dobrovolsky *et al., Phys. Earth Planet. Inter, 57*, 144, 1989.
(7) P. Morat et J.-L. Le Mouël, *C.R.A.S., 315*, II, 955, 1992.

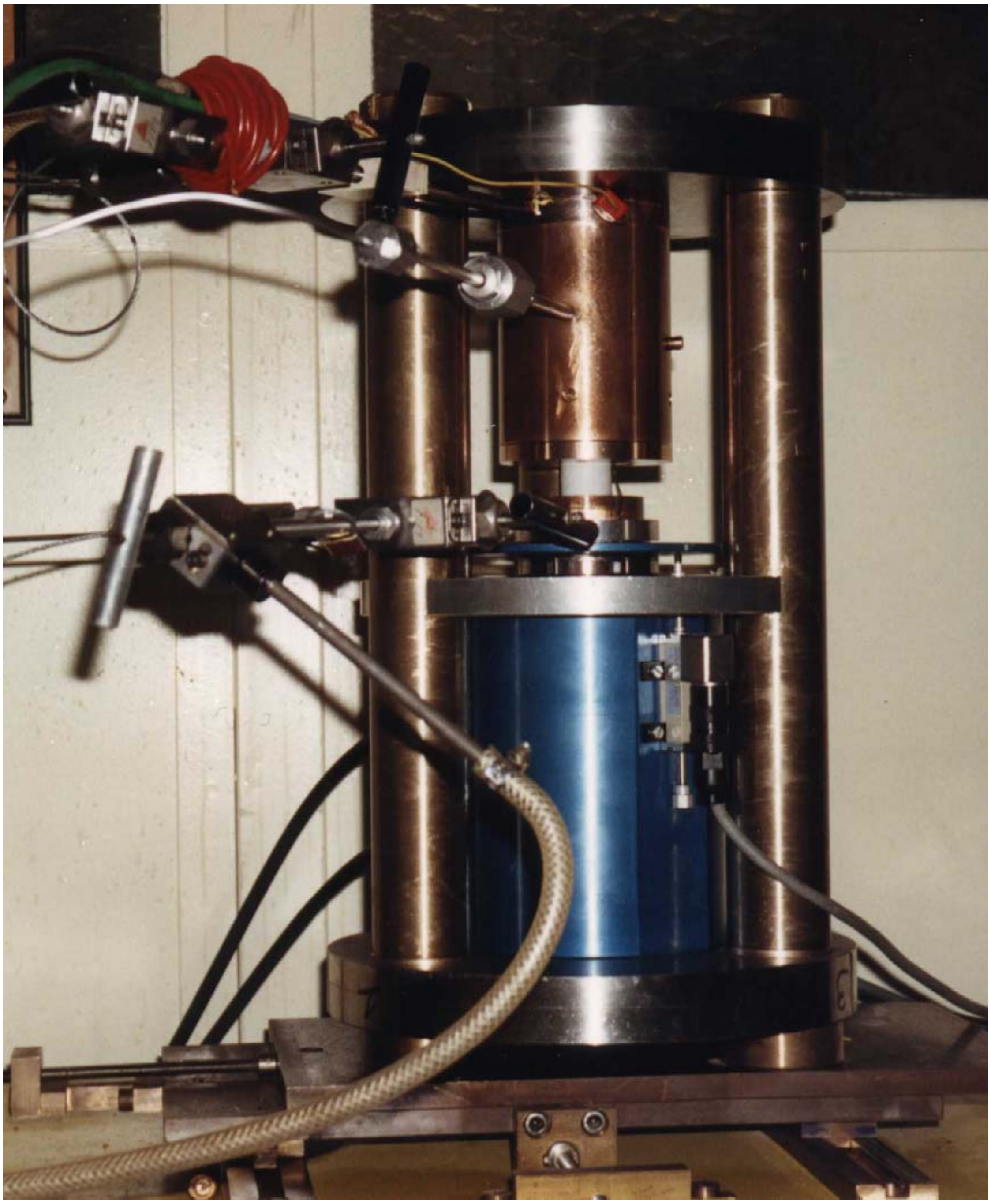

JOURNAL OF GEOPHYSICAL RESEARCH, VOL. 100, NO. B6, PAGES 10,197–10,209, JUNE 10, 1995

Streaming potential and permeability of saturated sandstones under triaxial stress: Consequences for electrotelluric anomalies prior to earthquakes

Laurence Jouniaux and Jean-Pierre Pozzi

Laboratoire de Géologie, Ecole Normale Supérieure, Paris

Abstract. The streaming potential, due to fluid circulation in rock, was measured on saturated sediments (Fontainebleau sandstones). The electrokinetic coupling coefficient, which is the ratio of the streaming potential and the excess pore pressure, is proportional to the fluid resistivity. Additionally, for a fluid conductivity of 10^{-3} S/m, the electrokinetic coupling coefficient varies from 10 to 6642 mV/0.1 MPa for sample permeability in the range of permeabilities from 0.15×10^{-15} to 1220×10^{-15} m^2. The different values of the electrokinetic coupling coefficient have been explained by the effect of increasing surface conductivity which becomes nonnegligible compared to fluid conductivity for low permeability. When the sample is deformed under triaxial stress up to failure, the vertical permeability (along the principal stress) drops by about 0.20%/0.1 MPa when failure occurs. The typical variation of the electrokinetic coupling coefficient is a large increase beginning with the onset of the localization of the shear band at about 75% of the yield stress and stopping at the failure. This increase of the electrokinetic coupling coefficient is due to an increase of ζ potential in the shear zone when new surfaces are created and connected. Possible consequences of our results are given concerning the electrical fields which could appear during the preparation of an earthquake. It is shown that in some cases, self-potential anomalies reported in the deformed zone preceding an earthquake occurrence could be due to an increase of the electrokinetic coupling coefficient from 75% of the yield stress to rupture in the vicinity of one of the electrodes. Any variation of fluid resistivity or permeability in the vicinity of one electrode could change the electrokinetic coupling coefficient, inducing a surface electrokinetic potential anomaly. In regard to the interpretation of the electrokinetic effect which occurs at large distance from the epicenter, a larger electrokinetic potential anomaly could be measured between electrodes situated along a vertical fluid flow, for instance, in a shallow borehole. An electrokinetic potential anomaly up to 30 mV, for a fluid conductivity of 0.01 S/m and a rock permeability of 10^{-12} m^2, could be observed with a change of the underground water table level as slight as 50 cm (50 mbar). Moreover, if the permeability between the electrodes is increased by a factor of 8×10^3, the electrokinetic coupling coefficient could be enhanced by a factor up to 650.

Introduction

Surface observations of self-potential (SP) anomalies have been reported from numerous tectonically active areas in the world. Electrotelluric precursors to earthquakes appear from a few minutes to several days before the seism and can be observed as far as 300 km from the epicenter, with an intensity ranging from 10 to 100 mV. The correlation of SP anomalies with earthquake occurrences has often been emphasized as a possible means for predicting earthquakes [*Mizutani et al.*, 1976; *Corwin and Morrison*, 1977; *Ishido and Mizutani*, 1981; *Varotsos and Alexopoulos*, 1984a, b].

SP anomalies can be produced by a streaming potential, as a consequence of fluid pressure gradients; by a thermoelectric potential, as a consequence of a temperature gradient; by a chemical potential, as a consequence of a chemical gradient; or by these effects possibly acting together. The streaming potential effect in the crust may be a promising model to explain low-frequency electric and magnetic precursors to earthquakes. These electrokinetic effects may be produced by fluid percolation in the crust, driven by a pore pressure gradient related to precursory deformation. This model was first proposed by *Mizutani et al.* [1976], who assumed that dilatancy prior to earthquakes [*Nur*, 1972; *Scholz et al.*, 1973] enhances the permeability of the medium and allows the fluid to flow in the vicinity of the fault. *Murakami et al.* [1984] reported self-potential anomalies associated with an active fault, and anomalous time variations of the self-potential in the fractured zone of an active fault preceding the earthquake occurrence were measured [*Miyakoshi*, 1986]. *Dobrovolsky et al.* [1989] proposed a long-distance elastic effect inducing the fluid flow and an electrokinetic effect near the electrodes. *Bernard* [1992] proposed an electrokinetic model based on the triggering of fluid instabilities by strain perturbation. However, the long-distance effects are still controversial, as their observation requires the coincidence of very favorable circumstances to

Paper number 95JB00069.
0148-0227/95/95JB-00069$05.00

take into account a reasonable precursory strain and the fact that no coseismic electrical anomalies are observed. Recently, some evidence of streaming potential has been reported in a study of the electrical effect of the annual variation of the water saturation of rocks in an underground quarry [*Morat et al.*, 1992]. Electrokinetic effects were also proposed to explain the SP anomalies frequently observed in geothermal areas [*Corwin and Hoover*, 1979], or electrokinetic effects were used to monitor subsurface flow in geotechnical constructions [*Merkler et al.*, 1989].

Surface electrokinetic effects, calculated for several geometries and various pore pressure source distributions, only appear near lateral heterogeneities of conductivity, permeability, or generally of the streaming coupling coefficient C_s, which is the ratio between the electrokinetic potential and the excess pore pressure [*Nourbehecht*, 1963; *Fitterman*, 1978, 1979]. The study of this electrokinetic coupling coefficient and its variation prior to earthquakes is therefore essential to quantify electrotelluric effects better. Streaming potentials refer to the electrical signals produced when a fluid flows in a porous medium, and this effect can be quantified through experimental results. Few data of geophysical interest on streaming potential are available [*Somasundaran and Kulkarni*, 1973; *Ishido and Mizutani*, 1981; *Massenet and Van Ngoc*, 1985; *Morgan et al.*, 1989]. These experiments are done on crushed samples or capillaries at atmospheric pressure and could not reflect the behavior of natural rocks. We chose to measure the streaming potential on intact saturated sediments with a large range of permeabilities. As the spatial distribution of anomalies in electrotelluric potentials and geomagnetic variations is partly controlled by relative change in C_s, we must know how C_s is affected prior to an earthquake. Particularly, is the electrokinetic coupling coefficient affected during dilatancy? As the streaming potential is expected to be proportional to the fluid pressure gradient, how is it affected by changes of permeability? The streaming potential coupling coefficient C_s and the permeability have therefore been measured first on a series of undeformed sediments and then during the deformation of samples up to failure.

Electrokinetic Phenomena

Electrokinetic phenomena are due to the existence of an electric double layer formed at the solid/liquid interface. The currently accepted model of the rock/fluid interface is due largely to *Stern* [1924] [*Ishido and Mizutani*, 1981; *Morgan et al.*, 1989]. The double layer is made up of a layer of ions (the Helmoltz layer) adsorbed on the surface of the rock and of a diffuse mobile layer (the Gouy-Chapman zone) extending into the liquid phase. Figure 1 depicts the potential distribution: Φ_0, Φ_h, and ζ are the potentials at distances from the surface of zero, H, and S, respectively. H is the distance to the beginning of the diffuse zone. S is referred to as the shear plane. Under all conditions the double layer as a whole is electrically neutral: the charge of the surface layer C_0 is equal to the sum of the charges in the diffuse zone (C_d) and in the Helmoltz layer (C_h), appropriate charge signs being taken into account.

When a fluid is made to flow through a porous medium, there will be an occurrence of a potential, the so-called streaming potential, across the sample, because of the relative motion between the solid and the liquid. The streaming potential is just the reverse of electroosmosis. S is considered to be the closest plane to the surface on which fluid motion takes place. The potential on this plane is defined as the ζ potential, and it is the potential which is manifest in streaming potential measurements.

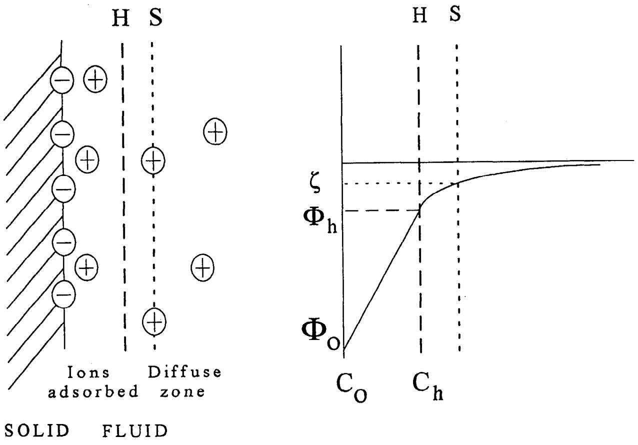

Figure 1. Scheme of the electrochemical solid/solution interface. Stern's model: C_0 is the charge density of the rock/fluid surface zone. Φ_0 is the surface potential. H is the plane between diffuse zone and adsorbed ions with a charge density C_h. S is the slipping plane with a corresponding ζ potential. Note that Φ_h and ζ can be positive or negative.

The Helmoltz-Smoluchowski equation is the relation governing the streaming potentials generated by fluids moving through porous media or capillaries [*Overbeek*, 1952; *Nourbehecht*, 1963]. In a porous medium the general relations between the electric current density I (A/m^2), the fluid flow J (m/s), and the forces of grad V and grad P are

$$-I = \frac{\sigma_f}{FF} \operatorname{grad} V - \frac{\varepsilon \zeta}{\eta FF^\circ} \operatorname{grad} P \qquad (1)$$

$$-J = -\frac{\varepsilon \zeta}{\eta FF^\circ} \operatorname{grad} V + \frac{k}{\eta} \operatorname{grad} P \qquad (2)$$

where σ_f and ε are the electrical conductivity and the dielectric constant of the fluid, ζ is the zeta potential, η is the dynamic viscosity of the fluid, k is the permeability of the porous medium, FF° is the formation factor ($\sigma_{\text{fluid}}/\sigma_{\text{rock}}$) with a very high fluid conductivity when surface conduction is absent, FF is the formation factor for the fluid conductivity being studied (i.e., possibly with surface conductivity), P is the pressure of the fluid, and V is the potential. The first term on the right-hand side of (1) represents Ohm's law and the second term in (2) represents Darcy's law. In a steady state equilibrium the convection current (due to grad P) is balanced by the conduction current (due to grad V). Equating these currents leads to

$$C_s = \frac{\Delta V}{\Delta P} = \frac{\varepsilon \zeta}{\eta \sigma_f} \frac{FF}{FF^\circ} \qquad (3)$$

which is the Helmoltz-Smoluchowski equation [*Dukhin*, 1974].

ΔV is the generated potential and ΔP is the applied pore pressure difference. This equation implies that the currents are of equal magnitude and opposite flow along the same

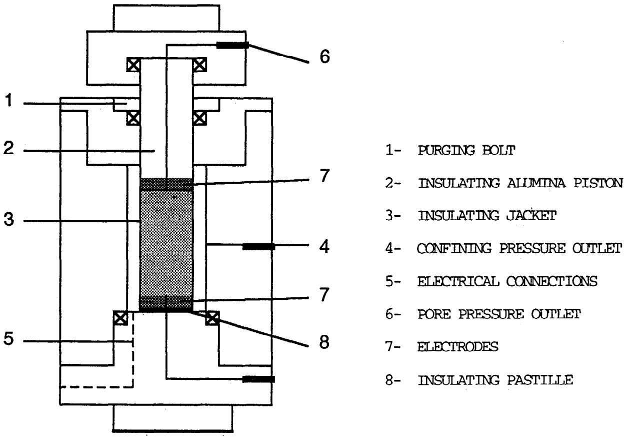

Figure 2. Nonmagnetic triaxial pressure cell and sample assembly.

path. The ratio $\Delta V/\Delta P$ is called the streaming potential cross-coupling coefficient C_s or simply the coupling coefficient. When surface conductivity is absent, $FF = FF^\circ$, and we have $C_s = \varepsilon\zeta/\eta\sigma_f$. The ratio FF°/FF can be also expressed for a circular cross section pore of radius a as

$$\frac{FF}{FF^\circ} = 1 \Bigg/ \left(1 + \frac{2S_s}{a\sigma_f}\right) \tag{4}$$

where σ_f is the fluid conductivity and S_s is the surface conductance [*Morgan et al.*, 1989]. We can note that the smaller the pore radius is, the greater the surface conductivity is.

Experimental Procedure

High-Pressure Cell

The sample assembly is shown in Figure 2. The samples were cut in cylinders (25 mm in diameter and 50 mm long) and dried at 70°C in vacuum for 8 hours. Then they were saturated with distilled water. The samples were subjected to a gradually increasing deviatoric stress up to failure, with a confining pressure of 10 MPa. The variations of the streaming potential, of resistivity, and of permeability with deformation were measured. Each measurement required 20–40 min to reach a stable state. A typical experiment lasted 8–11 hours. We used a triaxial cell servocontrolled in displacement by an hydraulic press. The entire cell is amagnetic, and the mobile insulating piston is made of alumina and has a central circular hole (Figure 2). The deformation was measured by a displacement sensor. The deformation of the press was not negligible and was taken into account by a calibration. The variations of axial stress, confining pressure, and pore pressure are independent. The sample was isolated from the confining fluid by an insulating jacket. The flow circuit is connected, at both ends of the sample, to an upstream and a downstream reservoir volume, where two sensors monitor the fluid pressure. Different valves allow us to keep the flow circuit open or closed. Air was removed from the flow system. The fluid was made to flow through the sample in the axial direction at each triaxial state of stress in order to measure permeability and electrokinetic potential. The two electrodes are made of beryllium bronze with a hole in the center and two linked circular grooves allowing the fluid to flow uniformly in the axial direction throughout the sample. The upper and lower electrodes are isolated from the conductive press and the cell by an insulating alumina piston and insulating pastille, respectively (Figure 2). The streaming potential and the resistance of the sample can not be measured at the same time, because the impedance meter disturbs the measurement of the streaming potential. The dielectric constant of the fluid is ε_{H_2O} at temperatures between 17°C and 24°C. The samples used were Fontainebleau sandstones (France), with a wide range of permeabilities. Using replicas method which produces resin casts of the pore space, we observed the porous medium of samples by electron microscope analysis. A resin is used to fill the pores, and the quartz grains are then dissolved with an acid. Different pore features have thus been shown.

Resistivity Measurement

The resistance of the sample was measured by an HP 4284A impedance meter at a frequency of 4 kHz to avoid polarizing the electrodes. The resistance of the different wires and connections is taken into account by the impedance meter. The confining fluid was checked to be nonconductive. The fluid present in the cylindrical hole of the insulating piston and insulating pastille is in contact with the sample and can provide a conduction path outside of the sample. The resistance R_w of this exterior conduction path was measured. The effect of R_w is to give a conduction path between the electrodes that is parallel with the conduction path through the sample. Thus the effective resistance between the electrodes R_m is $1/R_m = (1/R_s) + (1/R_w)$, where R_s is the resistance of the sample. The resistance of the sample, the resistivity of the fluid, and the streaming potential can not be measured simultaneously. During the experiment the resistance of the sample was measured just after the streaming potential measurement. We noted that the resistance of the sample changed when fluid was flowing through it. Fluid in the upstream reservoir has a constant resistivity of 2×10^3 Ω m in most of the cases. After flowing through the sample, fluid is usually more conductive, and we assumed that fluid resistivity after flowing through the sample was closer to fluid resistivity in the sample than fluid resistivity in the upstream reservoir. The resistivity ρ_w of the fluid, which has flowed through the sample, was used for the calculation of R_w and was measured out of the cell using a conductivity cell at each triaxial state of stress, as soon as the flow was stopped. This procedure allowed us to consider the resistivity of the sample (ρ_s) and the resistivity of the fluid (ρ_w) approximately equal to those that were present during the streaming potential measurement.

Streaming Potential Measurement

The streaming potential was measured during fluid flow (when permeability is $>10^{-15}$ m^2) by an HP 34401A voltmeter with an input resistance above 10^{10} Ω. The electrodes and the voltmeter were linked by coaxial wires, and the ground was connected to the press to avoid electrical noise. The lower electrode was connected to the ground of the streaming potential measurement. The resistance of the water in the insulating piston (R_w) is taken into account. Indeed, in this case, electrical current is no longer zero in the sample, and using the definition of electrokinetic coupling coefficient (equation (3)), the measured ΔV is related to the measured ΔP as

$$\frac{\Delta V}{\Delta P} = C_s \bigg/ \left(1 + \frac{R_s}{R_w}\right). \tag{3'}$$

Data were recorded, once per second, by a PC computer with an Institute of Electrical and Electronics Engineers interface. The flow could be reversed to measure the reverse streaming potential. The electrokinetic coupling coefficient was computed from the regression coefficient of five measurements. When permeability was less than 10^{-15} m^2, the streaming potential was measured during the pressure gradient diffusion.

Permeability Measurement System

Steady state flow method. The flow system was kept open at atmospheric pressure near the downstream reservoir, and the fluid was made to flow through the sample with a manual pump near the upstream reservoir. The pressure gradient ΔP across the sample was kept at a constant value. The rate of fluid flow Q (m^3/s) through the sample was measured during steady state fluid flow. The permeability k is simply given by Darcy's law,

$$Q = (kA\Delta P)/(\eta L), \tag{5}$$

where A is the cross-sectional area of the sample perpendicular to the direction of the flow and L is its length. This method can be used to measure permeabilities greater than 10^{-16} m^2. In all our experiments the fluid flow Q is proportional to the pressure gradient, and permeability values are computed from the regression coefficient determined from five measurements.

Transient flow method. The flow system is kept closed at the upstream and at the downstream reservoirs. A pressure pulse ΔP_0 (less than 10% the magnitude of the pore fluid pressure) is applied to the fluid reservoir connected to one end of the sample. The pressure gradient decay is then recorded in the fluid reservoirs at both ends of the specimen. *Brace et al.* [1968] analyzed the transient flow method and derived an expression for the pressure gradient as a function of time:

$$\Delta P(t) = \frac{2\Delta P_0 V_2}{V_1 + V_2} e^{-mt}, \tag{6}$$

where V_1 and V_2 are the upstream and downstream reservoir volumes ($V_1 = V_2 = 50 \times 10^{-6}$ m^3 in our experimental setup, large compared with the sample pore volume). A plot of the decay curve in terms of ln ($\Delta P(t)$) versus time gives a straight line with a slope m, and the permeability k can be determined by

$$k = (m\eta\beta L V_1 V_2)/[A(V_1 + V_2)] \tag{7}$$

where β is the compressibility of the pore fluid (0.42×10^{-9} Pa^{-1}). This method can be used to measure permeabilities in the range 10^{-16} m^2 to 10^{-24} m^2.

Results

We present streaming potential measurements on seven saturated samples of intact Fontainebleau sandstones with a large range of permeabilities.

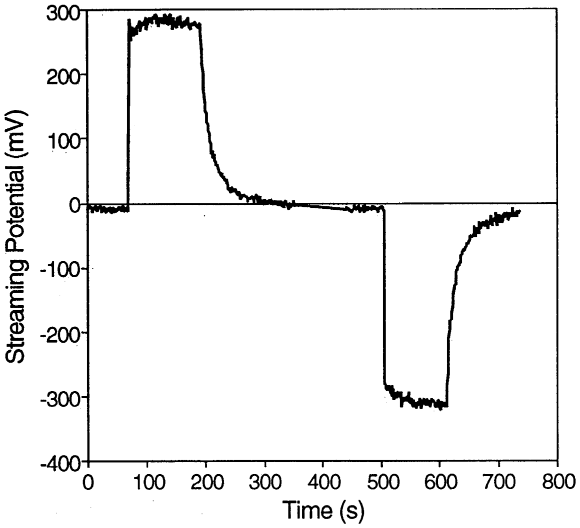

Figure 3. Example of measurement of streaming potential ΔV during a typical experiment: pressure difference ΔP = 0.1 MPa and fluid resistivity 600 Ω m. This measurement has been done on sample F313, with permeability $k = 13 \pm 3 \times 10^{-15}$ m^2, under hydrostatic pressure conditions p = 11.5 MPa.

Results on Undeformed Sediments

Streaming potential measurements. The streaming potential was first measured when the sample was subjected to a quasi-hydrostatic pressure of about 11.5 MPa: axial stress of 12 ± 0.5 MPa and confining pressure of 11 ± 0.1 MPa. We present a typical measurement of the streaming potential when the permeability of the sample was measured using the steady state flow method (for all our samples except F82) and when the permeability was measured using the transient flow method (for F82). In all our experiments the permeability was measured along the axial stress. The effects of the surface conductivity and of the fluid conductivity on the streaming potential will be discussed. We always observed negative electrokinetic coupling coefficients; the reported values are the absolute values of the electrokinetic coupling coefficients.

A typical streaming potential ΔV at a given pressure difference ΔP is shown in Figure 3 when the permeability is measured by the steady state flow method (sample F313). The streaming potential appears when the pressure difference is applied and still remains as long as the pressure gradient is maintained. The streaming potential drops to zero when the fluid flow is stopped. The sign of the streaming potential changes when the fluid flow is reversed. For this example the resistivity of the fluid was 600 Ω m. The streaming potential reaches about 300 mV (Figure 3) when the pressure difference is 0.1 MPa, leading to an electrokinetic coupling coefficient C_s of 540 mV/0.1 MPa, taking into account the resistance of the fluid in the cylindrical hole of the piston (R_w).

The permeability of sample *F*82, $k = 0.15 \pm 0.05 \times 10^{-15}$ m^2, was measured by the transient flow method. In this case the streaming potential was measured during the pressure gradient diffusion (Figures 4a and 4b). The fluid pressure before the pressure pulse was 10.03 MPa. The fluid resistivity was 1250 Ω m for this example. The potential

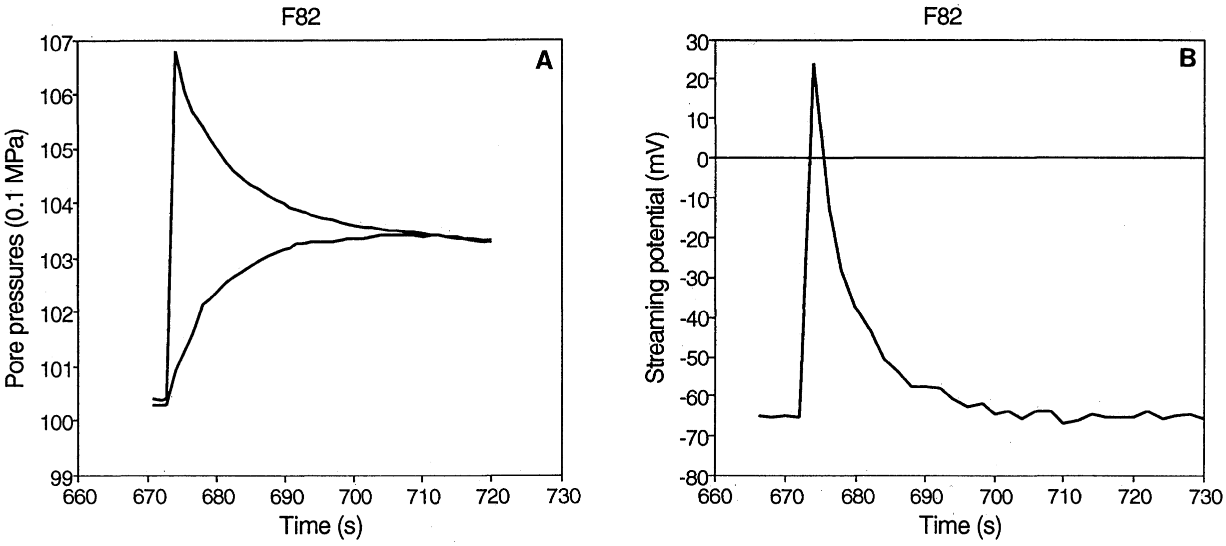

Figure 4. (a) Pressure gradient diffusion as a function of time: $\Delta P(t)$ during the transient flow method. (top) Behavior of pore pressure at the end of the sample where ΔP is applied. (bottom) Behavior of pore pressure at the other end of the sample. (b) Evolution of the streaming potential during this diffusion of pressure gradient $\Delta V(t)$. These measurements have been done on F82 in hydrostatic pressure conditions $p = 11.5$ MPa, permeability $k = 0.15 \pm 0.05 \times 10^{-15}$ m^2, fluid resistivity $\rho_f = 1250$ m.

changes from −65 to 24 mV (Figure 4b) when the pressure pulse is applied by increasing the pore pressure from 10.03 to 10.68 MPa (Figure 4a). This leads to a C_s of 13.7 mV/0.1 MPa (the resistance of the fluid in the cylindrical hole of the piston (R_w) was very large compared to the sample resistance). The evolution of the streaming potential with time is

$$\Delta V(t) = \frac{1}{\sigma_f} \int_{x_1}^{x_2} i_{\text{conv}}(t)\, dx \qquad (8)$$

with $i_{\text{conv}}(t) = \sigma_f C_s \partial P(t)/\partial x$, where $x_2 - x_1$ is the length of the sample. If we assume that C_s is constant, then $\Delta V(t) = C_s \Delta P(t)$, the pressure gradient being constant along its length, although it varies with time [*Brace et al.*, 1968]. A typical measurement (Figures 4a and 4b) shows that ΔV decreases more rapidly than ΔP. A possible interpretation is that the electrokinetic coupling coefficient is not exactly constant during the experiment. It seems that there is no threshold of pressure gradient to produce a streaming potential, the measurement being possible if the signal is greater than the noise.

Effect of surface conductivity. To estimate the contribution of the surface conductivity, we measured the conductivity of the sample $F313$ ($k = 13 \pm 3 \times 10^{-15}$ m^2 during the entire experiment) as a function of fluid conductivity with different NaCl concentrations. The resistance of the sample was measured as soon as the flow was terminated. The conductivity of the sample as a function of fluid conductivity is shown in Figure 5.

The results lead to $FF^0 = 91$ when fluid conductivity is larger than 2×10^{-3} S/m. For fluid conductivity below $\sigma_f = 2 \times 10^{-3}$ S/m the conductivity of the sample is no longer proportional to the fluid conductivity. Our measurements are usually done with $\sigma_f = 10^{-3}$ S/m and $FF = 61$, and we would have to multiply the "apparent" ζ potential by 1.5 if we wanted to have the "true" value of ζ for this sample (equation (3)).

The surface conductivity is the limit of the conductivity of the sample when fluid conductivity becomes very low. With the lowest fluid conductivity used in our measurements (Figure 5) being 10^{-3} S/m, the conductivity of the sample with this fluid allows us to overvalue the surface conductance: $S_s = 10^{-7}$ Ω^{-1}. For sandstones the pore radius is expected to be equal to 10^{-5} m. Then $2S_s/a = 2 \times 10^{-2}$ S/m is larger than the fluid conductivity $\sigma_f = 10^{-3}$ S/m for this sample, and the surface conductivity term is the major contributor to the streaming potential.

Effect of fluid conductivity. We measured C_s with different NaCl concentrations (Figure 6) with pH = 5 on the same sample $F313$. Different pore fluids were made to flow

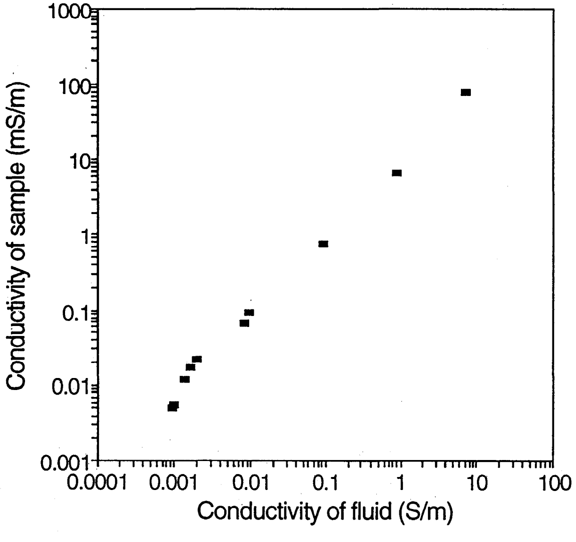

Figure 5. Rock conductivity versus fluid conductivity measured on sample F313 in hydrostatic pressure conditions $p = 11.5$ MPa.

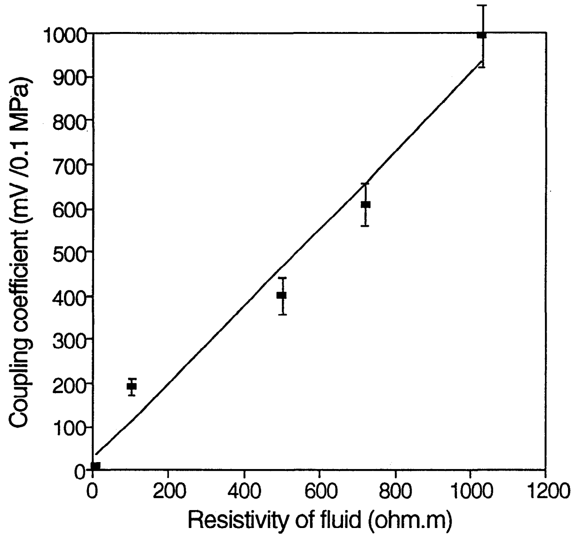

Figure 6. Electrokinetic coupling coefficient as a function of fluid resistivity for sample F313 in hydrostatic pressure conditions $p = 11.5$ MPa.

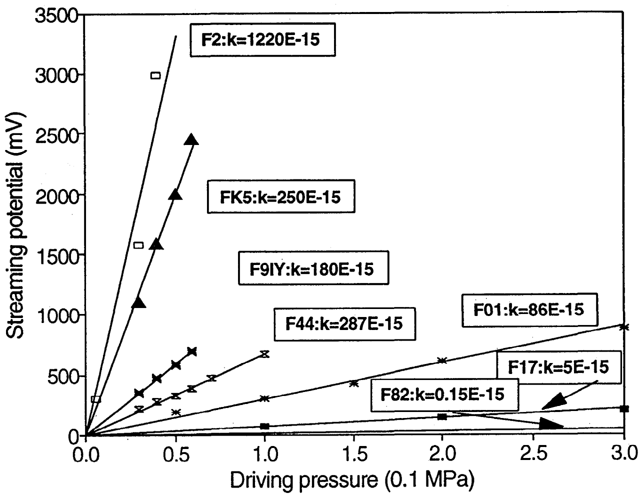

Figure 7. Streaming potential ΔV measurements with different applied driving pore pressures ΔP, on seven samples, in hydrostatic pressure conditions $p = 11.5$ MPa. Permeabilities range from $0.15 \pm 0.05 \times 10^{-15}$ to $1220 \pm 30 \times 10^{-15}$ m^2, corrected for a constant fluid resistivity $\rho_f = 10^3$ Ω m. The streaming potential is proportional to the driving pore pressure. The electrokinetic coupling coefficient $\Delta V/\Delta P$ (in absolute value) varies from 10 ± 1 to 6642 ± 611 mV/0.1 MPa.

through the sample from the most resistive to the most conductive fluid, waiting to reach a constant fluid resistivity out of the cell at each measurement of the streaming potential. We observed electrical instabilities when fluid conductivity was higher than 10^{-2} S/m. The electrokinetic potential was no longer constant when pore pressure difference was constant and abnormal variations at higher frequency up to 50% of the signal were observed. We used distilled water to avoid these electrical instabilities. The high fluid resistivity used enhances the chemical reactions between the matrix and the fluid. Changes in fluid resistivity when the fluid was made to flow through the sample were noted outside the cell, particularly before the failure. These changes resulted from the interaction between the rock and the fluid, and this interaction was dependent on deformation and cracking. The coupling coefficient was found to be proportional to the resistivity of the fluid which allowed us to compute electrokinetic coupling coefficients at a given fluid conductivity. As ε and η are constant, we can deduce that the ζ potential is constant, in first approximation, with different salinities of fluid. Notice that for pure quartz $\zeta = -2.8 \times 10^{-2}$ to $2.5 \times 10^{-2} \log_{10}\rho_f$, it means $\zeta = -100$ mV for a fluid resistivity of 10^3 Ω m and $\zeta = -50$ mV for a fluid resistivity of 10 Ω m [*Pride and Morgan*, 1991]. Moreover, *Ishido and Mizutani* [1981] found that ζ potential was dependant upon chemistry of the pore fluid. Nevertheless, it seems that ζ potential is constant with different conductivities for this sample and in this range of fluid conductivity. The linear dependence of the streaming potential versus the pressure gradient shows that (3) is verified with the term $FF/(\sigma_f FF^\circ)$ constant.

Relation between the streaming potential, fluid flow, and permeability. The relation between the streaming potential and the driving pressure, at a stress of about 11.5 MPa, was examined first and is shown in Figure 7. For sample F82 the slope of the straight line results from 10 measurements of pressure gradients and streaming potentials by the transient flow method, in the range 0.12–0.80 MPa. The slopes of the straight lines for the other samples result from five to seven measures by the steady state flow method. The various coupling coefficients were not measured with exactly the same fluid resistivity. As the coupling coefficients are proportional to the fluid resistivity, in first approximation they can be computed at a fixed fluid conductivity and then compared (Figure 7). There is a linear relation between the streaming potential and the driving pressure. It means that for a given sample the streaming potential is proportional to the flow rate of fluid. The coupling coefficient C_s, reported for a water resistivity of 10^3 Ω m, varies from 10 ± 1 to 6642 ± 611 mV/0.1 MPa.

For various samples (with $\varepsilon = 7.04\text{–}7.18 \times 10^{-10}$ F/m, $\eta = 0.951\text{–}1.049$ mPa s, $\sigma_f = 10^{-3}$ S/m), large values of the streaming coupling coefficient are obtained for large permeabilities (Figures 7 and 8a). The streaming coupling coefficient shows a linear variation with permeability on log-log coordinates with a slope of 0.7 (Figure 8a). The different values observed for the coupling coefficient could be produced by the ζ potential variations. But the ζ potential is expected to be of the same order of magnitude for all these Fontainebleau sandstones because the mineralogy is nearly identical. The apparent dependence of the coupling coefficient on permeability could be mainly due to the surface conduction effect, as the smaller the permeability is, the smaller the pore sizes in sandstones are expected to be. If surface conductivity is enhanced by smaller permeabilities, the conduction current tends to increase. As the conduction current equilibrates the convection current (which is constant), the electrical gradient tends to decrease, and the streaming coupling coefficient is decreased. This study has shown, using replicas method, different porous features reported in Table 1. These samples do not contain clay and have comparable size quartz grains ranging between 100 and 300 μm. Moreover, it has been shown that the surface conductivity for sample F313 ($k = 13 \pm 3 \times 10^{-15}$ m^2) is not negligible compared with the fluid conductivity. In order

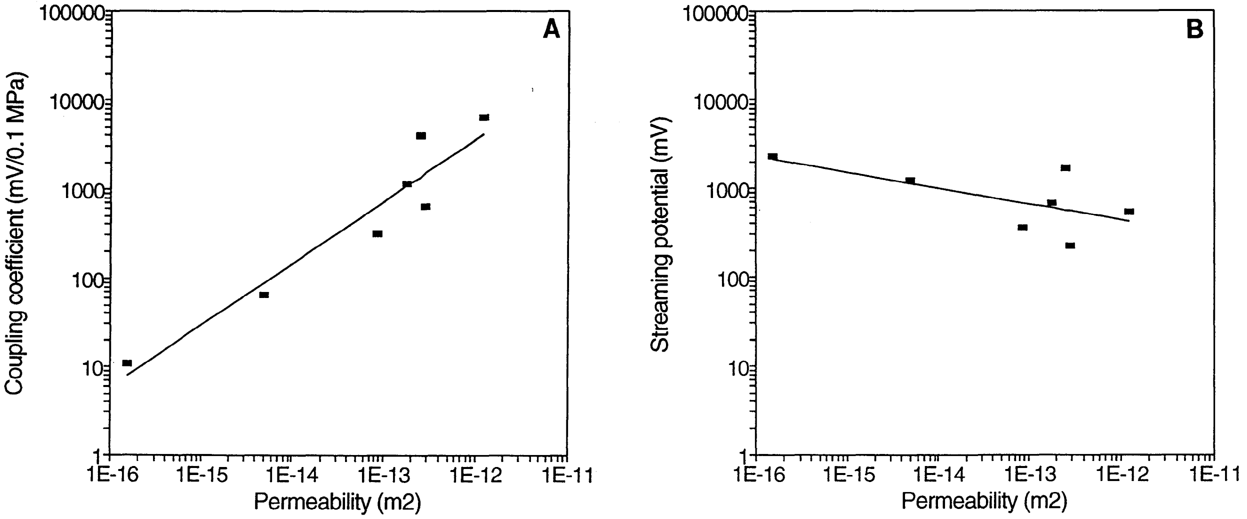

Figure 8. (a) Streaming coupling coefficient as a function of permeability. (b) Relation between the streaming potential and permeability at a constant fluid flow $Q = 10^{-7}$ m^3/s, calculated (solid line) with $\zeta = -21.9$ mV, fluid conductivity $\sigma_f = 10^{-3}$ S/m, or measured (rectangles) for different samples.

to know the exact effect of surface conductivity and the corrected ζ potential, the rock conductivity as a function of the fluid conductivity should be measured for each sample, which is beyond the scope of this paper. Our purpose is not to calculate the exact value of ζ potential for each sample but to know how the coupling coefficient varies with permeability. The coupling coefficient varies when the permeability changes as shown in Table 1 and in Figures 7 and 8a. The effect of surface conductivity has been quantified using a capillary model to express surface conductivity as a function of surface conductance and hydraulic radius. Then hydraulic radius has been related to permeability using Carman-Kozeny's law and computed values of streaming coupling coefficient are a good approximation of measured values.

We can deduce from (3) and (5) the relation between the streaming potential, the fluid flow, and the permeability [*Jouniaux and Pozzi*, 1995]:

$$\Delta V = \frac{L \varepsilon \zeta Q FF}{A \sigma_f k FF^{\circ}} \tag{9}$$

Table 1. Porosity, Permeability, and Electrokinetic Coupling Coefficient on Undeformed Sandstones

	Porosity, %	Permeability, $\times 10^{-15}$ m^2	Electrokinetic Coupling Coefficient, mV/0.1 MPa
F82	4.3*	0.15 ± 0.05	10 ± 1
F17		4.9 ± 1.2	65 ± 5
F01		86 ± 2	310 ± 24
F44	13	287 ± 7	661 ± 53
F9IY	9.9†	180 ± 4	1166 ± 93
FK5	10	250 ± 5	4002 ± 320
F2	20‡	1220 ± 30	6642 ± 611

With a fluid resistivity of 10^3 Ω m.

*Pore size 5–15 μm grain boundary porosity, important cementation.

†Pore size 10–30 μm grain boundary porosity, no cementation.

‡Pore size 30–50 μm large pores connected between poorly cemented grains.

The streaming potential ΔV increases if permeability decreases for a given fluid flow Q (the parameters L, A, ε, σ_f, and FF/FF° being constant), considering ζ constant. The dependence of ΔV at $Q = 10^{-7}$ m^3/s and $\sigma_f = 10^{-3}$ S/m with permeability k is shown in Figure 8b. The streaming potential ΔV shows a linear variation versus permeability on log-log coordinates of -0.18 slope with an average value of ζ of -21.9 mV (solid line). The difference between measurements (rectangles) and calculated variation (solid line) could be due to the different effects of surface conductivity, as explained above. The streaming potential is proportional to the fluid flow Q (with L, A, ε, ζ, σ_f, and FF/FF° constant) at a given permeability k, according to (9). We calculated the Darcian speed Q/A corresponding to the pore pressure gradient of $\Delta P = 0.1$ MPa for two samples. The samples F82 and F2 have a permeability of $0.15 \pm 0.5 \times 10^{-15}$ m^2 and $1220 \pm 30 \times 10^{-15}$ m^2, respectively. The deduced Darcian speed is 9.1 m/yr for F82 and 215 m/d for F2 which is higher than Darcian speeds in many geophysical contexts. The streaming potential as a function of Darcian speed depends on sample size, and we will not use this expression to predict the observed SP in the field. Note that electrokinetic coupling coefficient is independent of sample size and can be used for field measurements interpretation.

Results on Deformed Sediments

We present the behavior of the electrokinetic coupling coefficient and of permeability with deformation for three samples of Fontainebleau sandstones: F44, FK5, and F9IY. We first present the mechanical behavior, then the behavior of the electrokinetic coupling coefficient with deformation, and finally the behavior of permeability with deformation. The different features of the samples are reported in Tables 2 and 3. The effects of the deformation on these parameters for the three samples will be discussed, and we will try to explain the common features of the behavior of electrical properties and of permeability with deformation.

Mechanical behavior. The stress-strain curves for the samples F44, FK5, and F9IY are represented in Figures 9a, 9b, and 9c, respectively. The samples were subjected to an

Table 2. Principal Mechanical Features of the Samples F44, FK5, and F9IY

	Strain Rate, s^{-1}	Yield Stress, MPa	Deformation at Yield Stress, %	E, MPa
F44	9.5×10^{-7}	235	1.72	21,330
FK5	8.3×10^{-7}	260	1.52	28,870
F9IY	8.1×10^{-7}	249	1.50	27,450

E is the Young's modulus.

increasing hydrostatic pressure up to 10 MPa (point A). Then the axial pressure was gradually increased with a constant confining pressure of 10 ± 0.1 MPa. The average strain rate was between 8 and 9.5×10^{-7} s^{-1}. Failure occurred at a yield stress of about 250 MPa (point D). Young's modulus E, computed on the linear part of the curve, is between 21,000 and 29,000 MPa (Table 1).

Behavior of electrical properties with deformation. Previous studies on the same samples showed that electrical resistivity of the sample increases up to point C, which corresponds to 47%, 39%, and 40% of the yield stress for F44, FK5, and F9IY, respectively, and then decreases from point C to point D [*Jouniaux et al.*, 1992].

The variation of the coupling coefficient $\Delta V/\Delta P$, reported for a fluid resistivity of 10^3 Ω m, during the deformation of the samples F44, FK5, and F9IY is represented in Figures 10a, 10b, and 10c, respectively. The coupling coefficient decreases from point C to point L by 15.8% for F44, 45.2% for FK5, and 52% for F9IY. The coupling coefficient increases from point L to point D with a rate of 0.07–0.19%/0.1 MPa. The minimum value of the coupling coefficient, noted by point L, is obtained for a stress of 72–86% of the yield stress (Table 2).

Behavior of permeability with deformation. The permeability of the samples F44, FK5, and F9IY was measured by the steady state flow method, and its behavior with deformation is represented in Figures 11a, 11b, and 11c, respectively. First, the vertical permeability decreases (up to point C) by 0.007%/0.1 MPa, 0.013%/0.1 MPa, and 0.027%/0.1 MPa for F44, FK5, and F9IY (Figures 11a, 11b, and 11c). Then the permeability is changed by 0.0045%/0.1 MPa, −0.011%/0.1 MPa, and −0.014%/0.1 MPa for F44, FK5, and F9IY, respectively. Permeability dropped when failure occurred, with a rate of 0.017–0.020%/0.1 MPa (Table 3).

Discussion

Behavior of the Rock Resistivity with Deformation

Changes in the fluid resistivity for fluid that has flowed through the sample result from interaction between the rock and the fluid. Resistivity of the fluid often decreases from 50% of yield stress up to failure [*Jouniaux*, 1994]. A whiteish water was even sometimes observed just before the failure, denoting fine particles drained from the matrix. This effect can drastically affect the resistivity of the fluid up to 57% in some cases. These interactions are enhanced by our particular procedure of using a drained sample which is necessary to perform measurements of the streaming potential and of the permeability.

Variations of the sample resistivity are partly due to changes of the fluid resistivity. However, changes of the sample resistivity are mainly due to the closure of pores and subhorizontal microcracks (up to point C) and to the aperture of subvertical microcracks at the onset of dilatancy (from point C to point D) [*Brace and Orange*, 1968; *Brace*, 1975]. Indeed, the principal stress is always the vertical stress, and the increase of the deviatoric stress during the deformation induces the aperture of microcracks in the direction of the vertical stress. As a result the evolution of sample resistivity is the same in all our experiments, showing an increase up to point C and a decrease till the failure, although the magnitude of changes in fluid resistivity may be different [*Jouniaux et al.*, 1992; *Jouniaux*, 1994].

Studies done on Fontainebleau sandstones have shown brittle behavior [*Darve*, 1992] and an important dilatancy occurring at about 65% of the yield stress when the confining pressure is 10 MPa [*Kondo et al.*, 1991]. Point C, denoting the maximum resistivity of the rock during the deformation, occurs at 40–50% of the yield stress. These results are consistent with those of *Brace and Orange* [1968], who showed that maximum resistivity could occur before dilatancy detection.

Behavior of Permeability With Deformation

The changes of permeability are not similar for the three samples (Figures 11a, 11b, and 11c). At the beginning of the experiment, there is a path for the vertical fluid flow. First, the closure of pores and subhorizontal microcracks (up to point C) decreases the vertical permeability (Figures 11a, 11b, and 11c). Then the aperture of subvertical microcracks (from point C to point D) changes the permeability by increasing or decreasing it a little. The opened subvertical microcracks (after point C) do not strongly affect permeabil-

Table 3. Principal Features of the Behavior of Permeability and Electrokinetic Coupling Coefficient With Deformation

	Point A, $k \times 10^{-13}$ m^2	Point A C_s, mV/0.1 MPa	Point C, Percent of Failure	Point L, Percent of Failure	Increase Rate of C_s per 0.1 MPa From L to D, %	Decrease Rate of k at Failure per 0.1 MPa, %
F44	3.08 ± 0.08	531 ± 42	47	72	0.07	0.017
FK5	2.48 ± 0.06	4997 ± 399	39	86	0.13	0.020
F9IY	1.77 ± 0.04	1147 ± 92	40	73	0.19	0.020

Points A, C, L, and D refer to stress-strain curves given in Figures 9a, 9b, and 9c for samples F44, FK5, and F9IY, respectively. Increase rate of C_s and decrease rate of k are given for 0.1-MPa change in axial stress.

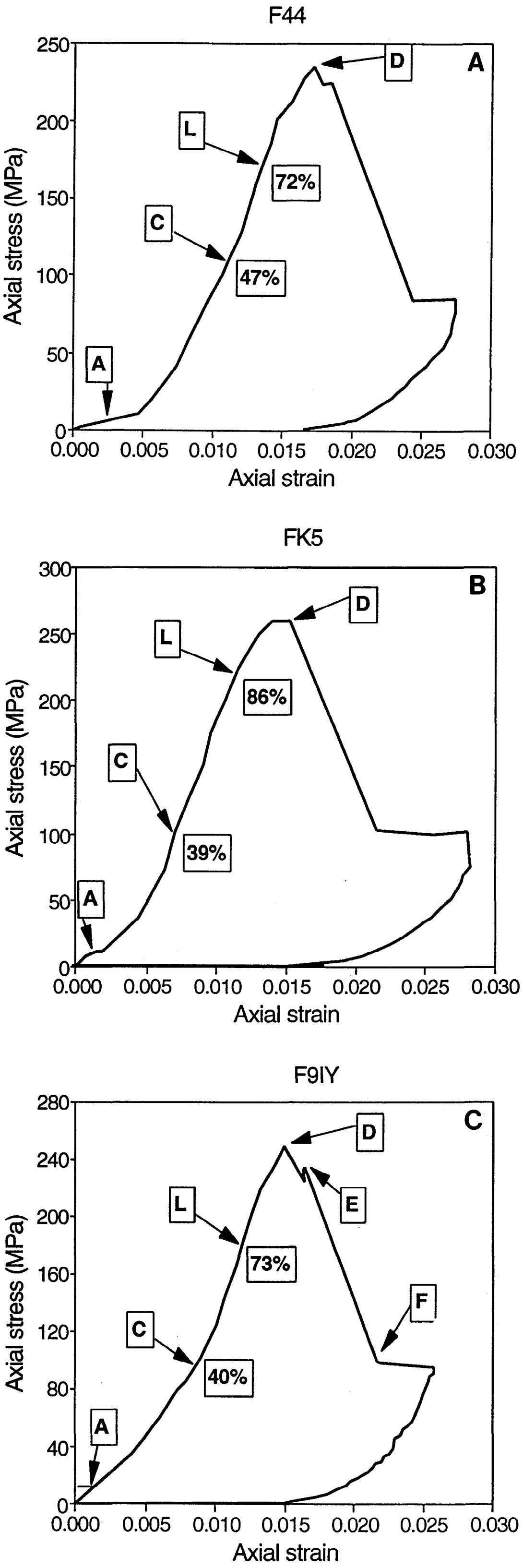

Figure 9. Axial stress-strain curve from triaxial deformation experiment to failure using a servocontrolled press in displacement. A indicates the point where samples were subjected to an increasing hydrostatic pressure up to 10 MPa, C indicates the point of maximum resistivity, L indicates the point of minimum electrokinetic coupling coefficient, D indicates the point of failure, *E* indicates Young's modulus computation point, F indicates the end of the first part of the weakening state, and percentages indicate percentages of strength. (a) Results for F44. (b) Results for FK5. (c) Results for F9IY.

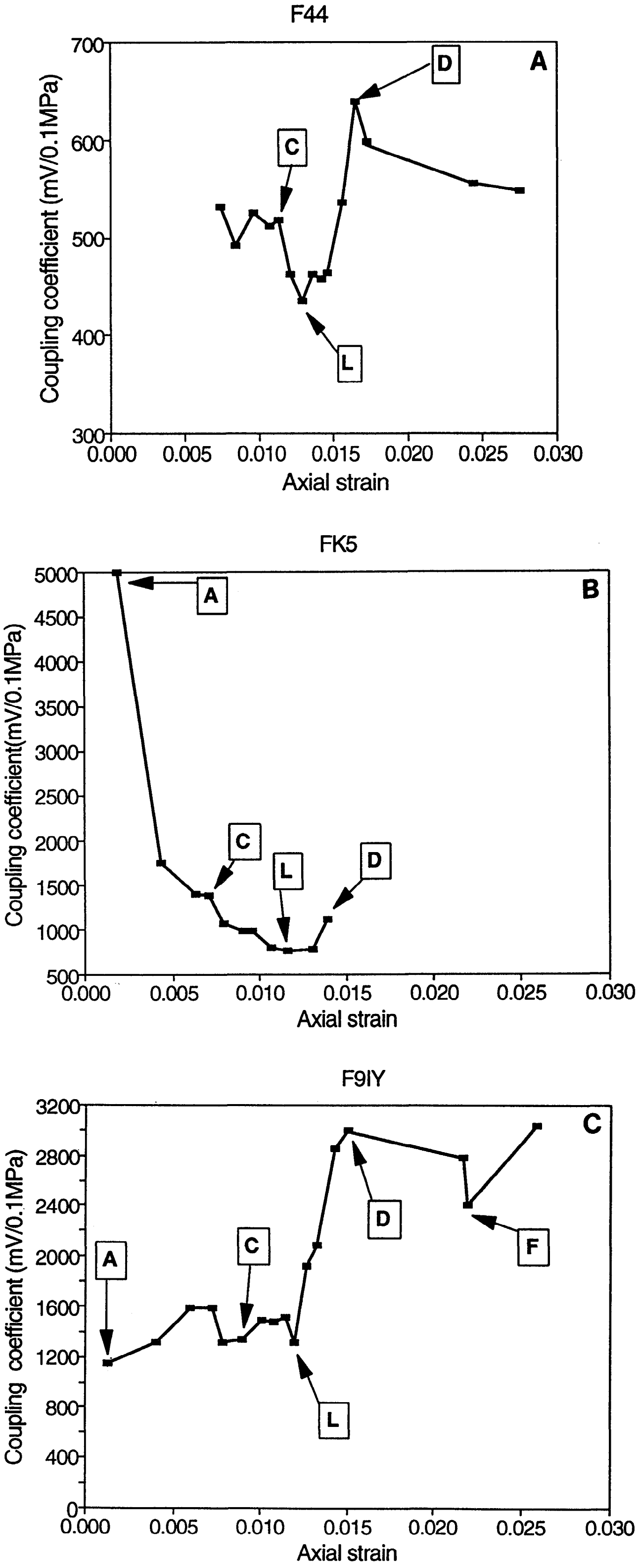

Figure 10. Variation in electrokinetic coupling coefficient (in absolute value) with the axial strain from triaxial deformation experiment to failure. A indicates the point where samples were subjected to an increasing hydrostatic pressure up to 10 MPa, C indicates the point of maximum resistivity, L indicates the point of minimum electrokinetic coupling coefficient, D indicates the point of failure, F indicates the end of the first part of the weakening state, and percentages indicate percentages of strength. (a) Results for F44. (b) Results for FK5. (c) Results for F9IY.

ity, showing that they are not connected. The confining pressure is kept at a constant value (10 MPa) during the experiment to measure permeabilities at the same effective pressure (confining pressure minus pore pressure), as permeability depends on the effective pressure [*Brace*, 1980]. When failure occurs, the confining pressure often increases by about 1.5–5 MPa. Permeability is then measured when the confining pressure is restored to 10 MPa. Hence the drop of permeability is due to the failure and not to an increase of the effective pressure. In all our experiments a drop in permeability is observed when failure occurs. This drop of permeability at failure is about 0.020%/0.1 MPa. The grain sizes are reduced during the deformation. At the end of the experiment the connections between the main microcracks, used for the fluid flow, are probably filled with finely crushed particles, inducing the sealing of the main microcracks and preventing the fluid from flowing easily through the sample. Nevertheless, the permeability is not changed by a factor higher than 3 during the entire deformation.

Behavior of the Electrokinetic Coupling Coefficient with Deformation

A general trend of the behavior of the coupling coefficient is noticeable from point C to failure (point D). Changes in the electrokinetic coupling coefficient are not similar to changes of permeability. Hence the evolution of the electrokinetic coupling coefficient is not related to changes of the permeability (Figures 10 and 11). Our measurements do not allow us to quantify the pore sizes related to the permeability measured during the deformation. We can not estimate the behavior of the surface conductivity during the deformation. The important variation of the electrokinetic coupling coefficient (reported at a constant fluid conductivity) with deformation results in a decrease from point C to point L and an increase from point L to failure (point D) (Figures 10a, 10b, and 10c). Point L, representing 72–86% of the yield stress, may correspond to the onset of the localization of the shear band (it is the growth and the propagation of cracks in an area in which a rearrangement of the grains is observed), and this area will be the way for the future failure. This localization of failure is known to occur after the onset of dilatancy and before failure [*Berthaud*, 1993]. The important increase of the electrokinetic coupling coefficient from the localization of failure (point L) to failure (point D) is thought to be due to an increase of ζ potential in the shear band where new surfaces are created and connected. The ζ potential is enhanced in the shear zone, and the increase of the electrokinetic coupling coefficient is measured at the sample scale when new cracks are connected (point L) allowing fluid to flow through these new cracks. Also, the creation of a shear zone makes the sample macroscopically heteroge-

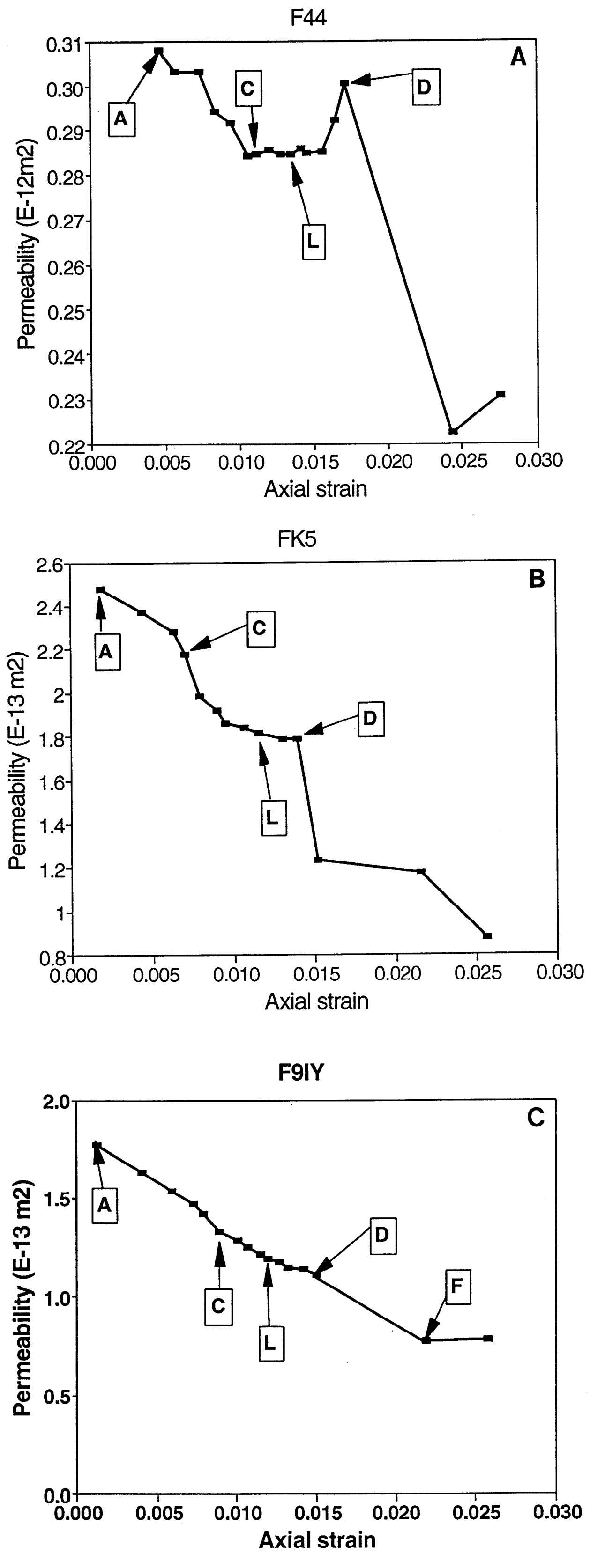

Figure 11. (opposite) Variation of permeability with axial strain from triaxial deformation experiment to failure. A indicates the point where samples were subjected to an increasing hydrostatic pressure up to 10 MPa, C indicates the point of maximum resistivity, L indicates the point of minimum electrokinetic coupling coefficient, D indicates the point of failure, F indicates the end of the first part of the weakening state, and percentages indicate percentages of strength. (a) Results for F44. (b) Results for FK5. (c) Results for F9IY.

neous. Charge separations may occur across the shear band in addition to the charge buildups at the ends of the sample.

Possible Consequences for Field Measurements

The major purpose of our study has been to measure representative values of the electrokinetic coupling coefficient under various conditions relevant to geophysical problems. We now give the possible consequences of our results for field measurements. The electrokinetic field due to fluid circulation can be measured horizontally by electrodes on the ground surface or vertically by electrodes buried at different depths.

Surface electrokinetic and magnetic anomalies have been computed in a layered Earth [*Fitterman*, 1978] and in a faulted half-space [*Fitterman*, 1979]. It has been shown that a boundary separating regions with different electrokinetic coupling coefficients, with a pressure in excess of hydrostatic at the electrokinetic coupling coefficient boundary, is required to develop a surface self-potential field due to subsurface fluid flow [*Nourbehecht*, 1963; *Fitterman*, 1979]. Moreover, these electrokinetic effects are proportional to $(C_1 - C_2)P$, where C_1 and C_2 are the electrokinetic coupling coefficients in region 1 and 2, respectively, and P is any pressure in excess of hydrostatic at the electrokinetic coupling coefficient boundary. Therefore these electrokinetic effects are changed if $(C_1 - C_2)$ or P is changed, leading to an electrokinetic potential anomaly.

In order to estimate changes of the difference between the electrokinetic coupling coefficients prior to an earthquake, we have to know the geophysical parameters influencing the electrokinetic coupling coefficient, especially those which could change during the mechanical process of preparation of an earthquake. Figure 12 shows the following (in absolute value). C is proportional to the fluid resistivity, as shown in Figure 6. C is inversely proportional to the fluid viscosity and depends thus on the fluid temperature and on the fluid nature. C is proportional to the ζ potential and depends on the nature of the rock and of the pore fluid chemistry. C decreases under the effect of the surface conductivity therefore by small pore sizes. C is thus lowered by low permeability and is enhanced by high permeability, as shown in Figure 7. C can increase by a factor up to 650 if permeability increases by a factor 8×10^3. C depends on the applied deformation, especially between about 75% of the yield stress and the failure, as shown in (Figures 10a, 10b, and 10c).

We will try to give some applications of the effects of these parameters, especially during the preparation of an earthquake, first in order to measure surface self-potential anomalies in the deformed zone, then to measure these anomalies at large distances from the epicenter.

Measurement of Electrokinetic Potential Anomalies in Deformed Zone

Dilatancy is commonly assumed to occur prior to an earthquake in the vicinity of the fault, allowing fluid flow variations through the fault and acting as the boundary of the heterogeneity and its vicinity, one side acting as region 1, the other as region 2 (Figure 13a). The permeability could be enhanced and the electrokinetic coupling coefficient would increase, as the effect of surface conductivity would decrease. The deformation itself could change the rock/fluid interaction. For instance, C could increase between about 75% of the yield stress and the failure at a rate up to 0.19% for 0.1 MPa of axial stress (Figures 10a, 10b, and 10c), using the effect of deformation on the electrokinetic coupling coefficient measured in our laboratory experiments. In order to measure the maximum of surface electrokinetic anomaly, it will be more convenient to measure the SP anomalies between an electrode buried where C is not changed, and an electrode near the site where a change of permeability is expected, dilatancy is expected, or a change of fluid conductivity is expected, assuming there is a fluid circulation through the fault separating the electrodes.

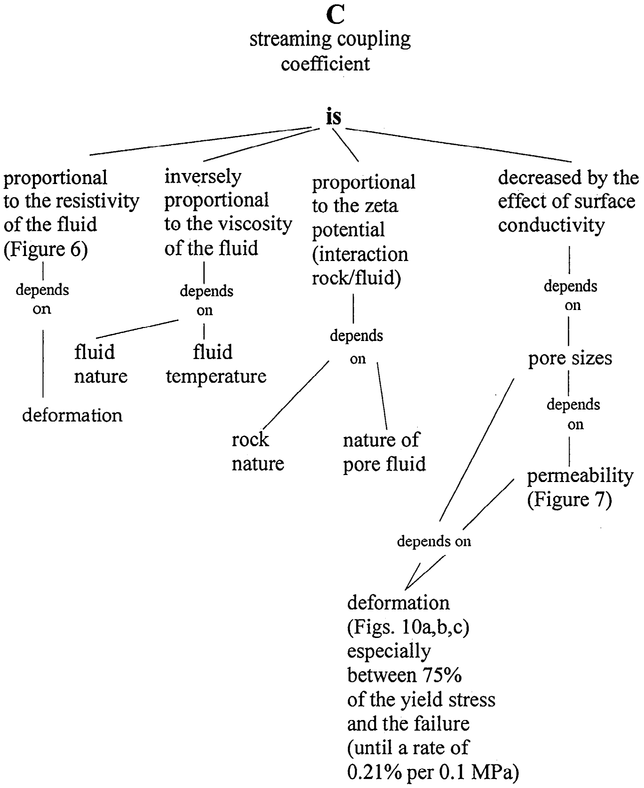

Figure 12. Schematic review of the physical parameters which have an influence on the electrokinetic coupling coefficient.

Miyakoshi [1986] reported SP anomalies at 3.2 km from the epicenter preceding an earthquake of $M = 5.6$, about 40 days and also 55 hours before the earthquake occurrence. The anomaly returned with the onset of the earthquake, reaching the initial level after 13 hours. The electrodes were fixed in an underground observation tunnel, and the maximum of the anomaly was 40 mV. He concluded that the anomaly was due to the change of the SP of the fractured fault rock in which one electrode was fixed, the other electrode being at a constant potential serving as a reference. Fluid was flowing through the Yamasaki fault, but this anomaly was not attributed to changes in the water migration through the fault on the basis of the time constant of the anomaly. Our measurements show that another interpretation can be proposed: the electrokinetic coupling coefficient of the rock near the electrode could be changed before the earthquake between about 75% of the yield stress and the rupture in the seismic zone. As the second electrode has

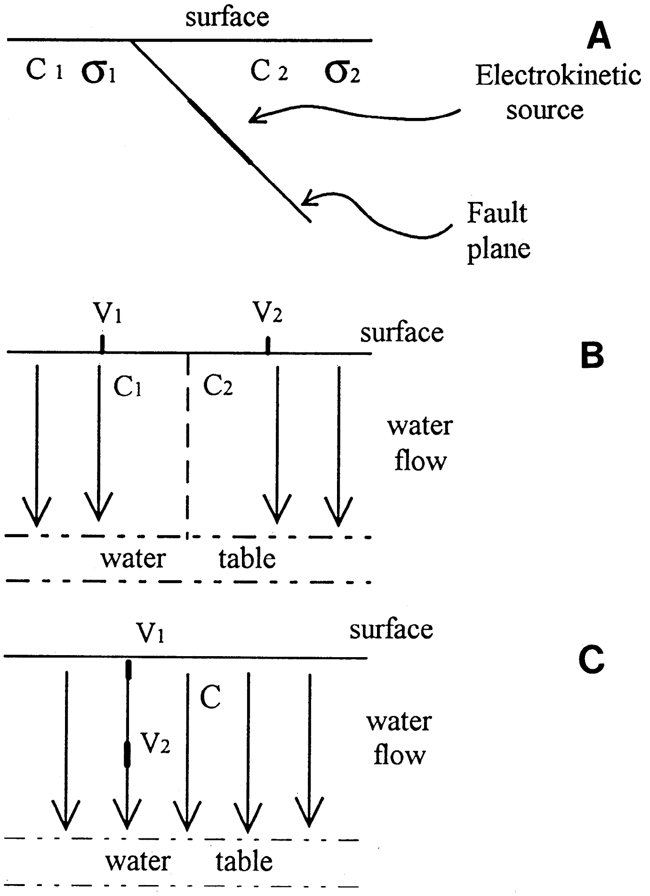

Figure 13. (a) Schematic view of fluid circulation and of lateral heterogeneity of electrokinetic coupling coefficient (C_1 and C_2) in the vicinity of a fault. (b) Schematic view of vertical fluid flow and lateral heterogeneity of electrokinetic coupling coefficient (C_1 and C_2) at large distances from the epicenter. V_1 and V_2 are the measured electric potentials. (c) Schematic view of vertical fluid flow at large distances from the epicenter, without lateral heterogeneity of electrokinetic coupling coefficient (C). V_1 and V_2 are the measured electric potentials.

shown a constant self-potential, one can suppose that it was buried in a rock with a constant coupling coefficient. Therefore the difference of the coupling coefficient could become greater, leading to an electrokinetic potential anomaly.

Measurement of Electrokinetic Anomalies at Large Distance From the Epicenter

Anomalies observed at large distances from the epicenter need a different interpretation. Indeed, electrokinetic currents produced in the deformed zone are expected to decrease very rapidly with the distance [*Bernard*, 1992]. Abrupt upheaval of underground water level is a phenomenon frequently observed postseismically. Large abnormal increases in water flow have been measured in springs and wells, beginning a few days after the seism, especially in major normal fault earthquakes, lasting 6–12 months, and observable at distances of the order of 50 km from the epicenter. Expelled water volumes were 0.2–0.5 km^3 for the two earthquakes studied by *Muir-Wood and King* [1993] of magnitude 7 and 7.3. The mechanism of such a water expulsion is still controversial, but we can assume that there is groundwater recharge during interseismic periods using the same mechanism. This recharge implies vertical fluid flows in shallow aquifers which could induce electrokinetic anomalies.

These anomalies will be detected at the surface, only if there is a lateral heterogeneity of the values of the electrokinetic coupling coefficient (Figure 13b). Electrokinetic potential anomalies will be proportional to vertical driving pore pressure. Hence any change of the vertical fluid flow could be detected prior to earthquakes. We must notice here that these surface measurements involve nonsaturated medium, and any computation and modeling in this case is beyond the scope of this paper.

Far from the epicenter when variations of the vertical fluid flow exist, the maximum of the electrokinetic effect will be measured between electrodes situated along the flow direction. In this case we assume that the ground is saturated. Thus the measurements will be similar to those made in the laboratory, and a lateral heterogeneity of the electrokinetic coupling coefficient is not needed (Figure 13c). The electric potential difference ΔV will be directly proportional to the vertical driving pore pressure, as shown in Figure 7, using the effect of permeability on the electrokinetic coupling coefficient measured in our particular laboratory experiments. Therefore an electrokinetic potential anomaly will be measured whenever the following occur. (1) The driving pore pressure is changed (equation (4)). Our measurements show that a streaming potential up to 30 mV, for a fluid conductivity of 0.01 S/m and a permeability of 10^{-12} m^2, could be produced by an underground water level change of 50 cm. Moreover, the streaming potential measurements could indicate when the water level change reverses, as the sign of the streaming potential will be reversed. (2) Fluid resistivity is changed, as the streaming potential is proportional to the fluid resistivity, assuming the driving pore pressure remains constant (4). (3) Permeability between the two electrodes is changed, inducing a different effect of surface conductivity (equation (4)). Our measurements show that if the permeability between the electrodes is increased by an amount of 8×10^3, the streaming potential could be enhanced by a factor of 650 (Figure 7), assuming that the driving pore pressure remains constant.

Conclusion

Streaming potential was measured along the direction of fluid flow on saturated samples of intact Fontainebleau sandstones. Streaming potential ΔV is proportional to the driving pore pressure ΔP. For a fixed driving pore pressure, streaming potential is proportional to the fluid resistivity. Electrokinetic coupling coefficient varies from 10 to 6642 mV/0.1 MPa when permeability changes from 0.15×10^{-15} to 1220×10^{-15} m^2. This has been explained by the effect of surface conductivity which is not negligible compared with fluid conductivity when the permeability is reduced.

When the sample is deformed under triaxial stress up to failure, permeability is changed at the most by a factor 3. The electrokinetic coupling coefficient $\Delta V/\Delta P$ reported for a constant fluid conductivity of 10^{-3} S/m increases from the localization of the shear band up to failure. This increase of the electrokinetic coupling coefficient just before failure is due to an increase of ζ potential in the shear zone when new surfaces are created and connected.

Possible consequences of our results to investigate the electric field which could appear during the preparation of an earthquake have been given. Self-potential anomalies observed in the deformed zone could be due to a large increase of the electrokinetic coupling coefficient from 75% of the yield stress to rupture. Far from the epicenter when variations of the vertical fluid flow exist in relation to an earthquake our measurements show that a vertical streaming potential of up to 30 mV could be induced by an underground water level change of 50 cm (for fluid conductivity 0.01 S/m and permeability 10^{-12} m^2). As shown in this paper, the streaming potential is strongly dependent on the permeability. An increase of 8×10^3 in permeability would enhance streaming potential by a factor of 650. This result could explain the strong influence of the site on the intensity of seismo-electrical signals.

Acknowledgments. This research was supported by ANDRA and the GRECO géomatériaux. It is a collaboration with C. Philippe, ENSAM, Paris. We thank S. Pride for fruitful discussions and the reviewers, D. Fitterman and P. Kasameyer, for their reviews and suggestions. This is ENS contribution 337 and CNRS-INSU-DBT contribution 3, thème Fluides et Failles.

References

Bernard, P., Plausibility of long distance electrotelluric precursors to earthquakes, *J. Geophys. Res.*, *97*, 17,531–17,546, 1992.

Berthaud, Y., Détection expérimentale de la localisation, rapport annuel, Group. de Rech. Coord. géomatériaux, Paris, 1993.

Brace, W. F., Dilatancy-related electrical resistivity changes in rocks, *Pure Appl. Geophys.*, *113*, 207–217, 1975.

Brace, W. F., Permeability of crystalline and argillaceous rocks, *Int. J. Mech. Min. Sci. Geomech. Abstr.*, *17*, 241–251, 1980.

Brace, W. F., and A. S. Orange, Electrical resistivity changes in saturated rocks during fracture and frictional sliding, *J. Geophys. Res.*, *73*, 5407–5420, 1968.

Brace, W. F., J. B. Walsh, and W. T. Frangos, Permeability of granite under high pressure, *J. Geophys. Res.*, *73*, 2225–2236, 1968.

Corwin, R. F., and D. B. Hoover, The self-potential method in geothermal exploration, *Geophysics*, *44*, 226–245, 1979.

Corwin, R. F., and H. F. Morrison, Self-potential variations preceding earthquakes in central California, *Geophys. Res. Lett.*, *4*, 171–174, 1977.

Darve, F. (Ed.), *Actes du Colloque Bilan et Perspectives du GRECO Géomatériaux*, pp. 19–52, GRECO géomatériaux, Paris, 1992.

Dobrovolsky, I. P., N. I. Gershenzon, and M. B. Gokhberg, Theory of electrokinetic effects occuring at the final stage in the preparation of a tectonic earthquake, *Phys. Earth Planet. Inter.*, *57*, 144–156, 1989.

Dukhin, S. S., *Surface and Colloid Science*, vol. 7, edited by E. Matijevic, John Wiley, New York, 1974.

Fitterman, D. V., Electrokinetic and magnetic anomalies associated with dilatant regions in a layered Earth, *J. Geophys. Res.*, *83*, 5923–5928, 1978.

Fitterman, D. V., Theory of electrokinetic-magnetic anomalies in a faulted half-space, *J. Geophys. Res.*, *84*, 6031–6040, 1979. (Correction, *J. Geophys. Res.*, *86*, 9585–9588, 1981.)

Ishido, T., and H. Mizutani, Experimental and theoretical basis of electrokinetic phenomena in rock-water systems and its applications to geophysics, *J. Geophys. Res.*, *86*, 1763–1775, 1981.

Jouniaux, L., Effets électriques et magnétiques liés aux circulations de fluides dans les roches sous contraintes, thèse de doctorat, Univ. Paris 6, 1994.

Jouniaux, L., and J. P. Pozzi, Permeability dependence of streaming potential in rocks for various fluid conductivities, *Geophys. Res. Lett.*, *22*, 485–488, 1995.

Jouniaux, L., et al., Resistivity changes induced by triaxial compression in saturated sandstones from Fontainebleau (France), *C. R. Acad. Sci., Ser. II*, *315*, 1493–1499, 1992.

Kondo, D., A. Haied, and J. P. Henry, Detection expérimentale de l'apparition de bandes de cisaillement dans les roches: Mesures extensométriques, rapport scientifique, pp. 219–228, GRECO géomatériaux, Paris, 1991.

Massenet, F., and P. Van Ngoc, Experimental and theoretical basis of self-potential phenomena in volcanic areas with reference to results obtained on Mount Etna, *Earth Planet. Sci. Lett.*, *73*, 415–429, 1985.

Merkler, G. P., et al. (Eds.), *Detection of Subsurface Flow Phenomena, Lect. Notes Earth Sci.*, vol. 27, pp. 197–210, Springer-Verlag, New York, 1989.

Miyakoshi, J., Anomalous time variation of the self-potential in the fractured zone of an active fault preceding the earthquake occurence, *J. Geomagn. Geoelectr.*, *38*, 1015–1030, 1986.

Mizutani, H., T. Ishido, T. Yokokura, and S. Ohnishi, Electrokinetic phenomena associated with earthquakes, *Geophys. Res. Lett.*, *3*, 365–368, 1976.

Morat, P., J. L. Le Mouël, G. Nover, and G. Will, Annual variation of the water saturation of a highly porous rock driven by a seasonal temperature variation and measured by an array of electrodes, *C. R. Acad. Sci.*, *315*, *Sér. II*, 1083–1090, 1992.

Morgan, F. D., E. R. Williams, and T. R. Madden, Streaming potential properties of Westerly granite with applications, *J. Geophys. Res.*, *94*, 12,449–12,461, 1989.

Muir-Wood, R., and G. C. P. King, Hydrological signatures of earthquake strain, *J. Geophys. Res.*, *98*, 22,035–22,068, 1993.

Murakami, H., H. Mizutani, and S. Nabetani, Self-potential anomalies associated with an active fault, *J. Geomagn. Geoelectr.*, *36*, 351–376, 1984.

Nourbehecht, B., Irreversible thermodynamic effects in inhomogeneous media and their applications in certain geoelectric problems, Ph.D. thesis, Mass. Inst. of Technol., Cambridge, 1963.

Nur, A., Dilatancy, pore fluids, and premonitory variations of t_s/t_p travel times, *Bull. Seismol. Soc. Am.*, *62*, 1217–1222, 1972.

Overbeek, J. T. G., Electrochemistry of the double layer, in *Colloid Science*, vol. 1, *Irreversible Systems*, edited by H. R. Kruyt, pp. 115–193, Elsevier, New York, 1952.

Pride, S. R., and F. D. Morgan, Electrokinetic dissipation induced by seismic waves, *Geophysics*, *56*, 914–925, 1991.

Scholz, C. H., L. R. Sykes, and Y. P. Aggrawal, Earthquake prediction: A physical basis, *Science*, *181*, 803–810, 1973.

Somasundaran, P., and R. D. Kulkarni, A new streaming potential apparatus and study of temperature effects using it, *J. Colloid Interface Sci.*, *45*, 591–600, 1973.

Stern, O., Zür theorie der electrolytischen doppelschicht, *Z. Elecktrochem.*, *30*, 508–516, 1924.

Varotsos, P., and K. Alexopoulos, Physical properties of the variations of the electric field of the Earth preceding earthquakes, I, *Tectonophysics*, *110*, 73–98, 1984a.

Varotsos, P., and K. Alexopoulos, Physical properties of the variations of the electric field of the Earth preceding earthquakes, II, Determination of epicenter and magnitude, *Tectonophysics*, *110*, 99–125, 1984b.

L. Jouniaux and J.-P. Pozzi, Laboratoire de Geólogie de L'Ecole Normale Supérieure, URA 1316 du C.N.R.S., 24, Rue Lhomond, 75231 Paris Cedex 05, France. (e-mail: jouniaux@magnetit.ens,fr; pozzi@magnetit.ens.fr)

(Received November 22, 1993; revised December 5, 1994; accepted December 29, 1994.)

C. R. Acad. Sci. Paris, t. 315, Série II, p. 1493-1499, 1992

Géophysique/*Geophysics*

Variation de résistivité sous contrainte triaxiale dans des grès de Fontainebleau saturés

Laurence Jouniaux, Jean-Pierre Pozzi, Marc Brochot et Claude Philippe

Résumé — Des expériences de déformation triaxiale menées jusqu'à la rupture, sur des échantillons de grès de Fontainebleau saturés avec de l'eau distillée, ont montré des variations de résistivité électrique importantes. La résistivité augmente avec la diminution de l'espace poreux en début de compression. Elle commence ensuite à décroître dès l'apparition de microfissures, liée à la dilatance. Cette diminution s'accélère bien avant qu'apparaissent les premiers signes de la rupture. Ces diminutions peuvent atteindre 0,065 % par 0,1 MPa (1 bar) : ceci constitue de nouvelles données pour comprendre le mécanisme physique responsable des anomalies de résistivité précédant et pouvant annoncer un séisme. La valeur des coefficients mesurés permet d'envisager des changements de contrainte beaucoup plus faibles que ceux estimés jusqu'à présent pour expliquer les chutes de résistivité observées *in situ*.

Resistivity changes induced by triaxial compression in saturated Sanstones from Fontainebleau (France)

Abstract — *Electrical resistivity of sandstones have been investigated through triaxial deformation experiments up to failure. The resistivity of a saturated rock first increases with the closure of pores; a decrease is observed which begins at the onset of dilatancy. The resistivity decreases more and more rapidly long before failure. The experimental decay of resistivity can reach 0.065% per bar, leading to stress changes estimation much lower than commonly derived from* in situ *observed changes of resistivity.*

Abridged English Version — Introduction. — Changes of electrical resistivity prior to earthquake have been observed by many authors ([1] to [4]). However, changes of resistivity measured in seismic areas are not always followed by an earthquake ([5], [6], [7]) and changes of resistivity do not occur systematically prior to an earthquake [8].

A few laboratory experiments were made in a deviatoric stress up to failure ([16], [17], [18]) and they showed a continuous decrease in resistivity until the fracture. These changes have been explained by the effects of dilatancy ([10], [11]). Available experimental determinations of resistivity decay under stress lead to unreasonable stress changes to explain the changes of resistivity observed *in situ*.

We measured permeability and changes of resistivity when water-saturated sandstones of Fontainebleau were subjected to triaxial stress up to failure.

Experimental procedure. — A cylindrical specimen was dried at 70°C in vacuum for 8 hrs., then it was saturated with water of resistivity 1,004 Ω.m, and subjected to a constant external confining pressure (10 MPa) and to gradually increasing axial stress. The sample was isolated from the confining fluid by a jacket. The permeability *k* was determined by Darcy's law. Resistance across the sample was measured at frequency of 4 kHz to avoid polarization of electrodes. It is notable that the fluid was made to flow through the sample at each triaxial state of stress in order to measure permeability and electrokinetic potential. As the press is servo-controlled in displacement, we have to wait for about 20-45 min. before each experiment to take into account the relaxation of the sample.

Results. — We present the results of 3 samples of sandstones from Fontainebleau : F 17, F 01 and F 36. The strain-stress curves are represented in Figures 1 *a*, 1 *b*, 1 *c* and the correlated changes of resistivity are shown in Figures 2 *a*, 2 *b*, 2 *c*.

Note présentée par Xavier Le Pichon.

0764-4450/92/03151493 $ 2.00 © Académie des Sciences

The sample was subjected to increasing hydrostatic pressure up to 10 MPa (point A). At this point, for F 17, F 01, and F 36, permeability was 5×10^{-15} m^2, 7.5×10^{-14} m^2 and 3×10^{-13} m^2 and resistivity 1.7, 6.0 and 6.0 kΩ.m respectively. Then the axial pressure was gradually increased with constant confining pressure of 10 MPa. The failure occurred at point D (*Fig.* 1 *a*, 1 *b*, 1 *c*) at 1.92% of deformation for F 17, 2.71% for F 01 and 2.44% for F 36. Large decreases in stress were observed for F 01 and F 36.

Variations of resistivity show the same trend for the 3 samples. The resistivity increases up to point B and more slowly until point C is reached, which corresponds to 87, 56 and 47% of yield stress and to 2.9, 16.3 and 27.9 kΩ.m for F 17, F 01 and F 36 respectively. Then the resistivity drops until failure (D) to 2.8, 7.7 and 4.7 kΩ.m for F 17, F 01 and F 36. The resistivity of F 36 increases up to E, then it drops until F (*Fig.* 2 *c*).

Samples F 01 and F 36 have the same physical behaviour with the same resistivity variation, while F 17, less brittle, has an increasing resistivity until 87% of yield stress (compared with 56 and 47%) and a drop of 3% (compared with 53 and 83%).

Discussion. — The increase of resistivity (up to C) is due to the closure of pores and the subhorizontal microcracks. From C to D the decrease of resistivity corresponds to the aperture of subvertical microcracks, at the onset of dilatancy. It is important to note that this phenomenon begins at 56 and 47% of yield stress for F 01 and F 36 and at only 87% for F 17, where important accommodation at grain boundaries delays the opening of microcracks.

Our observations are coherent with the results of experiments on deformation to failure for saturated samples. The rates of decay of resistivity 0.02, 0.042 and 0.065 per 0.1 MPa for F 17, F 01 and F 36 are important compared with the other laboratory experiments ([16], [17], [18]). For example a drop of 0.0078% per 0.1 MPa was observed for a sandstone from Pottsville [16].

Conclusion. — We observed important decreases of resistivity during experiments of deformation until failure, which constitute new data for understanding the physical mechanism responsible for resistivity anomalies prior to earthquakes. Resistivity changes of 10% commonly observed [3] predict large stress changes. These measures could allow modelling of much smaller stress changes.

Introduction. — Des phénomènes physiques précédant et pouvant annoncer des séismes, en particulier les changements de résistivité électrique, font actuellement l'objet de recherches actives.

Des changements significatifs de résistivité apparente ont été observés avant certains séismes en Russie [1], au Japon [2], ou aux États-Unis [3]. De même, d'importantes variations de potentiel électrique ont été mesurées lors d'observations pour la prévision sismique en Chine [4]. Certaines variations de résistivité électriques mesurées dans des régions sismiques n'ont pas été suivies par des séismes [5], mais reliées à des changements de température ou de salinité de l'eau [6], ou à la minéralisation d'argiles [7]. De plus il n'existe pas systématiquement de variations de résistivité avant un séisme [8].

D'importantes variations de conductivité électrique ont également été observées au sein d'édifices volcaniques [9].

Les variations de résistivité observées à grande échelle peuvent *a priori* résulter de plusieurs causes : la température, la nature du fluide, la variation du tenseur des contraintes et l'activité sismique. Mais les phénomènes physiques qui semblent précéder parfois les séismes sont reliés vraisemblablement à la même cause physique [10] : ces phénomènes ont été expliqués par des effets de la dilatance [11], due aux variations de contraintes qui précèdent les séismes et qui modifient la répartition des microfissures et du fluide, affectant la résistivité.

Des études de laboratoire ([12] à [15]) ont mesuré des variations de résistivité en fonction de différents paramètres : température, pression de confinement, pression axiale, pression de fluide, salinité du fluide, niveau de saturation, perméabilité. Quelques mesures ont été faites lors de rupture de roches ([16], [17]). Ces expériences montrent une diminution de la résistivité pendant la dilatance et jusqu'à la rupture, lorsque la contrainte triaxiale augmente et même lorsqu'elle est constante [18]. Mais les observations *in situ* sont souvent difficiles à corréler avec les mesures en laboratoire et le manque de données ne permet pas de déterminer à chaque fois le mécanisme responsable des variations de résistivité électrique apparente mesurées *in situ*.

Nous avons mesuré en laboratoire la résistivité électrique et la perméabilité d'échantillons de grès de Fontainebleau saturés pendant des expériences de déformation menées jusqu'à la rupture.

DISPOSITIF EXPÉRIMENTAL ET MODE OPÉRATOIRE. — Nous utilisons une cellule triaxiale en bronze au béryllium adaptée à une presse asservie en déplacement. Notre dispositif permet de faire varier de façon indépendante la contrainte axiale, la pression de confinement et la pression de pore, donc de créer dans la roche un état de déformation et de microfissuration bien contrôlé. La pression axiale maximale est de 450 MPa. La pression de confinement et la pression de pore peuvent atteindre 100 MPa. La cellule assure la sortie des signaux électriques provenant de deux électrodes en bronze au béryllium, aux extrémités de l'échantillon. Les échantillons sont cylindriques de diamètre 2,5 cm et de hauteur 4,8 cm. Une gaine isole l'échantillon du fluide de confinement et rend indépendantes la pression de fluide et la pression de confinement. L'impédance complexe est mesurée par un impédancemètre HP 4284 A (20 Hz à 1 MHz) à une fréquence de 4 kHz, pour éviter la polarisation des électrodes reconnue importante à des fréquences inférieures à 1 kHz [14].

Les échantillons sont séchés à 70°C sous vide pendant 8 h, puis saturés avec de l'eau distillée de résistivité 1 004 Ω.m. Enfin, ils sont soumis à une contrainte axiale croissante jusqu'à la rupture, sous une pression de confinement constante de 10 MPa. La résistivité est calculée à partir de la partie réelle de l'impédance mesurée. La perméabilité k est déterminée en mesurant le flux de fluide pour différents gradients de pression d'eau et en utilisant la loi de Darcy [19]

$$k=(Q\,l\,\eta)/(s\,\Delta P)$$

où k est la perméabilité, Q le débit volumique, l la longueur de l'échantillon, η la viscosité dynamique du fluide, s la section de l'échantillon, et ΔP la différence de pression de fluide appliquée entre les extrémités de l'échantillon. Nous vérifions la linéarité entre le flux et le gradient de pression pour chaque mesure de perméabilité.

La température varie de 20 à 24°C et nous en tenons compte pour la viscosité du fluide. Lorsque la pression axiale est changée, il est nécessaire d'attendre 20 à 45 mn environ pour atteindre un état d'équilibre, c'est-à-dire une pression axiale constante sur la courbe contrainte-déformation, en raison de la relaxation de l'échantillon.

Il faut noter que, pour chaque état triaxial, nous avons fait circuler l'eau à travers l'échantillon pour les mesures de perméabilité et de potentiel électrique. La pression de pore est laissée à la pression atmosphérique.

RÉSULTATS. — Nous avons étudié trois échantillons de grès de Fontainebleau : F 17, F 01 et F 36. En début d'expérience les perméabilités sont respectivement 5.10^{-15} m^2, $7{,}5.10^{-14}$ m^2 et 3.10^{-13} m^2 et les résistivités 1,7, 6,0 et 6,0 kΩ.m. Nous avons représenté la variation de la contrainte et la variation de la résistivité avec la déformation (*fig.* 1 *a*, 1 *b*, 1 *c*, 2 *a*, 2 *b*, 2 *c*).

L'échantillon est soumis à une contrainte hydrostatique jusqu'au point A (10 MPa); puis à une contrainte triaxiale croissante avec une pression de confinement constante de 10 MPa. La rupture se produit au point D. L'échantillon F 17 s'est déformé ductilement et une fissure est apparue à 1,92 % de déformation, marquée par une chute de contrainte de 7 sur 117 MPa. L'échantillon F 01 a eu une fracture fragile à 2,71 % de déformation, marquée par une chute de contrainte de 170 sur 290 MPa, ainsi que F 36 avec une chute de contrainte de 130 sur 240 MPa à une déformation de 2,44 %. Mais l'échantillon F 36 a supporté une réaugmentation de contrainte jusqu'à une déformation de 3,73 %.

Les courbes de variation de résistivité ont la même tendance pour les trois échantillons : la résistivité augmente beaucoup jusqu'au point B, représentant 1,1 % de déformation pour F 17, 0,9 % pour F 01 et 0,7 % pour F 36, ce qui correspond à une contrainte axiale de 46, 19 et 18 % de la contrainte de rupture pour F 17, F 01 et F 36. Puis la résistivité augmente plus lentement jusqu'au point C, représentant une déformation de 1,64, 1,73 et 1,42 %, ce qui correspond à une contrainte de 87, 56 et 47 % de la contrainte de rupture pour F 17, F 01 et F 36. La résistivité atteint alors 2,9, 16,3 et 27,9 kΩ.m pour F 17, F 01 et F 36. Puis à partir du point C la résistivité diminue jusqu'au point de rupture D, pour atteindre 2,8, 7,7 et 4,7 kΩ.m, soit une diminution de 3, 53 et 83 % pour une augmentation de contrainte de 15, 126 et 128 MPa pour F 17, F 01 et F 36. La résistivité de F 36 a de nouveau augmenté jusqu'au point E lorsqu'il s'est consolidé, puis a chuté avant une nouvelle rupture en F à 3,73 % de déformation.

Les échantillons F 01 et F 36 ont eu un comportement physique similaire et une variation de résistivité semblable. Alors que l'échantillon F 17, moins fragile, a vu sa résistivité augmenter jusqu'à 87 % de la contrainte de rupture (comparée à 56 et 47 %) puis diminuer de 3 % (comparé à 53 et 83 %).

INTERPRÉTATION ET DISCUSSION. — L'augmentation de la résistivité jusqu'au point C correspond à la fermeture des pores et de microfissures proches de l'horizontale. Ces fissures sont remplies d'eau initialement car l'échantillon est saturé, puis l'eau est expulsée, lorsque la pression augmente, et la résistivité s'accroît. Du point C au point D, la diminution de la résistivité correspond à une ouverture de microfissures plutôt verticales, lors de l'apparition de la dilatance. Il est important de noter que ce phénomène commence à 56 et 47 % de la contrainte de rupture pour les échantillons fragiles F 01 et F 36 et seulement à 87 % de la contrainte de rupture pour F 17. En effet, l'accommodation aux joints de grains pour F 17 est importante et retarde l'ouverture de microfissures verticales par rapport aux échantillons F 01 et F 36.

Les chutes de résistivité sont de 0,02, 0,042 et 0,065 % par 0,1 MPa (1 bar) pour F 17, F 01 et F 36, ce qui est important par rapport aux expériences menées jusqu'à présent. Il a été montré par exemple sur un grès de Pottsville une chute de 6,1 à 3 kΩ.m, soit 50 % lorsque la contrainte axiale augmente de 0 à 650 MPa (avec une pression de confinement

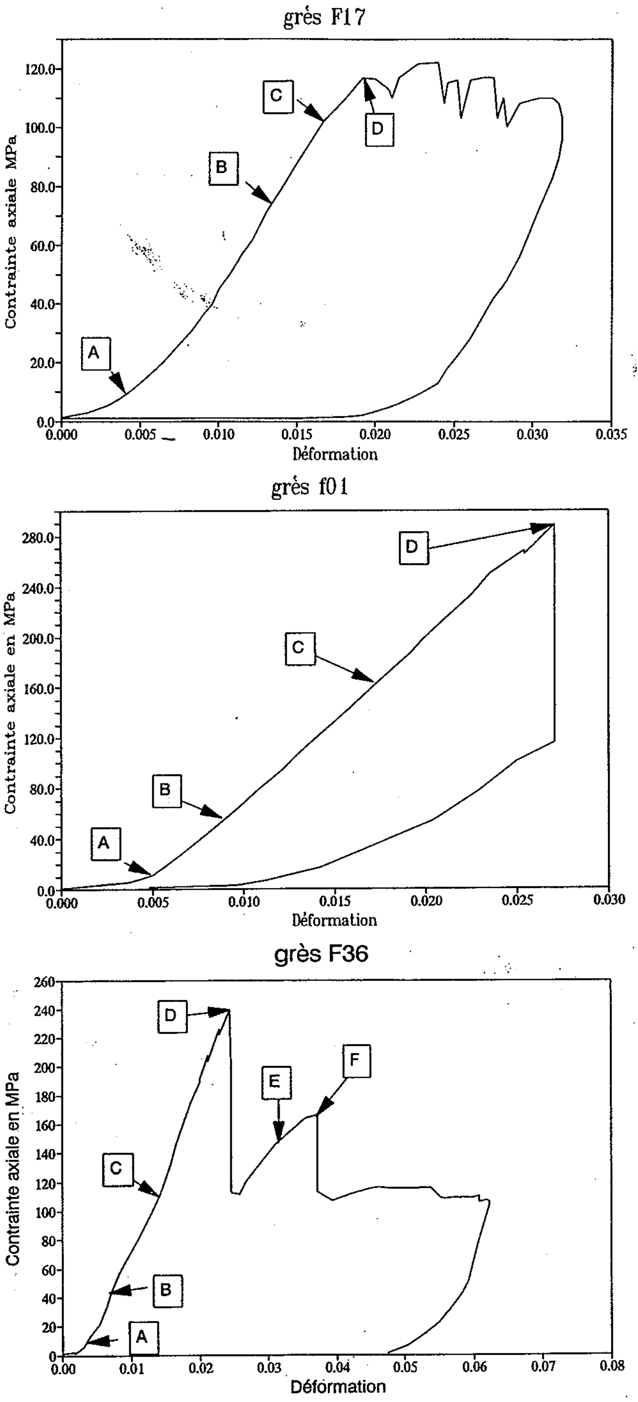

Fig. 1. – Courbe contrainte-déformation axiale pour les échantillons F 17 (1 *a*), F 01 (1 *b*) et F 36 (1 *c*) lors d'une expérience de déformation triaxiale menée jusqu'à la rupture avec une presse asservie en déplacement. C représente le point de résistivité maximale et D marque la zone de rupture.

Fig. 1. – Axial stress-strain curve for samples F 17 (1 a), F01 (1 b) and F36 (1 c) from triaxial deformation experiment to failure using a servo-controlled press in displacement. C indicates the point of maximum resistivity, D the failure zone.

de 150 MPa et une pression de fluide de 50 MPa), soit une chute de 0,0078 % par 0,1 MPa (1 bar) en moyenne. Des chutes plus importantes ont été mesurées sur de l'anorthosite (Wadhams) de 0,011 % par 0,1 MPa en moyenne, ou sur de la dunite (Spruce Pine) de 0,021 % par 0,1 MPa en moyenne [16]. Ces mesures montrent des diminutions de résistivité plus faibles que celles que nous avons observées, peut-être en raison des pressions effectives choisies (100 MPa au minimum).

CONCLUSION. — Nous avons donc observé des diminutions de résistivité importantes lors d'expériences de déformation menées jusqu'à la rupture, qui constituent de nouvelles données pour comprendre le mécanisme physique responsable des anomalies de résistivité précédant et pouvant annoncer un séisme. Les changements de résistivité de 10 % couramment mesurés [3] nécessitaient jusqu'à présent des changements de contraintes très importantes. Ces mesures permettraient de modéliser des changements de contraintes beaucoup plus faibles.

Cette étude a pu être menée grâce aux financements de ANDRA et du GRÉCOGÉOMATÉRIAUX. C'est une contribution 227 de l'E.N.S. et une contribution 510 du C.N.R.S.-I.N.S.U.-D.B.T., thème instabilités.

Note remise le 15 septembre 1992, acceptée le 9 octobre 1992.

RÉFÉRENCES BIBLIOGRAPHIQUES

[1] O. M. BARSUKOV, *Tectonophysics*, 14, 1972, p. 273-277.
[2] Y. YAMASAKI, *Tectonophysics*, 22, 1974, p. 159-171.
[3] S. K. PARK, *J. Geophys. Res.*, 96, 1991, p. 14.211-14.237.
[4] B. RALEIGH et coll., *E.O.S.*, 58, 1977, p. 236-272.
[5] H. F. MORRISON et R. FERNANDEZ, *J. Geophys. Res.*, 91, 1986, p. 11.618-11.628.
[6] Y. HONKURA et coll., *Tectonophysics*, 34, 1976, p. 219-230.
[7] D. V. FITTERMAN et T. R. MADDEN, *J. Geophys. Res.*, 82, 1977, p. 5401-5408.
[8] H. F. MORRISON et coll., *Geophys. Res. Let.*, 6, 1979, p. 139-141.
[9] J. ZLOTNICKI et J. L. LE MOUEL, *J. Geophys. Res.*, 30, 1988, p. 9157-9171.
[10] C. H. SCHOLZ et coll., *Science*, 181, 1973, p. 803-810.
[11] A. NUR et G. SIMMONS, *Earth. Planet. Scien. Let.*, 7, 1969, p. 183-193.
[12] W. F. BRACE et A. S. ORANGE, *J. Geophys. Res.*, 73, 1968, p. 5407-5420.
[13] D. LOCKNER et J. D. BYERLEE, *J. G. R.*, 90, 1985, p. 7837-7847.
[14] C. RUFFET, Y. GUEGUEN et M. DAROT, *Terra Res.*, 1991, p. 265-275.
[15] P. A. PÉZARD, *J. Geophys. Res.*, 95, 1990, p. 9237-9264.
[16] W. A. BRACE et A. S. ORANGE, *J. Geophys. Res.*, 73, 1968, p. 1433-1445.
[17] W. A. BRACE, *Pure Appl. Geo.*, 113, 1975, p. 207-217.
[18] D. A. LOCKNER et J. D. BYERLEE, *Pure Appl. Geo.*, 124, 1986, p. 659-676.
[19] A. E. SCHEIDEGGER, 3rd edition, University of Toronto Press, 1974.

L. J. et J. P. P. : *Laboratoire de Géologie, École normale supérieure, U. A. n° 1316 du C.N.R.S., 24, rue Lhomond, 75252 Paris Cedex 05;*

M. B. et C. P. : *Département Structures, École nationale supérieure des Arts et Métiers, 151, boulevard de l'Hôpital, 75013 Paris.*

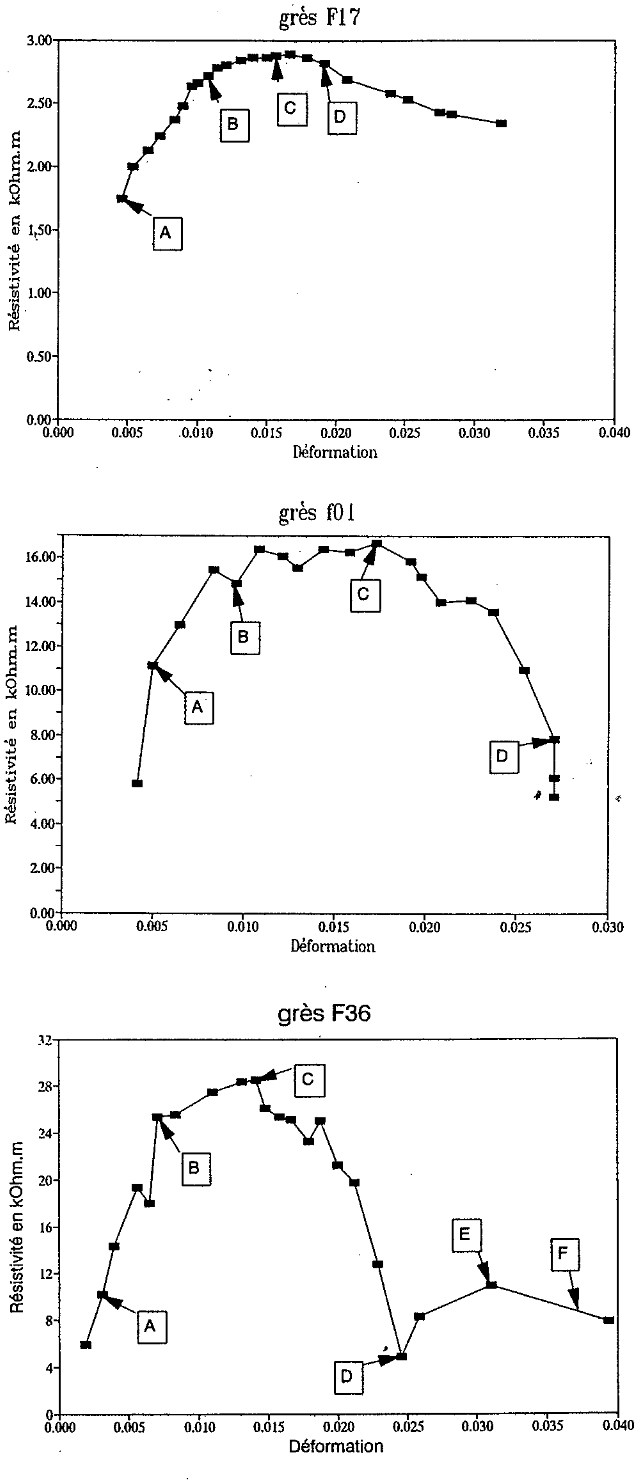

Fig. 2. — Variation de la résistivité avec la déformation axiale pour les échantillons F 17 (2 *a*), F 01 (2 *b*) et F 36 (2 *c*) lors d'une expérience de déformation triaxiale menée jusqu'à la rupture. C représente le point de résistivité maximale et D marque la zone de rupture.

Fig. 2. — Variation in resistivity with axial strain for samples F 17 (2 *a*), *F* 01 (2 *b*) *and F* 36 (2 *c*) *from triaxial deformation experiment to failure. C indicates the point of maximum resistivity, D the failure zone.*

Électrofiltration dans les zones volcaniques et zones de subduction

On verra dans cette partie les travaux relatifs aux effets d'électrofiltration responsables des anomalies de Potentiel Spontané observées sur les volcans, ainsi que les travaux reliés à la problématique de circulation des fluides dans le prisme d'accrétion de Nankai (Japon). Cette partie sera illustrée par une sélection des articles suivants :

Sur les zones volcaniques :

- ***Illustration*** de Potentiels Spontanés sur un volcan
- Jouniaux, L., Bernard, M.-L., Zamora, M., and J.-P. Pozzi, Streaming potential in volcanic rocks from Mount Pelee, ***J. Geophys. Res***., 2000.
- Fontaine F., Rabinowicz, M., Boulègue J., and Jouniaux L., Constraints on hydrothermal processes on basaltic edifices: Inferences on the conditions leading to hydrovolcanic eruptions at Piton de la Fournaise, Réunion Island, Indian Ocean, ***Earth Planet. Sci. Lett***., 2002.

Sur les zones de subduction :

- Bourlange, S., Jouniaux, L., and Henry, P., Data report: Permeability, compressibility, and friction coefficient measurements under confining pressure and strain, Leg 190, Nankai Trough, ***Proc. ODP, Sci. Results***, 2004.
  Open access : http://www-odp.tamu.edu/publications/190196SR/215/215.htm
- Henry, P., L. Jouniaux, E.J. Screaton, S. Hunze, and D. M. Saffer, Anisotropy of electrical conductivity record of initial strain at the toe of the Nankai accretionary wedge, ***J. Geophys. Res***., 2003.
- Jouniaux, L., J.-P. Pozzi, J. Berthier. and P. Massé, Detection of fluid flow variations at the Nankai Trough by electric and magnetic measurements in boreholes or at the seafloor, ***J. Geophys. Res***., 1999.
- Jouniaux L., Lallemant S., and Pozzi J.-P., Changes in the permeability, streaming potential and resistivity of a claystone from the Nankai prism under stress, ***Geophys. Res. Letters***, 1994.

Le principal encadrement que j'ai effectué, pour cette partie, a été celui de Sylvain Bourlange pour sa thèse de doctorat, soutenue en 2003.

- **Électrofiltration en zone volcanique.**

De nombreuses observations faites sur les volcans montrent des anomalies de potentiel électrique [*Aubert and Kieffer*, 1984 ; *Finizola et al.*, 2002 ; 2004 ; *Lénat et al.*, 2000] et de champ magnétique, dont on pense que l'origine est l'électrofiltration induite par les montées hydrothermales [voir illustration ci-après]. Le but à long terme serait de détecter des variations de régime hydrothermal par un suivi temporel des Potentiels Spontanés. Mais l'interprétation de ces Potentiels Spontanés nécessite une modélisation contrainte par des mesures de laboratoire représentatives. Nous avons montré que de fortes variations d'électrofiltration sur des échantillons de la Montagne Pelée sont liées en partie à la conductivité de surface et aux différents mécanismes d'éruption [*Jouniaux et al.*, *JGR*, 2000] (*INSU - PNRN*). Des mesures d'électrofiltration ont été effectuées sur des cendres du Misti (Pérou), (*coll. Université de Clermont-Ferrand - ACI Catastrophes Naturelles*), en quantifiant les effets de la chimie des solutions dans ce milieu, ceci pour mieux comprendre les anomalies de potentiel sur les volcans (co-direction de la thèse de Xavier Guichet, 2002). Jusqu'à présent, la plupart des suivis de Potentiels Spontanés sur les volcans se font en réitérant les mesures, et non en continu. Au Japon, sur le volcan Unzen, des mesures en continu ont été réalisées et une augmentation de l'anomalie de Potentiel Spontané de 500 à 600 mV a été détectée 3 mois avant une première extrusion de magma [*Hashimoto and Tanaka*, 1995]. À ma connaissance aucune modélisation rigoureuse des phénomènes électrocinétiques en zone volcanique n'a été effectuée. Dans le cadre de l'ACI - Catastrophes Naturelles, j'avais mesuré la perméabilité d'échantillons du Piton de La Fournaise pour contraindre la modélisation de la circulation hydrothermale dans cet édifice [*Fontaine et al., EPSL, 2002*]. Une fois le champ de pression hydrique connu, il est possible de modéliser les potentiels électrocinétiques à l'aide des équations couplées entre champ de pression et champ électrique. Cette modélisation n'est pas facile, et il faut tenir compte des variations de résistivité électrique du sol. Récement, des modélisations numériques ont montré que la première cause des potentiels spontanés sur les volcans ayant une zone non saturée importante n'était pas liée aux remontées hydrothermales mais à la distribution de conductivité électrique de la structure [*Ishido*, 2004 ; 2006]. L'interprétation des variations de Potentiels Spontanés sur les volcans est donc encore un sujet de débats.

- **Électrofiltration en zone de subduction.**

Les effets électriques et magnétiques dus aux circulations d'eau dans le prisme de Nankai ont été modélisés afin de savoir s'il est possible d'utiliser de telles mesures pour détecter les variations de circulation de fluide existant dans les prismes d'accrétion, elles-mêmes éventuellement liées au cycle sismique [*Jouniaux et al.*, *JGR*, 1999] (collaboration avec le laboratoire LETI du CEA de Grenoble ; programme franco-japonais Kaiko-Tokai). Nous avons montré que des signaux de 3 mV et de 3 nT pourraient être représentatifs de variations de 20 % dans les circulations d'eau dans les chevauchements du prisme.

J'ai ensuite effectué, avec Sylvain Bourlange (thèse de doctorat, 2003), des mesures de perméabilité d'échantillons du prisme de Nankai (collectés par P. Henry, leg ODP 190) dans des conditions de pression in situ [*Bourlange et al.*, *P.ODP*, 2004], et nous avons essayé de quantifier l'anisotropie de perméabilité. Ces mesures sont nécessaires pour l'étude de la propagation du décollement à la base du prisme d'accrétion. Une des motivations était d'arriver à déduire la perméabilité à faible pression effective (pression de confinement moins pression de pore) car on pense que de fortes surpressions sont présentes dans les prismes. Nous avons donc effectué des mesures, par la méthode dite du « pulse », c'est-à-dire en appliquant un gradient de pression d'eau et en suivant la diffusion de la pression [Fig. F1 dans *Bourlange et al.*, 2004], à des pressions effectives de l'ordre de 1 à 2.5 MPa, sous conditions hydrostatiques ou déviatoriques (avec fracturation), et nous avons mesuré des valeurs de perméabilité de l'ordre de 2-6 x 10^{-19} m^2 [Fig. F2 dans *Bourlange et al.*, *P.ODP*, 2004]. Ces valeurs ont ensuite été utilisées pour déduire un temps de diffusion de la pression de pore in - situ et conclure qu'une surpression pouvait être maintenue seulement pendant des épisodes transitoires pouvant constituer des épisodes de propagation du décollement [*Bourlange et al*., 2003]. Ces travaux ont fait suite à des mesures de variation de potentiel électrocinétique, de perméabilité, et de conductivité électrique lors de la déformation d'un échantillon du prisme de Nankai (provenant du Leg 131), et qui avaient montré une augmentation à la fois de la perméabilité et du potentiel d'électrofiltration pendant la déformation [*Jouniaux et al.*, *GRL*, 1994]. Par la suite, des mesures d'anisotropie de conductivité électrique sur des matériaux constitutifs du prisme d'accrétion de Nankai (provenant du Leg 190), ont été effectuées par P. Henry, qui a proposé d'utiliser ces mesures pour quantifier la déformation dans ces sédiments [*Henry et al*., *JGR*, 2003].

L'étude du prisme d'accrétion de Nankai se poursuit avec le projet IODP Nantroseize, avec un volet de forage qui sera mis en oeuvre à l'automne 2007 et se développera en 2008. Un des co-chefs européens de ce projet est Siegfried Lallemant (Univ. Cergy Pontoise). Sylvain Bourlange (Gocad, École Nationale de Géologie de Nancy) sera embarquant sur un des Legs. Il est probable qu'un projet national se développe, peut-être piloté par P. Henry (Collège de

France, Aix-en-Provence) et C. David (Univ. Cergy-Pontoise), et que l’équipe Physique des Roches de l’institut de Physique du Globe de Strasbourg y participe.

POTENTIELS SPONTANES SUR LES VOLCANS

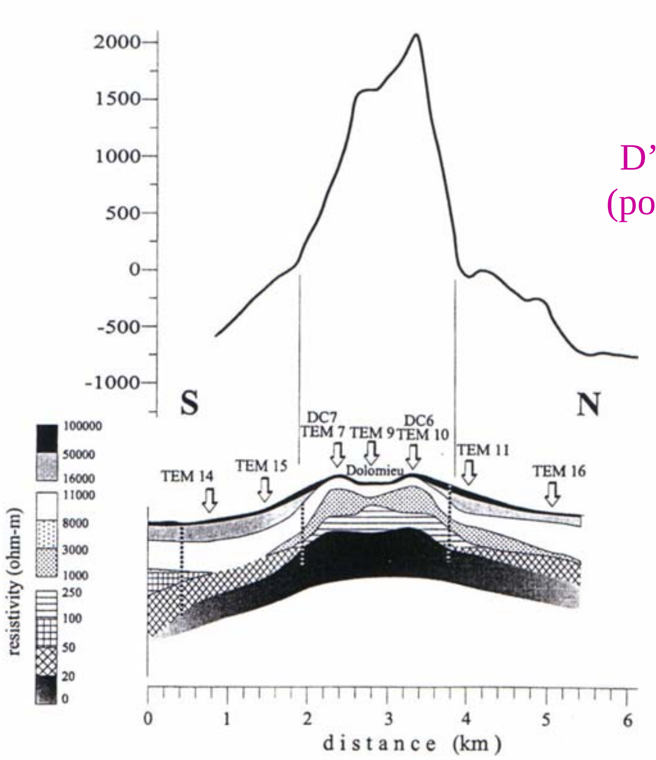

ORIGINE:
POTENTIEL
D'ELECTROFILTRATION
(potentiel électrique induit par
circulation de fluide :
migration ionique)

Lénat et al., 2000

BUT:
DETECTION DES VARIATIONS DE LA
SOURCE THERMIQUE

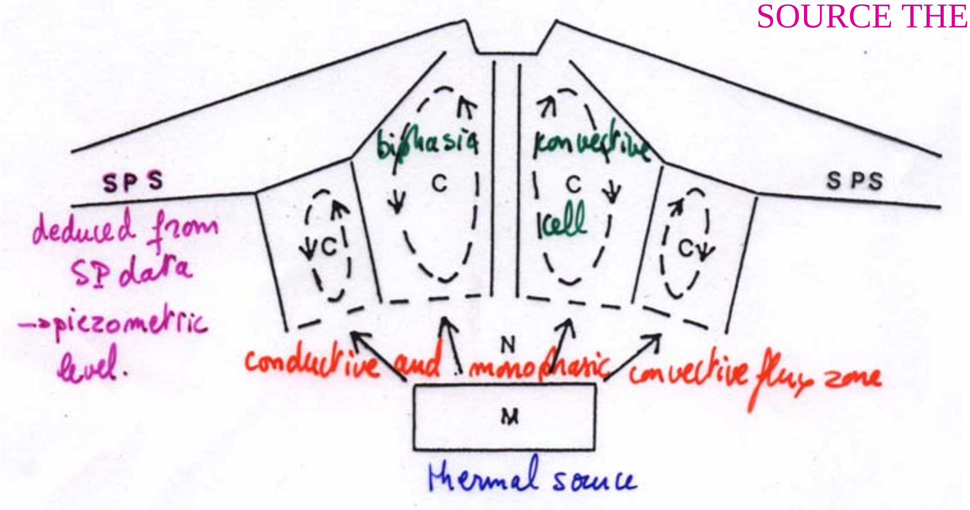

Aubert and Dana, 1994

JOURNAL OF GEOPHYSICAL RESEARCH, VOL. 105, NO. B4, PAGES 8391–8401, APRIL 10, 2000

Streaming potential in volcanic rocks from Mount Pelée

Laurence Jouniaux
Ecole Normale Supérieure de Paris, Unité Mixte de Recherche 8538, CNRS, Paris

Marie Lise Bernard and Maria Zamora
Institut de Physique du Globe de Paris, ESA 7046, CNRS, Université Denis Diderot, Paris

Jean Pierre Pozzi
Ecole Normale Supérieure de Paris, Unité Mixte de Recherche 8538, CNRS, Paris

Abstract. Streaming potential and electric conductivity have been measured in a laboratory on 11 consolidated samples coming from five deposits of the different evolutionary stages of Mount Pelée volcano. The streaming potential coupling coefficient ranges from –35 to –4905 mV MPa^{-1} and increases with increasing permeability. This increase is mainly due to the dependency of rock effective conductivity with permeability. The permeability of the samples varies from 0.146×10^{-12} to 34×10^{-12} m^2. The zeta potential, at pH = 7 and water conductivity of 2.1×10^{-4} S m^{-1}, is relatively small for the majority of the samples. It ranges from –4 to –19 mV. According to water conductivity analysis on Mount Pelée, streaming potential coupling coefficients of –25 to –406 mV MPa^{-1} can be expected for this volcano.

1. Introduction

Monitoring of electric and magnetic anomalies has been proposed as a means of predicting earthquakes [*Mizutani et al.*, 1976; *Fenoglio et al.*, 1995; *Trique et al.*, 1999] or volcanic eruptions [*Zlotnicki et al.*, 1998]. Magnetic observations made on La Soufrière volcano (Guadeloupe, France) have shown magnetic variations that could be induced by electric fields related to deep-water circulation (approximately at a depth of 5 km) [*Pozzi et al.*, 1979]. Water circulation is also thought to be the main agent of the strong magnetic signals observed on Piton de La Fournaise volcano (Réunion Island, France) [*Zlotnicki and Le Mouël*, 1990].

Self-potential (SP) anomalies can be produced by a streaming potential, as a consequence of fluid pressure gradients (an electrokinetic phenomenon); by a thermoelectric potential, as a consequence of a temperature gradient; by a chemical potential, as a consequence of a chemical gradient; or by these effects possibly acting together. Indeed, SP anomalies have been shown to be related to hydrothermal activity (two-phase water and steam flow) in geothermal areas and on active volcanoes [*Zohdy et al.*, 1973; *Anderson and Johnson*, 1976; *Corwin and Hoover*, 1979; *Michel and Zlotnicki*, 1998].

Electrokinetic phenomena were proposed as a possible mechanism for generating SP anomalies observed in geothermal areas [*Corwin and Hoover*, 1979; *Revil and Pezard*, 1998]. Some significant SP variations have been observed associated with volcanic activity and can precede eruptive episodes [*Aubert and Kieffer*, 1984; *Malengreau et al.*, 1994]. SP anomalies are commonly thought to be induced by electrokinetic phenomena because, thermoelectric and chemical coefficients are smaller than the electrokinetic coefficient [*Nourbehecht*, 1963; *Sill*, 1983; *Fitterman*, 1979; *Perrier et al.*, 1998, 1999]. SP surveys performed on Etna, Lamonga, and Merapi volcanoes have shown that the amplitude of the anomalies was related to the vapor flow, and the main source of these SP anomalies was thought to be electrokinetic [*Aubert and Dana*, 1994]. In some areas there is a good spatial correlation on active volcanoes between rising two-phase convective cells and positive SP anomalies [*Aubert et al.*, 1984; *Aubert and Baubron*, 1988]. SP measurements on La Fournaise volcano (Réunion Island, France) have shown a huge positive anomaly of amplitude more than +1850 mV on the cone. This anomaly suggests that hydrothermal ascendant circulations within the cone are induced by a magmatic complex source at least at 2 km depth beneath the summit [*Zlotnicki et al.*, 1994]. Recent SP measurements on Unzen volcano (Kyushu Island, Japan) showed a positive anomaly as large as +1000 mV per 500 m in the vicinity of the newly extruded lava dome. The most reasonable mechanism

Paper number 1999JB900435.
0148-0227/00/1999JB900435$09.00

for this anomaly is thought to be streaming potentials associated with subsurface hydrothermal convection [*Hashimoto and Tanaka*, 1995]. A sharp increase of +500 to +600 mV in SP was detected 3 months preceding the first extrusion of lava and was considered to be a result of the growth of the hydrothermal system. Moreover, *Fujinawa et al.* [1992] measured an anomalous vertical electric field of about +30 mV a few days prior to, and a month after, a minor volcanic eruption of Mount Mihara. These anomalous variations were thought to be generated by electrokinetic phenomena induced by variations of hydrothermal circulation around the crater, or by variations of crack density, due to volcanic activity.

Modeling of all these observations needs a good understanding of electrokinetic phenomena in volcanic rocks, specially the effect of the most influential parameters on streaming potential. These effects can be quantified in the laboratory. Few laboratory data of geophysical interest on streaming potential are available [*Ahmad*, 1964; *Somasundaran and Kulkarni*, 1973; *Ishido and Mizutani*, 1981; *Jouniaux et al.*, 1994; *Pozzi and Jouniaux*, 1994; *Jouniaux and Pozzi*, 1995a, b, 1997; *Lorne et al.*, 1999a, b], and few can be applied directly to volcanic environments [*Massenet*, 1983; *Massenet and Van Ngoc*, 1985; *Antraygues and Aubert*, 1993].

We present in this paper laboratory measurements of streaming potential and electric conductivity on 11 volcanic samples representative of the main lithologies and textures of the Mount Pelée volcano.

2. Electrokinetic Phenomena

Electrokinetic phenomena are induced by the relative motion between the fluid and the rock. Minerals forming the rock develop an electric double layer when in contact with an electrolyte, usually resulting from a negatively charged mineral surface. An electric field is created perpendicular to the surface of the mineral which attracts counterions (usually cations) and repulses anions in the vicinity of the pore-matrix interface. The electric double layer is made up of the Stern layer, where cations are adsorbed on the surface, and the Gouy diffuse layer, where the number of counterions exceeds the number of anions (for a detailed description, see *Adamson* [1976] and *Hunter* [1981]). The streaming potential is due to the motion of the diffuse layer induced by a fluid pressure difference along the interface. The zeta potential is defined at the slipping plane or shear plane (i.e., the potential within the double layer at the zero-velocity surface). In a porous medium the electric current density and the fluid flux are coupled [*Overbeek*, 1952; *Nourbehecht*, 1963], so that the streaming potentials are generated by fluids moving through porous media.

The parameter that quantifies this coupling is the streaming potential coupling coefficient or, simply, the coupling coefficient, defined by

$$C_S = \frac{\Delta V}{\Delta P} = \frac{\epsilon \zeta}{\eta \, \sigma_{\text{eff}}} , \qquad (1)$$

where ΔV is the generated electrical potential, ΔP is the applied pore pressure difference, ϵ is the dielectric constant of the pore fluid ($\epsilon = 7\times10^{-10}$ F m^{-1}), ζ is the zeta potential, η is the dynamic viscosity of the pore fluid ($\eta = 10^{-3}$ Pa s), and σ_{eff} is the effective conductivity defined by

$$\sigma_{\text{eff}} = F \, \sigma_r , \qquad (2)$$

where F is the formation factor and σ_r is the rock electrical conductivity at the fluid conductivity used for electrokinetic measurements.

If surface conductivity is negligible, $\sigma_{\text{eff}} = \sigma_f$, and we have

$$C_S = \frac{\epsilon \zeta}{\eta \, \sigma_f} , \qquad (3)$$

which is the Helmholtz-Smoluchowski equation [*Ishido and Mizutani*, 1981]. When we want to be free from the effect of the effective conductivity, another parameter, C', independent on this conductivity is defined,

$$C' = \frac{\Delta V}{\Delta P} \sigma_{\text{eff}} = \frac{\epsilon \zeta}{\eta} , \qquad (4)$$

where C' is called the electrokinetic coefficient.

For a complete development of the equations governing the coupled electro-magnetics and flow of the porous media, see *Pride* [1994] and *Revil et al.* [1999a, b], for modeling of electrokinetics in porous rocks see *Coelho et al.* [1996] and *Bernabé* [1998], and for further details on surface conductivity, see *Revil and Glover* [1997, 1998].

3. Experimental Procedures

Streaming potential and electric conductivity measurements have been performed on 11 consolidated samples coming from five deposits of the different evolutionary stages of Mount Pelée. This explosive volcano, located in the north end of Martinique Island in the Lesser Antilles (France), is mainly composed of andesitic pyroclastic materials. The sampling represented different lithologies and textures typically found on this volcano (dense or porous block, pumice, and scoria). Mineralogical and chemical compositions are relatively constant [*Westercamp*, 1976; *Fichaut et al.*, 1989; *Vincent et al.*, 1989]. Plagioclase, orthopyroxene, clinopyroxene, and a few magnetite are the main phenocrystals (with the following mean proportion: 33% plagioclase, 8% pyroxene, and 2.8% magnetite). The groundmass of the samples ranges from 52 to 63%. It is composed of variable percentages of glass and microcrystals. The proportion of the different mineral phases and the groundmass varies from one eruption to another. A short description of the samples is presented in Table 1.

3.1. Sample Preparation

Two samples were cored on each block of rock: (1) cylinder, 23 mm in diameter and 25–50 mm length, for porosity, permeability, and electrical conductivity measurements, and (2) cylinder, 2.5 cm in diameter and 48 mm long, for streaming potential measurements. The

Table 1. Description of the Samples

Stage	Eruption	Sample	Deposit	Description
Paleo–Pelée		MA701 (1)	volcanic breccias	vesicular andesite blocks
		MA701 (3)	volcanic breccias	vesicular andesite blocks
Neo–Pelée	Saint Vincent	MF201 (1)	scoria flows	andesite scoriaceous blocks
	Saint Vincent	MF201 (2)	scoria flows	andesite scoriaceous blocks
	Saint Vincent	MF201 (3)	scoria flows	andesite scoriaceous blocks
Modern stage	P1	F3	Pelean nuees ardentes	lightly vesicular andesite block
	P1	M	Plinian fallout	andesitic pumice
	1902	K	Pelean nuees ardentes	vesicular grey andesite
	1902	J	Plinian fallout	white andesitic pumice
	1929	R	Block-and-ash flows	vesiculated andesite
	1929	Q	Block-and-ash flows	highly vesicular andesite

end faces of the samples were ground flat and parallel to within 0.025 mm.

3.2. Porosity and Air Permeability Measurements

The matrix mass density ρ_m was measured with a pycnometer on 2–3 g of rock reduced on fine powder (10 μm). The porosity was measured with the triple weighing method: the sample was first oven dried at 70°C for at least 48 hours, slowly cooled to room temperature, and then saturated with degassed water under vacuum. The sample is weighed before saturation, and after saturation and immersed (saturated sample) within the water. These three measurements and the matrix mass density allow us to calculate the connected, ϕ_C, and trapped porosity, ϕ_T. The trapped porosity is the part of porosity not accessible under vacuum. The experimental error on porosity was less than 1%.

The air permeability k was measured, at atmospheric pressure, with a falling head permeameter (see *Bourbié and Zinszner* [1985] for a description of the apparatus). The accuracy is within 1% for permeabilities greater than 10^{-16} m^2. The Klinkenberg effect is only significant in the three less permeable samples, and it is always less than 6%. Measurements were repeated several times for reliability.

3.3. Electric Conductivity Measurements

In order to determine the electrical formation factor F, the electrical conductivity of the rock was measured, at room conditions, when the samples were saturated successively with a distilled water and with at least seven aqueous NaCl solutions with conductivities increasing from 6×10^{-4} to 17 S m^{-1}. The electrical conductivity measurements were performed with two-pole electrodes, a technique consisting in the measure of the electrical impedance of the samples, at different frequencies (varying from 100 to 100 kHz), by placing the sample between two stainless steel electrodes, connected to an impedance meter (HP4263A). Filter paper disks soaked with the saturating solution were put between the electrodes and each end of the sample to reduce contact resistance and to prevent polarization effects. A clamping system held the sample between the electrodes with the same constant force for each sample. The electrolyte conductivity was measured with a conductivity cell (Knick 702).

The following experimental procedure was used:

1. The sample was first dried for at least 48 hours at 70°C, cooled to room temperature, and placed in a container under dynamic vacuum for 4 hours. The container was then filled with distilled and degassed water and left under vacuum for 48 hours.
2. Samples were inserted quickly inside an insulating adhesive jacket to limit water evaporation during measurements and to prevent electrolyte conduction on the external surface sample. The electrical impedance of the sample and the conductivity of the solution were then measured.
3. After these measurements the samples were dried and again saturated with a degassed NaCl solution of 2×10^{-4} mol L^{-1}, and the electrical measurements were performed. The saturation conditions and the procedure of measurements were those described in the previous paragraph.
4. This procedure was reiterated for the other six NaCl solutions. Between two measurements, with two different saline solutions, the samples were carefully cleaned by saturating them several times with distilled water. The relative experimental error was less than 1% and 0.5% for rock conductivity and fluid conductivity measurements, respectively.

The formation factor was determined by nonlinear inversion of the experimental data, using the *Revil and Glover* [1998] model:

$$\sigma_r = \frac{\sigma_f}{F} H(\xi), \tag{5}$$

$$H(\xi) = 1 - t^f_{(+)} + F\xi + \frac{1}{2}\left(t^f_{(+)} - \xi\right) \times \left(1 - \frac{\xi}{t^f_{(+)}} + \sqrt{\left(1 - \frac{\xi}{t^f_{(+)}}\right)^2 + \frac{4F\xi}{t^f_{(+)}}}\right), \tag{6}$$

where $t^f_{(+)}$ is the Hittorf number of the cations (fraction of the electrical current carried in the free electrolyte by the cations), F and Φ are the formation factor and the porosity, respectively, and the dimensionless parameter ξ is defined by *Kan and Sen* [1987]

$$\xi = \frac{\sigma_S}{\sigma_f} = \frac{2}{3}\left(\frac{\Phi}{1-\Phi}\right)\frac{\beta_S Q_V}{\sigma_f}, \qquad (7)$$

where σ_S is the surface conductivity, β_S is the surface mobility of the counterions, and Q_V is the excess surface charges per unit of pore volume. The inversion procedure is described by *Bernard* [1999]. Only the data unaffected by the polarization effects were used for the inversion. For most of the samples the frequency which allows the electric impedance to be a pure resistance is 10 kHz.

3.4. Streaming Potential Measurements

The samples were first saturated with deionized water under vacuum for 8 hours. Electrical potential was measured while water was made to flow through the sample using the apparatus described in Figure 1. A silicone jacket was put around the sample to ensure the separation of the water and the confining fluid. A confining pressure (maximum 300 kPa) could be applied using the compressed air. The axial load was applied using lead weights of 50 kg, so that the axial stress on the sample was of the order of 1 MPa. This system allows a water to circulate through the sample with a maximum pressure gradient of 300 kPa. The water pressure, measured with a manometer, was controlled by applying compressed air pressure to a water reservoir at one end of the sample while the other end was maintained at atmospheric pressure. The tubing circuit was not closed, so that there was no possible electric current leakage through the water within the tubing. Most of the tubing is plastic, and the few metallic parts of the apparatus were grounded. The electric potential was measured by two silver-chloride electrodes of length 40 mm, which were made by electrolysis of a silver rod in salt water of concentration 10^{-1} mol L^{-1}. The electrodes were put in the water circuit near the ends of the sample but not within the water circulation to avoid the electrical noise due to water movement near the electrodes. The two electrodes are connected by two coaxial cables to a high-input impedance (above 10^{10} Ω) volt meter. The resistance of the sample was usually several hundred kΩ to a maximum of 1 MΩ, which is low compared to the input impedance of the volt meter, therefore allowing accurate measurements of the potentials.

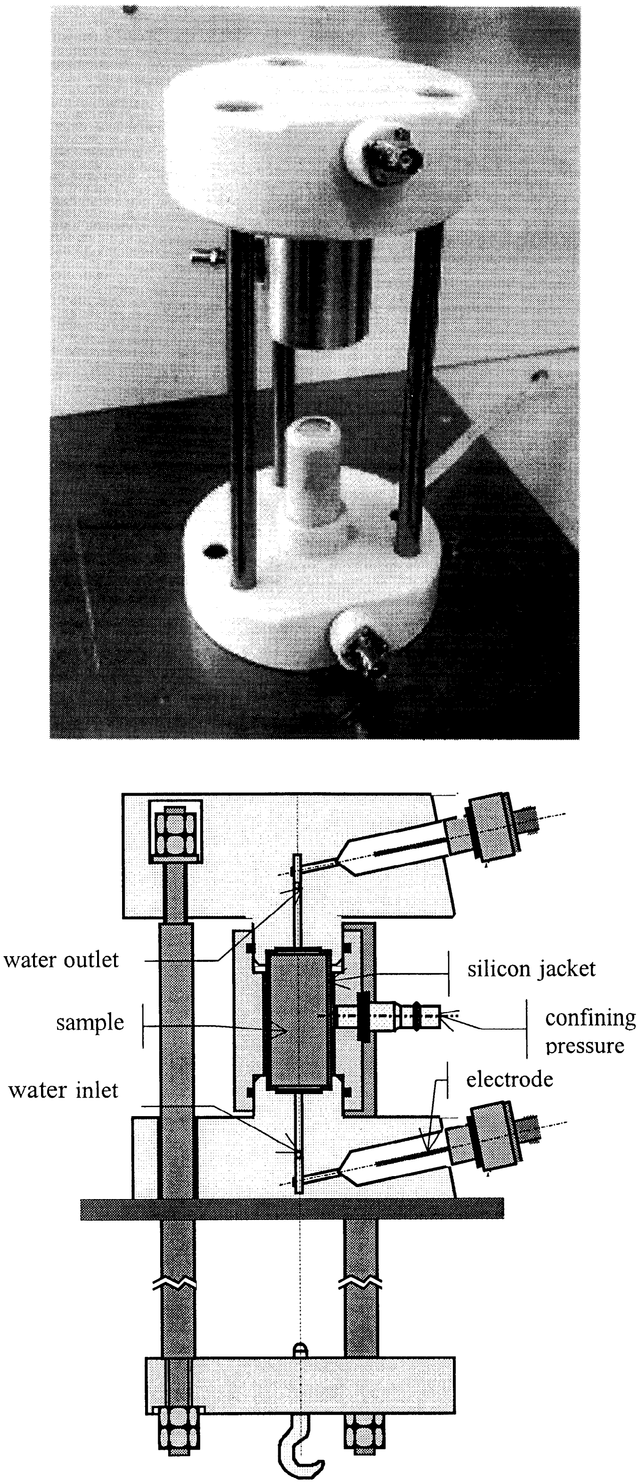

Figure 1. Apparatus used for electrokinetic measurements.

Streaming potential measurements were performed once equilibrium in water pH and water conductivity was attained: first, deionized water was made to flow through the sample, then collected, transferred to the upstream reservoir, and flowed through the sample again. The same procedure was repeated until the conductivity and pH of the water after flowing through the sample were constant. The volume of water flowing through the sample during this procedure ranged between 5 and 1000 cm^3, depending on the sample permeability (volume of the sample is 23.6 cm^3). Once the water conductivity and pH were constant, the streaming potential was measured for various water pressure gradients (10–180 kPa). The water expelled from the sample was also analyzed. Samples with permeability below 10^{-13} m^2 were not tested, because the water flow produced with the applied pore pressures would have

Table 2. Connected and Trapped Porosities, Permeability, and Electrical Formation Factor for Each Sample

Sample	ϕ_C	ϕ_T	k	F	σ_r
R	32.8	3.1	10342	9	0.19
Q	38.0	3.8	34325	9	0.19
K	25.1	2.3	1604	17	0.22
MF201 (1)	36.3	2.6	1564	16	0.85
MA701 (3)	28.9	2.3	5124	19	0.41
J	57.5	6.8	393	31	0.68
F3	14.6	1.7	207	65	0.15
M	57.4	10.0	146	40	0.76
MF201 (3)	35.2	2.9	5765	9	1.34
MA701 (1)	24.0	0.1	257	18	1.01
MF201 (2)	28.0	1.6	1043	25	0.43

Note that ϕ_C indicates connected porosity, in percent, ϕ_T indicates trapped porosity, in percent, k indicates permeability, in 10^{-15}m^2, F indicates formation factor, and σ_r indicates the rock conductivity, in mS m^{-1}.

been too small to induce a measurable electrokinetic effect. For lower permeabilities an apparatus similar to the one used with the pulse method to measure low permeabilities is needed [*Jouniaux et al.*, 1994].

4. Results and Discussion

4.1. Porosity, Permeability, and Electrical Conductivity

Connected porosity in the samples ranges from 14.6 to 57.5%, and trapped porosity can reach 10% (Table 2). Permeability ranges from 0.146×10^{-12} to 34×10^{-12} m^2. The most permeable samples have permeabilities higher than 10^{-11} m^2, which corresponds to very permeable materials such as sand.

Figure 2 shows an example of the dependence of the rock electrical conductivity versus the saturating fluid conductivity, with the fit obtained using the *Revil and Glover* [1998] model. Formation factor values are reported in Table 2 and range from 9 to 65. We note a tendency of F to decrease with increasing permeability as shown in Figure 3. The relationship between permeability and formation factor is detailed by *Bernard* [1999]. The rock conductivities σ_r, at the fluid conductivities used for electrokinetic measurements (obtained directly or by extrapolation using the Revil and Glover model) are inferior to 1 mS m^{-1}, except for the scoria MF201(3), where it reaches 1.3 mS m^{-1} (Table 2).

4.2. Streaming Potential

The streaming potential has been measured for 4-11 differential fluid pressure, 3 or 4 times for each sample. Figure 4 shows only the last set of measurements (the three last sets of measurements giving the same results, the first set corresponding to the transitory phase). We see that the streaming potential is proportional to the driving pore pressure, as expected from (1). This linearity has been verified previously for sand [*Ahmad*, 1964, *Lorne et al.*, 1999a] and sandstone samples [*Jouniaux and Pozzi*, 1997].

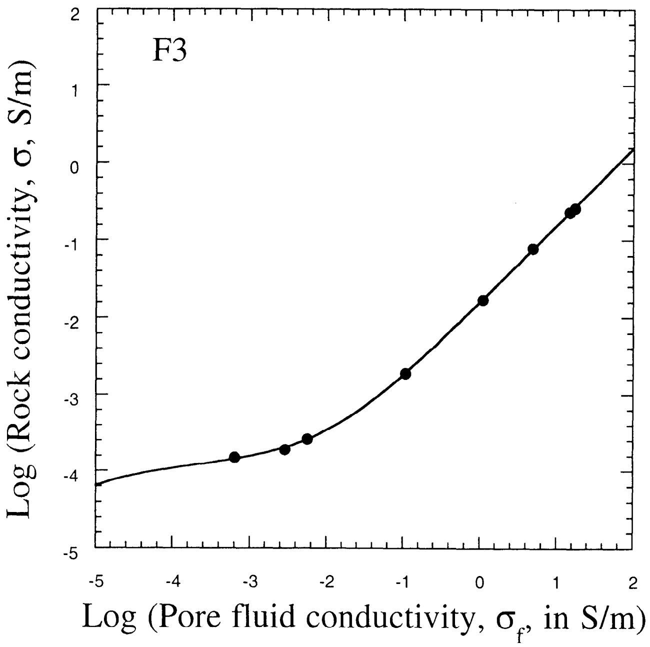

Figure 2. Rock electrical conductivity versus water conductivity, for sample F3.

For each sample, the coupling coefficient C_S has been deduced from the mean (from the three or four sets of measurements) of the slopes of the straight lines streaming potential versus driving pore pressure, by linear fit to the data, using least squares regression. The values of these coupling coefficients (Table 3) range from –35 to -4905 mV MPa^{-1} for a pH and conductivity of the water, in equilibrium with the the rock, varying from 6.2 to 6.9 and 0.23 to 2 mS m^{-1}, respectively.

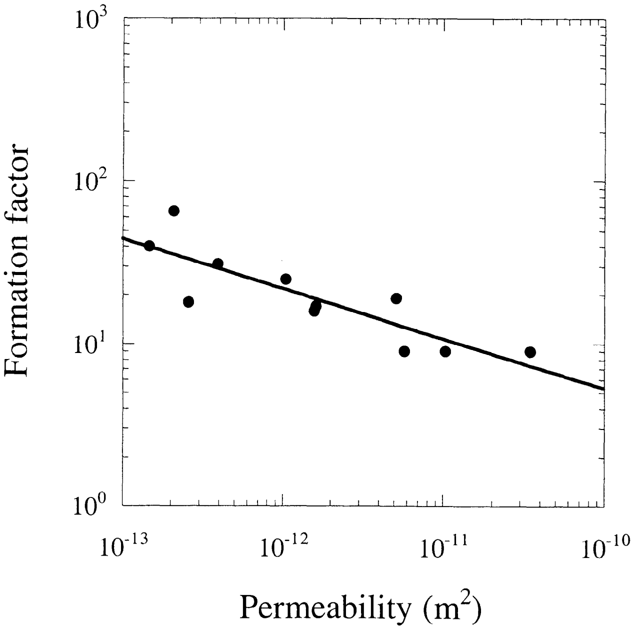

Figure 3. Formation factor versus permeability for all the studied samples.

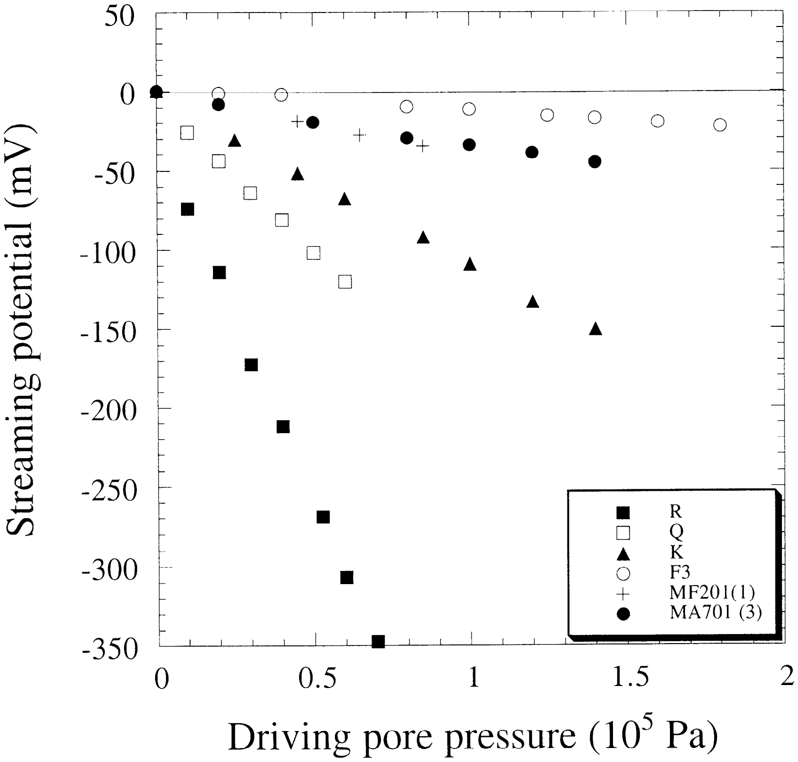

Figure 4. Measured streaming potential ΔV versus the applied pore pressure ΔP for six samples.

Figure 5 displays the variation of the coupling coefficient with porosity, formation factor, and permeability. No specific correlation is observed with porosity or formation factor. However, the coupling coefficient increases, by more than 2 orders of magnitude, with increasing permeability. This reliance of the coupling coefficient with permeability may be a consequence of a dependency of the effective conductivity σ_{eff} with permeability. Figure 6 exhibits this dependency. We observe a net decreasing of the effective conductivity, by more than 1 order of magnitude, with increasing permeability.

The dependency of the coupling coefficient on the permeability has been observed by *Antraygues and Aubert* [1993] on quartz sands (1.5 to 12 mm grain size) when these authors measured the electric potential along a vertical column of porous material in which upward vapor and a downward liquid water (vapor condensation) flows occurred, and by *Jouniaux and Pozzi* [1995a] on Fontainebleau sandstone samples, with permeabilities ranging from 0.15×10^{-15} to 1.2×10^{-12} m^2. *Jouniaux and Pozzi* [1995b] suggested that the decreasing coupling coefficient with the decreasing permeability of Fontainebleau sandstones could be induced by surface conductivity that may not be negligible, as first proposed for narrow cylindrical capillaries [*Broz and Epstein*, 1976]. In our samples, where the effective conductivity was measured instead of being inferred from surface conductance assumptions, we found a variation of the effective conductivity with permeability (Figure 6) of ~ 1.3 orders of magnitude. In order to be free of the dependence on the effective conductivity, the parameter C', which is independent from effective conductivity, has been calculated using (4). This parameter varies from -0.4 to -8.5 mV(MPa Ω m)$^{-1}$ (Table 3). Figure 7 shows the C' parameter as a function of permeability. We observe that the electrokinetic coefficient still varies by a factor 20 in the studied samples, but no clear dependence with permeability is noted.

4.3. The Zeta Potential

The macroscopic zeta potential is deduced for each sample, using (1). The values obtained are given in Table 3. The zeta potential ranges from −0.6 to −12.2 mV. These values are relatively low. Four samples have zeta potential, in absolute value, lower than 2 mV, indicating that for these samples the pH of the distilled water in equilibrium with these rocks is close to the pH_{pzc}. (Value pH_{pzc} represents the pH corresponding to the zero surface charge. At pH_{pzc} the zeta potential is zero). *Massenet and Van Ngoc* [1985] measured the zeta potential in samples of volcanic ashes (from Mount Etna). The mineralogical composition of these ashes is relatively close to the composition of our samples. They obtained values of zeta potential ranging from −26 to −34 mV for pH and fluid conductivity equivalent to these of our measurements. These values are superior to our values, but in the Mount Etna samples, $\text{pH}_{\text{pzc}} = 4.4$. These differences can emanate from differences in mineralogical composition and particularly from a different percentage of glass in the groundmass.

The zeta potential varies from more than 1 order of

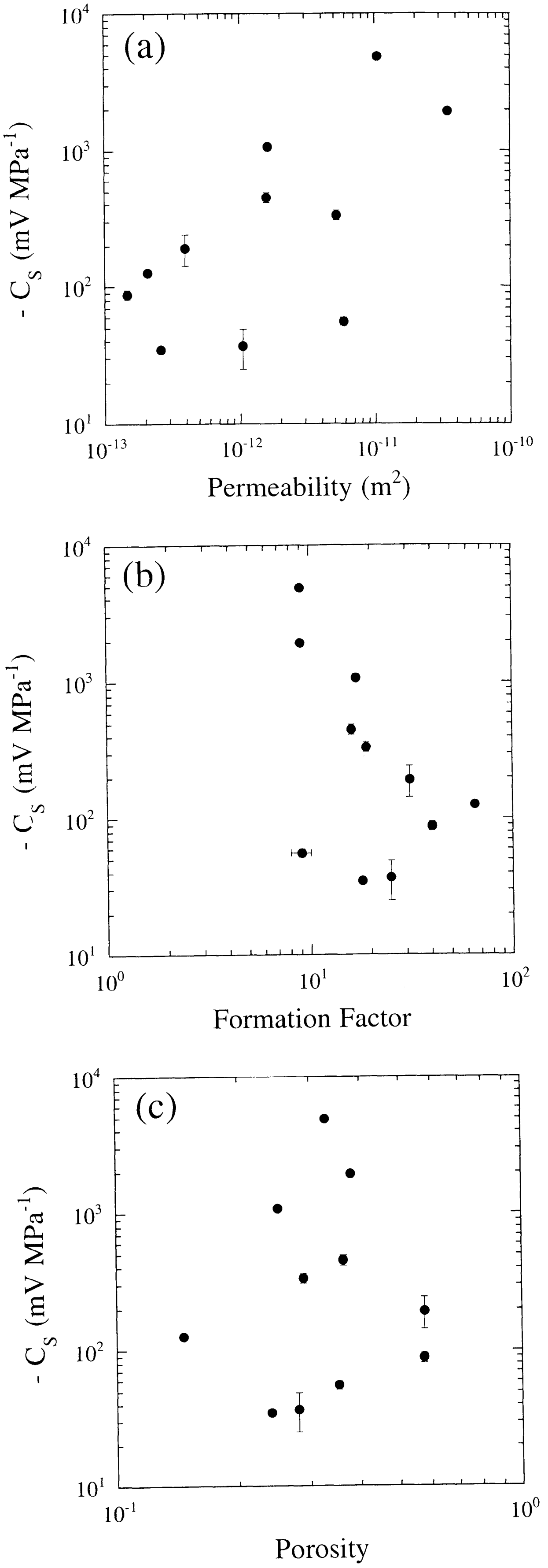

Figure 5. Measured coupling coefficient C_S versus (a) permeability, (b) formation factor, and (c) porosity.

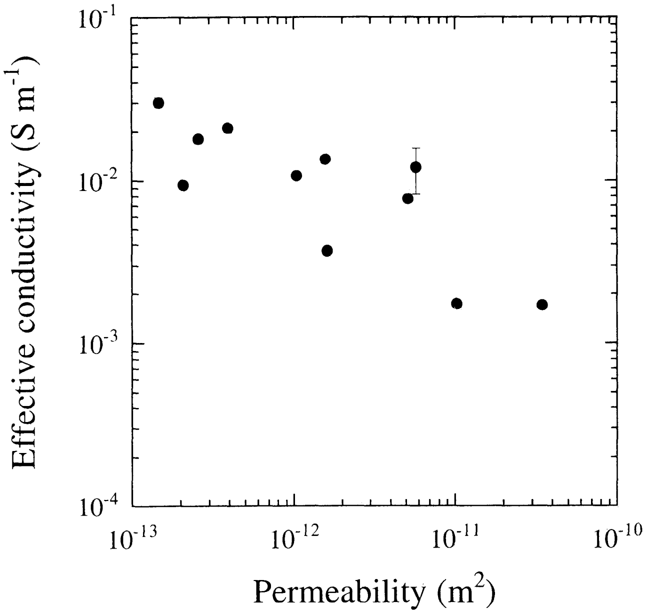

Figure 6. Measured effective conductivity σ_{eff} as a function of permeability.

magnitude in the studied samples. This variation cannot be due to the effective conductivity, since we take σ_{eff} into account to deduce the zeta potential. The effect of other parameters should be considered to explain this difference. The most influential parameters on the zeta potential are the mineralogical composition, the pH, the fluid conductivity, and the temperature [*Li and De Bruyn*, 1966; *Ishido and Mizutani*, 1981; *Revil et al.*, 1999a].

All the measurements were performed at the same temperature (25°C). The pH of the deionized water, at the equilibrium with the samples, pH_e, ranges from 6.2 to 6.9 (Table 3). It depends on the rock mineralogy. Thus, for the samples of the 1929 eruption, $\mathrm{pH}_e = 6.2$, while for Paleo-Pelée stage samples, $\mathrm{pH}_e = 6.6$. From the 1902 and P1 eruptions, which present a succession of the Plinian and Pelean mechanisms, in the samples emanating from the Pelean mechanism, $\mathrm{pH}_e = 6.4$. The two samples coming from the Plinian mechanism have different values of pH_e (6.7 and 6.9), problably because the Plinian samples exhibit more heterogeneous groundmass composition than the Pelean samples do (P. Besson, personal communication, 1999). The pH_e of the Saint Vincent stage samples are all different. This stage is characterized by variations of composition that are relatively important.

Water conductivity in equilibrium with the rock depends on the mineralogical composition and on the equilibrium pH and varies from 0.2 to 2 mS m^{-1} (Table 3). In order to compare the ζ potential obtained on the different samples in the same physical conditions, we must calculate the values of this potential at the same values of pH and water conductivity (or water concentration).

In the case of quartz systems, at pH close to 7 and for solutions containing K^+ or Na^+, the ζ potential may

Table 3. Fluid and Effective Conductivities, pH of the water, Coupling Coefficient, Electrokinetic Coefficient, and Zeta Potential for Each Sample.

Sample	σ_f	σ_{eff}	pH_e	C_S	C'	ζ	ζ_{cor}
R	0.34	1.7	6.2	-4905+15	-8.5	-12.2	-19
Q	0.23	1.7	6.2	-1940+30	-3.3	-4.7	-11
K	0.23	3.7	6.4	-1078+4	-4.0	-5.7	-11
MF201 (1)	1.31	13.6	6.8	-454+40	-6.2	-8.8	-11
MA701 (3)	0.34	7.7	6.6	-335+28	-2.6	-3.7	-7
J	0.74	21.0	6.7	-193+50	-4.1	-5.8	-9
F3	0.69	9.5	6.4	-127+5	-1.2	-1.7	-7
M	2.00	30.3	6.9	-88+7	-2.7	-3.8	-5
MF201 (3)	0.54	12.1	6.6	-56+4	-0.7	-1.0	-4
MA701 (1)	0.78	18.1	6.6	-35+2	-0.6	-0.9	-4
MF201 (2)	0.46	10.7	6.5	-37+12	-0.4	-0.6	-5

Note that σ_f indicates conductivity of fluid, in mS m^{-1}, σ_{eff} indicates effective conductivity, in mS m^{-1}, pH_e indicates the pH of the water at the equilibrium with the rock, C_S indicates coupling coefficient, in mV MPa^{-1}, C' indicates electrokinetic coefficient, in millivolt (MPa Ω m)$^{-1}$, ζ indicates zeta potential from equation (1), and ζ_{cor} indicates zeta potential from equation (8), in mV.

be analytically expressed as a function of temperature, pH, and fluid concentration [*Revil et al.*, 1999a] by

$$\zeta = c - d\,\text{pH} + b\log_{10}C_f \,, \qquad (8)$$

where C_f is the fluid concentration. The slopes b and d of (8) depend only on temperature. The zeta potential decreases in absolute value when the solution concentration increases. At 25°C, (8) provides b = –20 mV. This value is close to the one obtained by *Pride and Morgan* [1991], using a compilation of experimental data, who found b = –26 mV. The parameter c depends on temperature, on the total site density of the silica surface, and on the dissociation constant for

$$> \text{SiOH}^0 \quad \longleftrightarrow \quad > \text{SiO}^- + \text{H}^+ \qquad (9)$$

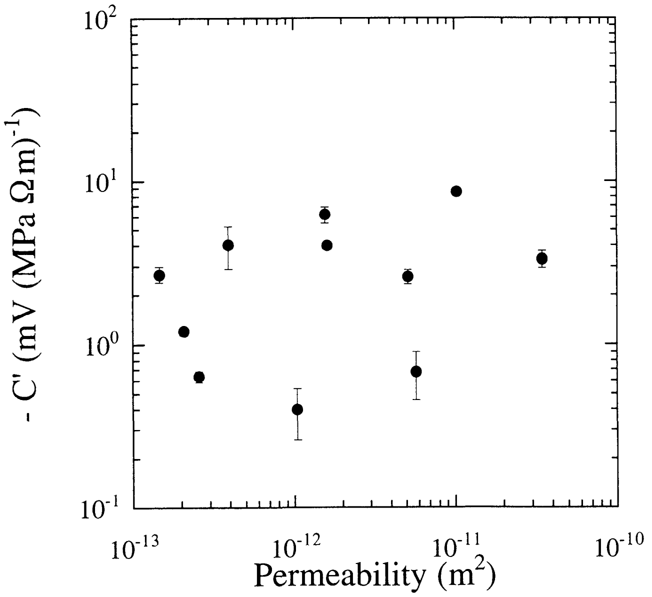

Figure 7. Computed parameter C' versus permeability.

For volcanic rocks, having usually a complex mineralogical composition, the effect of pH and fluid conductivity on zeta potential cannot be explained analytically, using microscopic approach, as for quartz systems. The effect of these parameters may only be inferred empirically using experimental data. Unfortunately, few experimental works exist in the literature concerning the effect of these parameters on zeta potential. In particular, only two studies explored the effect of pH and fluid conductivity on zeta potential in rocks having mineralogical compositions similar to our samples: the *Ishido and Mizutani* [1981] work which examined the effect of pH in an andesitic sample and the *Massenet and Van Ngoc* [1985] work which studied the effect of pH and fluid concentration in samples of volcanic ashes (from Mount Etna). The mineralogical composition of these ashes is relatively close to the composition of our samples.

In order to calculate the values of the ζ potential of our samples, in the same physical conditions, we assumed that the variation of the zeta potential with water concentration and pH can be described by a relation similar to that of (8), as for quartz systems. We used the measurements of *Massenet and Van Ngoc* [1985] at $6 \leq \text{pH} \leq 7$ and fluid concentration $\leq 10^{-3}$ mol L^{-1}, to deduce the values of b and d parameters. We used these values (b = 0.4 mV and d = 8 mV) to calculate zeta potential of our samples at C_f = 2.1×10^{-5} mol L^{-1} and pH = 7. The values of zeta potential at C_f = 2.1×10^{-5} mol L^{-1} and pH = 7, after pH and fluid concentration corrections (equation (8)), are given in Table 3. Figure 8 shows the zeta potential as a function of permeability before and after correction. We observe that after both corrections the dispersion of zeta potential is considerably reduced. The zeta potential ranges now from –4 to –19 mV. The zeta potential reflects differences in mineralogical composition of the samples. It is therefore related to the different eruption mechanisms, and we can observe that the lower values of zeta poten-

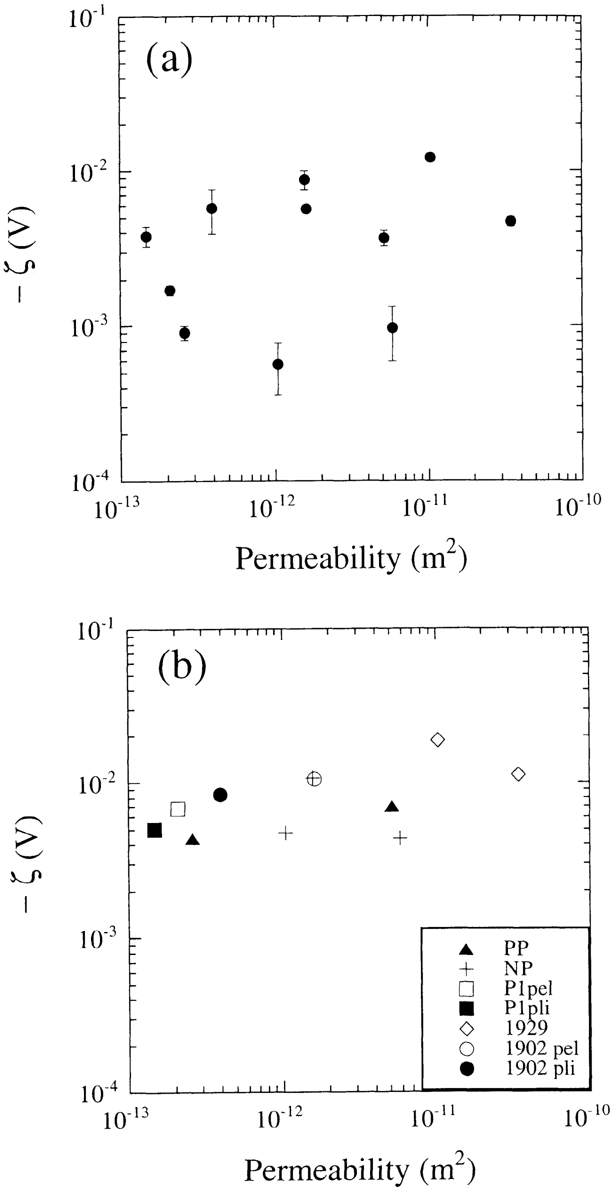

Figure 8. Zeta potential (a) deduced from equation (1) and (b) calculated from equation (8).

tial are obtained in the brecchias and scorias of Paléo- and Néo-Pelée stages, while the higher values are observed in the 1929 eruption. For the P1 and 1902 eruptions, zeta potential is more important in samples from Peléan mechanism. These observations show that the zeta potential is very sensitive to the weak mineralogical composition variations.

5. Streaming Potential on Volcanoes

SP surveys on mountainous areas usually show a negative correlation between electrical potential and topographic elevation, implying that the higher the topographic elevation, the lower the potential. Such a correlation between SP and topographic elevation is the result of steady state fluid flow caused by spatial variations in the elevation of the water table [*Ishido*, 1989]. Indeed, the electrokinetic coupling coefficient is usually negative for rocks, and positive charges are induced to move along the fluid flow from the top to the bottom of the topographic slope. This SP anomaly reflects the piezometric surface, and the amplitude of the anomaly is related to the thickness of the nonsaturated zone [*Aubert and Dana*, 1994]. This topographic effect in a volcanic area can be –1.6 mV m^{-1} [*Hashimoto and Tanaka*, 1995], –1.9 mV m^{-1} [*Lénat*, 1987], –3 mV m^{-1} [*Aubert and Lima*, 1986], –5 mV m^{-1} [*Aubert and Dana*, 1994], or larger, –10 mV m^{-1} [*Ishido*, 1989; *Hashimoto and Tanaka*, 1995]. In volcanic zones this topographic effect is modified by ascendant fluid flow, so that positive anomalies are usually observed, although it is not unusual to measure positive anomalies on extinct volcanoes too, induced by higher water-repellent levels. Large positive SP anomalies have been reported on La Fournaise volcano [*Zlotnicki et al.*, 1994], on Mount Somma-Vesuvius and Vulcano Island [*Di Maio et al.*, 1997], and on Unzen volcano [*Hashimoto and Tanaka*, 1995], and these anomalies are interpreted as the electric potentials generated by fluid flow in the hydrothermal ascendant circulations in the subsurface or greater depths. Recently, a huge anomaly of 4000 mV in self potential was reported on Misti volcano (south Peru) [*Finizola et al.*, 1998]. Since streaming potential is proportional to the pressure gradient (Figure 4), any source of fluid pressure gradient change will be an important factor for the electrokinetic process. Temporal monitoring of SP on volcanoes could reflect climatic variations [*Morat et al.*, 1992], variations in hydrothermal circulations resulting from crack closure or opening, fluid pressure increases induced by stress changes, or thermal fluctuations [*Malengreau et al.*, 1994].

Electrical resistivity of water sources and rivers on Mount Pelée has been measured to be 10–120 Ω m, with pH = 6.4. Sources of hot water (up to 73°C) showed also pH = 6.4. Moreover, resistivity of aquifers, measured via boreholes, was 20–72 Ω m [*Barat*, 1984]. Considering an average water electrical resistivity of 50 Ω m, one could expect a coupling coefficient of about –25 to –406 mV MPa^{-1} in this volcano.

6. Conclusion

The measured coupling coefficient on 11 samples from Mount Pelée volcano has been found to vary with permeability. This variation has been explained by the effect of the effective conductivity, of the pH, and of the fluid conductivity. The remaining variation of the zeta potential is due to the differences in mineralogy of the samples related to the eruption mechanisms.

This study demonstrates that it is important to perform electrokinetic measurements by controlling pH and ionic strength (or fluid conductivity) and by measuring the effective conductivity. A good understanding of the electrokinetic phenomenon on rock samples must involve joint measurements on intact samples and on crushed samples, in order to know the exact value of zeta potential in andesitic-water systems and its dependence on salinity and pH. The electrokinetic process in unsatured medium and the effect of temperature have been theoretically quantified recently [*Revil et al.*, 1999b]. The effects of vapor, and other gases, specially CO_2, on electrokinetics in volcanic samples, must be quantified in order to better understand the SP anomalies observed on volcanoes. Indeed, very recent measurements show that injected gases in soil, with various effects on pH, induced different SP responses [*Martinelli*, 1998].

Acknowledgments. This research is a collaboration with C. Philippe, ENSAM Laboratoire de Mécanique des Structures, Paris. We thank S. Jacquet and D. Corneille from ENSAM Paris and G. Marolleau from ENS Paris for the construction of the apparatus. The authors acknowledge fruitful exchanges with A. Revil, P. Besson and G. Boudon. The reviews of the manuscript by M. Aubert, P. Glover, and the Associate Editor greatly improved this paper. This research was supported by CNRS. This is a CNRS-INSU-PNRN contribution no. 215 (Thème risques volcaniques), a CNRS-INSU-PNRH contribution no. 216 (Thème circulation des fluides dans la croûte) and a EEC contribution of the Environmental and Climate Work programme (Volcanic risk). IPG contribution no. 1655.

References

Adamson, A.W., *Physical Chemistry of Surfaces*, Wiley-Interscience, New-York, 1976.

Ahmad, M., A laboratory study of streaming potentials, *Geophys. Prospect., 12,* 49–64, 1964.

Anderson, L. A., and G. R. Johnson, Application of the self-potential method to geothermal exploration in Long Valley, California, *J. Geophys. Res., 81,* 1527–1532, 1976.

Antraygues, P., and M. Aubert, Self potential generated by two-phase flow in a porous medium: Experimental study and volcanological applications, *J. Geophys. Res., 98,* 22,273–22,281, 1993.

Aubert, M., and J. C. Baubron, Identification of a hidden thermal fissure in a volcanic terrain using a combination of hydrothermal convection indicators and soil-atmosphere analysis, *J. Volcanol. Geotherm. Res., 35,* 217–225, 1988.

Aubert, M., and I. Dana, Interpretation of the self potential radial profiles in volcanology: Possibilities of the SP method for the monitoring of the active volcanoes, *Bull. Soc. Geol. Fr., 2,* 113–122, 1994.

Aubert, M., and G. Kieffer, Evolution d'une intrusion magmatique dans le flanc sud de l'Etna entre juin 1982 et juin 1983: Résultats de potentiel spontané (PS) et essai d'interprétation de l'éruption de 1983, *C. R. Acad. Sci., Ser. II, 298,* 379–382, 1984.

Aubert, M., and E. Lima, Hydrothermal activity detected by self-potential measurements at the N-S volcanic axis between the volcanoes Nevado de Colima and Volcan de Fuego de Colima, *Geofis. Int., 25,* 575–586, 1986.

Aubert, M., R. Auby, F. Bourlet, and Y. Bourlet, Contribution à la surveillance de l'áctivité de l'Etna à partir de l'étude des zones fumerolliennes, *Bull. Volcanol., 47,* 1039-1050, 1984.

Barat, A., Etude du role des eaux souterraines dans le mécanisme des éruptions phréatiques: Application à la Montagne Pelée de Martinique et à la Soufriére de Guadeloupe, Ph.D thesis, Univ. de Bordeaux, France, 1984.

Bernabé, Y., Streaming potential in heterogeneous networks, *J. Geophys. Res., 103,* 20,827–20,841, 1998.

Bernard, M. L., Etude expérimentale des propriétés physiques des roches pyroclastiques de la montagne Pelée, Ph.D thesis, Univ. Paris 7, Paris, 1999.

Bourbié, T., and B. Zinszner, Hydraulic and acoustic properties as a function of porosity in Fontainbleau sandstone, *J. Geophys. Res., 90,* 11,524–11,532, 1985.

Broz, Z., and N. Epstein, electrokinetic flow through porous media composed of fine cylindrical capillaries, *J. Colloid Interface Sci., 56,* 605–612, 1976.

Coelho, D., M. Shapiro, J. F. Thovert, and P. M. Adler, Electroosmotic phenomena in porous media, *J. Colloid Interface Sci., 181,* 169–190, 1996.

Corwin, R. F., and D. B. Hoover, The self-potential method in geothermal exploration, *Geophysics, 44,* 226–245, 1979.

Di Maio, R., P. Mauriello, D. Patella, Z. Petrillo, S. Piscitelli, A. Siniscalchi, and M. Veneruso, Self-potential, geoelectric and magnetotelluric studies in Italian active volcanic areas, *Ann. Geofis., XL-2,* 519–537, 1997.

Fenoglio, M.A., M. J. S Johnston, and J. D. Byerlee, Magnetic and electric fields associated with changes in high pore pressure in fault zones: Application to the Loma Prieta ULF emissions, *J. Geophys. Res., 100,* 12,951–12,958, 1995.

Fichaut, M., R. C. Maury, H. Traineau, D. Westercamp, J. L. Joron, A. Gourgaud, and C. Coulon, Magmatology of Mount Pelée (Martinique F.W.I.), III, Fractional crystallization versus magma mixing, *J. Volcanol. Geotherm. Res., 38,* 189–212, 1989.

Finizola, A., D. Ramos, and O. Macedo, Self-potential studies of hydrothermal systems structure on Misti and Ubinas volcanoes, South Peru, paper presented at the XXIII General Assembly, *Eur. Geophy. Soc.*, Nice, C194, 1998.

Fitterman, D. V., Theory of electrokinetic-magnetic anomalies in a faulted half-space, *J. Geophys. Res., 84,* 6031–6040, 1979. (Correction, *J. Geophys. Res.*, 86, 9585-9588, 1981.)

Fujinawa, Y., T. Kumagai, and K. Takahashi, A study of anomalous underground electric field variations associated with a volcanic eruption, *Geophys. Res. Lett., 19,* 9–12, 1992.

Hashimoto, T. and Y. Tanaka, A large self-potential anomaly on Unzen volcano, Shimabara peninsula, Kyushu Island, Japan, *Geophys. Res. Lett., 22,* 191–194, 1995.

Hunter, R. J., *Zeta Potential in Colloid Science*, Academic, London, 1981.

Ishido, T., Self-potential generation by subsurface water flow through electrokinetic coupling, in *Detection of Subsurface Flow Phenomena, Lecture Notes Earth Sci.*, Vol. 27, p. 121–131, Springer-Verlag, New York, 1989.

Ishido, T., and H. Mizutani, Experimental and theoretical basis of electrokinetic phenomena in rock-water systems and its applications to geophysics, *J. Geophys. Res., 86,* 1763–1775, 1981.

Jouniaux, L., and J.-P. Pozzi, Streaming potential and permeability of saturated sandstones under triaxial stress: Consequences for electrotelluric anomalies prior to earthquakes, *J. Geophys. Res., 100,* 10,197–10,209, 1995a.

Jouniaux, L., and J.-P. Pozzi, Permeability dependence of streaming potential in rocks for various fluid conductivities, *Geophys. Res. Lett., 22,* 485–488, 1995b.

Jouniaux, L., and J.-P. Pozzi, Laboratory measurements anomalous 0.1-0.5 Hz streaming potential under geochemical changes: Implications for electrotelluric precursors to earthquakes, *J. Geophys. Res., 102,* 15,335–15,343, 1997.

Jouniaux, L., S. Lallemant, and J.-P. Pozzi, Changes in the permeability, streaming potential and resistivity of a claystone from the Nankai prism under stress, *Geophys. Res. Lett., 21,* 149–152, 1994.

Kan, R., and P. N. Sen, Electrolytic conduction in periodic arrays of insulators with charges, *J. Chem. Phys., 86,* 5748–5756, 1987.

Lénat, J.-F., Structure et dynamique internes d'un volcan basaltique intraplaque océanique: Le Piton de La Fournaise (Ile de la Réunion), Ph. D thesis, Clermont-Ferrand II, France, 1987.

Li, H. C., and P. L. De Bruyn, electrokinetic and adsorption studies on quartz, *Sur. Sci., 5,* 203–220, 1966.

Lorne, B., F. Perrier, and J. P. Avouac, Streaming potential measurements, 1, Properties of the electrical double layer from crushed rock samples, *J. Geophys. Res., 104,* 17,857–17,877, 1999a.

Lorne, B., F. Perrier, and J. P. Avouac, Streaming potential measurements, 2, Relationship between electrical and hydraulic flow patterns from rock samples during deformation, *J. Geophys. Res., 104,* 17,879–17,896, 1999b.

Malengreau, B., J. F. Lénat, and A. Bonneville, Cartography and temporal observation of self-potential (SP) anomalies at Piton de la Fournaise, *Bull. Soc. Géol. Fr., 165,* 221–232, 1994.

Martinelli, G., The possible joint appearance of pre-seismic geochemical and geoelectrical anomalies in tectonically active areas, paper presented at the XXIII General Assembly, *Eur. Geophy. Soc.,* Nice, C171, 1998.

Massenet, F., Etude du phénomene de polarisation spontanée sur les volcans actifs et applications à la prospection et à la surveillance sur lEtna (Sicile), Ph. D thesis, Inst. Nat. Polytech. de Lorraine, Nancy, France, 1983.

Massenet, F., and P. Van Ngoc, Experimental and theoretical basis of self-potential phenomena in volcanic areas with reference to results obtained on mount Etna, *Earth Planet. Sci. Lett., 73,* 415–429, 1985.

Michel, S., and J. Zlotnicki, Self-potential and magnetic surveying of La Fournaise volcano (Réunion Island): Correlations with faulting, fluid circulation, and eruption, *J. Geophys. Res., 103,* 17,845–17,857, 1998.

Mizutani, H., T. Ishido, T. Yokokura, and S. Ohnishi, Electrokinetic phenomena associated with earthquakes, *Geophys. Res. Lett., 3,* 365–368, 1976.

Morat, P., J.-L. Le Mouël, G. Nover, and G. Will, Annual variation of the water saturation of a highly porous rock driven by a seasonal temperature variation and measured by an array of electrodes, *C. R. Acad. Sci., Ser. II, 315,* 1083–1090, 1992.

Nourbehecht, B., Irreversible thermodynamic effects in inhomogeneous media and their applications in certain geoelectric problems, Ph. D thesis, Mass. Inst. of Technol., Cambridge, Mass., 1963.

Overbeek, J. T. G., Electrochemistry of the double layer, in *Colloid Science*, vol. 1, *Irreversible Systems*, edited by H. R. Kruyt, pp. 115-193, Elsevier Sci., New York, 1952.

Perrier, F., M. Trique, B. Lorne, J. P. Avouac, S. Hautot, and P. Tarits, Electrical variations associated with yearly lake level variations, *Geophys. Res. Lett., 25,* 1955–1958, 1998.

Perrier, F., M. Trique, J. Aupiais, U. Gautam, and P. Shrestha, Electric potential variations associated with periodic spring discharge in western Nepal, *C. R. Acad. Sci. Paris, Ser. II, 328,* 73–79, 1999.

Pozzi, J.-P., and L. Jouniaux, Electric effects of fluid circulation in sediments and seismic prediction, *C. R. Acad. Sci., Ser. II, 328,* 73–77, 1994.

Pozzi, J. P., J. L. Le Mouël, J. C. Rossignol, and J. Zlotnicki, Magnetic observations made on La Soufrière volcano (Guadeloupe) during the 1976-1977 crisis, *J. Volcanol. Geotherm. Res., 5,* 217–237, 1979.

Pride, S. R., Governing equations for the coupled electromagnetics and acoustics of porous media, *Phys. Rev. B, Condens. Matter., 50,* 15,678–15,696, 1994.

Pride, S. R., and F. D. Morgan, electrokinetic dissipation induced by seismic waves, *Geophysics, 56,* 914–925, 1991.

Revil, A., and P. W. J. Glover, Theory of ionic-surface conduction in porous media, *Phys. Rev. B, Condens. Matter., 55,* 1757–1773, 1997.

Revil, A., and P. W. J. Glover, Nature of surface electrical conductivity in natural sands, sanstones, and clays, *Geophys. Res. Lett., 25,* 691–694, 1998.

Revil, A., and P. A. Pezard, Streaming electrical potential anomaly along faults in geothermal areas, *Geophys. Res. Lett., 25,* 3197–3200, 1998.

Revil, A., P. A. Pezard, and P. W. J. Glover, Streaming potential in porous media, 1, Theory of the zeta potential, *J. Geophys. Res., 104,* 20,021–20,031, 1999a.

Revil, A., H. Schwaeger, L. M. Cathles III, and P. D. Manhardt, Streaming potential in porous media, 2, Theory and application to geothermal systems, *J. Geophys. Res., 104,* 20,033–20,048, 1999b.

Sill, W. R., Self-potential modeling from primary flows, *Geophysics, 48,* 76–86, 1983.

Somasundaran, P., and R. D. Kulkarni, A new streaming potential apparatus and study of temperature effects using it, *J. Colloid Interface Sci., 45,* 591–600, 1973.

Trique, M., P. Richon, F. Perrier, J. P. Avouac, and J. C. Sabroux, Radon emanation and electric potential variations associated with transient deformation near reservoir lakes, *Nature, 399,* 137–141, 1999.

Vincent, P. M., J. L. Bourdié, and G. Boudon, The primitive volcano of Mount Pelée: Its construction and partial destruction by flank collapse, *J. Volcanol. Geotherm. Res., 38,* 1–15, 1989.

Westercamp, D., Petrology of the volcanic rocks of Martinique, West Indies, *Bull. of Volcanol., 39,* 175–200, 1976.

Zlotnicki, J., and J. L. Le Mouël, Possible electrokinetic origin of large magnetic variations at La Fournaise volcano, *Nature, 343,* 633–635, 1990.

Zlotnicki, J., S. Michel, and C. Annen, Self-potential anomalies and convective systems on La Fournaise volcano (Réunion Island, France), *C. R. Acad. Sci., Ser. II, 318,* 1325–1331, 1994.

Zlotnicki, J., G. Boudon, J. P. Viodé, J.-F. Delorne, and A. Mille, Hydrothermal circulation beneath Mount Pelée inferred by Self-potential surveying. Structural and tectonic implications, *J. Volcanol. Geotherm. Res., 84,* 73–91, 1998.

Zohdy, A. A. R., L. A. Anderson, and L. J. P. Muffler, Resistivity, self potential and induced polarization surveys of a vapor-dominated geothermal system, *Geophysics, 38,* 1130-1144, 1973.

Laurence Jouniaux, Jean Pierre Pozzi, Laboratoire de Géologie, Ecole Normale Supérieure de Paris, 24, rue Lhomond, F-75231, Paris cedex, France. Email: jouniaux@geologie.ens.fr

Marie Lise Bernard, Maria Zamora Laboratoire des Géomatériaux, Institut de Physique du Globe de Paris, 4 Place Jussieu, F-75252 Paris Cedex 05, France.

(Received December 9, 1998; revised November 30, 1999; accepted December 8, 1999.)

ELSEVIER
Earth and Planetary Science Letters 200 (2002) 1–14
EPSL
www.elsevier.com/locate/epsl

Constraints on hydrothermal processes on basaltic edifices: inferences on the conditions leading to hydrovolcanic eruptions at Piton de la Fournaise, Réunion Island, Indian Ocean

F.Jh. Fontaine[a,*], M. Rabinowicz[a], J. Boulègue[b], L. Jouniaux[c]

[a] *Laboratoire de Dynamique Terrestre et Planétaire, UMR 5562, 14 Avenue Edouard Belin, 31400 Toulouse, France*
[b] *Laboratoire de Géochimie, Physicochimie et Fluides Géologiques, UPMC, UPRESA 7047, 75252 Paris Cedex 05, France*
[c] *Ecole Normale Supérieure de Paris, Laboratoire de Géologie, UMR 8538, 24 rue Lhomond, 75231 Paris Cedex 05, France*

Received 7 September 2001; received in revised form 25 February 2002; accepted 7 March 2002

Abstract

The hydrothermal processes that occur on the active basaltic edifice of Piton de la Fournaise are investigated. The present-day volcanic activity concentrates in a west–east-oriented collapsed area, 13 km long and 6–8 km large, called Enclos Fouqué. Enclos Fouqué is open to the sea on its eastern side, while a horseshoe rim delimits its extension to the west, south and north. This forms a continuous cliff, 100–200 m high above the floor of Enclos Fouqué. Inside Enclos Fouqué, a 400 m high basaltic cone with two coalescent summit craters constitutes the most active area of the volcano. Beyond the western wall of Enclos Fouqué, a wide basaltic plateau called the Plaine des Sables stretches west for a few kilometers, until it reaches a cliff limiting its western part. To the north and south of this plateau, rivers notch the basaltic edifice, and along the slopes of the induced valleys springs flow. Geochemical data from these springs indicate hydrothermal activity within deep fractured media inside the plateau generated owing to west–east regional extension. On the floor of the Plaine des Sables, near the western wall of Enclos Fouqué, extensive ash deposits from a violent hydrothermal eruption have been recognized. Hydrothermal activity has also been detected in the deep (>100 m) porous layers of Enclos Fouqué, in an area surrounding the central cone. This circulation occurs in layers of vesiculated rocks that constitute a highly permeable and quasi-isotropic medium. Physical models are presented to illustrate the basic differences between the thermal regime of each hydrothermal system. We show that, in the periphery of the volcano, the fracture walls stabilize the hydrothermal circulation inside the fissure network, thus steadily draining the heat along the impermeable walls. Consequently, hot (230–240°C) rising convective currents with a finger shape, 150 m distant, reach the uppermost parts of the fracture. By contrast, inside the isotropic porous layers of the central area, the circulation is likely to be chaotic/turbulent because of the high permeability of the medium. This scatters the thermal energy through the whole porous media. Numerical models of the transient evolution of the hydrothermal circulation in the fractured medium are presented. They reveal that the fingers generated in the deep levels of the edifice move upward at a velocity of 15–150 m/yr, depending on the amplitude of the fracture

---

[*] Corresponding author. Tel.: +33-5-6133-2844; Fax: +33-5-6133-2900.
E-mail address: fontaine@pontos.cst.cnes.fr (F.J. Fontaine).

PII: S0012-821X(02)00599-X

permeability. The extensive character of the stresses in the Plaine des Sables, the velocity and the high temperature inside the hydrothermal flow constitute necessary conditions for the disruption of the fracture walls during boiling. Using a model of Germanovich and Lowell [J. Geophys. Res. 100 (1995) 8417–8434], these conditions are shown to be sufficient for the generation of huge (km^3 of deposits) hydrothermal eruptions in the periphery of the edifice, while only small (a few m^3 of deposits) hydrovolcanic events are shown to develop at the summit area. Accordingly, the ash deposits (0.6 km^3) recovered near the western wall of Enclos Fouqué are ascribed to the hydrothermal flow in fractures generated by the east–west extensional stresses.

Keywords: hydrothermal processes; volcanism; models; fractures; Piton de la Fournaise

1. Introduction

Hydrovolcanic phenomena are catastrophic eruptive/explosive events that sometimes accompany volcanic/magmatic activities. These events violently eject a mixture of water, steam and rock particles. According to Smith and McKibbin [2], these phenomena can be classified into two types: phreatomagmatic and steam-blast events. Phreatomagmatic eruptions occur when hot magmatic products contact groundwater or seawater. The erupted deposits contain amounts of fresh glassy magmatic products. Steam-blast events account for eruptions that did not involve the expulsion of juvenile rock. Among these steam-blast type eruptions, Smith and McKibbin [2] itemize: gas eruptions, when the driving fluid is gas or superheated steam, phreatic eruptions, when the driving fluid is groundwater (essentially of meteoric origin), and hydrothermal eruptions, which require a pre-existing hydrothermal system.

To understand the physical mechanisms driving hydrovolcanic events, the choice of a well studied and monitored site is fundamental. We focused our study on the Piton de la Fournaise which is one of the most active and monitored basaltic volcanoes in the world, erupting every 11–18 months [4]. Its build up started at least 500 000 years ago on the eastern flank of the Piton des Neiges (a nearby extinct volcano, Fig. 1) [3]. Thereafter, the volcanic activity moved to the east. Its present location results from three successive collapses separating four phases of magmatic activity [5] (Fig. 1). The youngest collapse, which formed the horseshoe structure called Enclos Fouqué (EF in Figs. 1 and 2), has been dated to 4000 years by analysis of cosmic ray-produced ^{3}He and ^{21}Ne [6]. The present-day volcanic activity (fourth magmatic phase) concentrates inside Enclos Fouqué which is composed of a 400 m high central cone, two diffuse rift zones and two coalescent – Bory (BC in Fig. 1) and Dolomieu (DC in Fig. 1) – summit craters. The magmatic activity is characterized by two preferential orientations for outlets: N10 and N170 (rift zones). A third orientation (N120, thought to be the main tectonic direction) has been evidenced, but is not involved in the present-day activity [5].

At the Piton de la Fournaise, except for a permanent fumarolic vent that has been active since 1986, there is no obvious hint of hydrothermal activity. In fact, the best evidence of hydrothermal activity comes from the geophysical studies of the volcano. It has been established by electric measurements (self-potential (SP) anomalies) that hydrothermal activity takes place in the active central cone. In fact, the positive SP anomalies (up to 2 V) detected inside the cone have been interpreted as convective ascending currents generated by thermal transfers via infiltrated meteoric water (6–10 m/yr) [7,8]. A shallow magmatic complex provides the necessary heat [5,9]. Recently, Lénat et al. [10] confirmed this hypothesis by studying the resistivity structure of the edifice. Indeed, the development of superficial layers (about a few hundred meters under the top of the cone) with low resistivities in the cone is associated to the influence of a coupled hydrothermal/magmatic complex. Nevertheless, little is known about hydrothermal activity that develops inside the cone. Particularly, the evidence of an aquifer has not been established yet.

Some arguments also lead to the hypothesis that hydrothermal activity develops in the periphery of the volcano. The western parts of the volcano are notched by deep valleys where erosion

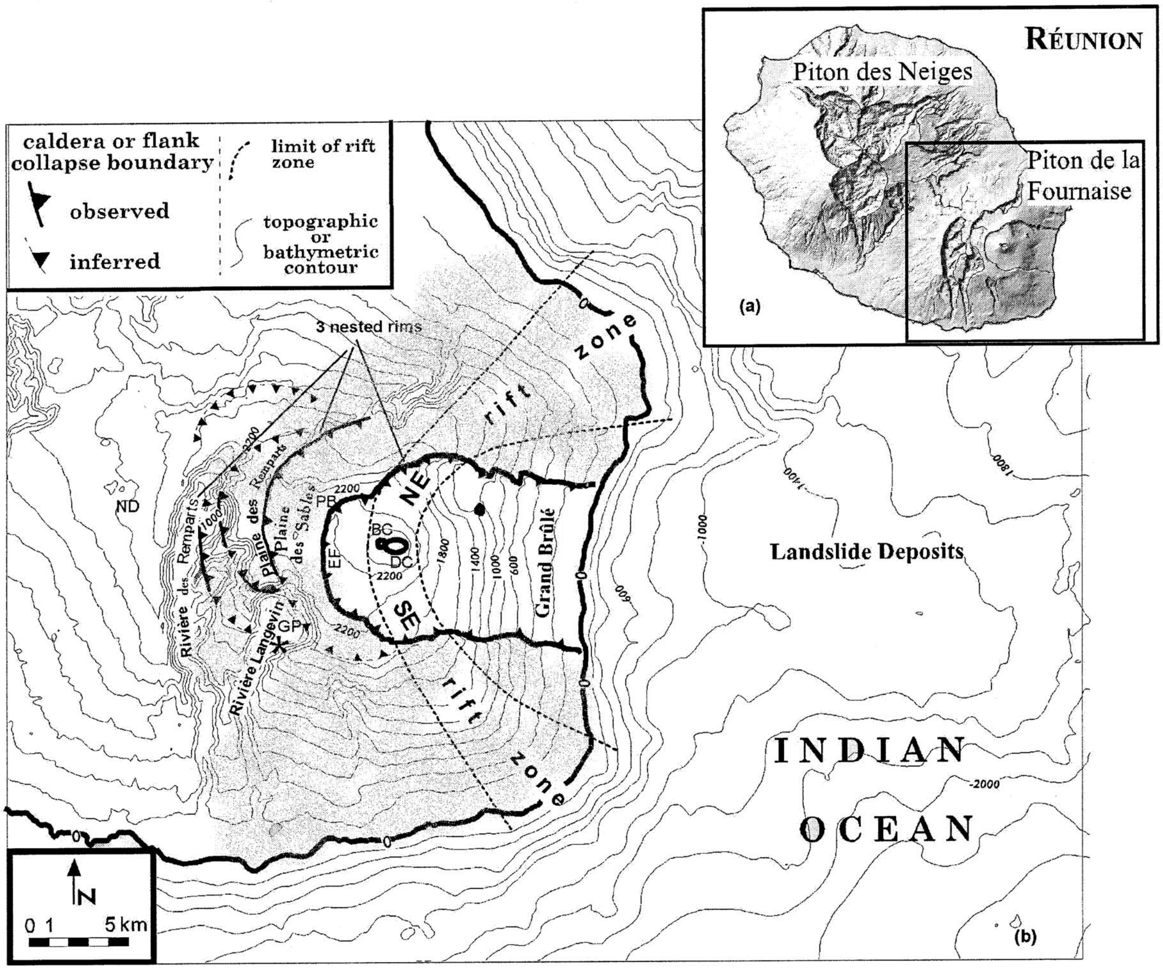

Fig. 1. (a) Réunion Island. (b) Main structures of the edifice of Piton de la Fournaise. EF: Enclos Fouqué; GP: Grand Pays circus; PB: Pas de Bellecombe; ND: Notre Dame area; BC: Bory Crater; DC: Dolomieu Crater; asterisk: location of the spring with anomalous $\delta^{13}C$ and fluor concentration. The gray area corresponds to the extension of the BAM. Also represented: the locations of the main fracture zone, N 10°, N 170° (rift zone northeast and southeast), and the lines of iso-elevation. Modified map after Lénat et al. [10].

digs rivers. The depth of these gorges lies between several hundred and a thousand meters. In the walls of Grand Pays (a collapse area upstream from Rivière Langevin, GP in Fig. 1), hydrothermal minerals have been recovered [11]. The resistivity structure under the Plaine des Sables (see Fig. 1) show the development of a conductive layer (resistivity $\leq 100\ \Omega$ m) at 1 km depth [10]. The interpretation of such conductive layers in the context of the Plaine des Sables is problematic, because it is an inactive area today. It has been inferred that these layers may be representative of a hydrothermally altered zone [10]. Moreover, gravimetric studies underneath the Grand Pays area (Fig. 1) show the settling of a dense intrusive complex, about 1 km below sea level. In fact, the presence of hydrothermal minerals and of a dense intrusive complex combined with the local extension suggests that Grand Pays is a potential area for geothermal exploitations [12]. Recent geochemical investigations by Boulègue et al. [13] show that local anomalies of dissolved fluoride and sulfate in springs of the eastern walls of Langevin valley are related to the input of hydrothermal related elements in the local aquifers. Locally $\delta^{13}C$ of dissolved carbonates are also typical of input of mantle-related CO_2 in contrast to most other cold springs in Réunion Island [13].

Hydrovolcanic events have been evidenced in the periphery of the volcano as well as along its axis. It has been shown that a particularly violent hydrovolcanic phase – which we called the Bellecombe Hydrovolcanic Events (BHE) – occurred in the periphery of the edifice. The resulting deposits of the BHE, the Bellecombe Ash Member (BAM), are scattered on the floor of the Plaine des Sables (see Fig. 1), near the western wall of Enclos Fouqué (EF in Figs. 1 and 2). The deposits are composed of units of pyroclastic flows and falls of phreatic, phreatomagmatic and hydrothermal origins. Their estimated volume reaches 0.6 km^3. The dating by ^{14}C of a piece of wood embedded in these deposits indicates similar ages for the formation of Enclos Fouqué and for the BHE (about 4000 years), suggesting that the formation of Enclos Fouqué is linked to the BHE [14].

In addition to the BHE, other hydrovolcanic events (mainly phreatomagmatic and phreatic ones) have been evidenced at the summit of the volcano. Important ‘historical’ phreatomagmatic/phreatic events (for example in 1791 and 1860) have been observed at the top central area, during a period (between 1760 and 1860) when Piton de la Fournaise was in quasi-permanent activity [14]. The conditions leading to such events have been inferred by Bachèlery [5] on the basis of the model of Jaggar and Finch [15]. The emission of a large volume of lava ($10–50\times10^6$ m^3 of lava) drives caldera and collapse formation, and rapid steam generation in response to water contacting hot rocks. These eruptions can be classified as ‘mixing eruptions’, caused by the mixing of groundwater with hot rocks [2]. The huge intensity of the historical events must be related to the particularly active period of the volcano (the event of 1791 is associated with the initiation of a crater, the Dolomieu Crater). In fact, during an eruptive crisis at Piton de la Fournaise, small hydrovolcanic events are observed at the summit of the volcano, as for instance in February–April 1982 [16].

In this study, we first develop, in Section 2, a consistent physical analysis of hydrothermal activity at Piton de la Fournaise, both in the periphery and along the axis of the edifice. On the basis of

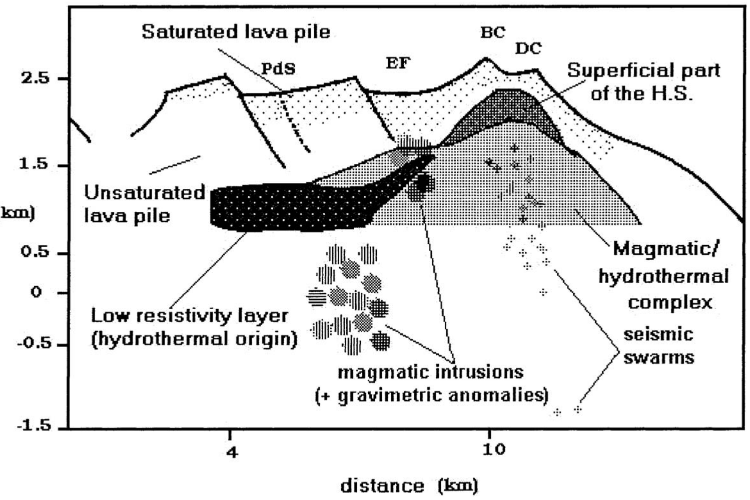

Fig. 2. West–east cross-section of Piton de la Fournaise, from the Plaine des Sables area (PdS) to the central top area, inferred from: resistivity data [10], seismic data [25], gravity data [19], self-potential (SP) data [7,8]. H.S.: hydrothermal system. Note the low-resistivity layer of the top central area, but also the low one of the periphery, beneath the PdS area. Modified cartoon after Lénat et al. [10].

this analysis, we finally (Section 3) discuss the mechanisms leading to hydrovolcanic events.

2. Hydrothermal circulation at the summit and in the periphery of Piton de la Fournaise: physical models

In this section, we show that the axial summit area of the volcano consists in a highly porous medium with a quasi-isotropic permeability field, and that in the periphery, buried layers of dense oceanites are fractured owing to local extension. Then, we present numerical models of hydrothermal convection in a fracture network surrounded by massive basaltic rocks. At the end of this section, we recall the characteristics of hydrothermal circulation in a highly permeable and isotropic porous medium. These models are used to assess the temperature and velocity fields of the hydrothermal flows at the summit and periphery of the volcano.

2.1. Constraints on the permeable media along the axis and in the periphery of the edifice

The eruptive axis constitutes a particular region in a volcanic edifice. The distribution of gas in the magmatic chamber is clearly three-dimensional. The roof of magma chambers being sloped, the volatiles exsolved during the degassing of magma accumulate along the axis of the chamber and ultimately trigger volcanic eruptions [17,18]. Thus, the resulting erupted lavas along the axis are highly vesiculated. The light gravimetric signature of the volcano's axis is consistent with this interpretation [19]. Because of the high concentration of connected voids, highly vesiculated lava is likely to be a highly permeable medium [20]. We measured the permeability of rocks collected at the summit area of Piton de la Fournaise using the apparatus of Jouniaux et al. [21]. The estimated porosity of the samples is about 24% and the permeability 4×10^{-11} m^2. This value is similar to Davis' estimates of the permeability of young porous basaltic lava: about 10^{-10} m^2 [22].

Magmatic overpressures and stresses generate fissures and fractures which enhance the permeability on a larger scale. At Piton de la Fournaise, an intense set of concentric fissures develops around the Dolomieu crater (DC in Fig. 1) and is thought to result from successive inflation and deflation of the structure due to magmatic inputs. An important network of radial fissures develops according to the directions of the rift zones (NE, SE) and to the main tectonic direction N120 (Fig. 1). Accordingly, these two sets of fissures likely increase the permeability inside the cone, but preserve its isotropy. In fact, it has been shown that this fissure network influences SP anomalies. Particularly, maximum positive SP anomalies concentrate where the density of concentric fissures is highest (Bory crater) [7]. The high permeability of the summit area of the Piton de la Fournaise explains that: (i) the meteoric water (6–10 m/yr) rapidly infiltrates the edifice and ii) all attempts to measure magmatic gas flux along the axis have been negative, indicating that the system is highly ventilated. Because gases accumulate along the axis of the magma chamber, gas-depleted magma likely crystallizes in the periphery, promoting the settlement of dense rocks. The positive gravimetric anomalies evidenced by Malengreau et al. [19] in the periphery of the volcano are consistent with the presence of dense, gas-depleted basaltic rocks buried about 1 km deep. Thus, our estimation of the distribution of porosity along the axis and in the periphery of the edifice is compatible with the gravimetric data. The small porosity of the rocks above these intrusions is seen in the lithostratigraphy of the walls of Rivière Langevin (Fig. 1). Particularly, massive oceanites (olivine-rich basalts) produced during the early development of Piton de la Fournaise (500 000 years ago) have been recognized at the base of valley Langevin [5]. At Grand Pays (GP, see Fig. 1), these massive oceanites are fissured and altered by paleo-hydrothermal flows [11]. It is likely that the deep crystallization of rocks occurs with a discontinuous pattern when the magma chamber is dying [19]. Accordingly, the dense bodies recovered on the west side of the volcano likely result from the crystallization of paleo-magma chambers. Rovetta [23] indicates that the permeability of such degassed volcanic rocks is about 10^{-18} m^2. The downward slopes to the north, south, and east of the volcano induce extension along its western wall (see Figs. 1 and 2). This extensive context triggers a westward fracturing of the edifice [24]. The fissure network kept open by the local tectonics favors the development of a hydrothermal circulation which mines the heat of the magmatic intrusion in the deep levels of the volcano.

To sum up, we suggest the geometry presented in Fig. 2 to describe the internal structure of the edifice from the westward Plaine des Sables area to the central cone (see Fig. 1). The presence of a magma chamber at sea level is inferred from the seismic data of Nercessian et al. [25].

2.2. *Hydrothermal activity in the fracture media of the periphery of the volcano*

The conceptual model presently developed has already been applied to describe hydrothermalism at mid-oceanic ridge [26,27], and also at continental rift zones [28]. The mathematical and numerical models have been extensively tested, and their full development can be found in previous publications from our group [26,27,29]. Using these codes, we now describe a conceptual model of the fracture, shedding light on the resulting hydrothermal activity.

2.2.1. *Conceptual model*

The fracture consists of a network of fissures parallel to the fault axis. Typically, the width of the fracture is about several tens of meters. The fissure connectivity along the fault can reach several kilometers and the network vertical extent a few kilometers. In fact, this depends on the nature of the fracturing and thus, on the local tectonics. The local extension keeps the fissures open, permitting fluid percolation. The fracture is surrounded by massive quasi-impermeable walls with a permeability of about 10^{-18} m^2 [23]. The result is that the heat in the walls essentially flows by conduction. We set 380°C as the temperature at the base of the fracture. This temperature corresponds to the demixion temperature of a slightly salted fluid. Let us note that it is the temperature and salinity in the fluid inclusions found in the hydrothermal minerals of the BAM [14]. At the temperature of demixion, two phases coexist: a brine and a fresher component. Because of its buoyancy, the fresh water moves above the critical interface and mixes the meteoric water. Thus, the deep horizon, below the interface, is filled with the brine. The tension at the interface between the fresh water and the brine stratifies convection on both sides of this interface [27]. Accordingly, the bottom of the convective layer of fresh water corresponds to a deep horizon inside the fracture but not to its bottom. At the top of the fracture two situations are possible, open or closed. Closed top conditions are reached if mineral diagenesis seals the system and/or if the fracture does not cross the whole height of the dense complex. This situation can result from an extensive context in the deep levels of the volcano coexisting with a compressive one at a higher elevation. When the hydrothermal circulation emerges in a porous aquifer, the top of the system is considered to be open. This last situation can be compared to the hydrothermal activity at the ridge crest below the pillow lava layer. The data from Piton de la Fournaise cannot aid the decision whether a given hydrothermal system is open or closed. Each of these two situations will be considered in this section. For the model with an open top, the fluid enters the fault at a temperature of 10°C and exits with a zero vertical temperature gradient ($\partial T/\partial z = 0$). For closed conditions, the temperature at the top is 10°C and no fluid flow crosses that interface.

A random perturbation to the initial conductive temperature regime triggers hydrothermal convection inside the permeable network. The heat transported by the flow is mined in the underlying hot rock. Such mining cools the deep layers on time scales of several Ma, i.e. much longer than the lifetime of the hydrothermal system (see below) [26]. The seismic data along the axis of the volcano show that the top of the magma chamber lies 2–2.5 km below the surface [25] (see Fig. 2). It indicates that the conductive gradient does not exceed 0.5°C/m. Thus, a temperature of 380°C is possible at a depth between 700 and 800 m. When the pressure is lithostatic, the fluid does not boil at that temperature and depth. Thus, the fluid circulation should be monophasic at the initiation of the hydrothermal activity. In the equations of convection given by Fontaine et al. [27], the fluid density (ρ_f) is pressure- and temperature-dependent while the viscosity (μ_f) only depends on the temperature. Accordingly, μ_f varies by a factor of 15 and ρ_f by more than 45%, for the range of temperature and pressure. Fig. 3 shows the geometry of the model (fracture+wall) adopted. In this model, the permeable network consists of a set of parallel fissures confined in a 'porous slot'. Each fissure is separated from the next by a massive quasi-impermeable wall (permeability $k_f = 10^{-18}$ m^2, and thickness $f = 1$ m). For symmetry reasons, the computed box is the half space of Fig. 3. The half fracture thickness ($d/2$) is about 15 m, and the half width of the system is 500 m. The height (H) of the whole system is 500 m, and its length (L) is 500 m. Springs which are known to be in contact with the hydrothermal system emerge from the wall of Rivière Langevin at an elevation of about 1600–1700 m, i.e. about 500 m below the floor of Enclos Fouqué. Hence, a value of 500 m for H is a minimum.

2.2.2. *Permeability amplitude and dynamical benchmarks*

Inside the fracture, the width of the fissure and their spacing are fundamental with regard to the permeability and porosity amplitude. The porosity is defined as: $\varepsilon = \delta/f$ and the permeability as: $k_f = \delta^3/12f$ where δ is the fissure aperture. Typically, for an aperture of about 0.1 mm and spacing of 1 m, the fracture permeability k_f is about 10^{-13} m^2 and the porosity ε is 10^{-4}. These values jump to 10^{-10} m^2 and 10^{-3}, respectively, for an aperture of 1 mm.

The fracture permeability k_f is a parameter whose amplitude is often difficult to assess. At Piton de la Fournaise, little is known about the permeability structure of the edifice. Particularly, the structure of the deep fracture system remains completely unknown. The study of marine hydrothermal systems has led to a few permeability measurements and estimations of the ridge crust. It seems that permeability amplitudes between 6×10^{-13} m^2 and 6×10^{-12} m^2 are lower bound values to generate vigorous hydrothermal activity such as those responsible for hot vents [30]. Such permeabilities are characteristic of fractures in the sheeted dike complex, which is a good analog of the fractured media in the periphery of the volcano because of the extensive context.

Inside the fracture, the permeability in the orthogonal direction is negligible because the wall permeability between two successive fissures is several orders of magnitude lower than the fracture permeability [27]. Consequently, the circulation is almost two-dimensional and confined in the vertical (xz) planes. Such sub-millimeter to millimeter apertures also allow thermal equilibrium to be reached between the fluid and the rock. Thus, fluid and solid temperatures are locally the same in the fault.

The vigor of the convection inside the fault de-

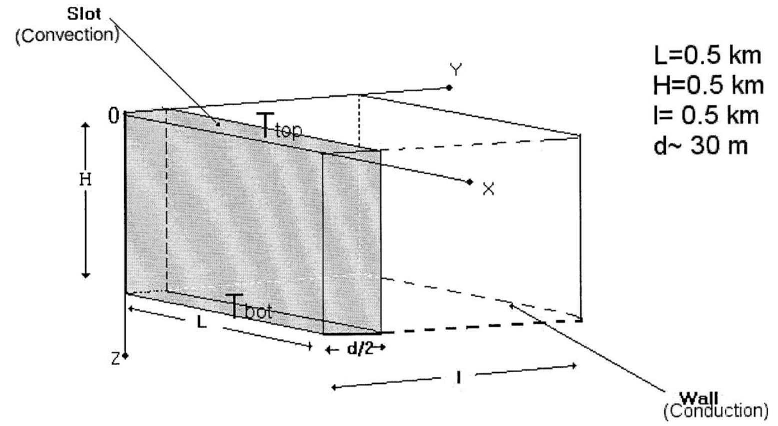

Fig. 3. Geometry of the half space modeled ($y \geq 0$). The flow and temperature fields are symmetrical on both sides of the $y = 0$ plane. $T_{top} = 10$°C, $T_{bot} = 380$°C.

pends on the non-dimensional Rayleigh number (Ra). Ra is defined as:

$$\mathrm{Ra} = \frac{\Delta\rho_\mathrm{f} g k_\mathrm{f} H}{\mu_0 k} \qquad (1)$$

where μ_0 is the viscosity of the fluid at 380°C ($\mu_0 = 7.3\times10^{-5}$ Pa s), g is the gravitational acceleration ($g = 10$ m/s^2), H is the height ($H = 500$ m), κ is the thermal diffusivity of the basalt ($\kappa = 10^{-6}$ m^2/s, and $\Delta\rho_\mathrm{f} = 440$ kg/m^3 is the drop in fluid density between 10°C and 380°C. Assuming a permeability range of 10^{-13} m^2 to 10^{-10} m^2, Ra ranges from 3×10^3 to 3×10^6, respectively. Because of numerical limitations, we are only able to run cases at the low end of this range of Ra.

We initiate convective circulation inside the fault by perturbing an initial conductive profile with a small random noise. Then, we iteratively resolve the temperature and flow fields inside the computing box (Fig. 3). Accordingly, we are able to follow the thermal and flow fields of the system with time.

2.2.3. *Physical properties*

In Fig. 4, we show two models giving the evolution of the hydrothermal flow during its first 20 years for an open and a closed top system. The Ra number of the experiments is 16 000, which corresponds to a fracture permeability k_f of 5×10^{-13} m^2.

Convection develops as fingers, i.e. the convective cells have a small aspect ratio. This is typical of convective processes in fractures thermally influenced by conductive impermeable walls [26]. The characteristic width of the fingers is about 70–80 m, and depends on the amplitude of Ra [26]. In both experiments, the bottom boundary layer is unsteady and thermal instabilities are initiated inside the layer. As seen in Fig. 4, these instabilities are lately collected by the ascending hot plumes. For the open top system, there is no boundary layer at the top of the system, and exit temperature reaches 240°C (0.65) (Fig. 4). For closed top conditions, the top thermal boundary is very thin (15–20 m, i.e. 3–4% of the whole height) and isotherms up to 230°C (0.6) reach the uppermost parts of the fault (Fig. 4). The transient snapshots (Fig. 4a–c) show that the hot thermal front travels from the bottom to the top of the fault in about 15–20 years, i.e. at a velocity of 10–15 m/yr. In fact, modeling shows that this velocity increases linearly with Ra [27]. This means that for $\mathrm{Ra} = 1.6\times10^5$, i.e. for a fracture permeability of 5×10^{-12} m^2, the hot front circulates at a velocity of about 100–150 m/yr. It has been shown that the thermal structure – and particularly the dimensionless asymptotic maximum exit temperature of 0.65 found for open systems – is independent of Ra, d, L and time t [26]. Fig. 4 shows that the convective process is much more developed along the axis of the fault than near the wall. This results from the horizontal thermal gradient across the fault. The convective circulation perturbs the conductive thermal field inside the walls on a distance less than 15 m (see Fig. 4d).

Finally, the mean amount of the heat flowing through the fracture is calculated by adding the mean value of the conductive flow at the top horizontal plane($\lambda^*\partial T/\partial z$, where λ^* is the conductivity of the porous medium in J m/s and T is the temperature in °C) to the advective one ($\rho_\mathrm{f} c_\mathrm{f} VT$, where $\rho_\mathrm{f} c_\mathrm{f}$ is the volumetric heat capacity of the fluid in J/m^3 and V the fluid velocity in m/s). After 20 years the heat flowing through the top interface stabilizes around 1.8×10^5 W. It corresponds to a mean of 12 W/m^2 flowing through the 500 m long, 30 m large top of the fracture. This heat is mainly transported by the three rising hot fingers seen in Fig. 4. Thus the power of one finger is less than 10^5 W and corresponds to a 100°C spring with a flow rate of about 0.1–0.2 l/s. 10^5 W is at least two orders of magnitude lower than the heat transported by oceanic vents [31]. As said before, the convective process inside the fault perturbs the conductive profile inside the walls on a distance less than 15 m. Accordingly, the heat anomaly due to a hot finger affects a surface of only 70×70 m^2. Such a heat anomaly is not easy to detect along the western part of the volcano because of the cold fluid circulation in the perched aquifers.

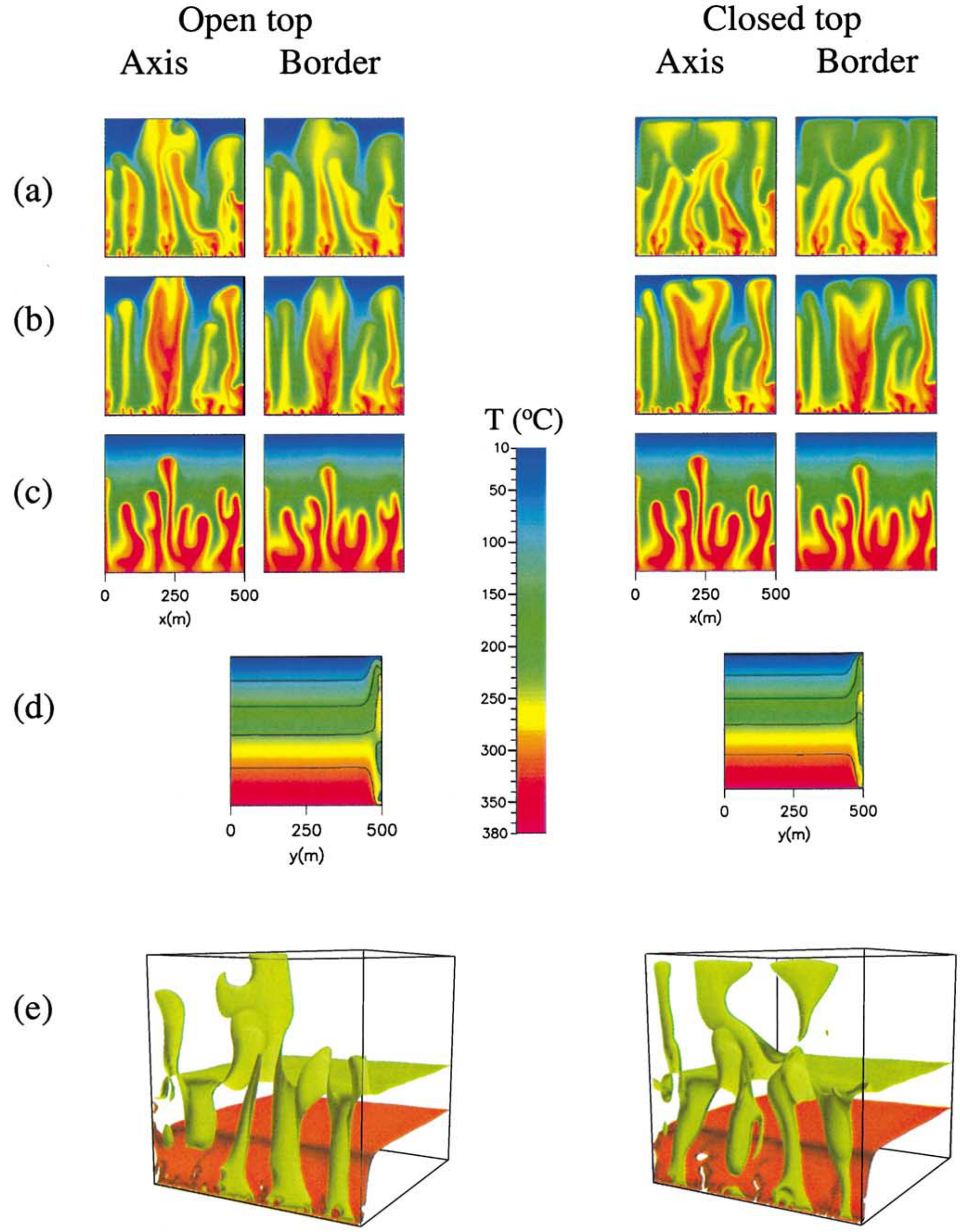

Fig. 4. Thermal characteristics of the hydrothermal flow for open/closed top systems. The Rayleigh number is 16000 ($k_f = 5\times10^{-13}$ m^2). The number of grid points in the x, y and z directions is: 256×64 (5 in the half-fracture, and 59 in the conductive wall)$\times256$, respectively. Panels a, b and c represent three snapshots of the thermal fields along the axis and border of the fault (xz planes) at time t: (a) $t=20$ years, (b) $t=11$ years, (c) $t=4$ years. Panels d show the thermal field in a cross-section (yz plane) at $x=250$ m and $t=20$ years. The temperature drops 74°C between two successive isolines. In panels e we also represent the location of the 240°C (light green) and 305°C (light red) three-dimensional isotherms inside the fault and the wall at $t=20$ years.

2.3. *Some inferences about hydrothermal activity at the summit of the volcano*

We have seen that the hydrothermal flows along the axis of the edifice develop in a highly porous medium with a quasi-isotropic permeability of about 10^{-10} m^2. The Rayleigh number Ra associated with this circulation ranges between 10^6 and 10^7. Although this range in Ra number is the same as that of the fractured system, the resulting physical regime is dramatically different. Numerical studies of convective processes in isotropic porous media at such a high Ra number are clearly beyond today's computer possibilities. It has been shown that the circulation exhibits a chaotic/turbulent regime beyond a Ra of 1200–1500 [32,33]. Hence, when $\mathrm{Ra} = 10^7$, the hydrothermal convection along the axis of the volcano is likely to be highly turbulent. The Nusselt number Nu (the ratio between convective/conductive heat transfer) increases roughly linearly with Ra ($\mathrm{Nu} \propto \mathrm{Ra}^e$, with $e \in (0.8,1.3)$) [32]. The result is that the thickness of the thermal boundary layers decreases roughly linearly with increasing Ra. If we consider that this relationship still holds at Ra up to 10^7, the hydrothermal system at the summit of the volcano has a few centimeters thick thermal boundary layer. As observed in numerical experiments of convection in fluids [34], a highly turbulent flow leads to the formation of some time/space-chaotic 'wispy tendrils'.

Also, hydrothermal systems perched in the edifice are likely to be biphasic. Studies of geothermal two-phase systems are numerous (see [35] for a review). Two types of two-phase systems can be distinguished: the majority is liquid-dominated and generates geysers or boiling hot springs; vapor-dominated systems are a minority and display fumaroles and acid springs. Some authors have developed numerical simulations of both types of two-phase systems [36]. However, the modeling of two-phase circulation in a porous medium with an isotropic permeability field and a Rayleigh number between 10^6 and 10^7 is impossible. Moreover, as said before, at Piton de la Fournaise, natural manifestations of the hydrothermal circulation such as hot springs or fumaroles are weak (only one diffuse fumarolic activity initiated in 1986). We propose that this is related to the airy character of the porous medium at the summit of the volcano.

To sum up, we see in this section that hydrothermalism of two types is likely to affect the edifice of the Piton de la Fournaise: the first one in a fractured, dense complex in the periphery of the volcano, and the second one in the porous layers of the top central area which constitutes a quasi-isotropic highly permeable medium. The thermal structure of both systems is basically different. In the fractured medium, the heat is drained along the walls of the fracture and fluids with asymptotic temperatures as high as 230–240°C reach the top of the fault. By contrast, the chaotic/turbulent two-phase circulation triggered in the porous layers of the central area leads to the formation of very thin thermal boundaries, and ascending currents swamp in the highly ventilated porous medium.

3. Discussion: hydrothermal eruptions at Piton de la Fournaise

The actual basic mechanisms of hydrothermal eruptions are not well known. Nevertheless, a recent model of Germanovich and Lowell [1] of the mechanisms of phreatic eruptions has pointed out some concepts that may be relevant to the mechanisms of hydrothermal eruptions. Their model is based on the crucial assumption that the medium where the fluid circulates has a 'two-scale' permeability: a main permeable crack network and a subsidiary one composed of a sub-network of micro-cracks, isolated cracks and dead-end cracks, which does not significantly contribute to the bulk permeability of the medium. A quantitative analysis shows that the amplitude of the main permeability must be greater than 10^{-12} m^2 and that of the subsidiary one about 10^{-18} m^2. The injection of a dike at shallow depth inside this saturated porous medium drives water to boil and superheated steam circulates inside the main permeable network. The upward transport of steam contributes to heat the rock above and on the sides of the intrusion. This flow generates a hot thermal wave, moving upward at a velocity of a few hundred meters per year, for a main permeability of 10^{-12} m^2. The heat transported by the wave is transferred to the fluid trapped inside the micro-cracks of the subsidiary network. Upon heating, the fluid-filled cracks of the low permeability medium are pressurized because of the thermal expansion of the fluid, and the cracks start to propagate according to the thermo-elastic stresses. Sufficient heating drives the fluid to boil inside the micro-cracks because of the pressure drop resulting from the volume increase of the cracks. Accordingly, the micro-cracks are filled with a mixture of water and steam and the *PT* conditions lie on the Clapeyron curve. The expanded fluid or steam in the micro-cracks migrates via the subsidiary permeability toward the main one. This leads to a relaxation of the elastic stresses generated because of the fluid expansion and boiling. With a subsidiary permeability of 10^{-18} m^2, the elastic stresses achieve relaxation in 1 year. According to Germanovich and Lowell [1], when the hot wave reaches the surface, the elastic stresses generated inside the rock lead to the failure of the rock in small pieces that can be projected upward. Thereafter, the front of failure propagates inward, down to the depth where the elastic stresses have already been relaxed. The model shows that the height of the excavated zone is directly related to the upward velocity of the hot front. Thus, the velocity of the ascending thermal wave being about a few hundred meters per year (for a main permeability of 10^{-12} m^2), and the relaxation time about 1 year, the excavated height of the crater likely reaches a few hundred meters. Germanovich and Lowell [1] show that the failure process is inhibited when the rock strength exceeds 10 MPa. Rock strengths have been shown to range between 7 MPa and 300 MPa, for sandstones and gabbros respectively [37]. Accordingly, the failure of gabbro can only be considered when extensional tectonic stresses overcome the essential part of the rock strength.

This model can explain the occurrence of the small hydrovolcanic events which occurred at the summit of Piton de la Fournaise [16]. The mean width of the dikes that inject at Piton de la Fournaise is about 1 m [38], and some recent volcanic activities have been attributed to the injection of dikes [39,40]. Ancient dike injections of degassed basalt that do not reach the surface and thus crystallize below the surface can create a local zone of low permeability, embedded in the porous basalts of permeability 10^{-10}–10^{-9} m^2 characteristic of the summit of the edifice. It is known that the eastern part of the central cone gradually moves to the sea at a rate of 20 cm/yr (between 1984 and 1989) because of the repeated injection of dikes in the rift zones (Fig. 1) [41], indicating that the rift zone is partly or wholly under extension. The model shows that the diameter of the crater resulting from such a hydrovolcanic eruption triggered by the intrusion of a 1 m thick dike is 2–6 m [1]. Accordingly, only small hydrovolcanic eruptions are expected at the summit of Piton de la Fournaise.

In fact, the model of Germanovich and Lowell [1] also applies to hydrothermal eruptions triggered by hydrothermal circulation in a fracture. As said before, the key assumption of the model is the presence of a medium with a ‘two-scale’ permeability: a main one where fluids transport the heat from the heat source and a subsidiary one where thermally expanding fluids in micro-cracks circulate. Clearly, the fracture geometry shown in Fig. 3 is consistent with this two-scale permeability: the set of interconnected fissures being responsible for the main permeability (with amplitude ranging between 10^{-13} and10^{-10} m^2 depending on the width of the fissures), and the meter thick quasi-impermeable walls of permeability of 10^{-18} m^2 (which separate one fissure from another) for the subsidiary network. Moreover, the extension that prevails inside the fracture is likely to favor the development of a hydrothermal eruption triggered by the mechanisms described by the model [1]. Our models of hydrothermal circulation in such a medium with a fracture permeability of 5×10^{-13} m^2 show that the convective circulation is able to drive hot fluids upward (‘fingers’), at a temperature up to 230–240°C.

In our models, we see that hot fingers of temperature about 230–240°C reach the top of the fracture. Provided that the fluid pressure there is not too high (less than 20–30 MPa), boiling will occur. The permeability of the subsidiary network of the fracture being 10^{-18} m^2, according to Germanovich and Lowell [1], the relaxation of elastic stresses occurs in 1 year. We have seen that, for fracture permeabilities of 5×10^{-13} m^2 and 5×10^{-12} m^2, the hot front moves upward at about 10–15 m/yr and 100–150 m/yr, respectively. Thus, the depth of craters can reach 15–20 m for $k_f = 5\times10^{-13}$ m^2 and 150–200 m for $k_f = 5\times10^{-12}$ m^2. The occurrence of craters deeper than 200 m is unlikely, because the hydrostatic pressure at these depths is very close to the boiling pressure of a 230–240°C fluid. It is noteworthy that these last values for a fracture permeability of 5×10^{-12} m^2 are consistent with that of the model of Germanovich and Lowell [1] for the same main permeability. This is due to the fact that their porous flow model is very close to that developed in this study. The initiation of the Enclos Fouqué formation [6] has been shown to be synchronous with the development of the BHE [14], i.e. about 4000 years ago. It is thus likely that it is the BHE, and particularly the hydrothermal eruption (phase 2), that triggered the development of the western rim bordering Enclos Fouqué.

The fracture network through emplaced dense rocks must be initiated owing to the extensional stresses generated by the eastern slopes of the edifice. Then, the fissures propagate toward the surface. The development of hydrothermal circulation inside the fracture leads to the formation of hot rising fingers, distant of about 150 m (Fig. 4). When a hot finger reaches the surface, a 150–200 m deep crater is generated. The time needed for the fingers to reach the surface is short (about 15 years for $k_f = 5\times10^{-13}$ m^2), if not very short (about 1 year for 5×10^{-12} m^2). This forms a series of craters following the plane of fracture forming a horseshoe rim on the western part of the edifice (Fig. 1). The series of craters, 150–200 m deep, distant of about 150 m, is likely to form a 200 m deep, discontinuous notch in the constitutive layers forming the ancient western slopes of Piton de la Fournaise 4000 years ago. Lithostratigraphic units with plastic rheology such as scories level favor landslides due to the destabilized eastern slopes of the volcano and the western notch. These landslides promote the separation of the eastern and western parts of the fracture zone, which initiates the formation of the depression of Enclos Fouqué. The hypothesis we propose for the sequence of events leading to the formation of Enclos Fouqué remains to be tested by specific field arguments. The development of fracturing in the rims of the craters could be tested. This needs extensive observations and sampling on the vertical wall of Enclos Fouqué.

4. Conclusion

With the help of the set of data collected on Piton de la Fournaise, we found that two types of hydrothermal processes develop inside the edifice. The first one, largely evidenced by electric and magnetic surveys, sets along the axis of the volcano, in the top central area. The lava that built up the central cone of Piton de la Fournaise is likely to constitute a porous medium, with a high, quasi-isotropic permeability up to 10^{-10} m^2. Recent geochemical data show that the second type of hydrothermal activity develops in the periphery of the volcano (4–5 km while moving to the west from the central cone). We infer that the extension that results from the destabilized eastern flank that is open to the sea opens pathways to convective fluid circulation by fracturing the dense medium that has crystallized in the periphery of the volcano. We show that fracture permeability ranges between 10^{-13} m^2 and 10^{-10} m^2, while the intrinsic permeability of the dense rock is about 10^{-18} m^2.

Numerical models emphasize the basic differences between the thermal fields of each type of hydrothermal activity. For the system along the axis of the volcano, chaotic/turbulent circulation leads to thermal energy scattering through the whole porous medium and to the formation of very thin eddies (as observed in turbulence in fluids). The fracture medium is modeled as a porous vertical slot that contains a fissure network. The fissures are separated from each other by a meter thick wall of permeability of about 10^{-18} m^2. The models show that, in the fracture medium, the heat is drained along the impermeable walls and hot fluids of temperature up to 240°C (fingers) reach the uppermost parts of the fracture.

With the model for phreatic eruptions developed by Germanovich and Lowell [1], we constrain the hydrovolcanic events that set at Piton de la Fournaise. This model is based on the fact that the medium where fluids circulate has a 'two-scale' permeability: a main one, composed of interconnecting fissures, and a subsidiary one, composed of a sub-network of fluid-filled micro-cracks that does not significantly contribute to the bulk permeability of the medium. The model shows that explosive/eruptive conditions can be reached when the fluid of the subsidiary network starts to boil leading to micro-crack pressurization. Because of: (1) the extensional stresses and (2) the overpressures due to boiling, the country rock can fail, initiating the hydrothermal eruption.

With this model, we show that only small phreatic/phreatomagmatic eruptions, responsible for crater formation of about 2–6 m in diameter, can develop at the summit of the volcano. We also show that the permeability structure of a fracture in the periphery of the central active area – i.e. the main permeable network of fissures that leads to fracture permeability between 10^{-13} m^2 and 10^{-10} m^2, and the subsidiary one of the separating walls of permeability 10^{-18} m^2 – is consistent with that of the model of Germanovich and Lowell [1]. Accordingly, we show that deep cratering is possible in the periphery of the volcano: crater depth can reach 150–200 m with fracture permeability of 10^{-12} m^2.

We relate such mechanisms to a huge hydrothermal eruption (more than 0.5 km^3 of ejected products) that set at the Piton de la Fournaise 4000 years ago. We link this catastrophic event to the initiation of the depression called Enclos Fouqué, which occurred at a similar age. Particularly, the western rim of Enclos Fouqué may be directly linked to the excavation of a series of 150–200 m deep craters. To this, we add that the discovery of older (30 000–20 000 years ago) deposits from possibly hydrothermal eruptions, 7–8 km from Enclos Fouqué while moving to the west, indicates that these catastrophic events may be recurrent through time, founding the hypothesis of future catastrophic events of the same type.

Acknowledgements

This work has been funded by the ECODEV, ACI CATNAT and INSU-Risques Naturels No. 309 programs. The computations were supported by the Centre National d'Etudes Spatiales (CNES). We wish to thank Dr. Michèle Allouche for English improvements, Philippe Labazuy and an anonymous reviewer for their constructive comments.***[AC]***

References

[1] L.N. Germanovich, R.P. Lowell, The mechanism of phreatic eruptions, J. Geophys. Res. 100 (1995) 8417–8434.

[2] T.A. Smith, R. McKibbin, Modelling of hydrothermal eruptions: a review, in: Proc. 19th NZ Geothermal Workshop, 1997, pp. 123–128.

[3] P.Y. Gillot, P. Nativel, Eruptive history of Piton de la Fournaise volcano, Réunion Island, Indian Ocean, J. Volcanol. Geotherm. Res. 36 (1989) 53–65.

[4] J. Dubois, J.L. Cheminee, Application d'une analyse fractale à l'étude des cycles éruptifs du Piton de la Fournaise (La Réunion): modèle d'une poussière de Cantor, C.R. Acad. Sci. 307 (1988) 1723–1729.

[5] P. Bachèlery, Le Piton de la Fournaise (Ile de la Réunion), Etude volcanologique, structurale et pétrologique, PhD thesis, 1981, 230 pp.

[6] T. Staudacher, C.J. Allègre, Age of the second caldera of the Piton de la Fournaise volcano (Réunion) determined by cosmic ray produced ^{3}He and ^{21}Ne, Earth Planet. Sci. Lett. 119 (1993) 395–404.

[7] B. Malengreau, J.-F. Lénat, A. Bonneville, Cartographie et surveillance temporelle des anomalies de polarisation spontanée (PS) sur le Piton de la Fournaise, Bull. Soc. Géol. Fr. 165 (1994) 221–232.

[8] S. Michel, J. Zlotnicki, Self-potential and magnetic surveying of La Fournaise Volcano (Réunion Island): Correlations with faulting, fluid circulation, and eruption, J. Geophys. Res. 103 (1998) 17845–17858.

[9] H. Bureau, F. Pineau, N. Metrich, M. Semet, M. Javoy, A melt and fluid inckusion study of the gas phase at Piton de la Fournaise volcano (Réunion Island), Chem. Geol. 147 (1998) 115–130.

[10] J.-F. Lénat, D. Fitterman, D.B. Jackson, P. Labazuy, Geoelectrical structure of the central zone of Piton de la Fournaise volcano (Réunion), Bull. Volcanol. 62 (2000) 75–89.

[11] J.-P. Ran con, Mise en évidence de 'diapirs' hydrothermaux: example des laves zéolitisées de la phase I du Piton de la Fournaise dans le cirque de Grand Pays, in: Evaluation du potentiel géothermique de l'Ile de la Réunion, Rapport Géologique, BRGM, 1981, pp. 135–137.

[12] A. Gérard, J.-P. Ran con, V. Barthes, Etude détaillée du site de Grand Pays, in: Evaluation du potentiel géothermique de l'Ile de la Réunion, BRGM, 1981, pp. 6–15.

[13] J. Boulègue et al., Fluids in Piton de la Fournaise: volatiles and volcanic activity, in: Report CEE-EVOP, Brussels, 1994, 42 pp.

[14] A. Mohamed-Abchir, Les cendres de Bellecombe: un évènement explosif majeur dans le passé récent du Piton de la Fournaise, Ile de la Réunion, PhD Thesis, 1996, 242 pp.

[15] T.A. Jaggar, R.V. Finch, The explosive eruption of Kilauea in Hawaii 1924, Am. J. Sci. 8 (1924) 353–374.

[16] P. Bachèlery, P.A. Blum, J.L. Cheminée, L. Chevallier, R. Gaulon, N. Girardin, C. Jaupart, F.X. Lalanne, J.L. Le Mouel, J.C. Ruegg, P.M. Vincent, Eruption at le Piton de la Fournaise volcano on 3th February 1981, Nature 297 (1982) 395–397.

[17] C. Jaupart, S. Vergniolle, The generation and collapse of a foam layer at the roof of a basaltic magma chamber, J. Fluid Mech. 203 (1988) 347–380.

[18] S. Vergniolle, C. Jaupart, Dynamics of degassing at Kilauea volcano, Hawaii, J. Geophys. Res. 95 (1990) 2793–2809.

[19] B. Malengreau, J.-F. Lénat, J.-L. Froger, Structure of Réunion Island (Indian Ocean) inferred from the interpretation of gravity anomalies, J. Volcanol. Geotherm. Res. 88 (1999) 131–146.

[20] J. Coudray, P. Mairine, E. Nicolini, J.-M. Clerc, Approche hydrogéologique du Piton de la Fournaise, in: J.F. Lénat (Ed.), Le Volcanisme de La Réunion, Monography, Centre de Recherches Volcanologiques, Clermont-Ferrand, 1990, pp. 307–355.

[21] L. Jouniaux, M.-L. Bernard, M. Zamora, J.-P. Pozzi, Streaming potential in volcanic rocks from Mount Pelée, J. Geophys. Res. 105 (2000) 8391–8401.

[22] S.N. Davis, Change in porosity and permeability of basalt with geologic time, in: Int. Symp. on Hydrology of Volcanic Rocks. UNESCO, Lanzarote, 1974.

[23] M.R. Rovetta, A similarity model of incremental fracture growth in submarine hydrothermal systems, J. Geophys. Res. 98 (1993) 4173–4182.

[24] L.L. Lavier, W.R. Buck, A.N.B. Poliakov, Factors controlling normal fault offset in an ideal brittle layer, J. Geophys. Res. 105 (2000) 23431–23442.

[25] A. Nercessian, A. Hirn, J.-C. Lépine, M. Sapin, Internal structure of Piton de la Fournaise volcano from seismic wave propagation and earthquake distribution, J. Volcanol. Geotherm. Res. 70 (1996) 123–143.

[26] M. Rabinowicz, J.-C. Sempéré, P. Genthon, Thermal convection in a vertical permeable slot: Implications for hydrothermal circulation along mid-ocean ridges, J. Geophys. Res. 104 (1999) 29275–29292.

[27] F.Jh. Fontaine, M. Rabinowicz, J. Boulègue, Permeability changes due to mineral diagenesis in fractured crust: Implications for hydrothermal circulation at mid-ocean ridges, Earth Planet. Sci. Lett. 184 (2001) 407–425.

[28] C. Tournier, P. Genthon, M. Rabinowicz, The onset of natural convection in vertical fault planes consequences for the thermal regime in crystalline basements and for heat recovery experiments, Geophys. J. Int. 140 (2000) 500–508.

[29] M. Rabinowicz, J. Boulègue, P. Genthon, Two- and three-dimensional modeling of hydrothermal convection in the sedimented Middle Valley segment, Juan de Fuca Ridge, J. Geophys. Res. 103 (1998) 24045–24066.

[30] A.T. Fisher, Permeability within basaltic oceanic crust, Rev. Geophys. 36 (1998) 143–182.

[31] M.K. Tivey, Modeling chimney growth and associated fluid flow at seafloor hydrothermal vent sites, in: S.E. Humphris et al. (Eds.), Seafloor Hydrothermal System: Physical, Chemical, Biological and Geological Interactions within Submarine Hydrothermal Systems, Geophys. Monogr. Ser. 91, AGU, Washington, DC, 1995, pp. 158–177.

[32] A.S.M. Cherkaoui, W.S.D. Wilcock, Characteristics of high Rayleigh number two-dimensional convection in an open-top porous layer heated from below, J. Fluid Mech. 394 (1999) 241–260.

[33] J.P. Caltagirone, P. Fabrie, Natural convection in porous media at high Rayleigh number, I, Darcy's model, Eur. J. Mech. B Fluids 8 (1989) 207–227.

[34] D.A. Yuen, U. Hansen, W. Zhao, A.P. Vincent, A.V. Malevsky, Hard turbulent thermal convection and thermal evolution of the mantle, J. Geophys. Res. Planets 98 (1993) 5355–5373.

[35] R.P. Lowell, Modeling continental and submarine hydrothermal systems, Rev. Geophys. 29 (1991) 457–476.

[36] S.E. Ingebritsen, M.L. Sorey, Vapor-dominated zones within hydrothermal systems; evolution and natural state, J. Geophys. Res. 93 (1988) 13635–13655.

[37] B.K. Atkinson, P.G. Meredith, Experimental fracture mechanims data for rocks and minerals, in: B.K. Atkinson (Ed.), Fracture Mechanics of Rocks, Academic Press, San Diego, CA, 1987, pp. 477–525.

[38] L. Stieltjes, D. Robert, Analyse structurale de l'ile de la Réunion: ses implications géologiques et géothermiques, in: Evaluation du potentiel géothermique de l'Ile de la Réunion, Rapport Géologique, BRGM, 1981, pp. 47–93.

[39] V. Cayol, F.H. Cornet, Three-dimensional modeling of the 1983–1984 eruption at Piton de la Fournaise Volcano, Réunion Island, J. Geophys. Res. 103 (1998) 18025–18037.

[40] F. Sigmundsson, P. Durand, D. Massonet, Opening of an eruptive fissure and seaward displacement et Piton de la Fournaise volcano measured by RADARSAT satellite radar interferometry, Geophys. Res. Let. 26 (1999) 533–536.

[41] J.F. Lénat, P. Bachèlery, Structure et fonctionnement de la zone centrale du Piton de la Fournaise, in: J.F. Lénat (Ed.), Le Volcanisme de La Réunion, Monograph, Centre de Recherches Volcanologiques, Clermont-Ferrand, 1990, pp. 43–74.

Mikada, H., Moore, G.F., Taira, A., Becker, K., Moore, J.C., and Klaus, A. (Eds.)
Proceedings of the Ocean Drilling Program, Scientific Results Volume 190/196

DATA REPORT: PERMEABILITY, COMPRESSIBILITY, AND FRICTION COEFFICIENT MEASUREMENTS UNDER CONFINING PRESSURE AND STRAIN, LEG 190, NANKAI TROUGH[1]

Sylvain Bourlange,[2, 3] Laurence Jouniaux,[2] and Pierre Henry[2, 4]

ABSTRACT

Permeability measured on three samples in a triaxial cell under effective confining pressure from 0.2 to 2.5 MPa ranges from 10^{-18} to 10^{-19} m^2. Overall, results indicate that permeability decreases with effective confining pressure up to 1.5 MPa; however, measurements at low effective pressure are too dispersed to yield a precise general relationship between permeability and pressure. When the effective pressure is increased from 1.5 to 2.5 MPa, permeability is roughly constant (~1–4 × 10^{-19} m^2). Samples deformed in the triaxial cell developed slickenlined fractures, and permeability measurements were performed before and after failure. A permeability increase is observed when the sample fails under low effective confining pressure (0.2 MPa), but not under effective pressure corresponding to the overburden stress. Under isotropic stress conditions, permeability decrease related to fracture closure occurs at a relatively high effective pressure of ~1.5 MPa. Coefficients of friction on the fractures formed in the triaxial cell are ~0.4.

INTRODUCTION

Permeability and storage coefficients are essential parameters controlling fluid flow and pore pressure regime. Knowledge of these param-

---

[1] Bourlange, S., Jouniaux, L., and Henry, P., 2004. Data report: Permeability, compressibility, and friction coefficient measurements under confining pressure and strain, Leg 190, Nankai Trough. *In* Mikada, H., Moore, G.F., Taira, A., Becker, K., Moore, J.C., and Klaus, A. (Eds.), *Proc. ODP, Sci. Results,* 190/196, 1–16 [Online]. Available from World Wide Web: <http://www-odp.tamu.edu/publications/190196SR/VOLUME/CHAPTERS/215.PDF>. [Cited YYYY-MM-DD]

[2] Laboratoire de Geologie, Ecole Normale Superieure UMR 8538, 24 rue Lhomond, 75231 Paris Cedex 05, France. Correspondence author: **bourlang@geologie.ens.fr**

[3] Present address: LIAD–ENSG, Rue du doyen Marcel Roubault, BP 40, 54500 Vandoeuvre, France.

[4] Present address: Chaire de Geodynamique, College de France, Europole de l'Arbois, BP 80, 13545 Aix en Provence Cedex 04, France.

Initial receipt: 29 July 2003
Acceptance: 14 January 2004
Web publication: 16 July 2004
Ms 190SR-215

eters under in situ conditions is therefore important in understanding deformation processes in accretionary complexes. Most permeability measurements on samples from the Nankai accretionary complex have been performed without pressure confinement (Taylor and Fischer, 1993) or at low confining pressure (<1 MPa) (**Gamage and Screaton,** this volume; Karig, 1993). Measurements of permeability under 1–5 MPa effective confining stress give lower values (Byrne et al., 1993). Here, we report measurements performed in the 0.5- to 2.5-MPa range in a triaxial cell with the main purpose of approaching in situ stress conditions. These measurements are indicative of the permeability of the unfractured sediment and may, therefore, constrain fluid flow out of the fault zones through the wallrock. The permeability of fractured zones may be higher, especially if the fractures are dilated because of a high fluid pressure. To investigate the effect of fracturing, samples were failed along drained paths at low (0.2 MPa) and relatively high (2.5 MPa) effective pressure and permeability was measured before and after fracturation. Slickenlined fractures formed during the failure tests with visual aspects similar to fractures observed on core samples, and it was possible to determine the friction coefficient of these surfaces. Experimental difficulties and time constraints limited the number of samples that could be processed; therefore, interpretations are preliminary.

METHODS AND SAMPLES

Permeabilities in this study were measured using a pulse decay method (Brace et al., 1968; Jouniaux et al., 1994, 1995). The pulse is a small step change (0.1–0.3 MPa) of differential fluid pressure imposed between pressure vessels connected at the ends of the sample. When a pressure pulse ΔP_0 is applied, the differential pressure $\Delta P(t)$ decays exponentially as a function of time, t:

$$\Delta P(t) = 2\Delta P_0 V_2/(V_1 + V_2)\ e^{-mt},$$

where

V_1, V_2 = the upstream and downstream reservoir volumes ($V_1 = V_2 = 50 \times 10^{-6}$ m^3 in our experimental setup),
t = time, and
m = a decay time constant (Fig. **F1**).

F1. Permeability measurement, p. 9.

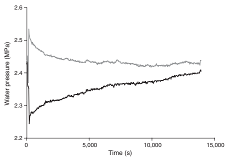

Plotting the decay curve in terms of ln[$\Delta P(t)$] vs. time t yields a straight line having a slope m, and the permeability k can be determined by

$$k = \mathrm{m}\mu(L/A) \times [\mathrm{Cup} \times \mathrm{Cd}/(\mathrm{Cup} + \mathrm{Cd})],$$

where

L = length of the sample,
A = cross-sectional area of the sample,
m = dynamic viscosity of pore fluid at temperature measurement (10^{-3} Pa·s at 20°C), and
[Cup × Cd/(Cup+Cd)] = storage of the pressure vessels (2.4×10^{-14} m^3/Pa).

Two GDS pressure controllers (50 cm^3 internal volume) in standby mode were used as constant-volume pressure vessels during pulse decay measurements. Forty-one measurements were performed with the pulse decay method at various levels of effective confining pressure (confining pressure – pore pressure) from 0.34 to 2.4 MPa.

We discarded measurements when an exponential could not be fitted to the data. The largest deviations from the ideal exponential curve correlate with room temperature variations and are attributed to the thermal expansion of water within the pressure controllers (or of the pressure controllers themselves). The pulse decay method requires a small pulse initial pressure difference (10%) compared to the effective pressure. Because the pressure pulse is at least 0.1 MPa (limited by the precision of the pressure gauges), measurements performed at effective confining pressure <1 MPa do not follow this condition. These measurements were retained when the exponential fit was good but yielded scattered results (Fig. F2).

F2. Permeability values and effective pressure, p. 10.

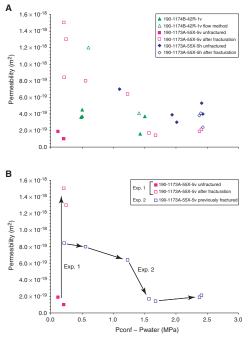

For comparison, two permeability measurements were performed from steady-state flow under a constant pressure gradient ΔP (0.1–0.28 MPa) with GDS pressure controllers in locked pressure mode. Time needed for these measurements is about twice the time needed using the pulse decay method. Permeability was calculated using Darcy's law:

$$k = Q\mu L/(A\times\Delta P).$$

Measurements were performed on three samples (diameter = 25 mm) from Ocean Drilling Program (ODP) Leg 190 (Moore, Taira, Klaus, et al., 2001; Moore et al., 2001) cored either in the vertical direction (v) or in the horizontal direction (h) (Table T1). The overburden stress was calculated by integrating the bulk density with depth. The effective overburden stress range is estimated assuming an overpressure ratio between 0 and 0.42 (maximum overpressure ratio determined for the underthrust sediments by Screaton et al. [2002]).

T1. Sample characteristics and estimated in situ overburden stress, p. 14.

RESULTS

Permeability

Permeability measurements were performed on sample 190-1174B-42R-1, 93–95 cm (vertical), under increasing isotropic pressure from effective pressures of 0.5–1.5 MPa over a period of 10 days (Fig. F2A). This sample was maintained at 0.5 MPa effective pressure for 8 days and absorbed 1262 mm^3 water without significant total volume change, showing that the sample was not fully saturated at the beginning of the experiment. We calculated an initial water saturation of 86%. Measurements made on Sample 190-1174B-42R-1, 93–95 cm (vertical), allowed a comparison of steady-state flow and pressure decay methods. The two measurements performed using the flow method (1.2×10^{-18} m^2 at an effective pressure of 0.6 MPa and 4.1×10^{-19} m^2 at an effective pressure of 1.41 MPa) are at the upper limit of the range of measurements done using the pulse decay method ($3.6–4.5 \times 10^{-19}$ m^2 at 0.5 MPa effective pressure and $1.6–3.7 \times 10^{-19}$ m^2 at 1.5 MPa effective pressure) but are compatible. The $1.2 \pm 0.2 \times 10^{-18}$ m^2 permeability value at 0.6 MPa effective pressure we obtained using the flow method is close to the 2.3×10^{-18} m^2 permeability measured using the same method on Sample 190-

1174B-42R-3, 133–150 cm (538 meters below seafloor [mbsf]), at the same effective pressure (Gamage and Screaton, this volume).

Sample 190-1173A-55X-5, 135–150 cm (vertical), was fractured during a failure test (experiment 1) performed at a low confining effective stress (0.2 MPa). This fracturation induced a single order of magnitude permeability increase from 1–2 × 10^{-19} m^2 to ~1.4 × 10^{-18} m^2 (Fig. F2B, exp. 1). The sample was removed from the triaxial press to observe the fracture (Fig. F3). This same sample (called "previously fractured" in Table T2) was used 2 days later for new permeability measurements under increasing isotropic conditions from 0.2 to 2.4 MPa effective pressure for 6 days (experiment 2). The evolution of confining and pore pressures and the permeability measurements are shown in Figure F4. Permeability decreased by nearly one order of magnitude from ~10^{-18} to ~10^{-19} m^2 from effective pressures of 0.5 to 1.5 MPa (Fig. F2B, exp. 2). Then the permeability remained nearly constant (~1.8 × 10^{-19} m^2) with increasing effective pressure.

F3. Sample 190-1173A-55X5, 135–150 cm (horizontal), p. 11.

Sample 190-1173A-55X-5, 135–150 cm (horizontal), was loaded along an isotropic path to a high confining effective stress (2.5 MPa). Permeability was measured first under isotropic conditions and then under deviatoric stress before and after failure. Failure occurred at 5.0 MPa of effective axial stress and 1.5% of deformation. The deformation rate was 4.2 × 10^{-9} s^{-1} during the hydrostatic stage (14 days) and 1.9–3.2 × 10^{-8} s^{-1} during the deviatoric stage (16 days). Permeability decreased by a factor of two (from ~8 to ~4 × 10^{-19} m^2) during isotropic loading as effective pressure increased from 1 to 2 MPa and then stayed roughly constant. Permeability decreased during failure and then recovered as the sample was deformed beyond the failure point. Photographs showing the fractures were taken after the experiments (Fig. F5).

T2. Permeability values and stress, strain conditions, p. 15.

F4. Evolution of confining and pore pressures, p. 12.

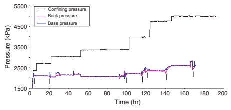

F5. Sample 190-1173A-55X5, 135–150 cm (vertical), p. 13.

All our permeability measurements performed in the triaxial cell are lower than measurements performed at a low effective stress (Taylor and Fisher, 1993; Gamage and Screaton, this volume), which range from 10^{-16} to 10^{-18} m^2 for samples from ~600 mbsf. However, they are in the same range as values measured at <1–5 MPa effective confining stress (Byrne et al., 1993), ranging 1.3 × 10^{-20} to 1.3 × 10^{-18} m^2. Byrne et al. (1993) also observed transient permeability variations with strain.

Overall results indicate permeability decreases with effective confining pressure as high as 1.5 MPa (Fig. F2A). This permeability reduction occurs with cumulative void decreases of 0.015–0.054 depending on the sample (Table T2). However, measurements at low effective pressure are too dispersed to yield a precise general relationship between pressure and permeability. When the effective pressure is increased as high as 2.5 Mpa, permeability is roughly constant (1–4 × 10^{-19} m^2) but the void ratio continues to decrease, reaching a final cumulative void ratio decrease of 0.08–0.10. Our results also suggest that fracturing does not affect permeability when the effective stress is more than ~1.5 MPa. They also show the enhancement of permeability by fracturing when effective stress is low, followed by the permeability decrease with the increase in effective stress, interpreted as fracture closure.

Bulk Compressibility Measurements

The bulk compressibilities of the samples were estimated using the volume of pore fluid expelled from the sample (ΔV) in response to an increase of the effective confining pressure in isotropic stress conditions and before the yield point. The compressibility is calculated as

$$\alpha = 1/V \times (\Delta V/\Delta P),$$

where V = the volume of the sample. Results show a value of 1.1 ± 0.2 × 10^{-8} Pa^{-1} for Sample 190-1174B-42R-1, 93–95 cm; 1.5 ± 0.2 × 10^{-8} MPa^{-1} for Sample 190-1173A-55X-5, 135–150 cm, in the vertical direction; and 1.4 ± 0.5 × 10^{-8} MPa^{-1} for the same sample in the horizontal direction. These compressibility values correspond to the elastic deformation of the sample. Compressibilities determined on the unloading curve were in the same range, confirming that the compressibilities were measured in the elastic domain of the samples.

These estimations can be compared with values deduced from the stiffness modulus derived from consolidation tests realized after Leg 131 (Moran et al., 1993). The compressibility is the inverse of the stiffness modulus. Before the yield point, Sample 131-808C-23R-3 (514 mbsf) showed a stiffness modulus of 50–250 MPa, corresponding to a compressibility of 4.0 × 10^{-9} to 2.0 × 10^{-8} Pa^{-1}. These different estimations remain in the same range.

Friction Coefficients

Friction coefficients were calculated for vertically and horizontally oriented Samples 190-1173A-55X-5, 135–150 cm (horizontal), and the same sample in the vertical direction. These samples were subjected to drained axial compression in the triaxial cell and developed slickenlined faultlike fractures during failure (Figs. F3, F5). The shear and normal stresses resolved on a rupture plane inclined at an angle of α from the vertical are as follows (Jaeger, 1959):

$$\tau = [(\sigma_1 - \sigma_3)/2] \times \sin(2\alpha), \text{ and}$$

$$\sigma_n = \{[(\sigma_1 + \sigma_3)/2] - [(\sigma_1 - \sigma_3)/2]\} \times \cos(2\alpha),$$

where

σ_1 = effective axial stress (axial stress – pore pressure) and
σ_3 = effective confining pressure.

As axial strain increases, axial stress reaches a peak stress corresponding to the failure of the sample. Then the stress reaches a plateau lower than the peak stress, corresponding to an axial strain increase at constant stresses. This plateau is interpreted as steady-state sliding on the previously formed fracture. The friction coefficient, μ, is calculated at this plateau (Byerlee, 1978):

$$\mu = \tau/\sigma_n.$$

Three friction coefficients were calculated on two samples (Table T3). Sample 190-1173A-55X-5 (horizontal) presented a friction coefficient of 0.40. The previously fractured Sample 190-1173A-55X-5 (vertical) presented a strain-stress curve with a plateau at 4.9 MPa axial effective stress, interrupted by a 45% drop in axial stress, followed by a new axial stress buildup to a second plateau at 5.2 MPa. The sudden drop in axial stress could be the result of oversliding (unstable sliding) on the fracture. The friction coefficients calculated at these two plateaus are 0.37 and 0.40. These friction coefficients are consistent with measurements per-

T3. Determination of friction coefficients, p. 16.

formed (usually at much higher effective pressure on the order of 100 MPa) on pure Ca smectite gouge during velocity-stepping direct shear experiments (Saffer et al., 2001) or on a gouge of a saturated mixture of ~60% quartz and ~40% montmorillonite (Logan and Ranenzahn, 1987) during steady-state sliding and on saturated illite (Morrow et al., 1992). Kopf and Brown (2003) measured friction coefficients of ~0.14 for purified smectite and ~0.25 for illite under a range of effective pressures of 1–30 MPa. They estimated, based on ring shear experiments and mineralogical composition, the friction coefficient on Nankai décollement to be 0.30–0.32. These values, lower than our measurements, were performed using elevated displacement. The values of Kopf and Brown (2003) may be representative of well-developed faults like the décollement, whereas our measured friction coefficients may be representative of fractures with shorter sliding, and therefore closer to initial failure conditions.

CONCLUSION

Permeability measurements show values of ~2–6 × 10^{-19} m^2 when the effective pressure is ~2.5 MPa and the drained compressibility of the sample is ~1.3 × 10^{-8} Pa^{-1}. If these values are representative of permeability and compressibility of fault wallrock under in situ conditions, diffusion of pore pressure in the wallrock would affect a characteristic length of 20–50 m in ~100–1000 yr. Considering that the fault zone itself is 20–30 m wide and that the diffusion distance varies with the square root of time, equilibration of pore pressure between the fault zone should be achieved in <100,000 yr. This implies that a higher pore pressure in the fault zone than in the surrounding sediments can be maintained only during transient events. These transient events may relate to slip events and to décollement propagation episodes (Bourlange et al., 2003).

Failure tests show that permeability increases as a result of the formation of a faultlike slip plane in the sample when confining stress is low. Sample 190-1173A-55X-5 (vertical) was fractured at 0.2-MPa confining effective stress, and this induced an increase of permeability by one order of magnitude. This fractured sample was then used in the triaxial cell for permeability measurements under increasing confining pressure. During this second phase, permeability decreased sharply between 1.23 and 1.57 MPa, whereas the sample experienced only a small (0.01) void ratio change (see Table T2; Fig. F2). This sharp permeability decrease likely corresponds to fracture closure. This suggests that once hydraulically conductive fractures have been formed, they may remain hydraulically conductive up to a relatively high confining stress (1.2 MPa). This permeability cycle presents similarity with transient increases in expelled water flow observed during sample loading (Byrne et al., 1993). These observations were interpreted as a transient increase in permeability associated with dilation and shear zone formation in the sample.

Friction coefficients determined in this study (0.37–0.40) are in the range expected for the clay-rich lithology and are not exceptionally low. This suggests a high fluid pressure is required inside the fault zone for decoupling at the décollement level. If a Coulomb wedge model is used (Dahlen, 1984), sliding along the décollement is allowed only when the excess pore pressure ratio, λ_b*, at the décollement is >0.6:

$$\lambda_b^* = (Pf - Ph)/(Pt - Ph),$$

where

Pf = interstitial fluid pressure,
Ph = hydrostatic fluid pressure, and
Pt = lithostatic pressure.

This value is significantly higher than the 0.47 value estimated from compaction curves (Screaton et al., 2002) at ODP Site 808. This suggests a higher pore pressure in the fault zone during episodes of sliding.

ACKNOWLEDGMENTS

We wish to thank Guy Marolleau at École Normale Supérieure (ENS) for maintaining our suffering triaxial cell, Jean Philippe Avouac and Frederic Perrier at the Commissariat à l'Ènergie Atomique/Direction des Applications Militaires (CEA/DAM) who provided us with three GDS cell controllers. This study was partly funded by Centre Nationale de la Recherche Scientifique (CNRS) and by the Geosciences "ad hoc" committee of Institut National des Sciences de l'Univers (INSU). This research used samples and data provided by the Ocean Drilling Program (ODP). The ODP is sponsored by the U.S. National Science Foundation (NSF) and participating countries under management of Joint Oceanographic Institutions (JOI), Inc.

REFERENCES

Bourlange, S., Henry, P., Moore, J.C., Mikada, H., and Klaus, A., 2003. Fracture porosity in the décollement zone of Nankai accretionary wedge using logging while drilling resistivity data. *Earth Planet. Sci. Lett.,* 209:103–112.

Brace, W.F., Walsh, J.B., and Frangos, W.T., 1968. Permeability of granite under high pressure. *J. Geophys. Res.,* 80:2225–2236.

Byerlee, J., 1978. Friction of rocks. *Pure Appl. Geophys.,* 116:615–626.

Byrne, T., Maltman, A., Stephenson, E., Soh, W., and Knipe, R., 1993. Deformation structures and fluid flow in the toe region of the Nankai accretionary prism. *In* Hill, I.A., Taira, A., Firth, J.V., et al., *Proc. ODP, Sci. Results,* 131: College Station, TX (Ocean Drilling Program), 83–101.

Dahlen, F.A., 1984. Non-cohesive critical Coulomb wedges: an exact solution. *J. Geophys. Res.,* 89:10125–10133.

Jaeger, J.C., 1959. The frictional properties of joints in rock. *Geofis. Pura Appl.,* 43:148–158.

Jouniaux, L., Lallemant, S., and Pozzi, J.-P., 1994. Changes in the permeability, streaming potential and resistivity of a claystone from the Nankai prism under stress. *Geophys. Res. Lett.,* 21:149–152.

Jouniaux, L., and Pozzi, J.-P., 1995. Streaming potential and permeability on saturated sandstones under triaxial stress: consequences for electrotelluric anomalies prior to earthquakes. *J. Geophys. Res.,* 100:10197–10209.

Karig, D.E., 1993. Reconsolidation tests and sonic velocity measurements of clay-rich sediments from the Nankai Trough. *In* Hill, I.A., Taira, A., Firth, J.V., et al., *Proc. ODP, Sci. Results,* 131: College Station, TX (Ocean Drilling Program), 247–260.

Kopf, A., and Brown, K.M., 2003. Friction experiments on saturated sediments and their implications for the stress state of the Nankai and Barbados subduction thrusts. *Mar. Geol.,* 202:193–210.

Logan, J.M., and Rauenzahn, K.A., 1987. Frictional dependence of gouge mixtures of quartz and montmorillonite on velocity, composition and fabric. *Tectonophysics,* 144:87–108.

Moore, G.F., Taira, A., Klaus, A., et al., 2001. *Proc. ODP, Init. Repts.,* 190 [CD-ROM]. Available from: Ocean Drilling Program, Texas A&M University, College Station TX 77845-9547, USA.

Moore, G.F., Taira, A., Klaus, A., and Leg 190 Scientific Party, 2001. New insights into deformation and fluid flow processes in the Nankai Trough accretionary prism: results of Ocean Drilling Program Leg 190. *Geochem. Geophys. Geosyst.,* 2:10.1029/2001GC000166.

Moran, K., Brückmann, W., Feeser, V., and Campanella, R.G., 1993. In-situ stress conditions at Nankai Trough, Site 808. *In* Hill, I.A., Taira, A., Firth, J.V., et al., *Proc. ODP, Sci. Results,* 131: College Station, TX (Ocean Drilling Program), 283–291.

Morrow, C., Radney, B., and Byerlee, J., 1992. Frictional strength and the effective pressure law of montmorillonite and illite clays. *In* Evans, B., and Wong, T.F. (Eds.), *Fault Mechanics and Transport Properties of Rocks:* San Diego, CA (Academic Press), 69–88.

Saffer, D.M., Fye, K.M., Marone, C., and Mair, K., 2001. Laboratory results indicating complex and potentially unstable frictional behavior of smectite clay. *Geophys. Res. Lett.,* 28:2297–2300.

Screaton, E., Saffer, D., Henry, P., Hunze, S., et al., 2002. Porosity loss within the underthrust sediments of the Nankai accretionary complex: implications for overpressures. *Geology,* 30:19–22.

Taylor, E., and Fisher, A., 1993. Sediment permeability at the Nankai accretionary prism, Site 808. *In* Hill, I.A., Taira, A., Firth, J.V., et al., *Proc. ODP, Sci. Results,* 131: College Station, TX (Ocean Drilling Program), 235–245.

Figure F1. Example of permeability measurement for the previously fractured Sample 190-1173A-55X-5, 135–150 cm (vertical), using the pulse decay method at 1.57 MPa effective pressure and 1.6 MPa effective axial stress. The two curves correspond to the pore pressure at both ends of the sample. The permeability deduced is 1.7 × 10^{-19} m^2.

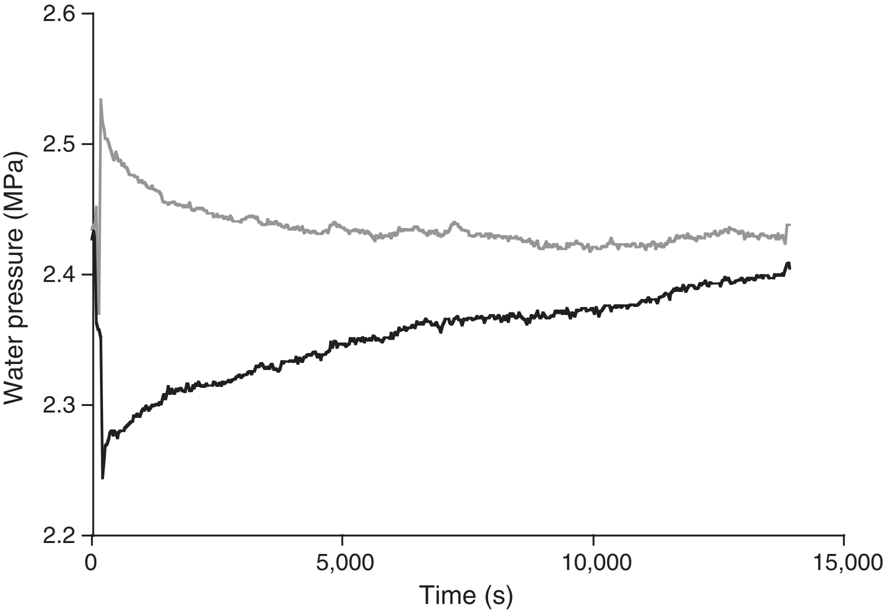

Figure F2. **A.** Permeability values as a function of the effective pressure for the four experiments. **B.** Permeability and effective pressure paths for experiments 1 and 2 on Sample 190-1173A-55X-5, 135–150 cm (vertical). v = vertical, h = horizontal. Pconf = confining pressure, P water = pore pressure.

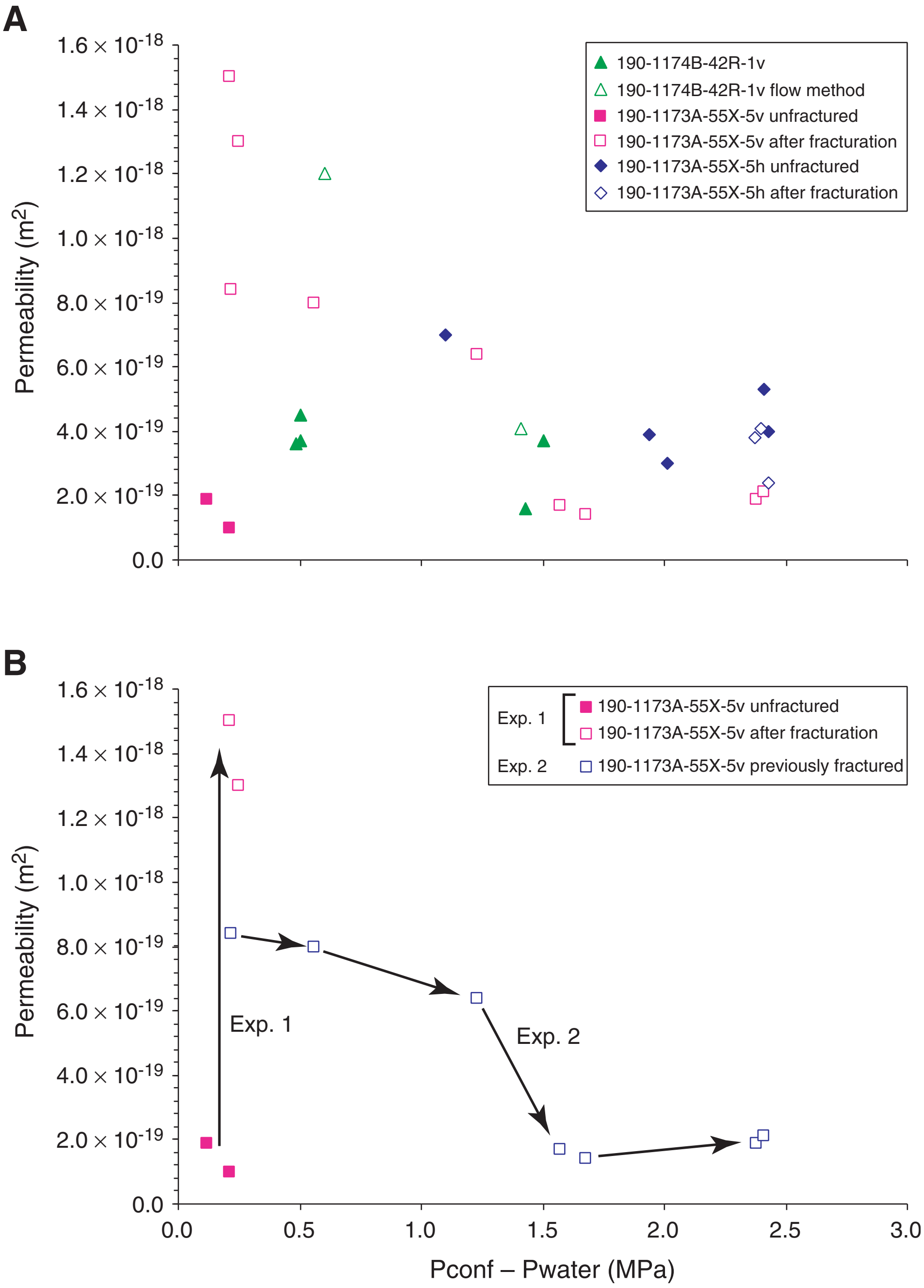

Figure F3. Sample 190-1173A-55X5, 135–150 cm (horizontal), after the experiment. Upper photograph shows the main fracture plane with a 30° angle, and two auxiliary fractures (one parallel to the main fracture and one conjugate at the bottom left of the sample). The lower photograph show the rupture plane, with visible striation.

Figure F4. Evolution of confining and pore pressures during experiment 2 on Sample 190-1173A-55X-5, 135–150 cm (vertical; previously fractured). Permeability measurements are indicated by arrows. The corresponding effective pressures of these measurements are, respectively, 0.22, 0.56, 1.23, 1.68, 1.57, 2.4, and 2.4 MPa.

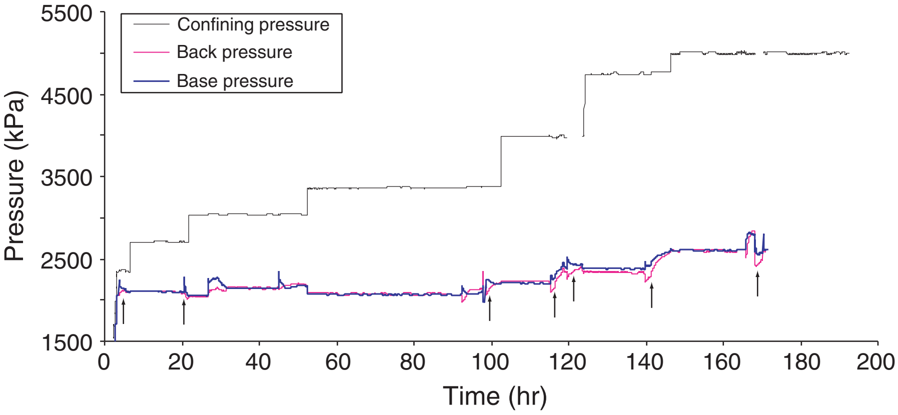

Figure F5. Sample 190-1173A-55X5, 135–150 cm (vertical), after the experiment.

Table T1. Sample characteristics and estimated in situ overburden stress.

Core, section, interval (cm)	Depth (mbsf)	Lithology	Porosity (%)	Length (mm)	Overburden stress (MPa)	Effective overburden stress (MPa)
190-1174B-42R-1, 93–95 (v)	535	Clay and silt	0.38	47.8	9.9	2.7–4.5
190-1173A-55X-5, 135–150 (v)	520	Clay and silt	0.43	41	8.8	2.1–3.6
190-1173A-55X-5, 135–150 (h)	520	Clay and silt	0.43	41.4	8.8	2.1–3.6

Note: v = vertical, h = horizontal.

Table T2. Permeability values and stress, strain conditions.

Core, section	Permeability (m^2)	Effective confining pressure (MPa)	Effective stress (MPa)	State	Deformation	Cumulative void ratio decrease
190-1174B-						
42R-1 (v)	$3.6 \pm 0.1 \times 10^{-19}$	0.48	0.5	Isotropic		
42R-1 (v)	$3.7 \pm 0.3 \times 10^{-19}$	0.5	0.5	Isotropic		
42R-1 (v)	$1.2 \pm 0.2 \times 10^{-18‡}$	0.6	0.6	Isotropic		
42R-1 (v)	$4.5 \pm 0.2 \times 10^{-19}$	0.5	0.5	Isotropic		**
42R-1 (v)	$4.1 \pm 0.15 \times 10^{-19‡}$	1.41	0.5	Isotropic		0.013
42R-1 (v)	$1.6 \pm 0.1 \times 10^{-19}$	1.43	1.4	Isotropic		0.013
42R-1 (v)	$3.7 \pm 0.3 \times 10^{-19}$	1.5	1.5	Isotropic		0.015
190-1173A-						
55X-5 (v)*	$1.9 \pm 0.6 \times 10^{-19}$	0.12	0.15	Isotropic		
55X-5 (v)*	$1.0 \pm 0.2 \times 10^{-19}$	0.21	0.2	Isotropic		
55X-5 (v)*	$1.5 \pm 0.2 \times 10^{-18}$	0.21	1	Deviatoric	Just fractured—0.015	
55X-5 (v)*	$1.3 \pm 0.2 \times 10^{-18}$	0.25	1.4	Deviatoric	Just fractured—0.028	
55X-5 (v)†	$8.4 \pm 0.4 \times 10^{-19}$	0.22	0.35	Isotropic	Previously fractured	**
55X-5 (v)†	$8.0 \pm 0.4 \times 10^{-19}$	0.56	0.55	Isotropic	Previously fractured	0.023
55X-5 (v)†	$6.4 \pm 0.4 \times 10^{-19}$	1.23	1.3	Isotropic	Previously fractured	0.044
55X-5 (v)†	$1.7 \pm 0.1 \times 10^{-19}$	1.57	1.6	Isotropic	Previously fractured	0.054
55X-5 (v)†	$1.4 \pm 0.2 \times 10^{-19}$	1.68	1.8	Isotropic	Previously fractured	0.054
55X-5 (v)†	$2.1 \pm 0.1 \times 10^{-19}$	2.41	2.2	Isotropic	Previously fractured	0.072
55X-5 (v)†	$1.9 \pm 0.1 \times 10^{-19}$	2.4	3.1	Deviatoric	Previously fractured—0.0357	0.094
55X-5 (h)	$7.0 \pm 1.2 \times 10^{-19}$	1.1	1.1	Isotropic	0.0005	0.023
55X-5 (h)	$3.0 \pm 1.1 \times 10^{-19}$	2	2	Isotropic	0.0034	0.048
55X-5 (h)	$3.9 \pm 0.3 \times 10^{-19}$	1.94	2	Isotropic	0.0034	0.048
55X-5 (h)	$5.3 \pm 0.2 \times 10^{-19}$	2.41	2.4	Isotropic	0.0046	0.053
55X-5 (h)	$4.0 \pm 0.2 \times 10^{-19}$	2.43	2.4	Isotropic	0.0051	0.062
55X-5 (h)	$2.4 \pm 0.3 \times 10^{-19}$	2.43	(5.0 to) 2.5	Deviatoric	0.015—after rupture	0.072
55X-5 (h)	$3.8 \pm 0.2 \times 10^{-19}$	2.37	2.4	Deviatoric	0.015—after rupture	0.072
55X-5 (h)	$4.1 \pm 0.3 \times 10^{-19}$	2.4	4.9	Deviatoric	0.0367—after rupture	0.078

Notes: v = vertical, h = horizontal. Sample 190-1173A-55X-5, 135–150 cm (vertical), was subjected to two experiments: * = experiment 1, † = experiment 2. ‡ = steady-state flow measurements; ** = reference state for the calculation of the void ratio decrease. The cumulative void ratio for Sample 190-1173A-55X-5 (horizontal) is taken in comparison to the void ratio at 0.3 MPa effective pressure.

Table T3. Determination of friction coefficients.

Core, section	Fracture angle (°)	(MPa) Axial effective stress	(MPa) Confining effective stress	Axial strain range of the plateau (%)	q/p	(MPa) Normal stress	(MPa) Shear stress	Friction coefficient
190-1173A-								
55X-5 (h)	30	5.5	2.4	3.2–3.6	0.9	3.1	1.3	0.40 ± 0.15
55X-5 (v)	35	4.9	2.4	3.1–3.6	0.77	3.2	1.2	0.37 ± 0.15
55X-5 (v)	35	5.2	2.4	5.1–5.2	0.84	3.3	1.3	0.40 ± 0.15

Note: v = vertical, h = horizontal. q/p = deviatoric stress/mean effective stress ratio.

JOURNAL OF GEOPHYSICAL RESEARCH, VOL. 108, NO. B9, 2407, doi:10.1029/2002JB002287, 2003

Anisotropy of electrical conductivity record of initial strain at the toe of the Nankai accretionary wedge

Pierre Henry[1,2] Laurence Jouniaux,[1] Elizabeth J. Screaton,[3] Sabine Hunze,[4] and Demian M. Saffer[5]

Received 4 November 2002; revised 1 April 2003; accepted 9 May 2003; published 3 September 2003.

[1] An approach based on March's theory is applied to measurements of the anisotropy of electrical conductivity on samples and is used to quantify initial strain at the toe of the Nankai accretionary wedge. A quantitative determination of strain is possible from simple assumptions: passive reorientation of flat pores forming the porous network and existence of a linear relationship between fabric tensor and electrical conductivity tensor. We show that this simple model correctly accounts for the increase of anisotropy with compaction at a reference site located in the trench (Ocean Drilling Program drill Site 1173). At the toe of the accretionary wedge (Site 1174), development of anisotropy in the horizontal plane and concurrent reduction of vertical plane anisotropy are observed. This can be explained by 12% horizontal ductile shortening, occurring after decollement initiation but before slip on imbricate thrust faults. Anisotropy in the underthrust sequence is correctly described by vertical compaction, consistent with decoupled stress states across the decollement. At Site 1174 the magnitude of ductile strain implies at least 75 m slip on the decollement. Ductile shortening is associated with porosity loss, implying partly drained conditions above the decollement. *INDEX TERMS:* 8105 Tectonophysics: Continental margins and sedimentary basins (1212); 3022 Marine Geology and Geophysics: Marine sediments—processes and transport; 8094 Structural Geology: Instruments and techniques; 5109 Physical Properties of Rocks: Magnetic and electrical properties; *KEYWORDS:* anisotropy of electrical conductivity, decollement, Nankai, strain, accretionary wedge

Citation: Henry, P., L. Jouniaux, E. J. Screaton, S. Hunze, and D. M. Saffer, Anisotropy of electrical conductivity record of initial strain at the toe of the Nankai accretionary wedge, *J. Geophys. Res.*, *108*(B9), 2407, doi:10.1029/2002JB002287, 2003.

1. Introduction

[2] Mechanical decoupling is essential for subduction and mountain building processes. Understanding how a synsedimentary or crustal decollement forms is thus an important problem in tectonics and geodynamics. One question asked is where decollement initiation occurs and how far ahead of the thrust front. In one extreme case, the decollement is a preexisting surface of mechanical decoupling and this discontinuity controls the deformation pattern from the beginning [e.g., *Beaumont and Quinlan*, 1994; *Doin and Henry*, 2001; *Karig and Morgan*, 1994]. Imbricate thrusting above a decollement may then be understood as a strain localization process of the bifurcation type [*Besuelle*, 2001; *Rudnicki and Rice*, 1975]. Alternatively, accretion of a new tectonic unit could be considered as one event, comprising stepwise decollement propagation, folding and thrusting. For example, accretion of new units could occur by fault propagation folding [*Allmendinger*, 1998; *Suppe*, 1985]. Processes may be distinguished from the pattern of early ductile strain. If mechanical decoupling occurs early, subhorizontal ductile shortening (also called layer parallel shortening) should occur within the section above the decollement before strain localization on thrust faults [*Averbuch et al.*, 1992; *Frizon de Lamotte*, 2002; *Sagnotti et al.*, 1998]. In fault propagation folding, ductile strain is associated with the folding and should concentrate in the forelimb of the folds [*Saint-Bezar et al.*, 2001]. Accretionary wedge toes are a special case of active fold and thrust belts, occurring under water and composed of high porosity sediments (30–70%). Because of this high water content and of their mechanical weakness, these sediments have the potential to record large ductile strains. They thus present an ideal case to study decollement initiation and imbricate thrusting. Studies of accretionary wedge toes by drilling have shown that ductile horizontal strain occurs in the toe region or in the trench and suggest early mechanical decoupling at the decollement level [*Housen*, 1997; *Morgan and Karig*, 1995a, 1995b; *Owens*, 1993]. Quan-

---

[1] Laboratoire de Géologie de l'Ecole Normale Supérieure, CNRS UMR 8538, Paris, France.

[2] Now at Departement de Geodynamique, College de France, Aix en Provence, France.

[3] Department of Geology, University of Florida, Gainesville, Florida, USA.

[4] Geowissenschaftliche Gemeinschaftsaufgaben-GCA, Hannover, Germany.

[5] Department of Geology and Geophysics, University of Wyoming, Laramie, Wyoming, USA.

0148-0227/03/2002JB002287$09.00

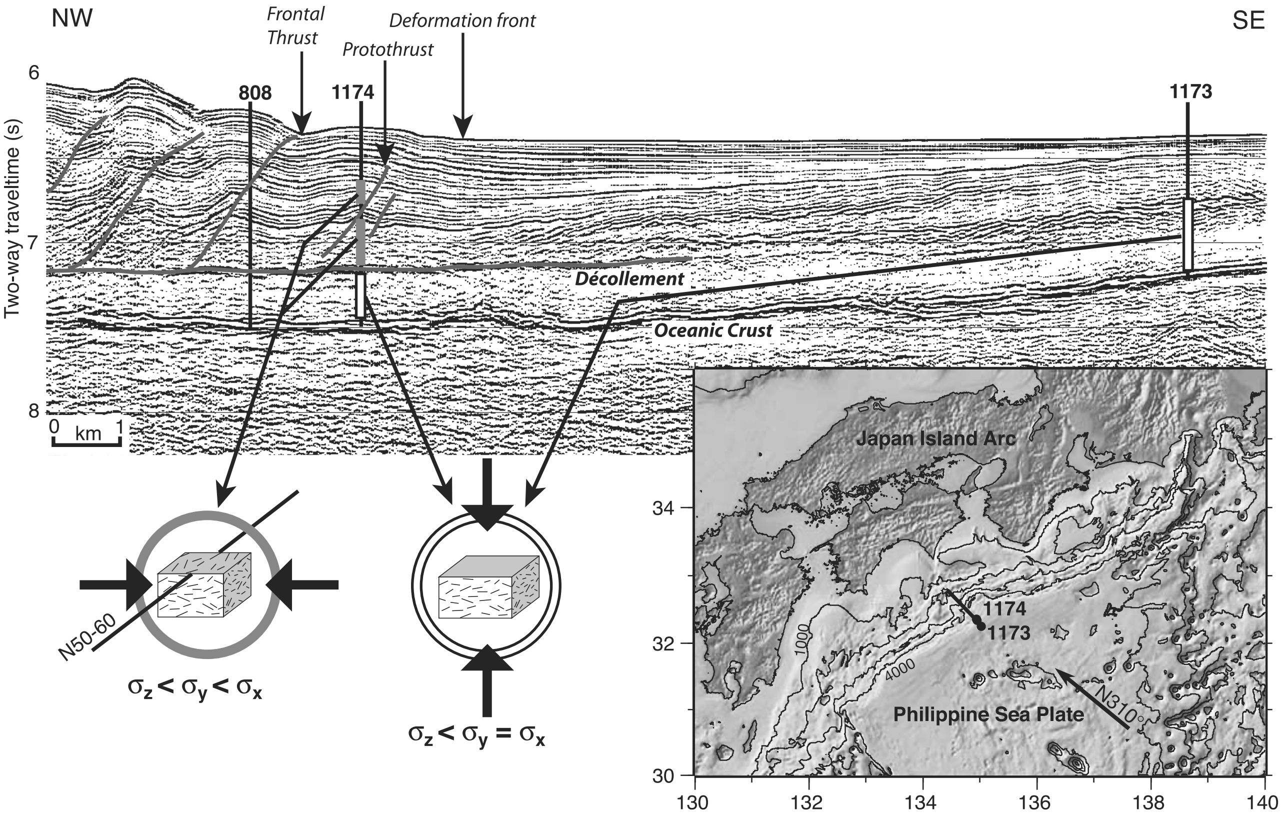

Figure 1. Location map and cross section of the toe of Nankai accretionary complex with the location of drill sites. Arrow on map shows N310° direction of Philippine Sea plate subduction. Results of anisotropy of electrical conductivity study are summarized. Vertical compaction occurs at Site 1173 and below the decollement level at Site 1174 (white bars). Sediments above the decollement (gray bars) record an additional component of horizontal strain.

tification of strain and determination of strain distribution and timing remain important problems.

[3] The anisotropy of magnetic susceptibility (AMS) is a commonly used indicator of strain [*Owens and Bamford*, 1976]. This measurement is very sensitive and has the advantage of yielding a complete six-component tensor. However, it is not, in general, used as a quantitative measurement of strain, in part because the mechanisms by which sediments acquire AMS are complex [*Rochette et al.*, 1992]. AMS as well as several other methods of strain determination have been tried at Site 808 at the toe of Nankai wedge, with ambiguous results [*Owens*, 1993; *Morgan and Karig*, 1993; *Brueckmann et al.*, 1993]. X-ray diffraction goniometry is a classic method of strain determination in sediment samples rich in layered silicates [*Evans et al.*, 1989]. This method indicates about 10% ductile horizontal shortening over the entire wedge section at Ocean Drilling Program (ODP) Site 808, but failed to give the correct vertical compaction strain component [*Morgan and Karig*, 1993]. Analyses of seismic profiles suggest a higher horizontal shortening in the trench, of 15–30% [*Morgan and Karig*, 1995a]. However, this latter value probably includes the effect of small-scale strain localization structures (faults or deformation bands), which are below seismic resolution. It should thus be considered as an upper bound to ductile strain. Anisotropy of *P* wave velocity has been measured on sample cubes during Leg 131 and appears to be affected by tectonic strain [*Brueckmann et al.*, 1993]. However, *P* wave anisotropy in the horizontal plane is too weak and noisy to be used for strain quantification. Electrical conductivity anisotropy is about 10 times larger and thus is easier to measure. Experimental work shows the anisotropy of electrical conductivity in clays follows strain, at least qualitatively [*Kuganenthira et al.*, 1996]. However, this property has been rarely used to assess strain in natural sediments.

[4] We here extend March's theory to include anisotropy of electrical conductivity measurements as the parameter measured to infer strain. In this approach, both clay particles and pores are idealized as flat disks, and reorganization with strain is treated as a passive rotation of the disks. This method is tested against data from the toe of Nankai accretionary wedge and yields consistent vertical and horizontal strain estimates. The deformation front of the wedge is defined by the onset of brittle deformation features (i.e., small scale faults) within the section above the decollement. The deformation front does not coincide with the frontal thrust, which is defined at the outcrop of the first thrust connecting the decollement and the seafloor (Figure 1). Site 808 was drilled through the frontal thrust during ODP Leg 131. Site 1174 was drilled during ODP Leg 190 in the zone between the deformation front and the frontal thrust, 1.8 km trenchward of Site 808 and

about 1.5 km landward of the deformation front. Site 1174 is thus a better location to study the onset of brittle deformation within the wedge section. At this location, two thrusts apparently offset sedimentary reflectors, and structural observations on cores define a zone of folding and fracturing between 463 and 500 meters below the seafloor (mbsf) that is designated as the protothrust [*Moore et al.*, 2001]. Site 1173 is a reference site located in the abyssal plain 14 km seaward of Site 808 and no compressive tectonic deformation is expected there. The present study is based on electrical conductivity measurements obtained at Sites 1173 and 1174. No anisotropy of electrical conductivity data are available at Site 808, which was drilled during an earlier cruise. However, electrical conductivity results from Site 1174 and Site 1173 alone are conclusive, and are compared with independent AMS and X-ray goniometry results.

2. Measurements

2.1. Method

[5] Complex electrical impedance of cubic samples cut from the core was measured on board the drill ship (Joides Resolution) with an impedance meter (Wayne-Kerr component analyzer), using two stainless steel electrodes [*Henry*, 1997; *Moore et al.*, 2001]. Filter papers soaked in seawater assured electrical contact between electrodes and sample. A zero reading was taken each time by measuring the impedance of the stacked two filters after they have been in contact with the sample. A frequency range of 20–30 kHz was selected for the measurements to minimize the imaginary part of the impedance, resulting in a phase angle of less than 3°. Conductivity along a given direction is computed from the real part of the conductance measured along this direction and from the dimensions of the sample. The three dimensions of the sample were measured with a caliper and are precise to within 0.1 mm.

[6] Conductivity (σ_x, σ_y, and σ_z, see notation section) is thus determined along three orthogonal axes in the core reference frame: z is vertical and x and y lie in the horizontal plane. The orientation of x and y axis relative to north is determined from magnetic remanence. Shipboard cryomagnetometer measurements after partial demagnetization in a 30 mT alternating field were obtained every 5 cm on the cores [*Moore et al.*, 2001]. These data are dense enough to allow reorientation of a majority of the measurements.

[7] All measurements were done at ambient conditions. The temperature in the laboratory was recorded during each sample measurement and varied between 24 and 29°C. A moderate pressure of about 1 bar was applied on the samples along the direction of measurement with a 10-pound weight. This applied pressure increased measurement reproducibility, and generally result in a small (less than 5%) increase of conductivity compared to measurements made without any applied pressure. Samples with apparent fissility displayed more sensitivity to pressure applied along the vertical axis, as cracks tend to open and fill with air when no pressure is applied.

[8] The measurement method does not give the complete electrical conductivity tensor, but only the diagonal terms in three directions. From these values, the horizontal anisotropy (a_H) or apparent anisotropy in the horizontal plane is defined as

$$a_H = 2(\sigma_x - \sigma_y)/(\sigma_x + \sigma_y), \tag{1}$$

and the vertical anisotropy (a_V) or average anisotropy over vertical planes as

$$a_V = 2\left(\frac{\sigma_x + \sigma_y}{2} - \sigma_z\right) \Big/ \left(\frac{\sigma_x + \sigma_y}{2} + \sigma_z\right). \tag{2}$$

Thus defined, the vertical anisotropy is invariant to rotation along the vertical axis, but this is not the case for the horizontal anisotropy. The anisotropy ratio (a) is defined the ratio of horizontal to vertical anisotropy:

$$a = a_H/a_V. \tag{3}$$

The normalized x axis conductivity (s_x) is defined as

$$s_x = 2\sigma_x/(\sigma_x + \sigma_y). \tag{4}$$

2.2. Results

[9] All measurements obtained on cube samples at Sites 1173 and 1174 are shown in Figure 2 along with porosity data and observations of bedding dip. In order to account for temperature variations in the lab, conductivity data are plotted as apparent formation factor, which is the ratio of seawater conductivity to sample conductivity at the same temperature ($F_a = \sigma_{\mathrm{seawater}}/\sigma$). It is apparent both for Sites 1173 and 1174 that the vertical anisotropy follows the compaction trends. This is best illustrated in the Lower Shikoku Basis Facies, which is composed of fairly homogeneous hemipelagic sediments. If apparent formation factor is plotted against porosity, the vertical and horizontal components appear to follow different generalized Archie's laws, with different exponents (Figure 3). At Site 1174, the vertical conductivity of samples from the decollement and above plot on an intermediate trend suggesting that tectonic strain results in a lower vertical anisotropy than the normal compaction trend.

[10] Average horizontal anisotropy is zero, which is expected for random sample orientation. At Site 1173, horizontal anisotropy is generally low and may reflect the natural dispersion of the measurements (Figure 2). At Site 1174 the scatter of horizontal anisotropy is higher in the section above the decollement. In order to identify a component of anisotropy in the horizontal plane, the normalized x axis conductivity and the anisotropy ratio are plotted as a function of orientation for all reoriented samples from above the decollement level, including those located above the protothrust zone (Figure 4a). A small but significant anisotropy is found, corresponding in average to a 6.6% horizontal anisotropy or to an anisotropy ratio of 28%, determined from a least square fit of all reoriented data. The direction of maximum conductivity is N52°. No significant anisotropy is found below the decollement but a few anomalous high conductivities measured between N0° and

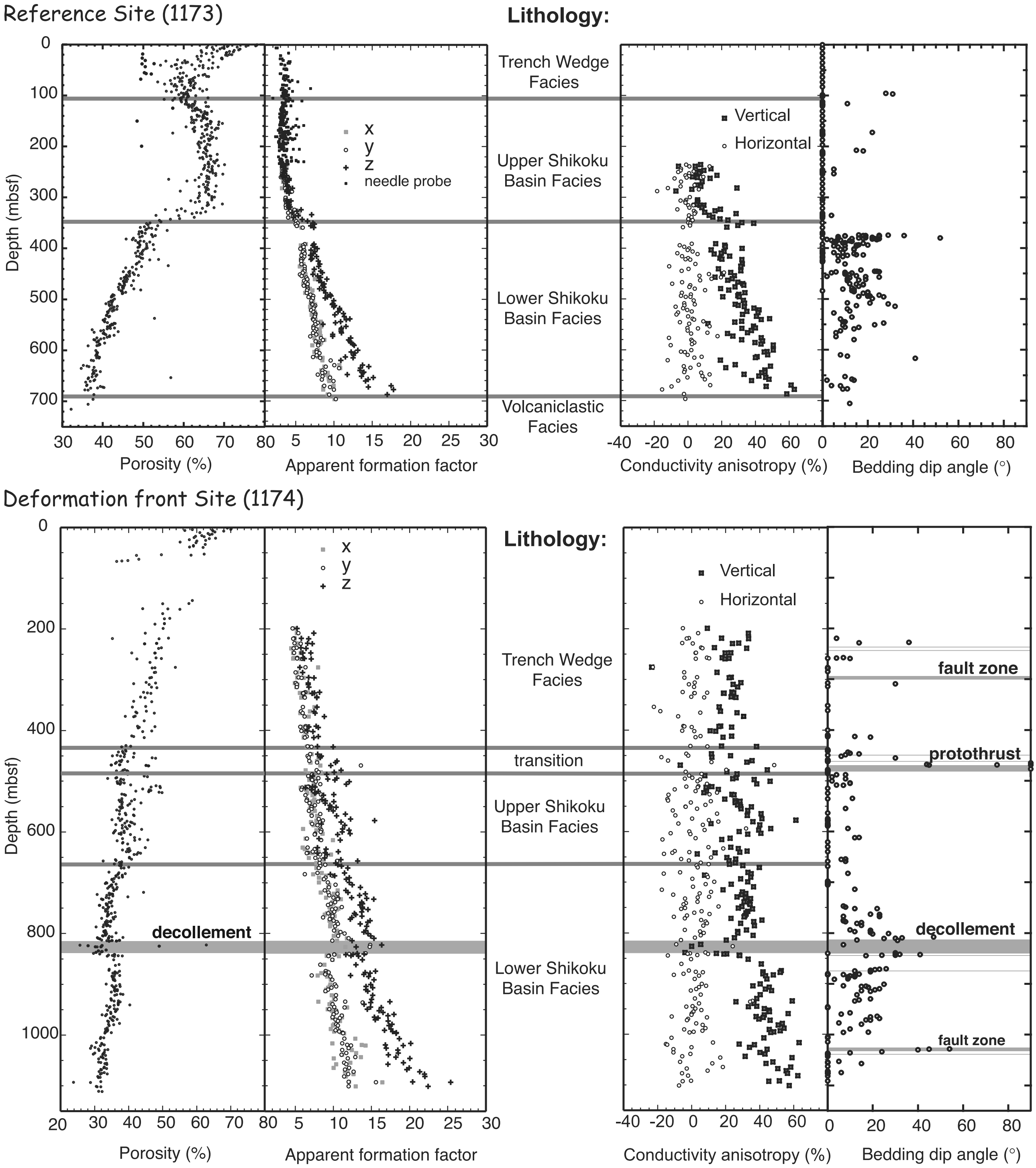

Figure 2. Measurements of apparent formation factor in all three directions (*x*, *y*, *z*) and of electrical conductivity horizontal and vertical anisotropy (see definitions in text) plotted next to porosity and bedding dip for Site 1173 (reference site) and Site 1174 (deformation front site). Needle probe measurements (using a four electrode array) were done on soft sediment cores from Site 1173 and did not measure significant anisotropy.

N20° may reflect discrete structures in these samples (Figure 4b).

2.3. Interpretation

[11] Interpretation of anisotropic physical properties in term of strain is based on the concept of an underlying relationship between fabric and anisotropy [*Owens and Bamford*, 1976]. Application of March's theory requires that the anisotropy signal is due to the reorientation of elongated or flat objects during nonisotropic strain. Clay particles and pores in clay matrix supported sediments, such as Nankai hemipelagites, are such objects. It is thus impor-

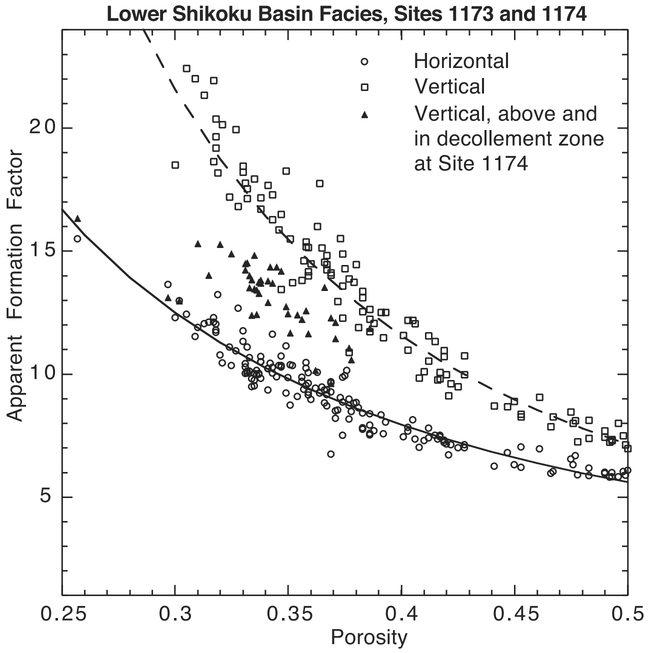

Figure 3. Apparent formation factors ($F_a = \sigma_{\mathrm{seawater}}/\sigma$) versus porosity for Lower Shikoku Basin Facies at both sites. Best fitting Archie's law determined from reference site (1173) is $F_a = 1.87\phi^{-1.58}$ for the horizontal component and $F_a = 1.58\phi^{-2.17}$ for the vertical component. Measurements at Site 1174 (deformation front) below the decollement level follow the same trends. In the decollement zone and above, the average horizontal component follows the same trend, but the vertical one does not. We interpret this as a consequence of strain.

tant to test whether the measured anisotropy truly reflects the microstructure of the sample or is the consequence of larger scale cracking during unloading. Indeed, the observation that fissility affects the measurements suggests that cracking may contribute to the anisotropy signal. However, the most fissile samples are from the lower trench wedge at Site 1174 and they appear to have only moderate vertical anisotropy, of 10–30%. Samples from the lower part of the Shikoku Basin facies had no apparent fissility but have stronger anisotropy.

[12] Further evidence arises from measurements of surface conductivity. Surface conductivity in clay rich sediments occurs primarily along the surfaces or the edges of the clay particles. The anisotropy of surface conductivity should thus depend primarily on the anisotropy of the clay particle distribution. Because the relative contribution of surface conductivity to total sample conductivity decreases with salinity [*Clavier et al.*, 1977; *Revil et al.*, 1998], measurements performed with a high salinity pore fluid are insensitive to surface conductivity effects. The anisotropy of electrical conductivity measured at high salinity should thus depend on the anisotropy of the pore distribution. For the Nankai hemipelagic sediments, fluid conductivity is in the 4–5 S/m range at room temperature, pore conductivity is dominant, but the surface conductivity term is not negligible [*Bourlange et al.*, 2003]. Sodium surface conductivity was determined on a limited number of samples by exchanging the pore fluid with NaCl solutions of conductivity 10, 20, 6 and, 3 S/m. Samples were left to equilibrate about 2 months in each solution and the vertical anisotropy measured after equilibration is plotted against fluid conductivity in Figure 5. The plotted curves correspond to the linear high salinity asymptotes determined for each sample for the vertical direction ($\sigma_V = \sigma_z$) and for the average of horizontal directions ($\sigma_H = (\sigma_x + \sigma_y)/2$):

$$\sigma = \sigma_{\mathrm{fluid}}/F + \sigma_{\mathrm{surface}}. \tag{5}$$

[13] The anisotropy of surface conductivity is the value extrapolated on these curves at the limit of zero fluid conductivity, whereas the limit at infinite conductivity gives the anisotropy of pore fluid conductivity. Anisotropy changes little with pore fluid conductivity and the anisotropy of surface and pore fluid conductivity are of the same order. This suggests they both have the same origin. Furthermore, anisotropy tends to decrease with fluid conductivity in samples having a vertical anisotropy of more than 40%. If, hypothetically, the anisotropy signal were due to preferred unloading crack orientation, anisotropy should vanish when the conductivity of the pore fluid equals that of the clay matrix. As this condition may only be met near the zero salinity limit, anisotropy from unloading cracks should always increase with salinity in the range of measurements. As this is not the case, it is likely that unloading cracks only have a minor influence on anisotropy. Measurements also suggest that the distribution of orientation of clay particles and pores are similar. Anisotropy of electrical conductivity may thus be used to infer strain.

[14] Another problem arises from incomplete determination of tensor geometry. Because the electrical conductivity measurements were only performed along three directions, the complete anisotropy tensor cannot be determined unless the directions of the principal axes are assumed or independently known. The horizontal plane anisotropy measured above the decollement may either correspond to a tensor coaxial to the core axes or, hypothetically, to a noncoaxial case. However, it can at least be shown that the horizontal plane anisotropy measured between 485 and 745 mbsf is not just the consequence of strata dip. Tensor algebraic properties imply that the horizontal plane anisotropy and the anisotropy ratio are always sinusoidal functions of azimuth. Many samples have a high anisotropy ratio and the best fitting sinusoidal corresponds to an anisotropy ratio of 36% along a N58 azimuth (Figure 6). Assuming that the compacted sediment is originally transversely anisotropic with a vertical axis of symmetry, the anisotropy ratio is a function of the dip angle and is computed by applying a rotation to the conductivity tensor. A 36% anisotropy ratio would require a dip of about 30°. However, no dip larger than 15° has been measured in the interval between 485 and 745 mbsf. The anisotropy ratio predicted for a 15° dip is always less than 10% and is too low to explain observations (Figure 6). More likely, the anisotropy tensor has lost its axial symmetry during strain and, like the AMS tensor [*Owens*, 1993; *Hisamitsu et al.*, 2001], is nearly coaxial to the core axis. However,

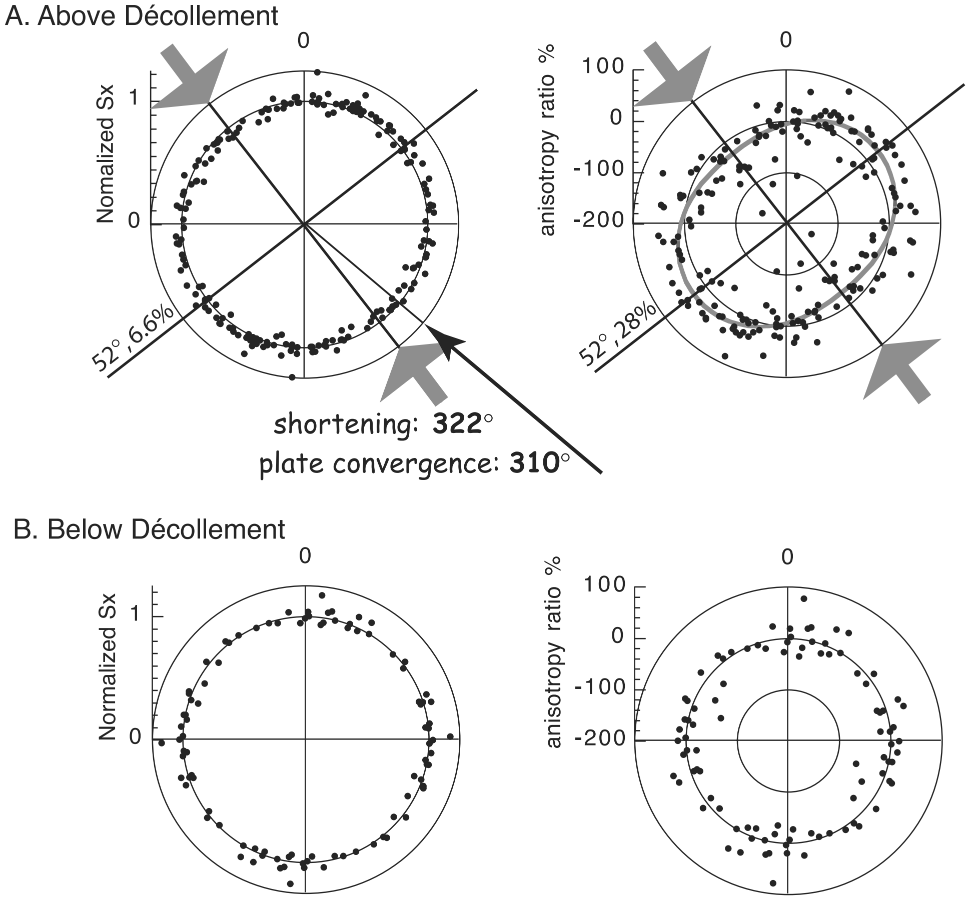

Figure 4. Polar plots of normalized conductivity and anisotropy ratio as a function of azimuth at the deformation front site (Site 1174). (a) Above the decollement. (b) Below the decollement. Data above the decollement display a maximum conductivity along a N52° direction, which is parallel to the deformation front and indicates ductile shortening along a N322° axis. Plate convergence is N310°.

one cannot exclude that the anisotropy signal in the zone from about 750 mbsf to the base of the decollement at 840 mbsf may also be affected by bedding dips.

3. Strain Computations

3.1. Assumptions and Definitions in March's Theory

[15] Relationships between strain and fabric in clay (or more generally phyllosilicates) can be obtained on the assumption that particles passively follow deformation, which is the fundamental assumption in March's theory (1932). This assumption is not generally valid because of electrostatic interaction between clay particles and recrystallization during diagenesis and metamorphism. It is also shown experimentally that large isotropic strains can destroy original anisotropy [*Kuganenthira et al.*, 1996], whereas it should have no effect according to March's theory. However, March's approach is considered as a good first approximation of strain even when there is extensive silicate recrystallization [*Evans et al.*, 1989]. Large isotropic strains are not expected at the Nankai sites except, perhaps, within the decollement zone.

[16] The orientation of a clay particle or of a flat pore is defined by the normal **n** to the particle or pore plane. When the material is subject to strain **S**, the assumption of passive reorientation results in the following equation [*Owens*, 1973]:

$$\mathbf{n}_{after} = \frac{{}^{t}\mathbf{S}^{-1} \cdot \mathbf{n}_{before}}{\|{}^{t}\mathbf{S}^{-1} \cdot \mathbf{n}_{before}\|}. \tag{6}$$

Note that **S** is a finite strain tensor and thus is I (not 0) in the absence of deformation. With this formula and for coaxial pure shear, the orientation of particles is not sensitive to the strain path but only to the finite strain between initial and final states.

[17] Two cases of strain are considered. Compaction strain is pure shear with vertical shortening and no strain on the horizontal axis. The strain tensor is a function of initial and final porosity:

$$\mathbf{S} = \begin{bmatrix} 1 & 0 & 0 \\ 0 & 1 & 0 \\ 0 & 0 & \dfrac{1-\phi_0}{1-\phi} \end{bmatrix}. \tag{7}$$

[18] Tectonic strain in the wedge may be approximated as horizontal pure shear, assuming all simple shear occurs within the decollement zone. Analysis of shear bands and slickenlined faults suggests that, in fact, the main principal

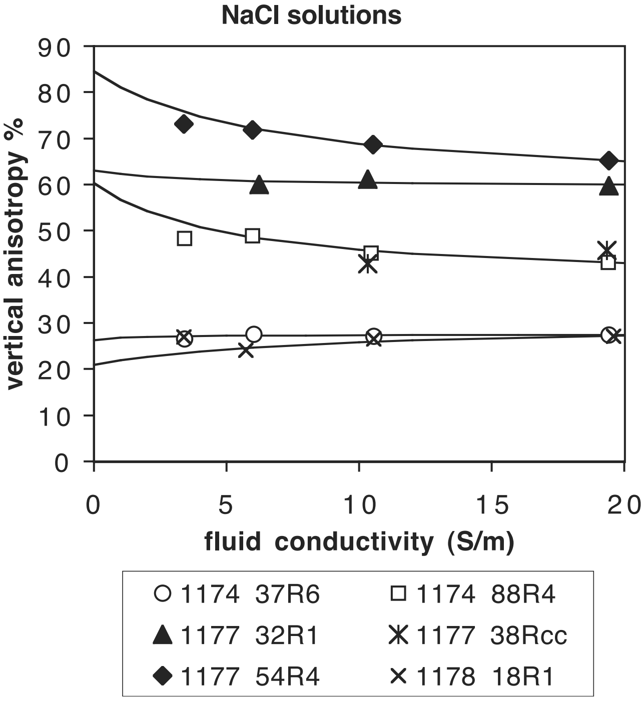

Figure 5. Vertical anisotropy as a function of conductivity of NaCl exchange solution. Fitting curves correspond to the high salinity asymptotes (see text).

stress axis dips slightly (up to 10°) during the phase of strain localization [*Moore et al.*, 2001]. The same may have been true during ductile distributed strain but this cannot be assessed with the electrical conductivity data because a small dip of the principal strain axis will not change results. In the horizontal pure shear model, the amount of horizontal shortening should be the same from the top of the column to the decollement. The strain tensor depends only on horizontal shortening and initial and final porosity:

$$\mathbf{S} = \begin{bmatrix} \dfrac{X}{X_0} & 0 & 0 \\ 0 & 1 & 0 \\ 0 & 0 & \dfrac{X_0}{X}\dfrac{1-\phi_0}{1-\phi} \end{bmatrix}. \tag{8}$$

3.2. Conductivity Anisotropy and Fabric: Assumptions and Model

[19] In order to relate the conductivity anisotropy with the fabric, let us assume that the pores in the clay matrix are flat and may be treated as disks conducting fluid only in their plane. For such a system, different physical approaches based on the noninteracting crack theory [*Kachanov*, 1993] or on a mean field approximation [*David*, 1985; *Gueguen and Dienes*, 1989; *Sausse et al.*, 2001] have resulted in a linear relationship between the permeability tensor and a tensor, $\boldsymbol{\alpha}$, that is a function of the pore distribution. The same approach can be applied to other transport properties such as the electrical conductivity tensor:

$$\boldsymbol{\sigma} = \sigma_i \mathbf{I} + C[(\mathrm{tr}\,\boldsymbol{\alpha})\mathbf{I} - \boldsymbol{\alpha}], \tag{9}$$

where σ_i represents the background conductivity (assumed isotropic) and C is a function of the geometry of the pores (which may not be ideal flat disks) and of the connectivity of the network. For electrical conductivity, $\boldsymbol{\alpha}$ is the sum of the contributions of surface and fluid conductivity for each disk shaped pore:

$$\boldsymbol{\alpha} = (1/V) \sum_{i:pore} v_i\left(\sigma_f + \Sigma_s/w_i\right)\mathbf{n}_i \otimes \mathbf{n}_i, \tag{10}$$

where V is rock volume, Σ_s is surface conductance, σ_f is fluid conductivity, and v_i and w_i are the volume and aperture of individual pores.

[20] In the assumed case, the flat disks represent the entire porous network and the background conductivity should be zero. For simplicity, we also assume that the distribution of orientation and the distribution of pore size (and aperture) are independent. Pore volume and pore aperture are thus replaced in equation (10) by their average, and (9) and (10) combined:

$$\boldsymbol{\sigma} = C\phi\sigma_f\left(1 + \Sigma_s/w\sigma_f\right)\left[\mathbf{I} - \frac{1}{N}\sum_{i\ pore} \mathbf{n}_i \otimes \mathbf{n}_i\right], \tag{11}$$

where ϕ is the porosity, w is average pore aperture, and N is the number of pores. The data that we model are dimensionless parameters (vertical anisotropy, horizontal anisotropy, anisotropy ratio and normalized x axis conductivity) that can be computed simply from the normalized anisotropy tensor:

$$\mathbf{A} = \left[\mathbf{I} - \frac{1}{N}\sum_{i\ pore} \mathbf{n}_i \otimes \mathbf{n}_i\right]. \tag{12}$$

3.3. Computation Results

[21] The anisotropy tensor is computed from a random realization of the pore distribution. An initially isotropic

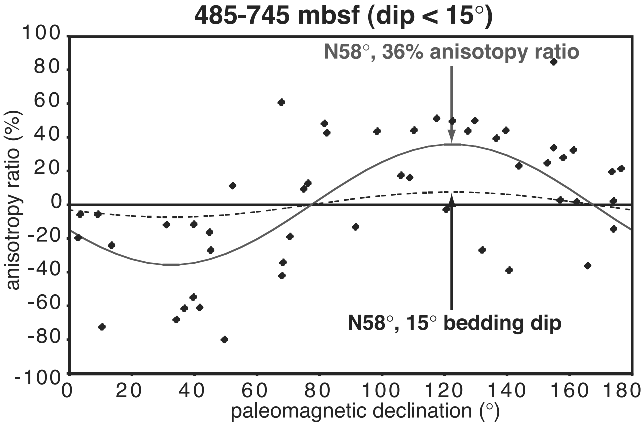

Figure 6. Comparison of the horizontal anisotropy ratio measured at Site 1174 between 485 and 745 mbsf and models. The maximum strata dip measured within this interval is 15°. Horizontal axis is magnetic declination and thus represents sample orientation. The solid curve is a best fit of the data assuming a fully anisotropic conductivity tensor (coaxial to the core axis). The dashed curve represents the anisotropy ratio that would result from tilting a transversely anisotropic medium by 15°.

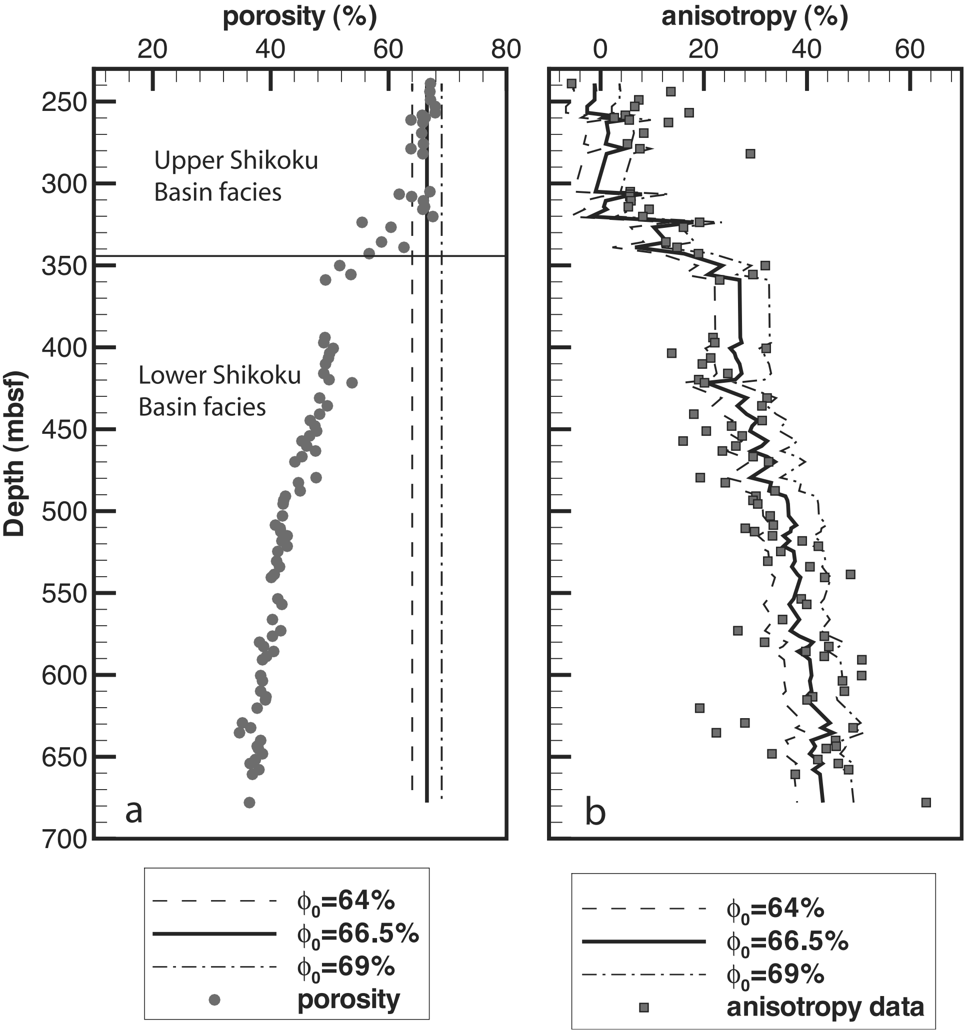

Figure 7. Predictions of compaction strain models at Site 1173 (reference site) and comparison with data. (a) Initial and final porosity. (b) Measured and computed vertical anisotropy.

population of 100,000 pores is defined by random determination of their normal vector. The strain operator is then applied to this distribution, following equation (6) and the anisotropy tensor is computed from equation (12).

[22] The method was first tested at Site 1173 (reference site), which presumably corresponds to a pure case of vertical compaction (equation (7)). The only adjustable parameter in this model is initial porosity ϕ_0. Computations are shown for three values of initial porosity (Figure 7). With an initial porosity of 69%, data from the Upper Shikoku Basin facies and the sharp change in porosity and anisotropy at its base are well fit. A lower initial porosity of 64% is required to fit data between 400 and 500 mbsf. The model with 66.5% initial porosity is the best fitting model if the entire depth range of data is considered. We conclude that this model is consistent with the behavior of the sediment during compaction.

[23] For Site 1174 (protothrust zone site) a vertical compaction model with an initial porosity of 67% approximates anisotropy data in the underthrust sequence (Figure 8). However, vertical anisotropy predicted with this compaction model is much too high in the section above the decollement. This observation and the horizontal anisotropy (see measurement section) were both used to constrain the amount of ductile strain using equation (8). This is also an important test of the method self-consistency. For moderate horizontal strains, the dependence of anisotropy on strain is close to linear and models with horizontal strain in the 10–15% range satisfy constraints on both horizontal and vertical anisotropy. Assuming 67% initial porosity, the best fitting model is with 12% shortening ($X/X_0 = 0.88$) (Figure 8). The computed horizontal anisotropy for this scenario is nearly constant but slightly decreases with depth from 6.8% at 200 mbsf to about 5.8% at 800 mbsf. The vertical anisotropy is within the range of data and follows, at least qualitatively, the variations in anisotropy associated with the high porosity intervals around 500 mbsf and 630 mbsf. The decollement zone itself appears as a zone of abnormally low anisotropy, which suggests additional strain not accounted for by the pure shear model.

3.4. Porosity Evolution

[24] Early occurrence of horizontal strain above the decollement suggests that the discontinuity in porosity observed across the decollement (4–5% at Site 1174, 5–6% at Site 808) is, at least in part, due to a discontinuity of

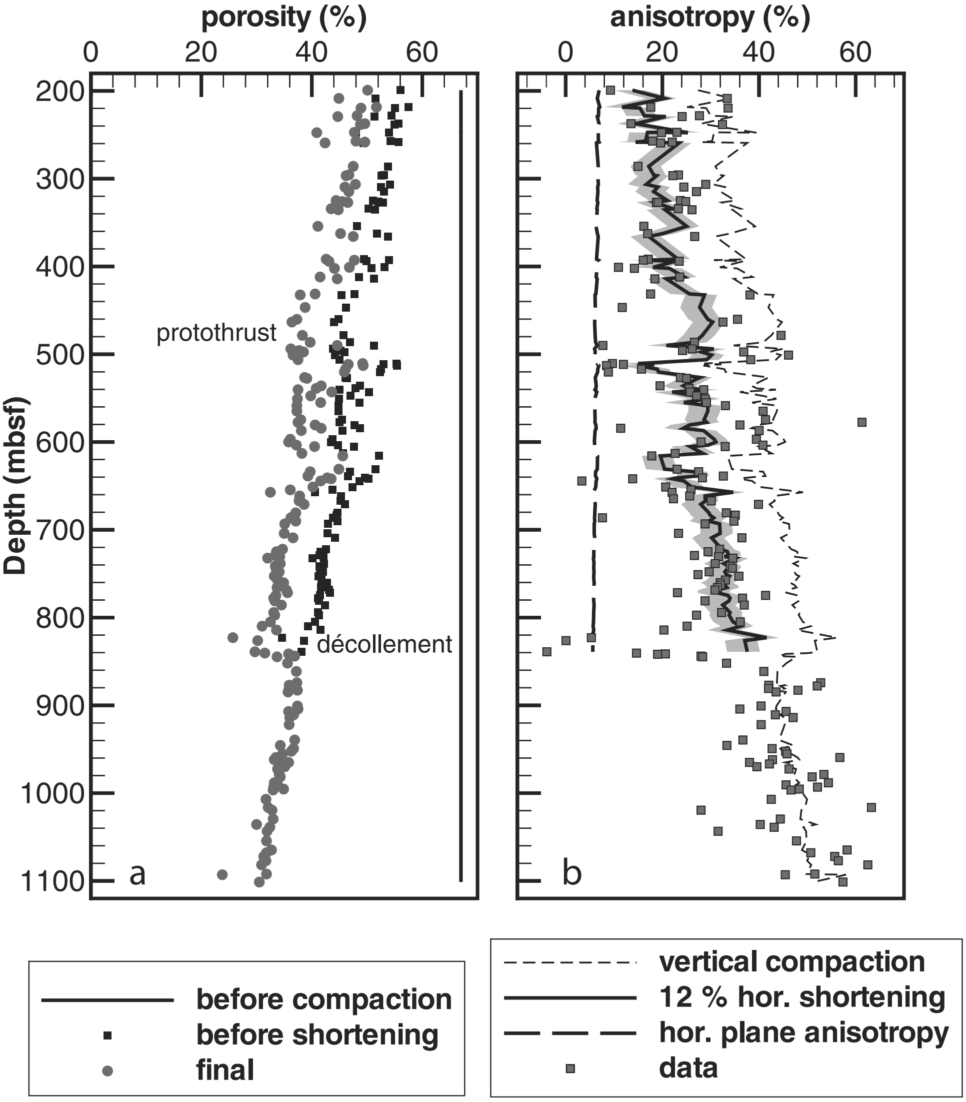

Figure 8. Predictions of strain models at Site 1174 (deformation front site) and comparison with data. (a) Porosity evolution. (b) Computed vertical anisotropy compared with data and the computed horizontal anisotropy. The gray area corresponds to the 10–15% range of horizontal strain, assuming 67% initial porosity. Horizontal anisotropy measurements are summarized on Figure 4.

the stress state [*Morgan and Karig*, 1995b]. In this hypothesis, ductile horizontal strain everywhere above the decollement should be associated with volume loss. As remarked in the assumptions and definitions section, the final state computed in the model does not depend on the strain path. However, it is possible to calculate the porosity at the beginning of horizontal shortening for different hypotheses. If horizontal shortening occurred under purely undrained conditions, the porosity before shortening is the final porosity. This would imply that the porosity jump existed even before shortening. If horizontal shortening is uniaxial (no associated thickening), then the porosity at the beginning of shortening is:

$$\phi_1 = 1 - \frac{X}{X_0}(1 - \phi). \qquad (13)$$

If ductile horizontal strain is truly uniaxial, the thickening of the sedimentary layers observed on the seismic profiles requires additional distributed (or diffuse) strain. As noted by *Morgan and Karig* [1995a], this additional strain may be the consequence of slip on small-scale faults. The porosities (ϕ_1) computed from equation (13) are plotted on Figure 8 and lie in continuity with the trend defined by measurements from the underthrust sequence. This coincidence may be explained if the porosity profile at the time of decollement initiation reflected compaction of homogenous sediments in a smoothly varying pore pressure regime. It is not possible to demonstrate which scenario is correct form the data available. However, the presence of only a small (<2%) porosity jump at the reference site (Site 1173) suggests that the uniaxial horizontal strain scenario may be a better approximation. Average pore pressure ratio (λ) in the underthrust sequence at Site 1174 has been estimated to 0.66 (corresponding to excess pore pressure ratio $\lambda^* = 0.42$, see definitions in the notation section) based on the analysis of compaction curves [*Screaton et al.*, 2002]. This moderate overpressuring is primarily due to sedimentary loading by rapid turbidite sedimentation in the trench [*Le Pichon et al.*, 1993; *Screaton et al.*, 2002] and may approximate the pore pressure regime in the formation on both sides of the decollement at the beginning of decollement initiation.

4. Discussion

[25] We showed that the evolution of electrical anisotropy with depth at the reference site follows the evolution of porosity. It also follows irregularities in the compaction curve. In the abyssal plain (Site 1173), a sharp porosity change at the lithological transition from Upper to Lower Shikoku Basin Facies corresponds to a sharp increase of anisotropy. This implies that the porosity change is associated with clay particle reorientation. At Site 1174, intervals of preserved high porosity are also found in the Upper Shikoku Basin Facies and correspond to zones of low anisotropy. Between these intervals, the sediment compacted and anisotropy increased. It is hypothesized that the evolution of porosity in the Upper Shikoku Basin Facies is controlled by silica diagenesis and that porosity loss is associated with a reorganization of the clay particles after the dissolution of grain contact cement [*Mikada et al.*, 2002; *Moore et al.*, 2001]. Observations on anisotropy of electrical conductivity agree well with this hypothesis.

[26] We estimate that about 12% subhorizontal ductile strain associated with porosity loss occurred at Site 1174 in the section above the decollement. Laboratory work on porous rocks shows that porosity exerts important control over the brittle-ductile transition [*Karig*, 1990; *Wong*, 1990]. Furthermore, triaxial tests on tuff samples from Nankai show that the amount of porosity reduction before failure is a function of effective stress [*Zhang et al.*, 1993]. We suggest that porosity reduction in the section above the decollement occurred prior to failure and could, in theory, be used to infer pore pressure conditions at failure. This, however, would require better laboratory constraints on the failure conditions in the hemipelagic lithologies.

[27] The results of the present study are also consistent with previous work that identified a change in strain axis orientation across the decollement at Nankai and Barbados wedge toes, using other methods such as AMS [*Housen*, 1997; *Owens*, 1993], X-ray goniometry [*Morgan and Karig*, 1993] and *P* wave anisotropy [*Brueckmann et al.*, 1993]. These results are consistent with new AMS results from Leg 190 [*Hisamitsu et al.*, 2001]. The underthrust sequence apparently continues to compact vertically whereas the entire sequence above the decollement is subject to horizontal strain. The present study also finds comparable quantitative estimates of ductile strain at Site 1174 (where deformation is at the protothrust stage) as previous work using X-ray goniometry at Site 808 (frontal thrust with 150 m throw) [*Morgan and Karig*, 1993]. This suggests that layer parallel shortening is 10–15% at both sites in spite of deformation processes being more advanced at Site 808 and strengthens the conclusion that ductile strain occurred prior to thrusting [*Morgan and Karig*, 1995a]. Furthermore, ductile horizontal shortening occurs both above and below the protothrust. It is thus shown that ductile strain occurs early in the process of strain localization in the section above the decollement and is not the consequence of thrust initiation (or propagation). However, distributed horizontal ductile strain (layer parallel shortening) should follow decollement initiation because it reflects strain decoupling.

[28] Comparison of results from anisotropy of electrical conductivity and X-ray goniometry is also interesting as a test of the methods. As noted in section 1, X-ray goniometry failed to give the correct vertical compaction strain [*Morgan and Karig*, 1993] and the anisotropy of electrical conductivity seems, with this respect, to give better results. One should note that the absence of a reference site in the earlier study may have been an obstacle to calibration but there are also fundamental differences. The X-ray goniometry is sensitive to clay particle orientation whereas the electrical method is mostly sensitive to pore orientation (at least for a high salinity pore fluid). We assumed that particles and pores have the same distribution of orientations and provided arguments in support of this hypothesis in the measurement interpretation section (section 2.3). We thus do not consider a discrepancy between particle and pore orientation distributions as the most likely explanation. The spatial resolution of methods is also different as the electrical method is sensitive to average pore orientation whereas X-ray goniometry may be affected by changes in crystalline network orientation at a scale smaller than particle size. Consequently, it is possible that the effect of small-scale crystalline disorder on the X-ray goniometry data partly masks the compaction signal. The X-ray goniometry method still appears sensitive to loss of axial symmetry during horizontal strain.

[29] The N052° direction of maximum conductivity in the section above the decollement implies shortening along a N322° direction, nearly perpendicular to the local strike of the deformation front and consistent with the anisotropy of magnetic susceptibility results [*Hisamitsu et al.*, 2001]. This direction is at a slight angle (12°) from the N310° direction of convergence [*Mazzotti et al.*, 2000; *Seno et al.*, 1993]. The direction of the principal stress axis inferred from slickenlined faults [*Lallemant et al.*, 1993] and deformation bands [*Ujiie et al.*, 2003] is closer to the direction of plate convergence. This suggests that some shear partitioning may be occurring even during strain localization. If ductile shortening is strictly normal to the trough axis, all of the small subduction obliquity must be taken up on faults.

[30] Layer parallel shortening at Site 1174 implies slip on the decollement seaward of the frontal thrust. The decollement reflector has strong amplitude below the trench wedge up to 5 km seaward of Site 1174. Deformation of the reflectors at the base of the trench wedge is observed on the seismic section up to the deformation front, 1.5 km seaward of Site 1174 (Figure 1). These may be considered as upper and lower bounds for the onset of sliding along the decollement. Assuming 10% horizontal shortening over 5 km, slip on the decollement due to ductile shortening alone may be as high as 500 m at Site 1174. Assuming shortening increases linearly from 0% to 10% over 1.5 km, a lower bound of 75 m for slip as Site 1174 is obtained. However, total slip is certainly larger due to thickening by small-scale deformation bands and faults. The decollement thus appears as the very first shear localization structure in

the system and is already a mature fault zone when imbricate thrusting is initiated.

5. Conclusions

[31] The anisotropy of electrical conductivity in clay rich sediment reflects the evolution of clay microfabric and can be used to quantify strain. At the toe of Nankai accretionary wedge, we estimate that 10–15% layer parallel shortening occurred before brittle failure in the entire section above the decollement.

[32] 1. In the abyssal plain (Site 1173), a sharp porosity change at the lithological transition from Upper to Lower Shikoku Basin Facies corresponds to a sharp increase of anisotropy. This very strong compaction gradient is thought to be a consequence of silica diagenesis.

[33] 2. Timing of deformation is as follows: (1) decollement initiation below the trench, (2) ductile layer parallel shortening in the section above the decollement, (3) strain localization in the section above the decollement, and (4) slip on imbricate thrusts. There may be some overlap between these phases. However, most of the ductile strain occurs after decoupled stress conditions are established at the decollement level and the decollement slips at least 150–500 m before significant slip occurs on the imbricate thrusts.

[34] 3. Layer parallel shortening is associated with porosity loss and can account for the change of porosity observed across the decollement. This also implies moderate pore overpressure in the formation above the decollement zone.

[35] 4. Fully understanding the process of decollement initiation would probably require drilling seaward of Site 1174, at a location where the decollement already acquired some reflectivity but where no deformation is apparent in the basin section.

Notation

σ	electrical conductivity.
σ_x	electrical conductivity along axis x (= σ_{xx} tensor term).
σ_H	average conductivity in horizontal plane (= $(\sigma_x+\sigma_y)/2$).
σ_V	conductivity along vertical axis (= σ_z).
a_H	horizontal anisotropy.
a_V	vertical anisotropy.
a	anisotropy ratio (= a_H/a_V).
s_x	normalized electrical conductivity along x axis (= σ_x/σ_H).
F_a	apparent formation factor (= $\sigma_{\text{seawater}}/\sigma$).
F	formation factor.
σ_{surface}	contribution of mineral surfaces to bulk conductivity.
$\mathbf{n}$	unit vector normal to particle or pore.
$\mathbf{S}$	strain tensor.
ϕ	porosity.
ϕ_0	initial porosity at deposition.
ϕ_1	porosity at the beginning of shortening.
X/X_0	horizontal strain.
σ_i	background conductivity (isotropic).
C	dimensionless conductivity factor.
$\mathbf{I}$	identity tensor.
$\boldsymbol{\alpha}$	pore distribution anisotropy tensor.
$\boldsymbol{\sigma}$	electrical conductivity tensor.
V	rock volume.
v_i	volume of pore i.
w_i	aperture of pore i.
σ_f	pore fluid conductivity (= σ_{fluid}).
Σ_s	surface conductance.
N	number of pores in volume V.
w	average aperture.
$\mathbf{A}$	normalized anisotropy tensor.
P_{fluid}	fluid pressure.
P_{hydro}	fluid hydrostatic pressure.
P_{seafloor}	pressure at the seafloor (hydrostatic).
P_{litho}	lithostatic pressure.
λ	pore pressure ratio $(P_{\text{fluid}} - P_{\text{seafloor}})/(P_{\text{litho}} - P_{\text{seafloor}})$.
λ^*	excess pore pressure ratio $(P_{\text{fluid}} - P_{\text{hydro}})/(P_{\text{litho}} - P_{\text{hydro}})$.

[36] **Acknowledgments.** We thank the leg 190 ODP crew for supporting an unrequired experiment and particularly Pieter Pretorius, who maintained the electrical resistivity device. We thank Maria Zamora at IPG Paris for advice and help with the determination of surface conductivities and Yves Gueguen (ENS Paris for theoretical discussions). We thank reviewers Julia Morgan, Peter Flemings, and Associate Editor Phil Wannamaker for their careful reading of the manuscript and their constructive comments. This work was supported by INSU "ad hoc ocean" fund.

References

Allmendinger, R. W., Inversed forward numerical modelling of trishear fault propagation fold, *Tectonics*, *17*, 640–656, 1998.

Averbuch, O., D. Frizon de Lamotte, and C. Kissel, Magnetic fabric as a structural indicator of the deformation path within a fold-thrust structure: A test case from the Corbière (NE Pyrenées France), *J. Struct. Geol.*, *14*, 461–474, 1992.

Beaumont, C., and G. Quinlan, A geodynamic framewok for interpreting crustal-scale seismic-reflectivity patterns in compressional orogens, *Geophys. J. Int.*, *116*, 754–783, 1994.

Besuelle, P., Compacting and dilating shear bands in porous rocks; theoretical and experimental conditions, *J. Geophys. Res.*, *106*, 13,435–13,442, 2001.

Bourlange, S., P. Henry, J. C. Moore, H. Mikada, and A. Klaus, Fracture porosity in the decollement zone of Nankai accretionary wedge using Logging While Drilling resistivity data, *Earth Planet. Sci. Lett.*, *209*, 103–112, 2003.

Brueckmann, W., K. Moran, and E. Taylor, Accoustic anisotropy and microfabric development in accreted sediment from the Nankai Trough, *Proc. Ocean Drill. Program Sci. Results*, *131*, 221–233, 1993.

Clavier, C., G. Coates, and J. Dumanoir, The theoretical and experimental bases for the dual-water model for the interpretation of shaly sands, paper presented at SPE 52nd Annual Fall Technical Conference, Soc. of Pet. Eng., Denver, Colo., 1977.

David, C., Modèle d'évolution de la permeabilité d'une roche, DEA thesis, Univ. Louis Pasteur, Strasbourg, France, 1985.

Doin, M. P., and P. Henry, Subduction initiation and continental crust recycling: The roles of rheology and eclogitization, *Tectonophysics*, *342*, 163–191, 2001.

Evans, K. F., G. Oertel, and T. Engelder, Apalachian stress study: 2. Analysis of Devonian shale core: Some implications for the nature of contemporary stress variations and Alleghanian deformation in Devonian rocks, *J. Geophys. Res.*, *94*, 7155–7170, 1989.

Frizon de Lamotte, D., Early record of tectonic magnetic fabric during inversion of a sedimentary basin. Short review and examples from the Corbières transfer zone (France), *Bull. Soc. Geol. Fr.*, *173*, 461–469, 2002.

Gueguen, Y., and J. Dienes, Transport properties of rocks from statistics and percolation, *Math. Geol.*, *21*, 1–13, 1989.

Henry, P., Relationship between porosity, electrical conductivity, and cation exchange capacity in Barbados wedge sediments, *Proc. Ocean Drill. Program Sci. Results*, *156*, 137–149, 1997.

Hisamitsu, T., K. Ujiie, and A. Taira, Magnetic fabric analysis of protodecollement zone at the toe of the Nankai accretionary prism, *Eos Trans. AGU*, *82*(47), Fall Meet. Suppl., Abstract T41A-0857, 2001.

Housen, B. A., Magnetic anisotropy of Barbados prism sediments, *Proc. Ocean Drill. Program Sci. Results*, *156*, 97–105, 1997.

Kachanov, M., Elastic solids with many cracks and related problems, *Adv. Appl. Mech.*, *30*, 259–445, 1993.

Karig, D.E., Experimental and observational constrains on the mechanical behavior in the toes of accretionary prisms, in *Deformation Mechanisms, Rheology and Tectonics*, edited by R. J. Knipe and E. H. Rutter, *Geol. Soc. Spec. Publ.*, *54*, 383–398, 1990.

Karig, D. E., and J. K. Morgan, Tectonic deformation; stress paths and strain histories, in *The Geological Deformation of Sediments*, edited by A. Maltman, pp. 167–204, Chapman and Hall, New York, 1994.

Kuganenthira, N., D. Zhao, and A. Anandarajah, Measurement of fabric anisotropy in triaxial shearing, *Géotechnique*, *46*, 657–670, 1996.

Lallemant, S. J., T. Byrne, A. Maltman, D. Karig, and P. Henry, Stress tensors at the toe of the Nankai accretionry prism: An application of inverse methods to slickenlined faults, *Proc. Ocean Drill. Program Sci. Results*, *131*, 103–122, 1993.

Le Pichon, X., P. Henry, and S. Lallemant, Accretion and erosion in subduction zones: The role of fluids, *Annu. Rev. Earth Sci.*, *21*, 307–331, 1993.

Mazzotti, S., X. Le Pichon, P. Henry, and S.-I. Miyazaki, Full interseismic locking of the Nankai and Japan-west Kurile subduction zones: An analysis of uniform elastic strain accumulation in Japan constrained by permanent GPS, *J. Geophys. Res.*, *105*, 13,159–13,177, 2000.

Mikada, H., J. C. Moore, K. Becker, and A. Klaus, *Proceedings of the Ocean Drilling Program*, *Initial Reports*, vol. 196, Ocean Drill. Program, College Station, Tex., 2002.

Moore, G. F., A. Taira, and A. Klaus, *Proceedings of the Ocean Drilling Program, Initial Reports,* vol. 190, Ocean Drill. Program, College Station, Tex., 2001.

Morgan, J. K., and D. E. Karig, Ductile strains in clay-rich sediments from hole 808C: Preliminary results using X-ray pole figure goniometry, *Proc. Ocean Drill. Program Sci. Results*, *131*, 141–155, 1993.

Morgan, J. K., and D. E. Karig, Kinematics and a balanced cross-section across the toe of the eastern Nankai accretionary prism, *J. Struct. Geol.*, *17*, 31–45, 1995a.

Morgan, J. K., and D. E. Karig, Decollement processes at the Nankai accretionary margin, southeast Japan: Propagation, deformation, and dewatering, *J. Geophys. Res.*, *100*, 15,221–15,231, 1995b.

Owens, W. H., Strain modification of angular density distribution, *Tectonophysics*, *16*, 249–261, 1973.

Owens, W. H., Magnetic fabric studies of samples from Hole 808C, Nankai Trough, *Proc. Ocean Drill. Program Sci. Results*, *131*, 301–310, 1993.

Owens, W. H., and D. Bamford, Magnetic, seismic and other anisotropic properties of rock fabrics, *Philos. Trans. R. Soc. London, Ser. A*, *283*, 55–68, 1976.

Revil, A., L. M. Cathles, S. Losh, and J. A. Nunn, Electrical conductivity in shaly sands with geophysical applications, *J. Geophys. Res.*, *103*, 23,925–23,936, 1998.

Rochette, P., M. Jackson, and A. Aubourg, Rock magnetism and the interpretation of anisotropy of magnetic susceptibility, *Rev. Geophys.*, *30*, 209–226, 1992.

Rudnicki, J. W., and J. R. Rice, Conditions for the localisation of the deformation in pressure sensitive dilatant materials, *J Mech. Phys. Solids*, *23*, 371–394, 1975.

Sagnotti, L., F. Speranza, A. Winkler, M. Mattei, and R. Funiciello, Magnetic fabric of clay sediments from the external northern Apennines (Italy), *Physics Earth Planet. Inter.*, *105*, 73–93, 1998.

Saint-Bezar, B., R. L. Hebert, C. Aubourg, P. Robion, R. Swennen, and D. Frizon de Lamotte, Magnetic fabric and petrographic investigation of hematite-bearing sandstones within ramp-related folds: Examples from the south Atlas Front (Morocco), *J. Struct. Geol.*, *24*, 1507–1520, 2001.

Sausse, J., E. Jacquot, B. Fritz, J. Leroy, and M. Lespinasse, Evolution of crack permeability during fluid-rock interaction. Example of the Brézouard granite (Vosges, france), *Tectonophysics*, *336*, 199–214, 2001.

Screaton, E. J., et al., Porosity loss within the underthrust sediments of the Nankai accretionary complex: Implications for overpressures, *Geology*, *30*(1), 19–22, 2002.

Seno, T., S. Stein, and A. E. Gripp, A model for the motion of the Philippine Sea Plate consistent with NUVEL 1 and geological data, *J. Geophys. Res.*, *98*, 17,941–17,948, 1993.

Suppe, J., *Principles of Structural Geology*, 537 pp., Prentice-Hall, Old Tappan, N. J., 1985.

Ujiie, K., A. J. Maltman, M. Sanchez-Gomez, T. Hisamitsu, and T. Nakano, Nature, distribution, and origin of deformation bands at the toe of the active accretionary prism, *J. Struct. Geol.*, in press, 2003.

Wong, T.-F., Mechanical compaction and brittle-ductile transition in porous sandstones, in *Deformation Mechanisms, Rheology and Tectonics*, edited by R. J. Knipe and E. H. Rutter, *Geol. Soc. Spec. Publ.*, *54*, 111–122, 1990.

Zhang, J., D. M. Davis, and T.-F. Wong, Failure modes of tuff samples from Leg 131 in the Nankai accretionary wedge, *Proc. Ocean Drill. Program Sci. Results*, *131*, 275–281, 1993.

P. Henry, Departement de Geodynamique, College de France, Europole de l'Arbois, Batiment Laennec, hall D, etage 2, BP 80, F-13545 Aix en Provence, France. (henry@geologie.ens.fr)

S. Hunze, Geowissenschaftliche Gemeinschaftsaufgaben-GCA, Stilleweg 2, D-30631 Hannover, Germany. (s.hunze@gga-hannover.de)

L. Jouniaux, Laboratoire de Géologie, Ecole Normale Supérieure, CNRS UMR 8538, 24 rue Lhomond, F-75231 Paris Cedex 05, France.

D. M. Saffer, Department of Geology and Geophysics, P.O. Box 3006, University of Wyoming, Laramie, WY 82071-3006, USA. (dsaffer@uwyo.edu)

E. J. Screaton, Department of Geology, University of Florida, P.O. Box 112120, Gainesville, FL 32611, USA. (screaton@geology.ufl.edu)

JOURNAL OF GEOPHYSICAL RESEARCH, VOL. 104, NO. B12, PAGES 29,293–29,309, DECEMBER 10, 1999

Detection of fluid flow variations at the Nankai Trough by electric and magnetic measurements in boreholes or at the seafloor

Laurence Jouniaux and Jean-Pierre Pozzi
École Normale Supérieure, Laboratoire de Géologie, UMR 8538, Paris, France

Jean Berthier and Philippe Massé
Laboratoire d'électronique, technologies et instrumentations, CEA, Grenoble, France

Abstract. Detection of changes in the flow rate of expelled fluids in accretionary prisms by monitoring of electric and magnetic fields is discussed. A numerical model of the electric and magnetic fields associated with fluid flow variations at the Nankai Trough is presented which gives a numerical solution of the coupled system of electric convection currents and conduction currents that directly determines the magnetic anomaly itself. Measurements in a borehole located between two vents are shown to be well adapted to detection of fluid flow variations using the vertical gradient of the electric potential and the horizontal magnetic field. The vertical electric field is about 10 mV/km up to 500 m depth where there is a lithologic reflector and about 50 mV/km below this reflector. The horizontal gradient of the magnetic field is 2 nT/km at the seafloor. Modelization with a lower fault conductivity and a larger décollement thickness has also been modeled. The vertical gradient of the horizontal magnetic field is ~5 to 15 nT/km. A variation of 3 mV and 1.5 to 3 nT at 600 m depth in a borehole could reveal a fluid flow rate variation of 20%, which is a reasonable fluid flow change based on some observations at short-scale time. Since a 1.5 to 3 nT anomaly seems easier to detect than a 3 mV anomaly, it is likely that the variation of the magnetic field would more sensitively reveal fluid flow variations. When monitoring the magnetic field at the seafloor, a change of 0.4 nT/km in the horizontal gradient could reveal a fluid flow rate variation of 20%.

1. Introduction

Accretionary prisms develop at some convergent margins from material offscraped at the deformation front. Accretionary prisms are composed of saturated sediments. As sediments deform, fluid pressure rises, and fluid is expelled both through tectonically induced consolidation and thermally induced dehydration processes. The décollement zone, essentially the plate boundary, separates the undeformed underthrust sediments from a complexly deformed accretionary prism. Fluid flow out of accretionary prisms occurs by distributed flow through intergranular permeability and by focused flow along fault zones and depends on large-scale permeability.

Elevated pore fluid pressure [*Westbrook et al.*, 1982] has long been recognized to maintain large parts of accretionary prisms near failure conditions [*von Huene and Lee*, 1982], resulting in complex interactions of strain regimes and fluid circulation. Expelled fluids from accretionary wedges have been shown to be transported from great depth within the prism [*Cloos*, 1984; *Moore et al.*, 1987; *Moore and Vrolijk*, 1992]. Changes of flow rate of expelled fluid could be related to the state of stress [*Moore*, 1989; *Vrolijk*, 1987; *Moore et al.*, 1988] and to seismic hazard by the seismic pumping mechanism [*Sibson et al.*, 1975]. Studies along the outer eastern Nankai accretionary wedge showed that the fluid circulation is mostly related to active faults and near-surface highly permeable zones [*Le Pichon et al.*, 1992].

The Nankai trench results from the subduction of the Philippine plate under Eurasia (Figure 1). The Kaiko-Nankai area has been studied through the Kaiko scientific project since 1984 [*Le Pichon et al.*, 1992]. Improvement in the detection of precursors of strong earthquakes in the Tokai area is of great importance as a magnitude 8 earthquake is expected in the eastern part of this area with an expected displacement on the fault about 4 m [*Ishibashi*, 1981]. Monitoring long-term variations of fluid flow at the toe of the east Nankai Trough has been proposed to improve the prediction of earthquakes in the region. Electrokinetic potentials on the ocean floor have been proposed to monitor long term variations of fluid flow thus giving way to a precursory electric signal [*Boulègue et al.*, 1985; *Segawa and Toh*, 1992; *Heinson and Segawa*, 1997].

In this paper a very simple analytic model is first considered, then a three-step finite element numerical calculation [*Massé and Berthier*, 1995] taking into account the convection current induced by electrokinetic phenomena and the conduction current (back current) is developed. We discuss the possibility of detecting the variations of flow rates of fluids expelled from an accretionary wedge by monitoring changes of the magnetic or electric field. In this paper we propose to model and to compare

Paper number 1999JB900102.
0148-0227/99/1999JB900102$09.00

the possibilities of measurements: vertical electric field and horizontal magnetic field measurements in borehole, horizontal electric field, and horizontal magnetic field measurements at the seafloor. In our model, hydraulic flow and electric current have been modeled to compute the magnetic and electric field induced by the coupling between the fluid flow and the electric current. The questions are as follows: (1) What are the calculated values of the electric and magnetic fields related to fluid circulation not only at the surface of the prism but also deep in the sediment? (2) What are the relative advantages of surface or borehole measurements? (3) What measurements or combination of measurements constitute the best experimental strategy to monitor fluid flow variations?

2. Electrokinetic Effect

When a fluid is flowing through porous sediments, a convection electric current is induced. The electric current density associated to this electrokinetic phenomenon is

$$J_{\text{conv}} = C_s \; \sigma_r \, \text{grad}\, P \qquad (1)$$

where grad P is the pressure gradient creating the fluid flow, σ_r is the electric conductivity of the formation, and C_s is the electrokinetic coupling coefficient (in V/Pa). The electrokinetic coupling coefficient is

$$C_s = \Delta V / \Delta P = (\varepsilon\zeta)/(\eta\, \sigma_f) \qquad (2)$$

where ζ is the zeta potential at the rock/fluid interface, and σ_f, ε, and η are the electric conductivity, the electric permittivity, and the shear viscosity of the circulating fluid, respectively. This expression is the Helmholtz-Smoluchowski equation, and it implies that the surface conductivity is small and negligible compared to the fluid conductivity σ_f [*Dukhin and Derjaguin*, 1974]. Note that the electric current is assumed to have the same path as the fluid flow in the porous medium. The electrokinetic coupling coefficient is positive or negative depending on the sign of zeta potential; it is negative for most rock. Electrokinetic phenomena are due to the existence of an electric double layer formed at the solid-liquid interface [*Stern*, 1924]. The double layer is made up of a layer of ions adsorbed on the surface of the matrix and of a diffuse mobile layer extending into the liquid phase. The zeta potential is the electric potential on the plane closest to the surface of the matrix on which fluid is in motion. In response to this convection current a conduction current or back current, governed by Ohm's law, is generated and the total electric current density J is related to the forces grad V and grad P by

$$J = J_{\text{conv}} + J_{\text{cond}} = C_s \; \sigma_r \, \text{grad}\, P - \sigma_r \, \text{grad}\, V \qquad (3)$$

where V is the electric potential [*Nourbehecht*, 1963].

3. Models

3.1. Simple Analytical Model

We have first developed a simplified analytical model to estimate the maximum electric and magnetic fields that could be induced by fluid flow. The fluid paths in accretionary prisms are commonly thought to be confined in the décollement and in the major thrust faults [*Moore*, 1989]. We have considered a simple geometry of two fault planes in which fluid is assumed to flow. These thrusts have an electrokinetic coupling coefficient C_s and an electric conductivity σ_r. The permeability inside these thrusts is assumed to be very high compared to the permeability of the sediments outside of these thrusts, so that the fluid flow mainly occurs in these thrusts. Note that this geometry of fluid paths can be seen at several space scales. We consider two extreme approaches, one where the total electric current density within the thrusts is assumed to be equal to the convection current J_{conv} and the other where the total electric current density within the thrusts is assumed to be zero.

3.1.1. Case of maximum electric current density in major thrusts. We consider first a case where the conduction current J_{cond} created in response to the convection current J_{conv} occurs mostly outside of the thrusts (Figure 2a). This configuration is possible if the electric conductivity outside of the thrusts is not very low compared to the one within the thrusts. Then the electric current density $J = J_{\text{conv}}$ inside the thrusts can produce a magnetic field

$$B_x = \mu_0 / 2J\, \Delta Z \qquad (4)$$

with ΔZ the width of the fault [*Durand*, 1953]. The magnetic field B_x induced by the fluid flow within the thrust is perpendicular to the direction of the electric current density sheet. B_x is independent of the distance to the thrust, as shown in Figure 2a. The magnetic field is uniform above and below each thrust with a discontinuity through the thrust. B_1 and B_2 are the magnetic fields induced by thrusts 1 and 2, respectively. Above and below the thrusts the magnetic fields add themselves - $(B_1{+}B_2)$ and $(B_1{+}B_2)$, respectively. Between the two thrusts the magnetic field will be lower since B_2 is subtracted from B_1. We assume here that the electric conduction current density J_{cond} outside of the thrusts induces a magnetic field that is equal to zero by symmetry. To have an idea of the order of the magnetic field that could be generated, let us calculate the electric current density J within the thrusts $J = J_{\text{conv}}$, defining the maximum total current density. Thus the magnetic field induced by this current density sheet is

$$B_x = \mu_0 / 2J_{\text{conv}}\, \Delta Z = \mu_0 / 2\; C_s \; \sigma_r \, \text{grad}\, P\, \Delta Z \qquad (4')$$

where grad P is the pressure gradient within the thrusts. If grad P $= \Delta P/\Delta Y =$ 10 MPa/km (hydrostatic pressure gradient ρg), $\sigma_r =$ 0.28 S/m and $C_s =$ -4 mV/ MPa (see section 3.2.2 for the justification of these values), the magnitude of the electric current density is $J_{\text{conv}} = 0.011$ mA/m^2. If we consider a width of fault $\Delta Z = 10$ m (for example, the décollement), $\mu_0/2 = 2\pi\, 10^{-7}$, the magnetic field is $B_x = 0.07$ nT. Above and below the two thrusts we could thus detect 0.14 nT by measuring the magnetic field inside the borehole.

Segawa and Toh [1992] computed the electric field at the ocean bottom induced by the streaming current density confined in a thrust and showed that the electric field at the ocean bottom was proportional to the electric current density. They assumed an electric convection current density $J_{\text{conv}} = 1$ mA/ m^2 and no conduction current, and computed an electric field of 0.075 mV/m at the seafloor just above the exit of the fluid flow (in P_0, for example, in Figure 2a) and of the order of 1μV/m at a distance of a few tens of meters from the entrainment of the fluid. Note that with a value of $J_{\text{conv}} = 0.01$ mA/ m^2 as we computed, the electric field at the seafloor computed by *Segawa and Toh* [1992] would be 2 orders of magnitude smaller, meaning 0.01 μV/m.

3.1.2. Case of zero electric current density in major thrusts. We consider now that the conduction current created in

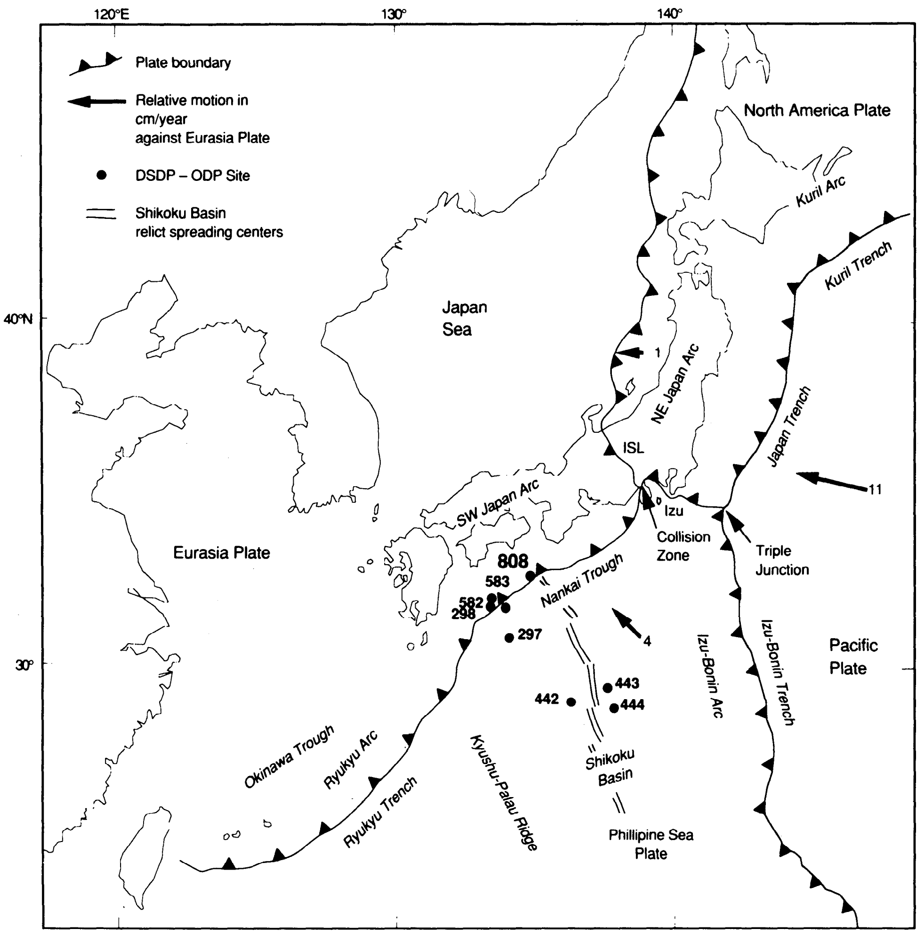

Figure 1. Location map, from Taira et al., 1991.

response to the convection current occurs mainly inside the thrusts (meaning that the electric conductivity inside the thrust is very high compared to the one in the adjacent sediments) and balances the convection current so that the total electric current density J is zero (Figure 2b). In this configuration, no magnetic field will be induced (equation (4)), and the electric field at the seafloor computed by *Segawa and Toh* [1992] would be zero, but the electric field within the thrusts will be maximum: $J = 0 = C_s\ \sigma_r$ grad $P - \sigma_r$ grad V leads to grad $V = C_s$ grad P. If we assume a hydrostatic pressure gradient in the thrust grad $P = 10$ MPa/km and an electrokinetic coupling coefficient $C_s = -4$ mV/MPa, the electric field within the thrust will be 0.04 mV/m. This electric field could be measured in different boreholes when they intercept the same thrust. For example, if the distance between P'_1 and P_1 is 300 m, we could expect to measure $V_1 - V'_1 = 12$ mV. The electric field can be monitored in the same well intercepting several thrusts. Thus we would be able to detect any difference of pressure gradients in the different thrusts considered.

The pressure gradient is a key factor needed to compute the electric field, since the electric field is directly proportional to the pressure field. We could even imagine that if there exists an overpressure in a homogeneous formation (no thrust), then an electric field will be induced. If we consider now that the pressure gradient along the thrust is closer to lithostatic [*Moore*, 1989] $\Delta P/\Delta Y = 30$ MPA/ km, J_{conv} is therefore 3 times greater than the calculation considered in the first case and $B_x = 0.21$ nT. Above and below the thrusts we could thus detect 0.42 nT. In the second case the electric field within the thrusts will be 0.12 mV/m. The electric current density is a key factor for computing the magnetic field since the magnetic field is directly proportional to this current density.

Since the real configuration will be included between the two extreme cases and the two pressure gradients (hydrostatic and lithostatic), we show here that the fluid circulation within thrusts could induce a maximum horizontal magnetic field of the order of 0.4 nT and a maximum electric field along the thrust of the order of 0.12 mV/m. We now develop a more realistic model which takes into account the coupled system of convection and conduction currents.

3.2. Numerical Model

This model proceeds in three steps: first, the hydraulic flow circulation is computed using Darcy's law; second, the streaming potential and current density are computed using Helmholtz-Smoluchowski's law and the pressure gradient from the previous hydraulic step;and third, the magnetic field is obtained from the Biot-Savart law and the electric current densities are obtained from the previous electrokinetic step. Our approach is very different from that of *Heinson and Segawa* [1997] since modeling the porosity reduction within the prism, they showed that décollement permeability has to be very high, and they computed the seafloor electric potential.

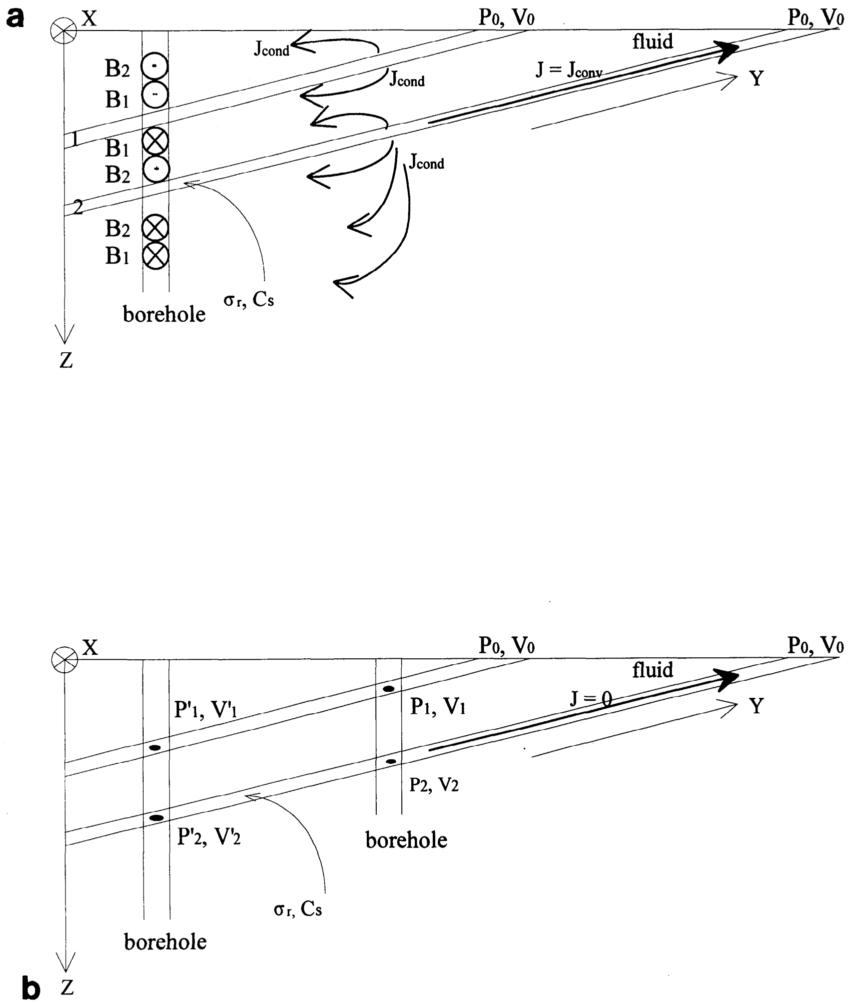

Figure 2. Geometry of the thrusts and borehole considered for the analytic model. *P* is the pressure and *V* is the electric potential. *B* is the magnetic field induced by fluid flow and is perpendicular to the figure. J_{cond} is the conduction current density. The total current density within the thrust is assumed (a) to be the convection density J_{conv} or (b) to be zero.

3.2.1. Geometry of the model. Hydraulic flow and electric current are modeled in a system of thrust faults connecting the décollement zone to the seafloor. The geometry of faults has been chosen from a seismic reflection study in the Nankai region seafloor from *Moore et al.* [1990] (Figure 3a). The subhorizontal interpreted reflector is a sedimentary horizon that has been disrupted by the thrust faulting. The thrust faults are spaced at 2 km. In the model the thickness of the ocean sediment is 1000 m above the décollement which is at the bottom, and the ocean above has a depth of 1000 m. The décollement is modeled as 50 m wide, and the faults are modeled as 10 m wide; the total lateral dimension investigated by the model is 48 km. The model is two-dimensional Cartesian and is shown in Figure 3b.

3.2.2. Physical parameters. Our model of fluid flow within an accretionary prism uses Darcy's law with matrix and faults being assigned different permeabilities. We consider different parts in the Nankai accretionary prism with different physical properties: the décollement and faults which are permeable and where most of the fluid flow takes place; the sediments which are less permeable and more conductive. The sediments above the near-horizontal reflector, called reflector A, are bedded sand, silt turbidites, and hemipelagic mud, whereas the sediments below the near-horizontal reflector are ash/tuff and hemipelagic mud [*Winkler and Stewart*, 1991]. Permeability data from accretionary prisms are limited to measurements from small samples and large scale inferences from their matrix or intergranular permeability range from 10^{-20} m^2 to 10^{-13} m^2 [*Moore and Vrolijk*, 1992]. Permeability of sediments above the reflector is about $2\text{x}10^{-15}$ m^2, and permeability of sediments below the reflector is about $5\text{x}10^{-17}$ m^2 [*Taylor and Fisher*, 1993]. The décollement zone is maintained by high fluid pressure [*Westbrook et al.*, 1982] and acts as a major conduit for fluid expulsion [*Cloos*, 1984; *Moore et al.*, 1987], and high fracture permeability is assumed to allow flow along the décollement [*Moore*, 1989]. Focused fluid flow is 3 to 5 orders of magnitude larger than distributed flow, probably representing the mean difference in permeability along these respective expulsion paths [*Screaton et al.*, 1990; *Henry and Le Pichon*, 1991; *Moore and Vrolijk*, 1992]. At the Barbados accretionary complex, observations of heat flow suggested high permeability (10^{-12} m^2) within the décollement zone [*Fisher and Hounslow*, 1990]. Moreover, *Heinson and Segawa* [1997] showed that permeability of the décollement must be ~4 orders of magnitude bigger than the permeability within the adjacent sediments to

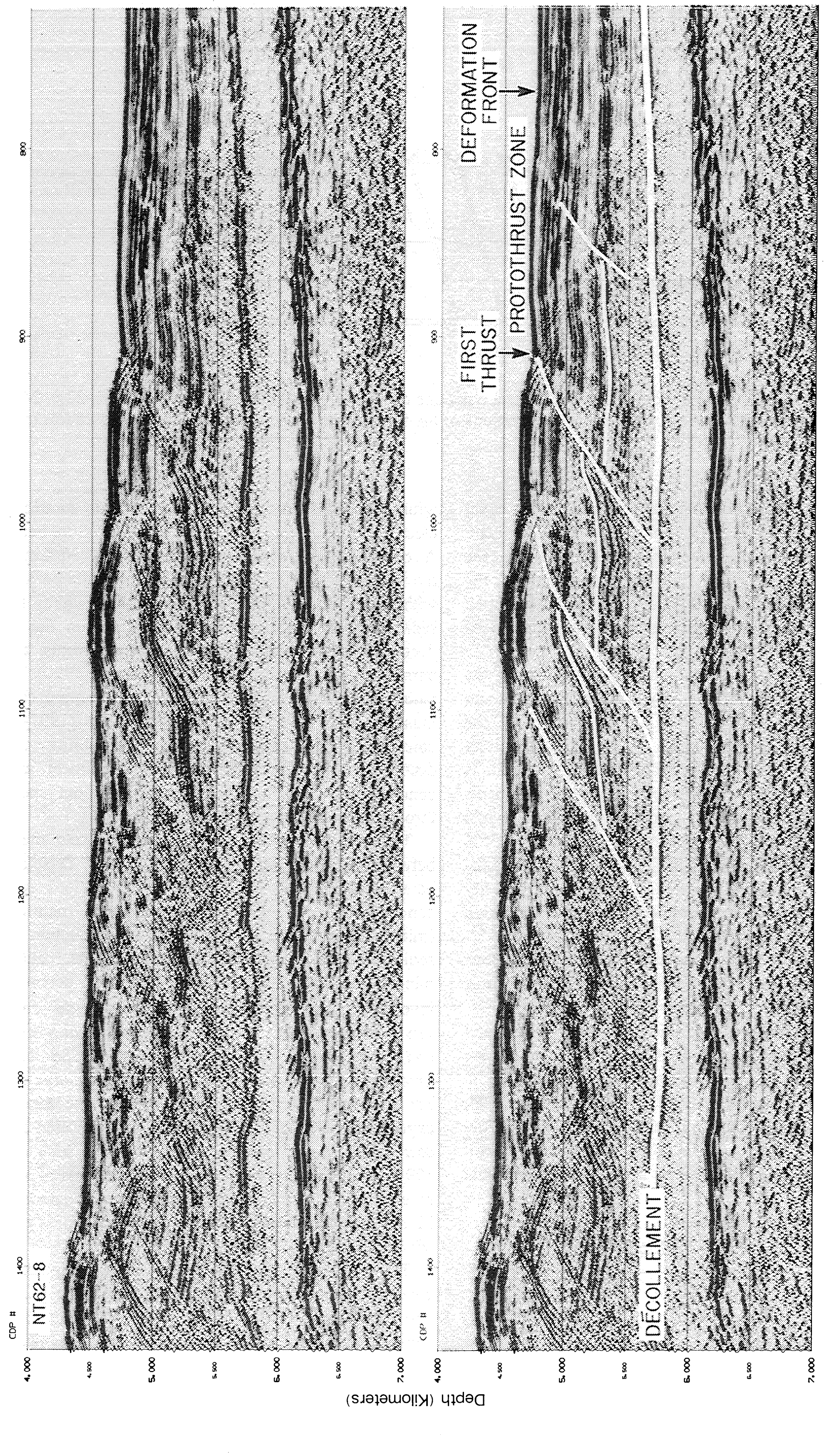

Figure 3a. Seismic profile on Nankai prism from *Moore et al.* [1990].

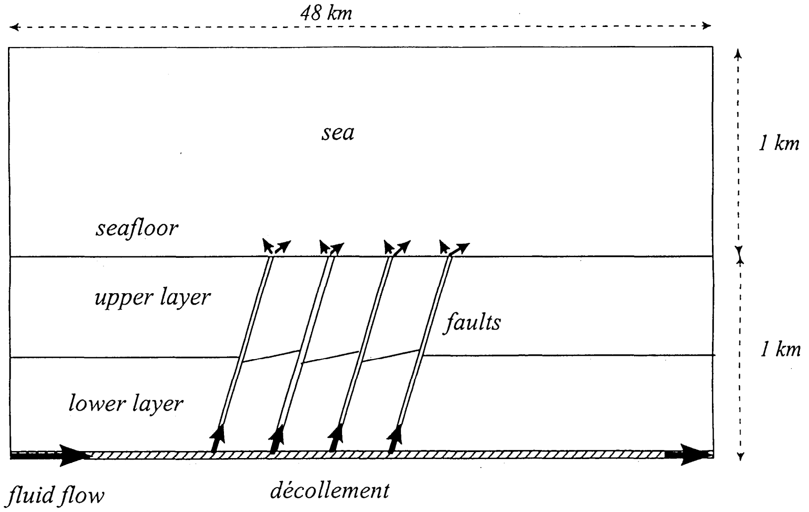

Figure 3b. Scheme of the model geometry. Lateral positions of the faults in the décollement are 20.1, 22.1, 24.1, and 26.1 km from the fluid source, and lateral positions of the vents at the seafloor are 22, 24, 26, and 28 km from the fluid source.

produce observed fluid flow. Permeability has been chosen equal to 10^{-13} m^2 in faults and 3.5×10^{-13} m^2 in the décollement. Therefore the difference in permeabilities between the décollement and the sediments is ~2 orders of magnitude for the sediments above reflector A and ~4 orders of magnitude for the sediments below reflector A. Permeabilities are assumed to be isotropic.

Geometry of the electric current path is governed by the contrast between the electric conductivity in the décollement and in the thrusts and the electric conductivity in the rest of the sediments. Formation factor F, which is the rock resistivity divided by the fluid resistivity, is therefore different in the faults and in the décollement and in the adjacent sediments. Sediments above reflector A have an average porosity Φ of 45%, while sediments below reflector A have an average porosity of 35% [*Hyndman et al.*, 1993; *Moran et al.*, 1993]. Porosity in the décollement zone is ~25% [*Hyndman et al.*, 1993], and porosity in the thrust faults has also been chosen equal to 25%. Formation factor F has been deduced from the equation $F=(3.8/\Phi)^{1.14}-4.755$ [*Taira et al.*, 1990] and is equal to 6.6 in sediments above reflector A and is equal to 10 below this reflector. In the thrust faults and in the décollement, formation factor is equal to 17.

The electric conductivity of the fluid σ_f is that of seawater inside the sediments above reflector A: σ_f = 5.3 S/m. As the chlorinity concentration has been shown to decrease with depth up to 20% at the décollement depth [*Gieskes et al.*, 1993; *Kastner et al.*, 1993], an average decrease of 10% in the fluid conductivity has been taken into account below the reflector A: σ_f = 4.8 S/m. A decrease of 20% has been taken into account within the décollement: σ_f = 4.2 S/m. Within the décollement the electrical conductivity is $\sigma_r = \sigma_f/F$ = 0.25 S/m, below reflector A, σ_r = 0.48 S/m, above reflector A, σ_r = 0.80 S/m, and within the thrusts, σ_r = 0.31 S/m. Note that since the porosity is lower within the thrusts and décollement than within the adjacent sediments, the conductivity is lower within the thrusts and décollement than within the adjacent sediments, although the permeability is larger [*Langseth and Moore*, 1990]. The physical parameters are summarized in Table 1. Our approach is different than the one from *Heinson and Segawa* [1997] since they considered only a change in permeability through the décollement compared to the prism sediment and assumed conductivity as a function of depth without special change through the décollement.

Table 1. Physical Parameters for the Model

	k, m^2	Porosity, %	F	σ_f, S/m
Sea				5.3
Upper layer	10^{-15}	45	6.6	5.3
Lower layer	5×10^{-17}	35	10	4.8
Décollement	3.5×10^{-13}	25	17 or 6	4.2
Fault	10^{-13}	25	17 or 6	5.3

The zeta potential (equation (2)) reflects the interaction between the fluid and the matrix, and it depends on many parameters such as the nature of fluids (ions concentration, conductivity, pH, temperature) and the nature of rocks (mineralogy, surface conductivity). In subduction zones, most sediments are terrigenous clastic deposits containing clay minerals such as smectite or illite. Streaming potential is usually investigated in quartz-water systems [*Ishido and Mizutani*, 1981], on sands and sandstones [*Sharma et al.*, 1987; *Jouniaux and Pozzi*, 1995a, 1997; *Lorne et al.*, 1998a, 1998b] or on limestones [*Jouniaux and Pozzi*, 1995b; *Jouniaux et al.*, 1996]. For a quartz system with NaCl solution the zeta potential is expected to be equal to -25 mV for a concentration of 10^{-1} mol/L corresponding to a conductivity of 1 S/m [*Pride and Morgan*, 1991; *Revil and Glover*, 1997]. Measurements of zeta potential by electrophoresis on kaolinite showed a zeta potential of about -32 mV with a solution of NaCl 10^{-1} mol/L for a pH 5.5 to 7.5 [*Poirier and Cases*, 1985].

The effect of temperature on the zeta potential is still controversial as only few studies are available [*Somasundaran and Kulkarni*, 1973; *Ishido and Mizutani*, 1981]; as a consequence, the zeta potential has been considered to be constant in our model without taking into account the effect of a thermal gradient. Moreover, the effect of methane detected in variable concentrations in fluids [*Moore and Vrolijk*, 1992] is not known on the zeta potential. In our model the zeta potential has therefore been chosen as constant and equal to -30 mV. This value leads to an electrokinetic coupling coefficient (equation (2)) $C_s = -4$ mV/MPa (with $\varepsilon= 7\text{x}10^{-10}$ F/m, $\eta = 10^{-3}$ Pa s, and $\sigma_f = 4.8$ S/m).

3.2.3. Three-step modeling. Electromagnetic models of electrokinetic phenomena require coupled modeling of fluid flow, electric (streaming) potential and magnetic field. The coupling of the potential gradient with the pressure gradient is taken into account. The electroosmotic coefficient term is negligible [*Fitterman*, 1978], leading to Darcy's law for the fluid flow. Such an approach has been implemented in the FLUX-EXPERT generation system "open codes" where an equation or a system of differential equations can be introduced by the user [*Massé and Berthier*, 1995, 1996] using the following options: second-order curvilinear finite elements, second-order curvilinear boundary elements, Gauss-Legendre approximations for integral calculations, Lagrangian second-order polynomials for test and interpolation functions, and incomplete Cholesky conjugate gradient method for solving linear systems.

3.2.3.1. Hydraulic modeling: The fluid is presumed to be injected into the décollement at the left of the model, and it flows within the décollement, the thrusts, and the sediments. The flow rate of water entering the décollement fault at its left end and exiting at its right end is not exactly known and is used here as a source to create fluid flow inside the thrusts. It is assumed that fluid velocities entering and exiting the décollement are 50 and 25 m/yr respectively, because these values will be shown to produce reasonable Darcian fluid flow velocities at the fault outlets on the seafloor. The model considered here is a steady state model.

Inside porous media the flow of water is sufficiently slow so that it is ruled by Darcy's law where the permeability coefficient is a tensor

$$u = -\frac{[k]}{\eta}\text{grad}\, P \tag{5}$$

where u is the Darcy fluid velocity, P is the pressure, and $[k]$ is the permeability tensor. The pressure gradient inducing the flow is either steady or slowly oscillating at a low frequency so that inertial effects are small compared to viscous ones. Taking into account the conservation of the flow rate, (5) yields

$$\text{div}(-\frac{[k]}{\eta}\text{grad}\, P) = 0 \tag{6}$$

The pressure computed here is in reality the excess pore pressure, meaning the pressure difference between total pressure and hydrostatic pressure.

To solve for the pressure, boundary conditions are needed either on the pressure itself or on the flux $F = -(k/\eta)$ grad $P.n$, where n is the vector normal to the fluid inlet. An initial state must be given for the pressure at the initial time step. At the boundaries of media of different properties, the mass flow is conserved, i.e.,

$$\rho_1\frac{[k_1]}{\eta}\text{grad}\, P_{n1} = \rho_2\frac{[k_2]}{\eta}\text{grad}\, P_{n2} \tag{7}$$

Boundary conditions for the excess pressure are zero at the two lateral ends inside the sea domain. There is no fluid flow perpendicular to the lateral sides in the sediments ($dP/dn = 0$) and no flow perpendicular to the bottom of the décollement ($dP/dn' = 0$, n' being the normal to the bottom). The sea is modeled as a medium of high permeability ($k = 5\text{x}10^{-9}$ m^2) which was determined only by consideration of convergence of the numerical system and not on a physical ground, since the fluid velocities inside the sea do not produce any electrokinetic phenomena. The dynamic viscosity of water is presumed constant in the whole computational domain and equal to 10^3 Pa s. Once the fluid pressure field has been calculated the Darcian fluid velocities are obtained from (5).

3.2.3.2. Streaming potential modeling: The frequency of the pressure oscillations being very low, the electromagnetic field conforms to the Maxwell equations in their static approximations (<100 Hz). The electric field being irrotational, it is given by $E = -$ grad V, where V is the electric scalar potential. Ohm's law states that the current density J is the sum of a conduction current and a convection current $J = \sigma_f E + \rho_e u$, where ρ_e is the electric charge. Then using (7) and the Debye approximation for the double layer [*Overbeek*, 1952], one obtains the Helmholtz-Smoluchowski expression for the total current density J:

$$J=-[G]\sigma_f\,\text{grad}\, V + [G]\frac{\varepsilon\zeta}{\eta}\text{grad}\, P \tag{8}$$

where[G] is a geometrical tensor linked to the global conductivity σ_r and fluid conductivity σ_f by the relation σ_r=[G] σ_f (G is the inverse of the formation factor F). In our application the pressure gradient is the source term, and the streaming potential V is the response to this source. Using the current conservation equation div $J = 0$, (8) can be written in the form

$$\text{div}([G]\sigma_f\,\text{grad}\, V) = \text{div}([G]\frac{\varepsilon\zeta}{\eta}\text{grad}\, P) \tag{9}$$

The coefficients G, ζ; σ_f, η, and ε have been kept inside the divergence because they are allowed to change spatially. At a boundary between two porous media the following relation holds:

$$-[G_1]\sigma_f\,\text{grad}\, V_{n1} + [G_1]\frac{\varepsilon\zeta}{\eta}\text{grad}\, P_{n1} - [G_2]\sigma_f\,\text{grad}\, V_{n2}$$

$$+ [G_2]\frac{\varepsilon\zeta}{\eta}\text{grad}\, P_{n2} = 0$$

The electrokinetic step has been divided into two consecutive substeps:

First, the streaming potential V is solved in (9) by considering only the part of the domain below the seafloor. The boundary conditions for V are then V=0 at the seafloor (this hypothesis will be shown to be valid at the next substep). On the lateral sides of the sediments the electric current is vertical ($dV/dn = 0$), and at the bottom of the décollement the current is horizontal ($dV/dn' = 0$). The potential is assumed uniform within the thickness of the décollement where the flow enters and exits the domain.

Second, the electric potential is computed in the sea using the electric current densities computed on the seafloor in the previous step and solving the equation div(σ_f grad V)=0. The potential is considered equal to zero at the two lateral ends of the sea region. Such an approach ensures the conservation of the electric current density J at the seafloor, but a very slight discontinuity is observed in the potential V. However, the discontinuity is negligible since the potential in the sea is about 1000 times less than the potential under the seafloor. If the potential computed at the seafloor is now taken as the limit boundary in order to compute the potential in the sediments, the results are not different.

3.2.3.3. Magnetic field modeling: The Maxwell laws in a quasi-static expression are curl $H = J$ and div $B = 0$, where H is the magnetic field (A/m) and B is the magnetic induction (in tesla). We can define a potential vector A such as B = curl A and choose the Coulomb gauge div $A = 0$. Recalling that $B = \mu H$, where μ is the magnetic permeability, the potential vector satisfies the relations div $A = 0$, and the Biot-Savart law

$$\mathrm{curl}\left(\frac{1}{\mu}\mathrm{curl}\,A\right) = -[G]\sigma_f\,\mathrm{grad}\,V + [G]\frac{\varepsilon\zeta}{\eta}\mathrm{grad}\,P \qquad (10)$$

The current densities J have been computed in the previous step for the whole computational domain. The natural boundary conditions between two different media are $(1/\mu_1)\mathrm{curl}\,A_\wedge n_1 + (1/\mu_2)\mathrm{curl}\,A_\wedge n_2 = 0$ and $A = 0$ at infinity.

The vector potential A is obtained by solving (10) with the following boundary conditions: $A_x = A_y = 0$ at the sea surface and at the two lateral ends of the computational domain. $A_x = 0$ at the lower boundary (below the décollement). The first boundary condition is valid only if the electric currents circulating outside the computational domain do not contribute to the magnetic field inside the domain. It is clear that such a hypothesis is not valid inside the domain close to the boundaries, but as we chose a large computational domain and as the level of the magnetic field is small (as will be shown in section 4.3), this hypothesis seems reasonable for the calculation in a restricted domain around the faulted zone. The second boundary condition is simply the consequence of no electric currents circulating downward from the décollement. The value of the magnetic permeability is constant over the whole domain and equal to that of a vacuum. As the calculation is two-dimensional, there exists only one component (normal to the domain) of the magnetic field.

4. Results

The results have been plotted in Plates 1-6 and Figures 4-6.

4.1. Fluid Circulation

The excess fluid pressure in the accretionary prism has been plotted over the whole computational domain in Plate 1a and in the fault system in Plate 1b. The pressure source is localized on the left side of the décollement. The numerical results show an excess pressure gradient inside the thrust faults of ~10 MPa/km. Fluid pressures in accretionary prisms are commonly high but range from hydrostatic to lithostatic [*Moore*, 1989]. At shallow depth the pressure gradient is thought to be almost hydrostatic (10 MPa/km) [*Moore*, 1989], meaning an excess pressure gradient near zero. Temperature measurements below clam colonies on the Nankai accretionary prism showed an excess pore pressure gradient of 10 Pa/m over 1-2 m depth [*Henry et al.*, 1992]. At depth the pressure gradient is closer to the lithostatic gradient (about 30 MPa/km) [*Moore*, 1989], meaning an excess pore pressure gradient of ~20 MPa/km. The *Hubbert and Rubey* [1959] dimensionless parameter λ, defined as the fluid pressure P_f divided by the vertical stress σ_z exerted by the lithostatic overburden $\lambda = P_f / \sigma_z$, allows us to quantify the overpressure. The graph of pressure from *Moore* [1989, Figure 10] shows λ of ~ 0.75 near the décollement and ~0.6 at a depth half that of the décollement (let us say 500 m depth in our case). *Westbrook et al.* [1982] reported that the low stresses required on the décollement on the lesser Antilles subduction zone are made possible by pore water within the décollement at pressure close to that of the lithostatic load (λ = 0.81 to 0.97). Water pressures approximately equivalent to the lithostatic load were inferred close to the décollement on the Barbados ridge complex [*Westbrook and Smith*, 1983]. Fluid pressures at near lithostatic values are also invoked to develop laterally extensive fractureways filled with dewatering fluids derived from deeper underthrust water-rich sediments [*Cloos*, 1984]. The pore fluid pressure ratio of *Hubbert and Rubey* [1959] has been generalized to the case of a submarine wedge [*Davis et al.*, 1983]: $\lambda = (P_f - \rho_w gD)/(\sigma_z - \rho_w gD)$, where $\rho_w gD$ is the hydrostatic pressure at the seafloor (10 MPa in our case since the seafloor is at 1 km depth). This parameter is equal to 1 when fluid pressure is equal to the lithostatic pressure and equal to ~0.4 when the fluid pressure is equal to the hydrostatic pressure. This coefficient has been predicted for various accretionary wedges from the pressure-dependent Coulomb wedge theory and has been shown to be ~0.7-0.9 [*Davis et al.*, 1983]. Recent study of the décollement propagation as a subhorizontal tension fracture requires also high pore pressure within the décollement [*Morgan and Karig*, 1995]. It seems therefore that λ of ~0.7-0.9 is considered as a reasonable value within the décollement. The value of λ deduced from our model is plotted in Figure 4. The λ values range from 0.65 to 1 within the décollement in the faults domain. Note that it is not the scope of this paper to deal with hydrofracture and that the realistic model is represented by the faults domain, not near the boundaries of the whole computational domain.

The distribution of the fluid velocity in the second fault is shown in Plate 2 in which the velocity vector has been plotted. The fluid velocity is of the order of 1 m/yr at the output of the thrust. Note that the upward Darcian fluid flow velocity in the Nankai region has been deduced from temperature measurements and has been found to be of the order of 10 m/yr at some fluid venting at the seafloor and of the order of 100 m/yr above the most active faults [*Le Pichon et al.*, 1992; *Henry et al.*, 1992]. The threshold of detection of the Darcian velocities deduced from these temperature measurements is 10 m/yr [*Henry et al.*, 1992], so that our computed values of the order of 1 m/yr seem to be reasonable values.

4.2. Streaming Potential

The electric potential repartition has been plotted in Plate 3a for the whole computational domain and for an enlargement of the fault zone in Plate 3b. The electric potential at the seafloor is constant and is < 1 mV in absolute value. As a consequence, the horizontal electric field is zero at the seafloor.

The electric potential increases with depth (in absolute value) up to > 45 mV near the décollement at the second fault. The electric potential has been plotted versus depth in Figure 5, just above the the second vent (squares) (lateral position 24,000 m in Plate 3b), and between the first and second vent (triangles) (lateral position 23,000 m in Plate 3b). The potential increases with depth, and the result of the least squares regression for the first 500 m depth shows that the potential is given by $V(\mathrm{mV}) = -0.9-0.005\mathrm{x}D_{\mathrm{epth}}(\mathrm{m})$ and $V(\mathrm{mV}) = 1.3-0.026\mathrm{xD}_{\mathrm{epth}}(\mathrm{m})$ for profiles above the vent and between the vents, respectively. Therefore the rate of potential increase with depth is larger when along a profile between two vents. Below reflector A at ~500 m depth, the rate of potential increase is larger, because the medium is less conductive (Figure 3 and Table 1), and the vertical electric field is between 90 and 100 mV/km (Figure 5). Note that far from the

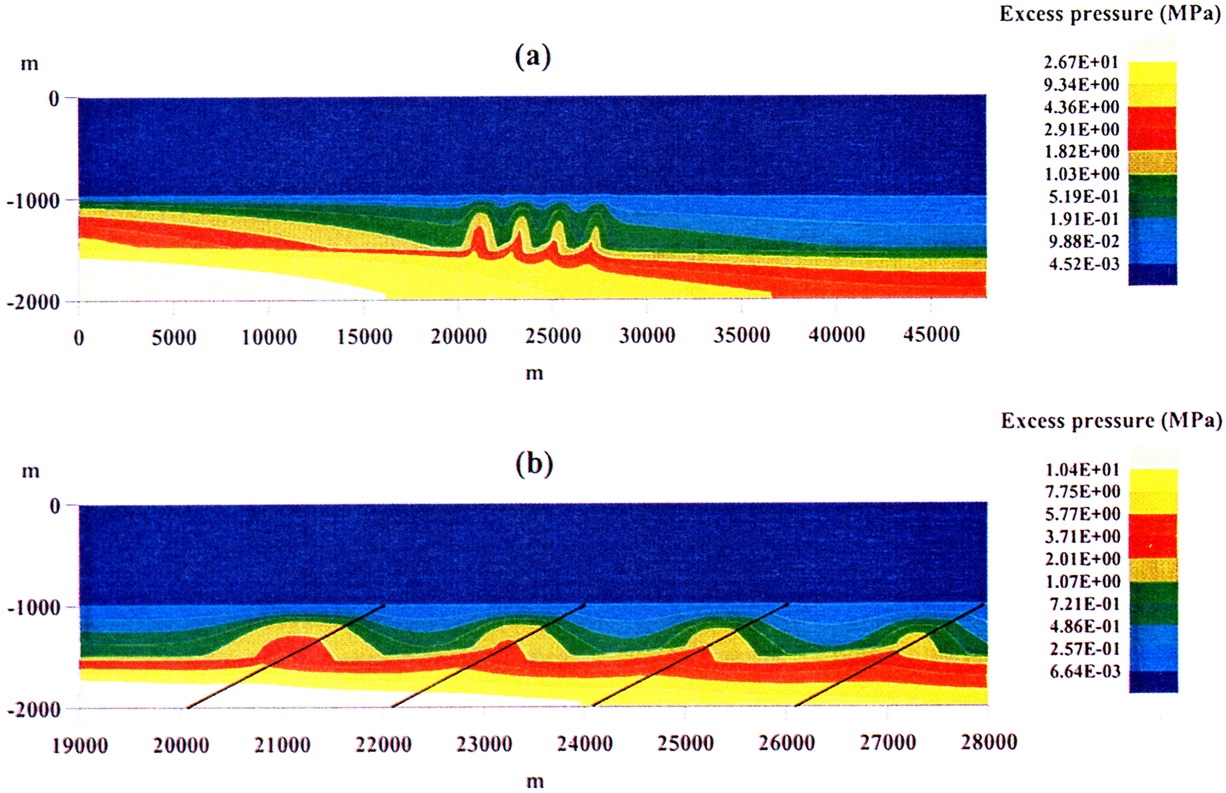

Plate 1. Pressure distribution (a) in the whole computational domain (48 km large) and (b) in the four thrusts domain (9 km large). The seafloor level is at -1000 m.

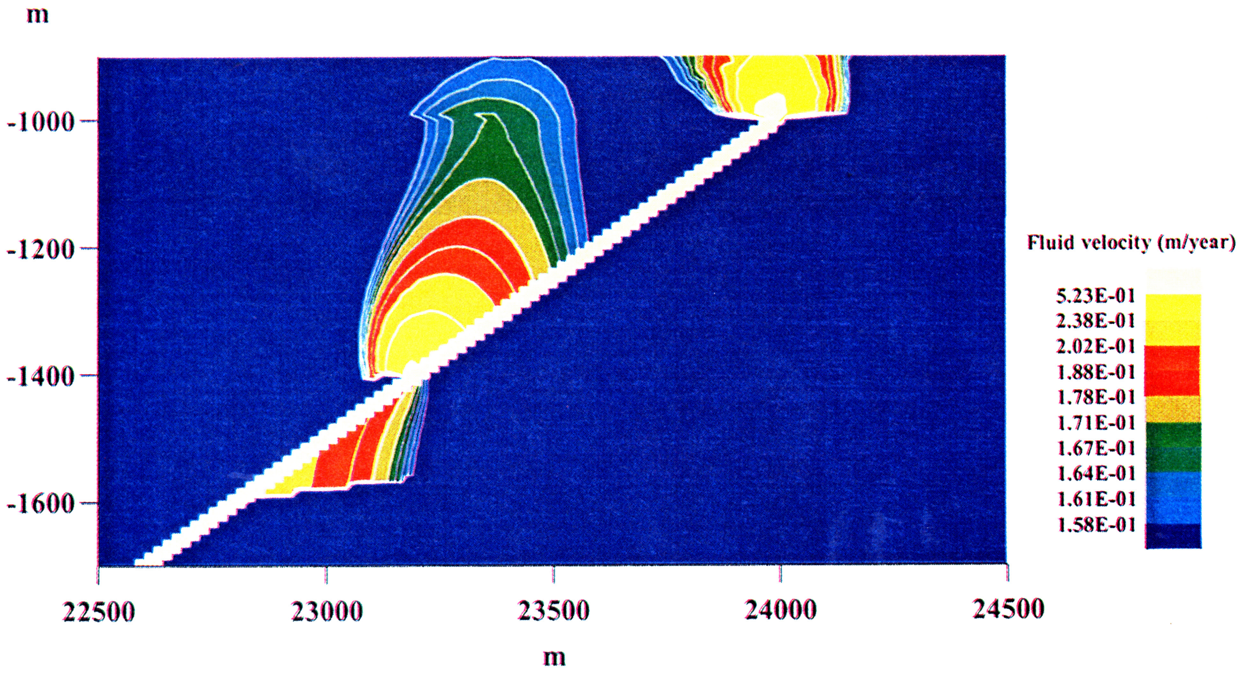

Plate 2. Distribution of fluid velocity within the second thrust (lateral location from 22.5 km to 24.5 km). The seafloor level is at -1000 m.

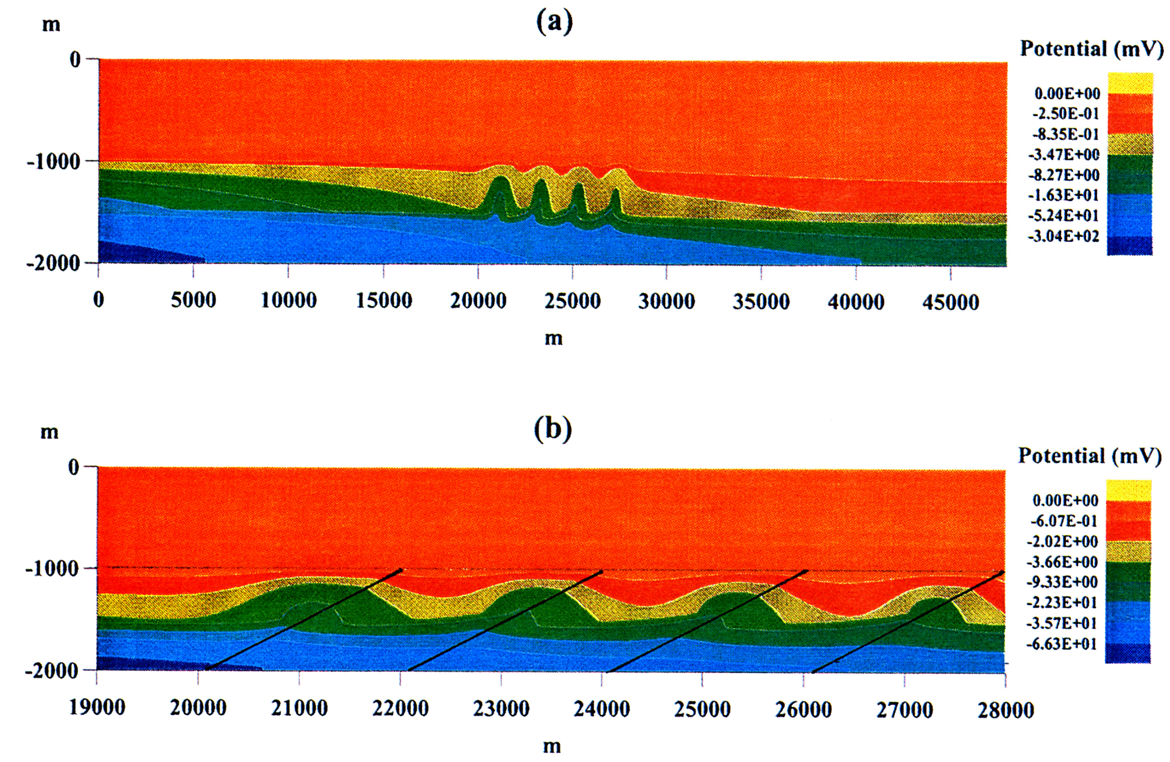

Plate 3. Streaming potential distribution (a) in the whole computational domain (48 km large) and (b) in the four thrusts domain (9 km large). The seafloor level is at -1000 m.

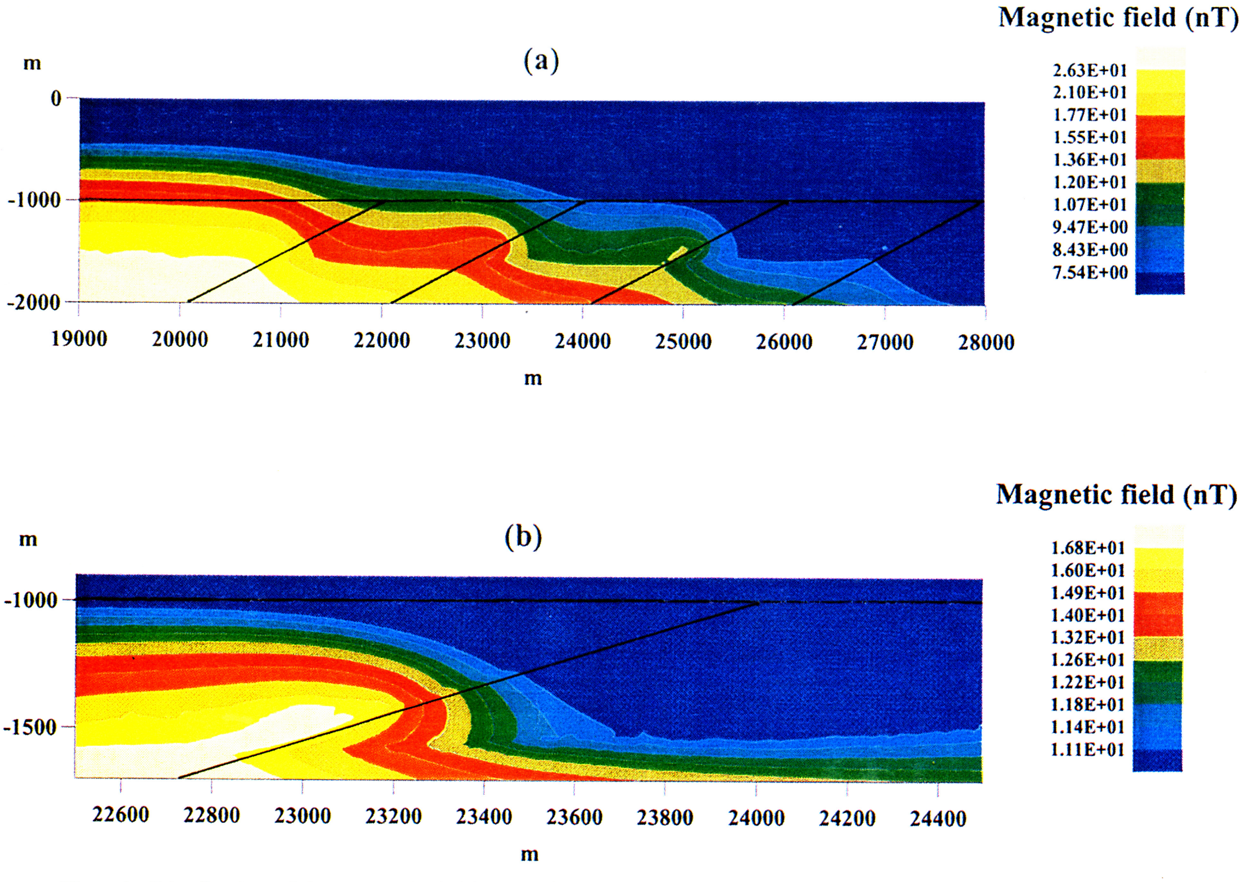

Plate 4. Distribution of the magnetic field (a) in the four thrusts domain and (b) in an enlargement in the vicinity of the second thrust. Seafloor level is at -1000 m.

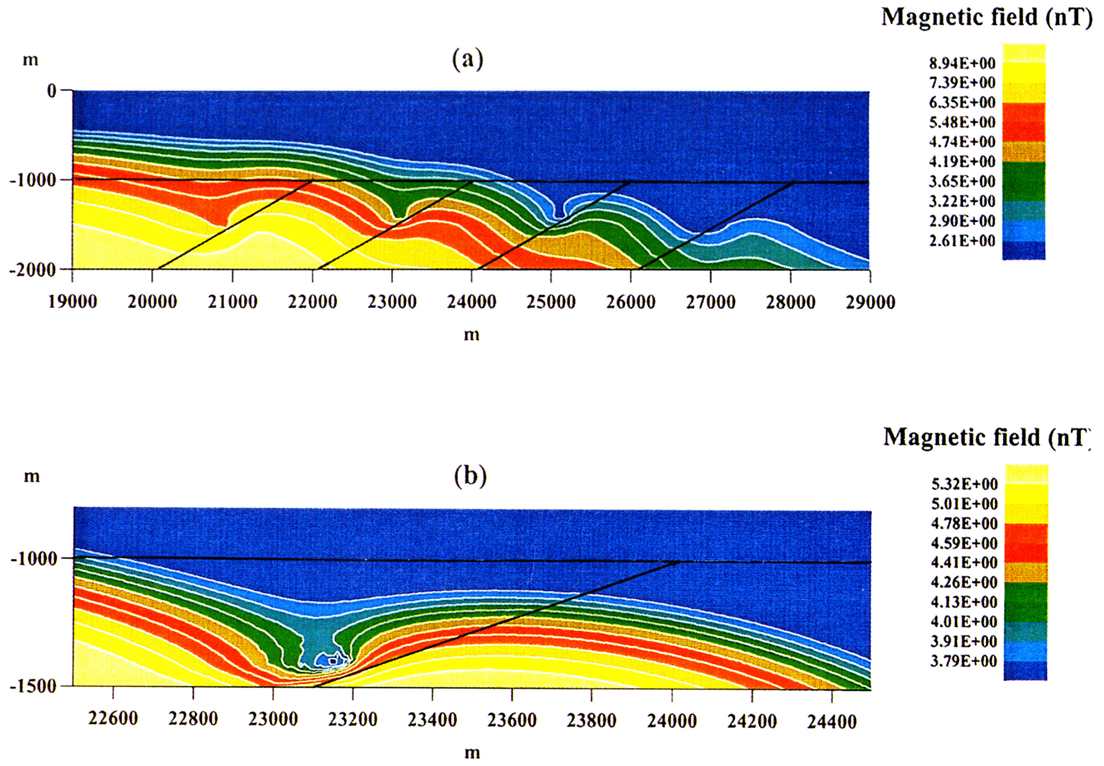

Plate 5. Distribution of the magnetic field in the case where the rock conductivity within the faults and in the décollement (décollement width is 50 m) is larger than in the surrounding sediments, (a) in the four thrusts domain and (b) in an enlargement in the vicinity of the second thrust. Seafloor level is at -1000 m.

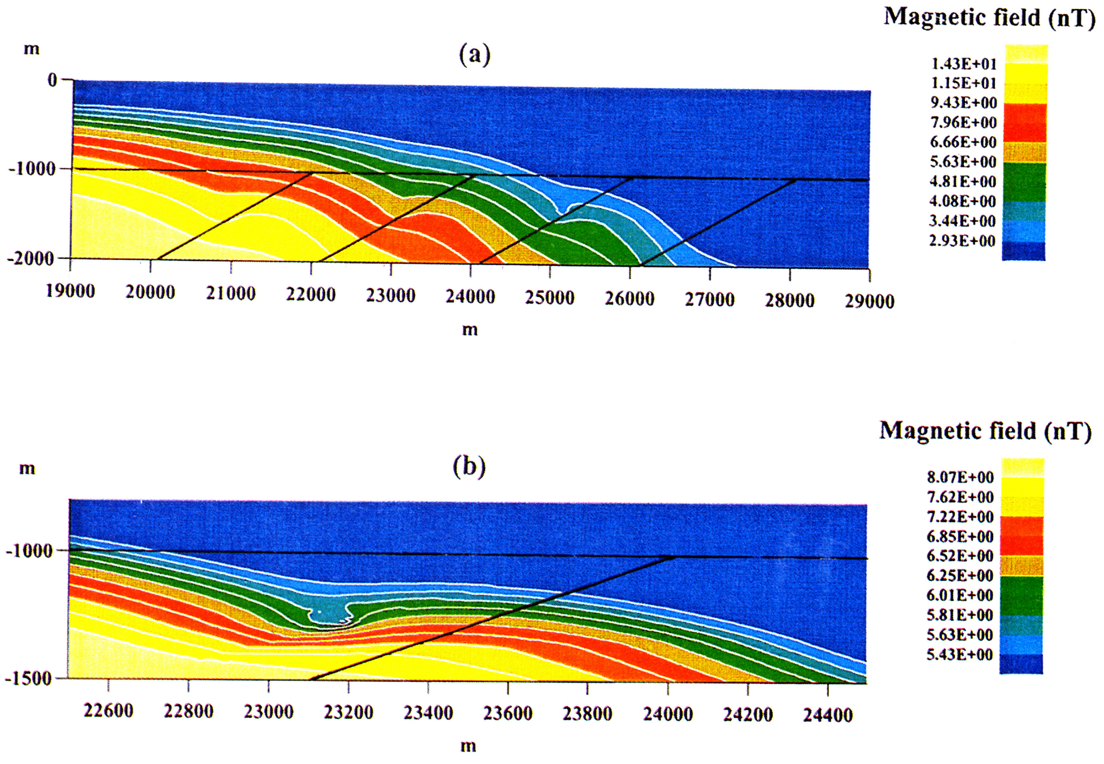

Plate 6. Distribution of the magnetic field when the décollement width is 20 m and in the case where the rock conductivity within the faults and in the décollement is larger than in the surrounding sediments, (a) in the four thrusts domain and (b) in an enlargement in the vicinity of the second thrust. Seafloor level is at -1000 m.

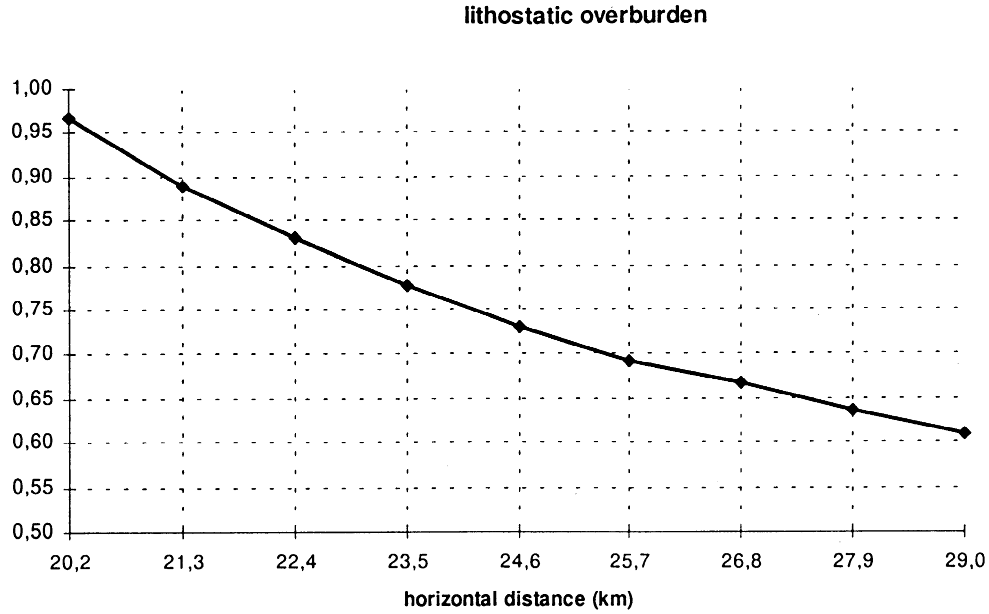

Figure 4. Values of the coefficient λ within the décollement in the thrusts domain for lateral position from 20.2 to 29 km.

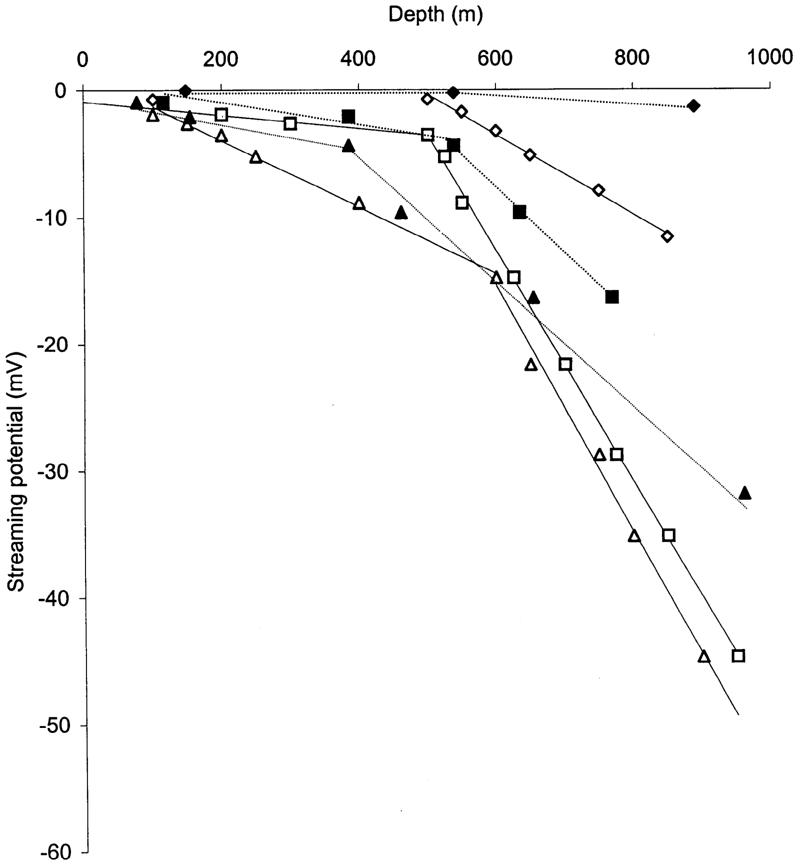

Figure 5. Streaming potential versus depth (below the seafloor) for lateral positions 24,000 m (squares) and 23,000 m (triangles), which are above the second vent and between the first and second vent, and for lateral position 45 km (diamonds) which is far from the source. Open symbols are for the case when F=17 in the décollement and in the faults and when the décollement width is 50 m. Solid symbols are for the case when F=6 in the décollement and in the faults and when the décollement width is 20 m.

fluid source, at 45 km, for example (Plate 3a) the vertical electric field is zero up to reflector A (Figure 5, diamonds) and of ~31 mV/km below this reflector A.

Because we take into account the conduction current in our model, we find a small current density of the order of 0.5-2x10^{-5} A/m^2, since the back current is opposite to the convection current. The faults clearly drain the electric current through the domain from the décollement to the sea.

4.3. Magnetic Field

The current density computed by our model is localized in the vertical plane, as the calculation is two-dimensional, and the magnetic field due to this current density will have a component perpendicular to this vertical plane. The horizontal magnetic field anomaly is shown in Plate 4a for the fault domain and in Plate 4b for the second fault.

The horizontal variation of the magnetic field at the seafloor is shown in Figure 6. The horizontal gradient of the magnetic field is ~2 nT/km at the seafloor in the faults domain (Figure 6). The vertical variation of the magnetic field above the second vent (lateral distance 24,000 m in Plate 4a) and between the first and second vent (lateral distance 23,000 m in Plate 4a) is shown Figure 6 (squares and triangles, respectively). The magnetic field increases with depth and for the first 400 m depth the magnetic field is given by B(nT) = 7.6+0.0077xD_{epth}(m) and B(nT) = 9.3+0.0149xD_{epth}(m) (open symbols) for profiles above the vent (squares) and between the vents (triangles), respectively. Therefore the rate of magnetic field increase with depth is larger between two vents. Then the rate of increase of the magnetic field is decreased around the 500 m depth where reflector A is located. The magnetic field is even constant between 400 and 700 m depth for the profile made between two vents since the isovalues of the field are distorted (Plate 4). Then the vertical gradient of the magnetic field is 11 nT/km at depth (Figure 6, open symbols). Note that far from the fluid source the vertical gradient of the magnetic field is zero (Plate 4a).

The model has been calculated with the physical parameters discussed above. In this paragraph we analyze the stability of the streaming potential against the possible variation of these parameters. As shown by Plates 1 and 3 the streaming potential reflects directly the excess pressure within the prism. If the pressure gradient is multiplied, for instance, by 2, the same increase is expected in the streaming potential (see equation (9)). If the fluid conductivity is decreased by 20% as discussed above, then the streaming potential is expected to be increased by 20% (see equation (9)). The streaming potential is proportional to the zeta potential within the electric double layer. The zeta potential is deduced from available measurements on a quartz-water system and kaolinite. Better constrained values can be expected from further experimental work [than *Jouniaux et al.*, 1994] on proper rocks from an accretionary prism.

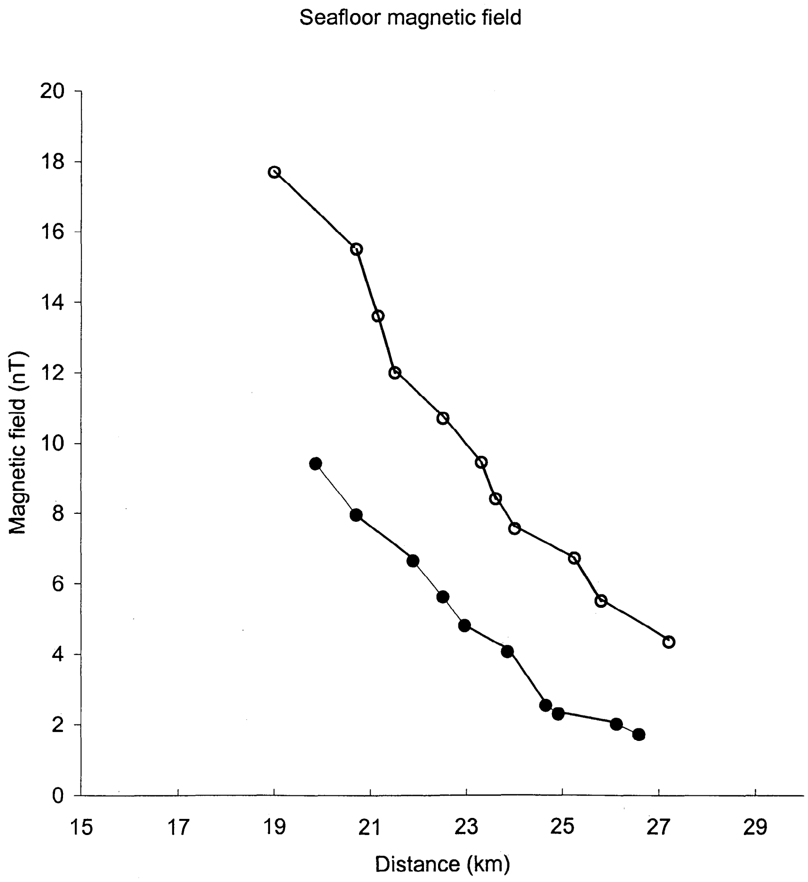

Figure 6a. Magnetic field at the seafloor for lateral positions from 19 to 27 km. Open symbols are for the case when F=17 in the décollement and in the faults and when the décollement width is 50 m. Solid symbols are for the case when F=6 in the décollement and in the faults and when the décollement width is 20 m.

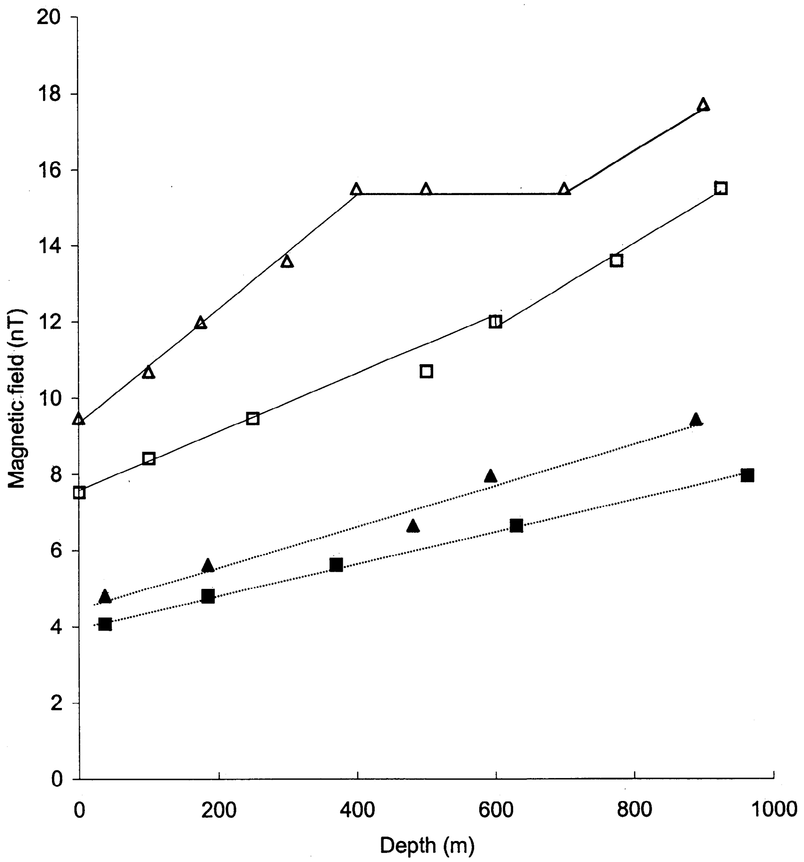

Figure 6b. Magnetic field versus depth (below the seafloor) for lateral positions 24,000 m (squares) and 23,000 m (triangles), which are above the second vent and between the first and second vent. Open symbols are for the case when F=17 in the décollement and in the faults and when the décollement width is 50 m. Solid symbols are for the case when F=6 in the décollement and in the faults and when the décollement width is 20 m.

4.4. Effect of Décollement Width and Conductivity

Since the permeability is higher in the faults and in the décollement because of fracture porosity, it might be possible that the conductivity is anomalously high along the fault and décollement and that the relationship between porosity and conductivity (described in section 3.2.2) is not appropriate for the fault zone and the décollement. A numerical simulation was performed where rock conductivity is increased in the faults and décollement. Formation factor was chosen to be equal to 6 in order to induce a rock conductivity of 0.88 S/m within the faults and 0.70 S/m within the décollement, compared to 0.80 and 0.48 S/m in the sediments above and below reflector A, respectively. The hydraulic results are not dependent on the formation factor since the formation factor is not included in the pressure and fluid flow computation (equations (5), (6), and (7)). The electric potential remains the same as in Plate 3, since both the electric convection current and conduction current are proportional to the formation factor (the inverse of G in equation (8) and (9)) but opposite in direction, so that the important parameter for the electric potential distribution is the water conductivity (see equation (9)). However, since the electric current density is changed, the magnetic field is changed (see equation (10)), so that it is decreased by about a factor 3 (Plates 5a and 5b).

Let us now test the effect of the décollement width on the results of the numerical model. The décollement width could be lower, for example, 20 m, and it might affect the electric potential and magnetic field results. A numerical simulation was performed with a décollement width of 20 m (Plate 6). In order to have reasonable overpressure (correct λ values between 0.7 and 0.9 in the décollement) in the faults zone the fluid velocity entering the décollement has been decreased, and the pressure gradient in the faults is decreased. The fluid velocity at the output of the thrust is decreased up to 0.2 m/yr for the second fault. In consequence, the electric potential is decreased by a factor 2 to 4, specially below the reflector A (Figure 5, solid symbols), the shape of the isovalues being the same, since the electric potential reflects directly the pressure field (equation (9)). The vertical electric field is 8.9 and 9.7 mV/km in the first 500 m depth for profiles above the vent (Figure 5, solid squares) and between the first and second vent (Figure 5, solid triangles). Below reflector A the vertical electric field is 48 to 52 mV/km (solid symbols, Figure 5). The horizontal gradient of the magnetic field remains about 2 nT/km, and the magnetic field is decreased by a factor 2 at the seafloor (Figure 6, solid symbols) and in depth (Figure 6): 4 and 5 nT/km for profiles above the vent (solid squares) and between the first and second vent (solid triangles), meaning that the total electric current density in the faults is decreased.

5. Discussion

When considering the first case of the simple analytical model where the electric current density is maximum within the faults (equal to the convection current) and all the conduction current is within the sediments, we know that the magnetic field is inversely proportional to the formation factor (see equation (4')), so that a decrease in the formation factor (from 17 to 6, as performed when considering an increase in rock conductivity within the faults) would induce an increase in the magnetic field. On the contrary, when all the conduction current is confined within the faults, the total electric current density within the fault is zero and no magnetic field is induced (see section 3.1). Therefore the results of the numerical modeling, showing that the magnetic field is reduced when the rock conductivity of the faults and décollement are increased, mean that the back conduction current is reduced within the sediments and increased within the faults and the décollement. The reducing of contribution of the faults, it is why the isovalues of the magnetic field have not exactly the same shape (Plates 5a and 5b compared to Plates 4a and 4b).

5.1. In Situ Measurements of Fluid Flow Variations

The results of the model permit discussion of the sensor geometry to best measure the two parameters that could potentially be followed to monitor fluid flow variations: the electric field and the magnetic field, assuming steadystate flow. If boreholes were drilled into the accretionary prism, the vertical electric field could be measured between the levels in the borehole and the seafloor. Since the rate of potential increase with depth is larger when doing a profile between two vents than above one vent, it would be more appropriate to perform measurements between two vents. In that case the expected values of the potential deduced from Figure 5 (solid symbols, when the conductivity is high (F=6) in the décollement and in faults and the décollement width is 20 m) are -4, -9.5, -14.5, and -25 mV at depths of 200, 400, 600, and 800 m, respectively. The deeper the borehole, the larger the measured electric field. It is shown here that with the chosen geometry and when the back current is taken into account, the electric field has to be measured in boreholes instead of at the seafloor as proposed by *Segawa and Toh* [1992], who found an horizontal electric field of ~1 μV/m.

A measurement of the magnetic field implies borehole measurement or seafloor measurement in the faults domain. For the borehole measurements, as for the electric measurements, it would be more appropriate to drill between two vents since the rate of increase of the magnetic field is larger there (Figure 6). A differential measurement performed between the seafloor and levels in the borehole, when the conductivity is high (F=6) in the décollement and in faults and the décollement width is 20 m, could yield a magnetic field intensity of 5.5, 6.5, 7.5, and 8.5 nT at depths of 200, 400, 600, and 800 m, respectively. The deeper the borehole, the larger the measured magnetic field.

Note that all the measurements could be performed in the same borehole drilled between two vents since it seems more appropriate for both electric and magnetic fields. Monitoring fluid flow variations implies the ability to follow the temporal variations of the electric and magnetic field.

5.2. Temporal Variations

Fluid inclusion analysis on rocks from the Kodiak accretionary complex showed that fluid pressures drop by 20% to 45% during the growth of quartz veins, suggesting that the deformation induces a local effect of fluid escaping to shallow levels in the subduction complex, possibly along an interconnected fracture network [*Vrolijk*, 1987]. The model proposed by Vrolijk implies cyclic variations of fluid pressure at near-lithostatic pressure. *Moore* [1989] proposed that episodicity of fluid flow along décollement zones may be explained by a deformational pumping mechanism by cycles of dilatation and flow to the décollement zone followed by failure and fluid expulsion along the décollement zone. Moreover, calculations based on thermal gradient and heat flow data from the Barbados accretionary complex are consistent with transient fluid flow along high-permeability conduits within the sediments, starting and stopping over intervals of decade to tens of thousands of years [*Fisher and Hounslow*, 1990]. At a shorter scale > 1 month, on the Nankai accretionary wedge, Darcy velocity deduced from temperature measurements to a depth of 60 cm over a very active fluid vent (fluid velocity of 100 m/yr) has shown fluctuations of ~15% which may be periodic and has shown an increase of 30% over the 1 month period of the observation [*Foucher et al.*, 1992]. We therefore consider a change of 20% in the fluid flow velocity due to a 20% change in the fluid pressure. The resulting variations in the streaming potential and magnetic field inside a borehole between two vents, when the conductivity is high (F=6) in the décollement and in faults and the décollement width is 20 m, are expected to be -1.9 mV and 1.3 nT at depth 400 m, -2.9 mV and 1.5 nT at depth 600 m, and -5 mV and 1.7 nT at depth 800 m. Direct fluid pressure measurements could be performed in borehole to complete these electric measurements. When monitoring the magnetic field at the seafloor, the variation is expected to be a change of 0.4 nT/km. Since the streaming potential is proportional to the fluid pressure, this justifies the use of a steadystate model in describing such variations of fluid pressure, streaming potential, and magnetic field anomaly. Note that if the fluid velocity change is only due to a permeability change (pressure gradient constant), then the streaming potential will remain constant (see equation (8)).

What about possible coupled change in permeability, fluid velocity, and fluid pressure? The permeability along the décollement is presumably much lower when pore pressure is low and fluid is not allowed to flow [*Fisher and Hounslow*, 1990]. High permeabilities are thought to be associated with anomalously high fluid pressures and fluid flow as implied by geochemical and thermal anomalies correlated with the décollement zone [*Gieskes et al.*, 1990; *Kastner et al.*, 1993]. Rhodochrosite filled veins in the scaly fabrics of the décollement zone at the Barbados ridge suggest that fluid pressures were sufficiently high to allow the décollement zone to open for fluid flow [*Moore et al.*, 1987]. If an increase in permeability and in pressure occurs in the décollement and in the major thrusts, the streaming potential will be increased, but only by the amount of the pressure increase as shown by equation (9).

Fluid flow can be deduced from pressure gradient measurements within venting clam colonies. In that case, some difficulties in inserting the probes into indurated sediments may arise [*Le Pichon et al.*, 1992]. Fluid flow can also be deduced from temperature measurements; however, only Darcian velocities > 10 m/yr can be reasonably estimated. Moreover, fluctuations in the bottomwater temperature may perturb the measurements. For example, data collected during the Kaiko-Nankai cruise at 2000 m depth were impossible to use because of a temperature variation at the bottom water of 1°C [*Henry et al.*, 1992].

The method that we propose to detect fluid circulation changes is therefore to monitor the vertical electric field and the horizontal magnetic field in a borehole and the magnetic field at the seafloor near the source. Since changes of fluid circulation that may be related to seismic activity are expected to have a long timescale variation, we need to monitor the electric field during several years with the technical problems that are implied. To measure the electric field, the electrodes must be very stable with time [*Filloux*, 1987; *Petiau and Dupis*, 1980; *Perrier et al.*, 1997]. In order to perform measurements in wells the boreholes must produce minimum perturbation of fluid circulation and in electric current paths. Therefore the use of the steel casing is not possible, and the use of an openhole causes the tools to be lost in the hole collapse.

The variations of the magnetic field are measurable, considering that a installed nuclear magnetic resonance (nmr) magnetometer has an accuracy of 0.05-0.1 nT with an appropriate reference for differential measurements. These nmr magnetometers measure the modulus of the magnetic field, i.e., the projection of the anomaly in the direction of the Earth's magnetic field to a first-order approximation. Note that the measurements at the seafloor are likely to be disturbed by the water movement at all scales from local bottom currents to large-scale oceanic streams as the "Kuroshio" western boundary ocean current [*Segawa and Toh*, 1992].

6. Conclusion

We showed that the fluid circulation in an accretionary prism could produce an electric field and a magnetic field due to electrokinetic coupling. The detection of fluid flow rate variations could be best performed by monitoring the vertical electric field and the vertical gradient of the horizontal magnetic field in a borehole drilled between two vents and by monitoring the horizontal gradient of the magnetic field at the seafloor. A variation of 3 mV and 1.5 to 3 nT at 600 m depth in a borehole could reveal a fluid flow rate variation of 20%, which is a reasonable fluid flow change based on some observations at short-scale time. Since a 1.5 to 3 nT anomaly seems easier to detect than a 3 mV anomaly, it is likely that the variation of the magnetic field would more sensitively reveal fluid flow variations. When monitoring the magnetic field at the seafloor, a change of 0.4 nT/km in the horizontal gradient could reveal a fluid flow rate variation of 20%.

Acknowledgments. We thank Pierre Henry for his highly fruitful conversations. The review of the manuscript by H. J. Tobin and two anonymous reviewers greatly improved the constraints of the model and the discussion. This research was supported by CNRS-INSU. This is CNRS-INSU-DBT contribution 161 thème fluides et failles, CNRS-INSU-PNRN contribution 159 thème risques sismiques, and CNRS-INSU-PNRH contribution 160 thème circulation des fluides dans la croûte.

References

Boulègue, J., X. Le Pichon, and J.T. Iiyama, Earthquake prediction in Tokai area (Japan), *C. R. Acad. Sci. Paris, Sér. II, 301*, 1217-1219, 1985.

Cloos, M., Landward-dipping reflectors in accretionary wedges: Active dewatering conduits?, *Geology*, *12*, 519-522, 1984.

Davis, D., J. Suppe, and F.A. Dahlen, Mechanics of fold-and-thrust belts and accretionary wedges, *J. Geophys. Res.*, *88*, 1153-1172, 1983.

Dukhin, S.S., and B.V. Derjaguin, *Surface and Colloid Science*, vol. 7, *Electrokinetic Phenomena*, edited by E. Matijevic, John Wiley, New York, 1974.

Durand, E., *Electrostatique et Magnétostatique*, pp. 499, Masson, Paris, 1953.

Filloux, J.H., Instrumentation and experimental methods for oceanic studies, in *Geomagnetism*, vol. 1, edited by J. A. Jacobs, pp. 143-248, Academic, San Diego, Calif., 1987.

Fisher, A.T., and M.W. Hounslow, Transient fluid flow through the toe of the Barbados accretionary complex: Constraints from Ocean Drilling Program Leg 110 heat flow studies and simple models, *J. Geophys. Res.*, *95*, 8845-8858, 1990.

Fitterman, D.V., Electrokinetic and magnetic anomalies associated with dilatant regions in a layered Earth, *J. Geophys. Res.*, *83*, 5923-5928, 1978.

Foucher, J.-P., P. Henry, X. Le Pichon, and K. Kobayashi, Time-variations of fluid expulsion velocities at the toe of the eastern Nankai accretionary complex, *Earth Planet. Sci. Lett.*, *109*, 373-382, 1992.

Gieskes, J.M., G. Bland, P. Vrolijk, H. Elderfield, and R. Barnes, Interstitial water chemistry-major constituents, in *Proc. Ocean Drill. Program Sci. Results*, *Part B*, *110*, 155-178, 1990.

Gieskes, J.M., T. Gamo, and M. Kastner, Major and minor element geochemistry of interstitial waters of site 808, Nankai Trough: An overview, in *Proc. Ocean Drill. Program*, *Sci. Results*, *131*, 387-396, 1993.

Heinson, G., and J. Segawa, Electrokinetic signature of the Nankai Trough accretionary complex: preliminary modelling for the Kaiko-Tokai program, *Phys. Earth Planet. Inter.*, *99*, 33-53, 1997.

Henry, P., and X. Le Pichon, Fluid flow along a décollement layer: A model applied to the 16°N section of the Barbados accretionary wedge, *J. Geophys. Res.*, *96*, 6507-6528, 1991.

Henry, P., J.-P. Foucher, X. Le Pichon, M. Sibuet, K. Kobayashi, P. Tarits, N. Chamot-Rooke, T. Furuta, and P. Schultheiss, Interpretation of temperature measurements from Kaiko-Nankai cruise: Modeling of fluid flow in clam colonies, *Earth Planet. Sci. Lett.*, *109*, 355-371, 1992.

Hubbert, M.K., and W.W. Rubey, Role of fluid pressure in mechanics of overthrust faulting, *Geol. Soc. Am. Bull.*, *70*, 115-166, 1959.

Hyndman, R.D., G.F. Moore, and K. Moran, Velocity, porosity and pore-fluid loss from the Nankai subduction zone accretionary prism, in *Proc. Ocean Drill. Program*, *Sci. Results*, *131*, 211-220, 1993.

Ishibashi K., Specification of soon-to-occur seismic faulting in the Tokai district, Central Japan, based upon seismotectonics, in *Earthquake Prediction: An International Review,* edited by D.W. Simpson and P.G. Richards, pp. 297-332, *Maurice Ewing Ser.*, vol. 4, Washington, D.C., 1981.

Ishido, T., and H. Mizutani, Experimental and theoretical basis of electrokinetic phenomena in rock-water systems and its applications to geophysics, *J. Geophys. Res.*, *86*, 1763-1775, 1981.

Jouniaux, L., and J.-P. Pozzi, Streaming potential and permeability of satured sandstones under triaxial stress: Consequences for electrotelluric anomalies prior to earthquakes, *J. Geophys. Res.*, *100*, 10197-10209, 1995a.

Jouniaux, L., and J.-P. Pozzi, Permeability dependence of streaming potential in rocks for various fluid conductivities, *Geophys. Res. Lett.*, *22*, 485-488, 1995b.

Jouniaux, L., and J.-P. Pozzi, Anomalous 0.1-0.5 Hz streaming potential measurements under geochemical changes: Consequences for electrotelluric precursors to earthquakes, *J. Geophys. Res.*, *102*, 15335-15343, 1997.

Jouniaux, L., S. Lallemant, and J.-P. Pozzi, Changes in the permeability, streaming potential and resistivity of a claystone from the Nankai prism under stress, *Geophys. Res. Lett.*, *21*, 149-152, 1994.

Jouniaux, L., M. Dubet, M. Zamora, and P. Morat, Physical properties of limestone from the quarry of Meriel, *C. R. Acad. Sci. Paris*, *Ser. IIa*, *322*, 361-367, 1996.

Kastner, M., H. Elderfield, W.J. Jenkins, J.M. Gieskes, and T. Gamo, Geochemical and isotopic evidence for fluid flow in the western Nankai subduction zone, Japan, in *Proc. Ocean Drill. Program*, *Sci. Results*, *131*, 397-413, 1993.

Langseth, M.G., and J.C. Moore, Introduction to special section on the role of fluids in sediment accretion, deformation, diagenesis, and metamorphism in subduction zones, *J. Geophys. Res.*, *95*, 8737-8741, 1990.

Le Pichon, X., K. Kobayashi, and Kaiko-Nankai Scientific Crew, Fluid venting activity within the eastern Nankai Trough accretionary wedge: A summary of the 1989 Kaiko-Nankai results, *Earth Planet. Sci. Lett.*, *109*, 303-318, 1992.

Lorne, B., F. Perrier, and J.-P. Avouac, Streaming potential measurements: 1. Properties of the electrical double layer from crushed rock samples, *J. Geophys. Res.*, *104*, 17857-17877, 1999a.

Lorne, B., F. Perrier, and J.-P. Avouac, Streaming potential measurements: 2. Relationship between electrical and hydraulic flow patterns from rock samples during deformation, *J. Geophys. Res.*, *104*, 17879-17896, 1999b.

Massé, P., and J. Berthier, Three dimensional finite element modelling of streaming potential and associated magnetic field in porous media, paper presented at *Conference on the Computation of Electromagnetics Fields* (COMPUMAG), Berlin, July 10-13, 1995.

Massé, P., and J. Berthier, Three dimensional finite element modeling of streaming potential and associated magnetic field, *Trans. Magn.*, *32*, 994-998, 1996.

Moore, G.F., T.H. Shipley, P.L. Stoffa, D.E. Karig, A. Taira, S. Kuramoto, H. Tokuyama, and K. Suyehiro, Structure of the Nankai Trough accretionary zone from multichannel seismic reflection data, *J. Geophys. Res.*, *95*, 8753-8765, 1990.

Moore, J.C., Tectonics and hydrogeology of accretionary prisms: Role of the décollement zone, *J. Struct. Geol.*, *11*, 95-106, 1989.

Moore, J.C., and P. Vrolijk, Fluids in accretionary prisms, *Revi. Geophys.*, *30*, 113-135, 1992.

Moore, J.C., and ODP Leg 110 Scientific party, Expulsion of fluids from depth along a subduction-zone décollement horizon, *Nature*, *326*, 785-788, 1987.

Moore, J.C., et al., Tectonics and hydrogeology of the northern Barbados Ridge: Results from Ocean Drilling Program Leg 110, *Geol. Soc. Am. Bull.*, *100*, 1578-1593, 1988.

Moran, K., W. Brückmann, V. Feeser, and R.G. Campanella, In-situ stress conditions at Nankai Trough, site 808, in *Proc. Ocean Drill. Project, Sci. Results*, *131*, 283-291, 1993.

Morgan, J.K., and D.E. Karig, Décollement processes at the Nankai accretionary margin, southeast Japan: Propagation, deformation, and dewatering, *J. Geophys. Res.*, *100*, 15221-15231, 1995.

Nourbehecht, B., Irreversible thermodynamic effects in inhomogeneous media and their applications in certain geoelectric problems, Ph.D. thesis, Mass. Inst. of Technol., Cambridge, 1963.

Overbeek, J.T., Electrochemistry of the double layer, in *Colloid Science*, vol.1, *Irreversible Systems*, edited by H. R. Kruyt, pp. 115-193, Elsevier, New York, 1952.

Perrier, F., et al., A one year systematic study of electrodes for long period measurements of the elctric field in geophysical environments, *J. Geomagnet. Geoelectr.*, *49*, 1677-1696, 1997.

Petiau, G., and A. Dupis, Noise, temperature coefficient, and long time stability of electrodes for telluric observations, *Geophys. Prospect.*, *28*, 792-804, 1980.

Poirier, J.E., and J.M. Cases, Sur l'origine et la nature de l'interaction adsorbat-adsorbant dans les systèmes à interactions faibles, in *Solid-Liquid Interactions in Porous Media*, pp. 447-462, Technip, Colloque Bilan, Nancy, France, 1985.

Pride, S.R., and F.D. Morgan, Electrokinetic dissipation induced by seismic waves, *Geophysics*, *56*, 914-925, 1991.

Revil, A., and P.W.J. Glover., Theory of ionic-surface electrical conduction in porous media, *Phys. Rev. B*, *55*, 1757-1773, 1997.

Screaton, E.J., D.R. Wuthrich, and S.J. Dreiss, Permeabilities fluid pressure and flow rates in the Barbados ridge complex, *J. Geophys. Res.*, *95*, 8997-9007, 1990.

Segawa, J., and H. Toh, Detecting fluid circulation by electric field variations at the Nankai Trough, *Earth Planet. Sci. Lett.*, *109*, 469-476, 1992.

Sharma, M.M., J.F. Kuo, and T.F. Yen, Further investigation of the surface charge properties of oxide surfaces in oil-bearing sands and sandstones, *J. Colloid Interface Sci.*, *115*, 9-16, 1987.

Sibson, R. H., J.M. Moore, and A.H. Rankin, Seismic pumping-a hydrothermal fluid transport mechanism, *J. Geol. Soc. London*, *131*, 653-659, 1975.

Somasundaran, P., and R.D. Kulkarni, A new streaming apparatus and study of temperature effects using it, *J. Colloid Interface Sci.*, *45*, 591-600, 1973.

Stern, O., Zür theorie der elektrolischen doppelschicht, *Z. Elektrochem.*, *30*, 508, 1924.

Taira, A., et al., Geological background and objectives, by shipboard scientific party, in *Proc. Ocean Drill. Program*, *Initial Rep.*, *131*, 5-14, 1991.

Taira, A., et al., Proceedings of the Ocean Drilling Initial Reports, vol. 131, site 808, p. 213, Ocean Drill. Program, College Station, Tex., 1990.

Taylor, E., and A. Fisher, Sediment permeability at the Nankai accretionary prism, site 808, in *Proc. Ocean Drill. Program*, *Sci. Results*, *131*, 235-243, 1993.

von Huene, R., and H. Lee, The possible significance of pore fluid pressure in subductions zones, edited by J.S. Watkins, and C.L. Drake, *Stud. Cont. Margin Geol.*, *34*, 781-791, 1982.

Vrolijk, P., Tectonically driven fluid flow in the Kodiak accretionary complex, Alaska, *Geology*, *15*, 466-469, 1987.

Westbrook, G.K., and M.J. Smith, Long décollements and mud volcanoes: Evidence from the Barbados ridge complex for the role of high pore-fluid pressure in the development of an accretionary complex, *Geology*, *11*, 279-283, 1983.

Westbrook, G.K., M.J. Smith, J.H. Peacock, and M.J. Poulter, Extensive underthrusting of underformed sediment beneath the accretionary complex of the Lesser Antilles subduction zone, *Nature*, *300*, 625-628, 1982.

Winkler, W.R., and N.J. Steward, Proceedings of the Ocean Drilling Program Scientific Results, vol. 131, site 808, Ocean Drill. Program, College Station, Tex., 1991.

J. Berthier, and P. Massé, LETI (CEA-Technologies avancées) DSYS, CEA Grenoble, 17 rue des Martyrs, 38054 Grenoble Cédex 9, France. (jberthier@cea.fr)

L. Jouniaux, and J.-P. Pozzi, Laboratoire de Géologie & CNRS UMR 8538, École Normale Supérieure, 24 rue Lhomond, 75231 Paris Cedex 05, France. (jouniaux@magnetit.ens.fr; pozzi@magnetit.ens.fr)

(Received June 8, 1998; revised March 10, 1999;
accepted March 11, 1999.)

GEOPHYSICAL RESEARCH LETTERS, VOL. 21, NO. 2, PAGES 149-152, JANUARY 15, 1994

Changes in the permeability, streaming potential and resistivity of a claystone from the Nankai prism under stress

Laurence Jouniaux, Siegfried Lallemant and Jean-Pierre Pozzi

Laboratoire de Géologie & CNRS URA 1316, Ecole Normale Supérieure, France

Abstract. Permeability is the critical factor governing fluid flow in accretionary prisms. Accretionary wedges are highly deformed, so permeability changes in an indurated claystone sample from the Nankai accretionary prism were measured during a triaxial stress experiment by the pulse decay method. Three zones were identified from the loading test. In zone I, the sample has deformed less than 1.3% and its permeability was 5.10^{-20} m^2. In zone II, the deformation reached 1.5% and the permeability was unstable with time. In zone III, the sample deformation reached 2% and its permeability reached 3.8 10^{-18} m^2. The permeability strongly decreased (from 3.2 10^{-18} m^2 to 1.7 10^{-19} m^2) with increasing effective pressure (from 2.3 to 10.8 MPa) after the sample was well deformed (zone III). The streaming potential was not measurable when the sample had a low permeability (zone I), but clearly occured when the permeability increased (zone III) : the streaming potential measured was 6 mV when the pore pressure pulse applied was about 1.17 MPa and the permeability 3.8 10^{-18} m^2. Our experiments suggest that shear deformation under low effective pressure increased the vertical permeability of sediments above the décollement. This increase in permeability may be detected by measuring the streaming potential. Variations of flow rate of expelled fluid in accretionary wedges may be detected by monitoring changes of electrokinetic potential, giving new insights on the state of stress related to the seismic cycles.

Introduction

Elevated pore fluid pressure has long been recognized to maintain large parts of accretionary prisms near failure conditions [von Huene and Lee, 1982], resulting in complex interactions of strain regimes and fluid circulation. Expelled fluids from accretionary wedges have been shown to be transported from great depth within the prism [Moore and Vrolijk, 1992]. The use of Darcy's law as governing equation of fluid flow in a prism [Henry and Wang, 1991] is probably reasonable as the high density of interconnected fractures probably approximates a Darcian continuum over large length scales. As expressed by Darcy's law, fluid pressure gradients are the driving force of fluid flow while rock permeability resists fluid flow. Pressure gradients change less than 1 order of magnitude, although permeability changes can be of 6 to 8 orders of magnitude [Moore and Vrolijk, 1992]. The permeability is thus the critical factor governing fluid flow in accretionary wedges. We present results from an experimental study of the changes of permeability associated with the deformation of an indurated claystone sample from the Nankai accretionary wedge. The permeability was measured as a function of the effective pressure for different states of axial strain. Variation of the electrical resistivity was measured during the experiment. We also measured the streaming potential during the measurement of permeability by pore pressure diffusion.

Paper number 93GL03293
0094-8534/94/93GL-03293$03.00

Sampling and experimental procedure

The two samples studied were obtained from leg 131 (hole 808C) of the Ocean Drilling Program, in the Nankai accretionary wedge. One sample was a tuff (sample 131-808C-54R-1, 68-72cm), collected from about 810 meters below the sea floor (mbsf), and the other was an indurated claystone (sample 131-808C-102R-1,121-126 cm), from about 1260 mbsf, with porosity of 23% and bulk density of 2.4 g/cm^3. Both samples were from below the décollement and thus belong to an undeformed sequence [Taira et al., 1992]. Samples were cut into cylinders : 20 mm in diameter and 40 mm long. They were saturated with distilled water and isolated from the confining pressure by a jacket. We used a press with controlled displacement. Variations of axial pressure, confining pressure and pore pressure were independant. Samples were first subjected to an axial stress and a confining pressure of 11±0.1 MPa, and a pore pressure of 9±0.1 MPa. These values were raised after a period of time sufficient to nearly equilibrate the pore pressure due to diffusion.

Vertical permeability was determined by the pulse decay method [Brace et al., 1968], which follows the decay of a small step change of pore pressure imposed at one end of a sample. When a pressure pulse ΔP_0 (less than 10% the magnitude of the total pore pressure) is generated, the differential pressure $\Delta P(t)$ decays exponentially as a function of time, t :

$$\Delta P(t) = 2\,\Delta P_0\, V_2 / (V_1 + V_2)\, e^{-mt} \qquad (1)$$

where V_1 and V_2 are the upstream and downstream reservoir volumes (V_1=V_2=50 10^{-6} m^3 in our experimental setup, large compared with the sample pore volume which is 2.9 10^{-6} m^3), t is time and m is a decay time constant. Plotting the decay curve in terms of $\ln(\Delta P(t))$ versus time t yields a straight line having a slope m, and the permeability k, can be determined by $k = (m\,\mu\,\beta\,L\,V_1\,V_2)/(A(V_1+V_2))$ where L is the length of the sample, A the cross-sectional area of the sample, μ the dynamic viscosity of pore fluid at temperature measurement (10^{-3} Pa.s at 20°C), and β is the compressibility of the pore fluid (0.42 10^{-9} Pa^{-1}). The pulse decay method is time-consuming because the diffusion of the pressure pulse across a clay sample can be about 24 hours and we must wait at each step for the total diffusion of the pore pressure inside the sample. Our apparatus was tested by measuring the permeability to water of a sample of Fontainebleau sandstone (France) with a porosity of 4.3% and a permeability to air of 4 10^{-16} m^2, giving us the opportunity to measure the permeability to water using two different methods. We found k=2.2 10^{-16} m^2 with the steady state flow method and k=1.1 10^{-16} m^2 with the pulse decay method, and concluded that our experimental method and the use of (1) yield reliable values of the permeability.

The pulse decay method has been used in triaxial tests on granite [Brace et al., 1968, Bernabé, 1987], and on samples of tuff [Zhang et al., 1993]. But permeability of argillaceous rocks is generally measured using a consolidation test [Taylor and Fisher, 1993]. Because the permeability of clays is supposed to be sensitive to the effective pressure [Brace, 1980], we made measurements of permeability at different states of effective stress.

The resistivity of the samples was measured at 4 kHz with an impedancemeter. The streaming potential is the difference of potential across a sample when a fluid is made to flow through it by a driving pressure ΔP. This streaming potential was measured by a voltmeter with an input resistance greater than $10^{10}\Omega$.

Experimental results

Permeability measurements

The sample of tuff had a permeability of 3.5 ± 1.5 10^{-20} m^2 (or 3.5 10^{-11} cm/s) when subjected to an axial stress and a constant confining pressure of 11 MPa, and a pore pressure of 9.2 MPa. Unfortunately, this sample was crushed because of a power cut and we could not make further measurements.

The second sample was exposed to an increasing deviatoric stress, with a confining pressure of 12 MPa, and a pore pressure of 9.2 MPa. The entire experiment lasted 11 days and the sample was deformed at an average strain rate of 2.3 10^{-8} s^{-1}. The timing of the measurements was kept as constant as possible. The differential stress (axial stress minus confining pressure) and the permeability as a function of the axial strain are represented in Figure 1. First, the permeability was 5 10^{-20} m^2, and remained almost constant up to the stress drop (Zone I). This stress drop, from 35 MPa to 10 MPa, occured during a 49 hours period. Then the permeability increased up to 1.1 and 3.3 10^{-18} m^2 (Zone II) and remained high : 3.2 to 3.8 10^{-18} m^2 when the sample was further deformed (Zone III). Zone II represents a critical deformation where the permeability was unstable. At the Zone I-II transition, two measures of permeability were made at constant axial strain : it decreased with time from 2 10^{-18} m^2 to 1.2 10^{-18} m^2 as shown in Figure 2. At the Zone II-III transition, permeability increased with time from 1.8 10^{-18} m^2 to 3.3 10^{-18} m^2. The time needed for each measure of permeability is shown by horizontal line.

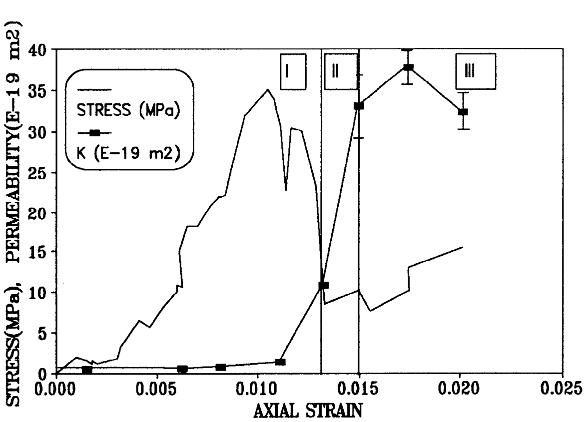

Fig. 1. : Differential stress (continuous line) and permeability as a function of axial strain (square dots). Zone II represents a critical strain where the permeability is unstable. Permeability changes from 5 10^{-20} m^2 to 3.8 10^{-18} m^2 in a narrow range of axial stress.

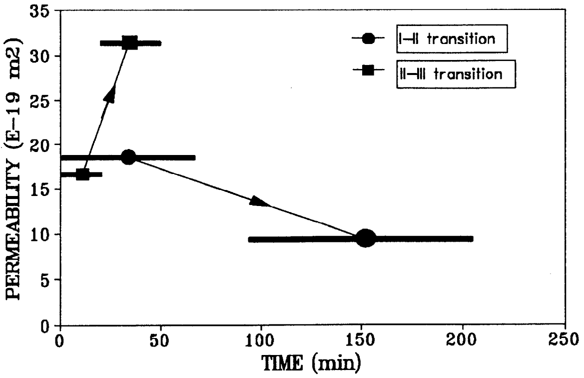

Fig. 2. : Evolution of the permeability with time at the I-II and II-III transitions (Fig.1.). The time needed for a permeability measurement is shown by horizontal line.

The permeability was then measured as a function of the effective pressure (confining pressure minus pore pressure) between 2 and 15 MPa. In zone I the permeability did not vary with the effective pressure as shown in Figure 3. On the other hand the permeability in zone III (after the last permeability measurement shown in Figure 1) became very sensitive to the effective pressure : the permeability decreased from 3.2 10^{-18} m^2 (P_e=2.3 MPa) to 1.7 10^{-19} m^2 (P_e=10.8 MPa). When the effective pressure was decreased by an increase of pore pressure to P_e=2.3 MPa, the permeability increased but did not recover its initial value (3.2 10^{-18} m^2). At the end of the experiment, no macroscopic shear fracture was observed. For this clay sample, the well-oriented clay flakes deformed by shear

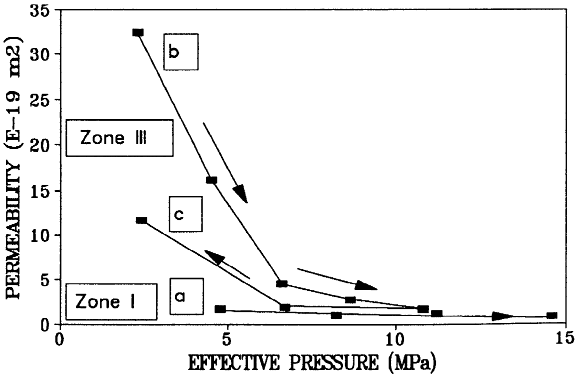

Fig. 3. : Permeability versus the effective pressure. a- in zone I, b- in zone III, by increasing confining presure; c- in zone III, by increasing pore pressure.

stress probably produced interconnected fluid volumes, resulting in an increase of permeability.

Electrical measurements

The resistivity decreased during the first stage of deformation, then it increased in zone II and III as shown in Figure 4. For this sample, the electrical conductivity was due not only to electrolytic conduction, but also to the surface conductivity. Moreover, the electrical conductivity of the fluid changed through chemical interaction during the 10 days of the experiment from 1500 Ω.m (initial saturating fluid) to 90 Ω.m at the end of the experiment (determined from collected water when the sample was taken off the cell), resulting in a complex behavior of the resistivity with the deformation. This behavior is opposite to that observed in sandstones, whose mechanical behavior is brittle with dilatancy, and whose electrical conductivity is only due to the electrolytic conduction [Jouniaux et al., 1992].

The streaming potential was not measurable when the sample had a low permeability (zone I), but clearly occured when the permeability increased (zone III). As shown in Figures 5a and 5b, electrical noise was recorded before the pore pressure pulse ΔP_0 was applied and during the diffusion of the pore pressure. The streaming potential occured just when the pore pressure pulse was applied. For this example, ΔP_0 is 11.7 bar, the streaming potential was 6 mV (-25 mV to -19 mV) while the noise was 2.5 mV. The same phenomenon was observed in the next state of deformation studied, when permeability was 3.2 10^{-19} m^2 (the last point in Figure 1). The streaming potential, produced by fluid percolation when a fluid is made to flow through a porous medium, is theoretically proportional to the driving pore pressure [Overbeek, 1952; Nourbehecht, 1963; Dukhin and Derjaguin, 1974; Morgan et al., 1989]. $C=\Delta V/\Delta P= -(\varepsilon\zeta)/(\eta\sigma)$ is called the electrokinetic coupling coefficient and depends on the fluid conductivity σ, the fluid viscosity η, the zeta potential ζ (potential at the rock/fluid interface), and the dielectric constant of fluid ε.

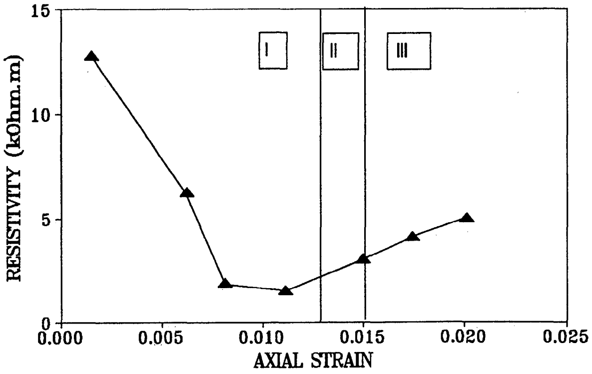

Fig. 4. : Electrical resistivity of the rock versus axial strain. The behavior of the resistivity includes the electrolytic conduction, the surface conductivity, and the chemical interaction.

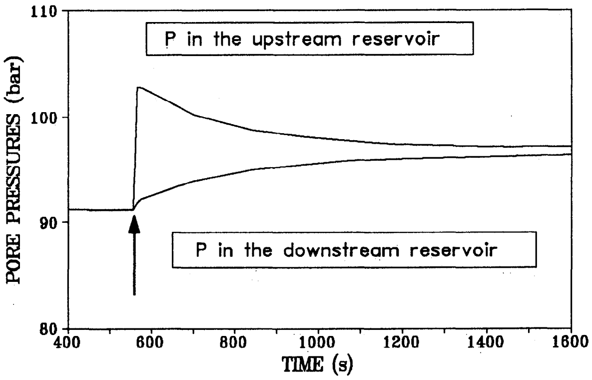

Fig. 5a. : Pulse decay as a function of time measured at maximum permeability. The arrow indicates the timing of the applied pressure pulse.

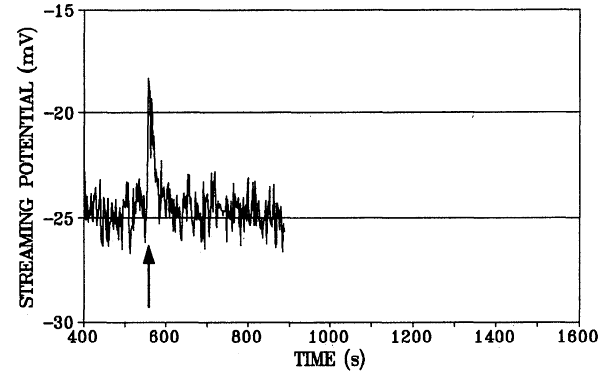

Fig. 5b. : Streaming potential as a function of time. The streaming potential only occured in Zone III of strain (Fig.1) when the pore pressure pulse was just applied. The permeability of the sample was 3.8 10^{-18} m^2. The arrow indicates the timing of the applied pressure pulse.

When the permeability of a sample is less than 10^{-17} m^2, the transient flow is described by a pressure diffusion law [Brace, 1968], and the volume flowing in the sample is the storage of fluid, due to the compressibilities of the fluid and of the solid. The evolution of the streaming potential with time is

$$\Delta V(t) = \frac{1}{\sigma}\cdot\int_{x_1}^{x_2} i_{conv}(t)dx, \text{ where } i_{conv}(t) = \frac{C\sigma\,\partial P(t)}{\partial x} \qquad (2)$$

and x_2-x_1 is the length of the sample. If we assume that C is constant, $\Delta V(t)=C\Delta P(t)$, the pressure gradient being constant along the length of the sample although it varies with time. The maximum streaming potential occurs when the pore pressure pulse ΔP is maximum. The streaming potential strongly decreased and was no longer measurable when ΔP fell below a critical value of 8 bar in our example. ΔV and ΔP showed two different time constants, 40 s and 165 s respectively, defined as the time when the signal decreased to half of its initial value. When ΔP_0 was applied, the Darcy's speed was 3.5 m/an, whereas it was 2.4 m/an when ΔP fell to this critical value. It seems that the volume flowing in the sample was not sufficient to produce a measurable streaming potential, as when a decrease in the permeability of a sample of sandstone induces a decrease in the electrokinetic coupling coefficient [Pozzi and Jouniaux, 1993].

Discussion and conclusion

The permeability of the indurated claystone increased almost by two orders of magnitude (from 5 10^{-20} m^2 to 3.8 10^{-18} m^2) when exposed to a deviatoric stress, even at small strain (0.015). We observed an unstable zone (zone II) where the permeability was unstable with time, at the same strain and without noticeable stress relaxation. When the sample was further deformed, the permeability remained high. Permeability showed only a slight variation with effective pressure at low axial strain and became very sensitive to the effective pressure at greater axial strain (from 3.2 10^{-18} m^2 to 1.7 10^{-19} m^2) in the range of effective pressure from 2.3 to 10.8 MPa. The streaming potential became measurable in Zone III. At a permeability greater than 3 10^{-18} m^2, a 6 mV streaming potential was produced in response to a pressure pulse of 1.17 MPa.

Although performed on only one sample, progressive shear deformation of an initially underformed sample from below the décollement is intended to approximate what happens to sequences of similar lithology that are naturally deformed above the décollement. Based on the geometry of the brittle structures in hole 808C, Lallemant et al. [1993] proposed that the 200m thick deformed claystone from above the décollement was subjected to high pore fluid pressure. Our experiments suggest that a shear strain under low effective pressure may be the cause of increased vertical permeability of these hemipelagic sequences. This increase of permeability may be detected by measuring the streaming potential. The streaming potential will be enhanced in cases of fresh water circulation relative to sea water circulation, because of the greater resistivity of fresh water. Changes of flow rates of fluids expelled from an accretionary wedge could be detected by monitoring changes of electrokinetic potential, as proposed by Boulègue et al. [1985], and related to the state of stress and the seismic hazard.

Acknowledgments : We thank P. Henry for fruitful discussions. This study is a collaboration with ENSAM (laboratoire de mécanique des structures). This research was supported by ANDRA, the GRECOgéomateriaux and INSU-Océanoscope. This is ENS contribution 309 and CNRS-INSU-DBT contribution 662, thème instabilités.

References

Bernabé, Y., The effective pressure law for permeability during pore pressure and confining pressure cycling of several crystalline rocks, J. Geophys. Res., 92, 649-657, 1987.

Boulègue, J., Le Pichon, X., and Iiyama, J.T., Earthquake prediction in Tokaï area (Japan), C. R. Acad. Sc. Paris, t. 301, Série II, n°16, 1217-1219, 1985.

Brace, W.F., Walsh, J.B., and Frangos, W.T., Permeability of granite under high pressure, J. Geophys. Res., 80, 2225-2236, 1968.

Brace, W.F., Permeability of crystalline and argillaceaous rocks, Int. J. Mech. Min. Sci. and Geomech. Abstr., 17, 241-251, 1980.

Dukhin, S.S., and Derjaguin, B.V., Surface and Colloïd Science, vol. 7, edited by E. Matijevic, John Wiley & Sons, New York, 1974.

Henry, P., and Wang, C.-Y., Modeling of fluid flow and pore pressure at the toe of the Oregon and Barbados accretionary wedges, J. Geophys. Res., 96, 20,109-20,130, 1991.

Jouniaux, L. et al., Resistivity changes induced by triaxial compression in saturated Sandstones from Fontainebleau, C. R. Acad. Sci. Paris, t. 315, Série II, 1493-1499, 1992.

Lallemant, S.J., et al., Stress tensors at the toe of the Nankai accretionary prism : an application of inverse methods to slickenlined faults, Proceedings of the Ocean Drilling Program, Scientific Results, 131, 103-122, 1993.

Moore, J.C. and Vrolijk, P., Fluids in Accretionary Prisms, Reviews of geophysics, 30,2, 113-135, 1992.

Morgan, F. D., et al., Streaming potentials properties of Westerly granite with applications, J. Geophys. Res., 94, 12449-12461, 1989.

Nourbehecht, B., Irreversible thermodynamic effects in inhomogeneous media and their applications in certain geoelectric problems, Ph. D. Thesis, M. I. T., Cambridge, Massachussetts, 1963.

Overbeek, J.Th.G., Colloïd Science, vol 1, edited by H.R. Kruyt, Elsevier, 115-193, 1952

Pozzi, J. P., and Jouniaux, L., Electrical effects of fluid circulation in sediments and seismic prediction, C. R. Acad. Sci. Paris, 1993, in press.

Reynolds, S.J. and Lister, G.S., Structural aspects of fluid-rock interaction in detachment zones, Geology, 15, 362-366, 1987.

Taira, A. et al., Sediment deformation and hydrogeology of the Nankai Trough accretionary prism : Synthesis of shipboard results of ODP Leg 131, Earth and Planetary Science Letters, 109, 431-450, 1992.

Taylor, E., and Fisher, A., Sediment permeability at the Nankai accretionary prism, site 808, Proceedings of the Ocean Drilling Program, Scientific Results, 131, 235-245, 1993.

von Huene, R., and Lee, H., The possible signifiance of pore fluid pressure and subduction zones, Studies of Continental Margin Geology, Am. Assoc. Pet. Geol. Mem., 34, 781-791, 1982.

Zhang, J., Davis, D.M., and Wong, T.-F., Failure modes of tuff samples from leg 131 in the Nankai accretionary wedge, Proceedings of the Ocean Drilling Program, Scientific Results, 131, 275-281, 1993.

L. Jouniaux, S. Lallemant and J-P Pozzi, Laboratoire de Géologie & CNRS URA 1316, Ecole Normale Supérieure, 24 rue Lhomond, 75231 Paris Cedex 05, France.

(Received August 30, 1993;
revised November 18, 1993;
accepted November 19,1993.)

Caractérisation des milieux superficiels par des excitations provoquées : conversions sismo-électro-magnétiques

On verra dans cette partie les travaux relatifs à un cas particulier d'électrofiltration : les conversions sismo-électro-magnétiques. Il s'agit des effets électriques et magnétiques liés à la propagation d'ondes sismiques dans un milieu poreux contenant de l'eau. Cette partie sera illustrée par une sélection des articles suivants :

- Article de vulgarisation : Pas un bruit, on scrute la Terre, ***ulp.sciences***, 2005.
- ***Photos*** du site du Laboratoire Souterrain à Bas Bruit (LSBB), Rustrel pays d'Apt
- ***Photos*** du montage expérimental au LSBB, Rustrel.
- Bordes, C., Jouniaux, L., Dietrich, M., Pozzi, J.-P., and S. Garambois, First Laboratory measurements of seismo-magnetic conversions in fluid-filled Fontainebleau sand, ***Geophys. Res. Lett.***, 2006.

Le principal encadrement que j'ai effectué, pour cette partie, a été celui de Clarisse Bordes pour sa thèse de doctorat, soutenue en 2005.

Les phénomènes sismo-électriques et sismo-magnétiques connaissent actuellement un regain d'intérêt suite à certaines expériences réussies [*Dupuis and Butler*, 2006 ; *Garambois and Dietrich*, 2001 ; *Beamish*, 1999 ; *Butler et al.*, 1996] et à des développements théoriques importants [*Garambois and Dietrich*, 2001 ; 2002 ; *Haarsten and Pride, 1997* ; *Pride*, 1994]. Il s'agit de conversion d'énergie sismique en énergie électromagnétique dans les milieux poreux. Des signaux électromagnétiques sont engendrés par la propagation des ondes sismiques dans le sous-sol grâce à des phénomènes de couplages électrocinétiques, à cause de l'existence d'un mouvement relatif entre les grains et l'eau, lié au passage de l'onde sismique. Les équations de transport électrique et hydrique exprimant le couplage entre les champs sismique et électrique ont été développées par S. Pride [1994]. Cela correspond à l'équation (2) en fonction de la fréquence de l'onde sismique. Il a été montré que le champ électrique est proportionnel à l'accélération sismique pour les ondes P, et que le champ magnétique est proportionnel à la vitesse sismique pour les ondes S [*Garambois and Dietrich*, 2001]. Les signaux accompagnant les ondes sismiques sont appelés « co-sismiques ». Il existe aussi un autre type de conversion sismo-électromagnétique à l'interface entre deux matériaux différents.

À une interface plane séparant deux milieux de caractéristiques différentes, une onde sismique crée une variation temporelle de la distribution des charges électriques de part et d'autre de l'interface, ce qui génère une perturbation électromagnétique qui se propage indépendamment de l'onde sismique, à partir de l’interface, avec une vitesse bien plus importante (de l’ordre de 125000 m/s dans un milieu poreux superficiel [*Garambois and Dietrich*, 2001]). Ce signal électromagnétique peut alors être détecté de manière quasi-instantané sur un réseau d’électrodes installé en surface.

Cette méthode pourrait être utilisée pour la détection à distance et la caractérisation des fluides dans le sous-sol. On s’intéresse donc à sa sensibilité au contenu en fluide, et à son potentiel en tant qu’outil d’imagerie et de caractérisation géophysique des formations superficielles, en particulier la caractérisation de couches géologiques de faible épaisseur. Les informations sismo-électriques ou sismo-magnétiques recueillies par des réseaux de dipôles électriques ou de magnétomètres peuvent donc servir à des études environnementales ou de géophysique de réservoir [*Thompson et al.*, 2005 ; *Thompson and Gist*, 1993].

Dans le cadre du projet ACI - eau sol environnement *(coordonné par M. Dietrich, LGIT Grenoble)*, j’ai assuré la co-direction de la thèse de Clarisse Bordes (2005) pour mettre au point un dispositif expérimental permettant de faire des mesures sismo-électriques et sismo-magnétiques sur du sable. Pour ce faire, nous avons travaillé au Laboratoire Souterrain à Bas Bruit (LSBB) de Rustrel, qui présente un environnement très peu bruité en ce qui concerne les champs électriques et champs magnétiques ambiants. Nous avons mis en évidence des signaux transitoires sismo-électriques et sismo-magnétiques, ayant pour origine l’électrofiltration [*Bordes et al., GRL*, 2006]. De plus, les temps des premières arrivées de ces signaux indiquent clairement que le champ sismo-électrique est couplé à la propagation des ondes P (vitesse aux environs de 1250 m/s), et que le champ sismo-magnétique est couplé à la propagation des ondes S (vitesse aux environs de 800 m/s), comme démontré dans la théorie de Pride [1994], mais encore jamais observé [Fig. 3 dans *Bordes et al., GRL*, 2006]. Les résultats de ces expériences posent encore beaucoup de questions, leur modélisation est assez compliquée. Deux articles sont en cours de rédaction. Néanmoins nous avons montré qu’une conversion sismo-magnétique était mesurable, même si nous n’avons pas pu quantifier la valeur du champ magnétique car nous n’avions pas de magnétomètre trois composantes. Il est donc envisagé de poursuivre les recherches dans ce domaine (voir Projets C-1).

Pas un bruit, on scrute la Terre

Dans une zone classée “secret défense” et qui n’apparaissait pas sur les cartes il y a encore dix ans, les chercheurs observent la Terre dans un silence presque parfait. C’est au cœur de la montagne, dans ce laboratoire hors du commun que Laurence Jouniaux expérimente une méthode pour “voir” le sous-sol.

Michel Dietrich, chercheur au Laboratoire de géophysique interne et de tectonophysique (LIGT)

Crédi Yves Orengo LGT

Le tunnel

Une longue galerie de deux kilomètres s’enfonce dans le massif karstique. Après une série de portes blindées, le tunnel débouche au coeur du laboratoire. À 500 mètres sous terre, au milieu du parc naturel du Lubéron, se niche une capsule blindée de 1250 m^3, suspendue à l’intérieur d’une alvéole de béton armé. Toutes ces protections et l’isolement du site font du Laboratoire souterrain à bas bruit (LSBB) l’un des lieux les plus calmes au monde : pas de bruit acoustique, ni mécanique ou électromagnétique. “*Le champ magnétique y est très faible et varie peu. Cette absence quasi-totale de bruits parasites nous assure des mesures non perturbées*”, explique Laurence Jouniaux, chargée de recherche au CNRS(1).

Avec Michel Dietrich, initiateur du projet, et Clarisse Bordes, doctorante en géophysique(2), elle y teste une nouvelle méthode d’imagerie et de caractérisation de roches-réservoirs. Dans un coin de la vaste capsule se trouve le dispositif : une colonne de plexiglas d’un mètre de haut et 8 cm de diamètre remplie de sable dans lequel s’intercalent des couches de kaolin. Une petite bille frappe le haut du montage pour provoquer une onde sismique. Dix électrodes et des magnétomètres répartis sur toute la hauteur de la colonne enregistrent les signaux électromagnétiques. “*Pour éviter toute perturbation, nous coupons aussi l’électricité et la ventilation pendant la manip,* raconte Laurence Jouniaux. *Il faut bien se couvrir.*”

L’expérience est basée sur un principe connu depuis les années 30, mais qui n’est testé sur le terrain que depuis une dizaine d’années. À l’interface entre deux couches de roches différentes, le passage d’une onde sismique crée une onde électromagnétique que l’on peut mesurer en surface. Il est alors possible de connaître certaines caractéristiques de l’interface et donc des roches qui la composent. “*Avec cette expérience, nous allons tenter de déterminer en laboratoire les paramètres pertinents auxquels cette méthode est sensible,* explique la géophysicienne. *Nous espérons pouvoir détecter des couches de roche peu épaisses, ce qui n’est généralement pas possible par d’autres moyens.*”

Une mince couche d’argile dans du calcaire est une barrière pour les liquides. Le savoir peut guider le forage d’un puits d’eau ou de pétrole. Les groupes pétroliers ont d’ailleurs été les premiers à s’intéresser à la technique et à lancer les essais sur le terrain. Les résultats ont incité des équipes académiques à continuer les recherches théoriques et les modélisations en laboratoire. “*Nous obtenons des données encourageantes, mais il y a encore du travail avant que la méthode ne devienne un outil utilisable sur le terrain*”, conclut la chercheuse.

M. E.

---

(1) Unité mixte de recherche ULP/CNRS 7516
Institut de physique du globe de Strasbourg,
EOST **http://ipgs.u-strasbg.fr**

(2) Unité mixte de recherche Université Joseph Fourier/CNRS 5559
LGIT **www-lgit.obs.ujf-grenoble.fr**

Crédit photo : Clarisse Bordes, LGT

Porte blindée

Crédit photo : Clarisse Bordes, LGT

Montage de l'expérience

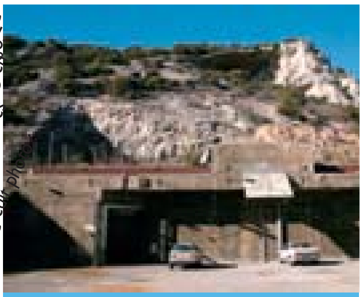

Crédit photo : Yves Orengo LGT

Entrée du LSBB

De la dissuasion nucléaire à la prospection géologique

Le LSBB est installé dans l’ancien poste de tir n°1 du plateau d’Albion. De là étaient commandés 18 missiles nucléaires sol-sol de la force de dissuasion française. Après son démantèlement en 1996, ce site exceptionnel a été racheté par la communauté de communes du pays d’Apt avec l’aide de la Région et transformé en laboratoire civil. Le LSBB accueille aujourd’hui 23 équipes venues d’Europe, du Canada et des États-Unis pour des recherches en hydrologie, sismologie ou physique des astroparticules.

http://lsbb.unice.fr

Site du Laboratoire Souterrain à Bas Bruit (LSBB)
Rustrel, Pays d'Apt

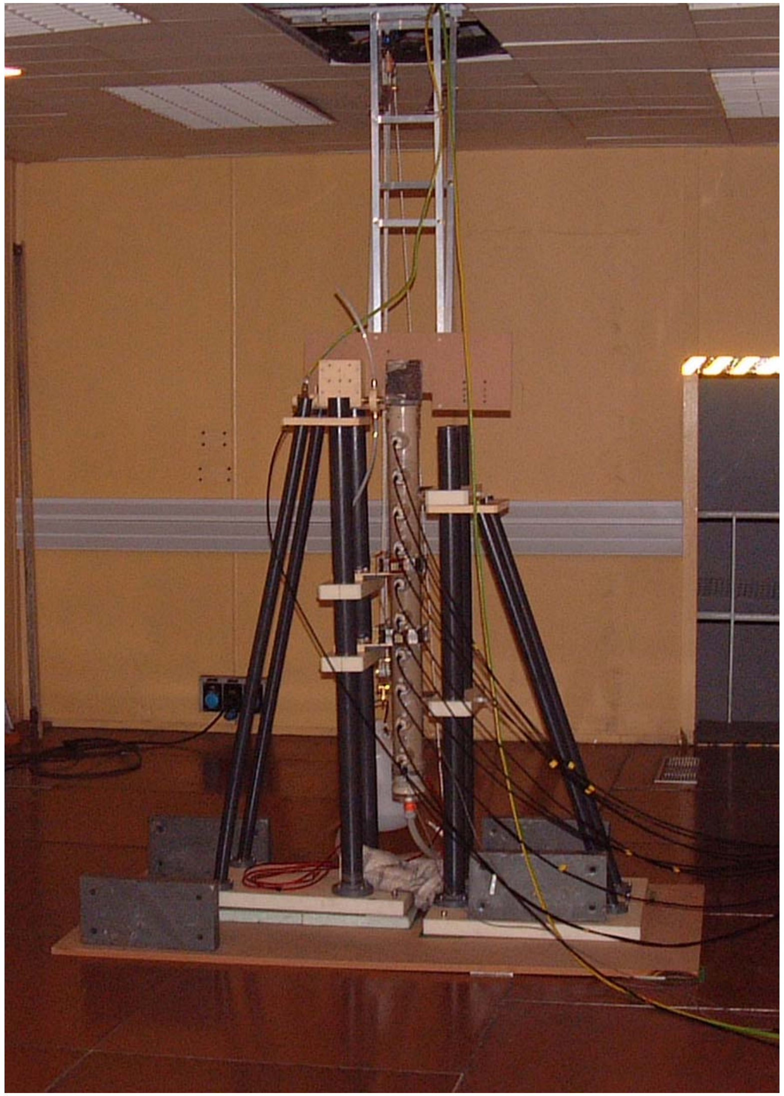

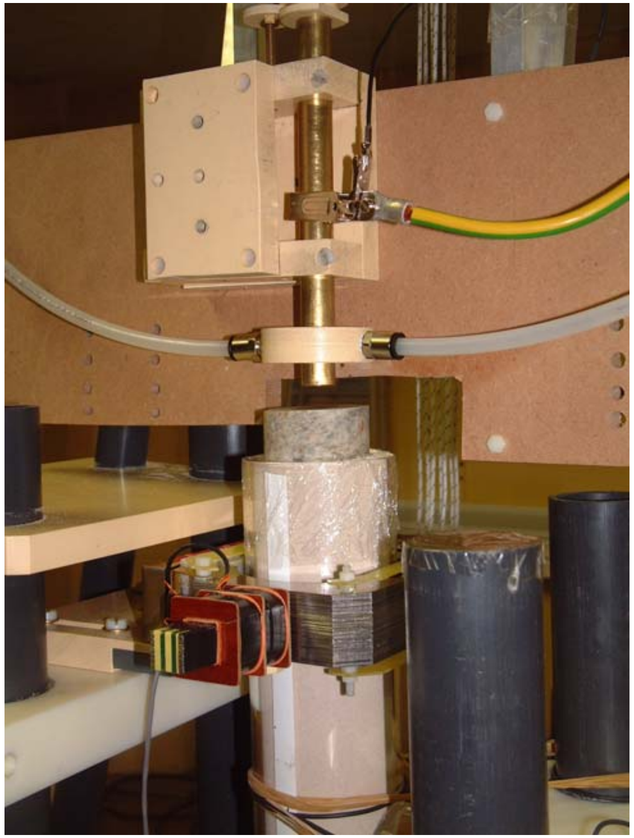

GEOPHYSICAL RESEARCH LETTERS, VOL. 33, L01302, doi:10.1029/2005GL024582, 2006

First laboratory measurements of seismo-magnetic conversions in fluid-filled Fontainebleau sand

C. Bordes,[1] L. Jouniaux,[2] M. Dietrich,[1] J.-P. Pozzi,[3] and S. Garambois[1]

Received 7 September 2005; revised 29 October 2005; accepted 16 November 2005; published 6 January 2006.

[1] Seismic wave propagation in fluid-filled porous materials induces electromagnetic effects due to small relative pore-fluid motions. In order to detect the seismo-magnetic couplings theoretically predicted by Pride (1994), we have designed a small-scale experiment in a low-noise underground laboratory which presents exceptional electromagnetic shielding conditions. Our experiment included accelerometers, electric dipoles and induction magnetometers to characterize the seismo-electromagnetic propagation phenomena. To assess the electrokinetic origin of the measured electric and magnetic fields, we compared records obtained in dry and fluid-filled sand. Extra care has been taken to ensure the mechanical decoupling between the sand column and the magnetometers to avoid spurious vibrations of the magnetometers and misinterpretations of the recorded signals. Our results show that seismo-electric and seismo-magnetic signals are associated with different wave propagation modes, thus emphasizing the electrokinetic origin of these effects. **Citation:** Bordes, C., L. Jouniaux, M. Dietrich, J.-P. Pozzi, and S. Garambois (2006), First laboratory measurements of seismo-magnetic conversions in fluid-filled Fontainebleau sand, *Geophys. Res. Lett.*, *33*, L01302, doi:10.1029/2005GL024582.

1. Introduction

[2] Observations of transient electromagnetic phenomena accompanying the seismic wave propagation in fluid filled porous media date back at least to the work of *Ivanov* [1940]. *Frenkel* [1944] gave the first quantitative explanations of these phenomena in term of electrokinetic effects at the pore scale until *Pride* [1994] developed a complete theory which prompted further studies.

[3] Early and pioneering work by *Martner and Sparks* [1959] and *Thompson and Gist* [1993] and more recent studies by *Takeuchi et al.* [1997], *Mikhailov et al.* [2000], and *Garambois and Dietrich* [2001] have concentrated on field measurements. Laboratory measurements were notably performed by *Zhu et al.* [2000], and *Zhu and Toksöz* [2005] whereas numerical simulations were performed by *Haartsen and Pride* [1997], *Garambois and Dietrich* [2002] and *White* [2005].

[4] Two kinds of seismo-electromagnetic effects are to be distinguished. The dominant contribution we are addressing in this paper corresponds to electrical and magnetic coseismic fields accompanying the body and surface waves. The second kind is generated at physico-chemical properties contrasts and consists of independently propagating electromagnetic waves.

[5] Seismo-electromagnetic studies have generally concentrated on the measurements of electrical fields as they require only a simple instrumentation. The investigation of seismo-magnetic fields has received much less attention mainly because of the high level of electromagnetic noise affecting the magnetic measurements. In order to minimize these disturbances, we have designed a laboratory experiment within the ultra-shielded chamber of the LSBB low-noise laboratory located in Rustrel, southern France.

[6] This paper describes the experimental apparatus as well as the first results (seismic, electric and magnetic responses) measured in homogeneous Fontainebleau sand. We show that seismo-magnetic conversions are weak but nevertheless measurable. Moreover, the different apparent velocities characterizing the seismo-electric and seismo-magnetic events emphasize that they are associated to different propagation modes.

2. Experimental Apparatus

[7] The LSBB facilities were originally an underground launching center for the ground-based component of the French strategic nuclear defense. A characterization of the electromagnetic shielding, performed by *Gaffet et al.* [2003], using a SQUID magnetometer showed that the noise level is below 2 $\mathrm{fT}/\sqrt{Hz}$ above 10 Hz.

[8] Our experimental apparatus was located within the shielded chamber and consisted of a porous sample, a seismic source and sensors. The whole experiment including the triggering of the mechanical source and the data acquisition was remotely controlled from outside the chamber to suppress electromagnetic perturbations from the instruments. All measurements were performed with a 24 bit seismic recorder (Geometrics StrataVisor NZ) using a 21 μs time sampling rate.

2.1. Seismo-Electromagnetic Measurements

[9] Our experiments were performed with two 1 m high and 8 cm diameter vertical Plexiglas columns filled with Fontainebleau sand (Figure 1). This sand contains 99% of silica with grain size smaller than 300 μm. The measured permeability of the sand is 5.8 10^{-12} m^2 and its bulk density 1.7727 10^3 kg/m^3, its electrical resistivity is 22 kΩ.m, and the water conductivity is 3.1 mS/m with a pH of 6.55 at

---

[1] Laboratoire de Géophysique Interne et Tectonophysique, Université Joseph Fourier, UMR 5559 Grenoble, France.

[2] Ecole et Observatoire des Sciences de la Terre, Université Louis Pasteur, UMR 7516 Strasbourg, France.

[3] Laboratoire de Géologie, Ecole Normale Superieure, Paris, France.

0094-8276/06/2005GL024582$05.00

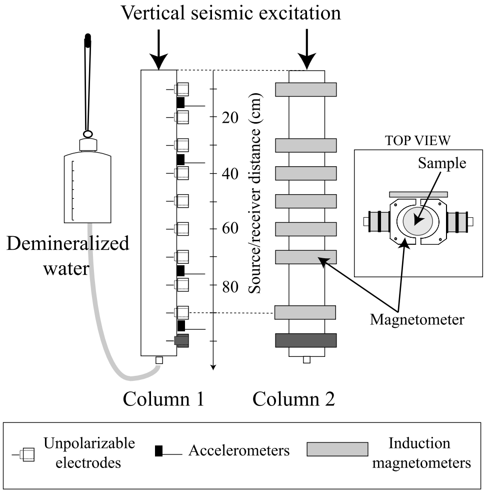

Figure 1. Experimental apparatus for seismo-electric and seismo-magnetic measurements: the column on the left is equipped with 10 unpolarizable electrodes and 4 accelerometers; the column on the right is used for seismo-magnetic measurements only. Magnetometers are fixed on an independent stand to avoid the transmission of disturbing vibrations.

20.5°C. The sand was compacted by vibrating the column during filling in order to minimize the pore space and high frequency seismic wave attenuation. The seismic velocities in the partially saturated sand can be estimated by considering reasonable values of the bulk frame modulus (1.3 10^9 Pa) and shear frame modulus (1.4 10^9 Pa). By using these values in relations given by *Pride and Haartsen* [1996] the computed *P* and *S* wave velocities are respectively equal to 1300 and 870 m/s.

[10] The first column was equipped with ten unpolarizable electrodes (silver rods and porous ceramics) spaced 10 cm apart along the column generatrix. These electrodes were previously used for streaming potential measurements and are described by *Guichet et al.* [2003]. We chose to use a common reference electrode at the bottom end of the column. Electrical measurements (mV) are normalized by the dipole spacing to provide equivalent electrical field (mV/m). However, since the input impedance of the recorder is not very high compared to the electrical resistance of the sand, the given electrical amplitudes are relative values. This column was also equipped with four accelerometers fixed on the outer Plexiglas surface.

[11] The second column was especially used for the seismo-magnetic measurements which are much more sensitive to external perturbations. Even if it is reduced within the capsule, we have to take into account the constant magnetic field. Indeed, the motions of the magnetometers may generate induction effects resembling coseismic effects and masking the seismo-magnetic signals of interest. We designed a suspension system for the seismic source on the capsule ceiling to avoid the transmission of mechanical vibrations to the magnetometers. Moreover, the magnetometers were fixed on a separate stand, and were isolated from ground vibrations by a soundproofing material. However, test accelerometers fixed on the magnetometers showed that residual vibrations arrive 5 ms after the seismic impacts. These disturbances appear later than the seismic and seismo-electromagnetic signals but are nevertheless in the time window considered (−1 ms to 10 ms).

[12] The upper magnetometer can be moved into seven locations which exactly correspond to the electrode positions in term of source-receiver spacing (Figure 1). The two missing locations correspond to the column fastening. The lower magnetometer is used as a common reference similarly to the electrical measurements, in order to cancel synchronous disturbances such as accelerometer radiation.

[13] The theory of *Pride* [1994] stipulates that in a homogeneous infinite fluid-saturated porous medium, the coseismic seismo-electric fields are traveling with longitudinal *P*-waves whereas seismo-magnetic signals are associated with transverse *S*-waves. For porous cylinders, we have to consider global and local deformations and their propagation in the structure. The maximum displacements due to a vertical seismic excitation are associated with extensional modes. In the elastic case, the extensional wave velocity is derived from Young's modulus E and total density ρ ($V_{ext}=\sqrt{E/\rho}$ = 1300 m/s) and is close to the *P*-wave velocity. Thus, waves propagating at a velocity of 1300 m/s will be associated with *P* and extensional modes whereas waves traveling at approximately 870 m/s will be associated with *S* waves. We used an induction magnetometer whose sensitivity on the radial and tangent components is quite constant in the 100 Hz to 2 kHz range.

2.2. EM Noise Free Pneumatic Seismic Source

[14] Piezoelectric seismic sources are often used for seismo-electric laboratory measurements [*Ageeva et al.*,

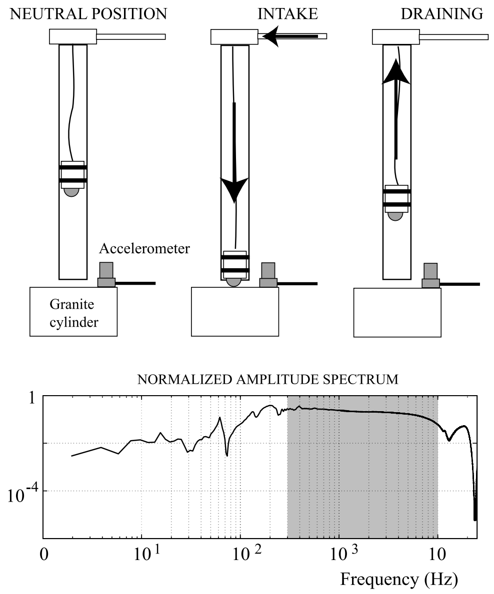

Figure 2. Pneumatic seismic source designed for the seismo-electromagnetic laboratory experiments: a rubis ball (6 mm) is projected with compressed air until it hits a granite cylinder resting on the top part of the sand column. The source time function of the mechanical excitation is measured with a piezo accelerometer on the granite plate.

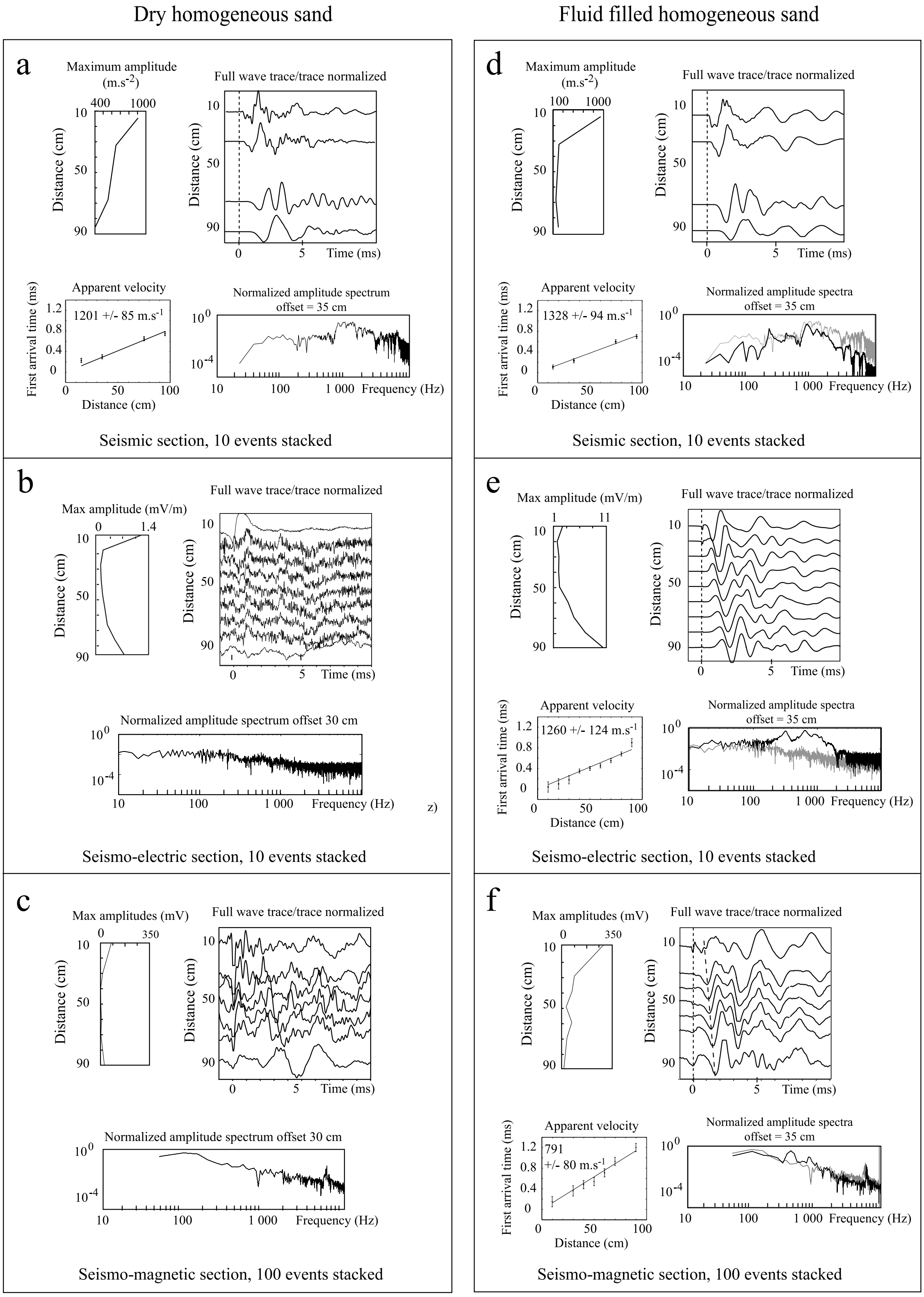

Figure 3. Seismic, seismo-electric and seismo-magnetic signals measured in homogeneous Fontainebleau sand normalized with respect to a 1000 m.s^{-2} vertical excitation. Amplitude spectra corresponding to dry conditions are shown in grey in the right-hand side panels for comparison. Apparent velocities have been estimated from the linear regression of first arrivals time.

1999; *Zhu et al.*, 2000]. These sources, however, are not well suited for seismo-magnetic measurements because of their intrinsic electromagnetic radiation. In order to minimize the magnetic perturbations generated by the seismic excitation, we built a pneumatic system (Figure 2) capable of generating a large number of impacts within a few minutes. This feature allows us to improve our data by stacking successive recordings.

[15] An accelerometer placed on the granite cylinder records the source time function. The latter is rather impulsive and has a broad-band spectrum ranging from 100 Hz to 10 kHz. To compare the records obtained from different shots, the signals are all normalized with respect to a reference excitation of 1000 m/s^2 ($\simeq$100 g).

3. Results

[16] Since our objective is to demonstrate the existence of seismo-electromagnetic fields due to fluid-grain interactions, we compared the electric, magnetic and seismic responses measured in dry and fluid-filled homogeneous sand. The signals presented in Figure 3 were obtained by stacking 10 accelerometric, 10 seismo-electric, and 100 seismo-magnetic records. The panels displayed in Figure 3 respectively present the seismic (top), seismo-electric (middle) and seismo-magnetic (bottom) responses obtained in dry sand (left) and fluid-filled sand (right). The spectra of seismic and electric signals were computed from the complete time sequences whereas the spectra of the magnetic signals were limited to the (-1 ms to 4 ms) time window.

3.1. Homogeneous Dry Sand

[17] The first arrivals of the accelerometric signals recorded in dry sand show an apparent velocity of 1201 ± 85 m/s in the 700 Hz to 3 kHz frequency range (Figure 3a). However, panels 3b and 3c show that the seismic wave propagation in homogeneous dry sand does not produce any coherent electromagnetic fields. The electrodes only pick up instrumental noise with amplitudes lower than 0.4 mV/m for an impact of 1000 m/s^2 (Figure 3b). Nevertheless, the trace located nearest to the source shows a weak signal (1.4 mV/m/1000 m/s^2) probably associated with a piezoelectric effect due to the excitation of quartz grains in perfectly resistive conditions. Similarly, the magnetic signals (Figure 3c) display low frequency noise caused by internal electronic disturbances of the magnetometers.

3.2. Fluid-Filled Homogeneous Sand

[18] The seismic records presented in Figure 3d are slightly modified by the presence of water. The lower frequency content of the signals seen in Figure 3d, as compared to Figure 3a, can be explained by the fact that in *Biot*'s [1956] theory, high frequencies are strongly attenuated due to fluid flow at the pore scale. The similarity of the apparent velocities of the first seismic arrivals in dry and saturated conditions is consistent with a fluid saturation lower than 80% according to the *Knight and Nolen-Hoeksema* [1990] measurements in rocks.

[19] When the sand is filled with water, electric and magnetic fields records are strongly modified. In particular, we observe that the amplitudes of the seismo-electric signals generated in the fluid-filled sand (10 mV/m/1000 m/s^2, Figure 3e) are 30 times larger than the electrical noise level in dry sand. The contributions of seismo-electric conversions are visible in both the time section and corresponding amplitude spectrum in the 200 Hz to 2 kHz range.

[20] By contrast, the maximum amplitudes of the seismo-magnetic signals are only 3 times as high as in dry sand. Consequently, seismo-magnetic signals are barely visible in the associated amplitude spectrum (Figure 3f). However, there is clear evidence of coherent arrivals in the time section. The presence of these events indicates some weak but non-zero seismo-magnetic coupling.

[21] The differences between the apparent velocities of the first arrivals of the seismo-electric (1260 ± 124 m.s^{-1}) and seismo-magnetic signals (791 ± 80 m.s^{-1}) indicate that these effects are associated with different propagation modes. This natural decomposition of the wave fields is consistent with *Pride*'s [1994] theory: the two wave propagation modes most likely correspond to longitudinal (or extensional modes) and to transverse modes.

[22] The detailed interpretation of the full waveforms is difficult because of the cylindrical geometry and finite length of the column which generate complex propagation modes in the sample. Further investigations relying on numerical simulations are needed to analyze the observed seismo-electric and seismo-magnetic conversions.

4. Conclusion

[23] The design of an experimental apparatus within the Low Noise Underground Laboratory allowed us to detect transient seismo-electric and seismo-magnetic signals in a fluid-filled sand column. Their electrokinetic origin has been verified by comparing records in dry and fluid-filled sand. In particular, our measurement protocol ensures that the transient magnetic fields are not due to spurious mechanical vibration of the magnetometers.

[24] The first arrival times of seismo-electric and seismo-magnetic fields clearly indicate that these two fields are coupled to different propagation modes, an observation that is consistent with *Pride*'s [1994] theory. Fast longitudinal modes generate only seismo-electric field whereas transverse modes are coupled to magnetic fields.

[25] Although rather weak, seismo-magnetic signals can be detected with sensitive induction magnetometers but would be difficult to measure outside of the ultra shielded chamber. Nevertheless, transverse modes could be enhanced by considering a horizontal seismic excitation that would generate stronger seismo-magnetic amplitudes. Our results emphasize the complementary nature of seismo-electric and seismo-magnetic measurements to estimate the properties of porous media especially in boreholes.

[26] **Acknowledgments.** This research was supported by CNRS and "ACI Eau et Environnement" of the French Ministry of Research. We are grateful to G. Waysand and S. Gaffet for helpful discussions and authorization to perform this experiment in the LSBB laboratory. We thank M. Auguste, D. Boyer, A. Cavaillou, G. Clerc, R. Guiguet and Y. Orengo for their technical help.

References

Ageeva, O. A., B. S. Svetov, G. K. Sherman, and V. Shipulin (1999), E-effect in rocks, *Russ. Geol. Geophys.*, *64*, 1349–1356.

Biot, M. A. (1956), Theory of propagation of elastic waves in a fluid-saturated porous solid: I. Low frequency range, *J. Acoust. Soc. Am.*, *28*(2), 168–178.

Frenkel, J. (1944), On the theory of seismic and electroseismic phenomena in a moist soil, *J. Phys.*, *8*(4), 230–241.

Gaffet, S., et al. (2003), Simultaneous seismic and magnetic measurements in the low-noise underground laboratory (lsbb) of Rustrel, France, during the 2001 January 26 Indian earthquake, *Geophys. J. Int.*, *155*, 981–990.

Garambois, S., and M. Dietrich (2001), Seismoelectric wave conversions in porous media: Field measurements and transfer function analysis, *Geophysics*, *66*, 1417–1430.

Garambois, S., and M. Dietrich (2002), Full waveform numerical simulations of seismoelectromagnetic wave conversions in fluid-saturated stratified porous media, *J. Geophys. Res.*, *107*(B7), 2148, doi:10.1029/2001JB000316.

Guichet, X., L. Jouniaux, and J.-P. Pozzi (2003), Streaming potential of a sand column in partial saturation conditions, *J. Geophys. Res.*, *108*(B3), 2141, doi:10.1029/2001JB001517.

Haartsen, M. W., and S. Pride (1997), Electroseismic waves from point sources in layered media., *J. Geophys. Res.*, *102*, 24,745–24,769.

Ivanov, A. G. (1940), Seismic-electric effect of second kind, *Izv. Akad. Nauk. USSR Geogr. Geophys.*, *5*, 699–726.

Knight, R., and R. Nolen-Hoeksema (1990), A laboratory study of the dependence of elastic wave velocities on pore scale fluid distribution, *Geophys. Res. Lett.*, (17), 1529–1532.

Martner, S. T., and N. R. Sparks (1959), The electroseismic effect, *Geophysics*, *24*(2), 297–308.

Mikhailov, O. V., J. Queen, and M. N. Toksöz (2000), Using borehole electroseismic measurements to detect and characterize fractured (permeable) zones, *Geophysics*, *65*, 1098–1112.

Pride, S. (1994), Governing equations for the coupled electromagnetics and acoustics of porous media, *Phys. Rev. B*, *50*, 15,678–15,695.

Pride, S., and M. W. Haartsen (1996), Electroseismic wave properties, *J. Acoust. Soc. Am.*, *100*, 1301–1315.

Takeuchi, N., N. Chubachi, and K. I. Narita (1997), Observations of earthquake waves by the vertical earth potential difference method, *Phys. Earth Planet. Inter.*, *101*, 157–161.

Thompson, A. H., and G. A. Gist (1993), Geophysical applications of electrokinetic conversion, *Leading Edge*, *12*, 1169–1173.

White, B. S. (2005), Asymptotic theory of electroseismic prospecting, *SIAM J. Appl. Math.*, *65*, 1443–1462.

Zhu, Z., and M. N. Toksöz (2005), Seismoelectric and seismomagnetic measurements in fractured borehole models, *Geophysics*, *70*(4), F45–F51.

Zhu, Z., M. W. Haartsen, and M. N. Toksöz (2000), Experimental studies of seismoelectric conversions in fluid-saturated porous media., *J. Geophys. Res.*, *105*, 28,055–28,064.

C. Bordes, M. Dietrich, and S. Garambois, Laboratoire de Géophysique Interne et Tectonophysique, Université Joseph Fourier, BP 53, F-38041 Grenoble Cedex 9, France. (cbordes@obs.ujf-grenoble.fr)

L. Jouniaux, Ecole et Observatoire des Sciences de la Terre, Université Louis Pasteur, F-67084 Strasbourg, France.

J.-P. Pozzi, Laboratoire de Géologie, Ecole Normale Superieure, F-75231 Paris, France.

C) PROJETS

Ma récente mobilité (2004) à l'Institut de Physique du Globe de Strasbourg m'a permis d'entamer des collaborations et d'envisager des projets, au sein de l'équipe « Physique des Roches », avec l'équipe « Proche Surface », et avec l'Institut de Mécanique des Fluides et des Solides (IMFS) de Strasbourg. D'autre part, je garde une collaboration étroite avec le LGIT (Grenoble), et maintenant avec l'ISTEEM (Montpellier), le LMIG (Pau) et Géoazur (Nice).

C-1. PHÉNOMÈNES TRANSITOIRES SISMO-ÉLECTROMAGNÉTIQUES

Suite aux résultats encourageants, mais partiels, obtenus lors de la thèse de Clarisse Bordes [2005 ; *Bordes et al.*, 2006], il est envisagé un développement des investigations des signaux transitoires sismo-électromagnétiques, à la fois (i) en laboratoire, au Laboratoire Souterrain à Bas Bruit (LSBB, Rustrel) ; (ii) sur le terrain, sur le site de Lavalette étudié par l'ISTEEM (Montpellier) ; et (iii) à l'aide de modélisations (LGIT, Grenoble). Pour ce faire nous avons donc rédigé une demande d'ANR (Transek), demande faite en 2005 (et non financée), par Michel Dietrich et moi-même, en collaboration avec Philippe Pézard (ISTEEM, Montpellier) et Stéphane Gaffet (Géoazur, Nice). En laboratoire, il s'agira, entre autres, de quantifier précisément les trois composantes du champ magnétique créé lors d'une conversion sismo-électromagnétique. Ce point nécessite le développement d'un capteur magnétique adapté, et des mesures dans un environnement à bas bruit (LSBB), ceci afin de savoir si les amplitudes des signaux engendrés sont suffisantes pour pouvoir espérer utiliser cette méthode sur le terrain.

C-2. EFFET DE LA SATURATION PARTIELLE SUR L'ÉLECTROFILTRATION

À ce jour, les seules mesures publiées dans la littérature concernant la dépendance de l'électrofiltration avec la saturation d'un milieu poreux sont celles de Guichet et al. [2003]. Ces mesures étaient assez grossières, et contraires à ce qu'il était envisagé, selon la théorie, de prendre comme loi d'évolution du couplage électrocinétique avec la saturation. On se pose donc encore la question, lors de l'interprétation d'observations, de savoir quelle loi exacte prendre pour les inversions. Afin de mener à bien une étude plus précise, un projet a été proposé (et financé) dans le cadre du réseau REALISE (coordonné par François Chabaux), en collaboration avec l'IMFS (François Lehmann, Philippe Ackerer). Il est ainsi prévu de quantifier l'électrofiltration lors d'écoulements dans un sable, en condition partiellement saturé, en couplant chaque mesure de potentiel électrique à une mesure de teneur en eau et une mesure de pression. Ceci devrait permettre de déduire une loi plus robuste de l'électrofiltration en fonction de la saturation.

C-3. ÉLECTROFILTRATION DANS UNE FRACTURE

L'influence de la géométrie de l'ouverture d'une fracture sur l'écoulement a été étudiée en laboratoire, dans le cadre du programme ACI - ECCO - PNRH (2003, 2004) « Transport et érosion dans une fracture ouverte : étude des couplages chimio-électro-hydro-mécaniques par une approche expérimentale », coordonné par Jean Schmittbuhl (équipe Physique des Roches). Il s'agissait d'intégrer les propriétés de la géométrie des fractures dans l'analyse de l'hydrodynamique et des couplages électriques, chimiques et mécaniques. Si le lien entre le champ de pression au sein de l'écoulement et le potentiel d'électrofiltration a été formalisé dans des milieux poreux et des conditions hydrodynamiques simples, qu'en est-il lorsque le champ de pression devient hétérogène du fait de la géométrie et/ou du régime d'écoulement ? Pour répondre à cette question, nous avons ajouté des électrodes au dispositif initial, au sein même de la fracture (*Maxime Mouyen*, stage de Master-1, 2006), afin de détecter les variations de potentiel électrique pendant l'écoulement dans la fracture. Ce projet est en cours et des améliorations expérimentales sont à apporter, grâce à l'aide précieuse d'Alain Steyer (équipe Physique des Roches). Dans le futur, nous aborderons l'analyse quantitative de l'érosion au sein de la fracture par une technique de colorimétrie en condition de film mince réactif épanché sur la surface de la fracture. Nous chercherons alors à savoir si le potentiel d'électrofiltration peut cartographier les zones de dissolution et de précipitation.

C-4. CARACTÉRISATION ÉLECTRIQUE D'ÉCHANTILLONS DE LA SOUTTE (VOSGES)

Je participe au programme ACI - FNS - ECCO (2003, 2004, 2005) « Waterscan : prospection et modélisation hydrogéophysique 4D », coordonné par P. Sailhac (équipe Proche Surface). L'équipe « Proche Surface » a instrumenté un terrain dans les Vosges, « La Soutte », pour suivre notamment de manière continue les Potentiels Spontanés. L'interprétation des observations en terme de circulation hydrique implique de connaître de nombreux paramètres tels que les précipitations, les perméabilités, les conductivités électriques, la température, et le coefficient de couplage d'électrofiltration. Nous avons donc commencé à mesurer l'électrofiltration et la conductivité électrique sur des échantillons prélevés sur le terrain de La Soutte (*Julia Holzhauer*, stage de Maîtrise, 2005). En 2006, des forages carottés ont été réalisés : il est donc envisagé de caractériser le couplage électrocinétique sur ces carottes, intactes, broyées, ou fissurées. Ceci permettra de déduire une ou plusieurs valeurs d'électrofiltration qui seront utilisées dans l'inversion des données, afin de mieux évaluer la sensibilité de l'interprétation au paramètre d'électrofiltration.

C-5. APPLICATION DES POTENTIELS SPONTANÉS SUR LES VOLCANS

L'interprétation des anomalies positives de Potentiel Spontané observées sur de nombreux volcans demande un effort de collaboration entre les différentes composantes de la communauté qui font les mesures de terrain (PS, conductivité électrique, CO_2, vapeur d'eau, température), qui développent des modèles directs ou inversent les données, et qui développent des mesures en laboratoire. Un certain nombre de collaborations avait été initié grâce au programme ACI - Catastrophes Naturelles (2001, 2002). Les anomalies positives de Potentiel Spontané sont en général interprétées par l'effet d'électrofiltration induit par les montées hydrothermales. Mais bien souvent cette interprétation ne tient pas compte des variations spatiales de conductivité électrique : une partie de la communauté scientifique se penche donc sur ce problème. De plus, les anomalies positives de potentiel sur les volcans peuvent être assez souvent anticorrélées aux flux de CO_2.

Dans le futur, il est prévu d'entreprendre des mesures sur des cendres volcaniques, en milieu non saturé, sous gradient de température, et avec la possibilité de faire circuler les mêmes gaz que ceux détectés sur les volcans. En particulier il est prévu de développer ces expériences sur des cendres du Misti (Pérou) ou du Lemptégy (Chaîne des Puys).

C-6. CARACTÉRISATION ÉLECTRIQUE DES GRANITES DU RINGELBACH (HAUTES-VOSGES)

Depuis de nombreuses années, le bassin versant du Ringelbach est étudié afin d'estimer ses réserves en eau. Pour ce faire, des études pluridisciplinaires ont permis d'améliorer la connaissance de la structure géologique générale de ce bassin et d'améliorer la modélisation hydrogéologique [*Baltassat et al.*, 2005] (projets ECCO - PNRH ; Région Alsace : Réseau REALISE, coordonnés par Bruno Ambroise, IMFS Strasbourg). Récemment, trois forages ont été réalisés, partiellement carottés. Des mesures géophysiques ont été menées en surface (conductivité électrique, Résonance Magnétique Protonique (RMP)) et des diagraphies réalisées par l'ISTEEM (Philippe Pézard, Montpellier). Nous avons donc proposé une caractérisation géophysique d'une partie des carottes prélevées (l'ISTEEM - Montpellier menant une étude complémentaire), à savoir des mesures de porosité, de perméabilité, de vitesses acoustiques, et de conductivité électrique, travail mené principalement par Bertrand Renaudié, en collaboration avec Thierry Reuschlé (équipe Physique des Roches). Ces mesures devraient permettre par la suite de contraindre l'apport des diagraphies effectuées.

RÉFÉRENCES

Archie, G.E., The electrical resistivity Log as an aid in determining some reservoir characteristics, *Transactions AIME, 146*, 54-62, 1942.

Aubert, M., and G. Kieffer, Evolution d'une intrusion magmatique dans le flanc sud de l'Etna entre juin 1982 et juin 1983, Résultats de potentiel spontané (PS) et essai d'interprétation de l'éruption de 1983,, *C. R. Académie des Sciences., Ser. II, 298,* 379-382, 1984.

Baltassat, JM, Legchenko, A., Ambroise, B., Mathieu, F., Lachassagne, P., Wyns, R., Mercier, JL, and JJ Schott, Magnetic resonance sounding (MRS) and resistivity characterisation of a mountain hard rock aquifer: the Ringelbach Catchment, Vosges Massif, France, *Near Surface Geophysics*, 267-274, 2005.

Beamish, D., Characteristics of near-surface electrokinetic coupling, *Geophys. J. Int.*, 137, 231-242, 1999.

Bernard, P., Plausibility of long distance electrotelluric precursors to earthquakes, *Journal of Geophysical Research, 97* (b12), 17531-17546, 1992.

Bordes, C., Jouniaux, L., Dietrich, M., Pozzi, J.-P., and S. Garambois, Laboratory measurements of seismo-magnetic conversions in fluid-filled Fontainebleau sand, *Geophys. Res. Lett.*, Vol. 33, No. 1, L01302, 10.1029/2005GL024582, 2006.

Bourlange, S., Henry, P., Moore, J.C., Mikada, H., and A. Klaus, Fracture porosity in the décollement zone of Nankai accretionary wedge using logging while drilling resistivity data, *Earth Planet. Sci. Lett.*, 209, 103-112, 2003.

Bourlange, S., Jouniaux, L., and Henry, P., Permeability, compressibility, and friction coefficient measurements under confining pressure and strain, Leg 190, Nankai Trough. *In* Mikada, H., Moore, G.F., Taira, A., Becker, K., Moore, J.C., and Klaus, A. (Eds.), *Proc. ODP, Sci. Results*, 190/196, 1–16, 2004.

open access: Online: http://www-odp.tamu.edu/ publications/190196SR/215/215.htm

Brace, W.F., Dilatancy-Related Electrical Resistivity Changes in Rocks, *Pure Appl. Geophys.*, 113, p. 207-217, 1975.

Butler, K.E., Russell, R.D., Kepic, A.W., and M. Maxwell, measurement of the seismoelectric response from a shallow boundary, *Geophysics*, 61, 1769-1778, 1996.

Darnet, M., and Marquis, G., Modelling streaming potential (SP) signals induced by water movement in the vadose zone, *J. Hydrology*, 285, 114-124, 2004.

Di Liberto, V., P.M. Nuccio, A. Paonita, Genesis of chlorine and sulphur in fumarolic emissions at Vulcano Island (Italy): assessment of pH and redox conditions in the hydrothermal system, J. of Volcanol. Geotherm. Res., 116, 137-150, 2002.

Doussan, C., Jouniaux, L., and J.-L. Thony, Temporal variations of SP and unsaturated water flow in loam and clay soils: a seasonal field study, *J. of Hydrology*, 267, 3/4, 172-184, 2002.

Dupuis, J.C., and K. Butler, Vertical seismoelectric profiling in a borehole penetrating glaciofluvial sediments, Geophys. Res. Lett., 33, L16301, 2006.

Finizola, A., J.-F. Lénat, O. Macedo, D. Ramos, J.-C. Thouret, F. Sortino, Fluid circulation and structural discontinuities inside Misti volcano (Peru) inferred from self-potential measurements, *Journal of Volcanology and Geothermal Research*, *135*,343-360, doi:10.1016/j.jvolgeores.2004.03.009, 2004.

Finizola, A., F. Sortino, J.F. Lénat, and M. Valenza, Fluid circulation at Stromboli volcano from self-potential and CO2 surveys, *Journal of Volcanology and Geothermal Research*, *116*, 1-18, 2002.

Fontaine F., Rabinowicz, M., Boulègue J., and Jouniaux L., Constraints on hydrothermal processes on basaltic edifices: Inferences on the conditions leading to hydrovolcanic eruptions at Piton de la Fournaise, Réunion Island, Indian Ocean, *Earth Planet. Sci. Lett.*, 200, 1-14, 2002.

Fraser-Smith, A.C., A. Bernardi, P.R. McGill, M.E. Ladd, R.A. Helliwelll and O.G. Villard Jr., Low-frequency magnetic field measurements near the epicenter of the Ms 7.1 Loma Prieta earthquake, *Geophys. Res. Lett.*, 17, 1465-1468, 1990.

Garambois, S., and M. Dietrich, Full waveform numerical simulation of seismoelectromagnetic wave conversions in fluid-saturated stratified porous media, *Journal of Geophysical Research*, *107* (B7), 10.1029/2001JB000316, 2002.

Garambois, S., and M. Dietrich, Seismoelectric wave conversions in porous media: Field measurements and transfer function analysis, *Geophysics*, 66, 1417-1430, 2002.

Guichet, X., L. Jouniaux, and N. Catel, Modification of streaming potential by precipitation of calcite in a sand-water system: laboratory measurements in the pH range from 4 to 12, *Geophysical Journal International*, 166, 445-**,** doi:10.1111/j.1365-246X.2006.02922.x, 2006.

Guichet, X., L. Jouniaux, and J.-P. Pozzi, Streaming potential of a sand column in partial saturations conditions, *J. Geophys. Res.*, 108, 2141, doi:10.1029/2001JB001517, 2003.

Haartsen, M., and S. Pride, Electroseismic waves from point sources in layered media, *J. Geophys. Res.*, 102, 24745-24769, 1997.

Hashimoto, T., and Y. Tanaka, A large self-potential anomaly on Unzen volcano, Shimabara peninsula, Kyushu island, Japan, *Geophys. Res. Lett., 22*, 191-194, 1995.

Henry, P., L. Jouniaux, E.J. Screaton, S. Hunze, and D.M. Saffer, Anisotropy of electrical conductivity record of initial strain at the toe of the Nankai accretionary wedge, *J. Geophys. Res.*,108, 2407, doi:10.1029/2002JB002287, 2003.

Hyndman, R.D., and P.M. Shearer, Water in the lower continental crust: modelling magnetotelluric and seismic reflection results, *Geophys. J. Int.*, 98, 343-365, 1989.

Ishido, T., Volcano monitoring using self-potential technique, *E.G.U.*, 2006.

Jouniaux, L., M. Zamora, and T. Reuschlé, Electrical conductivity evolution of non-saturated carbonate rocks during deformation up to failure, *Geophys. J. Inter.*, sous presse, 2006.

Jouniaux, L., Masuda, K., Lei, X., Nishizawa, O., Kusunose, K., Liu,L., and W. Ma, Comparison of the microfracture localization in granite between fracturation and slip of a pre-existing macroscopic healed joint by acoustic emission measurements, *J. Geophys. Res.*, 106, 8687-8698, 2001.

Jouniaux, L., Bernard, M.-L., Pozzi, J.-P., and M. Zamora, Electrokinetic in rocks: Laboratory measurements in sandstone and volcanic samples, *Phys. Chem. Earth*, 25, 329-332, 2000.

Jouniaux, L., M.L. Bernard, M. Zamora, and J.P. Pozzi, Streaming potential in volcanic rocks from Mount Pelée, *Journal of Geophysical Research*, *105*, 8391-8401, 2000.

Jouniaux, L., J.-P. Pozzi, J. Berthier. and P. Massé, Detection of fluid flow variations at the Nankai Trough by electric and magnetic measurements in boreholes or at the seafloor, *J. Geophys. Res.*, 104, 29293-29309, 1999.

Jouniaux, L. and Pozzi J.-P., Anomalous 0.1-0.5 Hz streaming potential measurements under geochemical changes: Consequences for electrotelluric precursors to earthquakes, *J. Geophys. Res.*, 102, 15335-15343, 1997**.**

Jouniaux, L., and J.-P. Pozzi, Streaming potential and permeability on saturated sandstones under triaxial stress: consequences for electrotelluric anomalies prior to earthquakes, *Journal of Geophysical Research*, *100*, 10197-10209, 1995 a.

Jouniaux L. and Pozzi J.-P., Permeability dependence of streaming potential in rocks for various fluid conductivities, *Geophys. Res. Letters*., 22, 485-488, 1995b.

Jouniaux L., Lallemant S., and Pozzi J.-P., Changes in the permeability, streaming potential and resistivity of a claystone from the Nankai prism under stress, *Geophys. Res. Letters***,** 21, 149-152, 1994.

Jouniaux L., Pozzi, J.-P., Brochot, M., et C. Philippe, Variation de résistivité sous contrainte triaxiale dans des grès de Fontainebleau saturés, *C. R. Acad. Sci. Paris,* t. 315, Série II, 1493-1499, 1992.

Lei, X.-L., K. Masuda, O. Nishizawa, L. Jouniaux, L. Liu, W. Ma, T. Satoh, K. Kusunose, Detailed analysis of acoustic emission activity during catastrophic fracture of faults in rock, *Jou. Struct. Geol.*, 26, 247-258, doi:10.1016/S0191-8141(03)00095-6, 2004.

Lénat, J.F., D. Fitterman, and D.B. Jackson, Geoelectrical structure of the central zone of the Piton de la Forunaise volcano (Réunion), *Bulletin of volcanology, 62* (2), 75-89, 2000.

Li, S.X., Pengra, DB, and PZ Wong, Onsager’s reciprocal relation and the hydraulic permeability of porous media, *Physical review E,* 51, 5748-5751, 1995.

Lockner, D.A., and J.D. Byerlee, Changes in complex resistivity during creep in granite, *Pure Appl. Geophys.*, 124, 659-676, 1986.

Lorne, B., Perrier, F., and J.-P. Avouac, Streaming potential measurements 2. relationship between electrical and hydraulic flow patterns from rock samples during deformation, *J. Geophys. Res.*, 104, 17879-17896, 1999.

Marquis, G. and Hyndman, R.D., Geophysical support for aqueous fluids in the deep crust: seismic and electrical relationships, *Geophys. J. Int.*, 110, 91-105, 1992.

Masuda, K., Jouniaux, L., Nishizawa, O., Lei, X., Liu, L., Ma, W., Satoh, T. And K. Kusunose, Fracture planes observed with X-ray CT images and AE hypocenter distribution, *Bull. Geol. Surv. Japan*, 48, 469-473, 1997.

Mizutani, H., T. Ishido, T. Yokokura, and S. Ohnishi, Electrokinetic phenomena associated with earthquakes, *Geophys. Res. Lett., 3*, 365-368, 1976.

Muir-Wood, R., and G. C. P. King, Hydrological signatures of earthquake strain, *J. Geophys. Res.*, 98, 22,035-22,068, 1993.

Nesbitt, B.E., Electrical resistivities of crustal fluids, *J. Geophys. Res.*, 98, 4301-4310, 1993

Olhoeft, G.R., Electrical properties of granite with implications for the lower crust, *J. Geophys. Res.*, 86, 931-936, 1981.

Onsager, L., Reciprocal relations in irreversible processes I: *Phys. Rev.*, 37, 405-426, 1931.

Perrier, F., Petiau, G., Clerc, G., Bogorodsky, V., Choquier, A., Erkul, E., Jouniaux, L., Lesmes, D., Macnae, J., Marquis, P., Meunier, J.M., Nascimento, D., Oettinger, G., Schwarz, G., Toh, H., Valiant, M.J., Vozoff, K. and Yazici-Cakin, O., A one year systematic study of electrodes for long period measurements of the electric field in geophysical environments, *Journal of Geomagnetism and Geoelectricity*, 49, 1677-1697, 1997.

Pinettes, P., Bernard, P., Cornet, F., Hovhannissian, G., Jouniaux, L., Pozzi, J.-P., and V. Barthès, On the difficulty of detecting streaming potentials generated at depth, *Pure and Applied Geophysics*, 159, 2629-2657, 2002.

Pride, S., Governing equations for the coupled electrmagnetics and acoustics of porous media, *Physical Review, 50* (B), 15678-15696, 1994.

Reppert, P.M., F.D. Morgan, D. Lesmes, and L. Jouniaux, Frequency dependent streaming potentials, *Journal of Colloid and Interface Science*, 234, 194-203, 2001.

Sill, W.R., Self-potential modelling from primary flows, *Geophysics*, 48, 76-86, 1983.

Thony, J.L, Morat, P., Vachaud, G., and Le Mouël, JL, Field characterization of the relationship between electrical potential gradients and soil water flux, *CR Acad. Sci. Paris*, 325, 317-321, 1997.

Thompson, A.H., et al., Field tests of electroseismic hydrocarbon detection, *SEG abstracts*, 2005.

Thompson, A.H, and G.A. Gist, geophysical applications of electro-kinetic conversion, *The Leading Edge*, 1169-1173, 1993.

Toutain, J.-P., M. Munoz, F. Poitrasson, and A.C. Lienard, Springwater chloride ion anomaly prior to a Ml=5.2 pyrenean earthquake, *Earth Planet. Sci. Lett.*, 1997.

Tsunogai, U. and Wakita Hiroshi, Precursory chemical changes in ground water: Kobe earthquake, Japan, *Science*, 269, 61-63, 1995.

Scholz, C.H., Sykes, L.R., and Y.P. Aggarwal, Earthquake prediction: a physical basis, *Science*, 181, 803-810, 1973.

Waxman, M.H., and L.J.M. Smits, Electrical conductivities in oil-bearing shaly sands, *Transactions AIME, 243*, 107-122, 1968.

Yoshida, S., Convection current generated prior to rupture in saturated rocks, *J. Geophys. Res.*, 106, 2103-2120, 2001.